Exclusive: Enforcement falls at Trump's FDA *p. 12*

Secrets to preventing burnout *p. 22*

Honesty goes up as temptations to steal increase *pp. 29 & 70*

Science

$15
5 JULY 2019
sciencemag.org

AAAS

TARGETED GENE INSERTION

New CRISPR function beyond microbial immunity

pp. 25 & 48

CONTENTS

5 JULY 2019 • VOLUME 365 • ISSUE 6448

94
Committees expecting coffee

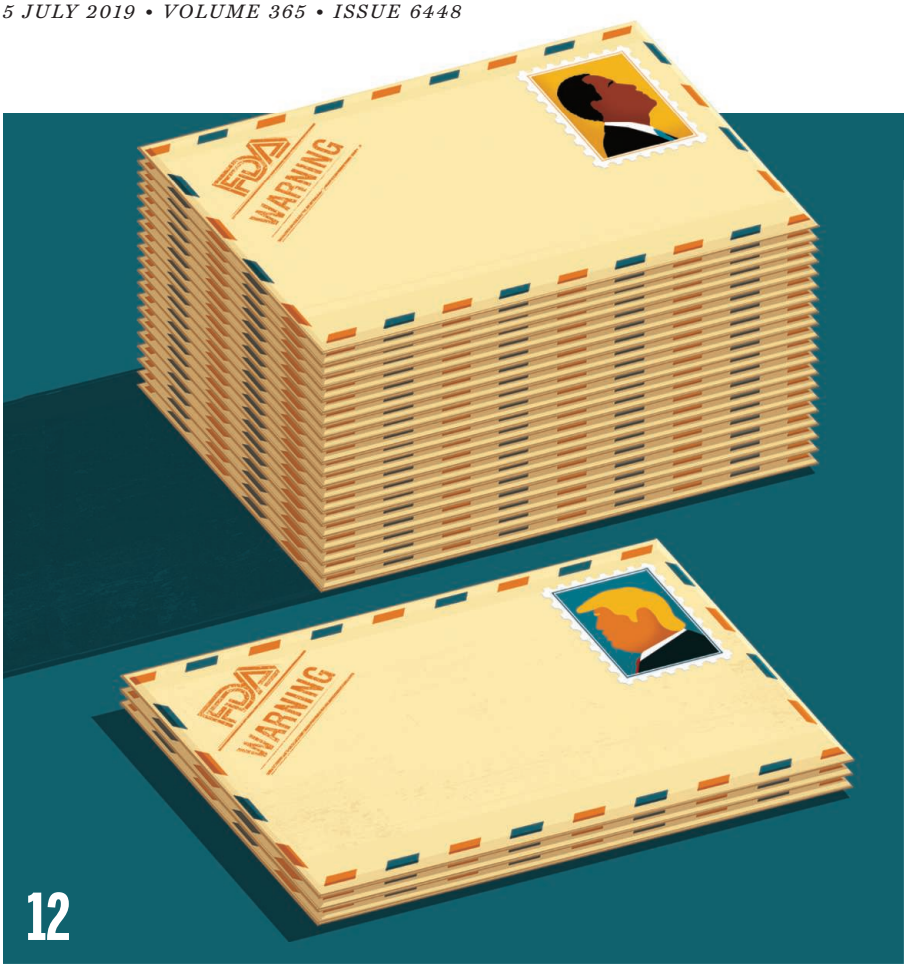

12

NEWS

IN BRIEF

IN DEPTH

FEATURES

INSIGHTS

LETTERS

PERSPECTIVES

Published by AAAS

PHOTO: VICTOR FRANKOWSKI

ON THE COVER

The bacterial CRISPR system is an adaptive immune defense mechanism. A new subtype of CRISPR is now shown to be co-opted by transposons to achieve their insertion into the targeted regions of the genome. This powerful CRISPR-Cas12k system can be programmed to achieve precise and efficient targeted gene insertion, which holds great potential in genome editing applications. See pages 25 and 48.
Image: Stephan Schmitz/Folio Art

SCIENCE (ISSN 0036-8075) is published weekly on Friday, except last week in December, by the American Association for the Advancement of Science, 1200 New York Avenue, NW, Washington, DC 20005. Periodicals mail postage (publication No. 484460) paid at Washington, DC, and additional mailing offices. The title SCIENCE is a registered trademark of the AAAS. Domestic individual membership, including subscription (12 months): $165 ($74 allocated to subscription). Domestic institutional subscription (51 issues): $1971; Foreign postage extra: Mexico, Caribbean (surface mail) $55; other countries (air assist delivery): $98. First class, airmail, student, and emeritus rates on request. Canadian rates with GST available upon request, GST #125488122. Publications Mail Agreement Number 1069624. **Printed in the U.S.A.**
Change of address: Allow 4 weeks, giving old and new addresses and 8-digit account number. **Postmaster:** Send change of address to AAAS, P.O. Box 96178, Washington, DC 20090–6178. **Single-copy sales:** $15 each plus shipping and handling; bulk rate on request. **Authorization to reproduce** material for internal or personal use under circumstances not falling within the fair use provisions of the Copyright Act can be obtained through the Copyright Clearance Center (CCC), www.copyright.com. The identification code for *Science* is 0036-8075. *Science* is indexed in the *Reader's Guide to Periodical Literature* and in several specialized indexes.

Published by AAAS

Science AAAS

Editor-in-Chief Jeremy Berg, jberg@aaas.org

Executive Editor Monica M. Bradford

EDITOR, INSIGHTS Lisa D. Chong **EDITORS, RESEARCH** Valda Vinson, Jake S. Yeston **DEPUTY EDITORS** Julia Fahrenkamp-Uppenbrink (UK), Stella M. Hurtley (UK), Phillip D. Szuromi, Sacha Vignieri **SR. EDITORIAL FELLOW** Andrew M. Sugden (UK) **SR. EDITORS** Gemma Alderton (UK), Caroline Ash (UK), Brent Grocholski, Pamela J. Hines, Paula A. Kiberstis, Marc S. Lavine (Canada), Steve Mao, Ian S. Osborne (UK), Beverly A. Purnell, L. Bryan Ray, H. Jesse Smith, Jelena Stajic, Peter Stern (UK), Valerie B. Thompson, Brad Wible, Laura M. Zahn **ASSOCIATE EDITORS** Michael A. Funk, Priscilla N. Kelly, Tage S. Rai, Seth Thomas Scanlon (UK), Keith T. Smith (UK), Yury V. Suleymanov **LETTERS EDITOR** Jennifer Sills **LEAD CONTENT PRODUCTION EDITORS** Harry Jach, Lauren Kmec **CONTENT PRODUCTION EDITORS** Amelia Beyna, Jeffrey E. Cook, Chris Filiatreau, Nida Masiulis, Suzanne M. White **SR. EDITORIAL COORDINATORS** Carolyn Kyle, Beverly Shields **EDITORIAL COORDINATORS** Aneera Dobbins, Joi S. Granger, Jeffrey Hearn, Lisa Johnson, Maryrose Madrid, Ope Martins, Shannon McMahon, Jerry Richardson, Alana Warnke, Alice Whaley (UK), Anita Wynn **PUBLICATIONS ASSISTANTS** Jeremy Dow, Alexander Kief, Ronmel Navas, Hilary Stewart (UK), Brian White **EXECUTIVE ASSISTANT** Jessica Slater **ASI DIRECTOR, OPERATIONS** Janet Clements (UK) **ASI SR. OFFICE ADMINISTRATOR** Jessica Waldock (UK)

News Editor Tim Appenzeller

NEWS MANAGING EDITOR John Travis **INTERNATIONAL EDITOR** Martin Enserink **DEPUTY NEWS EDITORS** Elizabeth Culotta, Lila Guterman, David Grimm, Eric Hand (Europe), David Malakoff **SR. CORRESPONDENTS** Daniel Clery (UK), Jon Cohen, Jeffrey Mervis, Elizabeth Pennisi **ASSOCIATE EDITORS** Jeffrey Brainard, Catherine Matacic **NEWS REPORTERS** Adrian Cho, Jennifer Couzin-Frankel, Jocelyn Kaiser, Kelly Servick, Robert F. Service, Erik Stokstad (Cambridge, UK), Paul Voosen, Meredith Wadman **INTERN** Alex Fox **CONTRIBUTING CORRESPONDENTS** Warren Cornwall, Ann Gibbons, Mara Hvistendahl, Sam Kean, Eli Kintisch, Kai Kupferschmidt (Berlin), Andrew Lawler, Mitch Leslie, Eliot Marshall, Virginia Morell, Dennis Normile (Shanghai), Elisabeth Pain (Careers), Charles Piller, Michael Price, Tania Rabesandratana (Barcelona), Emily Underwood, Gretchen Vogel (Berlin), Lizzie Wade (Mexico City) **CAREERS** Donisha Adams, Rachel Bernstein (Editor), Katie Langin **COPY EDITORS** Julia Cole (Senior Copy Editor), Cyra Master (Copy Chief) **ADMINISTRATIVE SUPPORT** Meagan Weiland

Creative Director Beth Rakouskas

DESIGN MANAGING EDITOR Marcy Atarod **GRAPHICS MANAGING EDITOR** Alberto Cuadra **PHOTOGRAPHY MANAGING EDITOR** William Douthitt **WEB CONTENT STRATEGY MANAGER** Kara Estelle-Powers **SENIOR DESIGNER** Chrystal Smith **DESIGNER** Christina Aycock **PHOTO EDITOR** Emily Petersen **GRAPHICS EDITOR** Nirja Desai **SENIOR SCIENTIFIC ILLUSTRATORS** Valerie Altounian, Chris Bickel **SCIENTIFIC ILLUSTRATOR** Alice Kitterman **SENIOR GRAPHICS SPECIALISTS** Holly Bishop, Nathalie Cary

CEO and Executive Publisher Rush D. Holt

Publisher, Science Family of Journals Bill Moran

DIRECTOR, BUSINESS SYSTEMS AND FINANCIAL ANALYSIS Randy Yi **DIRECTOR, BUSINESS OPERATIONS & ANALYSIS** Eric Knott **DIRECTOR OF ANALYTICS** Enrique Gonzales **MANAGER, BUSINESS OPERATIONS** Jessica Tierney **SENIOR BUSINESS ANALYST** Cory Lipman, Meron Kebede **FINANCIAL ANALYST** Alexander Lee **ADVERTISING SYSTEM ADMINISTRATOR** Tina Burks **SENIOR SALES COORDINATOR** Shirley Young **DIGITAL/PRINT STRATEGY MANAGER** Jason Hillman **QUALITY TECHNICAL MANAGER** Marcus Spiegler **ASSISTANT MANAGER DIGITAL/PRINT** Rebecca Doshi **SENIOR CONTENT SPECIALISTS** Steve Forrester, Antoinette Hodal, Lori Murphy **CONTENT SPECIALIST** Jacob Hedrick **DIGITAL PRODUCTION MANAGER** Lisa Stanford **CONTENT SPECIALIST** Kimberley Oster **DIGITAL AD-OPS SPECIALIST** Patrick Gerrits **ADVERTISING PRODUCTION OPERATIONS MANAGER** Deborah Tompkins **DESIGNER, CUSTOM PUBLISHING** Jeremy Huntsinger **SR. TRAFFIC ASSOCIATE** Christine Hall **SPECIAL PROJECTS ASSOCIATE** Sarah Dhere

ASSOCIATE DIRECTOR, BUSINESS DEVELOPMENT Justin Sawyers **GLOBAL MARKETING MANAGER** Allison Pritchard **DIGITAL MARKETING MANAGER** Aimee Aponte **MARKETING MANAGER** Shawana Arnold **MARKETING ASSOCIATES** Tori Velasquez, Mike Romano, Ashley Hylton **SENIOR DESIGNER** Kim Huynh **TRADE SHOW AND MEETINGS ASSOCIATE** Andrew Clamp

DIRECTOR AND SENIOR EDITOR, CUSTOM PUBLISHING Sean Sanders **ASSISTANT EDITOR, CUSTOM PUBLISHING** Jackie Oberst

DIRECTOR, BUSINESS STRATEGY AND PORTFOLIO MANAGEMENT Sarah Whalen **ASSOCIATE DIRECTOR, PRODUCT MANAGMENT** Kris Bishop **ASSOCIATE DIRECTOR, PRODUCT DEVELOPMENT AND SPJ** Hannah Heckner **SR. PRODUCT ASSOCIATE** Robert Koepke **DIGITAL PRODUCT STRATEGIST** Michael Hardesty **SPJ ASSOCIATE** Samantha Bruno Fuller

DIRECTOR, INSTITUTIONAL LICENSING Iquo Edim **ASSOCIATE DIRECTOR, RESEARCH & DEVELOPMENT** Elisabeth Leonard **SENIOR INSTITUTIONAL LICENSING MANAGER** Ryan Rexroth **INSTITUTIONAL LICENSING MANAGERS** Marco Castellan, Christos Skoutas **MANAGER, SYSTEMS AND OPERATIONS** Brian Holiahn **MANAGER, AGENT RELATIONS & CUSTOMER SUCCESS** Judy Lillibridge **SENIOR OPERATIONS ANALYST** Lana Guz **FULFILLMENT COORDINATOR** Melody Stringer

DIRECTOR, GLOBAL SALES Tracy Holmes **ASSOCIATE DIRECTOR, ADVERTISING SALES, US** Laurie Faraday **US EAST COAST AND MID WEST SALES** Glen Cox **US WEST COAST SALES** Lynne Stickrod **US SALES MANAGER, SCIENCE CAREERS** Claudia Paulsen-Young **US SALES REP, SCIENCE CAREERS** Tracy Anderson **ASSOCIATE DIRECTOR, ROW** Roger Goncalves **SALES REP, ROW** Sarah Lelarge **SALES ADMIN ASSISTANT, ROW** Bryony Cousins **DIRECTOR OF GLOBAL COLLABORATION AND ACADEMIC PUBLISHING RELATIONS, ASIA** Xiaoying Chu **ASSOCIATE DIRECTOR, INTERNATIONAL COLLABORATION** Grace Yao **SALES MANAGER** Danny Zhao **PROJECT MANAGER** Kilo Lan **ASCA CORPORATION, JAPAN** Kaoru Sasaki (Tokyo), Miyuki Tani (Osaka) **COLLABORATION/CUSTOM PUBLICATIONS/JAPAN** Adarsh Sandhu

DIRECTOR, COPYRIGHT, LICENSING AND SPECIAL PROJECTS Emilie David **RIGHTS AND LICENSING COORDINATOR** Jessica Adams **RIGHTS AND PERMISSIONS ASSOCIATE** Elizabeth Sandler **CONTRACTS AND LICENSING ASSOCIATE** Lili Catlett

---

MAIN HEADQUARTERS
Science/AAAS
1200 New York Ave. NW
Washington, DC 20005

SCIENCE INTERNATIONAL
Clarendon House
Clarendon Road
Cambridge, CB2 8FH, UK

SCIENCE CHINA
Room 1004, Culture Square
No. 59 Zhongguancun St.
Haidian District, Beijing, 100872

SCIENCE JAPAN
ASCA Corporation
Sibaura TY Bldg. 4F, 1-14-5
Shibaura Minato-ku
Tokyo, 108-0073 Japan

EDITORIAL
science_editors@aaas.org

NEWS
science_news@aaas.org

INFORMATION FOR AUTHORS
sciencemag.org/authors/science-information-authors

REPRINTS AND PERMISSIONS
sciencemag.org/help/reprints-and-permissions

MEDIA CONTACTS
scipak@aaas.org

MULTIMEDIA CONTACTS
SciencePodcast@aaas.org
ScienceVideo@aaas.org

INSTITUTIONAL SALES AND SITE LICENSES
sciencemag.org/librarian

PRODUCT ADVERTISING & CUSTOM PUBLISHING
advertising.sciencemag.org/products-services
science_advertising@aaas.org

CLASSIFIED ADVERTISING
advertising.sciencemag.org/science-careers
advertise@sciencecareers.org

JOB POSTING CUSTOMER SERVICE
employers.sciencecareers.org
support@sciencecareers.org

MEMBERSHIP AND INDIVIDUAL SUBSCRIPTIONS
sciencemag.org/subscriptions

MEMBER BENEFITS
aaas.org/membercentral

Science serves as a forum for discussion of important issues related to the advancement of science by publishing material on which a consensus has been reached as well as including the presentation of minority or conflicting points of view. Accordingly, all articles published in *Science*—including editorials, news and comment, and book reviews—are signed and reflect the individual views of the authors and not official points of view adopted by AAAS or the institutions with which the authors are affiliated.

Published by AAAS

EDITORIAL

Chinese scientists and security

Many scientific and economic successes in the United States are owed to the work of foreign-born scientists. Today, a substantial percentage of U.S patents and scientific publications are contributed by Chinese-born scientists. But there is increasing concern that China is unfairly and systematically attempting to capture intellectual property, trade secrets, and advanced technologies from the United States, all detrimental to productive long-term relationships. As part of the U.S. response to these threats, tenured Chinese-American scientists at top institutions of biomedical research were recently dismissed for purported violations of disclosure rules, breaches of confidentiality, or outright suspicion of espionage. As Congress seeks to protect the open and collaborative approach to science and technology from nefarious activities of foreign states, the scientific community must weigh in on the path forward.

We should remember that for years, scientific exchanges and collaborations with China were encouraged by U.S. policy-makers, including implicit support of China's Thousand Talents Program. Chinese-born as well as American-born federally funded scientists were publicly offered various positions in China over the years without opposition by relevant institutions. The "rules," now presented and enforced as severe violations of U.S. ethics and intellectual property regulations, were not rigorously implemented by officials at many U.S. institutions. The consternation, sense of targeted discrimination, and fear in the Chinese-American scientific community are thus understandable.

U.S. science and technology are a cornerstone of competitiveness and preeminence in the world, and the security and protection of this vital enterprise are of paramount importance. But unlike most other countries, the United States relies heavily on attracting the best and brightest in the world to its ecosystem of innovation because of an insufficient number of graduates in science, technology, engineering, and mathematics fields relative to the size and technological intensity of its economy. Would it be in the national interest to risk losing all or some of the extraordinarily productive Chinese-American scientific diaspora trained and supported for years in the United States?

In my experience in academia, government, and industry, most Chinese-born scientists prefer to stay in the United States for personal and family preferences. One can imagine the glee of Chinese officials at the prospect of thousands of Chinese-American scientists, whom they were unable to recruit until now, relocating back to China. So, what should be done?

Congress is conducting hearings and considering passing the Securing American Science and Technology Act of 2019 as part of the Defense Authorization bill—a good step forward. Although this bill is progressing at its usual pace in the legislative branch, time is not on our side. The executive branch should promptly establish a blue-ribbon panel composed of security experts, agencies representatives, academics, and prominent scientists and engineers under the auspices of the Office of Science and Technology Policy and the National Security Council to fully debate the facts, ways, and means to effectively protect U.S. science and technology while preserving the attractiveness of the United States to talented foreign-born scientists, most particularly from China. It should clearly define new rules of foreign scientific engagement; develop a risk matrix by area of science and technology to guide institutions; instruct agencies such as the Department of Commerce in the implementation of all rules of export or import controls and material and information transfers in a manner similar to that for dual-use research guidelines; mandate a compliance and education program for all concerned; and find explicit ways to reassure the Chinese-American scientific community at large.

> "...the United States relies heavily on attracting the best and brightest..."

No members of any community should be targeted because of their origins, rather than for what they may have intentionally and demonstrably done to harm U.S. science and technology. The United States should not risk losing critical intellectual assets such as productive foreign-born scientists and engineers to global competitors to serve short-term security concerns at the expense of long-term national interests.

–Elias Zerhouni

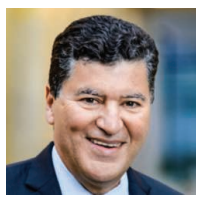

PHOTO: SANOFI PHOTOGRAPHERS

Elias Zerhouni
is an emeritus professor at Johns Hopkins University, Baltimore, MD, USA, and former director of the National Institutes of Health, Bethesda, MD, USA.
eliaszerhouni@gmail.com

10.1126/science.aay5212

NEWS

IN BRIEF

Edited by **Kelly Servick**

ARCHAEOLOGY

Paddlers to replicate ancient voyage

Five adventurers plan to paddle a hand-hewn log boat 200 kilometers from Taiwan, China, to the westernmost island of Okinawa, Japan, to show that Paleolithic voyagers could have made similar trips in migrating to the remote Pacific isles more than 30,000 years ago. Yousuke Kaifu, an archaeologist at Japan's National Museum of Nature and Science in Tokyo, dreamed up the project to solve the mystery of how early humans populated the Ryukyu Islands, in present-day Okinawa. Previous trials in the past 3 years using reed boats and bamboo rafts over shorter distances were unsuccessful. But the dugout canoe, hewn from a 1-meter-thick tree trunk using a primitive stone ax, has proved to be more buoyant and faster moving than the previous crafts. The crew of five includes a Maori man who will navigate by traditional methods of following the stars and judging winds and ocean swells. As *Science* went to press, the team awaited good weather to launch the voyage, which could take 30 to 40 hours. Kaifu says the chance of success "is not very high." Even if the attempt fails, the team expects to gain insights into the challenges of prehistoric ocean travel.

Citizenship question blocked

U.S. CENSUS | The U.S. Supreme Court last week told Commerce Secretary Wilbur Ross that he must do a better job of explaining his decision to add a citizenship question to the 2020 census. Writing the 5-4 opinion, Chief Justice John Roberts pointed to a "significant mismatch" between Ross's official stance—that he was acquiescing to the Department of Justice's request for better data to enforce the Voting Rights Act—and strong evidence that he had made up his mind months before he received such a request. The high court's ruling says, in effect, that Ross failed to meet the standards for justifying his actions under the Administrative Procedure Act (APA). "I'm pretty happy today," said John Thompson, who stepped down as director of the Census Bureau in June 2017 and has argued that adding the question could increase the cost and compromise the accuracy of the census. "Holding Secretary Ross accountable under APA … preserves the nation's statistical system."

LGBT survey shows discrimination

WORKPLACE | Harassment and exclusion are common experiences for members of sexual and gender minorities in the physical sciences, according to a survey released 26 June by the United Kingdom's Institute of Physics, Royal Astronomical Society, and Royal Society of Chemistry. It included responses from 637 scientists working in the United Kingdom, most of whom identified as lesbian, gay, bisexual, transgender, or another sexual or gender minority. A climate of discrimination had prompted 28% of respondents to consider leaving their jobs. And 16% said they had experienced "exclusionary, intimidating, offensive or harassing behaviour" in the past 12 months; among transgender people, that figure was 32%. The report highlights "areas for increased action" such as workplace training on transgender inclusion and correct pronoun usage.

PHOTO: NATIONAL MUSEUM OF NATURE AND SCIENCE/TOKYO

A log boat (below) will replace reed and bamboo crafts that failed in earlier seafaring trials.

Viruses blamed for pneumonia

GLOBAL HEALTH | Pneumonia kills nearly 1 million children every year, but the lung infection's precise cause can be hard to pinpoint, and doctors often prescribe antibiotics without knowing that bacteria are to blame. A new study has found that 61% of childhood pneumonia worldwide is caused by viruses. In 4252 pneumonia cases among children in Africa and Asia, researchers used nose and throat swabs and a variety of fluid samples to infer the cause of infection from a list of 30 pathogens. Viruses were the dominant culprits, the team reported last week in *The Lancet*, and one in particular—respiratory syncytial virus—accounted for nearly one-third of cases. The finding reveals the dramatic impact that sorely needed vaccines would have on the disease, the researchers say. Their new diagnostic approach might also help reduce the overuse of antibiotics.

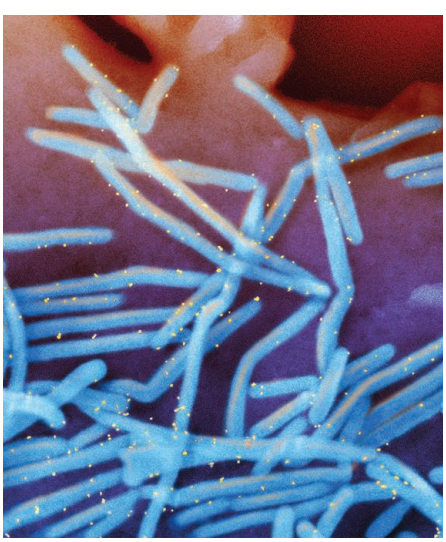

Respiratory syncytial virus (blue) causes nearly one-third of all pneumonia cases in children under age 5.

PHOTO: NATIONAL INSTITUTE OF ALLERGY AND INFECTIOUS DISEASES/NATIONAL INSTITUTES OF HEALTH

Contrails threaten climate

CLIMATE SCIENCE | Carbon emissions from aviation are a well-known contributor to climate warming. But another byproduct of planes—the white contrails they paint across the sky—has an even bigger effect. Contrails form when water vapor in a plane's exhaust freezes, and unlike low-level clouds that reflect sunlight to cool the atmosphere, they trap heat radiated from Earth's surface, warming it. A new model described last week in *Atmospheric Chemistry and Physics* is the first to classify contrail clouds separately from natural ones. Researchers predicted a threefold increase in contrail warming effects by 2050. They also estimated that a 50% reduction in airplane soot, which promotes the formation of contrails, would lead to a 15% decrease in those effects. But such reductions are unlikely; global air traffic is surging, and most pollution-reduction plans in the industry fail to consider climate impact beyond carbon dioxide emissions.

Pain society to shut down

PROFESSIONAL GROUPS | Under financial pressure from opioid lawsuits, the American Pain Society (APS) in Glenview, Illinois, announced last week that it would cease operations after its members overwhelmingly voted in favor of filing for bankruptcy. The 42-year-old organization has hosted an annual meeting, awarded small grants for basic research and early career scientists, and published *The Journal of Pain*. It has recently been among the defendants in opioid-related lawsuits and faced allegations it had represented drugmakers' interests and contributed to the overprescribing of the painkillers that led to the opioid epidemic. In a statement, APS described those suits as "spurious" and cited legal expenses as part of a "perfect storm," along with declining sponsorship, membership, and meeting attendance.

BY THE NUMBERS

142 million

People still at risk of the bacterial illness trachoma, the leading infectious cause of blindness—down 91% since 2002 thanks to the distribution of antibiotics and other public health campaigns (World Health Organization).

23%

Proportion of U.S. electricity generated by renewable sources as of April, the first month in which renewables surpassed coal's contribution—estimated at 20% (U.S. Energy Information Administration).

174

Bottlenose dolphins estimated to have stranded and died in the past year because of a harmful algal bloom along the southwest coast of Florida (U.S. National Oceanic and Atmospheric Administration).

Zambian river will keep flowing

ECOLOGY | After an outcry from conservation groups, the Zambian government has withdrawn approval for a dam on the 1100-kilometer Luangwa River, one of the longest free-flowing rivers left in southern Africa. The World Wildlife Fund (WWF) and other groups have opposed plans by a South African power company to create a 1510-square-kilometer reservoir, which researchers have determined would flood out parts of several tribal, hunting, and protected areas and shrink a wildlife corridor between two national parks. WWF freshwater scientist Michele Thieme called the Luangwa decision "a major win." Recent public opposition in Chile has killed similar projects on the Baker and Pascua rivers, two of the country's wildest waterways.

SCIENCEMAG.ORG/NEWS
Read more news from *Science* online.

SCIENCE POLICY

FDA enforcement actions plummet under Trump

Agency is sending many fewer warning letters

By **Charles Piller**

From monitoring clinical trials and approving medicines and vaccines, to ensuring the safety of blood transfusions, medical devices, groceries, and more, the U.S. Food and Drug Administration (FDA) is one of the nation's most vital watchdogs. By several measures, however, FDA's compliance and enforcement actions have plummeted since President Donald Trump took office, *Science* has found.

The agency's "warning letters"—a key tool for keeping dangerous or ineffective drugs and devices and tainted foods off the market—have fallen by one-third, for example. Such letters typically demand swift corrections to protect public health and safety. FDA records from Trump's inauguration through 22 May show the agency issued 1033 warning letters, compared with 1532 for the most recent equivalent period under former President Barack Obama. Compared with the start of the Obama presidency, Trump-era letters dropped by nearly half.

Warnings from the FDA Center for Devices and Radiological Health, which helps ensure the safety and quality of medical devices, and from some of the agency's district offices—including Philadelphia, Florida, and New York—have dropped even more steeply, by more than two-thirds. Two district offices have not issued a warning in more than 2 years. The numbers don't just reflect a new administration's slow start. FDA sent significantly fewer warning letters in the second year of Trump's presidency than in his first.

FDA watchers say they can't pinpoint what's driving the decline, but they are alarmed. "Those who think the Trump administration has not succeeded in its deregulatory efforts ought to look at these data," says Peter Lurie, an FDA executive under Obama and Trump and now executive director of the Center for Science in the Public Interest, a Washington, D.C., advocacy group. "Industry may well take the message from this that the cop is not on the beat as often."

Several other FDA actions under Trump show similar declines when measured against the end of the Obama administration. FDA inspection reports labeled "official action indicated"—typically a trigger for warning letters or similar actions—have fallen by about half under Trump and are continuing to trend downward. Even FDA's rare injunctions, a more forceful step than warnings to prevent sales or distribution of unsafe or otherwise illegal products, fell from 35 in the last part of the Obama administration to 26 under Trump. (During a comparable period at the start of the Obama years, FDA issued 51 injunctions.) The agency's "untitled letters"—for concerns that fall short of thresholds for formal warnings—also have dropped sharply under Trump.

"FDA's power to enforce its requirements is an important part of how it achieves its public health mission," says Patricia Zettler, a law professor at Ohio State University in Columbus and former FDA attorney. "If FDA is not using that power, it sends a signal that violations will be tolerated."

FDA did not dispute the enforcement and compliance data, which *Science* compiled from the agency's own public records. In a written statement, the agency responded, "Sometimes the actions we take are visible, like warning letters (or) recalls. … At other times, our actions to protect consumers are less discernible, but equally vital." Among the efforts that can obviate the need for warning letters, FDA noted, are meetings with companies, follow-up inspections, the threat of mandatory recalls, a new voluntary improvement pilot program for devicemakers, coordination with European regulators, and unspecified "regulatory and compliance measures" conducted "behind the scenes."

Scott Gottlieb, Trump's first FDA commissioner, defended his record after reviewing a summary of *Science*'s data. "We were pretty aggressive," he wrote in an email. "I don't think you can paint us with a political narrative—that just because we were a Republican administration, somehow we must have ratcheted down enforcement activity. We didn't."

Gottlieb, a physician and venture capitalist before being tagged for FDA, resigned in March and is now at the American Enterprise Institute, a conservative think tank in Washington, D.C. On his watch, Gottlieb said later in an interview, FDA made enforcement more efficient and expanded field resources. The agency's budget rose 21% from fiscal years 2016 to 2019. He says that under Trump, FDA issued guidance or beefed-up enforcement

ILLUSTRATION: STEPHAN SCHMITZ/FOLIO ART

on stem cells, vaping, dietary supplements, homeopathy, opioids, and generic drugs. He argues that warning letters and other such actions are imperfect enforcement measures.

The only significant exception to the downward trend on warning letters is FDA's Center for Drug Evaluation and Research (CDER), which assesses and approves new drugs and polices existing drugs for safety and efficacy. It has issued 188 warnings under Trump, compared with 116 in the most recent period under Obama. Many of the Trump-period letters concern opioid sales, or over-the-counter and generic drugs made in China and India, which have rapidly gained market share despite quality lapses documented by FDA and others.

Besides regulating consumer products, FDA protects subjects in clinical trials by reviewing informed consent and other ethical practices. In the most recent period under Obama, CDER issued 19 warnings concerning improper conduct of clinical investigations and protection of human subjects; under Trump the number fell to seven.

Michael Carome, who directs health research at the Washington, D.C., consumer advocate Public Citizen, points to clinical trials at Hennepin County Medical Center in Minneapolis, Minnesota, as an example of FDA's sluggish approach to human subjects protections. In July 2018, Public Citizen and more than 60 clinical scholars and ethicists complained to FDA about apparent lapses in informed consent and possible coercion of unwitting and vulnerable patients treated with powerful experimental drugs, including ketamine. The anesthetic and pain reliever was being tested to control agitation.

The next month, an FDA inspection of the trials validated some of Public Citizen's concerns. After a second inspection, FDA cited other serious transgressions. As first reported by Minneapolis's *Star Tribune*, these included failing to report to an oversight body that some patients developed serious breathing problems and movement disorders.

In May, the medical center's operator disputed most FDA findings, but agreed to make a few procedural changes. Nearly a year after the original complaint, FDA has yet to issue a warning letter. The agency declined to comment about the case. "It was among the more serious things I've seen in human subjects protection violations," says Carome, previously a Department of Health and Human Services official tasked with protecting human subjects. "Maybe [the FDA is] not taking appropriate action in some of these cases."

Even electronic cigarette enforcement has seen mixed results under Trump, despite Gottlieb's public stand against teen vaping. On the one hand, a special program to police retail sellers of tobacco and vaping products—such as convenience and grocery stores—issued about as many warnings and fines under Trump as at the end of the Obama years. Gottlieb says FDA put managers of large retail chains on notice to improve compliance. He also implemented a rule finalized under Obama that gave the e-cigarette industry a road map to comply with federal tobacco laws.

But warnings from the FDA Center for Tobacco Products, whose targets include wholesalers, online vendors, makers and suppliers of vaping liquids, and importers, dropped by one-third. Gottlieb's FDA also delayed from 2018 to 2022 an Obama-era deadline requiring e-cigarette–makers to submit products for premarketing review, reasoning that this would give the industry time to develop in ways that help adult smokers quit. (FDA recently advanced the deadline to 2021.)

Federal data show vaping among high school students shot up 78% from 2017 to 2018, and 48% among middle school students. Last year, FDA said it would restrict some sweet vaping flavors that entice children and began to enforce nicotine warnings on such products and crack down on improper marketing. But given the teen vaping epidemic, some critics view such moves as too little, too late. "Had we known there was going to be an epidemic of youth use … we would have made different decisions" and moved more quickly, Gottlieb concedes. He says that delaying the review deadline helped to ensure adequate guidance for industry, and was not responsible for the youth crisis.

Deregulatory pressure from the White House has had profound effects on several federal agencies, but whether and how it might explain the drop in some elements of FDA enforcement is unclear. The agency has few political appointees and is relatively decentralized. Some insiders say Gottlieb generally supported vigorous enforcement. But for some actions, including injunctions, FDA requires Department of Justice (DOJ) cooperation. Two people with personal knowledge of FDA enforcement, who decline to be named for fear of reprisals, say that under Trump, DOJ has blocked numerous strong injunction requests from FDA. One source says it became much harder to bring new injunction cases after Trump took office.

In its statement to *Science*, FDA did not address the allegations, but called DOJ a "strong partner." DOJ did not respond to queries.

Joshua Sharfstein, a health policy researcher at Johns Hopkins University in Baltimore, Maryland, who worked at FDA under Obama, including as its acting commissioner, says he hopes the data found by *Science* will prompt a closer look at the apparent declines in enforcement, and help clarify what has caused them. "The FDA's enforcement role is extremely important," he says. "If the FDA isn't doing enforcement, nobody's doing enforcement." ■

This story has been supported by the Science *Fund for Investigative Reporting.*

Watchdog off duty?

FDA enforcement actions are dropping under President Donald Trump. The number of warning letters and injunctions (through May 22) and Official Action Indicated (OAI) reports (through April 22) fell steeply from the equivalent periods before his inauguration.

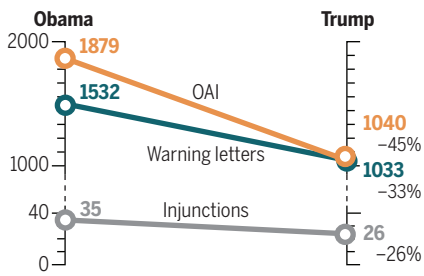

Centers of inaction

The decline in warning letters spans most FDA divisions.

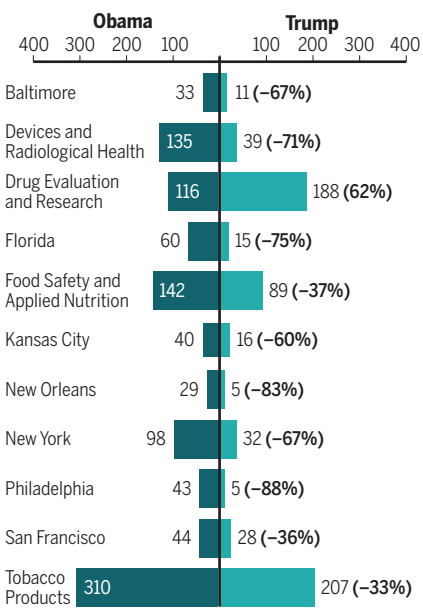

A tale of two presidents

Over a decade, warning letters and OAI reports rose and then waned, before a large Trump-era falloff.

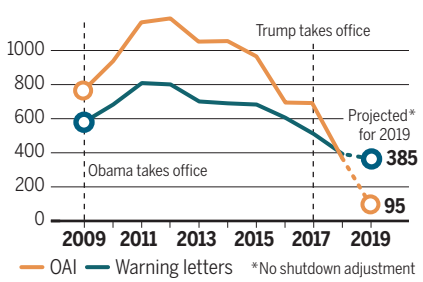

CREDITS: (GRAPHIC) N. DESAI/*SCIENCE*; (DATA) FDA

BIOMEDICAL RESEARCH

Details revealed on NIH probe of foreign ties

Official overseeing inquiry reveals undisclosed firings and returned funds from universities

By **Jeffrey Mervis**

A yearlong investigation by the National Institutes of Health (NIH) in Bethesda, Maryland, has fingered 180 scientists at more than 60 U.S. research institutions who NIH believes have violated the confidentiality of its peer-review system or failed to disclose financial ties to foreign organizations. But NIH has revealed few details of the investigation—including how it began and what it has learned.

Until now. Last week, the senior NIH official leading the agency's review of foreign ties talked with *Science* about the probe's substantial, and growing, scope.

This spring, two institutions—MD Anderson Cancer Center in Houston, Texas, and Emory University in Atlanta—announced that five faculty members had been dismissed in the wake of the NIH probe. But Michael Lauer, who directs NIH's $20 billion–plus extramural research program, says several other universities have cut ties with researchers in cases that have remained confidential. Lauer says some institutions have repaid NIH "hundreds of thousands of dollars" in grants after confirming what he termed "egregious" violations.

Lauer understands why some universities have kept quiet about those outcomes. "No organization wants to discuss personnel actions in a public forum," he says. At the same time, Lauer says NIH is, "to the extent possible, engaged in outreach" to the scientific community about the importance of ensuring research integrity and defending against foreign influence.

U.S. officials have become increasingly worried that foreign entities, especially those in China, are trying to manipulate the traditionally open U.S. research enterprise to their advantage. Their fears include the theft of intellectual property as well as economic and military espionage.

Lauer suspects some of the violations NIH has uncovered will result in the U.S. government banning scientists from receiving federal funds, a process called debarment. NIH has referred at least 18 cases to its parent agency, the Department of Health and Human Services, for further investigation. "We don't know where we'll end up," Lauer says. But in the meantime, he adds, "I wouldn't be surprised if other agencies follow our lead and start doing similar things."

Michael Lauer of the National Institutes of Health says undisclosed foreign ties had gone on for years before the agency noticed them.

Science could not independently verify some of Lauer's comments because of the secrecy surrounding NIH's investigation. But here are highlights of the conversation:

- NIH's current effort began after it learned in mid-2016 of a Federal Bureau of Investigation (FBI) case involving an MD Anderson researcher serving as an NIH reviewer. The FBI probe revealed that, despite strict rules to protect confidentiality, the researcher had shared grant proposals with several people. NIH has since found similar violations by other reviewers.

- Most disclosure violations came to light through NIH program staff poring over annual progress reports from grantees. They noticed that scores of U.S. researchers had reported affiliations with or funding from foreign institutions—particularly in China—in their research papers but failed to tell their home institutions or NIH about those arrangements.

- A majority of the scientists who have failed to disclose foreign ties hold multiple grants from NIH. "Most [of the scientists] are ethnically Chinese," Lauer says, "although some of our more serious cases are not." The researchers conduct studies in many fields, he adds.

- Many U.S. universities initially pushed back after receiving a letter, telling NIH that the named scientists had no such connections and that NIH "was blowing smoke." But those institutions later reversed course, Lauer says, after NIH supplied evidence such as grant numbers from foreign funders and employment contracts with foreign institutions. University officials were "surprised, shocked, and horrified" by the undisclosed ties, Lauer says.

- Some scientists targeted by the probe had NIH grants that provided salary for 8 months of work each year at their home institution. But investigations showed they had also agreed to work as much as 9 months a year at a foreign institution. A 17-month time commitment amounts to fraud, Lauer says. As a result, some institutions have returned salary funds to NIH.

- Some U.S.-based scientists participating in China's Thousand Talents Program, which seeks to build ties with scientists working outside China, signed contracts that stipulated their research results "must stay in China and cannot be reported to their American university." Others had contracts that required them to promote their Chinese affiliations in any publication.

"It's fascinating," Lauer says about the dual laboratories, overcommitments of time, and secret contracts by grantees that NIH says it has uncovered. The failure to report such arrangements "had been going on for a number of years, apparently. But it took a long time before we noticed it."

Many members of the Asian American community believe that U.S. agencies have been targeting Asian-born scientists simply for their participation in Thousand Talents and similar Chinese recruitment programs. But Lauer says NIH has no problem with U.S. scientists participating in Thousand Talents as long as they fully disclose that relationship. "Thousand Talents is not a threat [to the United States]," he says. "It's not the specific conduct we are focusing on, it's the failure to disclose it." ■

PHOTO: NATIONAL INSTITUTES OF HEALTH

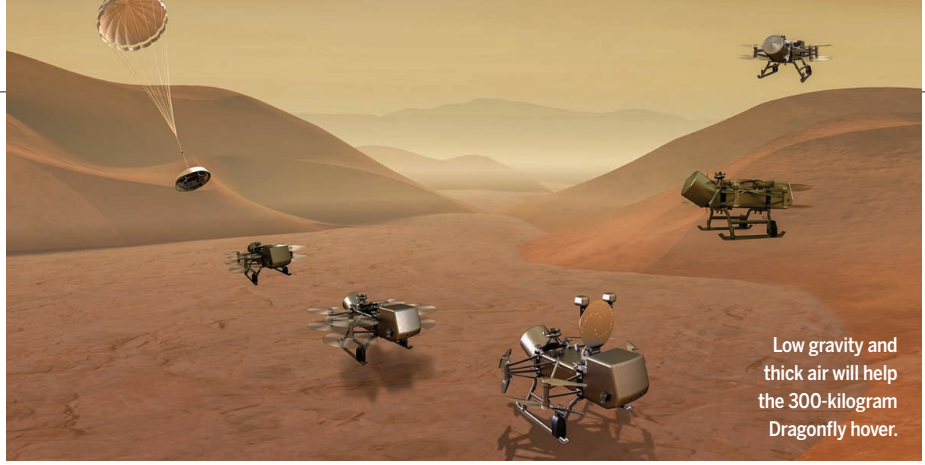

Low gravity and thick air will help the 300-kilogram Dragonfly hover.

PHOTO: JOHNS HOPKINS APL

PLANETARY SCIENCE

NASA to fly drone on Titan

Dragonfly quadcopter will scout saturnian moon for life

By **Paul Voosen**

On Earth's moon and Mars, driving is the best option for a robot explorer. But on Titan, Ralph Lorenz plans to fly. Telescopes indicated Saturn's largest moon had a thick, hazy atmosphere, sodden with methane. In such an environment, the best way to get around, Lorenz floated in a 2000 *New Scientist* article, would be a helicopter.

Two decades later, Lorenz's idea has turned into Dragonfly, a $1 billion mission selected last week by NASA for launch in 2026. Upon arrival in 2034, the craft, a quadcopter drone the size of a car, will take flight, periodically touching down on the icy surface in search of a chemistry that could foster life. "It doesn't get more interesting than a nuclear-powered quadcopter with drills and a neutron gun," says Lorenz, Dragonfly's project scientist at the Johns Hopkins University Applied Physics Laboratory (APL) in Laurel, Maryland, which will manage the mission.

NASA's pick is inspired, says Lindy Elkins-Tanton, a planetary scientist at Arizona State University in Tempe. "Titan might truly be the cradle for some kind of life," she says. "Whether life has emerged or not, Titan's hydrocarbon rivers and lakes, and its hydrocarbon snow, make it one of the most fantasylike landscapes in our solar system."

Titan was first explored by NASA's Cassini spacecraft. In 2005, it dropped the short-lived European Huygens probe into Titan's atmosphere. The surface it found was Earthlike, with plateaus, dune-filled deserts, and liquid seas at its poles. But on Titan, where temperatures average a frigid 94 K (-179° C), the "rocks" are made of water ice and the seas are filled with the hydrocarbons ethane and methane. Scientists believe the stew of organic molecules may have reacted to form amino acids and the bases that, on Earth, make up DNA's double helix. It's as if Titan has been conducting experiments on the origins of life for millions of years, says Elizabeth "Zibi" Turtle, a planetary scientist at APL and the mission's principal investigator. "Dragonfly is designed to go pick up the results of those experiments and study them," she says.

Given Titan's complex surface, a visit to a single site would not say much, so Dragonfly will hop between distant landing sites every couple of weeks. Titan's thick air and low gravity will allow the 300-kilogram copter, powered by a radioactive generator, to hover much more easily than on Earth.

The probe will target the moon's vast equatorial deserts, which likely contain a grab bag of material. It will search for impact craters or ice volcanoes, places that could have provided an energetic spark—and the liquid water—needed for organic reactions. Ultimately, it will reach the 80-kilometer-wide Selk crater, created by an impact large enough to melt Titan's water-ice crust and liberate oxygen, priming reactions that may be recorded in its outcrops.

During flight, Dragonfly can collect atmospheric measurements. Upon landing, an instrument on the copter's belly will fire neutrons at the surface and look for released gamma rays to detect basic terrain types, such as ammonia-rich ice or carbon-rich sand dunes. Its two landing skids will each carry a drill to take samples and feed them to an instrument to analyze their composition. The craft will also be able to sense vibrations induced by the tidal forces of Saturn. Those tremors could help gauge the depth and composition of the ocean thought to lie beneath the moon's crust.

Dragonfly may last up to 8 years before its radioactive power source peters out. ■

GENOME EDITING

CRISPR patent fight revived

U.S. patent office issues new interference declaration

By **Jon Cohen**

A surprise ruling last week reignited the high-profile patent fight over who invented a key application of the genome editor CRISPR. The 3-year-old battle pits parties represented by the University of California (UC) against the Broad Institute in Cambridge, Massachusetts. It revolves around the use of CRISPR, originally derived from a DNA-cutting system used by bacteria, in the more complex cells of eukaryotes—including humans, which means the outcome could shape the development of potentially lucrative CRISPR-based medical treatments.

Triggered by new patent claims from the UC group, the development resurrects contentious debates that calmed down after a court decision in September 2018 favoring the Broad Institute. The UC team, which represents Jennifer Doudna from UC Berkeley and her collaborators, had first published the use of CRISPR as a genome-editing tool in *Science* in June 2012, but they did not demonstrate that it worked in eukaryotes.

In January 2013, Broad's team, led by Feng Zhang, published a paper—also in *Science*—that described its success in mouse and human cells. After the U.S. Patent and Trademark Office awarded Broad several patents, UC requested what's known as an interference, contesting Broad's patents based on its own submitted patent. UC's attorneys argued that after the Doudna group's 2012 paper, it was "obvious" that CRISPR would work in eukaryotes.

The Patent Trial and Appeal Board (PTAB) ruled against UC in February 2017, and the U.S. Court of Appeals for the Federal Circuit denied UC's appeal 1 year later. In April 2018, however, UC filed new patent claims that highlighted its invention's utility in eukaryotic cells, prompting PTAB to rule that the two parties' claims now create an interference issue that needs to be examined in a hearing.

Eldora Ellison, a lead attorney for the UC team—who works at Sterne, Kessler, Goldstein & Fox in Washington, D.C., says

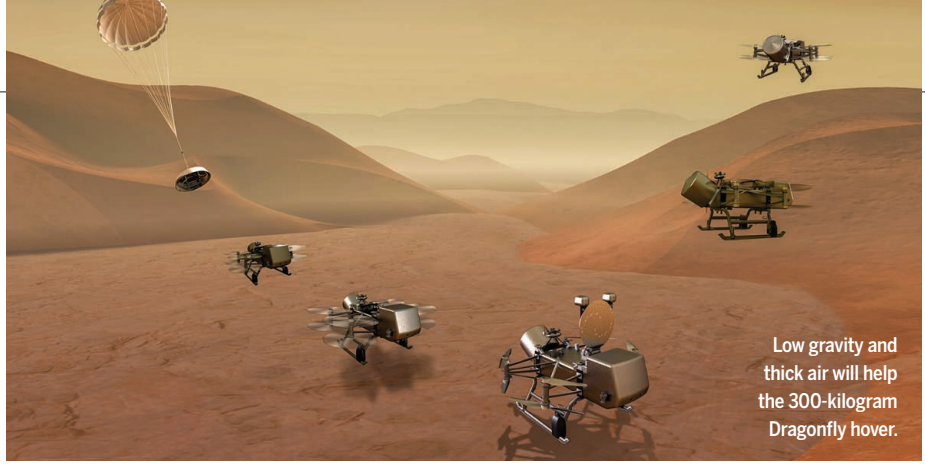

Low gravity and thick air will help the 300-kilogram Dragonfly hover.

PHOTO: JOHNS HOPKINS APL

PLANETARY SCIENCE

NASA to fly drone on Titan

Dragonfly quadcopter will scout saturnian moon for life

By **Paul Voosen**

On Earth's moon and Mars, driving is the best option for a robot explorer. But on Titan, Ralph Lorenz plans to fly. Telescopes indicated Saturn's largest moon had a thick, hazy atmosphere, sodden with methane. In such an environment, the best way to get around, Lorenz floated in a 2000 *New Scientist* article, would be a helicopter.

Two decades later, Lorenz's idea has turned into Dragonfly, a $1 billion mission selected last week by NASA for launch in 2026. Upon arrival in 2034, the craft, a quadcopter drone the size of a car, will take flight, periodically touching down on the icy surface in search of a chemistry that could foster life. "It doesn't get more interesting than a nuclear-powered quadcopter with drills and a neutron gun," says Lorenz, Dragonfly's project scientist at the Johns Hopkins University Applied Physics Laboratory (APL) in Laurel, Maryland, which will manage the mission.

NASA's pick is inspired, says Lindy Elkins-Tanton, a planetary scientist at Arizona State University in Tempe. "Titan might truly be the cradle for some kind of life," she says. "Whether life has emerged or not, Titan's hydrocarbon rivers and lakes, and its hydrocarbon snow, make it one of the most fantasylike landscapes in our solar system."

Titan was first explored by NASA's Cassini spacecraft. In 2005, it dropped the short-lived European Huygens probe into Titan's atmosphere. The surface it found was Earthlike, with plateaus, dune-filled deserts, and liquid seas at its poles. But on Titan, where temperatures average a frigid 94 K (-179° C), the "rocks" are made of water ice and the seas are filled with the hydrocarbons ethane and methane. Scientists believe the stew of organic molecules may have reacted to form amino acids and the bases that, on Earth, make up DNA's double helix. It's as if Titan has been conducting experiments on the origins of life for millions of years, says Elizabeth "Zibi" Turtle, a planetary scientist at APL and the mission's principal investigator. "Dragonfly is designed to go pick up the results of those experiments and study them," she says.

Given Titan's complex surface, a visit to a single site would not say much, so Dragonfly will hop between distant landing sites every couple of weeks. Titan's thick air and low gravity will allow the 300-kilogram copter, powered by a radioactive generator, to hover much more easily than on Earth.

The probe will target the moon's vast equatorial deserts, which likely contain a grab bag of material. It will search for impact craters or ice volcanoes, places that could have provided an energetic spark—and the liquid water—needed for organic reactions. Ultimately, it will reach the 80-kilometer-wide Selk crater, created by an impact large enough to melt Titan's water-ice crust and liberate oxygen, priming reactions that may be recorded in its outcrops.

During flight, Dragonfly can collect atmospheric measurements. Upon landing, an instrument on the copter's belly will fire neutrons at the surface and look for released gamma rays to detect basic terrain types, such as ammonia-rich ice or carbon-rich sand dunes. Its two landing skids will each carry a drill to take samples and feed them to an instrument to analyze their composition. The craft will also be able to sense vibrations induced by the tidal forces of Saturn. Those tremors could help gauge the depth and composition of the ocean thought to lie beneath the moon's crust.

Dragonfly may last up to 8 years before its radioactive power source peters out. ■

GENOME EDITING

CRISPR patent fight revived

U.S. patent office issues new interference declaration

By **Jon Cohen**

A surprise ruling last week reignited the high-profile patent fight over who invented a key application of the genome editor CRISPR. The 3-year-old battle pits parties represented by the University of California (UC) against the Broad Institute in Cambridge, Massachusetts. It revolves around the use of CRISPR, originally derived from a DNA-cutting system used by bacteria, in the more complex cells of eukaryotes—including humans, which means the outcome could shape the development of potentially lucrative CRISPR-based medical treatments.

Triggered by new patent claims from the UC group, the development resurrects contentious debates that calmed down after a court decision in September 2018 favoring the Broad Institute. The UC team, which represents Jennifer Doudna from UC Berkeley and her collaborators, had first published the use of CRISPR as a genome-editing tool in *Science* in June 2012, but they did not demonstrate that it worked in eukaryotes.

In January 2013, Broad's team, led by Feng Zhang, published a paper—also in *Science*—that described its success in mouse and human cells. After the U.S. Patent and Trademark Office awarded Broad several patents, UC requested what's known as an interference, contesting Broad's patents based on its own submitted patent. UC's attorneys argued that after the Doudna group's 2012 paper, it was "obvious" that CRISPR would work in eukaryotes.

The Patent Trial and Appeal Board (PTAB) ruled against UC in February 2017, and the U.S. Court of Appeals for the Federal Circuit denied UC's appeal 1 year later. In April 2018, however, UC filed new patent claims that highlighted its invention's utility in eukaryotic cells, prompting PTAB to rule that the two parties' claims now create an interference issue that needs to be examined in a hearing.

Eldora Ellison, a lead attorney for the UC team—who works at Sterne, Kessler, Goldstein & Fox in Washington, D.C., says

PTAB ruled in 2017 that there was no interference because Broad focused on eukaryotes and the UC patent made claims about the utility of CRISPR in "any environment." "What they said is, 'We're actually not going to have a fight at this point in time, because we think that these are two different inventions,'" Ellison says. "They kind of kicked the can down the road on who was first to invent the use of CRISPR in eukaryotes."

Now that UC has sharpened its claim to the use of CRISPR in eukaryotes, Broad "[looks] forward to participating in the interference process," according to a statement from the institute. Broad argues the new interference "challenges the validity of [UC's] eukaryotic claims." The ruling deems the Broad group the "senior party," which means UC "carries the burden of proof" and must convince PTAB that the Broad team did not invent the eukaryotic use of CRISPR.

Catherine Coombes, a patent attorney at HGF in York, U.K., who does not represent Broad or UC but is involved in CRISPR patent disputes, says the new interference "adds to the complexity of the landscape." The European Patent Office has granted what's known as "overlapping rights" to both groups and others who have filed CRISPR patent applications,

> ***"For human therapeutics, it is still too early to know where the key patents will lie."***
> **Catherine Coombes**, HGF

Coombes says—a temporary resolution in anticipation of future legal fights. "For human therapeutics, it is still too early to know where the key patents will lie," she adds, noting that CRISPR systems vary, using different enzymes that ultimately may make one version safer or more effective than another.

The patent uncertainty created by the new interference declaration may prod UC and Broad to cut a deal, Coombes says. Broad says in a separate statement that it has long hoped UC would enter a "patent pool," which effectively would allow both parties to earn money from their inventions without becoming ensnarled in legal wrangling.

The parties will discuss the interference with PTAB in a conference call on 5 August. If they do not reach a settlement, the interference hearing is expected in about 8 months. ■

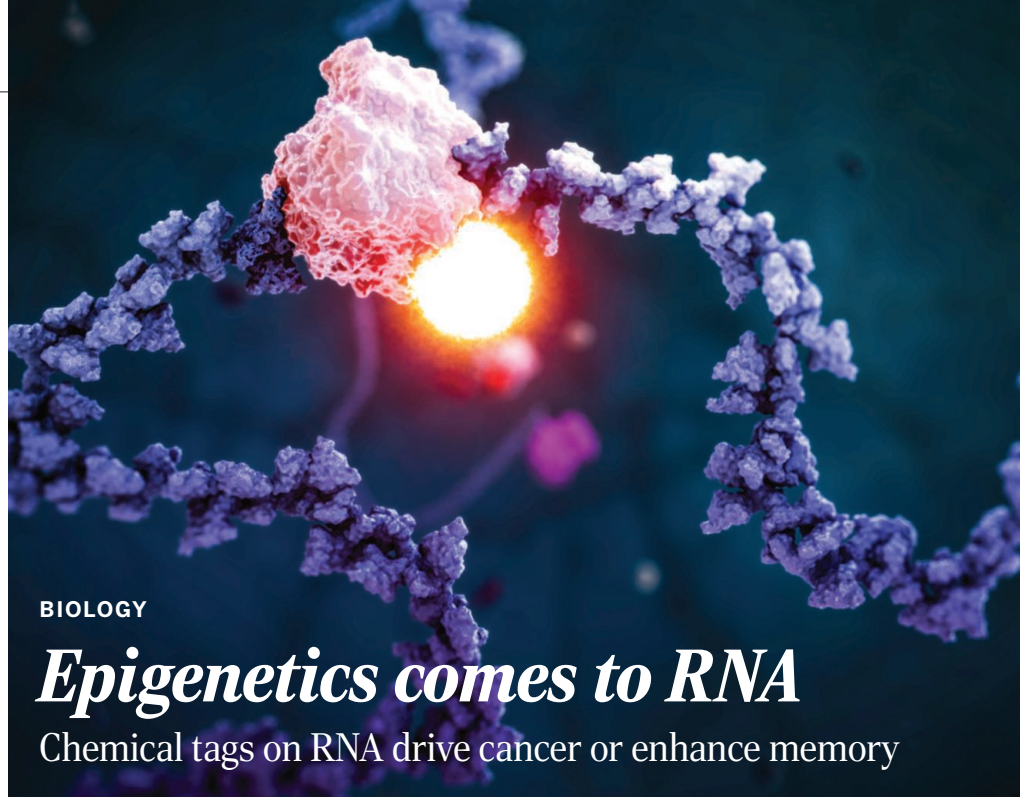

BIOLOGY

Epigenetics comes to RNA

Chemical tags on RNA drive cancer or enhance memory

By **Ken Garber**, *in Chicago, Illinois*

The idea that chemical tags on genes can affect their expression without altering the DNA sequence, once surprising, is the stuff of textbooks. The phenomenon, epigenetics, has now come to messenger RNA (mRNA), the molecule that carries genetic information from DNA to a cell's proteinmaking factories. At a conference here last month, researchers discussed evidence that RNA epigenetics is also critical for gene expression and disease, and they described a new chemical modification linked to leukemia.

Research has found that epigenetic marks decorate mRNAs like Christmas lights on a fence. The cell uses the marks "to determine where, when, and how much of the [associated] protein should be generated," RNA biologist Pedro Batista of the National Cancer Institute (NCI) in Bethesda, Maryland, said at the conference. What's more, says Michael Kharas of Memorial Sloan Kettering Cancer Center in New York City, mRNA modifications "can affect the viability of cells, whether cells divide, cancer, neurologic diseases." They are providing promising leads for drug developers. And, he adds, "There's so many [more] diseases these things could be important in, ones people aren't even looking at."

Modified mRNAs had been reported in the 1970s, but by 2008 they were largely forgotten. Then, Chuan He at the University of Chicago, Samie Jaffrey at Cornell University, and Gideon Rechavi at Tel Aviv University in Israel took a fresh look. Their teams focused on one mRNA modification called m^{6}A: a methyl group—a simple chemical unit—attached to some of an RNA molecule's adenine bases. He's group showed that a well-known enzyme removes this mRNA modification, indicating that m^{6}A has an important biological role, and Jaffrey's and Rechavi's groups developed mapping tools that showed it is widespread. Before the work, researchers knew mRNA epigenetic marks were there, but "they just didn't know how to actually look for them," says NCI researcher Shalini Oberdoerffer.

Of at least half a dozen modifications of mRNA, m^{6}A is the best studied. When proteins called readers attach to it, they direct the fate of the marked mRNA—which can vary dramatically.

For example, m^{6}A boosts gene expression needed for embryonic stem cells to properly differentiate into different cell types. But in blood stem cells, m^{6}A restricts differentiation. In leukemia—a disease of blood stem cells gone awry—m^{6}A sustains disease by keeping the cells in a stemlike state. In 2017, three groups, including Kharas's, independently showed that eliminating the enzyme that places m^{6}A on mRNA kills tumor cells in acute myeloid leukemia. At least three biotech companies are now developing experimental drugs to block such enzymes.

At the meeting, Tony Kouzarides of the University of Cambridge in the United Kingdom reported a new mRNA modification and an associated enzyme that drives leukemia. "I suspect there will be many, many more" links to leukemia, he said.

M^{6}A has also turned out to be critical in the brain. Through its readers, it controls the precise timing of new neuron formation during development in mice and enables

PHOTO: STORM THERAPEUTICS

An enzyme (pink) places a chemical mark (gold) on messenger RNA (blue), in an artist's concept.

axons to regenerate after nerve injury. The modification also enhances memory. When He's team knocked out the gene for an m^6A reader in mice, the otherwise normal animals had memory defects. Injecting a virus carrying the normal reader gene reversed the effect. And when the researchers chemically stimulated the neurons to mimic the addition of a new memory, they saw a burst of protein synthesis that depended on m^6A, they reported last year in *Nature*.

Several years ago, Oberdoerffer followed a hunch that cells might use another simple chemical unit, an acetyl group, on mRNA. Her team reported last year in *Cell* that many mRNA cytosine bases are acetylated. The change boosts translation by stabilizing the molecules, and perhaps also by helping mRNAs match up with the correct transfer RNAs (tRNAs), the small RNA molecules that read the mRNA and add an amino acid to a growing protein chain. When mRNA and tRNA complement each other, they bind, triggering the addition of the amino acid. But the system isn't exact—there are many more possible mRNA sequences than there are tRNAs, so tRNAs must somehow find (and bind to) some mRNAs that don't match.

Oberdoerffer's team found a clue to the mystery: an acetylated mRNA base often sits where a tRNA must recognize the mRNA despite a mismatch. The RNA modification's presence dramatically boosts gene translation, the researchers found. Oberdoerffer doesn't think the modification is necessary for correct mRNA-tRNA recognition, but it may strengthen binding. "I think we will learn that the genetic code as we know it is not a static entity," she says.

Like other fledgling areas of research, RNA epigenetics (also known as epitranscriptomics) has its skeptics. In 2016, one group reported in *Nature* it had found a new modification, m^1A, at more than 7000 sites across a cell's complement of mRNAs. But a year later in the same journal, another group claimed that at most 15 mRNA m^1A sites exist. "Because of that, everyone in the molecular biology community is a little bit suspicious about the validity of these [mRNA] modifications," Jaffrey says.

Other disputes rage over the functions of key enzymes and reader proteins. But epitranscriptomics is evolving fast. "We just need … a lot more knowledge about these things," He says. "We need to stay open minded. The field is still very young." ■

Ken Garber is a journalist in Ann Arbor, Michigan.

PHOTO: COURTESY OF LEON LEVY EXPEDITION TO ASHKELON

ARCHAEOLOGY

DNA reveals European roots of the ancient Philistines

3000-year-old burials identify the enemies of the biblical Israelites and shore up legends of Bronze Age migration

By **Ann Gibbons**

As a schoolgirl in Israel, Michal Feldman learned that the ancient Philistines, who lived between present-day Tel Aviv and Gaza during the Iron Age, were "the bad guys." In the Bible, they were the archenemies of the Israelites, who fought Samson's armies and sent Goliath into battle against David. "Philistine" is still a slur for an uncivilized barbarian.

Now a Ph.D. student in Germany, Feldman has found a new way to understand the Philistines. By analyzing DNA from 12th century B.C.E burials in the Philistines's renowned city of Ashkelon, her team has found that they were interlopers in the ancient Middle East. Their closest known kin were from southern Europe, the team reports this week in *Science Advances*.

Infant burials beneath Philistine houses in Ashkelon, Israel, yielded ancient DNA.

The DNA data suggest a kernel of truth to Greek and Middle Eastern legends that describe survivors who moved south after the catastrophic collapse of great Bronze Age civilizations of the Mediterranean in the late 13th and early 12th centuries B.C.E. "This [DNA] story of migration is tantalizingly close to those memories," says co-author Daniel Master of Wheaton College in Illinois, who leads excavations in Ashkelon, Israel. "This is about real people who are moving from real troubles, finding new families in a new home," adds Assaf Yasur-Landau, an archaeologist at the University of Haifa in Israel who was not part of the study. "It's the most basic human story."

Archaeologists have known for a century that the distinctive ceramic pots and other artifacts that suddenly appeared in 12th century B.C.E. Philistine cities resemble artifacts from the Mycenaean empire of Greece, the ancient power that, according to myth, battled Troy. Egyptian hieroglyphics depict a sea battle with people from the north whom 19th century scholars called the "Sea Peoples." But other scholars think Philistine culture spread when ancient empires in Turkey and Syria declined and local people filled the void.

Master invited Feldman's adviser, paleogeneticist Johannes Krause of the Max Planck Institute for the Science of Human History in Jena, Germany, to try to extract DNA from the teeth and inner ear bones of skeletons excavated in Ashkelon. The team analyzed 1.24 million sites across the genomes of 10 skeletons. Three of the oldest individuals, who lived 3500 to 3700 years ago, were not distinguishable genetically from local Levantine people. But DNA from four infants buried beneath the earthen floors of homes in Ashkelon 500 years later, when Philistine culture first appears, told a different story. They had inherited 25% to 70% of their DNA from southern European ancestors, and the closest matches were to ancient people from the Aegean, Sardinia, and Iberia. The remaining DNA was from local people, suggesting their European ancestors had quickly mated with their new neighbors. Indeed, two styles of pottery in neighboring houses suggest that Philistines and Levantines lived side-by-side in Ashkelon.

Just 200 year later, however, the DNA of three adults, presumably Philistines, fully matched that of local Levantine people. Intermarriage had swamped the genetic heritage of the European immigrants, Krause suggests.

With the study "we finally have real scientific proof that people moved into Ashkelon from Europe," says Kristian Kristiansen, an archaeologist at the University of Gothenburg in Sweden, who suspects they hailed from Italy. But it will take ancient DNA from across southern Europe to pinpoint their homeland. ■

The ethanol in Rob McGinnis's gloved hands was synthesized in the device behind him.

QUEST FOR FIRE

Rob McGinnis aims to use renewable energy to turn carbon dioxide and water into gasoline

By **Robert F. Service**, *in San Francisco, California; Photography by* **LiPo Ching**

On a warm March day here, you could almost mistake Rob McGinnis for a huckster newly arrived in a frontier town as he delivers a rapid-fire pitch to an audience of thousands of would-be investors. McGinnis, a chemical engineer and entrepreneur, isn't hawking snake oil, however: His elixir is gasoline. Nearly everyone in the developed world is hopelessly addicted to it. Collectively, we use nearly 3 trillion liters every year.

At the pitch fair, McGinnis wears the Silicon Valley entrepreneur uniform of jeans, a black T-shirt, and black leather biker boots. On a theater-size stage, he delivers his spiel, sandwiched between 3-minute presentations for an online personalized clothing store and an outfit that would rent scooters by the month. "We make gasoline from air, water, and electricity," McGinnis announces. "Today, gasoline sells for $3.50 a gallon in California. Next year, we will be selling it for $3 per gallon." Other startups peddling ideas at the fair foresee markets in the billions, but McGinnis aims higher. "We're talking about a $2 trillion [per year] gasoline market," he says.

If all that sounds too good to be true, it might be. "I hope they're right," says Olgica Bakajin, CEO of Porifera Inc., a San Leandro, California, company that has also worked on systems like those at the heart of McGinnis's fuelmaker. But she notes that McGinnis "is a good talker who sells things well."

He has convinced some powerful investors. In December 2018, he received $150,000 from Y Combinator, the Mountain View, California, seed funder hosting the pitch fair, to build a prototype of his air-to-gasoline–maker. The result was a refrigerator-size contraption of catalysts, tubes, electronics, and filters, assembled a week before the pitch fest.

But before the demo, the machine sprang a leak. Although it wasn't operating at the pitch fest, McGinnis's optimism was. He promised audience members that the repaired device would extract carbon dioxide (CO_2) from the air, add it to water, and use a catalyst to rearrange the chemical bonds to make hydrocarbons. The result: fossil fuel without the fossils. "It can sound like magic, but it's really just chemistry," McGinnis told the audience.

SYNTHESIZING GASOLINE, instead of refining it from oil, isn't a new idea. German chemists in the 1920s discovered they could turn coal into carbon monoxide (CO) and hydrogen—a combination known as synthesis gas. Catalysts, along with heat and pressure, could then transform synthesis gas into gasoline and other liquid hydrocarbons.

But McGinnis's setup requires no heat, pressure, or coal. It uses only air, water, and electricity, which can come from the sun or wind. And with those renewable resources becoming ever cheaper, he's betting he can deliver gasoline more economically—and far more cleanly—than companies that must find oil, drill for it, ship it, and refine it.

Several other startups and academic labs are pursuing the same dream. "There has been a lot of progress in the last few years" in turning CO_2 into more-complex compounds, says Peidong Yang, a pioneer in the field at the University of California, Berkeley.

Yet many of those efforts have stumbled over the expensive, energy-intensive steps needed to separate the hydrocarbons from the water they are produced in. Prometheus relies instead on a proprietary carbon nanotube membrane sieve that it says readily parts the hydrocarbons from water. "If they indeed have a low-energy separation process, that solves a big problem," Yang says.

"Rob's approach has a good chance of competing with fossil fuels," says Matthew Eisaman, a physicist at the State University of New York in Stony Brook who consults for Prometheus. Eisaman ran a now-mothballed research program at Google's research arm, Google X, that aimed to turn the CO_2 in seawater into liquid fuels.

Bruce Hinds, a nanotube membrane expert at the University of Washington in Seattle, says McGinnis's published results on his separation technology inspire confidence that the approach could work. "I'm highly encouraged," Hinds says.

McGinnis has long defied expectations. After high school, he enlisted in the Navy, which sent him to Bahrain during the first Gulf War. There, he cleared mines from battlefields and harbors. "I didn't want to do it," he says of his time in the service, but he needed money for school. He enrolled in Cabrillo College, a public community college near Santa Cruz, California, where he dreamed up an energy-efficient approach to desalinating water during a chemistry class. Today, most water desalination uses reverse osmosis, which employs energy to push water through a membrane that excludes salts. McGinnis planned instead to use forward osmosis, which relies on differences in the concentration of compounds on either side of a membrane to move water across; it consumes only about half as much energy. "I prototyped it in my kitchen," he says. "I wanted something to distinguish myself to [transfer] to a really good school."

His school plan worked, and McGinnis moved to Yale University for his junior year. He majored in theater and focused on playwriting. "It was really good training," he says. "A lot of what entrepreneurs do is tell stories."

But he never gave up on science. McGinnis canvassed the chemistry faculty to see whether anyone would let him use lab space in the evenings to pursue desalination. Menachem Elimelech, a Yale chemical engineer, agreed. McGinnis later pursued a Ph.D. in Elimelech's lab, constructed a forward osmosis demonstration, and helped launch a startup company called Oasys Water in Cambridge, Massachusetts, to commercialize the technology. Oasys built five large water treatment plants in China and was eventually bought out by its customer there.

Even before the buyout, McGinnis felt sidelined from decision-making. He left Oasys in 2012 to explore other ideas for improving membranes for separations, initially looking for even better ways to purify water. He chose to pursue membranes made from thin plastic sheets shot through with myriad carbon nanotubes—tiny hollow tubes made entirely from carbon atoms. Researchers at Lawrence Livermore National Laboratory in Califor-

Making fuel out of thin air

At the heart of a new fuelmaking machine are pipes shot through with tiny carbon mesh tubes that filter fuel from water using little energy. The fuel comes from an electrochemical process that combines water (H_2O) with carbon dioxide (CO_2) from the air.

Graphic by **Chris Bickel**

Combustion in reverse

Electricity and a copper surface convert CO_2 and H_2O into ethanol, an alcohol that can link into longer fuel molecules.

1 CO_2 reacts with H_2O to form carbonic acid (H_2CO_3).

2 Electricity converts carbonic acid to carbon monoxide (CO) and hydroxide (OH^-) on copper surface.

3 CO and H_2O react at copper surface to make ethanol.

4 Zeolite catalyst converts multiple alcohols to larger fuel molecules.

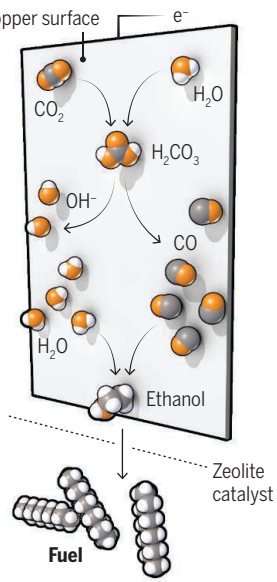

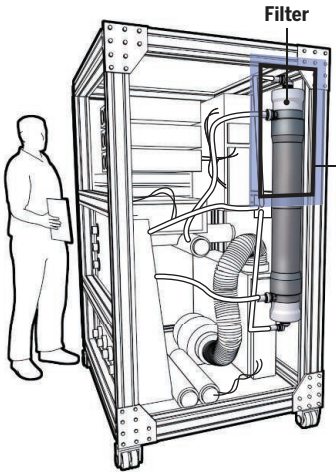

A prototype fuelmaker
Prometheus's machine houses the entire process, from CO_2 capture to ethanol synthesis. If the device is powered with renewable electricity, using the fuel releases zero net greenhouse gases.

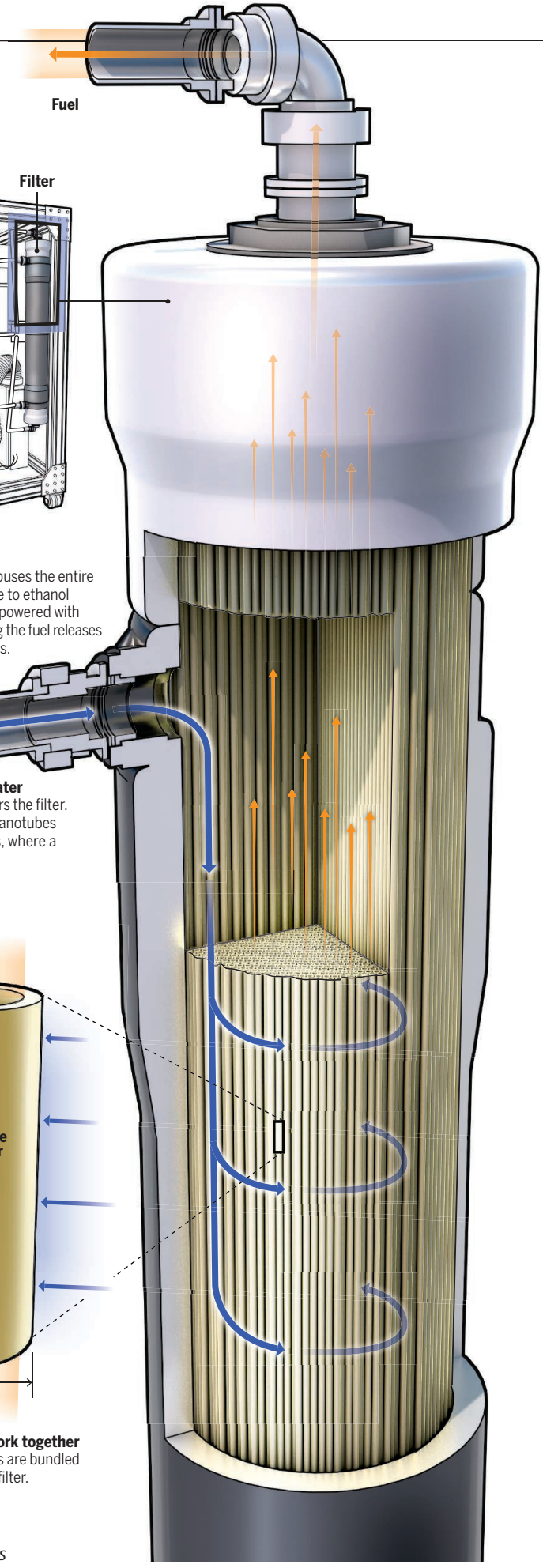

The ultimate filter

Cheap plastic sheets house trillions of carbon nanotubes per square meter, which zip alcohols through (orange) while blocking H_2O (blue).

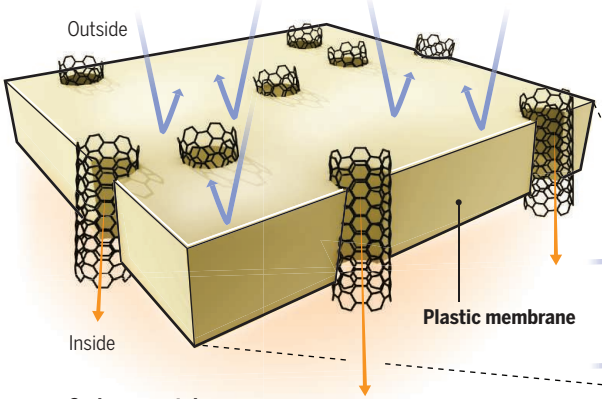

Carbon nanotubes
For filtering fuel, the best hollow carbon tubes are about 1 nanometer (nm) in diameter.

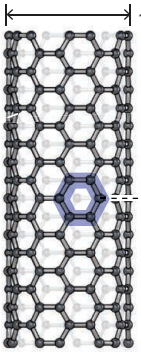

Atomic pattern
Connected rings of carbon atoms roll up into hollow tubes.

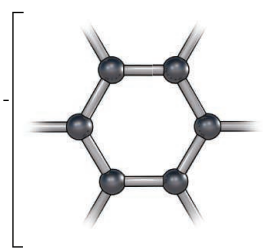

Published by AAAS

nia and elsewhere had shown that the tiny channels allow water to pass through while blocking other molecules. But the lab demonstrations employed dime-size membranes; larger membranes leaked and weren't uniform. "Carbon nanotube membranes never lived up to the hype," says Jeffrey McCutcheon, a membrane separation expert at the University of Connecticut (UConn) in Storrs who collaborates with McGinnis.

McGinnis thought he could solve the problem. He formed a company called MatterShift and received lab space in a startup incubator at UConn. After 5 years, he could make uniform membranes the size of a sheet of paper, consisting of carbon nanotubes embedded in a cheap commodity plastic called polyethersulfone.

The key, McGinnis says, was figuring out how to align vast numbers of nanotubes—roughly 2.5 trillion per square meter—so that most pierce the membrane perpendicularly, as ion channels on a cell surface do. Some researchers have speculated that magnetic fields are key to the process, but McGinnis isn't saying. "It's our secret sauce," he says.

In March 2018, he, McCutcheon, and colleagues reported one possible use for their membranes in *Science Advances*: filtering out organic contaminants, such as odor-causing compounds, from water, while applying only a fraction of the pressure used to push water through reverse osmosis membranes. But McGinnis sees that use as a demonstration rather than his primary commercial target.

In the past year, he and his team have come up with a way to transform their membranes from flat sheets into narrow hollow plastic fibers dotted with nanotube pores. The researchers can manufacture those fibers in a continuous process, McGinnis says, cutting them to any length and bundling them to make industrial filters.

THE NANOTUBE FILTERS can perform a far more important feat than removing contaminants, McGinnis says: They separate ethanol from water. Carbon nanotubes of the right diameter—about 1 nanometer—transport ethanol more quickly than water through their interior. McGinnis explains that ethanol's carbons have an affinity for the inside of the carbon nanotubes. So if the starting liquid contains at least 5% to 10% ethanol and a slight vacuum draws it through the filter, the alcohol molecules form a molecular conga line through the nanotubes, excluding nearly all water. The filtered solution winds up containing about 95% ethanol.

McGinnis and his team haven't published those separation results yet. But researchers led by Yang Decai from Dalian University of Technology (DUT) in China reported in August 2018 in *Nano Letters* that a similar carbon nanotube membrane was highly selective and fast at separating ethanol and butanol (another alcohol) from water.

If commercialized, such membranes could benefit biofuel companies that make ethanol from corn, McGinnis and others say. Fermentation leaves a solution of 10% ethanol in water. Today, ethanol producers use heat and 6-meter-tall distillation columns to boil off the ethanol, an energy-intensive process that costs about a third as much as the alcohol itself. McGinnis says his membranes could cut the distillation cost by 90% in an ethanol market worth $50 billion per year in the United States.

If the membranes work as claimed, "That by itself would be big," Peidong Yang says.

McGinnis is working to prove that they do. Last year, MatterShift and partners at UConn received a $900,000 grant from the Department of Energy to demonstrate their ethanol separation technology. Their test uses a 2-meter-high tube with 1400 nanotube-pocked fibers, with results expected this summer.

If either MatterShift's or DUT's membranes prove durable and long-lived, bioethanol producers should represent an eager market, says David Sholl, a chemical engineer at the Georgia Institute of Technology in Atlanta. McGinnis has already founded a company called MatterShift Biofuels to commercialize the technology. But he envisions a bigger future for his membranes: not just filtering ethanol fermented from corn or sugar, but also purifying fuel made from the air itself.

Synthesizing the fuel is the easy part. Peidong Yang's team and groups at Oak Ridge National Laboratory (ORNL) in Tennessee and the University of Illinois in Urbana have published papers in the past 3 years showing that electricity and nanosize copper catalysts can turn CO_2 and water into a mix of alcohols. And startups including a New Orleans, Louisiana, company called ReactWell are pursuing related approaches.

Thus far, the ORNL team has reported the highest efficiency, turning 23% of the electrical energy into fuel. But all the groups using the approach to make alcohols face the challenge of separating the fuel from the water. McGinnis says his membranes are the answer. They are "the new piece in the puzzle no one else has."

In the air-to-fuel machine he hoped to demonstrate at Y Combinator, the membranes filter a liquid that flows from a meter-wide chamber containing two electrodes dunked in water. When air blows through the chamber, the CO_2 it contains reacts with water, producing carbonic acid—the same molecule acidifying the oceans. That acid, in turn, reacts on a copper catalyst coating the negative electrode, or cathode, to create CO. The cathode also strips protons off water molecules, leaving behind negatively charged hydroxide ions. Those ions travel to a positively charged electrode, or anode, where they react to form water and oxygen gas. Meanwhile, at the cathode, multiple CO molecules and protons are transformed into ethanol and other alcohols.

The result is the alcohol and water mixture that goes through the nanotube fibers. Prometheus has repaired its machine since the pitch fair, and it produces "a pretty steady drip" of fuel, McGinnis says: 10 milliliters per hour of alcohol that trickles out a red valve in the back. Over the next month, McGinnis and his colleagues plan to increase the size of their electrodes and catalysts to raise the production rate to 50 to 100 milliliters per hour.

Ultimately, McGinnis plans to add a second catalytic step using commercially available catalysts called zeolites, which would convert the mix of alcohols to the larger hydrocarbon molecules found in gasoline. "All of the pieces of this process have been proved to work. But no one has put them all together," he says. "Until now." He expects the device, when optimized, to produce 20 liters of gasoline per week.

Once the machine is working efficiently, electricity will make up about one-third of its operating costs. Renewable electricity prices around the globe are falling, however, and they already sink near zero at certain times of the day in places where the sun blazes or the wind howls. Prometheus, McGinnis says, could easily ramp its electricity demands up and down to take advantage of the lowest rates, and the machines could be sited wherever renewable power is cheapest. Next year, the company plans to build a $500,000 shipping container–size demonstration plant that can produce hundreds of thousands of liters of fuel per year. And last month, it inked its first deal, to begin to sell carbon-neutral fuel to Boom Supersonic, a Denver company building a supersonic commercial airliner.

Even if all goes according to plan, McGinnis will face a long road to compete with the likes of ExxonMobil. He'll have to prove he can build a fuelmaker cheaply enough to make its gasoline affordable. That could be tough if turning it on makes sense only when renewable electricity prices bottom out. The fuelmaker also works only with a source of clean water. And before he can market his invention, he'll need to prove that his fuels can directly substitute for fossil-derived versions.

At the pitch fair, McGinnis stands next to his prototype and repeats his story for a steady stream of potential investors. "We want to replace all fossil gasoline," he says. "That would make the world a better place." A few hours later, he loads up his wares and moves on in the hope that one day his dreams turn into an energy revolution. ■

INSIGHTS

LETTERS

NEXTGEN VOICES

Pithy burnout prevention

We asked young scientists this question: **In exactly six words, what is the secret to preventing burnout?** In their succinct responses, scientists from around the world suggested ways to prioritize breaks, focus on the positive, and find inspiration in work, hobbies, and community. Our respondents urged researchers facing burnout to take care of themselves, whether that means setting boundaries or giving themselves permission to splurge. Follow NextGen on Twitter with hashtag #NextGenSci. See all NextGen Voices results at https://science.sciencemag.org/collection/nextgen-voices. —**Jennifer Sills**

Invest in hobbies

Improve a skill unrelated to research.
Ming-Ju Amy Lyu, *China*

Walk while listening to soothing songs.
Jian Zhang, *China*

Incorporate parkour tricks into coffee runs.
Raf Aerts, *Belgium*

Channel exhaustion to creativity; art works!
Shruti Sharma, *USA*

Sing loudly! It's socially acceptable screaming.
Tiffany Phu, *USA*

Rescue a dog, catalyst for joy.
Matt Joseph Kuhn, *USA*

Regenerate neurons by exercising. Start yesterday.
Athanasia Nikolaou, *Germany*

Do something that brings joy daily.
Carson Alice Wills, *USA*

Beer tastings count as field research.
Beth McKinnon Adamowicz, *USA*

Watch kitten videos during conference calls.
Aric S. Campling, *USA*

Cultivate community

Chilling with friends makes me fireproof.
Vanessa Karina Alves da Silva, *UK*

Work with people who respect you.
Marion White, *USA*

Tell your supervisor about your feelings.
Clara del Junco, *USA*

PHOTO: POPARTIC/ISTOCKPHOTO.COM

Published by AAAS

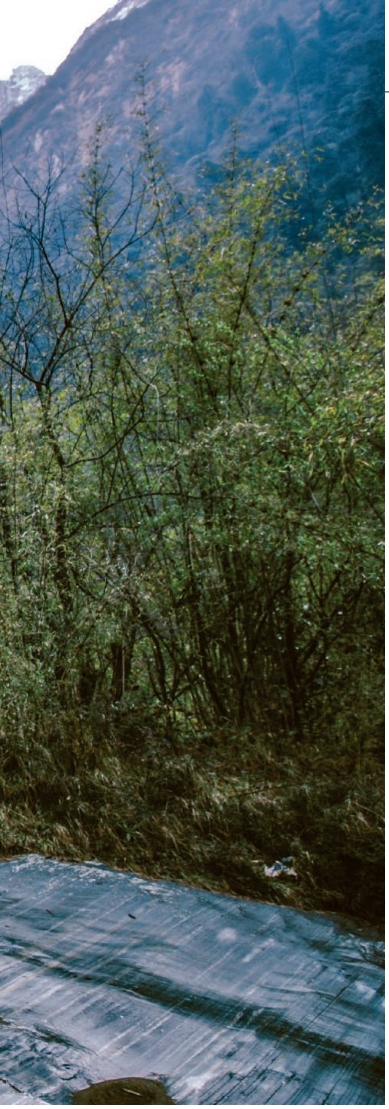

Intentionally cultivate honest, supportive work friendships.
Rosalie Shinwei Doerksen, *USA*

Margaritas with temporary friends at conferences!
Heather Burkin, *USA*

Recognize other people's confidence in you.
Jonathan Marquez, *USA*

Coffee with lab friends is indispensable.
Joel Henrique Ellwanger, *Brazil*

Team sports and friends outside academia.
Andrés S. Rigual Hernández, *Spain*

Cook elaborate meals for your friends.
Leah Cairns, *USA*

Take your time and get support.
Ingrid Zuniga, *Mexico*

Read bedtime stories to the kids.
Ben de Haas, *Germany*

Set intentional goals

Find permanent positions with permanent funding!
Sacha Escamez, *Sweden*

Find work that fits your personality.
Robert P. Tett, *USA*

Share long-term ambitions with collaborators.
Yuta Igarashi, *Japan*

Define your target. Focus on it.
Allison Matia, *USA*

Set relevant, achievable, and short-term goals.
Marcela Viviana Nicola, *Argentina*

Divide big projects into smaller tasks.
Lin Wang, *France*

Celebrate success

A glass of beer after brainstorming.
Luiz H. Varzinczak, *Brazil*

Dance, listen to music when stressed.
Karishma Shaik, *India*

Impromptu, solo dance parties to Toto.
Déna Jansen, *South Africa*

Recurring break to garden and hike.
Aminata Coulibaly, *USA*

Learn to enjoy the small successes.
Satyanarayana Subrahmanyam, *India*

Remember the wins and stay grateful.
Caitlin M. Aamodt, *USA*

Acknowledge and celebrate team's progress weekly!
Salma Kaochar, *USA*

Delight in the success of colleagues.
Catherine Carbone, *USA*

Find meaningful reward in the journey.
Carol Lee Wilkinson, *USA*

Maintain perspective

Try your best. Let it be.
Junxiang Cheng, *China*

Remember!
You are not your job.
Rachel Hale, *New Zealand*

Keep the big picture in mind.
Sarah Ch'ng, *Australia*

Recall why and how you started.
Jing Woei Li, *Hong Kong*

Have something more important in life.
Amanda Linnea Karolina Jonsson, *USA*

Love yourself more than your work.
Mallory Rose Peterson, *USA*

Recognize burnout's systemic, not personal failure.
Rachel Yoho, *USA*

See the inner child in everyone.
Joseph Michael Cusimano, *USA*

Focus on the joy of discovery.
Richard Gaughan, *USA*

Bonfire: Reviewer 2's comments as kindling.
Colin Murphy, *USA*

Prioritize self-care

Mindful breathing, 15 minutes every day.
Oriana Jovanović, *Hong Kong*

Sleep! Even Einstein got 10 hours.
Josiah Dykstra, *USA*

Appropriately titer your caffeine:ethanol ratio.
Kelvin Yen, *USA*

Invest in yourself and experiments equally.
Victoria Tokarz, *Canada*

Know limits; take care of yourself.
Ruwansha Galagedara, *Sri Lanka*

Resting creates space for great ideas.
Ingrid Olivares, *UK*

Internet-free day keeps burnout away!
Martin Schwarzer, *Czech Republic*

Regular breaks, including a postlunch nap.
Rambabu Korrapati, *India*

Talk with a mental health professional.
Carl Davidson Gandola, *USA*

Set boundaries

Delegate all tedious work to minions.
Thomas Alejandro Berrueta, *USA*

Work actual contract hours, not weekends.
Klaudija Daugelaite, *France*

Honor and respect work-life balance.
Shahienaz Hampton, *United Arab Emirates*

Remember, "breakthrough" starts with a "break."
Anne-Sophie Hafner, *Germany*

Thou shall not do it all!
Mac Kevin Ella Braza, *Philippines*

Realize long hours don't equal productivity.
Edward Lau, *USA*

Do not take on unnecessary responsibilities.
Evrim Fer, *Turkey*

The secret: Learn to say "No."
María Romina Schiaffino, *Argentina*

Refuse to do what doesn't matter.
Shervin Fatehi, USA

Splurge

Indulge in guilty pleasures without remorse.
Yong Tang, *USA*

Give yourself permission to be selfish.
Howard M. Huynh, *Canada*

Ignore serving size suggestions on snacks.
Do Soon Kim, *USA*

Eat cake...Didn't work? Eat more!
Michael Patrick Schwoerer, *USA*

Sugar is brain food. Keep snacking.
Emily Royse, *USA*

Coffee before lab. Goodbye, steady hands!
Mark Martin Jensen, *USA*

Ditch that coffee and just snooze.
Charles Teta, *South Africa*

Clean house. Just joking. Netflix binge.
Ken Dutton-Regester, *Australia*

Conference in Hawaii. Don't attend talks.
Soham Saha, *USA*

Deep breathing (if inhaling food counts)
Dhruv Patel, *USA*

10.1126/science.aay2936

PERSPECTIVES

Restored and regenerated forest in the Reserva Ecológica de Guapiaçu, Brazil illustrates how forests can regain maximum potential canopy cover.

ECOLOGY

Restoring forests as a means to many ends

An urgent need to replenish tree canopy cover calls for holistic approaches

By **Robin Chazdon** *and* **Pedro Brancalion**

Earth is approaching environmental thresholds that, if crossed, will create serious disruptions to ecosystems, economies, and society (*1*). To avoid the devasting effects of climate change and biodiversity loss, humanity must protect and restore native ecosystems (*2*). International conventions and organizations support forest restoration as a method for mitigating hazardous environmental shifts, but questions remain as to where and how to focus such restoration efforts. On page 76 of this issue, Bastin *et al.* (*3*) describe a new approach that advances our understanding of global tree distribution.

Prevailing views on how to assess forest cover and restoration opportunities might actually hinder rather than promote the large-scale action needed. Traditional methods for evaluating changes in forest cover are based on a dualistic (forest/nonforest) classification of land use that applies a subjective threshold to the 0 to 100% canopy-cover gradient (*4*). Bastin *et al.* move beyond this strict dichotomy with the use of direct photo-interpretation measurements that account for wooded lands that lie outside forest areas. The authors identify the global potential for enhanced tree canopy cover on the basis of variations in natural levels of tree cover, which has immediate implications for restoring forest cover. Test scenarios that assess how future climate change will affect global canopy cover emphasize the urgency of taking action now, as shifting responses of forests to climate change are already under way and will become far more pronounced.

This urgency of restoring tree cover does not justify short-term fixes that fail to produce environmentally and socially beneficial long-term outcomes. An assessment of the biophysical capacity for restoring global tree cover provides a necessary but insufficient foundation for evaluating where tree cover can be feasibly increased. The kinds of trees as well as how and where they are grown determine how and which people benefit. In some contexts, increasing tree cover can elevate fire risk, decrease water supplies, and cause crop damage by wildlife. Reforestation programs often favor single-species tree plantations over restoring native forest ecosystems. This approach can generate negative consequences for biodiversity and carbon storage (*5*), threaten food and land security, and exacerbate social inequities. How restored lands are governed determines how reforestation costs and benefits are distributed.

Without attention to these social and environmental issues, efforts to rapidly increase tree cover are likely to prove ineffective in the long term. Initiated by Germany and the International Union for Conservation of Nature in 2011, the Bonn Challenge has garnered 58 commitments to restore 170 million hectares of forest land by 2030. The Global Deal for Nature (*6*) proposes that 30% of Earth's surface be formally protected and an additional

Restoration systems deliver multiple benefits

A forest restoration system integrates structures (trunk and roots) that assimilate and distribute resources (soil) to initiate and sustain restoration outcomes (branches). The system ultimately delivers myriad benefits for nature and humanity (fruits). Restoration outcomes and benefits sustain the system, stabilize enabling conditions, and increase capital stocks.

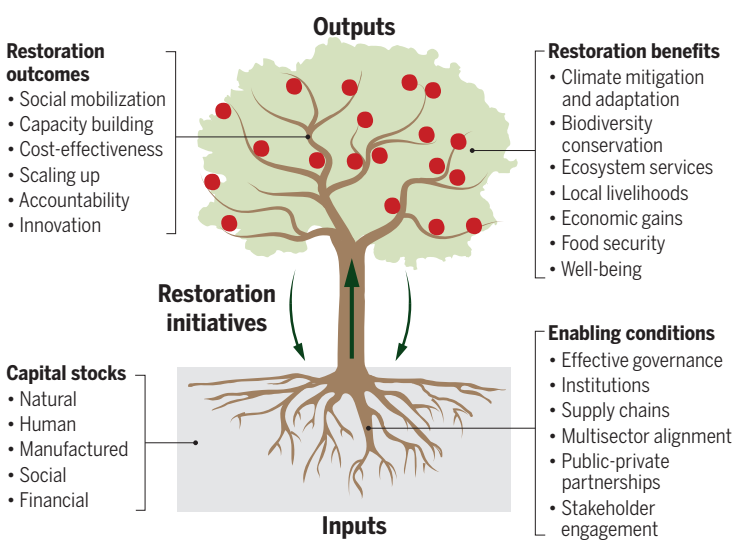

[1]*Department of Ecology and Evolutionary Biology, University of Connecticut, Storrs, CT 06269, USA.* [2]*Department of Forest Science, Universidade de São Paulo, Escola Superior de Agricultura Luiz de Queiroz, Piracicaba, São Paulo, Brazil. Email: robin.chazdon@uconn.edu; pedrob@usp.br*

CREDITS: (PHOTO) ROBIN CHAZDON; (GRAPHIC) N. CARY/*SCIENCE*

20% designated as climate stabilization areas by 2030, to stay within 1.5°C of global temperature rise.

Reaching ambitious restoration targets appears unlikely, however, without practical guidelines and tools, institutional alignment, accountability mechanisms, and a robust evidence base. Enormous gaps remain between high-level focus on restoration and implementation on the ground (*7*). Forest restoration programs are largely conducted on project scales by using approaches that are neither cost effective nor designed to achieve multiple benefits and long-term sustainable outcomes (*8*). In contrast to such site-based practices, forest and landscape restoration is a holistic approach; it aims to balance diverse types of tree cover to achieve multiple benefits, based on the local socio-ecological context and stakeholder engagement (*9*). This landscape approach is vital to reaching the global scales needed to reverse the effects of deforestation and land degradation.

Forest restoration is a mechanism to achieve multiple goals, including climate mitigation, biodiversity conservation, socioeconomic benefits, food security, and ecosystem services. A living tree helps to illustrate the components of a holistic forest restoration system (see the figure). The above-ground portions of the tree are the trunk (restoration initiatives), branches (restoration outcomes), and fruits (restoration benefits). Below the ground are soil (capital stocks) and root structures that assimilate and distribute resources and create enabling conditions.

Viewing restoration as a system also guides appropriate mechanisms to mobilize resources in cost-effective ways. One such mechanism is to use the best available spatial information to identify areas where the most beneficial and feasible restoration outcomes intersect (*10*). Bastin *et al.* clearly show that we have a narrow window of time in which to restore global tree cover. We need to act quickly, intelligently, holistically, and globally. Doing so will require planting and sustaining of restoration systems wherever new types of canopy cover are needed. ■

ILLUSTRATION: STEPHAN SCHMITZ

REFERENCES AND NOTES

1. W. Steffen *et al.*, *Proc. Natl. Acad. Sci. U.S.A.* **115**, 8252 (2018).
2. B. W. Griscom *et al.*, *Proc. Natl. Acad. Sci. U.S.A.* **114**, 11645 (2017).
3. Food and Agriculture Organization of the United Nations (FAO), *Global Forest Resources Assessment 2015. How Are the World's Forests Changing?* (FAO, 2015).
4. J.-F. Bastin *et al.*, *Science* **365**, 76 (2019).
5. S. L. Lewis *et al.*, *Nature* **568**, 25 (2019).
6. E. Dinerstein *et al.*, *Sci. Adv.* **5**, eaaw2869 (2019).
7. R. L. Chazdon *et al.*, *Conserv. Lett.* **10**, 125 (2017).
8. K. D. Holl, *Science* **355**, 455 (2017).
9. S. Mansourian, J. Parrotta, Eds., Forest Landscape Restoration: Integrated Approaches to Support Effective Implementation (Routledge, 2018).
10. P. H. S. Brancalion *et al.*, *Sci. Adv.* **5**, eaav3223 (2019).

10.1126/science.aax9539

GENOME EDITING

Inserting DNA with CRISPR

Inserting large DNA segments with CRISPR holds great promise for genetic engineering

By **Zhonggang Hou** *and* **Yan Zhang**

Most prokaryotes rely on the CRISPR-Cas system for adaptive immunity against viruses and mobile elements (*1*, *2*). Small RNAs produced from CRISPR direct Cas effector proteins to seek and destroy nucleic acids from invaders that have complementary target sites (*3*). There are multiple types of CRISPR, which are defined on the basis of their protein composition. Recently, RNA-guided nucleases from types II and V CRISPR systems, Cas9 and Cas12, have revolutionized genome editing by allowing programmed DNA sequence alterations (*4*). However, robust and targeted insertion of a large DNA segment into eukaryotic genomes has remained challenging. On page 48 of this issue, Strecker *et al.* (*5*) show that a CRISPR-associated transposase (CAST) mediates highly efficient, RNA-guided insertion of cargo DNA into the bacterial *Escherichia coli* genome. Moreover, Klompe *et al.* (*6*) report another CRISPR-guided DNA transposase system that operates similarly. These studies offer new tools that could transform genetic engineering and gene therapy research.

In a typical CRISPR application, Cas9 or Cas12 is directed by its guide RNA to the intended complementary genomic site flanked by a protospacer-adjacent motif (PAM), and creates a DNA double-strand break (DSB) (*4*). The outcome of gene editing largely depends on the repair of this DSB by the endogenous pathways in the host cell. Repair by end-joining DNA repair pathways often predominates and tends to introduce heterogeneous small DNA insertions or deletions (indels) that disrupt a gene's function. However, many applications require site-specific knock-in of large DNA segments, such as a therapeutic gene or reporter genes. This can be achieved through accurate DSB repair by the homology-directed repair (HDR) pathway, which requires long sequence homology between a supplied DNA template and the genomic regions flanking the insertion site. HDR is inefficient and often restricted to certain stages of the cell cycle or by cell type (*7*, *8*). Therefore, there is an urgent need for tools that enable robust and targeted DNA integration.

DNA transposons, also known as "jumping genes," can move from one genomic location to another, and their relocations and insertions are catalyzed by an enzyme complex called transposase. Since 2017, the CAST systems have been discovered through bioinformatics mining of new CRISPR variants (*9*, *10*). CAST comprises a miniature type I or V CRISPR-Cas encoded within a Tn7-like transposon. The mini-CRISPR systems encode protein machineries that either lack the Cas3 nuclease-helicase of the type I CRISPR system or carry inactivating mutations in the catalytic residues of Cas12k of the type V system. Accordingly, they could be competent for target sequence binding but not for DNA cleavage. It is speculated that these defective CRISPRs have been hijacked by Tn7-like transposons to serve a role other than

Department of Biological Chemistry, University of Michigan. 1150 W. Medical Center Drive, Ann Arbor, MI 48109, USA. Email: yzhangbc@med.umich.edu

prokaryotic adaptive defense. Instead, they might increase the evolutionary success of transposons by enabling their RNA-guided spread across bacterial genomes and other mobile DNA elements (*9*, *10*). The putative RNA-programmable nature of CAST contrasts with the poor target site selectivity of canonical transposases, which insert their cargo DNA semirandomly.

Strecker *et al.* established the functionality of two CAST loci from cyanobacteria *Scytonema hofmanni* (Sh) and *Anabaena cylindrica* (Ac) in vivo and elucidated the underlying mechanism. Each CAST locus is ~20 kilobases, comprising Tn7-like transposase genes (*tnsB*, *tnsC*, *tniQ*), additional cargo genes, and genes encoding a type V-K CRISPR and its effector Cas12k as well as trans-activating crRNA (tracrRNA), which is an invariant small RNA cofactor that is essential for Cas12k. The authors assayed potential transposition into plasmid DNA in the heterologous host *E. coli*. A helper plasmid encoding all CAST protein and RNA components was delivered into *E. coli*, together with a donor plasmid and a target plasmid (see the figure). Targeted donor integration occurred in one specific orientation, with an efficiency of 13 to 75%. Integration was guided by CRISPR-Cas12k, because it requires tracrRNA, a cognate target, and a 5′ flanking GTN PAM. Most notably, the insertion sites were clustered unidirectionally within a narrow window of DNA sequence, 60 to 66 base pairs for ShCAST and 49 to 56 base pairs for AcCAST, downstream from the PAM. Donor cargo DNA of up to 10 kilobases was integrated efficiently into the target plasmid.

The PAM and target sequence for CRISPR-Cas12k remain intact after transposition, yet they cannot support additional rounds of effective CAST integration into the same downstream region that already received a copy of the transposon. This observation resembles the "target immunity" phenomenon where bacterial T7 transposon avoids repeated insertion into the same site (*11*). Notably, the 5–base pair sequence before each integration site is duplicated to flank the other end of the inserted DNA. This is consistent with staggered single-stranded DNA gaps generated by T7 transposons (*12*), which are presumably sealed by gap-filling host factors. Taken together, CAST is a bona fide CRISPR-guided, prokaryotic transposon.

Strecker *et al.* reconstituted CAST-catalyzed DNA insertion in vitro and also demonstrated that CAST could be repurposed as a targeted DNA insertion tool for bacterial genome engineering. ShCAST was reprogrammed against 48 different target sites in noncoding regions of the *E. coli* genome and achieved targeted insertion at 29 loci. For a few sites, the efficiencies are impressively high (50 to 80%), obviating the need for positive selection to detect transposition. Insertions were also profiled on a genome-wide scale using unbiased deep sequencing. Approximately half of the total insertions were on-target, whereas the off-target insertions were scattered along the chromosome. Many of the top off-target sites occurred repeatedly between *E. coli* samples for distinct guide RNAs and thus are likely caused by a CRISPR-independent mechanism. Limiting the amount of transposase produced in the cells may help reduce off-target effects.

Klompe *et al.* characterize a transposon from bacteria *Vibrio cholerae* that employs a mini–type I CRISPR-Cas to insert cargo DNA in two possible orientations. The integration is CRISPR-guided and robust, and displays low (less than 10%) off-target activity.

Can we leverage the CRISPR-guided DNA transposase systems reported by Strecker *et al.* and Klompe *et al.* for highly efficient, targeted genome integration in eukaryotes? Compared to the current viral- or transposon-based therapeutic gene delivery into human cells (*13*), CRISPR-guided DNA transposase systems could be used to insert custom genes into the desired site and therefore avoid oncogenic risks associated with random genomic integration. Unlike Cas9- or Cas12-based editing tools, CRISPR-guided DNA transposase systems do not require DSB repair by the host HDR pathways, and therefore may enable highly efficient gene knock-ins in a wider variety of cell types and tissues. However, a limitation is that the terminal ends of the transposon will be incorporated together with the intervening cargo DNA, making applications that require "scarless" insertion impossible. The discovery of the CRISPR-guided DNA transposase systems again illustrates the power of bioinformatic mining of microbial genomes in uncovering new CRISPR variants with functions beyond defense (*9*, *10*). As more CRISPR-linked accessory genes are discovered, the noncanonical facets of CRISPR biology will be further revealed (*14*, *15*). ■

CRISPR-guided DNA insertion

CRISPR-associated transposase (CAST)–mediated DNA insertion is guided by CRISPR-Cas12k. The inserted transposon can include cargo DNA for genetic engineering.

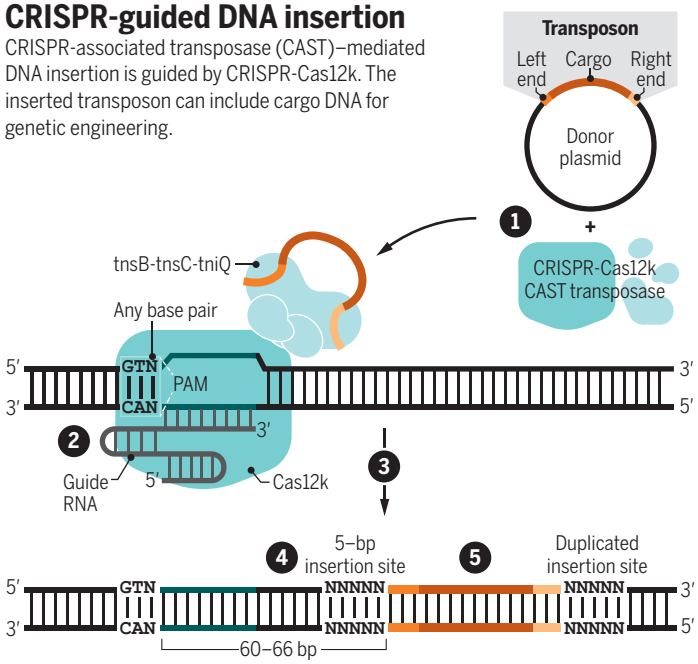

1 CAST system is delivered to cells.

2 CAST locates the target DNA sequence in host cells via guide RNA–target complementarity and a flanking PAM recognized by Cas12k.

3 CAST components mediate robust cargo DNA insertion, which does not require DNA double-strand break repair by host cell pathways.

4 Integration in the host genome occurs 60 to 66 base pairs (bp) downstream of PAM.

5 Transposon ends and the intervening custom DNA cargo are inserted in one orientation.

GRAPHIC: V. ALTOUNIAN/*SCIENCE*

REFERENCES AND NOTES

1. R. Barrangou *et al.*, *Science* **315**, 1709 (2007).
2. K. S. Makarova *et al.*, *Nat. Rev. Microbiol.* **9**, 467 (2011).
3. S. J. Brouns *et al.*, *Science* **321**, 960 (2008).
4. G. J. Knott, J. A. Doudna, *Science* **361**, 866 (2018).
5. J. Strecker *et al.*, *Science* **365**, 48 (2019).
6. S. E. Klompe, P. L. H. Vo, T. S. Halpin-Healy, S. H. Sternberg, *Nature* (2019). 10.1038/s41586-019-1323-z
7. M. Heidenreich, F. Zhang, *Nat. Rev. Neurosci.* **17**, 36 (2016).
8. A. C. Komor, A. H. Badran, D. R. Liu, *Cell* **168**, 20 (2017).
9. J. E. Peters, K. S. Makarova, S. Shmakov, E. V. Koonin, *Proc. Natl. Acad. Sci. U.S.A.* **114**, E7358 (2017).
10. G. Faure *et al.*, *Nat. Rev. Microbiol.* (2019). 10.1038/s41579-019-0204-7
11. A. E. Stellwagen, N. L. Craig, *EMBO J.* **16**, 6823 (1997).
12. R. Bainton, P. Gamas, N. L. Craig, *Cell* **65**, 805 (1991).
13. P. Kebriaei, Z. Izsvák, S. A. Narayanavari, H. Singh, Z. Ivics, *Trends Genet.* **33**, 852 (2017).
14. S. A. Shmakov, K. S. Makarova, Y. I. Wolf, K. V. Severinov, E. V. Koonin, *Proc. Natl. Acad. Sci. U.S.A.* **115**, E5307 (2018).
15. G. Faure, K. S. Makarova, E. V. Koonin, *J. Mol. Biol.* **431**, 3 (2019).

ACKNOWLEDGMENTS

Y.Z. acknowledges NIH (GM117268) and the Biological Sciences Scholar Award from University of Michigan for funding.

10.1126/science.aay2056

OCEAN SCIENCE

Seaweed, seaweed everywhere

Floating *Sargassum* seaweed species are spreading in the Atlantic Ocean

By **James Gower**[1] *and* **Stephanie King**[2]

Thanks to the gas vesicles that give the *Sargassum* genus its name, the open-ocean seaweed species *S. natans* and *S. fluitans* float freely in the ocean. On page 83 of this issue, Wang *et al.* (*1*) report that patches and lines of these seaweeds have grown and spread through the Caribbean and across the north equatorial Atlantic to the west coast of Africa and the Gulf of Guinea, forming what the authors call the great Atlantic *Sargassum* belt. Other species of *Sargassum*, such as *S. muticum* (*2*) and *S. horneri* (*3*), have also increased their range recently but are rooted and are probably being spread through shellfish shipments and ship ballast water. It is the freely floating species that are providing the major changes noted by Wang *et al.*

Greek and Roman classical authors reported strange seaweeds in the Atlantic beyond the Strait of Gibraltar, but Columbus was the first to give definite reports of *Sargassum*, during his voyage to the Americas (*4*–*6*). Later, Jules Verne, in his novel *20,000 Leagues Under the Sea*, gave Captain Nemo a submarine for exploring the world's oceans, partly to enable him to cross the Sargasso Sea, the area of the North Atlantic gyre where *Sargassum* tends to accumulate. *Sargassum* does not pose a problem to modern shipping, but dense mats would have affected sailing vessels when wind speeds were low; furthermore, it would have suggested dangerously shallow waters to sailors who lacked charts, were unsure of their position, and were used to seeing seaweed only near shore.

S. natans and *S. fluitans* are highly visible to optical sensors on modern satellites, thanks to the high infrared reflectance of the chlorophyll a pigment that is present in all photosynthesizing plants. For plants floating on the ocean, this gives high contrast, seen against the low infrared reflectance of seawater. Furthermore, this pigment has low reflectance at visible wavelengths and high reflectance in the infrared, separated by a sharp increase (a red edge) at a wavelength of ~700 nm. This allows imaging instruments with suitable spectral bands to discriminate between floating plant life and clouds, haze, foam, or reflected sunglint, which lack this red edge. However, patches of *Sargassum* are often much smaller than the spatial resolution (300 to 1000 m) of ocean-monitoring satellite imagers. The satellites therefore probably miss many smaller patches but can detect larger accumulations well enough to map the major concentrations of *Sargassum*.

Sargassum seaweeds have washed up on an ocean beach in Playa del Carmen, Mexico, in May 2019.

PHOTO: VICTOR RUIZ/AP PHOTO

When first observed by satellite, *Sargassum* in the Gulf of Mexico during the "high *Sargassum* year" of 2005 formed patches and sinuous lines across the northern parts of the Gulf (*7*). Studies by satellite of its movement in the years 2002 to 2010 (*8*) showed an annual pattern in which it grew in spring in the western Gulf of Mexico, moved east into the eastern Gulf and Loop Current, then into the Atlantic Gulf Stream and Sargasso Sea in the fall. This picture was consistent with the distributions reported from earlier ship observations (*2*–*4*, *9*–*11*), although the Gulf of Mexico was not previously seen as an area with substantial *Sargassum* growth. Before 2011, satellite data showed no sign of major quantities of *Sargassum* in the Caribbean or equatorial Atlantic.

This picture changed dramatically in 2011 (*12*), when large amounts of *Sargassum* were observed in the Caribbean and equatorial Atlantic. Since then, this great Atlantic *Sargassum* belt has continued to grow in density and areal extent, albeit with considerable interannual variation and with an unexplained annual cycle, as shown by Wang *et al.* Where it has drifted ashore in large amounts, especially on Caribbean beaches (see the photo), *Sargassum* can have a substantial negative impact on tourism. On the other hand, floating *Sargassum* at sea is an important habitat for many marine species, and the overall long-term impact on tourism is not clear. The recent change in distribution suggests an important, but so far undetermined, change in the marine environment. As Wang *et al.* suggest, increased nutrients from coastal upwelling and from the Amazon River may be a cause of this change.

Sargassum species are easy to track from space. Other marine species of plants or animals that have low spectral contrast, do not form extended patches, or live at depth below the water surface could also vary widely in spatial distribution, without this being as evident. Also, floating marine garbage, especially plastics, is known to accumulate in similar patterns but has thus far proved impossible to see by satellite. This is largely explained by the lack of infrared contrast and of the red edge of chlorophyll a.

Observers in the Caribbean, Brazil, and Africa have called the *Sargassum* influx since 2011 unprecedented (*12*). However, there is no easy way of determining past distributions, and it remains unclear whether similar changes in *Sargassum* distribution have occurred before, although DNA techniques may one day give an answer. In the future, the *Sargassum* distribution may shrink back to its traditional territory, centered on the Sargasso Sea, or it may spread into other oceans. In either case, present satellite sensors are well suited to watch. ■

[1]*Fisheries and Oceans Canada, North Saanich, BC, Canada.* [2]*Sea This Consulting, Nanaimo, BC, Canada. Email: jim.gower@dfo-mpo.gc.ca*

REFERENCES AND NOTES

1. M. Wang *et al.*, *Science* **365**, 83 (2019).
2. A. T. Critchley, W. F. Farnham, T. Yoshida, T. A. Norton, *Bot. Mar.* **33**, 551 (1990).
3. Q. Xing *et al.*, *IEEE Geosci. Remote Sens. Lett.* **14**, 1815 (2017).
4. O. Kruemmel, *Petermanns Geogr. Mitt.* **37**, 129 (1891).
5. O. Winge, "Report on the Danish oceanographical expeditions 1908–10 to the Mediterranean and adjacent seas," vol. III, misc. paper no. 2 (1923), pp. 3–34.
6. J. H. Ryther, *Sci. Am.* **194**, 98 (1956).
7. J. Gower, C. Hu, G. Borstad, S. King, *IEEE Trans. Geosci. Remote Sens.* **44**, 3619 (2006).
8. J. F. R. Gower, S. A. King, *Int. J. Remote Sens.* **32**, 1917 (2011).
9. A. E. Parr, *Bull. Bingham Oceanogr. Collect.* **6**, 1 (1939).
10. J. N. Butler *et al.*, *Bermuda Biol. Sta. Spec. Publ.* No. 22 (1983).
11. B. E. Lapointe, *Limnol. Oceanogr.* **40**, 625 (1995).
12. J. Gower, E. Young, S. King, *Remote Sens. Lett.* **4**, 764 (2013).

ACKNOWLEDGMENTS

The authors are grateful to the Grid Processing on Demand project of the European Space Agency for providing composite imagery for tracking *Sargassum*. J.G. acknowledges the emeritus scientist program of Fisheries and Oceans Canada.

10.1126/science.aay0989

SIGNALING

Integrating stress responses and immunity

Stress is required to assemble immune signaling complexes during infection

By **Philippe Pierre**

The integrated stress response (ISR) is a gene expression program that protects cells from amino acid deprivation, oxidative stress, or stress in the endoplasmic reticulum (ER) that is caused by protein misfolding and aggregation (*1*). Phosphorylation of the eukaryotic initiation factor 2α (eIF2α) initiates the ISR, but it also has a role in innate immunity (*2*, *3*). In particular, eIF2α is important to harness the full capacity of different immune cells to produce inflammatory cytokines or type-I interferon in response to microbial cues. On page 47 of this issue, Abdel-Nour *et al.* (*4*) reveal that in response to bacterial infection, the ISR promotes expression of heat shock protein family B-member 8 (HSPB8), which controls the assembly of signaling hubs for inflammatory cytokine production. This involves the formation of amyloid fibrils, which are also associated with neuroinflammation and neurodegeneration. Thus, understanding these regulatory processes may reveal new targets for the prevention of inflammation.

eIF2α is a member of the heterotrimeric eIF2 complex that is required for most forms of eukaryotic translation initiation. It mediates the binding of initiating methionine transfer RNA to the ribosome in a guanosine triphosphate (GTP)–dependent manner. eIF2α phosphorylation on Ser^{51} creates a dominant negative form of the eIF2 initiation factor that inhibits translation. In response to different stressors, eIF2α phosphorylation is mediated by four stress-specific eIF2α kinases (EIF2AK1–4) that are individually responsible for a global reduction of protein synthesis and a distinct activating transcription factor 4 (ATF4)–dependent gene expression program (*5*). For example, accumulation of misfolded proteins in the ER lumen (*6*) promotes the dissociation of HSPA5 chaperone protein (also called BIP) from the ER-lumenal domain of PKR-like ER kinase (PERK, also called EIF2AK3). This causes PERK to oligomerize and phosphorylate eIF2α in the cytosol, which reduces secreted protein synthesis while favoring ATF4 translation and initiates the ISR to restore ER homeostasis.

Abdel-Nour *et al.* show that intracellular bacterial infection promotes the dissociation of HSPB8 from the oxidative stress–activated kinase heme-regulated inhibitor (HRI, also called EIF2AK1), which activates this kinase. This leads to increased phosphorylation of eIF2α, mirroring PERK activation. The process of HSP-dependent activation of HRI highlights that all members of this kinase family, including EIF2AK2 (also called PKR) and EIF2AK4 (also called GCN2), are negatively regulated through cycles of interaction with HSP proteins (*7*). Thus, negative feedback control of activated EIF2AKs by HSPs is likely to be a key regulatory component of the ISR and potentially other biochemical pathways (see the figure). Two protein phosphatase 1 (PP1) cofactors, PP1 regulatory subunits 15A and 15B, are considered the main negative regulators of eIF2α phosphorylation (*8*). Investigating the interplay between the inhibitory HSPs and these PP1 cofactors will therefore be key to further understanding how the ISR is terminated and how protein synthesis returns to equilibrium after stress resolution.

A surprising discovery of Abdel-Nour *et al.* is that expression of HSPB8 also controls the pro-inflammatory response to *Salmonella*, *Shigella*, *Listeria*, or *Citrobacter* infection. Cytokine expression is dependent on HRI activation, which directly releases HSPB8 and increases ATF4- and ATF3-dependent expression, through the phosphorylation of eIF2α. This pathway is important for the activation of several key innate immunity signaling pathways because it promotes the assembly of signaling adaptors such as receptor-interacting protein 2 (RIP2), mitochondrial antiviral-signaling protein (MAVS), or TIR domain–containing adapter protein inducing interferon-β (TRIF) into protein aggregates that constitute supramolecular organizing centers (SMOCs, also called signalosomes), which transduce signals (*9*). A discriminative feature of TRIF- or MAVS-containing SMOCs, compared to other signalosomes (*10*), is their capacity to adopt an alternative folding pattern and associate within protofilaments, thereby forming amyloid fibrils. These fibrils are emerging as key signaling platforms following the detection of microbial or danger signals (*11*). However, their aggregation-prone properties can be cytotoxic and trigger inflammation independently of microbial stimuli, as demonstrated by their association with neurodegenerative pathologies such as Parkinson's disease (PD) (*12*, *13*).

The integrated stress response in inflammation

Stress-dependent release of HSPs, such as HSPB8, from EIF2AKs promotes eIF2α phosphorylation and subsequent ATF4-dependent gene expression: the ISR. Concomitant microbial triggering of innate immune sensors releases HSPB8 from HRI and favors the assembly of SMOCs and downstream pro-inflammatory cytokine expression. ISRIB inhibits this pro-inflammatory process by counteracting eIF2α phosphorylation.

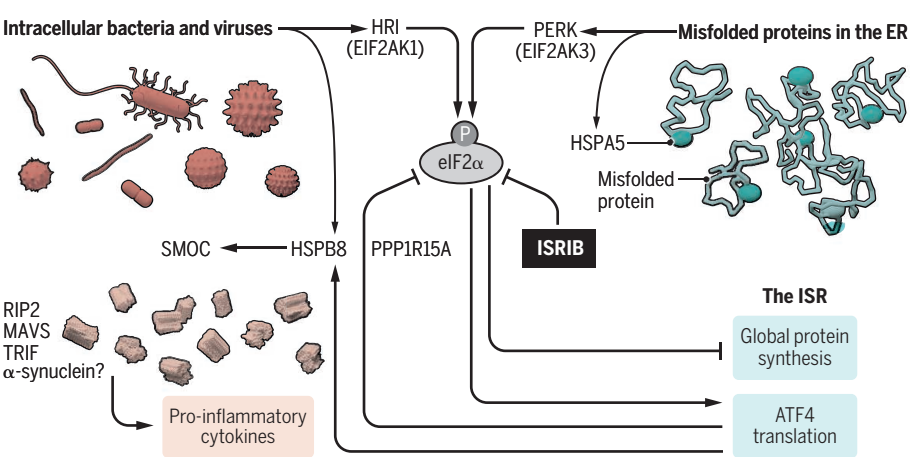

ATF4, activating transcription factor 4; eIF2α, eukaryotic initiation factor 2α; EIF2AK, eIF2α kinase; ER, endoplasmic reticulum; HRI, heme-regulated inhibitor; HSP, heat shock protein; ISR, integrated stress response; MAVS, mitochondrial antiviral-signaling protein; PPP1R15A, protein phosphatase 1 regulatory subunit 15A; RIP2, receptor-interacting protein 2; SMOC, supramolecular organizing center; TRIF, TIR domain-containing adapter protein inducing interferon-β.

GRAPHIC: A. KITTERMAN/*SCIENCE*

Aix Marseille Université, CNRS, INSERM, CIML, Marseille, France, and Institute for Research in Biomedicine (iBiMED) and Ilidio Pinho Foundation, Department of Medical Sciences, University of Aveiro, 3810-193 Aveiro, Portugal.
Email: pierre@ciml.univ-mrs.fr

Assembly and removal of amyloid SMOCs should therefore be tightly regulated to avoid adverse effects and progression toward uncontrolled inflammation. HRI and HSPB8 are likely to play key roles in this regulation. However, it remains unexplained how the paradoxical situation of increasing the expression of specific chaperones to promote SMOC assembly and inducing translation of pro-inflammatory mediators can occur when protein synthesis is concomitantly inhibited by the phosphorylation of eIF2α by HRI.

These observations raise questions about the capacity of cells to respond to the formation of signaling fibrils and the establishment of an HRI-dependent ISR that could induce pro-inflammatory cytokine release during sterile (that is, noninfectious) neurodegeneration. Neuroinflammation is a major component of PD progression, characterized by neuronal cytoplasmic inclusions composed mainly of aggregated α-synuclein called Lewy bodies (*12*). In addition to RIP2, MAVS, and TRIF, Abdel-Nour *et al.* showed that overexpression of α-synuclein alone activated HRI-dependent responses, including expression of HSPB8. Interestingly, the small-molecule drug ISRIB, which reverses the downstream effects of eIF2α phosphorylation (*14*), reduced the capacity of infected cells to produce pro-inflammatory cytokines, mimicking a deficit in HRI or eIF2α phosphorylation. Given that memory consolidation is inherently limited by ISR activation in neurons, ISRIB-treated mice display significant enhancement in spatial and fear-associated learning (*15*) while also being protected from protein aggregation–mediated disease. The capacity of ISRIB to reduce neuroinflammation in response to amyloid SMOC signaling might therefore explain some of these pharmacological effects. ■

REFERENCES AND NOTES

1. R. C. Wek, *Cold Spring Harb. Perspect. Biol.* 10.1101/cshperspect.a032870 (2018).
2. N. Cláudio *et al.*, *EMBO J.* **32**, 1214 (2013).
3. J. Grootjans *et al.*, *Nat. Rev. Immunol.* **16**, 469 (2016).
4. M. Abdel-Nour *et al.*, *Science* **365**, eaaw4144 (2019).
5. M. E. Fusakio *et al.*, *Mol. Biol. Cell* **27**, 1536 (2016).
6. S. S. Cao, R. J. Kaufman, *Curr. Biol.* **22**, R622 (2012).
7. A. Roobol *et al.*, *Biochem. J.* **465**, 213 (2015).
8. H. P. Harding *et al.*, *Proc. Natl. Acad. Sci. U.S.A.* **106**, 1832 (2009).
9. J. C. Kagan, V. G. Magupalli, H. Wu, *Nat. Rev. Immunol.* **14**, 821 (2014).
10. X. Tan *et al.*, *Annu. Rev. Microbiol.* **72**, 447 (2018).
11. J. Sohn, S. Hur, *Curr. Opin. Struct. Biol.* **37**, 134 (2016).
12. E. Emmanouilidou, K. Vekrellis, *Brain Pathol.* **26**, 398 (2016).
13. J. K. Ryu *et al.*, *Nat. Immunol.* **19**, 1212 (2018).
14. C. Sidrauski *et al.*, *eLife* **4**, e05033 (2015).
15. C. Sidrauski *et al.*, *eLife* **2**, e00498 (2013).

ACKNOWLEDGMENTS

P.P. is supported by grants from FRM DEQ 20140329536 and DCBIOL Labex ANR-11-LABEX-0043 funded by the French government program Investissements d'Avenir, and by the Ilídio Pinho foundation and FCT (Fundação para a Ciência e a Tecnologia) and projects PTDC/IMI-IMU/3615/2014, POCI-01-0145-FEDER-016768, and POCI-01-0145-FEDER-030882.

10.1126/science.aay0987

PHOTO: R. ASHRAFOV/SHUTTERSTOCK

A lost wallet returned to its owner serves as a new proxy for the finder's civic honesty.

BEHAVIORAL ECONOMICS

Financial temptation increases civic honesty

Altruism and self-image, not selfishness, drive surprising findings

By **Shaul Shalvi**

Does temptation shape dishonesty? For example, when a person finds a wallet on the street and decides to return it to its owner, it may be because the contents of the wallet are not very tempting or, alternatively, because people care about complying with norms of good conduct, that is, civic honesty. Scientists commonly explore such questions about human honesty through artificial laboratory tasks, but such studies have not provided conclusive evidence about the extent to which people are honest in natural circumstances. On page 70 of this issue, Cohn *et al.* (*1*) describe a field experiment involving 17,000 people in 40 countries to provide a new measure of honesty. The results show just how prevalent civic honesty is, and they raise many questions, such as how environments can be designed to foster civic honesty.

Cohn *et al.*'s work is a prime example of the theoretical models that emerge when economics and psychology interact. Traditionally, economic models have assumed that humans act as rational economic agents who seek to serve their self-interest to increase material gain. To better predict human behavior, behavioral economic models incorporate nonmaterial utilities, such as altruistically caring for others' outcomes (*2*) or seeking to maintain a positive self-image (*3*, *4*). To test these models, behavioral scientists often engage participants in tasks that enable them to be honest or instead to lie in order to increase their pay. For example, in a task that rewards participants

Amsterdam School of Economics, University of Amsterdam, Amsterdam, Netherlands. Email: s.shalvi@uva.nl

according to their self-reported outcome of a private rolling of a die, participants, on average, report higher numbers than would be expected if they were honest, indicating that people lie, but only to a modest extent (*5*, *6*). Because participants' die rolls are private, the modest amount of lying suggests that people are concerned with maintaining a positive self-image.

Such laboratory tasks are limited by their artificial nature and by the fact that it is unclear to participants who would benefit from their honesty or suffer from their dishonesty. The question is whether such settings predict honesty outside the lab, where dishonesty often harms others. Recent work suggests that lab tasks do fairly well, revealing a positive correlation between participants' reported die roll numbers (as a proxy for dishonesty) and their tendency to free-ride on public transport (*7*) or to not return undeserved payment (*8*). Furthermore, in countries with high levels of corruption, participants report higher die roll numbers (*9*). What is still missing, however, is a direct measure for how prevalent honesty is in a natural setting, where people face varying degrees of temptation and have a clear idea of the person or group that benefits from honesty and is harmed by dishonesty.

To disentangle the influence of self-interest, self-image, and altruism in a field experiment, Cohn *et al.* handed wallets to front-desk employees at major institutions, including banks, theaters, and other public offices, claiming to have found them on the street. Each wallet contained a grocery list, a key, and three identical business cards, providing people with a way to show civic honesty by returning the wallet to its owner. To vary temptation, different amounts of money were also included in some of the wallets. Cohn *et al.* conducted many control tests and analyses to rule out the possibility that people would return the wallet out of fear of being identified or punished.

Whereas selfishness predicts that people will be less likely to return wallets containing money, altruism and the desire to maintain a positive self-image predict the opposite pattern. In 38 of the 40 countries studied, wallets with money were returned more often than wallets without money, which supports the idea that people are not purely selfish. Moreover, wallets with more money (US$94.15) were more likely to be returned than wallets with less money (US$13.45). The effect not only contradicts rational economic thinking, it is rather surprising. Both laypeople and expert economists predicted the exact opposite pattern of results in surveys reported by the authors.

Furthermore, a key is valuable to the wallet's owner, not the wallet's finder. In the United States, the United Kingdom, and Poland, the authors added an experimental treatment in which wallets included money but no key. Doing so allowed them to assess the specific contribution of altruism to honesty. Indeed, adding a key increased the likelihood of the wallet being returned. Taken together, these results support the idea that people care about others as well as caring about being honest.

Cohn *et al.*'s study provides a new way to assess human honesty. The work evokes numerous questions. By having the grocery list and business cards written in the local language, the authors identified the wallet owner as local. Our globalized world, however, is diverse. People of different ethnicities, backgrounds, and nationalities interact. Prosocial and honest behaviors are often parochial (*10*–*12*); people find it worthwhile to act kindly toward members of their own group but not members of other groups. The results reported by Cohn *et al.* may thus scale down when civic honesty is expressed toward nonlocals, including tourists or immigrants.

Also, showing civic honesty does not just mean returning a lost wallet. It is about acting in a socially desirable way, against one's selfish interests. Understanding when people are likely to engage in civic honesty—such as by whistleblowing in response to suspected organizational wrongdoing, or by obeying rules even when exposed to others' corrupt behavior—is important. By continuing to push the methodological boundaries and the proxies used to assess sensitive behaviors such as honesty, researchers aspire to figure out how to better design our environments and organizations to foster such desired behaviors. ■

REFERENCES AND NOTES

1. A. Cohn, M. A. Maréchal, D. Tannenbaum, C. L. Zünd, *Science* **365**, 70 (2019).
2. E. Fehr, K. M. Schmidt, in *Handbook of the Economics of Giving, Altruism and Reciprocity*, S.-C. Kolm, J. M. Ythier, Eds. (North-Holland, 2006), vol. 1, pp. 615–691.
3. R. Bénabou, J. Tirole, *Q. J. Econ.* **126**, 805 (2011).
4. N. Mazar, O. Amir, D. Ariely, *J. Mark. Res.* **45**, 633 (2008).
5. U. Fischbacher, F. Föllmi-Heusi, *J. Eur. Econ. Assoc.* **11**, 525 (2013).
6. P. Gerlach, K. Teodorescu, R. Hertwig, *Psychol. Bull.* **145**, 1 (2019).
7. Z. Dai, F. Galeotti, M. C. Villeval, *Manage. Sci.* **64**, 1081 (2018).
8. J. Potters, J. Stoop, *Eur. Econ. Rev.* **87**, 26 (2016).
9. S. Gächter, J. F. Schulz, *Nature* **531**, 496 (2016).
10. H. Bernhard, U. Fischbacher, E. Fehr, *Nature* **442**, 912 (2006).
11. C. K. De Dreu *et al.*, *Science* **328**, 1408 (2010).
12. S. Shalvi, C. K. W. De Dreu, *Proc. Natl. Acad. Sci. U.S.A.* **111**, 5503 (2014).

ACKNOWLEDGMENTS

This work was funded by the European Research Council (ERC-StG-637915).

Published online 20 June 2019
10.1126/science.aax5034

LIGHT METALS

Processing magnesium at room temperature

In situ microscopy experiments show how pyramidal slip increases magnesium's ductility

By **Gwénaëlle Proust**

Aluminum (Al) alloys are often used for lightweight applications such as airframes, but with proper alloying elements and heat treatments, magnesium (Mg) alloys can reach strengths comparable to those of some Al alloys but be 35% lighter (*1*). Nonetheless, the use of Mg alloys has been limited by their poor processability at room temperature and low corrosion resistance

"The low ductility of Mg alloys is associated with their hexagonal crystalline structure."

(*2*). The latter can be improved either with additional alloying elements (*2*) or by refining their grain size (*3*). Improvements to the ductility of Mg, which controls its processability, will require better understanding of its plastic deformation mechanisms and the parameters controlling their activities. On page 73 of this issue, Liu *et al.* (*4*) offer new insight into how Mg deforms, and more specifically, on the role of slip along the pyramidal planes of its unit cell in accommodating large deformation (see the figure).

The potential for energy savings with lighter alloys is especially appreciated by the transportation industry (*5*). In recent years, the Volkswagen group has used around 14 kg of Mg in the Audi A4 and A6, and General Motors has used 26 kg in the GMC Savana (*6*). The forming of wrought Mg alloys—shaping them by rolling, extruding, or forging—is costly and time consuming

School of Civil Engineering, The University of Sydney, NSW 2006, Australia. Email: gwenaelle.proust@sydney.edu.au

because of the low deformation capability of these alloys at low temperatures. Shaping processes at room temperature require repeated cycles of small deformation and thermal annealing to prevent cracking. The production of bars, rods, sheets and plates at high temperatures can avoid low-temperature multiple-stage processing (*7*), but high-temperature deformation methods come with a substantial energy penalty.

Improving the ductility of Mg alloys at low temperatures would not only decrease the cost associated with their production but also would create microstructures in the alloy that could potentially improve their performance for structural applications. The low ductility of Mg alloys is associated with their hexagonal crystalline structure. Most other engineering metals are more ductile because they have a cubic crystalline structure that allows the dislocations that accommodate plastic deformation to move more readily. The structure in Mg has only limited ways for dislocations to easily glide, so deformation must be accommodated by other mechanisms, such as twinning, grain boundary sliding, and recrystallization (see the figure). The diversity of the deformation mechanisms available results in the high plastic anisotropy of Mg, which limits its ability to accommodate deformation in the directions normal to the loading direction. The deformation mechanisms that operate depend on processing parameters such as temperature, loading direction, deformation rate, and grain size (*8*, *9*).

At low temperatures, some of these mechanisms are not available, which results in cracking. Different approaches have been proposed to improve the ductility of Mg at room temperatures, including grain refinement (*10*), modification of texture (the distribution of the various crystallographic orientations present in the material) (*11*), and alloying (*12*). All these approaches aim to increase the activity of nonbasal slip (basal slip being the most favorable slip mode in Mg and its alloys); more specifically, to accommodate deformation along the *c* axis of the Mg hexagonal unit cell, $\langle c + a \rangle$ dislocations (ones that move in the direction in the unit cells that combines the $\langle c \rangle$ and $\langle a \rangle$ unit vectors) should glide on pyramidal planes.

There are actually two types of pyramidal planes in Mg: type I in the $(10\bar{1}1)$ plane and type II in the $(11\bar{2}2)$ plane. Because these two types of planes have different atomic densities, the energy required to move dislocations on them is different. To date, no consensus has been reached on which of these types of planes is prevalent during Mg deformation (*13*). The other difficulties come from studies showing contradictory results regarding the mobility of the $\langle c + a \rangle$ dislocations in pure Mg. Ahmad *et al.* stated that $\langle c + a \rangle$ dislocations are essentially sessile (immobile) but that this problem can be overcome with proper alloying (*14*). Kumar *et al.* showed that although $\langle c + a \rangle$ dislocations on pyramidal type I planes become sessile, the ones on pyramidal type II planes remain glissile under stress (*15*).

Liu *et al.* present results related to both controversies. They used advanced in situ transmission electron microscopy (TEM) mechanical testing techniques to apply a compressive load at room temperature on Mg micropillars fabricated from single crystals. Both pyramidal type I and pyramidal type II planes participate to plastically deform Mg. Their recording of the visualized deformation synchronized with the mechanical response of the material showed unequivocally the relation between strain accommodation and the formation and motion of $\langle c + a \rangle$ dislocations. They also used three-dimensional reconstruction techniques on the TEM images captured at different tilting angles to identify the planes (pyramidal type I or II) on which different dislocations are lying and to even identify dislocation cross-slip. The glissile character of the dislocations is confirmed on both types of pyramidal planes by molecular dynamics simulations in which $\langle c + a \rangle$ dislocations nucleate because of compressive loading along the *c* axis, instead of by being artificially introduced in the model. The reversibility of dislocation motion is demonstrated through cyclic loading observed during in situ TEM testing.

The findings of Liu *et al.* reinforce the idea that promoting $\langle c + a \rangle$ dislocation activity in Mg can increase its processability. Using the proposed molecular dynamics model, it will become possible to identify microstructures that are favorable to increase ductility in Mg and its alloys at room temperature. The combined experimental and modeling approach used in this study can be repeated on different Mg alloys to confirm and better understand the role of alloying elements in the ductility of Mg, which will allow the development of new wrought Mg alloys. ■

Mapping magnesium deformation

Atoms in magnesium accommodate strain through several mechanisms when the metal is deformed. Liu *et al.* studied one mechanism, slip along pyramidal planes, with electron microscopy while the metal was strained.

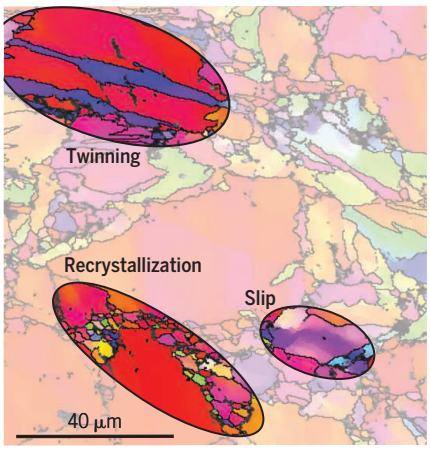

Accommodating strain Changes in microstructure characterized with electron backscatter diffraction that resulted from straining a magnesium alloy are shown as changes in color and smaller grains. Three different mechanisms—slip, twinning, and recrystallization—simultaneously accommodate strain in this sample.

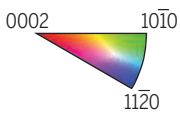

Packing atoms

Two families of pyramidal planes can accommodate deformation in this hexagonal close-packed metal.

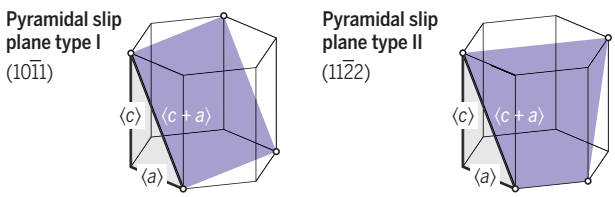

GRAPHIC: A. KITTERMAN/*SCIENCE*

REFERENCES AND NOTES

1. I. Polmear, D. StJohn, J.-F. Nie, M. Qian, Ma, *Light Alloys - Metallurgy of the Light Metals* (Elsevier, ed. 5, 2017).
2. W. Xu *et al.*, *Nat. Mater.* **14**, 1229 (2015).
3. D. Song *et al.*, *Mater. Des.* **166**, 107621 (2019).
4. B.-Y. Liu *et al.*, *Science* **365**, 73 (2019).
5. T. M. Pollock, *Science* **328**, 986 (2010).
6. D. Sameer Kumar, C. Tara Sasanka, K. Ravindra, K. N. S. Suman, *Am. J. Mater. Sci. Technol.* **4**, 12 (2015).
7. C. Moosbrugger, L. Marquard, *Engineering Properties of Magnesium Alloys* (ASM International, 2017).
8. S. R. Agnew, O. Duygulu, *Int. J. Plast.* **21**, 1161 (2005).
9. M. W. Vaughan *et al.*, *Acta Mater.* **168**, 448 (2019).
10. P. Lukáč, Z. Trojanová *Mater. Eng. Mater. Inž.* **18**, 111 (2011).
11. E. Dogan, M. W. Vaughan, S. J. Wang, I. Karaman, G. Proust, *Acta Mater.* **89**, 408 (2015).
12. Z. Wu, R. Ahmad, B. Yin, S. Sandlöbes, W. A. Curtin, *Science* **359**, 447 (2018).
13. Z. Ding *et al.*, *Acta Mater.* **146**, 265 (2018).
14. R. Ahmad, B. Yin, Z. Wu, W. A. Curtin, *Acta Mater.* **172**, 161 (2019).
15. A. Kumar, B. M. Morrow, R. J. McCabe, I. J. Beyerlein, *Mater. Sci. Eng. A* **695**, 270 (2017).

ACKNOWLEDGMENTS

I thank I. Karaman and his team at Texas A&M University for the Mg specimen used to illustrate the article and acknowledge Microscopy Australia for use of the microscopy characterization equipment at the Australian Centre for Microscopy and Microanalysis at the University of Sydney.

SUPPLEMENTARY MATERIALS

science.sciencemag.org/content/365/6448/30/suppl/DC1

10.1126/science.aax9732

NEUROSCIENCE

Targeting microglia in brain disorders

The heterogeneity of brain immune cells could be exploited therapeutically

By Josef Priller[1,2,3] and Marco Prinz[4,5,6]

When the neuroscientist Pío del Río Hortega first characterized "microglia" in 1919 using silver carbonate staining of animal and human brain tissues, he was impressed by the morphological plasticity and capacity to phagocytose (ingest) of the resident immune effector cells, called microglia (*1*). A century later, technological advances in molecular biology, imaging, and single-cell analysis have provided fascinating insights into the dynamic changes of microglia in response to aging and brain diseases, revealing their potential as therapeutic targets.

Microglia are specialized tissue-resident macrophages in the central nervous system (CNS). They develop from immature yolk sac progenitor cells during early embryogenesis and persist throughout life. Microglia rely on cytokine signaling, such as activation of colony-stimulating factor 1 receptor (CSF1R) and transforming growth factor–β1 (TGF-β1), for their survival. Notably, heterozygous loss-of-function mutations in the human *CSF1R* gene cause an autosomal-dominant progressive degenerative white-matter disorder called adult-onset leukoencephalopathy with axonal spheroids and pigmented glia (ALSP), and homozygous *CSF1R* mutations cause brain malformations with almost complete absence of human microglia (*2*). A somatic BRAF-Val^{600}Glu mutation in human microglia results in late-onset neurodegeneration in individuals with histiocytosis (excess of macrophages) (*3*). This suggests that microglial dysfunction can be the primary cause of neurological diseases in humans.

Microglia can also promote neurodegeneration secondary to infections (e.g., HIV infection), exposure to misfolded proteins (as occurs in many neurodegenerative disorders), or CNS injury. Whereas microglia were traditionally considered to quickly respond to any pathological event in the brain and to help restore homeostasis (albeit at the price of potential bystander damage, such as through the release of toxic molecules or pro-inflammatory mediators), it is now becoming clear that this passive role of microglia in responding to damage falls short in reflecting their complex functions in the CNS. Indeed, microglia may themselves initiate neural dysfunction and neurodegeneration through loss of homeostatic and/or gain of aberrant function (see the figure). Consistently, many genetic alterations that are associated with increased risk for neurological and psychiatric disorders, including schizophrenia, autism spectrum disorder, frontotemporal dementia, and Alzheimer's disease (AD), affect genes that are highly expressed by microglia. As a result, microglial functions have emerged as possible targets for CNS disorders.

Given their embryonic origin and dependence on self-maintenance in the absence of turnover with circulating monocytes, microglia may be much more vulnerable to aging and degeneration than previously assumed. Recent transcriptomic studies have revealed substantial age-dependent changes in the expression of genes involved in cell motility, adhesion, axonal guidance, and immune function in microglia, reminiscent of the changes observed in some neurodegenerative diseases (*4*). The sialic acid–binding receptor CD22 is up-regulated on aged microglia, and CD22 blockade restores microglial homeostasis and improves cognitive function in aged mice (*5*), underscoring the therapeutic potential of targeting microglial functions. A disease-associated microglia state was recently identified in the brains of AD transgenic mice that may exert protective functions by clearing amyloid-β protein aggregates, which are thought to be pathological in AD (*6*). These neurodegeneration-associated microglia express many of the genes that have been associated with increased risk for AD and other neurodegenerative disorders in genome-wide association studies, including cathepsin D (*CTSD*), lipoprotein lipase precursor (*LPL*), TYRO protein tyrosine kinase–binding protein (*TYROBP*), apolipoprotein E (*APOE*), and triggering receptor expressed on the myeloid cells 2 (*TREM2*). Single-cell transcriptomic analysis of the prefrontal cortex in humans with AD pathology confirmed the presence of disease-associated microglia signatures (*7*). Among the most highly expressed genes in microglia were secreted phosphoprotein 1 (*SPP1*), protein tyrosine phosphatase receptor type G (*PTPRG*), apolipoprotein C1 (*APOC1*), and *APOE*, all of which have been associated with increased risk of AD.

Disease-associated microglia states were also discovered in the brains of humans with multiple sclerosis (MS), including SPP1^{+} microglia and CTSD^{+} microglia (*8*). Their transcriptional profiles resembled those of microglia phenotypes identified in a mouse model of demyelination, which is a hallmark of MS pathology (*8*). In contrast to neurodegeneration-associated microglia, increased expression of genes involved in interactions with other immune cells, including CD74, and the major histocompatibility complex (MHC) class II molecules, was detected in MS-associated microglia. This may reflect the chronic neuroinflammation that is observed in MS.

Technological advances in single-cell mass cytometry have enabled the validation of some of the transcriptional signatures of disease-associated microglia at the protein level (single-cell proteomics) (*9*). These studies detected differences in the immunophenotypic signatures of microglia between mouse models of neurodegeneration and neuroinflammation; whereas the former showed up-regulation of CD14 in a small subset of microglia, the latter were characterized by the global up-regulation of MHC class II and stem cell antigen 1 (SCA1) in microglia. Future lineage-tracing studies will help to determine whether disease-associated microglia are a distinct, albeit heterogenous population, a mixture of different subpopulations, or a reflection of dynamic states of microglia.

From a therapeutic perspective, it would seem attractive to specifically target these disease-associated microglia phenotypes based on the molecular signatures according to the type of neuropathology. The modulation of checkpoint mechanisms that normally keep microglia in a homeostatic state and are down-regulated during the development of disease-associated microglia, such as the receptors CX3C chemokine receptor 1 (CX3CR1), P2Y purinoceptor 12 (P2Y12). and TGF-β1 receptor (TGFBR1), as well as the TREM2-APOE pathway, appears particularly promising (*6*). By contrast, long-term depletion of microglia or administration of immunosuppressant drugs may not be the preferred treatment choice for neuropsychiatric disorders due to the resulting loss of homeostatic functions of microglia, such as the modulation of synaptic plasticity, the supply of trophic factors for neurons and other

[1]Department of Neuropsychiatry, Charité and BIH, Berlin, Germany. [2]DZNE, Berlin, Germany. [3]University of Edinburgh and UK DRI, Edinburgh, UK. [4]Institute of Neuropathology, Medical Faculty, University of Freiburg, Freiburg, Germany. [5]Signalling Research Centres BIOSS and CIBSS, University of Freiburg, Freiburg, Germany. [6]Center for Basics in NeuroModulation, Freiburg, Germany. Email: josef.priller@charite.de; marco.prinz@uniklinik-freiburg.de

types of glia, and the participation in pathogen defense.

Microglia are highly dependent on environmental signals to maintain their homeostatic phenotype. This results in distinct brain region–dependent transcriptional identities, which are associated with differential vulnerability to aging (*4*). Immune profiling of human brain microglia by single-cell proteomics recently revealed a core immunophenotypic signature with considerable regional heterogeneity (*10*). Notably, microglia subsets in the frontal and temporal cortex expressed higher amounts of mannose receptor C type 1 (CD206) compared to microglia subsets in the subventricular zone and thalamus that expressed higher levels of the proliferation markers cyclin A, cyclin B1, and Ki67. These findings have important therapeutic implications because microglia may be targeted not only in a disease-specific, but also in a brain region–specific, manner. This refined approach could facilitate the treatment of CNS disorders with regionally confined pathology, such as stroke or Parkinson's disease, by enabling site-specific modulation of microglial function that spares nonaffected tissue.

Unfortunately, microglia cannot be easily accessed in the CNS. The blood-brain barrier, which is formed by tight junctions between endothelial cells in cerebral blood vessels, regulates the trafficking of cells and larger molecules into the CNS. As an exception to the rule, the choroid plexuses and circumventricular organs contain fenestrated blood vessels that facilitate exchange processes with the periphery. The therapeutic relevance of these gates into the CNS from peripheral blood has yet to be fully explored. Initial attempts to target genetically engineered hematopoietic cells injected into the blood to sites of damage in the brain in order to replace microglia relied on CNS irradiation (*11*). In two landmark clinical studies on inherited peroxisomal and lysosomal storage disorders (X-linked adrenoleukodystrophy and metachromatic leukodystrophy) that result in severe motor and cognitive deficits, children were treated successfully with chemotherapy, which also conditions the CNS for immune cell engraftment. This was followed by reinfusion of hematopoietic stem cells that were genetically corrected ex vivo with lentiviral vectors, resulting in expression of the deficient proteins in the CNS (*12*, *13*).

Dysfunctional microglia can also be depleted locally or throughout the brain with pharmacological inhibitors of CSF1R signaling or with liposome-encapsulated bisphosphonates that trigger apoptosis specifically of microglia. As the microglial population is under strong homeostatic pressures, rapid replenishment occurs from local pools (*14*). The newly engrafted cells temporarily acquire functions that are distinct from those of preexisting dysfunctional microglia (*14*). The process of replenishment also provides an opportunity to introduce gene-modified cells. Competition of myeloid cells (such as monocytes and macrophages) for niches within the CNS that have been generated by the loss or dysfunction of microglia can affect the efficiency of replacement with engineered cells. The factors that govern competitive engraftment are not fully understood and have yet to be exploited therapeutically. Aged microglia or microglia carrying genetic and/or epigenetic defects may have a competitive disadvantage. Thus, future attempts to modify the function of microglia or microglia subpopulations, e.g., by gene editing, on a whole-brain or region-specific level need to consider microglia population dynamics. Along these lines, it is important to note that somatic mosaicism (cell clones with distinct acquired mutations) in microglia plays a role in CNS disorders, such as histiocytosis and ALSP (*3*, *15*). The selection of the (regionally) "fittest" microglia may be exploited for therapeutic purposes, e.g., gene-edited microglia may outcompete microglia with disease-causing mutations, and microglia may be engineered that maintain homeostatic functions or resist toxic microenvironments.

Many obstacles need to be overcome before microglia can be exploited for the therapy of CNS disorders. It is likely to be important to develop drugs that specifically target disease-associated microglia states without affecting homeostatic microglia or peripheral tissue macrophage populations. These compounds would need to cross the blood-brain barrier to gain access to the brain parenchyma, and in the case of gene engineering, efficient vectors for human microglia need to be available that do not trigger inflammation. The protocols for the engraftment of genetically engineered myeloid cells in the human CNS also need to be optimized. Interventions may need to be temporally restricted if disease-associated microglia are dynamic states. Thus, the development of new radioligands for positron emission tomography (PET)–based monitoring of microglial activity in the human brain, e.g., isotope-labeled ligands for P2Y12 or TREM2 receptors, will be of importance. Dynamic modulation of microglial function (activation and inhibition) to account for the spatiotemporally differential roles of disease-associated microglial states, and for the complex interactions of microglia with other immune cells, such as border-associated brain macrophages, astrocytes, oligodendrocytes, and peripheral immune cells, as well as endothelial cells, will be required over the disease course, which is a daunting task. Nevertheless, our understanding of the cross-talk between microglia and other cell types in the CNS and periphery has substantially increased in recent years and may eventually allow us to modulate microglial function indirectly and without ingress into the CNS. Given the lack of effective therapeutic options for many neurological and psychiatric diseases, further understanding and eventual targeting of microglial functions in the CNS could hold promise. ■

Microglial heterogeneity

Regional heterogeneity of microglia can be observed during homeostasis. During pathology, disease-associated microglia emerge with distinct transcriptional profiles that reflect specific activation states.

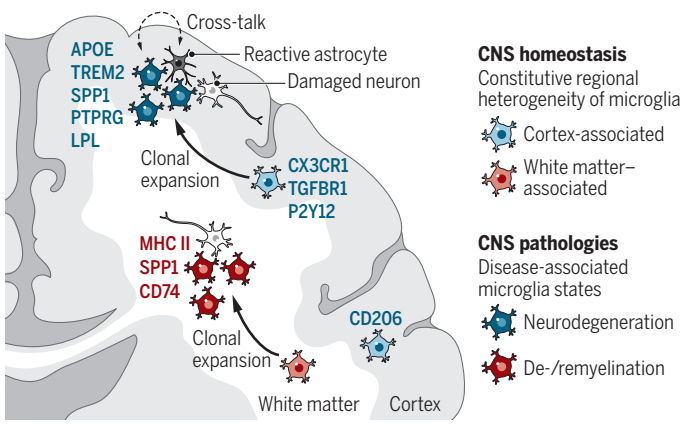

GRAPHIC: KELLIE HOLOSKI/*SCIENCE*

REFERENCES AND NOTES

1. P. Río-Hortega, *Bol. Soc. Esp. Biol.* **VIII**, 91 (1919).
2. N. Oosterhof *et al.*, *Am. J. Hum. Genet.* **104**, 936 (2019).
3. E. Mass *et al.*, *Nature* **549**, 389 (2017).
4. K. Grabert *et al.*, *Nat. Neurosci.* **19**, 504 (2016).
5. J. V. Pluvinage *et al.*, *Nature* **568**, 187 (2019).
6. H. Keren-Shaul *et al.*, *Cell* **169**, 1276 (2017).
7. H. Mathys *et al.*, *Nature* 10.1038/s41586-019-1195-2 (2019).
8. T. Masuda *et al.*, *Nature* **566**, 388 (2019).
9. B. Ajami *et al.*, *Nat. Neurosci.* **21**, 541 (2018).
10. C. Böttcher *et al.*; NBB-Psy, *Nat. Neurosci.* **22**, 78 (2019).
11. J. Priller *et al.*, *Nat. Med.* **7**, 1356 (2001).
12. N. Cartier *et al.*, *Science* **326**, 818 (2009).
13. A. Biffi *et al.*, *Science* **341**, 1233158 (2013).
14. L. Zhan *et al.*, *PLOS Biol.* **17**, e3000134 (2019).
15. F. S. Eichler *et al.*, *Brain* **139**, 1666 (2016).

ACKNOWLEDGMENTS

J.P. and M.P. are coordinators of the DFG SFB/TRR167.

10.1126/science.aau9100

POLICY FORUM

RESEARCH REGULATION

Regulating genetic biohacking

Emphasize community engagement, not perfect compliance

By **Patricia J. Zettler,[1] Christi J. Guerrini,[2] Jacob S. Sherkow[3,4,5]**

Just as the popularization of computers in the late 1970s and early 1980s gave rise to computer hacking, the recent accessibility and affordability of relatively easy (and widely hyped) genome-editing technologies and resources has spurred interest in genetic "biohacking"—molecular genetics experiments performed outside institutional laboratories by individuals who may have little formal scientific training. Regulation of the work of professional scientists and traditional scientific institutions is robust, although it still faces scrutiny in the wake of He Jiankui's genome-editing experiments on Chinese twins (*1*). However, regulation of genetic biohacking has received far less attention, even though, like traditional scientific research, it is likely to produce a range of innovations while posing a number of risks to public health. Here, we explore these risks and the consequences of understanding that some instances of regulatory failure for biohacking are inevitable. And, where they are not, we suggest that agencies, policy-makers, and private parties have the opportunity to improve oversight of genetic biohacking using the tools they currently possess.

GENETIC BIOHACKING

Experiments to modify genetic expression that once required specialized training and substantial investments in equipment and reagents can now be conducted for a few hundred dollars and with a basic instruction manual. Genomic sequencing can be done using portable pocket devices, some of which cost less than a plane ticket. The rise of direct-to-consumer genetic testing has also resulted in individual access to raw genetic data, fueling a variety of health, wellness, ancestry, and relative identification services that offer to interpret those data.

As these technologies go mainstream, some individuals have begun conducting genetic experiments outside of traditional scientific labs, such as those associated with universities, research institutions, and regulated corporate entities. Some of these experiments have involved humans, although thus far they appear to be limited to self-experimentation with one's own body—an activity that has an ancient pedigree in traditional medical research.

The motivations of these genetic biohackers, some of whom lack any formal training in biology, are diverse and often complex. Some appear to be motivated by normative beliefs in a "right to do science." Others place a high value on bodily autonomy or creative expression—a right to experiment on themselves or use genome editing for expressive purposes. Some view biohacking as a means of self-care, where, for example, they experiment with alternatives to (sometimes expensive) regulated drugs. Still others harbor views that traditional scientific institutions are poor regulators of themselves or are slow and needlessly cumbersome. And some, frankly, are moved by anti-government sentiments.

Reflecting these diverse motives, recent reports of genetic biohacking include a broad array of experiments: genetic modification of bacteria, yeast, plants, nonhuman mammals—and also humans, in the form of genetic self-experimentation. This includes, for example, self-injecting homemade genetic material in attempts to change the expression of muscle growth factors to improve strength or to treat diseases such as HIV or herpes (*2*). Where self-experimentation is undertaken by groups that coordinate their efforts, these activities can begin to look like decentralized clinical trials. Some biohackers might also attempt to experiment on others. Although there are no documented instances of this to date, biohackers have reported (and expressed concerns about) being approached by individuals asking for help treating their own or their family members' health conditions. Genetic biohacking of this sort—experimentation on oneself and others—poses public health risks. These include interventions with poor safety or efficacy, a lack of true informed consent, and the introduction and uptake of unsafe and unproven "therapies" into commerce. The democratization of genetic biohacking exacerbates these public health risks because many experiments make use of easy-to-obtain materials and equipment purchased from companies that cater to the do-it-yourself (DIY) market or freely provided by other biohackers.

There are other emerging areas of DIY science, such as neurohacking and self-manufacture of traditional pharmaceutical products, that do not focus on molecular genetics but that similarly raise public health concerns. Genetic biohacking, however, is especially easy, affordable, and a particularly popular and promising form of DIY science that poses unclear but potentially serious or far-reaching risks. These include, for example, sick individuals foregoing

[1]Moritz College of Law, The Ohio State University, Columbus, OH 43210, USA. [2]Center for Medical Ethics and Health Policy, Baylor College of Medicine, Houston, TX 77030, USA. [3]Innovation Center for Law and Technology, New York Law School, New York, NY 10013, USA. [4]Department of Health Policy and Management, Columbia University Mailman School of Public Health, New York, NY 10032, USA. [5]Center for Advanced Studies in Biomedical Innovation Law, University of Copenhagen Faculty of Law, DK-2300 Copenhagen, Denmark. Email: zettler.25@osu.edu, christi.guerrini@bcm.edu, jacob.sherkow@nyls.edu

known, effective treatments in the hope of cheaper and unproven DIY genetic interventions or, at an extreme, harmful germline modifications. As has been the case for "alternative" cancer treatments and autologous stem cell transplants, hype and access to biological reagents have the potential to pose substantial public health concerns. Genetic biohacking communities, therefore, should be an important focus for regulating DIY science.

GOVERNMENT REGULATION

As biohacking has become more prevalent and public, scholars, ethicists, and regulators have voiced concerns that government oversight may be absent or inadequate to address the risks that these activities may pose. Indeed, biohackers sometimes work in private, whereas traditional research is conducted in teams overseen by institutions. Biohackers generally do not obtain ethical review of their work, in contrast to traditional biological research. Furthermore, biohackers are often self-funded and are thus not typically accountable to private or agency funders, unlike their traditional, professional counterparts.

Contrary to the conventional wisdom, however, genetic biohacking does not occur in a legal or ethical "wild west" (*1*). In the United States, there are a number of laws and regulations that appear to be relevant. We focus on the U.S. regulatory landscape because the United States is a popular site for genetic biohacking and the home of the earliest community laboratories. Unlike some European countries, the United States does not ban genome editing conducted outside of licensed laboratories, although it is not unlikely that such a ban would be proposed if it is discovered (as it was with He) that some genetic biohackers have crossed generally observed lines of ethics or safety. Our objective is to help U.S. regulators better prepare for that day. Although our recommendations may not precisely translate to other countries because each jurisdiction has a unique regulatory system and philosophy, they may nonetheless be broadly informative of potential regulatory responses.

The U.S. Food and Drug Administration (FDA), for example, has extensive power to regulate the public health impacts of genetic biohacking, with jurisdiction that reaches farther than many biohackers realize. In many circumstances, the things used by genetic biohackers—such as raw biological materials, traditional drug products, and DIY CRISPR kits—are, by statute, FDA-regulatable drugs. Other articles, such as human gene therapy products, also come within FDA's purview over biologics (*3*). Moreover—and contrary to popular belief—money need not always change hands for an item to fall within FDA's jurisdiction, a wrinkle important for biohackers who freely provide or exchange materials (*4*). This view of FDA's authority was bolstered in November 2017 when, in response to concerns about individuals using DIY CRISPR kits for self-experimentation, the agency stated that "any use of CRISPR/Cas9 gene editing in humans [is] gene therapy" and therefore subject to regulation (*5*).

FDA has yet to vigorously enforce its power in this area. To date, it has not taken public enforcement action against any biohackers conducting genome editing. But this is consistent with FDA's flexibility to exercise "enforcement discretion" in deciding which violations merit formal action given limited enforcement resources. Genetic biohacking may also make it practically difficult for FDA to identify violations that do occur, especially when committed by individual experimenters or small-scale biohacking communities.

Even so, this does not mean that new or more powerful regulations are warranted. Where FDA has chosen not to formally wield its enforcement power, the agency still has a role in community engagement—education, warning, and standard-setting for activities that pose public health risks and that otherwise fall within its purview. An important function of the agency is to encourage communication and disclosure for traditional, commercial research (*6*). Through its longstanding role in assessing drugs and biological products, FDA is the government regulatory agency equipped with the expertise to assess the safety and effectiveness of genetic biohacking. FDA involvement, therefore, may help to realize the promise of genetic biohacking through guiding biohacking efforts toward interventions that live up to the communities' hopes.

Although FDA has begun to show interest in genetic biohacking—as evidenced by its November 2017 statement and the participation of officials in a 2018 "bio-citizen" workshop hosted not by the agency but by the Woodrow Wilson Center (*5*, *7*)—the agency has seemingly not yet taken the reins through a proactive effort to deeply engage with or understand biohacking communities. Given some biohackers' continued confusion about FDA's authority over their work, the agency might begin by clarifying the boundaries of its jurisdiction, in lay terms and in sufficient detail to cover diverse biohacking activities, while seeking feedback from biohacking communities on how FDA could best exercise its authority in this space. This would provide biohacking communities more certainty about where they stand and potentially encourage new and innovative biohacking activities that might have been deterred by uncertainty about FDA enforcement. At the same time, these activities will help the agency to avoid repeating the mistakes it made with the stem cell industry, where the rapid expansion of clinics offering unproven interventions to patients is attributed to years of uncertainty around the scope of FDA jurisdiction and limited agency engagement. The agency also could draft guidances about typical genetic biohacking experiments and identify staff as points of contact for those engaged in genetic biohacking who would like to communicate with the agency. FDA's lack of current engagement is a shame, but not one that merits revamping of the agency's powers.

A similar approach has thus far proved successful for other federal authorities in different contexts. The risks posed by biohacking in the context of "bioterrorism," for example, have been the subject of study by the Federal Bureau of Investigation's (FBI) Biological Countermeasures Unit (*8*). To police the threat of biohacking-mediated bioterrorism, and in contrast to FDA's work, the FBI has developed strong relationships with community labs, where some genetic experimentation is occurring.

Efforts at community engagement should focus on the potential public health harms posed by genetic biohacking, such as adverse effects from the administration of homemade gene therapies, contamination of the environment from poorly kept genetic reagents (such as viral vectors), and the forgoing of traditional treatments in favor of DIY experimental ones. Specific risks (and potential benefits) of genetic biohacking involving humans will depend on the context of their use. Thus, assessment should include, for example, ascertaining whether a homemade genetic intervention is intended as a therapy for a disease with no known treatment, a disease for which there are known effective treatments, or for some other purpose, such as an enhancement or aesthetic use.

PRIVATE REGULATION

Genetic biohacking is also potentially subject to U.S. laws that are enforced by private rather than government actors. These may fill some of the gaps in public regulators' ambit (*9*). Patent owners, for example, can impose ethical restrictions on licensees, such as the Broad Institute's licenses for its CRISPR patents to Bayer (formerly Monsanto), with conditions that Bayer avoid research activities that are potentially harmful to public health, including tobacco research and germline editing (*10*). Such li-

cense restrictions can—and should—be used to police commercial manufacturers of genome-editing kits and reagents popular in biohacking communities, just as they have previously been used to prevent activities that pose national security, environmental, or public health risks (*11*). Even without a license in place, patent owners can enforce restrictions through threats of patent infringement litigation against any recalcitrant biohackers or manufacturers of biohacking products. A similar model was proposed as an attempt to restrict the use of "gene drive technology"—inheritable versions of CRISPR designed to drive a specific allele through generations of a population (*12*). Beyond patents, people injured by genetic biohacking materials could potentially bring tort law claims against biohackers and component suppliers to seek compensation for their injuries. A person injured while using a DIY CRISPR kit, for example, would likely be able to sue the seller of the kit—a potentially strong deterrent to marketers of unsafe biohacking materials.

Apart from these legal mechanisms, some biohacking communities have adopted their own ethics restrictions, which, even if not intended to do so, might indirectly avoid harms to public health caused by genetic biohacking. The International Genetically Engineered Machine (iGEM) Competition, for example, requires its participants to comport with a strict program of bioethics (*13*). The International Gene Synthesis Consortium—a group of commercial suppliers of genetic materials—developed protocols for screening orders and verifying customers in an effort to prevent dangerous uses. For example, protocols may instruct suppliers to decline orders for delivery to home addresses or post office boxes (*9*). Although this is an important effort, some biohackers have nonetheless devised ways to pass such screening by, for instance, registering businesses for the purpose of obtaining institutional addresses.

Another example of self-governance is community labs' adoption of safety policies, which often include standards detailed in the cornerstone of biosafety practices in the United States, the Biosafety in Microbiological and Biomedical Laboratories guidance document. These policies include restrictions on experimentation in humans, one of the riskiest forms of genetic biohacking with the largest potential negative consequence to public health. A grant-funded effort spearheaded by North Carolina State University is currently under way to understand and improve on community labs' safety policies with guidance from biosafety officers established in three labs. Analogously, a code of ethics adopted in 2011 by an organization of DIY biologists, DIYbio.org, remains an important touchstone for experiments (*14*).

Given that many biohackers who conduct work at home are also members of community labs (*15*), their safety policies have the potential to go a long way in promoting safety in genetic biohacking. Outside the norms of community labs and traditional scientific institutions, many who engage in biohacking activities nonetheless rely on each other for materials and information, providing a positive downstream effect to community labs' ability to police the conduct of biohacking communities. These collaborations might also encourage transparency between biohackers affiliated with community labs and those outside the community lab niche.

Like government regulation, private governance of this sort is important and laudable but not a perfect or comprehensive solution. Private actors may not be inclined to regulate conduct that poses few risks to them, even if safety risks to others are numerous, obvious, and serious. In other cases, the social stigma of violating community norms may simply be an ineffective deterrent. Additionally, community labs' private governance efforts only weakly reach genetic biohacking communities focused on human experimentation or in locations where community labs are absent.

MOVING FORWARD

The existence of public and private governance mechanisms to mitigate the public health risks and encourage the innovative potential of biohacking—even if currently infrequently used—means that regulators can better implement these mechanisms rather than rely on new ones to be grafted into law. For example, calls for bans on biohacking, such as those from a consumer advocacy organization in Australia, go too far. The tools for public and private regulators to manage biohacking's public health risks are largely already available. But they must be used better.

As with other issues pertaining to public health, this also means that the future of regulating biohacking lies not only in more stringent policing, but in better education of its participants and a realistic understanding that violations will be inevitable. Education would help private actors to understand the risks posed by certain forms of biohacking and to appreciate FDA's role in both consumer protection and fostering of innovation (*6*). Likewise, public regulators such as FDA would benefit from engaging with stakeholders to better understand genetic biohacking activities, its participants' perspectives, and biohacking communities' potential for self-governance—much as it already does with the pharmaceutical industry. Even with limited enforcement resources, agencies such as FDA have an opportunity to advance public health by working with biohacking communities as their practices and norms are being developed—and before potentially problematic norms of risk, secrecy, and mavericks become widespread.

No government or private policy will ever achieve perfect compliance, even in traditional scientific settings—as He's experiments painfully demonstrate. There will always be "rogue actors" who may maintain connections with their institutional communities even after being "caught" (*1*). Striving for perfect compliance comes with substantial burdens, including throttling the development of new technologies, expending scarce enforcement resources, and facing political backlash. Appreciating this should allow policy-makers and regulators—both public and private—to understand that different genetic biohacking activities will pose different risks and should merit different approaches, and to tailor existing regulatory mechanisms to mitigate genetic biohacking's risks while amplifying its potential. ■

REFERENCES AND NOTES

1. R. A. Charo, *N. Engl. J. Med.* **380**, 976 (2019).
2. E. Baumgaertner, *New York Times*, 15 May 2018; www.nytimes.com/2018/05/14/science/biohackers-gene-editing-virus.html.
3. 42 U.S.C. § 262(i).
4. 21 U.S.C. § 331.
5. FDA, "Information About Self-Administration of Gene Therapy," www.fda.gov/BiologicsBloodVaccines/CellularGeneTherapyProducts/ucm586343.htm.
6. R. S. Eisenberg, *Mich. Telecommun. Technol. Law Rev.* **13**, 345 (2007).
7. T. Kuiken, E. Pauwels, S. W. Denton, "The Rise of the New Bio-Citizen: Ethics, Legitimacy, and Responsible Governance in Citizen-Driven Biomedical Research and Innovation" (Woodrow Wilson Center, July 2018); www.wilsoncenter.org/article/the-rise-the-new-bio-citizen-workshop.
8. H. Wolinsky, *EMBO Rep.* **17**, 793 (2016).
9. S. M. Maurer, *Self-Governance in Science* (Cambridge Univ. Press, 2017).
10. C. J. Guerrini, M. A. Curnutte, J. S. Sherkow, C. T. Scott, *Nat. Biotechnol.* **35**, 22 (2017).
11. S. O'Connor, *Berkeley Technol. Law J.* **21**, 1017 (2006).
12. A. Regalado, *MIT Tech. Rev.* (20 October 2016); www.technologyreview.com/s/602633/stop-gene-spills-before-they-happen/.
13. C. Vilanova, M. Porcar, *Nat. Biotechnol.* **32**, 420 (2014).
14. DIYbio, "Draft DIYbio Code of Ethics from North American Congress" (2011); https://diybio.org/codes/code-of-ethics-north-america-congress-2011/.
15. D. Grushkin, T. Kuiken, P. Millet, *Seven Myths and Realities About Do-It-Yourself Biology* (Woodrow Wilson Center, 2013); www.wilsoncenter.org/publication/seven-myths-and-realities-about-do-it-yourself-biology-0.

ACKNOWLEDGMENTS

We thank I. Canfield for research assistance. C.J.G.'s involvement in development of this manuscript was funded in part by National Human Genome Research Institute grant K01-HG009355.

10.1126/science.aax3248

Karen Lloyd and Donato Giovannelli investigate primitive microbes in Costa Rica as part of their work with the Deep Carbon Observatory.

PHOTO: TOM OWENS

CHEMISTRY

The grand story of carbon

A geologist offers a melodic meditation on one of Earth's most abundant elements

By **Nicola Pohl**

Although organic chemistry is often described as the science of carbon, Robert Hazen's latest book, *Symphony in C*, makes clear that this vital element cannot be contained by such a disciplinary boundary.

Despite its abundance and importance, the location and cycling of carbon on Earth are not yet well understood. Ever-increasing atmospheric concentrations of its dioxide form lend urgency to a more accurate accounting of this element. However, it is Hazen's enthusiasm, the string of shareable facts presented, and the introduction of so many interesting scientists that make this book such a fascinating read.

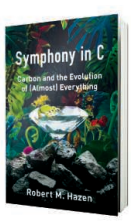

Symphony in C
Carbon and the Evolution of (Almost) Everything
Robert M. Hazen
Norton, 2019. 313 pp.

Trained as a geologist, Hazen also has a deep love of music, which manifests in the symphonic form that superficially organizes the book's content into four alchemical movements: earth, air, fire, and water. In the first section, "Earth"—the most well-developed of the book—Hazen discusses carbon-based minerals, offering a wonderful account of how mineralogy has gradually turned from a purely observational science to one that can predict missing carbon-containing minerals.

Hazen brings a distinct and intentionally personal perspective to this topic as head of the Deep Carbon Observatory (DCO), which brings together hundreds of scientists around the world to understand how carbon moves in all its forms in and around our planet. In 2015, the DCO started the "Carbon Mineral Challenge" to find the almost 150 carbon-containing minerals predicted to exist on or near Earth's surface. Some of these predicted minerals, including a sodium lead carbonate called abellaite and green middlebackite, have already been found.

The extreme pressures and temperatures hundreds of miles below Earth's surface form denser crystalline minerals, but almost none of the ~400 currently known carbon minerals are in high-pressure phases. Hazen has been fascinated by experimental efforts to mimic these extreme pressures since he was a graduate student, and he details the methods being used to reach 80,000-fold or greater atmospheres of pressure. Such high pressures do not lead only to simple structures, we learn. Additional surprises await when Hazen explores deeper toward Earth's core.

The second section, "Air," starts with a very brief history of Earth before discussing carbon in the air—primarily carbon dioxide—and its cycling through the atmosphere. Hazen finishes this section with a wonderful discussion of the biases that humans, including scientists, have and the challenges they bring to forming a more integrated picture of the world. "Carbon science is like that—a blending of concepts and principles from every branch of research," he writes. "So, perhaps when we seek to understand the limits to knowledge—the nature of the unknowable—our own human limitations need to be placed at the top of the list."

"Fire" is devoted to the many ways we manipulate carbon, using it to create plastic materials, for example, as well as other products of modern organic chemistry. Here, Hazen presents an almost random assortment of historical anecdotes about carbon-based materials, from methane to neoprene to paper, giving the reader a sense of the diverse forms carbon can take. This section is the shortest, and readers hoping for more detail might turn instead to Mark Miodownik's recent book, *Liquid Rules* (reviewed in *Science* on 8 February 2019) (*1*).

The final movement is the most speculative as Hazen describes the many scenarios that may account for the origins of carbon-based life forms. He makes clear his own biases—he believes that mineral surfaces were crucial to the formation of the small organic building blocks of life, for example—as he gallops through a history of this field.

The final pages of the book end with a very personal look at what Hazen calls the "human carbon cycle"—exploring how we consume and expel carbon—and examines our responsibility to our carbon-based home. "If we are wise, if we can temper our wants with a renewed sense of awe and wonder, if we can learn to cherish our rhapsodically beautiful carbon-rich world as it so urgently deserves, then we may hope to leave an unrivaled, priceless legacy for our children, their children, and all the generations to come." Given the incredibly wide range of the earlier chapters, this philosophical ending fits.

Throughout *Symphony in C*, science is presented as a living and very human endeavor. Hazen fills the book with scientists and collaborators from around the world and with his own research stories. An eight-page insert of photos, which depict not only mineral structures and timelines of Earth's evolution but also the men and women working to extend our knowledge, reinforces the human part of the grand story of carbon. The rapid pace of research in the areas presented could quickly warrant another overview, but for now, this very readable account should inspire a much broader interest in carbon. ■

The reviewer is at the Department of Chemistry, Indiana University, Bloomington, IN 47405, USA. Email: npohl@indiana.edu

REFERENCES AND NOTES

1. S. Brandt, *Science* **363**, 591 (2019).

10.1126/science.aaw7726

ARTIFICIAL INTELLIGENCE

Unsettling robots and the future of art

An AI-driven artist's exhibition hints at, but never fully explores, the ethics of algorithms

By **Chiara Ambrosio**

My train ride from London to Oxford is filled with anticipation. Having just watched the latest season of *Black Mirror*, I anticipate the same blending of wit, unintended consequences, and dystopian paradox from the new exhibition that has just opened at the Barn Gallery in St John's College, Oxford.

Unsecured Futures is the solo show of the first ultrarealistic humanoid robot artist, Ai-Da. A versatile artist, Ai-Da dabbles in drawing and painting as well as sculpture and performance. "She" is the result of a large multidisciplinary team that features artists, curators, computer scientists from the universities of Oxford and Leeds, and Cornwall-based company Engineered Arts.

Unsecured Futures
Lucy Seal, curator
The Barn Gallery, St John's College, University of Oxford
Through 6 July 2019

The press release feeds my sense of expectation, promising me that she is absolutely unique: "Ai-Da's ability as a robot to draw and paint from sight has never been achieved before and makes Ai-Da an artist in her own right, as well as a world first."

As I enter the gallery space, the exhibition synopsis advises that Ai-Da produces art "but she is also the art herself, highlighting tensions of transhumanism [sic], biotechnological advances, and how we will come to redefine our views of creativity." And there is more: Ai-Da aims to raise questions on a host of pressing social issues, ranging from how "necessary ethical discussions" about technology are "painfully lagging behind" to addressing "the frailty of our environment." The text concludes with a nod to George Orwell, Aldous Huxley, and Aleksandr Solzhenitsyn.

In three corners of the gallery, large screens show close-ups of Ai-Da performing an original piece, *Poetry of Consolation*, based on the prison literature of Fyodor Dostoyevsky, Oscar Wilde, and Severinus Boethius. The artwork label, a printed A4 sheet of paper blue-tacked to the wall and typed in 12-point font, cryptically explains that the original texts are used "as the input data for AI [artificial intelligence] algorithms based on Markov chains." It then swiftly moves to draw comparisons between prison literature and "the pain and suffering of animals housed in unsuitable captive environments."

Along one of the gallery walls, Ai-Da's pencil portraits of Charles Babbage, Alan Turing, Ada Lovelace (the robot's namesake), Karel Čapec, and Leonardo da Vinci and the robot's own self-portrait are hung side by side—inscribing Ai-Da in the long history of creativity, computing, and invention.

Ai-Da's paintings are the most visually spectacular items on display. Rich tones of red, yellow, and green and thick brushstrokes suggest a human touch. The position of the lights draws the viewer's gaze directly to the center of each work, heightening the "shattered" composition of the abstract paintings.

PHOTO: VICTOR FRANKOWSKI

The reviewer is at the Department of Science and Technology Studies, University College London, London WC1E 6BT, UK. Email: c.ambrosio@ucl.ac.uk

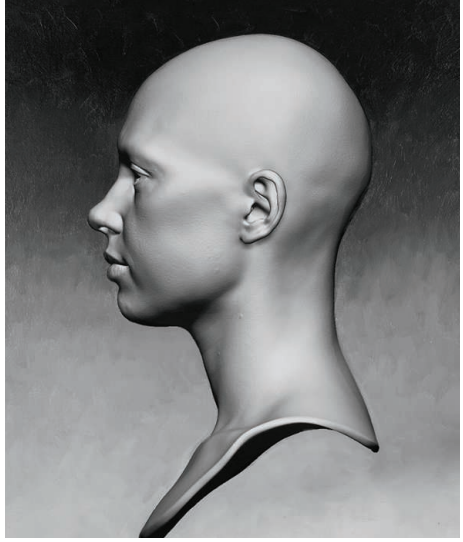

Artificial neural networks create the foundation for Ai-Da's abstract paintings, plotting the coordinates onto a Cartesian plane. Artist Suzie Emery applies oil paint to canvas renderings to create the final works. Sculptures based on Ai-Da's virtual renderings, including one based on a CT scan of a real bee, also appear in the exhibition.

PHOTOS: VICTOR FRANKOWSKI

Labels state that coordinates from Ai-Da's drawings are "plotted onto the Cartesian plane and then run through AI algorithms." The digital versions of the artworks were transferred on canvas and overlaid with oil paint by artist Suzie Emery.

On the train home, I cannot stop thinking about the paintings. How are neural networks "trained" to obtain them? How does Ai-Da choose the color of her artworks?

My questions are interrupted by an email from the exhibition's press office, which kindly puts me in contact with the Oxford-based computer scientist behind the paintings, Aidan Gomez. In a clear and detailed email, he explains how he uses logs of Ai-Da's motor instructions to wire the large neural network that creates the foundational design for the paintings. He tells me that he chooses the color palette, clarifying, however, that "it is the network's responses that dictate which colour lands at each point on the canvas, the lightness, the intensity, and so forth." He shares digital proofs, which provide an exciting glimpse at what the images look like before they are transferred on canvas and overlaid with paint. He stresses that Emery's artistic input is the decisive factor in the final form of the paintings.

Gomez's clear answers remain overshadowed—in the exhibition as well as in the press—by the hype around a female-presenting robot that produces original art. On my return home, I turn on the television and there is Ai-Da, with her flamboyant creator, Aidan Meller. As she quietly draws, Meller makes bold statements about ethics in the digital age and how we need to rethink creativity. A welcome reference to philosopher Margaret Boden creeps in but remains unexplained.

We need public engagement, he continues. But thus far, the appearance of Ai-Da has produced exactly the opposite effect: a cacophony of fashionable terms that will alienate a nonacademic audience and infuriate an academic one. We are already asking big questions about technology and about algorithms in particular. Virginia Eubanks's *Automating Inequality*, Safiya Umoja Noble's *Algorithms of Oppression*, and Cathy O'Neil's *Weapons of Math Destruction*, albeit not concerned with art in the digital age, are only a few examples of how technology does not only need to be questioned—it needs to be questioned rigorously and unpretentiously.

That mysterious algorithms and a random list of social issues live separate lives in the dazzling space of *Unsecured Futures* is a worrying sign of what can happen when a narrow conception of art joins the hype around AI and its applications. "Tensions of transhumanism," "ethics," and "public engagement" become empty terms, waved for effect and never probed. The result is an overload of information that polarizes opinion, fosters divides, and obliterates the critical potential of art as research in its own right.

As a philosopher, part of my job is to articulate questions that will take us beyond shallow slogans and commonplace assumptions. I found depth in Suzie Emery's brushstrokes, which compelled me to ask how Ai-Da's paintings came to be. I found depth in Aidan Gomez's honest answers about the uncertainties surrounding color processing in a neural network. I am certain that other collaborators, overshadowed by the lights of press conferences and television interviews, have equally interesting stories to tell.

Giving more space to the "how" of art and science is difficult and time consuming. It requires investigating the details. But only when this component is brought to the fore can we begin articulating interesting questions about our relationship with technology. ■

10.1126/science.aay1956

RESEARCH

A simplified route for polarization imaging

Rubin et al., *p. 43*

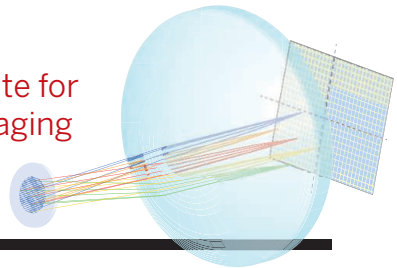

IN *SCIENCE* JOURNALS

Edited by **Stella Hurtley**

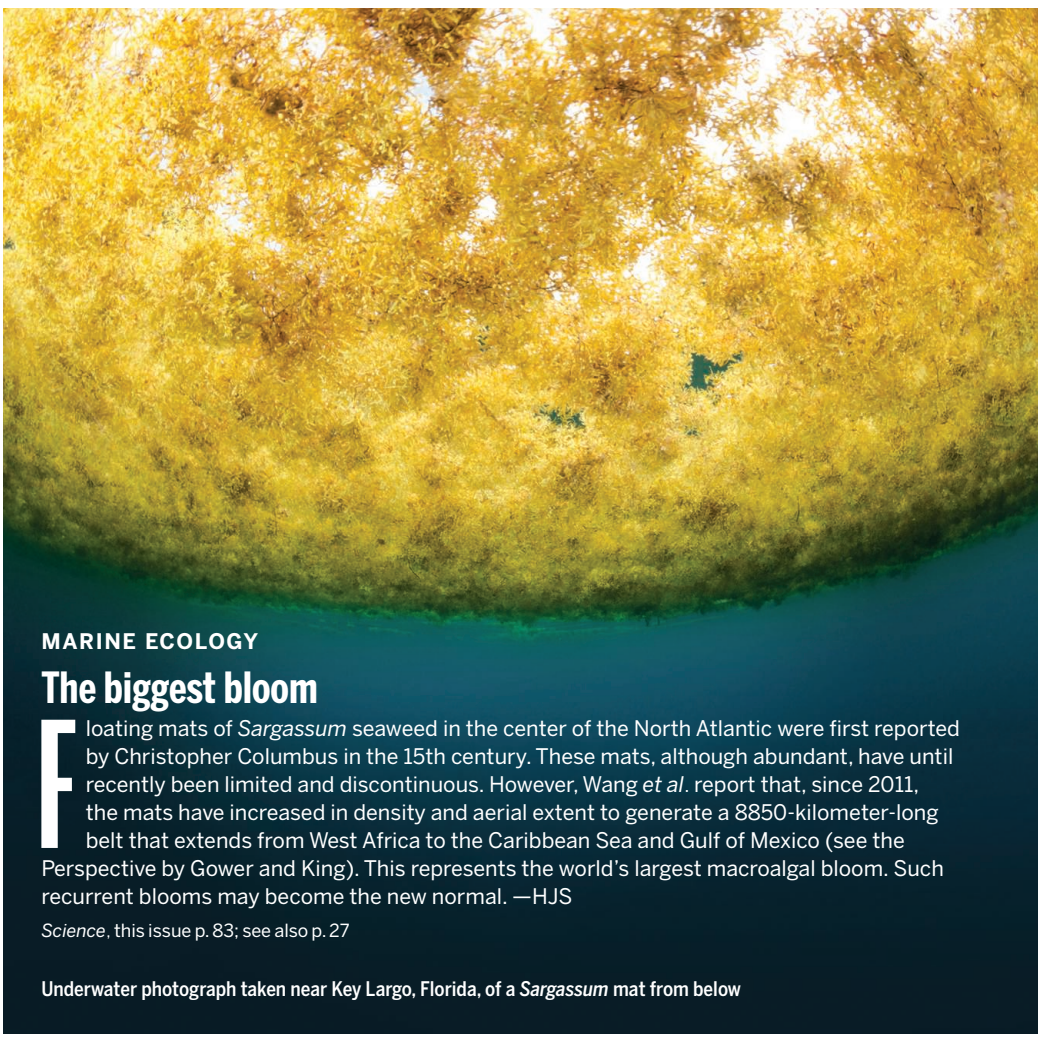

MARINE ECOLOGY

The biggest bloom

Floating mats of *Sargassum* seaweed in the center of the North Atlantic were first reported by Christopher Columbus in the 15th century. These mats, although abundant, have until recently been limited and discontinuous. However, Wang *et al*. report that, since 2011, the mats have increased in density and aerial extent to generate a 8850-kilometer-long belt that extends from West Africa to the Caribbean Sea and Gulf of Mexico (see the Perspective by Gower and King). This represents the world's largest macroalgal bloom. Such recurrent blooms may become the new normal. —HJS

Science, this issue p. 83; see also p. 27

Underwater photograph taken near Key Largo, Florida, of a *Sargassum* mat from below

CRISPR BIOLOGY

Beyond adaptive immunity

Prokaryotic CRISPR-Cas systems defend bacterial cells from phage and plasmid infection. Strecker *et al.* characterized a CRISPR-Cas system that functions beyond adaptive immunity (see the Perspective by Hou and Zhang). Type V-K CRISPR-Cas from cyanobacteria was associated with a Tn7-like transposon and a natural nuclease–deficient effector Cas12k. Cas12k directed the insertion of Tn7-like transposons into target sites via RNA-guided Tn7 transposition. This system was reprogrammed to efficiently and specifically insert DNA both in vitro and into the *Escherichia coli* genome. —SYM

Science, this issue p. 48; see also p. 25

RESTORATION ECOLOGY

The potential for global forest cover

The restoration of forested land at a global scale could help capture atmospheric carbon and mitigate climate change. Bastin *et al.* used direct measurements of forest cover to generate a model of forest restoration potential across the globe (see the Perspective by Chazdon and Brancalion). Their spatially explicit maps show how much additional tree cover could exist outside of existing forests and agricultural and urban land. Ecosystems could support an additional 0.9 billion hectares of continuous forest. This would represent a greater than 25% increase in forested area, including more than 500 billion trees and more than 200 gigatonnes of additional carbon at maturity. Such a change has the potential to cut the atmospheric carbon pool by about 25%. —AMS

Science, this issue p. 76; see also p. 24

PROTEIN DYNAMICS

Refilling the proton pump

Proteins are dynamic. Rearrangements of side chains, secondary structure, and entire domains gate functional transitions on time scales ranging from picoseconds to milliseconds. Weinert *et al.* used time-resolved serial crystallography to study large conformational changes in the proton pump bacteriorhodopsin that allow for redistribution of protons during the pumping cycle. They adapted methods used for x-ray free electron lasers to synchrotron x-ray sources. Large loop movements and a chain of water molecules were central to regenerating the starting state of bacteriorhodopsin. —MAF

Science, this issue p. 61

LIGHT METALS

Smaller but more ductile

Poor ductility is one limiting factor in widespread use of strong but lightweight magnesium

CREDITS: (PHOTO) CHRIS GUG/ALAMY STOCK PHOTO; (GRAPHIC) RUBIN *ET AL.*

alloys in cars, trains, and planes. The usual way to try to circumvent this poor ductility is by adding other elements, which can be costly. Liu *et al.* show that very small samples of pure magnesium are much more ductile than previously believed (see the Perspective by Proust). The small samples suppress the deformation twinning that causes fractures in larger samples. Avoiding this mechanism should allow development of high-ductility magnesium and other metal alloys. —BG

Science, this issue p. 73; see also p. 30

BEHAVIORAL ECONOMICS

Honesty and selfishness across cultures

Rationalist approaches to economics assume that people value their own interests over the interests of strangers. Cohn *et al.* wanted to examine the trade-off between material self-interest and more altruistic behaviors (see the Perspective by Shalvi). They distributed more than 17,000 wallets containing various sums of money in 355 cities across 40 countries. In contrast to what rationalist theories of economics predict, citizens were more likely to return wallets that contained more money. The findings also reveal a high level of civic honesty across nations. —TSR

Science, this issue p. 70; see also p. 29

CANCER

Putting CAR T cells in idle

Chimeric antigen receptor T (CAR T) cells can be an effective cell therapy for cancer. Unfortunately, excessive activation of CAR T cells can occasionally cause severe, even lethal, toxicity. Existing approaches can suppress overactive CAR T cells, but these generally kill the CAR T cells, which abrogates both their toxicity and their antitumor effects. In contrast, Mestermann *et al.* identified dasatinib as a drug that can temporarily inactivate CAR T cells. This helps reduce acute toxicity and allows the T cells to recover their antitumor effects after the drug is removed. —YN

Sci. Transl. Med. **11**, eaau5907 (2019).

GUT MICROBIOME

Inheriting microbiome variation

In mice, the bacterial species in the gut microbiome are maternally inherited. Yardeni *et al.* found reduced gut microbiome species diversity in mice with variations in mitochondrial DNA (mtDNA) that were associated with increased reactive oxygen species (ROS) production. When pups were cross-fostered, the gut microbiome species after weening reflected not the microbiota community of the nursing mother but rather the inherited mtDNA variation. Pharmacological or genetic reductions in mitochondrial ROS levels increased microbiome diversity. —ERW

Sci. Signal. **12**, eaaw3159 (2019).

CHEMICAL PHYSICS

A panoramic view of photodissociation

As light pulses get shorter in time, they correspondingly get broader in frequency. Kobayashi *et al.* take advantage of both properties of attosecond pulses to elucidate iodine monobromide (IBr) photodissociation by detecting ultrafast bromine and iodine spectral shifts simultaneously. A preliminary burst of light weakens the I–Br bond. Then, as the atoms fly apart, they reach a configuration where the bond vibration can couple ground and excited electronic states. The broadband probe pulse reveals rapid changes in each atom's electronic structure at this juncture. —JSY

Science, this issue p. 79

IN OTHER JOURNALS

Edited by **Caroline Ash** *and* **Jesse Smith**

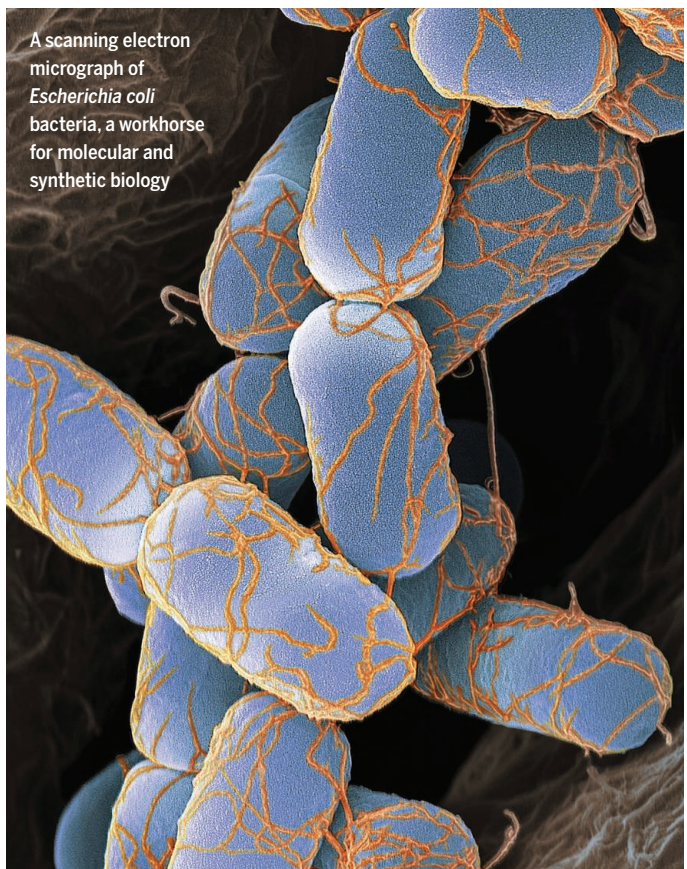

A scanning electron micrograph of *Escherichia coli* bacteria, a workhorse for molecular and synthetic biology

METABOLIC MODELING

Predicting resource use in microbes

A bacterial cell is a microscopic, self-replicating factory that hosts thousands of interconnected chemical reactions. Metabolism varies with input materials and environment and can be manipulated in the lab to yield desired products. Bulović *et al.* created a package of tools to automate construction of models of metabolite flux in bacteria. A key step is optimization of parameters using experimental data, but the predictions were robust even when limited information was available. The authors model a strain of *Escherichia coli* engineered to fix carbon, demonstrating that such models can be useful planning tools for synthetic biology. —MAF

Metab. Eng. **55**, 12 (2019).

CANCER

Microbial stages of colorectal cancer

Colorectal cancers develop in a multistage process from polyploid adenomas to carcinomas and more advanced disease stages. Increasingly, some bacterial species in the gastrointestinal microbiota have been linked to colorectal cancer development. Yachida *et al.* mapped the fecal microbiome contents of 616 individuals undergoing colonoscopy. They found significant increases of specific bacterial species with

PHOTO: MARTIN OEGGERLI/SCIENCE SOURCE

COASTAL PROTECTION

Storm protection services

The tropics are at increasing risk of storm damage as the climate warms—a major worry, as coasts also concentrate human populations. Many coastlines in the tropics are, or once were, bordered by mangrove woodland. Mangroves colonize and stabilize the intertidal zone, not only providing habitats for terrestrial and marine organisms but also buffering storm surges, winds, and saline intrusion. However, these forests are at risk owing to land reclamation for building, agriculture, and other economic activities. Hochard *et al.* calculated the global value of mangroves in protecting human activities against tropical cyclone damage. From 23 mangrove-fringed countries, they observed human activity by satellite mapping of nighttime light. Regions with narrow (6-meter) strips of mangrove suffer greater permanent economic loss over the next 6 years than do communities protected by 25 meters of mangroves or more, despite disaster-mitigation responses. This work underscores the importance of restoring natural infrastructure for the benefit of vulnerable communities, as well as biodiversity. —CA

Proc. Natl. Acad. Sci. U.S.A. **116**, 12232 (2019).

Coastal mangrove forests near Krabi, Thailand

different stages of colorectal cancer, indicating that these might be biomarkers of disease that can be used in diagnosis. —GKA

Nat. Med. **25**, 968 (2019).

SIGNAL TRANSDUCTION

Receptor get-together for hematopoiesis

Wnt signaling is involved in many organismal processes. What is poorly understood in each pathway is which Wnt ligand requires which receptor. Blood-cell proliferation and specialization (hematopoiesis) requires specific Wnt and Frizzled ligand and receptor pairs. Grainger *et al.* discovered a role for a distinct receptor type in Wnt signaling. Labeling Frizzled9b protein in human cells with a peroxidase enzyme allowed closely associated proteins to be isolated and identified by mass spectroscopy. The most enriched protein was the epidermal growth factor receptor. Experiments inhibiting epidermal growth factor receptor function also supported its role in regulation of Wnt signaling, perhaps by modulating receptor internalization. —LBR

Nat. Cell Biol. **21**, 721 (2019).

DEVELOPMENTAL BIOLOGY

Coordinating organs

Although individuals vary in size and shape, body parts are largely proportional. But what mechanisms monitor relative size between organs? In the larva of the fruit fly, *Drosophila*, adult body parts arise from structures called imaginal discs. When growth of one *Drosophila* imaginal disc is inhibited, similar size restriction is seen in other imaginal discs. Boulan *et al.* show that upon injury, the stress response transcription factor Xrp1 activates expression of a hormone-like peptide called Dilp8. Dilp8 is key for coordination between organs. Furthermore, the small ribosomal subunit protein Rps12 senses tissue growth and regulates Xrp1. Together, the Rps12-Xrp1-Dilp8 regulatory program maintains appropriate body proportions by delaying growth to coordinate interorgan size. —BAP

Dev. Cell **49**, 811 (2019).

APPLIED PHYSICS

Flipping the bits with current

Using magnetic fields to write information into memory storage limits the physical bit density of magnetic media. Hong *et al.* present a proof-of-principle demonstration of using spin-polarized currents instead of magnetic fields for the writing process, which could potentially increase this density. The magnetic bit was a multilayer structure with cobalt-iron-boron as the magnetic layer. A scanning tip—through which the spin-polarized current tunneled into the bit—was coated with a similar multilayer. The researchers were able to control the magnetization of the bit with the current by placing the tip only 3 angstroms away—a distance that will need to be increased for commercial applications. —JS

Appl. Phys. Lett. **114**, 243101 (2019).

CLIMATE CHANGE

High-latitude stakes

Sea ice in the Arctic is disappearing rapidly because of climate warming, a process which then accelerates warming owing to the absorption of solar radiation by a sea that is no longer covered by highly reflective ice. How much additional heating would complete loss of that sea ice cover cause? Pistone *et al.* use satellite observations to estimate how much solar energy would be added to the climate system were all the sea ice in the Arctic to melt. They calculate that heating would increase by an amount equivalent to that which would result from 1 trillion tons of carbon dioxide emissions, approximately 25 years of current fossil fuel use. —HJS

Geophys. Res. Lett. 10.1029/2019GL082914 (2019).

PHOTO: CRYSTITE RF/ALAMY STOCK PHOTO

ALSO IN *SCIENCE* JOURNALS

Edited by **Stella Hurtley**

METASURFACES

A metasurface polarization camera

Imaging the polarization of light scattered from an object provides an additional degree of freedom for gaining information from a scene. Conventional polarimeters can be bulky and usually consist of mechanically moving parts (with a polarizer and analyzer setup rotating to reveal the degree of polarization). Rubin *et al.* designed a metasurface-based full-Stokes compact polarization camera without conventional polarization optics and without moving parts. The results provide a simplified route for polarization imaging. —ISO

Science, this issue p. 43

AFRICAN GENETICS

East African genetics and pastoralism

The origin and spread of domestic animals across the globe also affected the underlying genetic composition of human populations. In Africa, however, it has been difficult to identify the impact of interactions among migrating food producers and local hunter-gatherers. Prendergast *et al.* wanted to discern the timing and movement of husbandry and pastoralism and its effects on foraging communities in Africa. They sequenced 41 ancient eastern African human genomes from individuals that lived approximately 100 to 4000 years ago. Surprisingly, relatively little genetic mixture occurred at the same time as the spread of pastoralism. —LMZ

Science, this issue p. 44

PROTEIN STABILITY

Glycine N-degron regulation revealed

For more than 30 years, N-terminal sequences have been known to influence protein stability, but additional features of these N-end rule, or N-degron, pathways continue to be uncovered. Timms *et al.* used a global protein stability (GPS) technology to take a broader look at these pathways in human cells. Unexpectedly, glycine exposed at the N terminus could act as a potent degron; proteins bearing N-terminal glycine were targeted for proteasomal degradation by two Cullin-RING E3 ubiquitin ligases through the substrate adaptors ZYG11B and ZER1. This pathway may be important, for example, to degrade proteins that fail to localize properly to cellular membranes and to destroy protein fragments generated during cell death. —SMH

Science, this issue p. 45

NEURODEVELOPMENT

Temporal code underlies circuit formation

Olfactory neurons respond to various odorants according to which olfactory receptors, of many, they express. During development, axons from olfactory neurons that express the same olfactory receptor converge to share the same glomeruli. Nakashima *et al.* now show that, in mice, the neurons build these connections according to shared patterns of activity. When the olfactory receptor is triggered, it causes its cell not simply to fire but to fire in specific patterns. Neurons that speak the same code end up connected at the same glomerulus. —PJH

Science, this issue p. 46

CELL BIOLOGY

Linking protein misfolding and innate immunity

Multiple innate immune sensors undergo rapid assembly into large complexes known as signalosomes. This is an essential step during cellular responses to microbes and danger signals. How this process is regulated to avoid accumulation of potentially toxic protein aggregates remains poorly understood. Abdel-Nour *et al.* identified a pathway, dependent on heme-regulated inhibitor, eukaryotic initiation factor 2α, activating transcription factor 4, and heat shock protein B8, which controls the folding and scaffolding of innate immune sensors, allowing optimal proinflammatory signaling (see the Perspective by Pierre). The pathway appears to mirror the endoplasmic reticulum unfolded protein response (UPR), and so was named the cytosolic UPR (cUPR). The cUPR may represent a general mechanism to control protein misfolding in cells. —SMH

Science, this issue p. 47; see also p. 28

CELL BIOLOGY

ER-phagy keeps cells healthy

In eukaryotic cells, about one-third of all proteins are targeted to the endoplasmic reticulum (ER), which serves as a hub for secretory protein traffic and quality control. Cui *et al.* studied a protein known as Lst1 in yeast and SEC24C in mammalian cells that is involved in loading secretory cargo into vesicles that are delivered to the Golgi complex. In response to stress caused by starvation or misfolded aggregate-prone secretory proteins, Lst1 acted to promote an additional function—ER-phagy. Together with autophagy receptors on the ER, Lst1 targeted ER domains for degradation to avert protein aggregation, thus preserving cellular health. —SMH

Science, this issue p. 53

BIOCHEMISTRY

Oxygen sensing across kingdoms

The ability to sense and respond to changes in oxygen levels is critical for most forms of life. To date, mechanistic studies of this process in mammals have focused on the oxygen-sensitive stability of a transcription factor called hypoxia-inducible factor. Masson *et al.* discovered an enzymatic oxygen sensor in humans that is functionally identical to plant cysteine oxidases, enzymes that control responses to hypoxia in plants. The human and plant enzymes convert the N-terminal cysteine in substrate proteins to cysteine sulfinic acid, a modification that ultimately targets the proteins for degradation. Oxygen sensing is impaired in many human diseases, and further study of the human enzyme could help in the development of strategies for therapeutic intervention. —PAK

Science, this issue p. 65

NEUROSCIENCE

Brain immune cells in disease

The microglia are brain-resident macrophages that are important for homeostasis. Recent studies show that microglia are also involved in various brain diseases, such as multiple sclerosis and Alzheimer's disease. In a Perspective, Priller and Prinz discuss how these disease-associated microglia exhibit alterations that are specific to the type of disease. This specificity suggests avenues by which microglia might be targeted to overcome brain pathology. —GKA

Science, this issue p. 32

IMMUNOLOGY

Hypertension-induced alarm signal

Human hypertension is a highly prevalent disease known to be associated with chronic low-grade inflammation. Zhao *et al.* used mouse models to look for hypertension-induced proinflammatory molecules that contribute to T cell activation and inflammation. They found consistent elevations in plasma levels of the alarmin molecule adenosine triphosphate in hypertensive mice. Increased adenosine triphosphate (ATP) concentrations promoted T cell responses by enhancing expression of the CD86 costimulatory molecule on antigen-presenting cells, an effect mediated through the P2X7 purinergic receptor. Elevations of plasma ATP were also detected in a cohort of hypertensive human patients when compared with normotensive controls. Thus, ATP release and the ATP-P2X7 signaling axis represent potential targets to help rein in the proinflammatory sequelae associated with chronic hypertension. —IW

Sci. Immunol. **4**, eaau6426 (2019).

RESEARCH ARTICLE SUMMARY

METASURFACES

Matrix Fourier optics enables a compact full-Stokes polarization camera

Noah A. Rubin, Gabriele D'Aversa, Paul Chevalier, Zhujun Shi, Wei Ting Chen, Federico Capasso*

INTRODUCTION: Polarization describes the path along which light's electric field vector oscillates. An essential quality of electromagnetic radiation, polarization is often omitted in its mathematical treatment. Nevertheless, polarization and its measurement are of interest in almost every area of science, as well as in imaging technology. Traditional cameras are sensitive to intensity alone, but in a variety of contexts, knowledge of polarization can reveal features that are otherwise invisible. Determination of the full-Stokes vector—the most complete description of light's polarization—necessitates at least four individual measurements. This results in optical systems that are often bulky, reliant on moving parts, and limited in time resolution.

RATIONALE: We introduce a formalism—matrix Fourier optics—for treating polarization in paraxial diffractive optics. This formalism is a powerful generalization of a large body of past work on optical elements in which polarization may vary spatially. Moreover, it suggests a path to realizing many polarization devices in parallel using a single optical element. We can then design diffraction gratings whose orders behave as polarizers for an arbitrarily selected set of polarization states, a new class of optical element. The intensity of light on a set of diffraction orders is then dictated by the polarization of the illuminating light, making these gratings immediately applicable to full-Stokes polarization imaging.

RESULTS: We theoretically investigate these gratings and develop an optimization scheme for their design. Our diffraction gratings were realized with dielectric metasurfaces in which subwavelength, anisotropic structures provide for tunable polarization control at visible frequencies. Characterization of the fabricated gratings shows that they perform as designed. Notably, an arbitrary set of polarizations may be analyzed by a single unit cell, in contrast to past approaches that relied on interlacing of several individually designed diffraction gratings, increasing the flexibility of these devices.

These gratings enable a snapshot, full-Stokes polarization camera—a camera acquiring images in which the full polarization state is known at each pixel—with no traditional polarization optics and no moving parts (see panel A of the figure). Polarized light from a photographic scene is incident on the grating inside of a camera. The polarization is "sorted" by the specially designed subwavelength metasurface grating. When combined with imaging optics (a lens) and a sensor, four copies of the image corresponding to four diffraction orders are formed on the imaging sensor. These copies have each, effectively, passed through a different polarizer whose functions are embedded in the metasurface. The four images can be analyzed pixel-wise to reconstruct the four-element Stokes vector across the scene. Several examples are shown at 532 nm, both indoors and outdoors. The figure depicts an example photograph of two injection-molded plastic pieces, a ruler and a spoon (illuminated by a linearly polarized backlight), that show in-built stresses (see panels C to E of the figure) that are not evident in a traditional photograph (panel B). The camera is compact, requiring only the grating (which is flat and monolithically integrated, handling all the polarization analysis in the system), a lens, and a conventional CMOS (complementary metal–oxide–semiconductor) sensor.

CONCLUSION: Metasurfaces can therefore simplify and compactify the footprint of optical systems relying on polarization optics. Our design formalism suggests future research directions in polarization optics. Moreover, it enables a snapshot, full-Stokes polarization imaging system with no moving parts, no bulk polarization optics, and no specially patterned camera pixels that is not altogether more complicated than a conventional imaging system. Our hardware may enable the adoption of polarization imaging in applications (remote sensing, atmospheric science, machine vision, and even onboard autonomous vehicles) where its complexity might otherwise prove prohibitive. ■

ON OUR WEBSITE

Read the full article at http://dx.doi.org/10.1126/science.aax1839

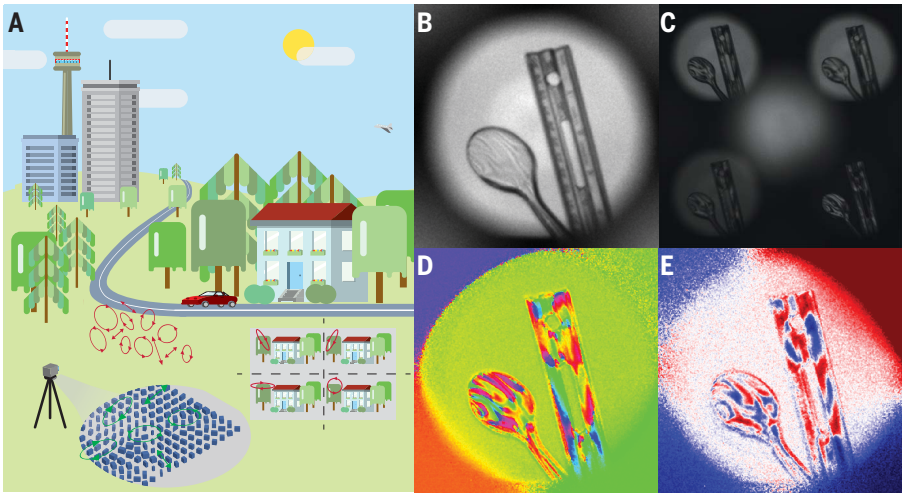

Metasurface-based polarization camera. (**A**) Photographic scenes contain polarized light that is invisible to traditional, intensity-based imaging, which may reveal hidden features. Our camera uses a metasurface (inset) that directs incident light depending on its polarization, forming four copies of an image that permit polarization reconstruction. (**B** to **E**) A plastic ruler and spoon are photographed with the camera. (B) A monochrome intensity image (given by the S_0 component of the Stokes vector) does not reveal the rich polarization information stemming from stress-birefringence readily evident in (C) to (E), which show a raw exposure, azimuth of the polarization ellipse, and the S_3 component of the Stokes vector that describes circular polarization content, respectively.

The list of author affiliations is available in the full article online.
*Corresponding author. Email: capasso@seas.harvard.edu
Cite this article as N. A. Rubin *et al.*, *Science* **365**, eaax1839 (2019). DOI: 10.1126/science.aax1839

RESEARCH ARTICLE

METASURFACES

Matrix Fourier optics enables a compact full-Stokes polarization camera

Noah A. Rubin[1], Gabriele D'Aversa[1,2], Paul Chevalier[1], Zhujun Shi[3], Wei Ting Chen[1], Federico Capasso[1]*

Recent developments have enabled the practical realization of optical elements in which the polarization of light may vary spatially. We present an extension of Fourier optics—matrix Fourier optics—for understanding these devices and apply it to the design and realization of metasurface gratings implementing arbitrary, parallel polarization analysis. We show how these gratings enable a compact, full-Stokes polarization camera without standard polarization optics. Our single-shot polarization camera requires no moving parts, specially patterned pixels, or conventional polarization optics and may enable the widespread adoption of polarization imaging in machine vision, remote sensing, and other areas.

Polarization refers to the path traversed by light's electric field vector. As a fundamental characteristic of light, polarization and its measurement are of great interest in almost all areas of science and in imaging technology as well. Traditionally, polarization is spoken of as a property of a beam of light. However, advances in the last few decades in holographic media, micro- and nanofabrication, and other areas have enabled the practical realization of optical elements with tailored, spatially varying polarization properties, even on a subwavelength scale, at optical frequencies. In these devices, the polarization state of light can be varied controllably, point-to-point across an optical element.

Work of this nature now has an extensive literature across several disciplines of optics under various names, including diffractive optics (*1*, *2*), polarization holography (*3*–*6*), and nanophotonics (metasurfaces) (*7*, *8*), in addition to appreciable attention from the liquid crystal community (*9*, *10*). These devices exhibit different behavior depending on the polarization of illuminating light, so a natural question that arises is how they can be designed to implement many polarization-dependent functions in parallel.

We consider a generalization of work in this area, which we call matrix Fourier optics, that suggests new design strategies for the design of polarization optics not previously achievable in a single element. In particular, we apply it to the design of metasurface diffraction gratings that can analyze several arbitrarily specified polarization states in parallel.

[1]Harvard John A. Paulson School of Engineering and Applied Sciences, Harvard University, Cambridge, MA 02138, USA. [2]Section de Physique, École Polytechnique Fédérale de Lausanne, CH-1015 Lausanne, Switzerland. [3]Department of Physics, Harvard University, Cambridge, MA 02138, USA.
*Corresponding author. Email: capasso@seas.harvard.edu

Matrix Fourier optics

We present a general way of viewing diffraction from a polarization-dependent obstacle. In the plane-wave expansion (or angular spectrum) picture of optics, an electromagnetic disturbance $U(x,y)$ in a plane can be considered as being formed from the interference of many plane waves incident at different angles. An individual plane wave in this set is characterized by its in-plane wave-vector (k_x, k_y) and a weight given by the Fourier transform of the optical field as

$$A(k_x,k_y)=\iint_{-\infty}^{+\infty}U(x,y)e^{i(k_x x+k_y y)}dx\,dy \quad (1)$$

Each plane wave with its weight $A(k_x,k_y)$ can be individually propagated forward in space to form the field at a different position (Fig. 1A). This formalism can treat light's interaction with simple obstacles. If a planar obstacle having a transmission function $t(x,y)$ (e.g., Young's double slit, or a diffraction grating) is illuminated by an incident field of magnitude E_0 (which may also be spatially-varying), the field immediately following the obstacle, $t(x,y)E_0$, can be handled in this way.

This intuitive understanding of optical wave propagation is the basis of the field broadly known as Fourier optics (*11*) and underpins much of modern optical physics, including imaging and holography. Notably, however, this picture is a scalar one and does not include light's polarization. Nonetheless, it is possible to conceive of optical elements in which polarization-dependent properties vary as a function of space. Then, instead of the scalar transmission function $t(x,y)$, we may consider that an optical element is associated with a matrix-valued function $\tilde{J}(x,y)$. Here, $\tilde{J}(x,y)$ denotes the local Jones matrix (*12*), the way in which the Jones polarization vector is modified, at each point. (In this work, matrix quantities are denoted by a tilde.)

We consider that such an optical element with a Jones matrix profile $\tilde{J}(x,y)$ is illuminated by a field described by the Jones vector ket $|E_0\rangle$ (in acknowledgment of its polarized nature). The field immediately after the obstacle is then given by $\tilde{J}(x,y)|E_0\rangle$. This field, too, can be propagated by plane-wave expansion as given by the Fourier transform

$$|A(k_x,k_y)\rangle = \iint_{-\infty}^{+\infty}\tilde{J}(x,y)|E_0\rangle e^{i(k_x x+k_y y)}dx\,dy \quad (2)$$

which is now vector-valued. If the incident wave is a normally incident, uniform plane-wave, it will carry no space-dependence and can be removed from the integral. The only integral to be evaluated, then, is given by

$$\tilde{A}(k_x,k_y)=\iint_{-\infty}^{+\infty}\tilde{J}(x,y)e^{i(k_x x+k_y y)}dx\,dy \quad (3)$$

which is a Fourier integral distributed across each of the four elements of the 2 × 2 Jones matrix yielding a Fourier coefficient $\tilde{A}(k_x,k_y)$ which is itself a Jones matrix (Fig. 1B).

This matrix Fourier transform is physically significant. Instead of an amplitude and phase, as in traditional Fourier optics, a given direction (k_x,k_y) is associated with a polarization-dependent behavior given by the Jones matrix operator $\tilde{A}(k_x,k_y)$. In a sense, this description decouples the optical element described by $\tilde{J}(x,y)$ from the polarization of the illuminating light: The interaction of all possible incident polarizations with $\tilde{J}(x,y)$ is handled at once by the matrix Fourier transform $\tilde{A}(k_x,k_y)$.

In this work, we specialize to polarization-dependent diffraction gratings—that is, elements in which $\tilde{J}(x,y)$ is a periodic function and the angular spectrum $\tilde{A}(k_x,k_y)$ is discrete, yielding diffraction orders. Diffraction gratings simply reveal the consequences of this matrix Fourier optics, in particular, that it can be inverted and used as a design strategy for multifunctional polarization optics. Suppose there is a set of desired polarization devices to be realized (e.g., polarizers, waveplates, optically active elements, or any behavior that can be described by a Jones matrix) having the Jones matrices $\{\tilde{J}_k\}$ and a set of diffraction orders $\{\ell\}$. The Fourier series expansion

$$\tilde{J}(x,y)=\sum_{k\in\{\ell\}}\tilde{J}_k e^{i(k_x x+k_y y)} \quad (4)$$

represents a single optical element realizing all of these (potentially complicated) polarization-dependent functions in parallel with each order implementing its own polarization device (Fig. 1C). In the case of a grating, the Fourier transform

Eq. 3 becomes a Fourier series in Eq. 4 with the optical elements $\{\tilde{J}_k\}$ as coefficients. We refer to such a diffraction grating as a matrix grating.

This way of viewing polarization-dependent diffraction has not seen wide acknowledgment or use in the literature of polarization [with some limited exceptions in diffractive optics (*13*, *14*) and polarization ray-tracing (*15*, *16*)]. In a common strategy, optical elements—especially in the field of metasurfaces—are often designed so that when a given polarization is incident, the output polarization state is uniform across the element and a scalar phase profile is imparted. When the orthogonal polarization is incident, the output polarization state is again uniform and a second phase profile is experienced. In this way, optical elements with different functions for chosen linear, circular, and arbitrary elliptical polarization bases (*7*, *8*, *17*) can be realized. Notably, what is widely referred to as the "geometric" or "Pancharatnam-Berry" phase, at least as it relates to this problem, is a subcase of that approach, being used to create scalar phase profiles for circularly polarized light (*2*, *9*, *18*–*21*). In other past work, polarization is understood to vary with space, but a particular incident polarization state is assumed (*22*, *23*). These past design strategies are subcases of the matrix approach presented here.

Parallel polarization analysis by unitary polarization gratings

The formalism presented in the last section is general. Equation 4 provides a prescription for the realization of a diffractive element implementing arbitrary polarization behavior, but does not specify the nature of the desired optical functions (contained in $\{\tilde{J}_k\}$) or how the resulting $\tilde{J}(x,y)$ should be practically realized.

We focus on cases in which $\{\tilde{J}_k\}$, the behaviors implemented by the grating orders, are polarization analyzers. This choice is not a fundamental one, but it is highly relevant for practical applications: Analyzers are perhaps the most fundamental polarization element and, moreover, devices that project light onto different states of polarization are of practical use in polarimetry, the measurement of light's polarization state (*24*). A diffraction order k behaving as a polarizer can be described by a Jones matrix that is a dyadic (outer product) expressed as

$$\tilde{J}_k = a_k |p_k\rangle\langle q_k| \tag{5}$$

Equation 5 describes a Jones matrix analyzing for the chosen Jones vector $|q_k\rangle$ in accordance with Malus' law: When $|q_k\rangle$ is incident, intensity transmission is maximum. If instead the orthogonal polarization $|q_k^{\perp}\rangle$ with $\langle q_k^{\perp}|q_k\rangle = 0$ arrives, the output light is quenched. The light emerging from $\tilde{J}_k$ will carry the polarization state $|p_k\rangle$. (A traditional polarizer familiar from laboratory experience has $|p_k\rangle = |q_k\rangle$). Finally, a_k is a complex (scalar-valued) weight.

Once the desired analyzers $\{\tilde{J}_k\}$ are specified (Eq. 5), the grating $\tilde{J}(x,y)$ can be derived by Eq. 4. What physical optical element should implement the resulting $\tilde{J}(x,y)$? A highly convenient realization medium takes the form of metasurfaces (*25*, *26*)—subwavelength-spaced arrays of nanophotonic phase shifters—composed of dielectric pillars possessing form birefringence (*7*, *8*). Locally, the Jones matrix of these metasurfaces may be well-approximated by a linearly birefringent waveplate (*8*) given by

$$\tilde{J}(x,y) = R(\theta(x,y)) \begin{pmatrix} e^{i\phi_x(x,y)} & 0 \\ 0 & e^{i\phi_y(x,y)} \end{pmatrix} R(-\theta(x,y)) \tag{6}$$

Stated differently, such a metasurface can realize a sampled matrix grating where $\tilde{J}(x,y)$ is locally of the form of Eq. 6. The use of dielectric metasurfaces obeying Eq. 6 is, again, not a fundamental choice, but an especially convenient one: ϕ_x, ϕ_y, and θ are all easily and continuously adjusted by varying the dimensions and angular orientation of a simple dielectric pillar, easily fabricated lithographically (R is a 2×2 rotation matrix). We refer to metagratings structured from these elements simply as "gratings," but in contrast to more generic diffraction gratings, it should be understood that the gratings here possess special polarization properties owing to their subwavelength features.

By inspection, Eq. 6 describes a Jones matrix that is (i) unitary everywhere—that is, $\tilde{J}^{\dagger}\tilde{J} = \mathbb{1}$ for all (x,y), with $\mathbb{1}$ the 2×2 identity matrix—and more specifically, (ii) linearly birefringent, having linear polarizations as its eigenvectors for all (x,y).

From the completely general matrix picture presented we have made two specific choices that the diffraction orders of the grating should behave as analyzers and that the grating should locally resemble Eq. 6, implying the above two constraints. But are these choices mathematically consistent with one another? That is, for a general set of diffraction orders $\{\ell\}$ implementing the polarization analyzers $\tilde{J}_k = a_k|p_k\rangle\langle q_k|$ for $k \in \{\ell\}$, will the $\tilde{J}(x,y)$ mandated by Eq. 4 obey the form of Eq. 6 for all (x,y)?

This question is a matrix analog of extensive work conducted on phase-only gratings (*27*, *28*). We show in the supplementary text (section S1) that the linear birefringence required by Eq. 6 implies that the $\tilde{J}_k$ must be symmetric mandating that each take the form $\tilde{J}_k = a_k|q_k^*\rangle\langle q_k|$. That is, the output polarization of each analyzer must be the complex conjugate of the Jones vector being analyzed for; this is equivalent to a mirroring about the equatorial plane of the Poincaré sphere, a change in sign of the third (chiral) Stokes component. Physically, this means that the analyzer leaves the polarization ellipse's shape unchanged while reversing the handedness of its rotation, a generalization of a key conclusion of (*7*) and (*8*).

Accepting this constraint guarantees linear birefringence (that is, matrix symmetry) for all (x,y), but not necessarily unitarity everywhere. This unitarity restriction in particular implies that, if we insist on a matrix grating with exactly n orders that are polarization state analyzers, the form of Eq. 6 can only be matched everywhere if $n = 2$ and the polarizations analyzed for are strictly orthogonal (as proven in supplementary text section S1) (*17*).

Design strategy and optimization

If we insist on using a single-layer metasurface obeying Eq. 6 everywhere, then we may not have all light confined to an arbitrary set of diffraction orders acting as polarization state analyzers. But

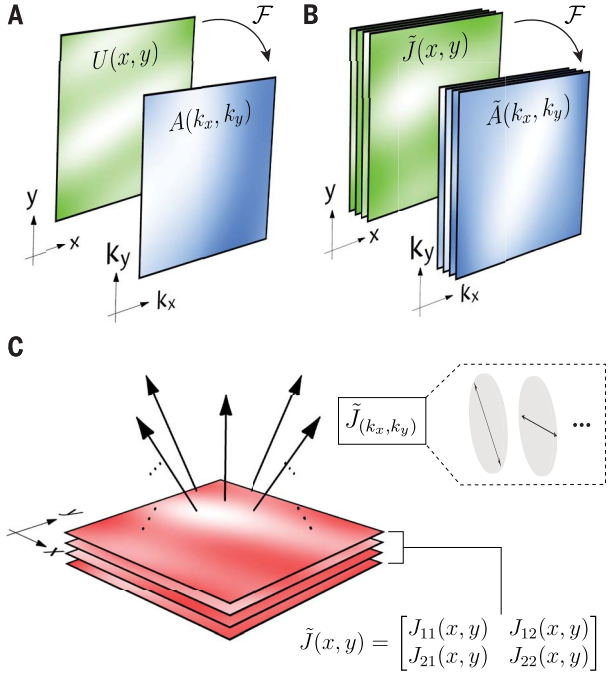

Fig. 1. Matrix Fourier Optics. (**A**) A scalar optical field $U(x,y)$ has a plane-wave expansion $A(k_x,k_y)$ obtained by Fourier transform ($\mathcal{F}$) that permits its propagation forward in space. (**B**) An obstacle implementing a 2×2 Jones matrix $\tilde{J}(x,y)$ that varies with space (and thus contains four scalar functions, which are schematically represented as different planes here) has a Fourier-domain representation $\tilde{A}(k_x,k_y)$ that is also a Jones matrix. $\tilde{A}(k_x,k_y)$ encodes the behavior of direction (k_x,k_y) as a function of incident polarization. (**C**) If $\tilde{J}(x,y)$ represents a periodic grating, its orders are described by Jones matrix coefficients $\tilde{J}_{(k_x,k_y)}$, each describing an independent polarization device, for instance, a configuration of birefringent plates. The grating implements many such devices in parallel.

what if some light is allowed to leak into other diffraction orders? Then, the $\tilde{J}_k$ of some orders could behave as analyzers for arbitrary polarization states with a limited amount of leakage into other diffraction orders (implementing their own $\tilde{J}_k$) so that the overall grating formed in Eq. 4 is still unitary everywhere. In other words, the grating can function as a coupled system in which neighboring diffraction orders compensate for desired polarization-dependent behavior on a selected few in a way that preserves overall unitarity for all (x, y).

Here, we seek to design a grating $\tilde{J}(x, y)$ that locally obeys Eq. 6 with a set of diffraction orders $\{\ell\}$ each having $\tilde{J}_k$ that are analyzers for an arbitrarily specified set of polarization states $\{|q_k\rangle\}$ as defined in Eq. 5 with as little light as possible leaking into diffraction orders outside of $\{\ell\}$. This is a question of optimization. We define the quantities $I_q^k = \langle q_k|\tilde{J}_k^\dagger\tilde{J}_k|q_k\rangle$, the power on diffraction order k when the preferred polarization $|q_k\rangle$ is incident, and $I_{q^\perp}^k = \langle q_k^\perp|\tilde{J}_k^\dagger\tilde{J}_k|q_k^\perp\rangle$, the power on diffraction order k when the orthogonal polarization $|q_k^\perp\rangle$ with $\langle q_k^\perp|q_k\rangle = 0$ is incident. The sum $\sum_{k\in\{\ell\}} I_q^k$ should be maximized to keep as much light as possible in the orders of interest. Simultaneously, the contrast of each order given by $\eta = (I_q^k - I_{q^\perp}^k)/(I_q^k + I_{q^\perp}^k)$—the polarization sensitivity of the order to the desired polarization $|q_k\rangle$—should be as close to unity as possible to constrain the $\tilde{J}_k$ to act as the desired analyzers (in the sense of Eq. 5). This can be addressed with gradient-descent. We reserve detailed discussion of this optimization to the supplementary text [sections S1 and S2, where we also describe a path to an analytical form of the solution using variational methods (*17*, *27*, *28*)].

Many previous works have considered diffraction gratings capable of splitting, and thus analyzing, light on the basis of its polarization state. However, these works have generally taken a scalar approach, seeking to impart opposite blazed grating phase profiles on orthogonal polarization states. Consequently, several individually designed gratings must be interlaced (often called "spatial multiplexing" or "shared aperture") (*29*–*32*) or, equivalently, cascaded in series (*1*, *33*) to create a grating whose orders analyze for any more than two polarization states. This is inherently problematic: These configurations cannot implement polarimetry with any less than six measurements (whereas four is the minimum required), compromising sensor space. Moreover, the polarization states of the analyzers cannot be arbitrarily specified. Interlacing different gratings also introduces unwanted periodicity, mandating loss of light to out-of-plane diffraction. The matrix approach of this work shows that interlacing is not necessary—all functions can be integrated into a single grating—and moreover, affords possibilities not achievable by interlacing. The tetrahedron grating that we will present, as a simple example, is not possible by simple interlacing as none of its four analyzer states are orthogonal to any of the others.

Experiment

Tetrahedron grating design

Gratings implementing parallel polarization analysis are of practical interest for Stokes polarimetry (*24*, *34*) which requires a minimum of four projective polarization state measurements. For maximum fidelity of Stokes vector reconstruction, these four states should be as distinct from one another as possible, accomplished by choosing analyzer states corresponding to a tetrahedron inscribed in the Poincaré sphere (polarization state space) (*35*–*37*). We use the matrix formalism and optimization scheme described above to design a two-dimensional diffraction grating analyzing for these four polarization states on its innermost four orders. The leftmost panel of Fig. 2A gives a map of these orders and the polarization ellipses ($\{|q_k\rangle\}$) they are designed to analyze for in k-space. These diffraction orders and desired polarization states can be fed into the aforementioned optimization, yielding a numerical $\tilde{J}(x, y)$ that is locally of the form of Eq. 6 (unitary and linearly birefringent). It is then straightforward to map the locally required

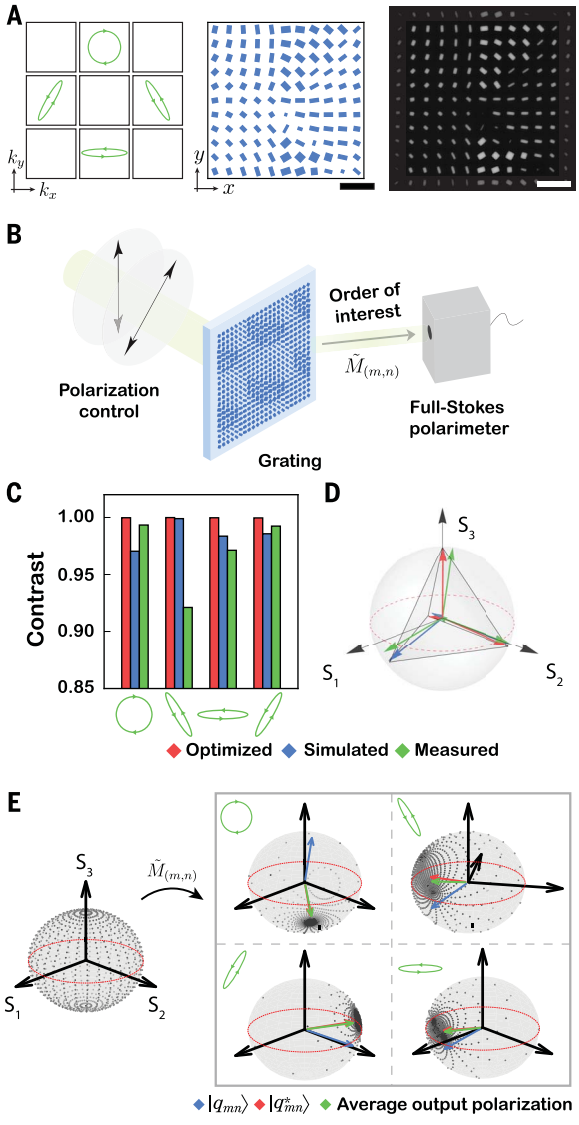

Fig. 2. Matrix gratings for arbitrary parallel polarization analysis. (**A**) A 2D grating unit cell is designed to analyze four polarization states corresponding to a tetrahedron inscribed in the Poincaré sphere. On the left is a map of the diffraction orders and the polarization ellipses they analyze in k-space. The designed 11 × 11 element grating unit cell containing TiO_2 rectangular pillars implementing this at $\lambda = 532$ nm is shown in design (middle) and as-fabricated [scanning electron micrograph (SEM), right]. Scale bar, 1 μm. (**B**) The grating is illuminated by light whose polarization is varied while recording the output polarization on a single diffraction order with a full-Stokes polarimeter permitting reconstruction of the order's 4 × 4 experimental Mueller matrix $\tilde{M}_{(m,n)}$. (**C**) The polarization contrast of each order is shown. Each order is labeled by the polarization ellipse it analyzes, and results from the analytical grating design (as-optimized, red), a full-wave simulation of the grating (blue), and experiment (green) are given. (**D**) The polarizations analyzed by each order [for which they have the contrasts given in (C)] of the tetrahedron grating are shown on the Poincaré sphere alongside a tetrahedron indicating the desired analyzer polarizations as predicted by the optimization, a full-wave simulation, and as-measured. (**E**) A set of 1024 uniformly sampled input polarization states on the Poincaré sphere can be operated on by an experimentally determined Mueller matrix $\tilde{M}_{(m,n)}$ to form a distorted set of states depicting output polarization as a function of input. Each sphere on the right represents the behavior of one of the four engineered grating orders, whose designed analyzer polarizations are shown. On each, a blue arrow denotes the measured analyzer polarization $|q_{(m,n)}\rangle$ from (C), a red arrow the equator-mirrored polarization $|q^*_{(m,n)}\rangle$, and a green arrow the average output polarization over all points which, according to the formalism here, should overlap with the red one. (In some cases, the overlap of red and green arrows is too close to permit visual discrimination.)

Jones matrix (ϕ_x, ϕ_y, θ) to geometries of actual structures by referring to a library of such structures in a material platform/wavelength regime of interest (*8*).

In this work, that material platform is TiO_2 pillars fabricated with an e-beam lithography and atomic layer deposition technique extensively documented elsewhere (*38*). This permits operation at technologically important visible wavelengths, aiding the camera application discussed below. We stress, however, that neither TiO_2 nor visible wavelengths are central to this work. The grating unit cells presented here have 11 such elements to a side with an interelement separation of 420 nm so that the diffraction angle at $\lambda = 532$ nm is $\theta_D \sim 6.6°$ (paraxial). The subwavelength spacing of the pillar elements themselves assures that radiative orders may only stem from the collective unit cell of 11 × 11 elements. The grating unit cell designed by optimization for the tetrahedron case is shown in Fig. 2A (top and bottom, respectively), both in design and as-fabricated (electron micrograph, right). This unit cell is tessellated hundreds of times to create a grating.

Mueller matrix polarimetry and results

In polarization optics, the Jones and Mueller matrices describe polarization-dependent behavior. Of the two, only the Mueller matrix is directly observable, being a description of optical intensities rather than electric fields. To that end, we perform Mueller matrix polarimetry, that is, the experimental determination of the 4 × 4 Mueller matrix $\tilde{M}_{(m,n)}$ of each of the four grating orders (m, n) of interest (as a 2D grating, the orders are labeled by two integer indices). The grating is illuminated with laser light at $\lambda = 532$ nm in several (at least four) different input polarization states with known Stokes vectors $\{\vec{S}_{in}\}$. As the polarization switches between the different known inputs, a full-Stokes polarimeter can be placed on the order of interest to record the corresponding output Stokes vectors, $\{\vec{S}_{out}\}$. The matrix $\tilde{M}_{(m,n)}$ linking $\{\vec{S}_{in}\}$ to $\{\vec{S}_{out}\}$ can then be numerically determined from the data in the least-squares sense. This is sketched in Fig. 2B and discussed in more detail in supplementary text section S3 (*17*).

In analyzing the results, it is difficult to make a direct comparison of matrix quantities. Instead, because each order of interest is designed to act as a polarization analyzer, it makes sense to ask the following questions: Do the orders act as analyzers? For which polarizations? And, with what efficiency?

The first question is addressed by Fig. 2C, which plots the polarization contrast of each diffraction order. Each group of bars in Fig. 2C corresponds to the diffraction order designed to analyze for the polarization ellipse shown below it. Each group contains three color-coded bars: one for the numerically optimized $\tilde{J}(x, y)$, one for a full-wave simulation, and one for measurement. On the left of Fig. 2D, the contrast (the normalized difference between the intensity on that order when its preferred polarization is incident versus the orthogonal one) is plotted. An ideal polarizer would have 100% contrast. The numerically optimized result predicts near perfection (100%). In a simulation of the grating design, the contrast decreases somewhat, and then again as measured in actuality. However, the four orders of the measured grating all show polarization contrasts in excess of 90%—the designed orders of the grating do act as polarizers (analyzers).

Second, it must be verified that the orders act as analyzers for the polarization states specified in the design. In Fig. 2D, the polarization states for which each grating order has maximum output intensity (as-optimized, in simulation, and as-measured) are plotted on the Poincaré sphere alongside the tetrahedron representing the goal of the design. It can be seen that these analyzer polarizations are close to their desired counterparts (there are no notable mixups in Fig. 2D, whereby one analyzer polarization lands very far away appearing to be closer to another, falsely exaggerating correspondence).

Figure 2, C and D, shows that the metasurface grating implements four arbitrarily specified analyzers in parallel with no polarizers or waveplates, lending validity to the matrix approach underlying its design. We address the question of efficiency in the supplementary text (section S3) (*17*). The grating's diffraction efficiency cannot be quantified with a single number—it is polarization dependent. Averaged over all possible input polarizations, efficiency in terms of power diffracted into the four orders of interest over incident power exceeds 50%, high enough to enable practical use.

The data contained in Fig. 2, C and D, are derived from the first row of the Mueller matrix, which dictates the intensity S_0 of the outgoing beam. The remainder of the Mueller matrix controls the output beam's polarization state. This can be visualized by individually operating on a set of input Stokes vectors that uniformly sample the Poincaré sphere (1024 dots) with each order's measured Mueller matrix $\tilde{M}_{(m,n)}$ and plotting the set of Stokes vectors that result as a new, distorted set of dots. This is shown for each of the four orders of interest in Fig. 2E on four spheres. If each behaved as a perfect analyzer (compare to Eq. 5), all polarizations would be mapped into a single point in the distorted diagram at the state corresponding to $|p_k\rangle$. The grating is not perfect in experimental reality, so the spheres in Fig. 2E

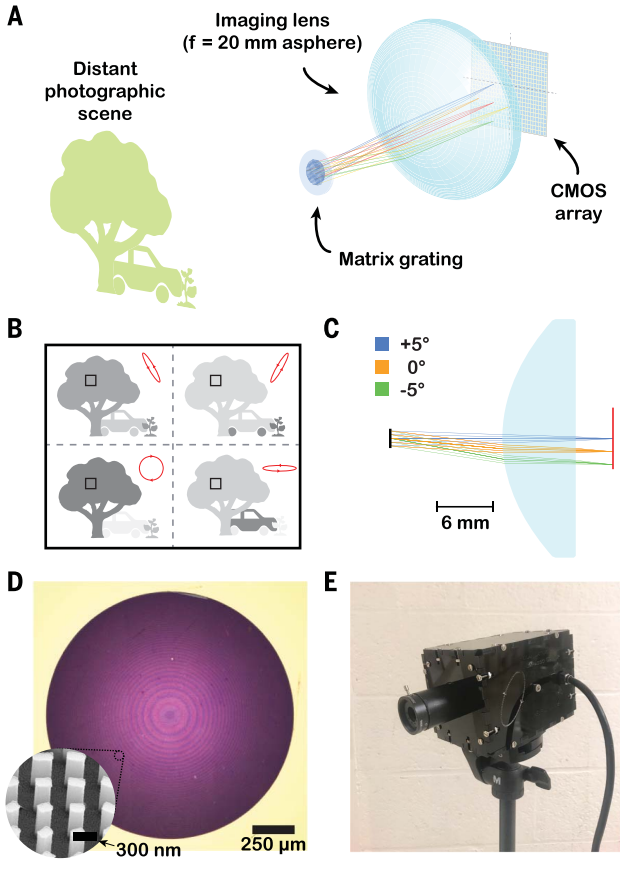

Fig. 3. Metagrating full-Stokes polarization camera. (**A**) A matrix metagrating (as in Fig. 2) is integrated with an aspheric lens to image four diffraction orders onto four quadrants of a CMOS imaging sensor. A ray trace of one diffraction order is shown. The camera is designed to image far-away objects, so each color corresponds to different parallel ray bundles incident on the grating from different angles over a ±5° FOV. Not shown: A 10-nm bandpass filter at 532 nm and an aperture in front of the grating to limit the FOV to prevent overlap of the four subimages. (**B**) Each copy of the image on each quadrant has been analyzed along a different polarization. Pixel-wise differences in intensity can be used to synthesize a single polarization image of the scene in which the full Stokes vector is known at each point. (**C**) A clearer side view of the ray trace in (A). Blue, orange, and green correspond to ray bundles incident at +5°, 0°, and −5°, respectively. (**D**) Optical microscope image of the grating sample, which is 1.5 mm in diameter and shows Fresnel zones owing to the weak, polarization-independent lensing effect imposed on top of the metagrating. An SEM inset shows the subwavelength, form-birefringent TiO_2 pillars comprising the metasurface. (**E**) The imaging system in (A) can be packaged into a practical, portable prototype with adjustable focus. The essential part of the camera, as shown in (C), is about 2 cm long. The prototype here is larger for ease of optomechanical mounting.

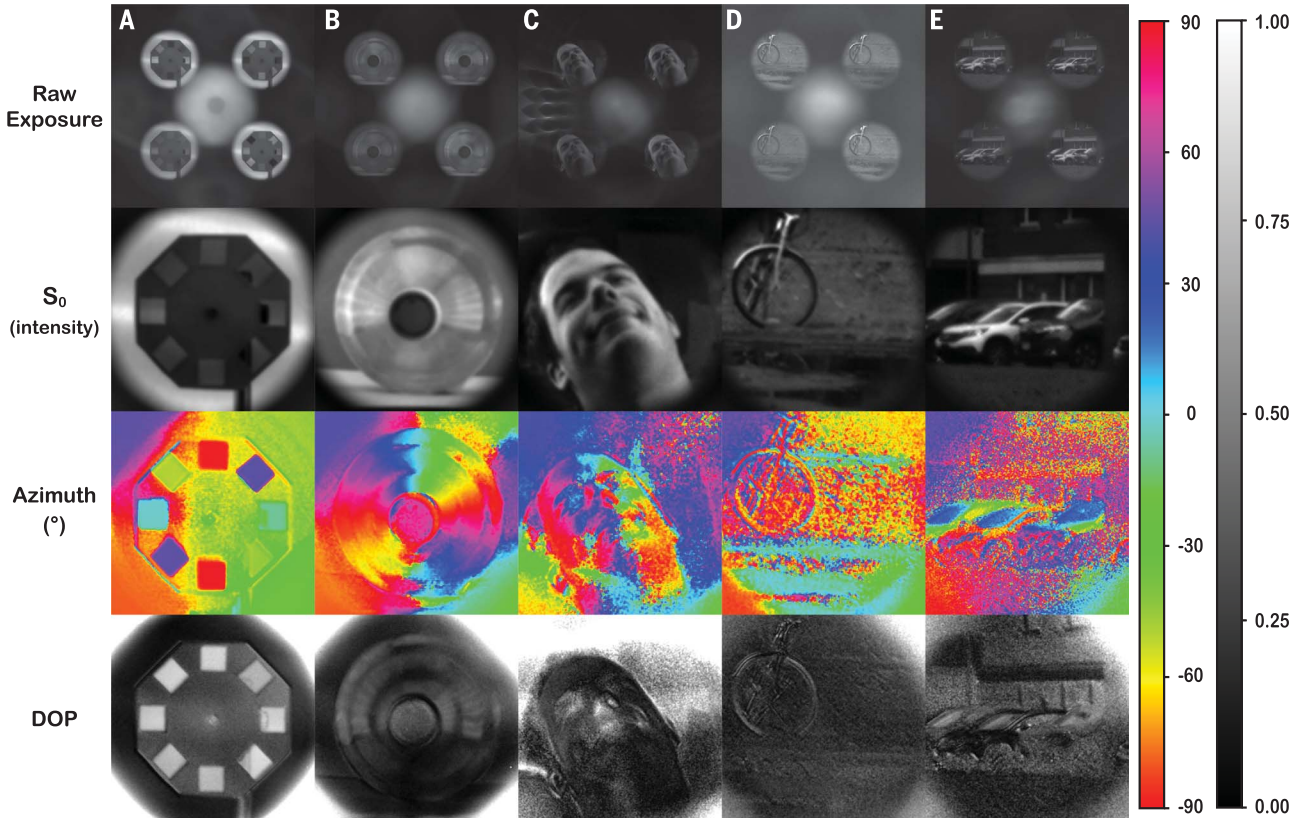

Fig. 4. Full-Stokes polarization imagery. Indoor (**A** to **C**) and outdoor (**D** and **E**) photography with the camera depicted in Fig. 3. In each case, the raw unprocessed exposure, S_0 (the traditional monochrome intensity image), the azimuth of the polarization ellipse [in degrees, given by $\arctan(S_2/S_1)$], and the degree of polarization (DOP, given by $\sqrt{S_1^2+S_2^2+S_3^2}/S_0$) are shown. See text for detail on each case. Indoor images were acquired with exposures on the order of 100 ms, outdoor images with exposures on the order of 10 ms. In both cases, polarization imagery can be acquired at video framerate. The bright disk in the center of each raw exposure is zero-order light that does not interact with the grating and thus forms a defocused image of the scene. All images are at a single color (green, $\lambda \sim 532$ nm).

contain points distributed over the entire sphere; the extent to which these points are concentrated in one direction and extremely sparse elsewhere illustrates that each diffraction order does indeed act as an analyzer. For each grating order in Fig. 2E, a blue arrow corresponds to the polarization being analyzed (copied from Fig. 2D) ($|q_{(m,n)}\rangle$ in the notation of Eq. 5). A green arrow shows the polarization on the grating order averaged over the set of incident polarizations. Finally, a red arrow depicts $|q^*_{(m,n)}\rangle$, which has flipped handedness with respect to $|q_{(m,n)}\rangle$ and is thus mirrored about the equator of the sphere. According to the picture presented above, the linear birefringence of the grating elements implies that the output must necessarily take on the form of $|q^*_{(m,n)}\rangle$. This aspect of the theory is supported by the close overlap of the red and green arrows in each plot of Fig. 2E.

In the supplementary text, results are given for a second grating, an octahedron grating, in which six diffraction orders act as analyzers (*17*).

Full-Stokes polarization imaging

We now apply these matrix gratings in an area of great practical interest. If paired with four detectors, the tetrahedron grating presented above could function as a single-component, compact, and integrated full-Stokes polarimeter (a sensor to measure the polarization state of a beam), an area where metagratings (*29*–*32*) and integrated approaches (*39*, *40*) have recently attracted considerable interest (*34*). However, for a variety of applications (*41*–*44*), a polarization camera, or imaging polarimeter, is of even more utility. A polarization camera captures the Stokes vector at each point in an image. In the case of the four-element Stokes vector, this necessitates four independent image acquisitions along independent polarization directions, which may be taken sequentially in time ("division-of-time," limiting temporal resolution and often requiring moving parts), by patterning a focal plane array with micropolarizers ("division-of-focal-plane," requiring expensive fabrication, usually without offering full-Stokes vector determination, and mandating loss of photons to absorptive micropolarizer elements), or by simultaneous capture of the image along four paths each with independent polarization optics ("division-of-amplitude," substantially increasing system bulk and complexity) (*41*).

Grating-based approaches are not new to polarimetry (*24*, *45*) (and imaging polarimetry), particularly in the liquid crystal (*46*) and, more recently, metasurface literatures (*29*–*32*). Owing to the limitations of previous approaches, however, multiple gratings—either cascaded in series or patterned adjacent to one another—are required to implement the measurements necessary for full-Stokes vector determination. The matrix gratings here are free from this complication and full-Stokes imaging can be implemented with a single polarization element, promising wide-ranging applications in machine vision and remote sensing.

Design of an imaging system

The task here is to integrate a metagrating into a photographic imaging system. The tetrahedron grating described above is chosen because it offers full-Stokes determination with only four measurements, the minimum necessary. We developed an imaging system composed of this grating (implemented with a TiO_2 metasurface as above) followed by an aspheric lens ($f = 20$ mm, whose choice is discussed in supplementary text section S4) and a standard monochrome complementary metal–oxide–semiconductor (CMOS) imaging sensor. This is depicted in Fig. 3A. Relative to Fig. 2A, the grating is rotated by 45°

so that each of its orders forms an image of the scene on one quadrant of the imaging sensor. Each quadrant then contains a version of the photograph analyzed along its characteristic polarization—these images can be simultaneously acquired and the Stokes vector $\vec{S}$ reconstructed pixel-wise (Fig. 3B), forming a monochromatic polarization image.

Simple ray tracing is used to optimize all aspects of the system: the separation of the grating and the asphere, the separation of the asphere and the imaging sensor, and finally, the grating period (and thus, the diffraction angle θ_D). The goal of the optimization is to take parallel ray bundles over a ±5° field-of-view (FOV)—which are assumed to emerge from a very distant object—and focus them within the bounds of a quadrant of the sensor. An azimuthally symmetric, polarization-independent (scalar) phase profile is added on top of the matrix grating during the design and is experienced by all diffraction orders. This produces a weak lensing effect that aids in imaging. The design focuses on just one grating order. However, the other three will be imaged to their respective quadrants by default because the system is rotationally symmetric.

A real ray trace of the imaging system is shown in Fig. 3A with a clearer side view in Fig. 3C. The ray colors correspond to parallel bundles incident at different angles on the matrix grating. The optimized grating has $N = 10$ elements at a 420-nm pitch, yielding $\theta_D = 7.3°$ at $\lambda = 532$ nm.

In Fig. 3D a microscope image of the 1.5-mm sample is shown. The sample is surrounded by metal to block stray light and displays Fresnel zones stemming from the weak lensing imparted on top of the grating (whose periodicity is too small to see at this magnification).

Finally, the entire system can be packaged into a prototype for practical use in polarization photography as shown in Fig. 3E with variable focus. The size of this prototype is much larger than is strictly necessary to permit easy optomechanical mounting—as is shown in Fig. 3C, the functional part of the system is only ~2 cm long. An aperture in front of the camera permits control of the FOV so that the four copies of the image do not overlap, and a 10-nm bandpass filter at 532 nm behind the sample prevents the dispersive nature of the grating from interfering with imaging. This is important to note — if a broad band of illuminating wavelengths were introduced to the imaging system, the grating would effectively smear the images together, with spatial and spectral information colocated on the sensor. The bandwidth of dye filters used in conventional color sensors (~100 nm for the Bayer filter) is too wide to effectively address this. For color or hyperspectral polarization imaging, a different approach could be employed, such as the use of a tunable filter at the input or incorporation of the grating into a pushbroom scanning system where only one space dimension is acquired at a time (as is common in remote sensing).

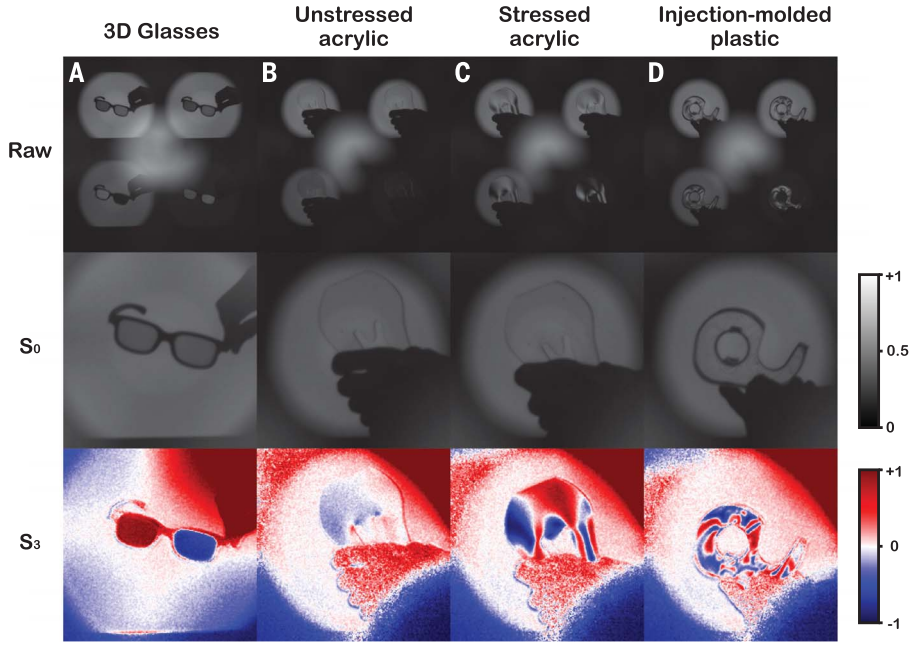

Fig. 5. Polarization imaging of S_3. Example imagery from the camera making explicit use of S_3, part of its full-Stokes capability. All images are acquired with a backlight linearly polarized at 45°. In each example, raw sensor acquisition, S_0 (traditional intensity image), and S_3 are shown. (**A**) 3D glasses are seen to contain opposite circular polarizers, invisible to the traditional intensity image. (**B** and **C**) A laser-cut acrylic piece is stressed by hand-squeezing and displays stress birefringence evident in the S_3 image. (**D**) An injection-molded plastic part (a tape dispenser) has complex, in-built stresses that are visible in the S_3 channel of the polarization image. Edge artifacts in these images and those in Fig. 4 are discussed in the supplementary text (section S4) (*17*).

Polarization imaging

The metagrating camera can then be used for practical full-Stokes photography. The raw sensor acquisition approximates Fig. 3B. To form a polarization image, the four image copies must be aligned (registered) to one another, forming the vector $\vec{I} = [I_0\ I_1\ I_2\ I_3]^T$ of measured intensity from the four quadrants at each pixel. If the polarizations analyzed for by each diffraction order are precisely known (calibration), the Stokes vector at each pixel can be computed as $\vec{S} = A^{-1}\vec{I}$, where A is a matrix whose rows are these analyzer Stokes vectors. Image registration and polarimetric calibration are addressed simultaneously with an angle-dependent method (supplementary text section S4) (*17*).

In a polarization image, $\vec{S} = [S_0\ S_1\ S_2\ S_3]^T$ is known at each pixel, which does not admit easy visualization. Instead, images can be formed from scalar quantities derived from the Stokes vector. In the literature of polarization imaging, two parameters of the polarization ellipse are commonly used. The first is the azimuth angle, $\arctan(S_2/S_1)$, which yields the physical orientation of the polarization ellipse. The second is the degree of polarization, given by $p = \sqrt{S_1^2 + S_2^2 + S_3^2}/S_0$, which quantifies the degree to which light is (or is not) fully polarized. Finally, an image can be formed of just S_0 which, as the intensity of the light, yields a traditional monochrome photograph.

In Fig. 4, exemplar photographs captured by the polarization imaging system are shown. For each, images of the raw acquisition on the sensor, S_0, the azimuth angle, and the degree of polarization (DOP) are shown. In all of these images, the illuminating light is unpolarized and diffuse, that is, incident from all directions. The indoor images in Fig. 4 are taken under diffuse light-emitting diode illumination, whereas outdoor images are acquired in broad daylight. In the raw exposures, a bright disk in the center represents zero-order light that does not interact with the grating and thus forms a defocused version of the image (some stray light is also present).

Next, we describe each example. Figure 4A constitutes a simple test—a paper frame holding eight sheets of polarizing film whose axes are arranged radially outward with image-forming light allowed to transmit from behind. A traditional photograph sees no difference between the sheets (S_0), but an image of the azimuth accurately reveals their angular orientations. Moreover, the DOP image shows that light passing through the sheets is highly polarized relative to the surrounding surface.

Figure 4, B to E, examine the polarization dependence of specular reflection (*47*). Unpolarized light becomes partially polarized upon specular reflection in a direction perpendicular to the plane of incidence. In Fig. 4B, a conventional plastic soda bottle is imaged head-on. From an intensity image (S_0), the bottle's curved shape could not be ascertained a posteriori. The azimuth image, however, displays smooth, continuous change around the top of the bottle evidencing its conical shape and could be used

in three-dimensional (3D) reconstruction; indeed, the polarized nature of specular reflection has been used as a means of depth imaging (*47*–*50*). Figure 4C illustrates the same concept for a more complicated object — the face of one of the authors. Its 3D nature is not discernible from the S_0 image (as opposed to, say, a mere printed photograph of a face), but the azimuth image traces its contour and could be used in 3D facial reconstruction.

Figure 4, D and E, depict outdoor scenes. In Fig. 4D, a bicycle is seen parked on a grassy field after rain on the Harvard campus. In front of it is a boundary between grass and asphalt, as well as a puddle. In the azimuth image, a strong delineation is seen between the wet pavement, where the polarization direction is well-defined parallel to the ground, and the grass and puddle, where the azimuth is somewhat random because the reflection is diffuse. Moreover, the azimuth reveals the presence of an asphalt walkway in the rear of the image, which is difficult to see in the intensity image. In Fig. 4E, a row of cars is photographed. Cars illuminated by sunlight are a favorite target in polarization imaging literature because the windshields tend to yield strong polarization signatures. This is seen for all three cars in the azimuth image, where the windshields and auto bodies have definite polarization azimuths and in the DOP image where the windshields are highly polarized relative to the rest of the car and background.

We note, however, that the examples in Fig. 4 make only indirect use of S_3, the chiral Stokes component, through the DOP. Many existing polarization cameras, particularly using the division-of-focal-plane approach, are unable to measure S_3 (*42*). Figure 5, however, directly demonstrates the full-Stokes capability of the camera. In Fig. 5, objects are illuminated from behind by light linearly polarized at 45° from a liquid crystal computer display. In each case, the raw sensor acquisition, S_0, and S_3 are shown. Figure 5A depicts a pair of 3D glasses whose frames contain opposite circular polarizers. This is not visible in the traditional intensity image S_0, but is readily seen in the S_3 image where each lens has a ±1 value. In Fig. 5B, a piece of acrylic is held in front of the camera, displaying little chiral component. Upon squeezing (Fig. 5C), no change is perceptible in the traditional photograph, but considerable information is now visible in S_3 stemming from stress birefringence (the photoelastic effect). This is also evident in Fig. 5D where an injection molded plastic part—a tape dispenser—displays an in-built, complicated distribution of stress in S_3 not visible with traditional photography. Visualization of stress fields is an important application of polarization imaging, one that is readily accomplished with the camera presented here.

These examples demonstrate powerful applications in machine vision, remote sensing, and other areas. The camera presented here requires no conventional polarization optics, offers simultaneous data acquisition with no moving parts, does not require an imaging sensor specially patterned with micropolarizers, and is compact and potentially mass-producible. Moreover, the camera's simplicity—just a single grating with an imaging lens—suggests that these gratings could be designed around existing, conventional imaging systems to create polarization-sensitive ones.

Conclusion

We have introduced a general picture of polarization-dependent diffraction from polarization-sensitive obstacles. This matrix Fourier optics describes optical elements that can enact many polarization-dependent functions in their diffraction patterns. In this work, we applied this picture to the case of periodic gratings analyzing arbitrary polarizations in parallel, characterized these gratings, and showed how they enable a polarization camera with no additional polarization optics, moving parts, or specialized sensors. Practical polarization photography with this camera was demonstrated.

Our work generalizes a large body of research in polarization-sensitive diffractive optics and metasurfaces. Its emphasis is on the collective behavior of many elements at once as expressed in the Fourier transform, rather than the point-by-point consideration of each element alone, and thus advances design strategies in these areas beyond simple phase profiles. Moreover, this work suggests several interesting directions of research in multifunctional polarization optics. For instance, although polarization analyzers (polarizers) have been studied here, the matrix approach is quite general: Gratings implementing a wide variety of polarization operators on their orders [e.g., waveplates, optically active media, and possibly more exotic behavior (*51*)] could be envisioned. The constraint of linearly birefringent elements is by no means fundamental, and with the freedom afforded by lithographic fabrication, elements with more complex polarization responses (*52*) or multilayer structures could be used to realize these behaviors. This work illustrates the ability of metasurfaces to markedly simplify the architecture of systems using polarization optics. Gratings enabled by the approach here present a simpler means of full-Stokes polarization imaging that can be easily extended to other imaging systems and wavelengths. These compact, lightweight, and passive devices could enable the widespread adoption of polarization imaging.

REFERENCES AND NOTES

1. G. Cincotti, Polarization gratings: Design and applications. *IEEE J. Quantum Electron.* **39**, 1645–1652 (2003). doi: 10.1109/JQE.2003.819526
2. E. Hasman, G. Biener, A. Niv, V. Kleiner, Space-variant polarization manipulation. *Prog. Opt.* **47**, 215–289 (2005). doi: 10.1016/S0079-6638(05)47004-3
3. A. W. Lohmann, Reconstruction of Vectorial Wavefronts. *Appl. Opt.* **4**, 1667 (1965). doi: 10.1364/AO.4.001667
4. T. Todorov, L. Nikolova, N. Tomova, Polarization holography. 1: A new high-efficiency organic material with reversible photoinduced birefringence. *Appl. Opt.* **23**, 4309–4312 (1984). doi: 10.1364/AO.23.004309; pmid: 18213314
5. T. Todorov, L. Nikolova, K. Stoyanova, N. Tomova, Polarization holography. 3: Some applications of polarization holographic recording. *Appl. Opt.* **24**, 785 (1985). doi: 10.1364/AO.24.000785; pmid: 18217026
6. L. Nikolova, P. Ramanujam, *Polarization Holography* (Cambridge Univ. Press, 2009).
7. J. P. Balthasar *et al*., Metasurface Polarization Optics: Independent Phase Control of Arbitrary Orthogonal States of Polarization. *Phys. Rev. Lett.* **118**, 113901 (2017). doi: 10.1103/PhysRevLett.118.113901; pmid: 28368630
8. A. Arbabi, Y. Horie, M. Bagheri, A. Faraon, Dielectric metasurfaces for complete control of phase and polarization with subwavelength spatial resolution and high transmission. *Nat. Nanotechnol.* **10**, 937–943 (2015). doi: 10.1038/nnano.2015.186; pmid: 26322944
9. C. Oh, M. J. Escuti, Achromatic diffraction from polarization gratings with high efficiency. *Opt. Lett.* **33**, 2287–2289 (2008). doi: 10.1364/OL.33.002287; pmid: 18923598
10. J. Kim *et al*., Fabrication of ideal geometric-phase holograms with arbitrary wavefronts. *Optica* **2**, 958 (2015). doi: 10.1364/OPTICA.2.000958
11. J. W. Goodman, *Introduction to Fourier Optics* (Roberts, 2005).
12. R. C. Jones, A New Calculus for the Treatment of Optical Systems! Description and Discussion of the Calculus. *J. Opt. Soc. Am.* **31**, 488 (1941). doi: 10.1364/JOSA.31.000488
13. I. Moreno, M. J. Yzuel, J. Campos, A. Vargas, Jones matrix treatment for polarization fourier optics. *J. Mod. Opt.* **51**, 2031–2038 (2004). doi: 10.1080/09500340408232511
14. I. Moreno, C. Iemmi, J. Campos, M. J. Yzuel, Jones matrix treatment for optical Fourier processors with structured polarization. *Opt. Express* **19**, 4583–4594 (2011). doi: 10.1364/OE.19.004583; pmid: 21369291
15. W. Urbańczyk, Optical Transfer Function for Imaging Systems Which Change the State of Light Polarization. *Opt. Acta (Lond.)* **33**, 53–62 (1986). doi: 10.1080/713821863
16. J. P. McGuire, R. A. Chipman, Diffraction image formation in optical systems with polarization aberrations I: Formulation and example. *J. Opt. Soc. Am. A* **7**, 1614 (1990). doi: 10.1364/JOSAA.7.001614
17. See supplementary materials.
18. Z. Bomzon, V. Kleiner, E. Hasman, Pancharatnam—Berry phase in space-variant polarization-state manipulations with subwavelength gratings. *Opt. Lett.* **26**, 1424–1426 (2001). doi: 10.1364/OL.26.001424; pmid: 18049626
19. M. Berry, Quantal Phase Factors Accompanying Adiabatic Changes. *Proc. R. Soc. Lond. A Math. Phys. Sci.* **392**, 45–57 (1984). doi: 10.1098/rspa.1984.0023
20. E. Hasman, V. Kleiner, G. Biener, A. Niv, Polarization dependent focusing lens by use of quantized Pancharatnam–Berry phase diffractive optics. *Appl. Phys. Lett.* **82**, 328–330 (2003). doi: 10.1063/1.1539300
21. D. Lin, P. Fan, E. Hasman, M. L. Brongersma, Dielectric gradient metasurface optical elements. *Science* **345**, 298–302 (2014). doi: 10.1126/science.1253213; pmid: 25035488
22. N. A. Rubin *et al*., Polarization state generation and measurement with a single metasurface. *Opt. Express* **26**, 21455–21478 (2018). doi: 10.1364/OE.26.021455; pmid: 30130853
23. R. Zhao *et al*., Multichannel vectorial holographic display and encryption. *Light Sci. Appl.* **7**, 95 (2018). doi: 10.1038/s41377-018-0091-0; pmid: 30510691
24. R. M. A. Azzam, Stokes-vector and Mueller-matrix polarimetry [Invited]. *J. Opt. Soc. Am. A Opt. Image Sci. Vis.* **33**, 1396–1408 (2016). doi: 10.1364/JOSAA.33.001396; pmid: 27409699
25. N. Yu *et al*., Light propagation with phase discontinuities: Generalized laws of reflection and refraction. *Science* **334**, 333–337 (2011). doi: 10.1126/science.1210713; pmid: 21885733
26. P. Genevet, F. Capasso, F. Aieta, M. Khorasaninejad, R. Devlin, Recent advances in planar optics: From plasmonic to dielectric metasurfaces. *Optica* **4**, 139 (2017). doi: 10.1364/OPTICA.4.000139
27. L. A. Romero, F. M. Dickey, Theory of optimal beam splitting by phase gratings. I. One-dimensional gratings. *J. Opt. Soc. Am. A Opt. Image Sci. Vis.* **24**, 2280–2295 (2007). doi: 10.1364/JOSAA.24.002280; pmid: 17621332
28. L. A. Romero, F. M. Dickey, The Mathematical Theory of Laser Beam-Splitting Gratings. *Prog. Opt.* **54**, 319–386 (2010). doi: 10.1016/S0079-6638(10)05411-9
29. A. Pors, M. G. Nielsen, S. I. Bozhevolnyi, Plasmonic metagratings for simultaneous determination of Stokes parameters. *Optica* **2**, 716 (2015). doi: 10.1364/OPTICA.2.000716
30. W. T. Chen *et al*., Integrated plasmonic metasurfaces for spectropolarimetry. *Nanotechnology* **27**, 224002 (2016). doi: 10.1088/0957-4484/27/22/224002; pmid: 27114455

31. S. Wei, Z. Yang, M. Zhao, Design of ultracompact polarimeters based on dielectric metasurfaces. *Opt. Lett.* **42**, 1580–1583 (2017). doi: 10.1364/OL.42.001580; pmid: 28409803
32. E. Arbabi, S. M. Kamali, A. Arbabi, A. Faraon, Full-Stokes Imaging Polarimetry Using Dielectric Metasurfaces. *ACS Photonics* **5**, 3132–3140 (2018). doi: 10.1021/acsphotonics.8b00362
33. T. Todorov, L. Nikolova, Spectrophotopolarimeter: Fast simultaneous real-time measurement of light parameters. *Opt. Lett.* **17**, 358–359 (1992). doi: 10.1364/OL.17.000358; pmid: 19784327
34. A. Martínez, Polarimetry enabled by nanophotonics. *Science* **362**, 750–751 (2018). doi: 10.1126/science.aau7494; pmid: 30442792
35. R. Azzam, I. Elminyawi, A. El-Saba, General analysis and optimization of the four-detector photopolarimeter. *J. Opt. Soc. Am. A* **5**, 681 (1988). doi: 10.1364/JOSAA.5.000681
36. D. S. Sabatke *et al*., Optimization of retardance for a complete Stokes polarimeter. *Opt. Lett.* **25**, 802–804 (2000). doi: 10.1364/OL.25.000802; pmid: 18064189
37. J. S. Tyo, Design of optimal polarimeters: Maximization of signal-to-noise ratio and minimization of systematic error. *Appl. Opt.* **41**, 619–630 (2002). doi: 10.1364/AO.41.000619; pmid: 11993905
38. R. C. Devlin, M. Khorasaninejad, W.-T. Chen, J. Oh, F. Capasso, Broadband high-efficiency dielectric metasurfaces for the visible spectrum. *Proc. Natl. Acad. Sci. U.S.A.* **113**, 10473–10478 (2016). doi: 10.1073/pnas.1611740113; pmid: 27601634
39. A. Espinosa-Soria, F. J. Rodríguez-Fortuño, A. Griol, A. Martínez, On-Chip Optimal Stokes Nanopolarimetry Based on Spin-Orbit Interaction of Light. *Nano Lett.* **17**, 3139–3144 (2017). doi: 10.1021/acs.nanolett.7b00564; pmid: 28388061
40. W. Wu, Y. Yu, W. Liu, X. Zhang, Fully integrated CMOS-compatible polarization analyzer. *Nanophotonics* **8**, 467–474 (2019). doi: 10.1515/nanoph-2018-0205
41. J. S. Tyo, D. L. Goldstein, D. B. Chenault, J. A. Shaw, Review of passive imaging polarimetry for remote sensing applications. *Appl. Opt.* **45**, 5453–5469 (2006). doi: 10.1364/AO.45.005453; pmid: 16855644
42. F. Snik *et al*., *Proceedings of the SPIE* **9099** (2014).
43. S. G. Demos, R. R. Alfano, Optical polarization imaging. *Appl. Opt.* **36**, 150–155 (1997). doi: 10.1364/AO.36.000150; pmid: 18250656
44. J. S. Tyo, M. P. Rowe, E. N. Pugh Jr., N. Engheta, Target detection in optically scattering media by polarization-difference imaging. *Appl. Opt.* **35**, 1855–1870 (1996). doi: 10.1364/AO.35.001855; pmid: 21085310
45. Y. Cui, R. M. A. Azzam, Sixteen-beam grating-based division-of-amplitude photopolarimeter. *Opt. Lett.* **21**, 89–91 (1996). doi: 10.1364/OL.21.000089; pmid: 19865314
46. M. W. Kudenov, M. J. Escuti, E. L. Dereniak, K. Oka, White-light channeled imaging polarimeter using broadband polarization gratings. *Appl. Opt.* **50**, 2283–2293 (2011). doi: 10.1364/AO.50.002283; pmid: 21614123
47. L. B. Wolff, T. E. Boult, Constraining object features using a polarization reflectance model. *IEEE Trans. Pattern Anal. Mach. Intell.* **13**, 635–657 (1991). doi: 10.1109/34.85655
48. S. Rahmann, N. Canterakis, in *Proceedings of the 2001 IEEE Computer Society Conference on Computer Vision and Pattern Recognition* (2001), pp. 149–155.
49. A. Kadambi, V. Taamazyan, B. Shi, R. Raskar, *Proc. IEEE International Conference on Computer Vision* (2015), pp. 3370–3378.
50. N. M. Garcia, I. de Erausquin, C. Edmiston, V. Gruev, Surface normal reconstruction using circularly polarized light. *Opt. Express* **23**, 14391–14406 (2015). doi: 10.1364/OE.23.014391; pmid: 26072802
51. A. Cerjan, S. Fan, Achieving Arbitrary Control over Pairs of Polarization States Using Complex Birefringent Metamaterials. *Phys. Rev. Lett.* **118**, 253902 (2017). doi: 10.1103/PhysRevLett.118.253902; pmid: 28696764
52. C. Menzel, C. Rockstuhl, F. Lederer, Advanced Jones calculus for the classification of periodic metamaterials. *Phys. Rev. A* **82**, 053811 (2010). doi: 10.1103/PhysRevA.82.053811

ACKNOWLEDGMENTS

We acknowledge M. Tamagnone, Y.-W. Huang, V. Ginis, S. Kheifets, Z. Li, A. Zaidi, and A. Dorrah (all of Harvard University) for helpful comments. **Funding:** N.A.R. acknowledges support from the National Science Foundation Graduate Research Fellowship Program (GRFP) under grant no. DGE1144152. This work was supported by the Air Force Office of Scientific Research under grant nos. FA9550-18-P-0024, FA9550-16-1-0156, and FA9550-14-1-0389 (MURI). We also acknowledge support from a Physical Sciences and Engineering Accelerator grant from Harvard University's Office of Technology Development and a gift from the Google Accelerated Science team. F.C. acknowledges support from King Abdullah University of Science and Technology (KAUST) Office of Sponsored Research (OSR) under grant no. OSR-2016-CRG5-2995. This work was performed in part at the Center for Nanoscale Systems (CNS), a member of the National Nanotechnology Coordinated Infrastructure (NNCI), which is supported by the National Science Foundation under NSF award no. 1541959. CNS is part of Harvard University. **Author contributions:** N.A.R. conceived the experiment and fabricated the gratings. G.D. wrote grating design codes and performed experimental characterization. N.A.R. and Z.S. clarified theoretical aspects of the work. W.T.C. contributed to camera design. N.A.R. and P.C. assembled the camera prototype, wrote camera software, and acquired the images in Figs. 4 and 5. N.A.R. and F.C. wrote the manuscript. F.C. supervised the research. **Competing interests:** A provisional patent application (US 62/834,343) has been filed on the subject of this work. **Data and materials availability:** All data needed to evaluate the conclusions in the paper are present in the paper and/or the supplementary materials.

SUPPLEMENTARY MATERIALS

science.sciencemag.org/content/365/6448/eaax1839/suppl/DC1
Materials and Methods
Supplementary Text
Figs. S1 to S22
Tables S1 and S2
Movie S1
References (*53*–*57*)

28 February 2019; accepted 8 May 2019
10.1126/science.aax1839

RESEARCH ARTICLE SUMMARY

AFRICAN GENETICS

Ancient DNA reveals a multistep spread of the first herders into sub-Saharan Africa

Mary E. Prendergast*†, Mark Lipson*†, Elizabeth A. Sawchuk*†, Iñigo Olalde, Christine A. Ogola, Nadin Rohland, Kendra A. Sirak, Nicole Adamski, Rebecca Bernardos, Nasreen Broomandkhoshbacht, Kimberly Callan, Brendan J. Culleton, Laurie Eccles, Thomas K. Harper, Ann Marie Lawson, Matthew Mah, Jonas Oppenheimer, Kristin Stewardson, Fatma Zalzala, Stanley H. Ambrose, George Ayodo, Henry Louis Gates Jr., Agness O. Gidna, Maggie Katongo, Amandus Kwekason, Audax Z. P. Mabulla, George S. Mudenda, Emmanuel K. Ndiema, Charles Nelson, Peter Robertshaw, Douglas J. Kennett, Fredrick K. Manthi, David Reich*

INTRODUCTION: Cattle, sheep, and goats appeared in eastern Africa 5000 years ago, catalyzing the spread of herding throughout sub-Saharan Africa. Archaeologists have long debated the geographic origins of eastern Africa's first herders, the extent to which people moved with livestock, and relationships among food-producing and foraging communities. In this work, we integrate ancient DNA with archaeological, linguistic, and genetic evidence to explore how pastoralism developed within this region, establishing the roots of one of Africa's dominant economic strategies.

RATIONALE: Research into the spread of herding has been limited by patchy archaeological data and poorly preserved human remains. Ancient DNA has the potential to untangle patterns of movement and interaction underlying this economic and cultural transition.

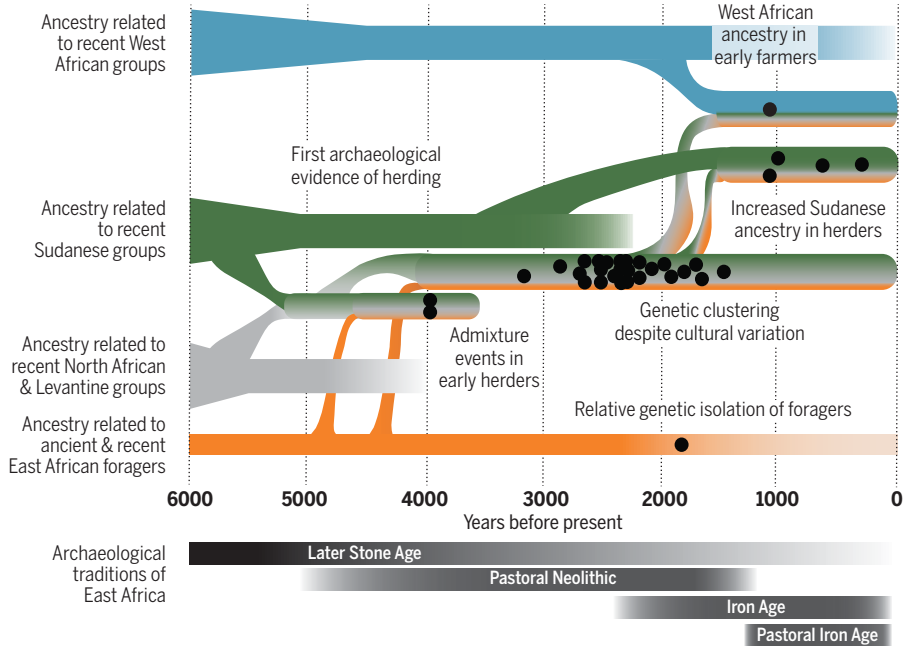

Admixture events contributing to ancestry of ancient eastern Africans. Results were inferred from genome-wide ancient DNA data from 41 individuals from archaeological sites in Kenya and Tanzania, analyzed together with published ancient and present-day genetic data. Black circles represent reported individuals, placed at their median calibrated radiocarbon dates (six individuals, five of whom have forager-related ancestry, had insufficient collagen for dating and thus are not represented here). Ancestry components depicted in green and gray continue to the present day (outside of eastern Africa) but are truncated for readability.

We generated genome-wide ancient DNA data from the remains of 41 individuals (35 directly radiocarbon dated) associated with Later Stone Age (n = 3), early pastoral and Pastoral Neolithic (n = 31), Iron Age (n = 1), and Pastoral Iron Age (n = 6) traditions in what are now Kenya and Tanzania to study how ancient individuals were related to each other and to people living today.

RESULTS: We document a multistep spread of herding and farming into eastern Africa. Ancient individuals genetically correlate with their archaeological associations: Later Stone Age individuals form part of a forager genetic cline, early pastoral and Pastoral Neolithic individuals are most closely related to present-day Afro-Asiatic speakers, and Pastoral Iron Age individuals show affinities to present-day Nilotic speakers. A child buried at an Iron Age agricultural site has shared ancestry with western Africans and Bantu speakers.

ON OUR WEBSITE

Read the full article at http://dx.doi.org/10.1126/science.aaw6275

We propose a four-stage model that fits the data. First, admixture in northeastern Africa created groups with approximately equal proportions of ancestry related to present-day Sudanese Nilotic speakers and groups from northern Africa and the Levant. Second, descendants of these northeastern Africans mixed with foragers in eastern Africa. Third, an additional component of Sudan-related ancestry contributed to Iron Age pastoralist groups. Fourth, western African–related ancestry, similar to that found in present-day Bantu speakers, appeared with the spread of farming.

We also observe a high frequency of a Y chromosome lineage associated with the spread of pastoralism, as well as a single individual with a genetic variant conferring adult lactase persistence. We do not detect any differentiation among individuals associated with two distinctive Pastoral Neolithic artifact traditions, suggesting that these represent cultural rather than ancestral differences.

CONCLUSION: Archaeological and now genetic evidence suggest complex spreads of herding and farming in eastern Africa involving multiple movements of ancestrally distinct peoples as well as gene flow among these groups. Models formulated on the basis of ancient DNA are a starting point for further exploration through additional archaeological, linguistic, and genetic research. ■

The list of author affiliations is available in the full article online.
*Corresponding author. Email: mary.prendergast@slu.edu (M.E.P.); mlipson@genetics.med.harvard.edu (M.L.); elizabeth.sawchuk@stonybrook.edu (E.A.S.); reich@genetics.med.harvard.edu (D.R.)
†These authors contributed equally to this work.
Cite this article as M. E. Prendergast *et al.*, *Science* **365**, eaaw6275 (2019). DOI: 10.1126/science.aaw6275

RESEARCH ARTICLE

AFRICAN GENETICS

Ancient DNA reveals a multistep spread of the first herders into sub-Saharan Africa

Mary E. Prendergast[1,2]*†, Mark Lipson[2]*†, Elizabeth A. Sawchuk[3]*†, Iñigo Olalde[2], Christine A. Ogola[4], Nadin Rohland[2], Kendra A. Sirak[2], Nicole Adamski[2,5], Rebecca Bernardos[2], Nasreen Broomandkhoshbacht[2,5]‡, Kimberly Callan[2,5], Brendan J. Culleton[6], Laurie Eccles[7], Thomas K. Harper[7], Ann Marie Lawson[2,5], Matthew Mah[2,5,8], Jonas Oppenheimer[2,5]§, Kristin Stewardson[2,5], Fatma Zalzala[2,5], Stanley H. Ambrose[9], George Ayodo[10], Henry Louis Gates Jr.[11], Agness O. Gidna[12], Maggie Katongo[13], Amandus Kwekason[12], Audax Z. P. Mabulla[12], George S. Mudenda[13], Emmanuel K. Ndiema[4], Charles Nelson[14], Peter Robertshaw[15], Douglas J. Kennett[16], Fredrick K. Manthi[4], David Reich[2,5,8]*

How food production first entered eastern Africa ~5000 years ago and the extent to which people moved with livestock is unclear. We present genome-wide data from 41 individuals associated with Later Stone Age, Pastoral Neolithic (PN), and Iron Age contexts in what are now Kenya and Tanzania to examine the genetic impacts of the spreads of herding and farming. Our results support a multiphase model in which admixture between northeastern African–related peoples and eastern African foragers formed multiple pastoralist groups, including a genetically homogeneous PN cluster. Additional admixture with northeastern and western African–related groups occurred by the Iron Age. These findings support several movements of food producers while rejecting models of minimal admixture with foragers and of genetic differentiation between makers of distinct PN artifacts.

Domestic sheep, goats, and cattle of southwest Asian origin were first introduced to northeastern Africa ~8000 calibrated years before the present (B.P.) and spread into eastern Africa beginning ~5000 B.P., ultimately reaching southernmost Africa by ~2000 B.P. (*1*, *2*). How pastoralism—a way of life centered on herding animals—spread into eastern Africa is unclear. Livestock appear in northern Ethiopia and Djibouti relatively late [~4500 to 4000 B.P. (*3*)] and are poorly documented elsewhere in the Horn of Africa and in South Sudan. Instead, the earliest known domesticated animals in sub-Saharan Africa are found in Kenya at the beginning of the Pastoral Neolithic (PN) (~5000 to 1200 B.P.) era near Lake Turkana, where archaeological evidence documents groups that pursued fishing and herding and constructed elaborate monumental cemeteries (*4*–*6*). Although livestock spread quickly through the Turkana Basin, herding practices were not transmitted farther south for many hundreds of years. Sheep, goats, and pottery typical of Turkana began to trickle into Kenya's south-central Rift Valley ~4200 B.P. (*7*, *8*), but it was not until ~3300 B.P. that specialized pastoralism spread across Kenya and northern Tanzania, transforming the economic, social, and physical landscapes of the region (*9*–*11*).

The core PN era (~3300 to 1200 B.P.) in Kenya and Tanzania witnessed the development of diverse herder societies, some heavily reliant on livestock (*2*). However, pastoralism did not fully replace Later Stone Age (LSA) economies present in the region since ~50,000 B.P., creating a mosaic of herding and foraging communities on the landscape. Two contemporaneous pastoralist traditions have been identified: Elmenteitan and Savanna Pastoral Neolithic (SPN) (*12*, *13*). Elmenteitan sites are found between the central Rift Valley and the western Lake Victoria Basin of Kenya. Occupants used a particular obsidian source, left behind distinctive lithic and ceramic traditions, and practiced primarily cremation burial. By contrast, SPN sites are found across a wider part of Kenya and Tanzania. Occupants used different obsidian sources, had greater diversity in material culture, and mainly buried their dead in cairns. The heterogeneous SPN category likely encompasses multiple groups. Some distinctions between SPN and Elmenteitan traditions, such as mortuary practices, are variable (*6*), and relationships between PN groups—both cultural and genetic—remain uncertain. In addition, little is known about herder interactions with LSA foragers or about relationships among later PN herders and the first iron-using herders after ~1200 B.P. By this time, farming is also documented in the region (*14*, *15*).

Archaeologists have debated the cultural and genetic affinities of the first pastoralists in eastern Africa and the role that movement of people played in the spread of herding to the region. Because the oldest instances of livestock remains and associated pottery and stone tool traditions have been found near Lake Turkana, it has been hypothesized that pastoralism was introduced by migrants from Sudan and/or Ethiopia, potentially in a series of small movements, and that their descendants gave rise to PN traditions farther south (*12*, *13*, *15*, *16*). However, there are no unambiguous cultural connections between Kenya's earliest herders and northern groups, and archaeological evidence supports the local adoption of herding to some degree (*8*, *16*, *17*). Other archaeological and linguistic evidence has been jointly used to hypothesize two expansions into eastern Africa: an initial expansion of herders speaking Afro-Asiatic (specifically proto–Southern Cushitic) languages from the Horn of Africa linked with the SPN, and a second expansion of herders speaking Nilo-Saharan (specifically Nilotic) languages linked with the Elmenteitan.

People of the second expansion have also been hypothesized to be ancestral to some Iron Age groups (*18*, *19*). One subset of Rift Valley sites is designated Pastoral Iron Age (PIA) (~1200 B.P. to recent years) on the basis of material culture and evidence for herding, whereas other sites appear connected to farming and are classified into early, middle, and later Iron Age (IA) (~2500 B.P. to recent) variants (*2*, *14*). Iron-working first entered eastern Africa via the Lake Victoria Basin ~2500 B.P. and spread toward the coast by 2000 B.P. (*14*). This expansion may have brought

[1]Division of Humanities, Saint Louis University, 28003 Madrid, Spain. [2]Department of Genetics, Harvard Medical School, Boston, MA 02115, USA. [3]Department of Anthropology, Stony Brook University, Stony Brook, NY 11790, USA. [4]Department of Earth Sciences, National Museums of Kenya, Nairobi, Kenya. [5]Howard Hughes Medical Institute, Harvard Medical School, Boston, MA 02115, USA. [6]Institutes for Energy and the Environment, Pennsylvania State University, University Park, PA 16802, USA. [7]Department of Anthropology, Pennsylvania State University, University Park, PA 16802, USA. [8]Broad Institute of Harvard and MIT, Cambridge, MA 02142, USA. [9]Department of Anthropology, University of Illinois Urbana-Champaign, Urbana, IL 61801, USA. [10]Department of Public and Community Health, School of Health Sciences, Jaramogi Oginga Odinga University of Science and Technology, Bondo, Kenya. [11]Hutchins Center for African and African American Research, Harvard University, Cambridge, MA 02138, USA. [12]National Museums of Tanzania, Dar es Salaam, Tanzania. [13]Livingstone Museum, Livingstone, Zambia. [14]Academy for Lifelong Learning, Western Washington University, Bellingham, WA 98225, USA. [15]Department of Anthropology, California State University, San Bernardino, CA 92407, USA. [16]Department of Anthropology, University of California, Santa Barbara, CA 93106, USA.

***Corresponding author. Email: mary.prendergast@slu.edu (M.E.P.); mlipson@genetics.med.harvard.edu (M.L.); elizabeth.sawchuk@stonybrook.edu (E.A.S.); reich@genetics.med.harvard.edu (D.R.)**

†These authors contributed equally to this work. ‡Present address: Department of Anthropology, University of California, Santa Cruz, CA 95064, USA. §Present address: Department of Biomolecular Engineering, University of California, Santa Cruz, CA 95064, USA.

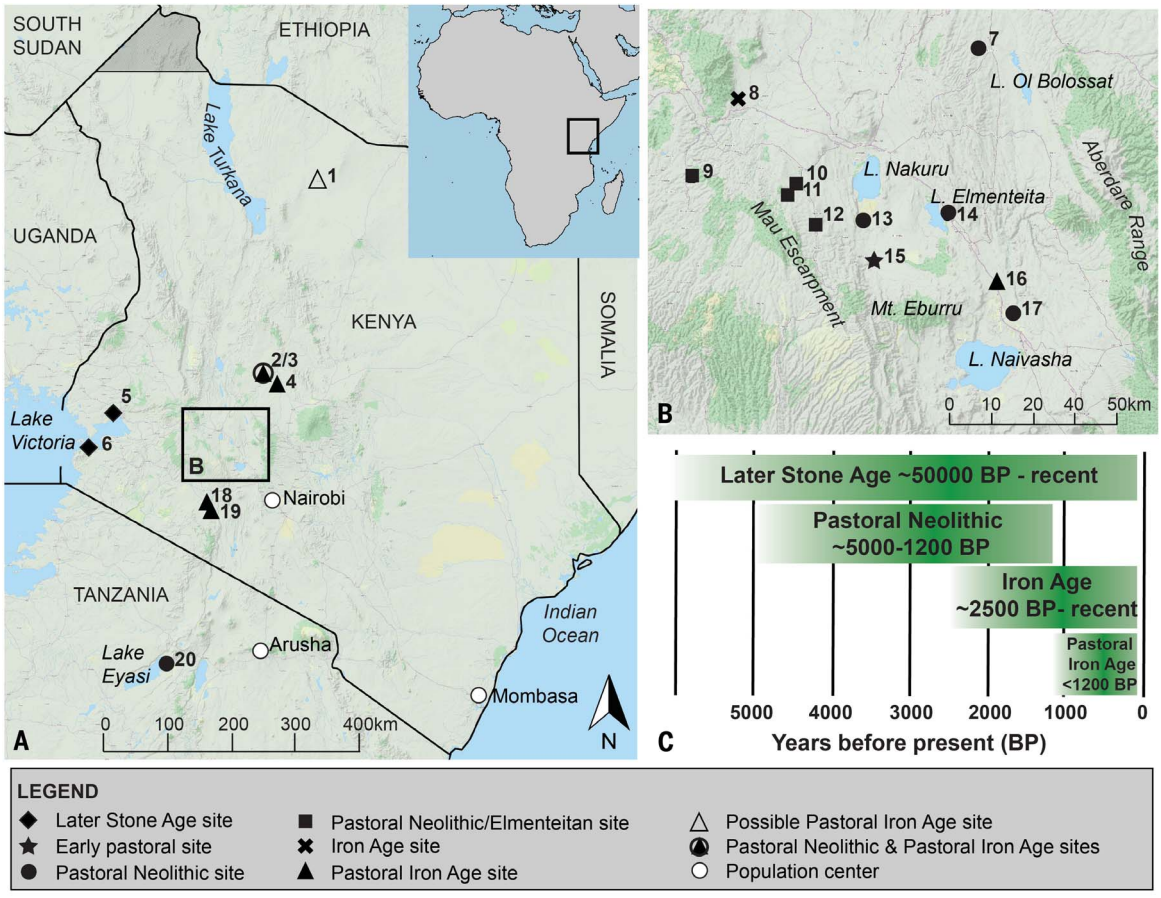

Fig. 1. Map of the study area and regional chronology. (**A**) Locations of sampled archaeological sites in Kenya and Tanzania, with (**B**) detail of the south-central Rift Valley. (**C**) A timeline for eastern African archaeological traditions highlights their degree of overlap and diffuse endpoints. Numbers in (A) and (B) correspond to sites listed in Table 1. Location of 7 is approximate. [Terrain basemaps: © www.thunderforest.com; data: © www.osm.org/copyright; adapted under CC-BY-SA 2.0]

early IA farmers, thought to have spoken Bantu languages originating in equatorial western Africa, into contact with PN herders, although iron-working is not widely attested among herders until ~1200 B.P. at PIA sites (*2*, *15*). Alternatively, PIA sites may reflect other iron-working traditions entering from the north, potentially associated with additional movements of Nilotic-speaking pastoralists into and within the Rift (*2*). This complex mosaic of foragers, herders, and farmers gave rise to much of the present day ethnolinguistic landscape of eastern Africa (*20*).

Rigorous testing of models for the spread of herding has been inhibited by several factors. A spatial and chronological gap exists between the earliest evidence of pastoralism in the Turkana Basin and the later PN expansion, with few material culture similarities. Additionally, relationships among PN and diverse Iron Age groups remain poorly understood. Human skeletal material from relevant contexts tends to be fragmentary, limiting bioarchaeological analysis, and reliable radiocarbon dates are rare. Finally, the persistence of foraging groups raises questions about interaction networks during this period (*12*, *15*), as well as whether food production spread primarily via demic expansion or via local adoption of novel practices and livestock.

To address these debates, we generated genome-wide ancient DNA data from individuals buried at sites associated with LSA (n = 3), early pastoral and PN (n = 31), IA (n = 1), and PIA (n = 6) archaeological traditions in what are now Kenya and Tanzania (Fig. 1, Table 1, and table S1). We extracted DNA from a combination of tooth and bone samples and enriched for a targeted set of ~1.2 million single nucleotide polymorphisms (SNPs) (*21*). Surprisingly, given the tropical climate and variable curatorial conditions, we obtained excellent data quality, with a median of approximately 0.51× coverage, or 440,000 SNPs covered by at least one sequence, for the 41 newly reported individuals (from a total of 67 sequencing libraries; table S2). The data scored well in standard ancient DNA authenticity metrics for all but two individuals [I12391 and I13970, whom we excluded from genome-wide analyses but for whom we obtained Y chromosome and mitochondrial DNA (mtDNA) haplogroups (*21*)]. We also generated direct radiocarbon dates for 35 individuals (tables S3 and S4 and fig. S1). We analyzed these data jointly with sequences from published ancient African individuals (*22*–*27*) as well as from people living in eastern Africa today (*28*–*31*).

Overview of genetic affinities of ancient eastern Africans

We used principal components analysis (PCA) of the genome-wide data to visualize the genetic structure of the ancient individuals (Fig. 2 and table S5). We defined PCs using a small set of present-day groups [southern Africans, northeastern Africans, and non-Africans (*21*)] and projected a large number of diverse individuals onto these axes. An alternative analysis with western Africans additionally used to compute the axes yielded almost identical results (fig. S2). Present-day groups from Sudan mostly lie along a cline extending from Copts (upper right, near individuals from northern Africa and the Levant) to Nilotic speakers such as Dinka and Nuer (lower left). Afro-Asiatic speakers (mostly from Ethiopia) form a second cline, with the right end near Sudanese Beja and Nubians and the left end extending toward eastern African foragers [who themselves form a south-to-north gradient (*22*)]. Present-day Kenyans largely fall in the space

Table 1. Ancient individuals reported in this study, ordered by start of calibrated radiocarbon date range. Site codes, where available, follow a standardized system for Africa (*49*). Calibrated years before the present were calibrated in OxCal v.4.3.2 (*50*), modeling for an unspecified mixture of IntCal13 (*51*) and SHCal13 (*52*) curves and rounding to the nearest decade. PN, Pastoral Neolithic; ELM, Elmenteitan; IA, Iron Age; PIA, Pastoral Iron Age; LSA, Later Stone Age. N/A, not applicable; ND, not determined. Prob., probably; cov., coverage.

Lab ID	Site	Map no.	Latitude (°)	Longitude (°)	Archaeological association	Genetic cluster	Sex	mtDNA haplogroup	Y chromosome haplogroup	Average cov. (reads per site)	Uncalibrated years before present (lab no.)	Calibrated years before present (B.P.), 2σ
I12533	Prettejohn's Gully (GsJi11)	15	−0.545	36.106	Early pastoral?	PN outlier	M	K1a	E2(xE2b); E-M75	0.83	3670 ± 20 (PSUAMS-4982)	4080–3890
I12534	Prettejohn's Gully (GsJi11)	15	−0.545	36.106	Early pastoral?	PN outlier	F	L3f1b	N/A	0.69	3640 ± 20 (PSUAMS-4983)	4060–3860
I8874	Cole's Burial (GrJj5a)	14	−0.442	36.267	PN	PN cluster	M	L3i2	E1b1b1a1a1b1; E-CTS3282	3.90	3070 ± 20 (PSUAMS-4723)	3350–3180
I8809	Kisima Farm, A5/Porcupine Cave	2	0.458	36.709	PN	PN cluster	M	M1a1	E1b1b1b2b2a1; E-M293	3.48	2855 ± 20 (PSUAMS-4510)	3030–2860
I8820	Kisima Farm, A5/Porcupine Cave	2	0.458	36.709	PN	PN cluster	F	M1a1f	N/A	0.07	2675 ± 20 (PSUAMS-4717)	2840–2740
I12398/9*	Rigo Cave (GrJh3)	12	−0.464	35.971	PN/ELM	PN cluster	M	L3f	E1b1b1b2b2a1; E-M293	0.89	2480 ± 20 (PSUAMS-4945); 2570 ± 15 (PSUAMS-4946)	2710–2380; 2750–2510
I8759	Naishi Rockshelter	13	−0.458	36.081	PN	PN outlier	M	L3x1a	E1b1b1b2b; E-V1515 (prob. E-M293)	0.07	2550 ± 15 (PSUAMS-4715)	2750–2500
I13980	Gishimangeda Cave	20	−3.476	35.348	PN	PN cluster	M	HV1b1	E1b1b1a1b2; E-V22	2.72	2530 ± 20 (PSUAMS-5655)	2740–2490
I13981	Gishimangeda Cave	20	−3.476	35.348	PN	PN cluster	F	L0a	N/A	0.36	2510 ± 20 (PSUAMS-5656)	2730–2460
I8758	Naishi Rockshelter	13	−0.458	36.081	PN	PN cluster	M	L0a2d	A1b(xA1b1b2a); A-P108	0.29	2470 ± 15 (PSUAMS-4624)	2700–2370
I8804	Keringet Cave?†	9	−0.358	35.699	PN	PN cluster	M	L4b2a1	A1b1b2; A-L427	0.50	2465 ± 20 (PSUAMS-4716)	2700–2360
I8923	Rigo Cave (GrJh3)	12	−0.464	35.971	PN/ELM	PN cluster	M	M1a1b (likely)	E1b1b1b2b2; E-V1486 (prob. E-M293)	0.15	2440 ± 20 (PSUAMS-4512)	2690–2350
I13979	Gishimangeda Cave	20	−3.476	35.348	PN	PN cluster	F	L3x1	N/A	2.56	2410 ± 20 (PSUAMS-5654)	2490–2350
I8922	Rigo Cave (GrJh3)	12	−0.464	35.971	PN/ELM	PN cluster	M	L4b2a2c	E1b1b1b2b2a1; E-M293	2.79	2400 ± 15 (PSUAMS-4725)‡	~2460–2350
I8814	Naivasha Burial Site	17	−0.663	36.410	PN	PN cluster	F	L4b2a2b	N/A	2.53	2400 ± 20 (PSUAMS-4784)	2480–2340
I13978	Gishimangeda Cave	20	−3.476	35.348	PN	PN outlier	F	L4b2a1	N/A	0.56	2355 ± 20 (PSUAMS-5653)	2400–2310
I8830	Naivasha Burial Site	17	−0.663	36.410	PN	PN cluster	M	M1a1b	xBT (prob. A)	0.10	2320 ± 20 (PSUAMS-4720)	2360–2210
I8920	Naivasha Burial Site	17	−0.663	36.410	PN	PN cluster	M	L3h1a1	E1b1b1b2b2a1; E-M293	1.68	2310 ± 15 (PSUAMS-4724)	2350–2210
I8919	Naivasha Burial Site	17	−0.663	36.410	PN	PN cluster	M	L4a1	A1b1b2b; A-M13	1.84	2255 ± 20 (PSUAMS-4789)	2340–2160
I8918	Naivasha Burial Site	17	−0.663	36.410	PN	PN cluster	M	L3x1a	E1b1b1b2b2a1; E-M293	2.45	2235 ± 20 (PSUAMS-4744)	2320–2150

Lab ID	Site	Map no.	Latitude (°)	Longitude (°)	Archaeological association	Genetic cluster	Sex	mtDNA haplogroup	Y chromosome haplogroup	Average cov. (reads per site)	Uncalibrated years before present (lab no.)	Calibrated years before present (B.P.), 2σ
I13762	Gishimangeda Cave	20	−3.476	35.348	PN	PN cluster	M	L3i2	E1b1b1b2b2a1; E-M293	1.81	2140 ± 15 (PSUAMS-5458)	2150–2020
I10719	Njoro River Cave II	11	−0.389	35.917	PN/ELM	PN cluster	F	L3h1a2a1	N/A	1.11	2070 ± 15 (PSUAMS-4758)	2110–1930
I13970	Gishimangeda Cave	20	−3.476	35.348	PN	N/A	F	L3h1a2a1	N/A	0.03	2030 ± 20 (PSUAMS-5650)	2000–1900
I13977	Gishimangeda Cave	20	−3.476	35.348	PN	PN cluster	M	L0f2a1	E1b1b1b2b2; E-V1486 (prob. E-M293)	0.30	2005 ± 20 (PSUAMS-5652)	2000–1890
I8808	Jawuoyo Rockshelter	5	−0.067	34.667	LSA	Forager cline	M	L4b2a2c	E1b1b1a1b2; E-V22	1.37	1895 ± 15 (PSUAMS-4783)	1880–1750
I8805	Egerton Cave (GrJh10)	10	−0.375	35.933	PN/ELM	PN cluster	F	L0a1d	N/A	3.79	1880 ± 15 (PSUAMS-4741)	1870–1740
I12384	Ol Kalou	7	−0.300§	36.400§	PN	PN cluster	M	L3d1d	E1b1b1b2b2a1; E-M293	0.51	1800 ± 20 (PSUAMS-4940)	1810–1620
I13972	Gishimangeda Cave	20	−3.476	35.348	PN	PN outlier	M	T2+150	E1b1b1b2b2; E-V1486 (prob. E-M293)	0.09	1780 ± 25 (PSUAMS-5651)	1740–1580
I12394	Keringet Cave (GrJg4)	9	−0.358	35.699	PN/ELM	PN cluster	F	K1a	N/A	0.42	1585 ± 15 (PSUAMS-4943)	1530–1400
I8892	Ilkek Mounds	16	−0.603	36.374	PIA	PIA cluster	M	L0f2a	E2(xE2b); E-M75	0.10	1170 ± 15 (PSUAMS-4788)	1170–980
I8802	Deloraine Farm (GqJh6)	8	−0.183	35.809	IA	IA other	M	L5b1	E1b1a1a1a1a; E-M58	2.65	1160 ± 15 (PSUAMS-4625)	1170–970
I8901	Kisima Farm, C4	3	0.458	36.709	PIA	PIA cluster	M	L3h1a1	E2(xE2b); E-M75	0.02	1110 ± 15 (PSUAMS-4743)	1060–940
I12391	Kasiole 2 (GvJh54)	18	−1.326	35.939	PIA	N/A	M	L3h1a2a1	E1b1b1b2b; E-V1515 (prob. E-M293)	0.02	1110 ± 15 (PSUAMS-4942)	1060–940
I12381	Laikipia District Burial (GoJl45)	4	0.380	36.893	PIA	PIA cluster	F	L0a1c1	N/A	0.92	635 ± 15 (PSUAMS-4939)	650–560
I12379	Emurua Ole Polos (GvJh122)	19	−1.396	35.983	PIA/recent	PIA cluster	M	L3h1a2a1	E1b1b1b2b2a1; E-M293	3.38	270 ± 15 (PSUAMS-4938)	420–160
I13763	Gishimangeda Cave	20	−3.476	35.348	PN	Forager cline	F	ND	N/A	0.01	Insufficient collagen	N/A
I13982	Gishimangeda Cave	20	−3.476	35.348	PN	Forager cline	F	ND	N/A	0.02	Insufficient collagen	N/A
I13983	Gishimangeda Cave	20	−3.476	35.348	PN	Forager cline	M	ND	BT (low cov.; prob. B)	0.02	Insufficient collagen	N/A
I8904	Kokurmatakore	1	3.132	37.433	PIA?¶	PN outlier?	M	L3a2a	E1b1b1; E-M35 (not E-M293)	0.09	Insufficient collagen	N/A
I8930	White Rock Point (GrJb2)	6	−0.450	34.321	LSA	Forager cline	M	L2a4	BT(xCT) (low cov.; prob. B)	0.03	Insufficient collagen	N/A
I8931	White Rock Point (GrJb2)	6	−0.450	34.321	LSA	Forager cline	F	L0a2 (likely)	N/A	0.03	Insufficient collagen	N/A

*Samples are from the same individual but provided slightly different radiocarbon dates. †The context of this individual is uncertain; see (*21*) for details. ‡Indirect date on a bone that may be from a different individual (table S1). All other dates are direct on the individual for whom DNA data are reported. §Approximate location. ¶New attempts to date this individual failed, but a published date on bone apatite from this individual suggests a PIA association, despite genetic clustering with PN individuals; see (*21*) for details.

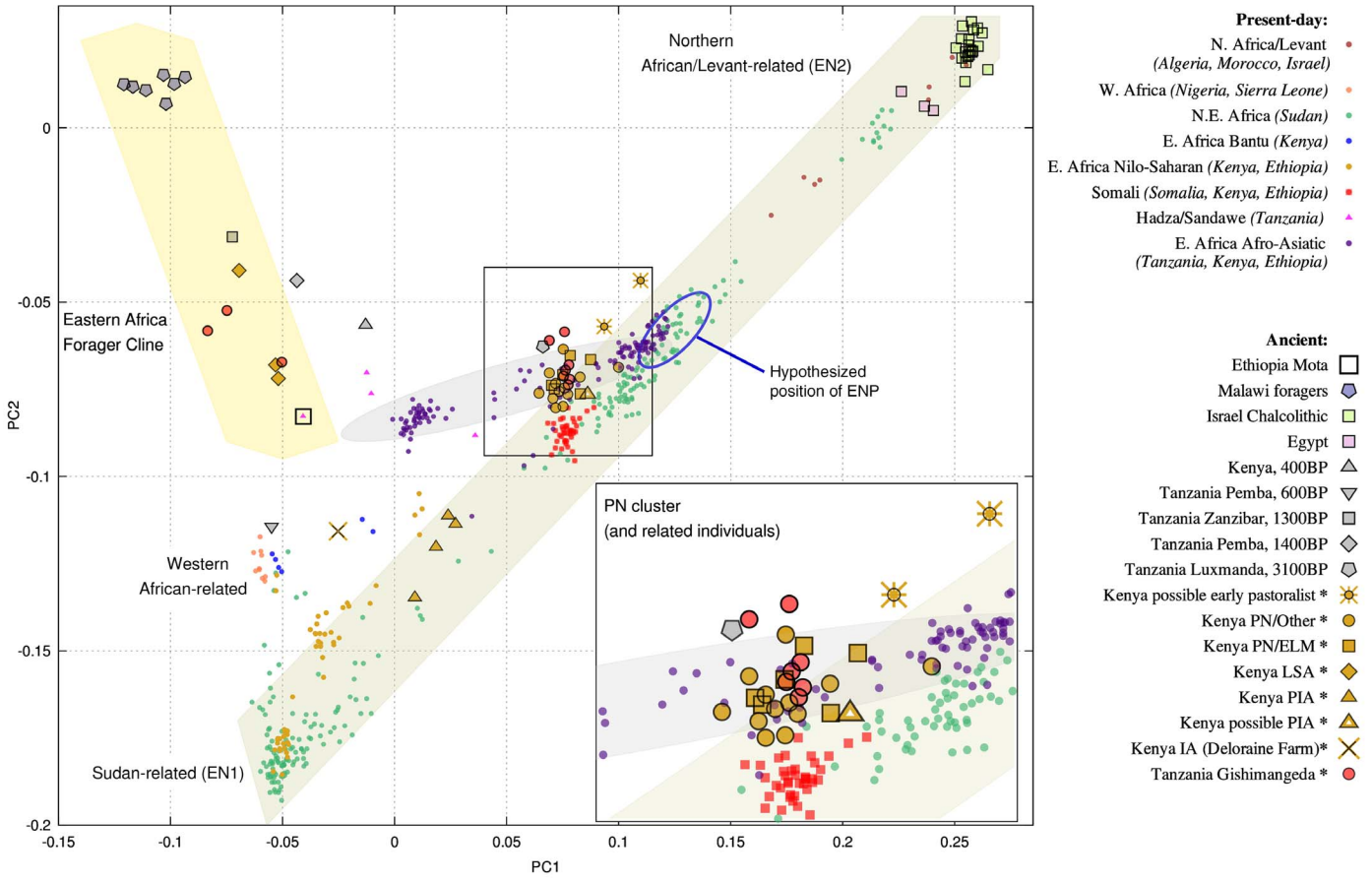

Fig. 2. Principal components analysis. Shaded regions are drawn to highlight notable clines of ancestry. Ancient individuals from this study are indicated in the key with asterisks. Dates for published ancient individuals outside of Kenya and Tanzania are ~4500 B.P. for Mota, ~8100 to 2500 B.P. for Malawi foragers, ~6500 to 5800 B.P. for Israel Chalcolithic, and ~3600 to 2000 B.P. for Egypt. ELM, Elmenteitan; LSA, Later Stone Age; PN, Pastoral Neolithic; IA, Iron Age (I8802); PIA, Pastoral Iron Age; ENP, early northeastern pastoralist. See (*21*) for more details and table S5 for the full list of individuals shown.

between Sudanese, Ethiopians, and western Africans, with their language family affiliations tending to predict their broad-scale genetic affinities.

The positions of ancient eastern Africans on the PCA strongly correlate with archaeological associations. The three individuals from LSA cultural contexts all cluster with previously reported ancient foragers, falling intermediately between those from southern Ethiopia (Mota) and coastal Tanzania (Zanzibar and Pemba islands), consistent with their geographic position (*22*, *24*). Individuals from pastoralist contexts [including one from Luxmanda in Tanzania (*22*)] are highly differentiated from foragers, with the exception of three individuals uncertainly assigned a pastoral context at Gishimangeda Cave in Tanzania, who cluster with foragers. PN individuals, including Elmenteitan and those within the heterogenous SPN category (whom we refer to as "other PN"), mostly form a tight cluster near present-day Afro-Asiatic speakers, with a small number of modest outliers, including the two individuals buried at Prettejohn's Gully, whose earlier date (~4000 B.P.) coincides with the initial limited spread of herding into the area. Finally, five Iron Age individuals are shifted to the left in the PCA: four PIA individuals toward Nilotic speakers and an IA child from Deloraine Farm (I8802)—the earliest agricultural site in Kenya's Rift Valley (*32*)—toward western Africans and Bantu speakers.

We also examined the uniparentally inherited loci (mtDNA and Y chromosomes) of the sampled individuals. The most pronounced pattern is the high frequency among the PN individuals (7 to 12 out of 17 males; table S6) of the E-M293 haplogroup (E1b1b1b2b2a1), a Y chromosome lineage that has been hypothesized to be associated with the spread of pastoralism in the Horn of Africa, Kenya, and Tanzania and from there to southern Africa, on the basis of its present-day distribution and diversity (*33*, *34*). Other males also carried haplogroups most frequently found in present-day eastern Africa, with the exception of E-M58 (E1b1a1a1a1a; predominantly western African) in the IA individual I8802, consistent with his position in the PCA. The observed mtDNA lineages form more of a mosaic pattern, including types most closely associated with eastern and northeastern Africans, eastern African foragers, and northern Africans and western Eurasians (table S7).

Formal modeling of admixture

To obtain quantitative inferences about the genetic relationships among the ancient and present-day individuals, we used the *qpAdm* software (*35*, *36*), which provides a flexible framework for testing admixture models and estimating mixture proportions. Guided by the PCA, we began by using three groups of individuals—present-day Dinka (*28*), ancient Chalcolithic-period individuals from Israel (*25*), and the ~4500 B.P. forager from Mota, southern Ethiopia (*24*)—to represent distinct components of ancestry plausibly found in ancient and present-day eastern Africans, with present-day western Africans among the outgroups (*21*). Note that the use of these proxy groups in *qpAdm* modeling does not imply an assumption that they are directly ancestral to the true sources contributing to the individuals we analyzed. Instead, for a model to be properly formulated, the reference groups only need to be more closely related to the true sources

than are the outgroups, without substantially different admixture (35). Thus, for example, ancestry related to the Chalcolithic Israel reference individuals could plausibly have originated anywhere in northeastern Africa or the Levant and could have been present in northeastern Africa for many thousands of years. We use the Chalcolithic individuals in this study because we lack genetic data from a phylogenetically adjacent reference group from Egypt, Sudan and/or South Sudan, or the Horn. Additionally, *qpAdm* does not require any assumptions regarding the internal phylogeny relating the references and outgroups, and it provides both standard errors for mixture proportion estimates and a *P* value for overall model fit quality (35).

Our *qpAdm* modeling reveals that the PN individuals had substantial proportions of all three ancestry components (~40% each for those represented by Dinka and by the Chalcolithic Israel individuals and ~20% related to Mota) (Fig. 3 and tables S8 and S9), with no evidence of western African–related ancestry. The individuals from Prettejohn's Gully can also be well modeled using the same three components, but in a modestly different ratio. The Iron Age group as a whole (including the more recent ~300 B.P. individual from Emurua Ole Polos but excluding the possible PIA individual from Kokurmatakore) does not fit well under a three-way model, but the fit improves markedly when we exclude the Deloraine Farm individual I8802 (P = 0.009 versus 0.0003). The remaining four individuals (who are confidently assigned to PIA contexts) are inferred to have substantially more Sudan (Dinka)–related ancestry (~60%) than is seen in the PN. We also observe similar patterns for present-day groups falling near the ancient individuals in PCA [using data from (31)], whereby the three-way model fits better for Afro-Asiatic– and Nilo-Saharan–speaking groups than for Bantu-speaking groups (table S8). Consistent with the PCA results, Afro-Asiatic speakers are inferred (as in PN) to have relatively even proportions of the components represented by Dinka and by Chalcolithic Israel (but with varying proportions of Mota-related ancestry), whereas Nilo-Saharan speakers are inferred to have more Sudan-related ancestry. Alternative model formulations in which we use either ancient individuals from Taforalt in Morocco (27) in place of the Chalcolithic Israel group or present-day Lemande from Cameroon (28) in place of Dinka (with Dinka moved to the outgroup set) fit significantly worse for most test groups (table S8).

From these results, we formulated a four-part hypothesis to explain the origins of the ancestries in the sampled eastern African groups. First, admixture in northeastern Africa, likely associated with the spread of pastoralism, created groups (as yet unsampled with ancient DNA) with approximately equal proportions of ancestry related to (i) present-day Nilotic speakers such as Dinka and Nuer and (ii) sampled ancient and present-day groups from northern Africa and the Levant. We refer to this combination as early northeastern African pastoralist-associated ancestry (henceforth "early northeastern pastoralist," or ENP) and the two subcomponents as EN1 and EN2. Second, descendants of these groups mixed with local foragers in eastern Africa, leading to the ~20% Mota-related ancestry in the PN individuals. Third, an additional period of Sudan-related gene flow occurred before the Iron Age and contributed to PIA groups. Fourth, close to the same time, western African–related ancestry related to present-day Bantu speakers [also seen in an individual buried on Pemba Island ~600 B.P. (22)] appeared in the Rift Valley (notably at Deloraine Farm), in association with the spread of farming.

To test these hypotheses and gain further insight into changes in ancestry over time, we carried out a second round of analysis in *qpAdm* using pairs of reference groups linked more closely with each historical phase. For the initial spread of pastoralism, we used Hadendowa [Sudanese Beja (29)] plus Mota. It is likely that

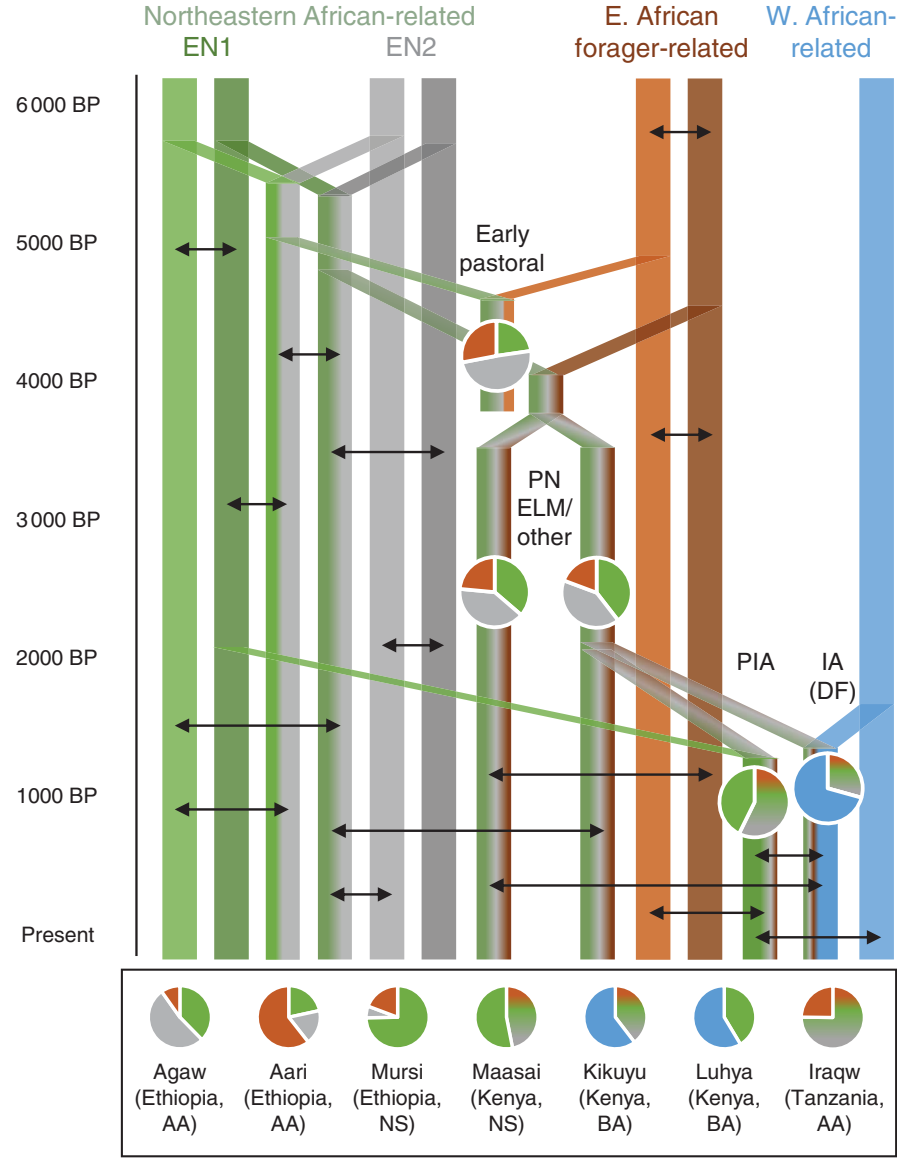

Fig. 3. Proposed model of admixture for ancestry in eastern Africans. Solid-color bars represent lineages of northeastern African (EN1/Sudan-related in green, EN2 in gray), eastern African forager-related (orange), and western African-related (blue) ancestry, and mixed-color bars represent admixed groups (hypothesized early northeastern pastoralists, green plus gray). Pie charts show ancestry proportions for sampled ancient (embedded in figure at approximate date points) and present-day (bottom) groups inferred from *qpAdm* (PN-related ancestry as mixed-color sections). Black arrows represent likely ongoing interactions and not specific admixture events inferred from the data. EN1 and EN2, early northeastern pastoralist source groups; PN, Pastoral Neolithic; ELM, Elmenteitan; PIA, Pastoral Iron Age; IA (DF), Iron Age (Deloraine Farm); AA, Afro-Asiatic; NS, Nilo-Saharan; BA, Bantu.

the genetic landscape of northeastern Africa has changed substantially since the time of the events we are modeling, so we do not propose that Hadendowa are descended directly from ENP; rather, we chose them to serve as a proxy for the (approximate) mixture of ancestries hypothesized to be present in the true ENP-related source (on the basis of the PCA and *qpAdm* results above). This two-way model yields a good fit for the PN individuals ($P = 0.45$) but not for Iron Age individuals (either the PIA cluster or the IA individual from Deloraine Farm) or present-day Nilotic- and Bantu-speaking groups (all $P < 1 \times 10^{-6}$; table S8). We also attempted to fit PN as a mixture of possible early Kenyan pastoralist (represented by Prettejohn's Gully) and forager-related ancestry, but this combination was rejected ($P < 1 \times 10^{-6}$ using either Mota or the three Kenyan LSA individuals to represent the forager component), suggesting that the two ancient pastoralist groups are not simply differentiated by their proportions of forager-related ancestry.

Finally, to study later transformations, we built models using PN as one proxy source and Dinka (Sudan-related), Mota (forager-related), or Lemande (western African-related) as the other. We obtain improved fits for the Iron Age individuals and for present-day Kenyan Nilotic- and Bantu-speaking groups in this framework: The PIA cluster can be fitted as a mixture of ~57% PN-related and ~43% Sudan-related ancestry, whereas the Deloraine Farm individual can be modeled as a mixture of ~29% PN-related and ~71% western African–related ancestry (Fig. 3). Similar models also yield good fits for present-day Maasai (~47% PN-related and ~53% Sudan-related) and Kikuyu (~40% PN-related and ~60% western African–related), whereas Luhya can be fit as a mixture of Sudan-related (~41%) and western African–related (~59%) ancestry (Fig. 3).

We also used direct tests of asymmetry in allele frequencies to investigate the fine-scale genetic structure of the PN cluster and related individuals (table S10). First, in agreement with their colocalization in PCA, we do not detect any significant differences in allele-sharing between Elmenteitan and other PN individuals relative to a set of 27 comparison groups, including the Iron Age and possible early pastoralist groups from this study (maximum nominal Z score = 2.1; see also Fig. 4). There are hints of differentiation (maximum $Z = 2.6$) between the main PN cluster and individual I8904 from Kokurmatakore [previously dated to the PIA (*37*)], but this individual's ancestry is much more similar to other PN individuals than to PIA (Fig. 2 and table S10). We also find only minor asymmetry between the primary Kenyan and Tanzanian PN clusters (maximum $Z = 2.5$). However, four PN-period individuals who appear as outliers on PCA do have statistically significant ancestry differences as compared with the PN cluster. In particular, two individuals from Gishimangeda Cave (I13972 and I13978) and the previously reported ~3100 B.P. pastoralist individual from Luxmanda in Tanzania (*22*) have evidence of more or different forager-related ancestry relative to Sudan-related ancestry [e.g., f_4(Ancient South African foragers, Dinka; X, PN) > 0, $Z = 3.2$, 5.1, and 6.8, respectively; Fig. 4 and tables S8 and S10], whereas individual I8759 (an early PN individual buried at Naishi Rockshelter in Kenya) has evidence of less forager-related ancestry [e.g., f_4(Ancient South African foragers, Europeans; I8759, PN) < 0, $Z = -4.4$]. We also confirm the differences in ancestry between the PN cluster and the two possible early pastoralist individuals from Prettejohn's Gully (both $Z > 5$). Although the individuals from Prettejohn's Gully fall relatively far apart on PCA (Fig. 2), their ancestry is only weakly differentiated via f statistics (maximum $Z = 2.2$; table S10).

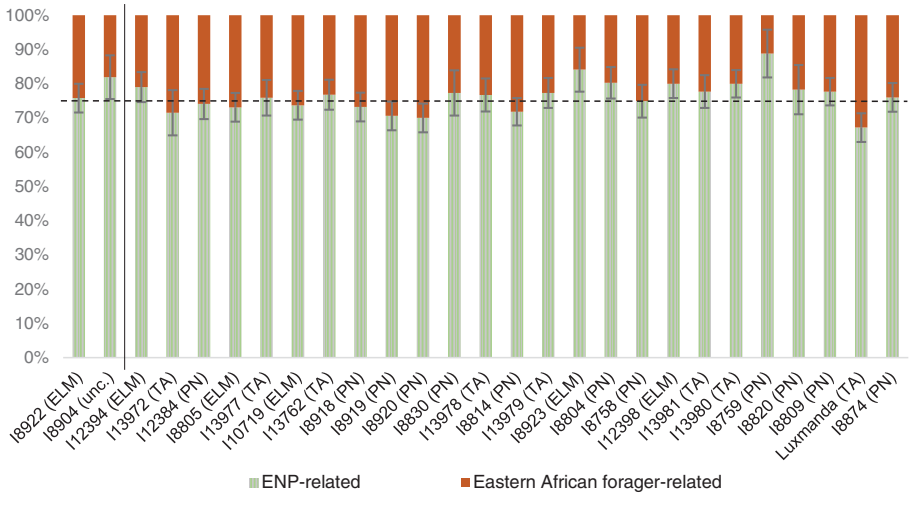

Fig. 4. Mixture proportions for PN individuals. Results are from a two-component *qpAdm* model using Hadendowa (green-and-gray striped bars) and the ancient individual from Mota, Ethiopia (orange bars) as proxy sources [for early northeastern pastoralist (ENP) and eastern African forager–related ancestry, respectively]. Radiocarbon-dated individuals (to the right of the solid line) are ordered from most ancient on the right (I8874, 3350 to 3180 B.P.) to most recent on the left (I12394, 1530 to 1400 B.P.). Bars show two standard errors in each direction. The dashed line represents the Kenya PN group-level estimate (74.7 ± 1.0% ENP-related ancestry). Note that the linear regression coefficient for forager-related ancestry is not significantly nonzero as a function of date ($R^2 = 0.03$, $P = 0.39$) or latitude ($R^2 = 0.03$, $P = 0.37$). ELM, Elmenteitan; PN, other Kenyan Pastoral Neolithic; TA, Tanzanian PN [including the Luxmanda individual from (*22*)]; unc., uncertain.

Dates of admixture

The fact that we observe tight clustering of PN individuals via PCA and *qpAdm*, with little if any spatial or temporal structure as revealed by direct dating (Fig. 4 and table S9), suggests that the admixture responsible for forager-related ancestry in the PN had largely ceased before the lifetimes of our sampled individuals. To test this hypothesis, we used the MALDER software (*38*, *39*) to estimate dates of admixture for pairs of high-coverage individuals with similar direct radiocarbon dates and locations (*21*). All pairs have inferred dates that point to distant average times of admixture (mean ~4600 B.P. for PN and ~5300 B.P. for Prettejohn's Gully; Fig. 5 and table S10), with the concordance among the PN estimates providing an independent line of evidence for a lack of substantial ongoing mixture. We infer a more recent average date (~2200 B.P.) for two late PIA individuals, likely associated with additional Sudan-related ancestry (table S11). Our power to detect multiple waves of admixture is limited with ancient data, but for one pair of PN individuals from Naivasha Burial Site, we are confidently able to identify two separate events, the first at ~5100 B.P. and the second at ~4000 B.P. We also infer two waves for a pair of individuals from Gishimangeda Cave, dating to ~6000 B.P. and ~4000 B.P. In light of our *qpAdm* results, and given the associated MALDER amplitudes (table S11), these multiple dates plausibly represent estimates of the times of (i) the formation of admixed ENP ancestry and (ii) admixture in eastern Africa between local foragers and descendants of the first mixture, leading to the three-component ancestry of PN individuals. In this context, the single (and intermediate) estimated dates for other PN pairs can be interpreted as averages of these two processes (Fig. 5).

Incorporating genetic evidence into models for the spread of food production

The four-phase model emerging from our genetic and radiocarbon dating results builds on archaeological reconstructions for the spread of herding into eastern Africa, supporting some theories while rejecting others that until now have been considered plausible. Under a proposed "moving frontier" model, herders entering new environments would interact in diverse ways with Indigenous foragers, resulting in varying cultural responses and blurred archaeological boundaries

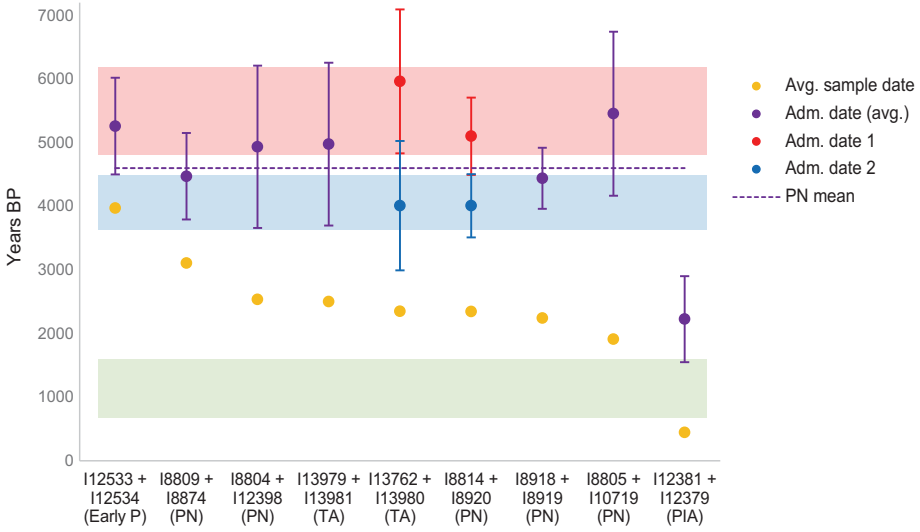

Fig. 5. Dates of admixture inferred for pairs of ancient individuals. Bars show two standard errors in each direction. The shaded areas represent implied periods of admixture (Adm.): ENP (early northeastern pastoralist; red), forager-related (blue), and additional Sudan-related (green). Early P, early pastoralists; PN, Pastoral Neolithic; PIA, Pastoral Iron Age; TA, Tanzanian PN. See also table S11.

as groups adopted some of each other's cultural practices. In the ensuing "static frontier," more intensive herding and/or competition would transform initial relationships into more stable, long-term patterns (*40*). Archaeologists interpret the construction of cemeteries by the first herders in the Turkana Basin and the apparent trickle of people with similar material culture into the south-central Rift Valley as part of a moving frontier, whereas the explosion of pastoralist cultures in the PN reflects more established, static herder-forager relationships (*6*, *15*).

On the basis of genetic data from a wide sampling of PN individuals, we infer two phases of admixture associated with the spread of pastoralism: the first likely ~6000 to 5000 B.P. in northeastern Africa and the second ~4000 B.P. between this admixed ENP group and eastern African foragers. Archaeological data show that the Nile Valley was important for herders seeking reliable water sources toward the end of the African Humid Period (~7000 to 6000 B.P.) (*1*, *41*). Herders plausibly traced the White Nile southward, following unknown trajectories through South Sudan and/or southern Ethiopia to arrive in the Turkana Basin ~5000 B.P. (*5*, *6*). Alternatively, they may have moved via the Horn of Africa, but current evidence for herding in that region postdates that of Turkana (*3*). Our results support archaeological hypotheses that no matter the routes they took, early herders interacted with local foragers as they spread (*16*, *42*). In eastern Africa, extensive forager-herder interactions have been proposed, both in the Turkana Basin and during the initial trickle of herding into the south-central Rift Valley (*6*–*10*, *16*, *17*). Either area, or another unsampled region, could have witnessed the admixture we document between descendants of the (already admixed) ENP group and local foragers, giving rise to the groups who then developed the PN cultural traditions of southern Kenya and northern Tanzania.

Our attempts to extract DNA from early herders in Turkana were unsuccessful (*21*), so the genetic ancestry (or ancestries) of the first eastern African pastoralist groups remains uncertain. However, some lineages may be reflected in a man and a woman buried at Prettejohn's Gully ~4000 B.P. There are few associated artifacts, but the individuals' genetic profiles suggest that they may represent an initial limited dispersal of herders into the south-central Rift Valley that did not leave large numbers of descendants. Previously, evidence of herding before ~3300 B.P. was limited to Turkana-related Nderit pottery found sporadically, and usually undated, in the area (*8*), and to sheep or goat remains associated with a date of ~4200 B.P. at a site 33 km south of Prettejohn's Gully (*7*). Genetically, the two individuals are most similar to those from PN sites, but they fall outside the range of sampled PN (and present-day) variation and cannot be modeled as directly related to PN. They also have a suggestively older date of admixture, and the male individual (I12533) carries a Y chromosome haplogroup (E2; E-M75) not found in any of our sampled PN individuals. Our results thus imply at least two chronologically distinct movements of herders through eastern Africa, consistent with archaeological evidence of complex spreads (*2*), while adding new information by showing that one group (the one that gave rise to the PN cluster) was eventually much more demographically successful than the others.

Although Prettejohn's Gully may represent a limited trickle of herders into the south-central Rift Valley, numerous PN sites after ~3300 B.P. attest to successful specialized pastoralism. Archaeologists attribute this florescence to herder innovations that allowed them to overcome environmental and disease barriers, likely facilitated by strong social networks reflected in widespread material cultural traditions (*8*–*11*). The dense cluster of PN individuals in our PCA—including burials >450 km apart—suggests that these networks formed among people with shared ancestry, with the close relatedness perhaps reinforced by ongoing mobility and gene flow. Moreover, it is notable that individuals in our sample buried with distinctive Elmenteitan material culture display minimal genetic differentiation from those of other PN burials. Strong Elmenteitan material cultural traditions may reflect maintenance of social boundaries, but our results do not support the view that these people were genetically distinct (*12*, *18*). In comparison to present-day groups, all PN individuals (associated with both the SPN and Elmenteitan material cultures) show the greatest genetic affinity to Afro-Asiatic speakers, supporting the hypothesis that the initial large-scale expansion of pastoralism in eastern Africa was linked to the spread of Afro-Asiatic languages (*18*, *19*).

With regard to the moving frontier model, we find that although sampled PN individuals carry ~20% admixture from local forager groups, almost all of this gene flow occurred well before the core PN era, as herders entered new environments. By contrast, the rapid spread of pastoralists into Kenya and Tanzania after ~3300 B.P. involved minimal gene flow between herders and foragers, plausibly due to the formation of a static frontier along which social barriers prevented large-scale gene flow, despite possible social and economic interaction (*8*, *15*). Alternatively, population densities of foragers may have been so low that gene flow between the groups had little demographic impact on the more numerous pastoralists (*12*). Static frontiers were not absolute, however, in agreement with ethnographic and ethnohistoric records that testify to some intermarriage between foragers and food producers (*43*, *44*). Today, for example, the Eyasi Basin is an important interaction zone for diverse foraging and food-producing groups (*44*) and is home to speakers of each of the four main African language phyla. In our data, the ancestries of the individual buried at Luxmanda (*22*), the southernmost known PN site (*11*), and two newly reported individuals from Gishimangeda Cave in the Eyasi Basin attest to additional admixture with foragers beyond the events contributing to the possible early pastoralists from Prettejohn's Gully and to the main PN cluster. Furthermore, at Gishimangeda Cave, we observe three individuals clustering genetically with foragers, which may reflect social ties between people with different ancestry and/or ways of life. However, given that the three forager-related individuals produced insufficient collagen for radiocarbon dating and genetic data with substantially lower coverage than that of the pastoralist-related individuals, we speculate that the observation of distinct ancestry types is more likely to be a consequence of multiple burial phases at the site (i.e., greater antiquity for the forager-related individuals).

Low frequency of genetic adaptation to milk consumption

To test whether the success of PN groups in eastern Africa was aided by genetic adaptations linked to diet, we also evaluated the sequenced individuals for presence or absence of genetic variants associated with adult lactase persistence (LP) (table S12). Although our coverage is limited for some individuals and some SNPs, we observe only one instance of an LP-conferring mutation, in individual I13762, from Gishimangeda Cave in Tanzania. This individual, who falls within the main PN genetic cluster and lived during the later PN (2150 to 2020 B.P.), carried the derived allele at the rs145946881 (G/C-14010) SNP, which is the most common LP mutation found among eastern African groups today. The other ancient individuals could possibly have carried different variants conferring the same phenotype, but the assayed SNPs are found at high frequencies in some present-day eastern African groups and thus are likely to have been important historically (*45*). This finding suggests that eastern African pastoralists were mostly lactose intolerant as recently as 3000 to 1000 years ago and that the LP alleles only recently rose in frequency, although our results also demonstrate that the G/C-14010 mutation was present and could have been a target for natural selection by the PN period. Direct evidence for dairying is currently lacking in the region, despite the specialized pastoralist lifestyle inferred from faunal remains at PN sites (*8*). However, culinary innovations such as fermentation could have enabled dairy consumption even in the absence of LP.

Increasing complexity in the Iron Age

The eastern African Iron Age can be summarized archaeologically as a mosaic in which foragers, herders, and early farmers with distinct traditions and ways of life overlapped in space and time (*2*, *14*, *15*, *19*). This complexity is reflected in the ancient individuals we analyzed. The young boy buried at Deloraine Farm—the site with the earliest direct evidence of farming in the Rift Valley (*32*)—shows affinity to western Africans and speakers of Bantu languages (both genome-wide and on the Y chromosome). This is the earliest documentation of western African–related ancestry in eastern Africa, in a region where today such ancestry is widespread and the majority of people speak Bantu languages (*46*).

The Deloraine Farm child's genetic distinctiveness as compared with the PN cluster is notable in light of similarities in artifacts between Elmenteitan sites and Deloraine Farm, viewed as evidence of continuity from the Elmenteitan to the Iron Age (*32*, *47*). By contrast, four PIA individuals spanning an ~800-year period show greater affinity to present-day Nilotic speakers and are associated with an influx of Sudan (Dinka)–related ancestry. Similarities between archaeologically and ethnographically documented material culture suggest that PIA sites may be associated with ancestors of present-day Kenyan Nilotic speakers such as the Kalenjin or Maasai (*32*, *47*). Both the PIA individuals and present-day Maasai retain substantial components of PN-related ancestry, showing that the ancestry composition of PIA and more recent pastoralists reflects mixture with previously established herder groups in eastern Africa. For other groups, such as Luhya (who speak a Bantu language), there is little evidence of PN-related ancestry, suggesting that their ancestors spread into Kenya without mixing substantially with local herders. Boundaries between foragers and food producers may have been maintained during the Iron Age, as we do not observe a significant increase in forager ancestry in the PIA or IA individuals, but we cannot rule out a small proportion of additional forager-associated admixture. Overall, we caution that these interpretations are limited by small sample sizes and may not reflect the more nuanced regional dynamics within this mosaic.

Genetic diversity of eastern African foragers

Archaeological evidence of foragers across Holocene eastern Africa encompasses an array of material culture and subsistence traditions (*48*). This study adds to our understanding of LSA genetic variation by reporting ancient DNA from additional foragers without pastoralist-related admixture, including from fisher-foragers near Lake Victoria who may have been living contemporaneously with PN herders in the broader region. These individuals fall in an intermediate position between Ethiopian and Tanzanian foragers on a genetic cline that is well correlated (among sampled ancient individuals) with geographical location (*22*). Broadly, however, the similarity of foragers buried in the Victoria and Eyasi basins to individuals living on the Kenya coast and in Ethiopia and coastal Tanzania (*22*, *24*) suggests that shared forager ancestry extended widely across the region, as also attested by present-day genetic data (*20*).

Outlook

Genome-wide data from 41 ancient eastern Africans show that archaeological complexity during the spreads of herding and farming is also reflected in genetic patterns, which indicate multiple movements of and gene flow among ancestrally distinct groups of people. We identify three components of ancestry harbored by ancient pastoralists and propose a sequence of admixture events to explain our observations; future archaeological and ancient DNA research in the Turkana Basin, the Horn of Africa, and other parts of northeastern Africa will be necessary to confirm the earliest stages of the spread of herding into the region. At the other end of our timeframe, we document multiple admixture events affecting Iron Age groups associated with heterogeneous economic, cultural, and linguistic patterns. This complexity can be further explored through additional comparisons of genetic and archaeological diversity. Ancient DNA offers a new source of information about eastern African Holocene prehistory, and an important next direction is to integrate this information rigorously with insights provided by the longer-established disciplines of archaeology and linguistics.

Materials and methods summary

Human skeletal remains from eastern African archaeological sites, including the petrous portion of the skull, teeth, and other bones, were sampled from the National Museums of Kenya and Tanzania and the Livingstone Museum in Zambia, following protocols to minimize both destruction and contamination. Bioarchaeological data on the analyzed individuals, along with detailed information about archaeological context, are provided in the full materials and methods (*21*). DNA was extracted from bone powder in dedicated clean rooms at Harvard Medical School using protocols optimized for ancient DNA. Illumina sequencing libraries were prepared with uracil-DNA-glycosylase (UDG) to reduce deamination-induced errors. Before sequencing, libraries were enriched for molecules overlapping ~1.2 million genome-wide SNPs. Of the 77 samples processed for this study, 43 (from 41 distinct individuals) provided genome-wide ancient DNA data. Direct radiocarbon dates were generated at the Pennsylvania State University (PSU) Radiocarbon Laboratory via accelerator mass spectrometry (AMS).

Raw sequencing data were filtered and aligned to the human reference genome. One sequence per individual was chosen randomly from those overlapping each targeted SNP to represent that individual at that position. On the basis of authenticity metrics, two individuals were excluded from genome-wide analyses. The other 39 individuals were analyzed in conjunction with published genetic data from ancient individuals and present-day groups, using a variety of statistical approaches. Multiple population genetics methods were applied to investigate proportions, sources, and dates of admixture, with a particular emphasis on testing of proposed admixture models through the *qpAdm* software.

REFERENCES AND NOTES

1. F. Marshall, E. Hildebrand, Cattle before crops: The beginnings of food production in Africa. *J. World Prehist.* **16**, 99–143 (2002). doi: 10.1023/A:1019954903395
2. P. Lane, in *Pastoralism in Africa: Past, Present and Future*, M. Bollig, M. Schnegg, H.-P. Wotzka, Eds. (Berghahn, 2013), pp. 105–143.
3. J. Lesur, E. A. Hildebrand, G. Abawa, X. Gutherz, The advent of herding in the Horn of Africa: New data from Ethiopia, Djibouti and Somaliland. *Quat. Int.* **343**, 148–158 (2014). doi: 10.1016/j.quaint.2013.11.024
4. J. Barthelme, *Fisher-Hunters and Neolithic Pastoralists in East Turkana, Kenya* (British Archaeological Reports International Series, BAR Publishing, 1985), vol. 254.
5. E. A. Hildebrand *et al*., A monumental cemetery built by eastern Africa's first herders near Lake Turkana, Kenya. *Proc. Natl. Acad. Sci. U.S.A.* **115**, 8942–8947 (2018). doi: 10.1073/pnas.1721975115; pmid: 30127016
6. E. A. Sawchuk, S. T. Goldstein, K. M. Grillo, E. A. Hildebrand, Cemeteries on a moving frontier: Mortuary practices and the spread of pastoralism from the Sahara into eastern Africa. *J. Anthropol. Archaeol.* **51**, 187–205 (2018). doi: 10.1016/j.jaa.2018.08.001
7. S. H. Ambrose, Chronology of the Later Stone Age and Food Production in East Africa. *J. Archaeol. Sci.* **25**, 377–392 (1998). doi: 10.1006/jasc.1997.0277

8. D. Gifford-Gonzalez, Early pastoralists in East Africa: Ecological and social dimensions. *J. Anthropol. Archaeol.* **17**, 166–200 (1998). doi: 10.1006/jaar.1998.0322
9. D. Gifford-Gonzalez, "Animal disease challenges" fifteen years later: The hypothesis in light of new data. *Quat. Int.* **436**, 283–293 (2017). doi: 10.1016/j.quaint.2015.10.054
10. F. Marshall, K. M. Grillo, L. Arco, in *Sustainable Lifeways: Cultural Persistence in an Ever-Changing Environment*, N. Miller, K. Moore, K. Ryan, Eds. (Univ. of Pennsylvania Museum of Archaeology and Anthropology, 2011), pp. 38–73.
11. K. M. Grillo *et al*., Pastoral Neolithic settlement at Luxmanda, Tanzania. *J. Field Archaeol.* **43**, 102–120 (2018). doi: 10.1080/00934690.2018.1431476
12. S. H. Ambrose, in *From Hunters to Farmers: The Causes and Consequences of Food Production in Africa*, J. D. Clark, S. A. Brandt, Eds. (Univ. of California Press, 1984), pp. 212–239.
13. S. H. Ambrose, in *Encyclopedia of Prehistory. Volume 1: Africa*, P. N. Peregrine, M. Ember, Eds. (Kluwer Academic Publishers, 2001), pp. 97–109.
14. A. Crowther, M. E. Prendergast, D. Q. Fuller, N. Boivin, Subsistence mosaics, forager-farmer interactions, and the transition to food production in eastern Africa. *Quat. Int.* **489**, 101–120 (2018). doi: 10.1016/j.quaint.2017.01.014
15. P. Lane, The 'moving frontier' and the transition to food production in Kenya. *Azania* **39**, 243–264 (2004). doi: 10.1080/00672700409480402
16. J. Bower, The Pastoral Neolithic of East Africa. *J. World Prehist.* **5**, 49–82 (1991). doi: 10.1007/BF00974732
17. C. Marean, Hunter to herder: Large mammal remains from the hunter-gatherer occupation at Enkapune ya Muto rockshelter. *Afr. Archaeol. Rev.* **10**, 65–127 (1992). doi: 10.1007/BF01117697
18. C. Ehret, in *From Hunters to Farmers*, J. D. Clark, S. A. Brandt, Eds. (Univ. of California Press, 1984), pp. 26–35.
19. S. H. Ambrose, in *The Archaeological and Linguistic Reconstruction of African History*, C. Ehret, M. Posnansky, Eds. (Univ. of California Press, 1982), pp. 104–157.
20. L. B. Scheinfeldt *et al*., Genomic evidence for shared common ancestry of East African hunting-gathering populations and insights into local adaptation. *Proc. Natl. Acad. Sci. U.S.A.* **116**, 4166–4175 (2019). doi: 10.1073/pnas.1817678116; pmid: 30782801
21. Materials and methods are available as supplementary materials.
22. P. Skoglund *et al*., Reconstructing prehistoric African population structure. *Cell* **171**, 59–71.e21 (2017). doi: 10.1016/j.cell.2017.08.049; pmid: 28938123
23. C. M. Schlebusch *et al*., Southern African ancient genomes estimate modern human divergence to 350,000 to 260,000 years ago. *Science* **358**, 652–655 (2017). doi: 10.1126/science.aao6266; pmid: 28971970
24. M. Gallego Llorente *et al*., Ancient Ethiopian genome reveals extensive Eurasian admixture in Eastern Africa. *Science* **350**, 820–822 (2015). doi: 10.1126/science.aad2879; pmid: 26449472
25. É. Harney *et al*., Ancient DNA from Chalcolithic Israel reveals the role of population mixture in cultural transformation. *Nat. Commun.* **9**, 3336 (2018). doi: 10.1038/s41467-018-05649-9; pmid: 30127404
26. V. J. Schuenemann *et al*., Ancient Egyptian mummy genomes suggest an increase of Sub-Saharan African ancestry in post-Roman periods. *Nat. Commun.* **8**, 15694 (2017). doi: 10.1038/ncomms15694; pmid: 28556824
27. M. van de Loosdrecht *et al*., Pleistocene North African genomes link Near Eastern and sub-Saharan African human populations. *Science* **360**, 548–552 (2018). doi: 10.1126/science.aar8380; pmid: 29545507
28. S. Mallick *et al*., The Simons Genome Diversity Project: 300 genomes from 142 diverse populations. *Nature* **538**, 201–206 (2016). doi: 10.1038/nature18964; pmid: 27654912
29. N. Hollfelder *et al*., Northeast African genomic variation shaped by the continuity of indigenous groups and Eurasian migrations. *PLOS Genet.* **13**, e1006976 (2017). doi: 10.1371/journal.pgen.1006976; pmid: 28837655
30. L. Pagani *et al*., Ethiopian genetic diversity reveals linguistic stratification and complex influences on the Ethiopian gene pool. *Am. J. Hum. Genet.* **91**, 83–96 (2012). doi: 10.1016/j.ajhg.2012.05.015; pmid: 22726845
31. S. Fan *et al*., African evolutionary history inferred from whole genome sequence data of 44 indigenous African populations. *Genome Biol.* **20**, 82 (2019). doi: 10.1186/s13059-019-1679-2; pmid: 31023338
32. S. H. Ambrose, D. Collett, F. Marshall, Excavations at Deloraine, Rongai, 1978. *Azania* **19**, 79–104 (1984). doi: 10.1080/00672708409511329
33. B. Trombetta *et al*., Phylogeographic refinement and large scale genotyping of human Y chromosome haplogroup E provide new insights into the dispersal of early pastoralists in the African continent. *Genome Biol. Evol.* **7**, 1940–1950 (2015). doi: 10.1093/gbe/evv118; pmid: 26108492
34. B. M. Henn *et al*., Y-chromosomal evidence of a pastoralist migration through Tanzania to southern Africa. *Proc. Natl. Acad. Sci. U.S.A.* **105**, 10693–10698 (2008). doi: 10.1073/pnas.0801184105; pmid: 18678889
35. W. Haak *et al*., Massive migration from the steppe was a source for Indo-European languages in Europe. *Nature* **522**, 207–211 (2015). doi: 10.1038/nature14317; pmid: 25731166
36. I. Lazaridis *et al*., Genetic origins of the Minoans and Mycenaeans. *Nature* **548**, 214–218 (2017). doi: 10.1038/nature23310; pmid: 28783727
37. D. Stiles, S. C. Munro-Hay, Stone cairn burials at Kokurmatakore, northern Kenya. *Azania* **16**, 151–166 (1981). doi: 10.1080/00672708109511289
38. P.-R. Loh *et al*., Inferring admixture histories of human populations using linkage disequilibrium. *Genetics* **193**, 1233–1254 (2013). doi: 10.1534/genetics.112.147330; pmid: 23410830
39. J. K. Pickrell *et al*., Ancient west Eurasian ancestry in southern and eastern Africa. *Proc. Natl. Acad. Sci. U.S.A.* **111**, 2632–2637 (2014). doi: 10.1073/pnas.1313787111; pmid: 24550290
40. J. Alexander, in *Early Frontiers in Southern Africa*, M. Hall, G. Avery, D. M. Avery, M. L. Williams, A. J. B. Humphreys, Eds. (British Archaeological Reports International Series, BAR Publishing, 1984), vol. 207, pp. 12–23.
41. R. Haaland, G. Haaland, in *Oxford Handbook of African Archaeology*, P. Mitchell, P. Lane, Eds. (Oxford Univ. Press, 2013), pp. 541–553.
42. F. Hassan, in *The Origins and Development of African Livestock: Archaeology, Genetics, Linguistics, Ethnography*, R. Blench, K. MacDonald, Eds. (UCL Press, 2000), pp. 61–86.
43. L. Cronk, *From Mukogodo to Maasai: Ethnicity and Cultural Change in Kenya* (Westview, 2004).
44. F. Marlowe, *The Hadza: Hunter-Gatherers of Tanzania* (Univ. Of California Press, 2010).
45. A. Ranciaro *et al*., Genetic origins of lactase persistence and the spread of pastoralism in Africa. *Am. J. Hum. Genet.* **94**, 496–510 (2014). doi: 10.1016/j.ajhg.2014.02.009; pmid: 24630847
46. S. A. Tishkoff *et al*., The genetic structure and history of Africans and African Americans. *Science* **324**, 1035–1044 (2009). doi: 10.1126/science.1172257; pmid: 19407144
47. J. E. G. Sutton, Deloraine: Further excavations and the Iron Age sequence of the central Rift. *Azania* **28**, 103–125 (1993). doi: 10.1080/00672709309511650
48. S. B. Kusimba, in *The Oxford Handbook of African Archaeology*, P. Mitchell, P. Lane, Eds. (Oxford Univ. Press, 2013).
49. C. M. Nelson, A standardized site enumeration system for the continent of Africa. *Nyame Akuma* **40**, 62–67 (1993).
50. C. Bronk Ramsey, Bayesian analysis of radiocarbon dates. *Radiocarbon* **51**, 337–360 (2009). doi: 10.1017/S0033822200033865
51. P. J. Reimer *et al*., INTCAL13 and MARINE13 radiocarbon age calibration curves 0–50,000 years cal BP. *Radiocarbon* **55**, 1869–1887 (2013). doi: 10.2458/azu_js_rc.55.16947
52. A. Hogg *et al*., SHCal13 Southern Hemisphere calibration, 0–50,000 years cal BP. *Radiocarbon* **55**, 1889–1903 (2013). doi: 10.2458/azu_js_rc.55.16783

ACKNOWLEDGMENTS

We thank S. Mallick for consultation on data analysis, M. Meyer for sharing optimized oligonucleotide sequences for single-stranded library preparation, and R. Pinhasi for advising on techniques for minimally invasive sample preparation. **Funding:** M.E.P. started this research as a fellow of the Radcliffe Institute for Advanced Study at Harvard University. D.R. was supported by U.S. National Institutes of Health grant GM100233, an Allen Discovery Center grant, and a grant from the John Templeton Foundation and is an investigator of the Howard Hughes Medical Institute. Radiocarbon work was supported by the NSF Archaeometry program (grant BCS-1460369) to D.J.K. and B.J.C. **Author contributions:** M.E.P., E.A.S., and D.R. conceived of the study and designed it with C.A.O., F.K.M., A.Z.P.M., and M.K. M.E.P., E.A.S., C.A.O., S.H.A., G.A., H.L.G., A.O.G., M.K., A.K., A.Z.P.M., G.S.M., E.K.N., and F.K.M. obtained skeletal samples for analysis or facilitated sampling. M.E.P., E.A.S., S.H.A., C.N., and P.R. assembled archaeological and anthropological information. B.J.C., T.K.H., and L.E. performed radiocarbon analysis, and D.J.K. supervised this analysis. N.R., N.A., N.B., K.C., A.M.L., J.O., K.S., and F.Z. performed ancient DNA laboratory and data processing work, and N.R. also supervised this work. M.L., I.O., K.A.S., R.B., and M.M. analyzed genetic data. M.E.P., M.L., E.A.S., and D.R. wrote the manuscript with input from all coauthors. **Competing interests:** The authors declare no competing interests. **Data and materials availability:** The aligned sequences are available via the European Nucleotide Archive under accession number PRJEB31373. The genotype datasets used for analyses are included as supplementary materials (data S1). Skeletal samples were exported and repatriated under materials transfer agreements with the curating institutions; see the supplementary materials and methods for details on research permissions.

SUPPLEMENTARY MATERIALS

10 January 2019; accepted 13 May 2019
Published online 30 May 2019
10.1126/science.aaw6275

RESEARCH ARTICLE SUMMARY

PROTEIN STABILITY

A glycine-specific N-degron pathway mediates the quality control of protein *N*-myristoylation

Richard T. Timms, Zhiqian Zhang, David Y. Rhee, J. Wade Harper, Itay Koren*, Stephen J. Elledge*

INTRODUCTION: The ubiquitin-proteasome system is the major route through which the cell achieves selective protein degradation. The E3 ubiquitin ligases are the major determinants of specificity in this system, which is thought to be achieved through their selective recognition of specific degron motifs in substrate proteins. However, our ability to identify these degrons and match them to their cognate E3 ligase remains a major challenge.

RATIONALE: It has long been known that the stability of proteins is influenced by their N-terminal residue, and a large body of work over the past three decades has characterized a collection of N-end rule pathways that target proteins for degradation through N-terminal degron motifs. Recently, we developed Global Protein Stability (GPS)–peptidome technology and used it to delineate a suite of degrons that lie at the extreme C terminus of proteins. We adapted this approach to examine the stability of the human N terminome, allowing us to reevaluate our understanding of N-degron pathways in an unbiased manner.

RESULTS: Stability profiling of the human N terminome identified two major findings: an expanded repertoire for UBR family E3 ligases to include substrates that begin with arginine and lysine following an intact initiator methionine and, more notably, that glycine positioned at the extreme N terminus can act as a potent degron. We established human embryonic kidney 293T reporter cell lines in which unstable peptides that bear N-terminal glycine degrons were fused to green fluorescent protein, and we performed CRISPR screens to identify the degradative machinery involved. These screens identified two Cul2 Cullin-RING E3 ligase complexes, defined by the related substrate adaptors ZYG11B and ZER1, that act redundantly to target substrates bearing N-terminal glycine degrons for proteasomal degradation. Moreover, through the saturation mutagenesis of example substrates, we defined the composition of preferred N-terminal glycine degrons specifically recognized by ZYG11B and ZER1.

ON OUR WEBSITE

Read the full article at http://dx.doi.org/10.1126/science.aaw4912

We found that preferred glycine degrons are depleted from the native N termini of metazoan proteomes, suggesting that proteins have evolved to avoid degradation through this pathway, but are strongly enriched at annotated caspase cleavage sites. Stability profiling of N-terminal peptides lying downstream of all known caspase cleavages sites confirmed that $Cul2^{ZYG11B}$ and $Cul2^{ZER1}$ could make a substantial contribution to the removal of proteolytic cleavage products during apoptosis. Last, we identified a role for ZYG11B and ZER1 in the quality control of *N*-myristoylated proteins. *N*-myristoylation is an important post-translational modification that occurs exclusively on N-terminal glycine. By profiling the stability of the human N-terminome in the absence of the *N*-myristoyltransferases NMT1 and NMT2, we found that a failure to undergo *N*-myristoylation exposes N-terminal glycine degrons that are otherwise obscured. Thus, conditional exposure of glycine degrons to ZYG11B and ZER1 permits the selective proteasomal degradation of aberrant proteins that have escaped N-terminal myristoylation.

CONCLUSION: These data demonstrate that an additional N-degron pathway centered on N-terminal glycine regulates the stability of metazoan proteomes. $Cul2^{ZYG11B}$- and $Cul2^{ZER1}$-mediated protein degradation through N-terminal glycine degrons may be particularly important in the clearance of proteolytic fragments generated by caspase cleavage during apoptosis and in the quality control of protein *N*-myristoylation. ■

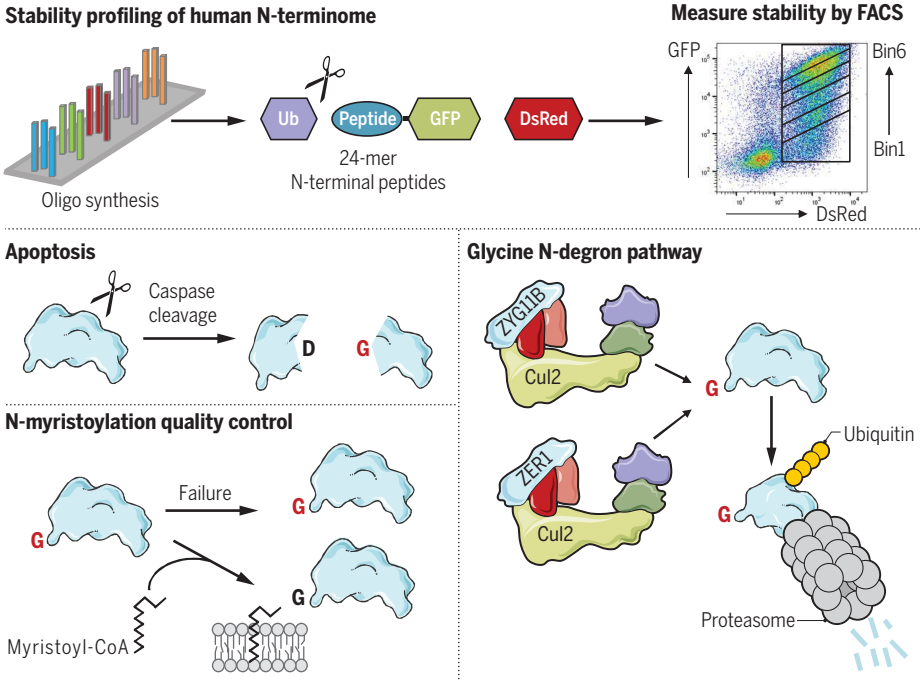

The glycine N-degron pathway. Stability profiling of the human N-terminome revealed that N-terminal glycine acts as a potent degron. CRISPR screening revealed two Cul2 complexes, defined by the related substrate adaptors ZYG11B and ZER1, that recognize N-terminal glycine degrons. This pathway may be particularly important for the degradation of caspase cleavage products during apoptosis and the removal of proteins that fail to undergo *N*-myristoylation.

The list of author affiliations is available in the full article online.
*Corresponding author. Email: itay.koren@biu.ac.il (I.K.); selledge@genetics.med.harvard.edu (S.J.E.)
Cite this article as R. T. Timms *et al.*, *Science* **365**, eaaw4912 (2019). DOI: 10.1126/science.aaw4912

RESEARCH ARTICLE

PROTEIN STABILITY

A glycine-specific N-degron pathway mediates the quality control of protein *N*-myristoylation

Richard T. Timms[1,2], Zhiqian Zhang[1,2], David Y. Rhee[3], J. Wade Harper[3], Itay Koren[1,2]*†, Stephen J. Elledge[1,2]*

The N-terminal residue influences protein stability through N-degron pathways. We used stability profiling of the human N-terminome to uncover multiple additional features of N-degron pathways. In addition to uncovering extended specificities of UBR E3 ligases, we characterized two related Cullin-RING E3 ligase complexes, $Cul2^{ZYG11B}$ and $Cul2^{ZER1}$, that act redundantly to target N-terminal glycine. N-terminal glycine degrons are depleted at native N-termini but strongly enriched at caspase cleavage sites, suggesting roles for the substrate adaptors ZYG11B and ZER1 in protein degradation during apoptosis. Furthermore, ZYG11B and ZER1 were found to participate in the quality control of *N*-myristoylated proteins, in which N-terminal glycine degrons are conditionally exposed after a failure of *N*-myristoylation. Thus, an additional N-degron pathway specific for glycine regulates the stability of metazoan proteomes.

The ubiquitin-proteasome system (UPS) is the major route through which eukaryotic cells achieve selective protein degradation (*1*). The specificity of this system is provided by E3 ubiquitin ligases, of which more than 600 are encoded in the human genome. E3 ligases recognize specific sequence elements, known as degrons, that are present in substrate proteins (*2*). However, although a detailed knowledge of the specificity of E3 ligases for degrons will be essential for achieving a systems-level understanding of the UPS, our current knowledge of degron motifs remains remarkably sparse (*3*).

The first degrons to be discovered were located at the N terminus of proteins (*4*). N-terminal degrons are targeted by N-degron pathways [formerly known as N-end rule pathways (*5*)], of which there are two main branches: the Arg/N-degron pathway, through which UBR-family E3 ligases target N-termini typically generated through endoproteolytic cleavage (*6*, *7*), and the Ac/N-degron pathway, through which proteins bearing acetylated N-termini are targeted for degradation by the E3 ligase MARCH6 (also known as TEB4) (*8*, *9*). In addition, a Pro/N-degron pathway was recently described, through which proteins harboring an N-terminal proline residue are degraded by the GID E3 ligase complex (fig. S1) (*10*). Theoretically, these pathways have the capacity to target the majority of cellular proteins, but the extent to which they affect protein stability in a physiological context remains unclear. For example, loss of N-terminal acetyltransferase (NAT) enzymes has minimal effect on protein stability in yeast (*11*), which is inconsistent with a widespread role for the Ac/N-degron pathway.

Previously, we modified the Global Protein Stability (GPS) system (*12*) to develop a high-throughput method to characterize degron motifs in human proteins (*13*). This approach is based on a lentiviral expression vector that encodes two fluorescent proteins: DsRed, which serves as an internal reference, and green fluorescent protein (GFP) fused to a short peptide of interest, which is translated from an internal ribosome entry site (IRES). Because both DsRed and the GFP-peptide fusion protein are expressed from the same transcript, the GFP/DsRed ratio can be used to quantify the effect of the peptide sequence on the stability of GFP (*13*). We exploited the ubiquitin-fusion technique (*4*) to adapt this "GPS-peptidome" approach to search for N-terminal degron motifs. We thereby directly examined the contribution of N-terminal sequences to protein stability in human cells.

Stability profiling of the human N-terminome using GPS-peptidome technology

We synthesized an oligonucleotide library encoding the first 24 amino acids of the primary isoform(s) of all human proteins, both with and without an initiator methionine (~50,000 sequences). These were cloned into the "Ub-GPS" expression vector between the ubiquitin gene and GFP (Fig. 1A). Upon expression of the constructs in human embryonic kidney (HEK) 293T cells, proteolytic cleavage of the ubiquitin moiety by endogenous deubiquitinating enzymes led to the exposure of the peptides at the N terminus of GFP (Fig. 1A). We used fluorescence-activated cell sorting (FACS) to partition the population into six bins of equal size on the basis of the stability of the peptide-GFP fusion. The stability of each fusion was then quantified with Illumina sequencing, with each peptide assigned a protein stability index (PSI) score ranging between 1 (maximally unstable) and 6 (maximally stable) according to the proportion of sequencing reads in each bin (data file S1).

We began by assessing the effect of the initiator methionine on protein stability. Overall, peptide-GFP fusions that lacked an initiator methionine were much less stable than their counterparts with an initiator methionine (Fig. 1B). However, this effect was only observed for certain N-terminal residues (Fig. 1C). Reporters that begin with amino acids bearing small side chains (C, V, G, P, T, A, and S) were generally relatively stable and exhibited little or no difference in overall stability, whether or not they were preceded by an upstream methionine residue. (Single-letter abbreviations for the amino acid residues are as follows: A, Ala; C, Cys; D, Asp; E, Glu; F, Phe; G, Gly; H, His; I, Ile; K, Lys; L, Leu; M, Met; N, Asn; P, Pro; Q, Gln; R, Arg; S, Ser; T, Thr; V, Val; W, Trp; and Y, Tyr.) This is consistent with efficient cleavage of the initiator methionine by methionine aminopeptidases when the following amino acid has a sufficiently small radius of gyration (*14*). By contrast, peptide-GFP fusions that begin with all other residues (except methionine itself) were generally stable only when preceded by an upstream methionine residue and were greatly destabilized in the absence of an initiator methionine (Fig. 1, C to F).

Overall, these data provide strong support for a central role of the Arg/N-degron pathway in protein quality control. Whereas proteins bearing native N-termini [methionine itself, or C/V/G/P/T/A/S, from which methionine is normally removed (*14*)] are broadly stable, proteins bearing aberrant N-termini (R/K/H/W/Y/F/L/I/D/E/N/Q, without a preceding methionine) are all highly unstable. The latter residues correspond perfectly to the primary type I (R/K/H), primary type II (W/Y/F/L/I), secondary (D/E), and tertiary (N/Q) N-terminal degrons of the Arg/N-degron pathway (fig. S1A). Crucially, however, when these residues were preceded by methionine—as they would be in the context of normal protein synthesis—broad stabilization was observed (Fig. 1F).

Computational identification of destabilizing N-terminal motifs

Subsequently, we focused on understanding the factors that determined the stability of peptide-GFP fusions synthesized with an initiator methionine. Stability scores for these fusions were distributed bimodally, with approximately one-third

[1]Division of Genetics, Department of Medicine, Howard Hughes Medical Institute, Brigham and Women's Hospital, Boston, MA 02115, USA. [2]Department of Genetics, Harvard Medical School, Boston, MA 02115, USA. [3]Department of Cell Biology, Harvard Medical School, Boston, MA 02115, USA. ***Corresponding author. Email: itay.koren@biu.ac.il (I.K.); selledge@genetics.med.harvard.edu (S.J.E.)** †Present address: The Mina and Everard Goodman Faculty of Life Sciences, Bar-Ilan University, Ramat-Gan, 5290002, Israel.

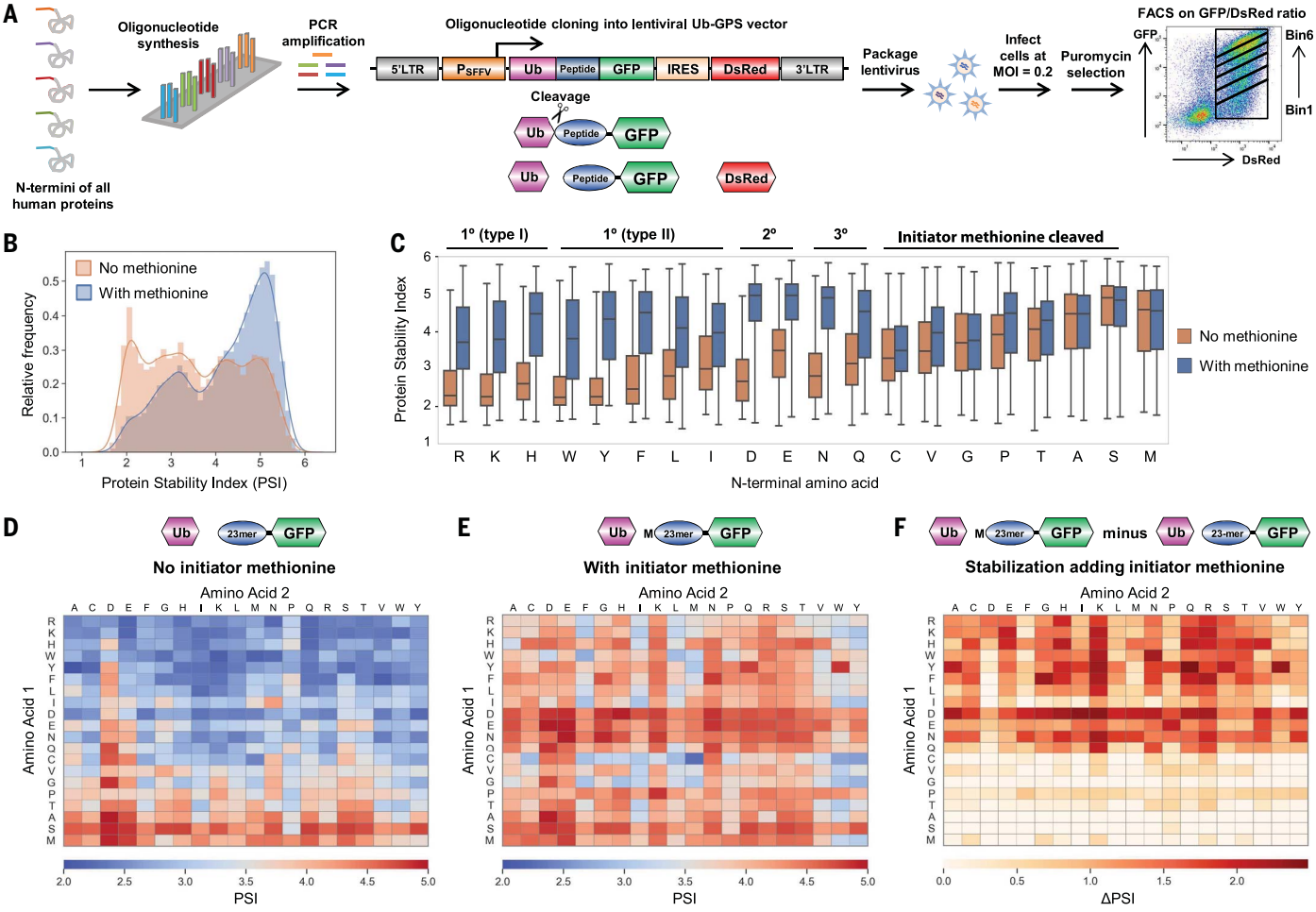

Fig. 1. GPS profiling of the human N-terminome. (**A**) Schematic representation of the N-terminome GPS screen, in which the first 24 residues of all human proteins were expressed in the Ub-GPS vector as N-terminal fusions to GFP. (**B**) Distribution of protein stability scores observed from the screen depicted in (A). (**C**) Boxplots showing the distribution of stability scores for all peptides that begin with the indicated amino acid, when encoded either with (blue boxes) or without (orange boxes) an upstream methionine residue. (**D** to **F**) Heatmaps depicting the mean stability score for all peptides that begin with the indicated two amino acids, when encoded either with (E) or without (D) an upstream methionine residue; (F) illustrates the difference between the two.

of the library exhibiting significant instability (Fig. 1B, blue histogram). One key factor that strongly influenced stability was amino acid composition (Fig. 2, A and B). For example, aspartic acid and glutamic acid were depleted from unstable peptides and enriched among the stable peptides, whereas hydrophobic residues such as tryptophan, phenylalanine, isoleucine, and leucine showed the opposite pattern. This effect is not specific to the N terminus, however, because similar rules govern the stability of reporter constructs in which peptides are fused at the C terminus of GFP (*13*).

Most amino acids exerted a similar effect on stability regardless of their position across the 24-amino acid peptide, but we noticed that certain residues exerted differing effects specifically when encoded at the second position (Fig. 2, A and B). We therefore performed a computational analysis to identify motifs that might promote instability specifically when located at or near the N terminus of the peptide. For all possible combinations of dipeptide motifs, we compared the mean stability of all peptide-GFP fusions harboring the motif within the first seven N-terminal amino acids with those harboring the motif at an internal position in the 24-amino acid peptide (Fig. 2C and data file S2). Over 80% of the top 100 candidate destabilizing N-terminal motifs could be grouped into one of four categories solely based on the identity of the second residue: Lysine was present downstream of the initiator methionine in 26 motifs, arginine in 24 motifs, glycine in 22 motifs, and cysteine in nine motifs (Fig. 2D). Reporters that encode these residues at the second position were significantly less stable than reporters that contain these residues at any internal position (Fig. 2E), and globally, peptide-GFP fusions that begin MC-, MR-, MG-, and MK- exhibited the lowest mean stability (Fig. 2F). Thus, considering initiator methionine removal, this analysis identified N-terminal glycine and cysteine in addition to MR- and MK- as candidate destabilizing N-terminal motifs.

Exploring the substrate repertoire of UBR family E3 ligases

Next, we sought to identify the cellular machinery targeting each class of putative N-terminal degron. We began by investigating a role for UBR family E3 ligases. UBR1, UBR2, and UBR4 have been shown functionally to participate in the recognition of N-degrons (*15*), and so, through sequential rounds of CRISPR/Cas9–mediated gene disruption, we attempted to create a single-cell clone that lacks all three of these UBR proteins. Despite screening ~40 clones, we were unable to identify a clone in which simultaneous ablation of UBR1, UBR2, and UBR4 proteins was observed with immunoblot, suggesting that such a triple-mutant cell may not be viable. However, we were able to generate clones that express substantially reduced levels of two or more of the proteins (Fig. 3A). Ub-GPS reporters in which the initiator methionine of GFP was replaced with either arginine (R), lysine (K), or tyrosine (Y) were strongly destabilized in wild-type cells, but

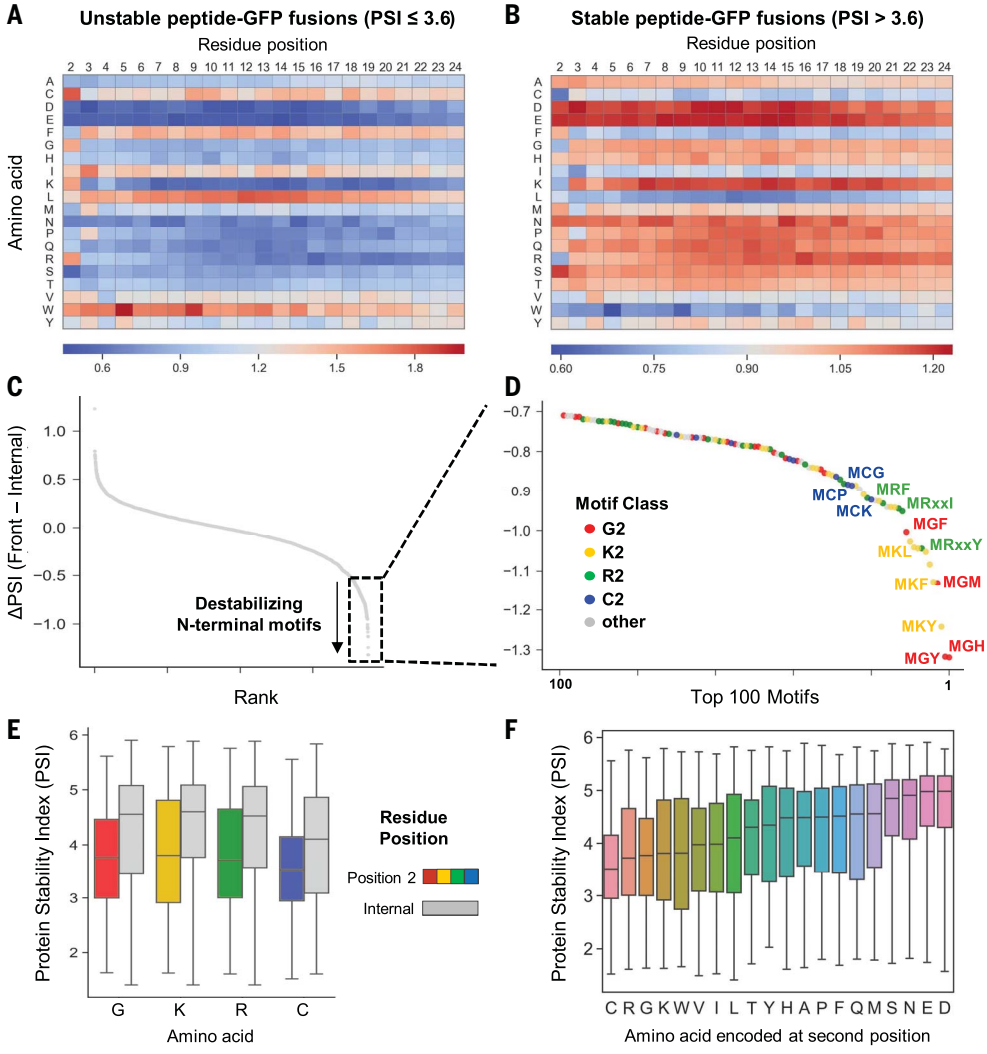

Fig. 2. Identification of degron motifs located at protein N-termini. (**A** and **B**) The effect of peptide composition on protein stability. Shown are heatmaps depicting the relative depletion (blue) or enrichment (red) of each amino acid across all positions of the 24-amino acid peptide among (A) unstable peptides versus (B) stable peptides. (**C** to **F**) Computational prediction of N-terminal degrons. (C) For all possible combinations of dipeptide motifs, the mean difference in stability between peptides that contain the motif at the extreme N terminus (that is, immediately following the initiator methionine) was compared with all peptides that contain the motif at any other internal position in the peptide. (D) Classes of N-terminal degrons. The majority of the top 100 predicted destabilizing N-terminal motifs encoded either glycine (G2), lysine (K2), arginine (R2), or cysteine (C2) at the second position; some example motifs are annotated. (E) Boxplots showing the distribution of stability scores for all peptides in which the indicated residues were encoded at the second position (colored boxes) versus any other internal position within the peptide (gray boxes). (F) Boxplots showing the distribution of stability scores for all peptides with the indicated residues encoded at the second position.

this effect was abrogated in UBR knockout (KO) clone 1 and clone 3 (fig. S2A) and completely abolished in clone 2 (Fig. 3B).

We created a panel of Ub-GPS constructs in which either 23-amino acid peptides (Fig. 2C) or 3-amino acid peptides (fig. S2B) that harbor example degron motifs downstream of an initiator methionine were fused to the N terminus of GFP. In both cases, loss of UBR proteins resulted in the stabilization of reporters bearing three of the classes of degrons motifs: MK-, MR-, and N-terminal cysteine. However, loss of UBR proteins had little or no effect on the stability of the GFP-fusion proteins bearing N-terminal glycine, suggesting a role for additional E3 ligase(s) in the recognition of this particular N-terminal degron.

It was not surprising that UBR E3 ligases targeted N-terminal cysteine, given that nitric oxide–mediated oxidation and subsequent arginylation of N-terminal cysteine renders it a substrate for the Arg/N-degron pathway (*16*). That said, ATE1 disruption only led to modest stabilization of two peptide-GFP substrates that expose N-terminal cysteine (fig. S2, C and D), suggesting that additional routes to UBR-mediated degradation must also exist. UBR-mediated degradation of proteins that begin MK- and MR- was unexpected, however, suggesting that in addition to targeting truncated proteins bearing abnormal N-termini, UBR ligases might also target certain intact proteins that bear their initiator methionine. To confirm that the initiator methionine of these substrates was intact, and thus rule out the possibility that methionine removal was instead exposing canonical Arg/N-degrons, we used mass spectrometry to examine the N terminus of two example peptide-GFP UBR substrates expressed in UBR KO clone 2 (fig. S3A). In both cases, we were readily able to detect the intact N-terminal peptide with the initiator methionine present, whereas we could not detect any peptides corresponding to a putative processed form without an initiator methionine (fig. S3B).

To further examine this property of UBR proteins, we directly compared the stability of the entire Ub-GPS N-terminome library in wild-type cells versus UBR KO clones 1, 2, and 3 (Fig. 3D and data file S3A). Loss of UBR proteins had little effect on the overall stability of reporters synthesized with an N-terminal methionine; only 570 peptide-GFP fusion proteins (<3% of the N-terminome library) exhibited substantial stabilization (>0.8 PSI units) in any of the UBR mutant clones compared with control cells (Fig. 3E). Sequence analysis of the UBR substrates revealed a clear preference for particular N-terminal degron motifs (Fig. 3F and fig. S4, A to H). Consistent with our previous data (Fig. 2C and fig. S2B), peptides starting MC-, MK-, and MR- were all enriched. Peptides starting ML- and MI- were also overrepresented, and for three example peptides in each case, we validated that they were stabilized in UBR KO clone 2 (fig. S4I). In *Saccharomyces cerevisiae*, Ubr1 has been shown to target proteins that start MΦ- (where Φ is a bulky hydrophobic residue, W/F/Y/L/I) for degradation (*17*); however, unlike peptides that start ML- and MI-, we did not observe enrichment for peptides that start MF- or MY- among the UBR substrates, and observed only weak enrichment for peptides that start MW-.

Last, only a small proportion of all peptides in the library that begin MK-, MR-, ML-, or MI- were UBR substrates, suggesting that additional

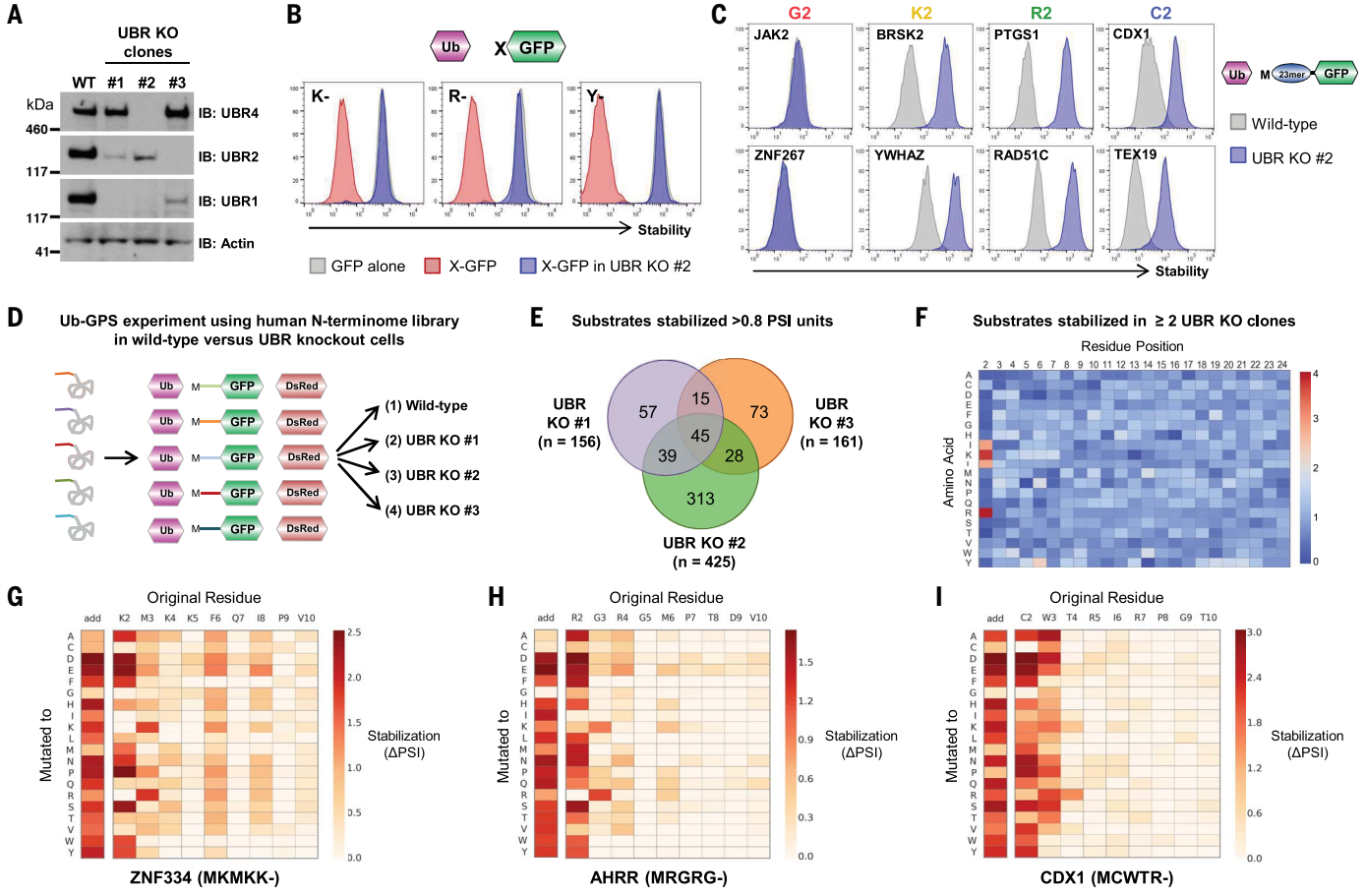

Fig. 3. Assessing the repertoire of UBR substrates among the human N-terminome. (**A** to **C**) Assessing UBR-mediated degradation through N-terminal degron motifs. (A) CRISPR/Cas9–mediated generation of clones expressing reduced levels of UBR1, UBR2, and UBR4. (B) Functional validation of UBR KO clones. Optimal Arg/N-end rule substrates were highly unstable in wild-type cells but not in UBR KO clone 2, as measured with flow cytometry (fig. S2A). (C) UBR proteins target example peptide-GFP reporters in which lysine, arginine, or cysteine, but not glycine, are encoded at the second position. N-terminal peptides derived from the indicated genes were expressed in wild-type or UBR KO clone 2 by using the Ub-GPS system, and their stability was assessed by means of flow cytometry. (**D** to **F**) Global identification of N-terminal UBR substrates. (D) Schematic representation of the GPS screen. (E) Venn diagram summarizing the substrates stabilized >0.8 PSI units across the three UBR KO clones. (F) Heatmap showing the relative enrichment (red) or depletion (blue) of each amino acid across all positions of the 24-amino acid peptide comparing peptides stabilized in two or more of the UBR KO clones relative to the whole N-terminome library (fig. S4). (**G** to **I**) Characterization of N-terminal UBR degrons through saturation mutagenesis. Each of the first 10 residues of the N-terminal peptides derived from (G) ZNF334 (beginning MK-), (H) AHRR (beginning MR-), and (I) CDX1 (beginning MC-) were mutated to all other possible residues, and their stabilities were measured by means of FACS and Illumina sequencing. The darker the color, the greater the degree of stabilization as compared with that of the wild-type sequence (fig. S5).

residues were essential for degron recognition. Analysis of the composition of all the UBR substrates identified in each category highlighted preferred residues enriched at downstream positions (fig. S4, E to H). Furthermore, for some example peptides that start MK-, MR-, and MC-, we defined the N-terminal UBR degron in detail by performing saturation mutagenesis experiments. We created a Ub-GPS library in which each of the residues from position 2 to position 10 of the 24-amino acid peptide were mutated to all other possible amino acids and measured the stability of the resulting peptide-GFP fusions by means of FACS and Illumina sequencing (data file S4A). These experiments confirmed the critical importance of the lysine, arginine, or cysteine residue encoded at the second position but also demonstrated that certain mutations at the third or fourth position could prevent degron recognition (Fig. 3, G to I, and fig. S5). These data also confirmed the requirement for these degron motifs to be positioned at the extreme N terminus because addition of just a single upstream amino acid (that is, immediately after the initiator methionine) resulted in stabilization of the peptide-GFP fusions (Fig. 3, G to I, and fig. S5, column "add").

N-terminal glycine can act as a potent degron

We next focused on the one class of N-terminal degron motif that was not a substrate for UBR-mediated degradation: N-terminal glycine. To validate that N-terminal glycine did indeed constitute a degron motif, we performed a series of mutagenesis experiments on a panel of unstable Ub-GPS reporters in which 24-amino acid peptides starting MG- were fused to the N terminus of GFP (Fig. 4A and fig. S6A). In each case, the glycine residue was indeed critical for instability because a single substitution converting the glycine residue to serine (G2S) was sufficient to inhibit degradation (Fig. 4A and fig. S6A, left). Moreover, the position of the glycine residue at the extreme N terminus was also critical because addition of a single serine residue upstream of the glycine (add S) stabilized the peptide-GFP fusions to a similar extent (Fig. 4A and fig. S6A, center). Last, consistent with the notion that the initiator methionine is constitutively cleaved when followed by a small

residue such as glycine, deletion of the initiator methionine (ΔMet) had no stabilizing effect on any of the peptide-GFP fusions (Fig. 4A and fig. S6A, right).

For some example peptides, we defined the N-terminal glycine degron in detail by performing saturation mutagenesis experiments (data file S4A). This confirmed the absolute requirement for the exposure of glycine at the extreme N terminus because addition of any single amino acid upstream of the glycine resulted in stabilization of the peptide-GFP fusion (Fig. 4B and fig. S6, B to G, column "add"). The size of the degron motif appeared to be relatively small, but some substitutions at the residues immediately downstream of the exposed glycine did exert a stabilizing effect (Fig. 4B and fig. S6, B to G).

Cul2^{ZYG11B} and Cul2^{ZER1} target N-terminal glycine

We began the search for the E3 ligase(s) responsible for targeting N-terminal glycine by using the small molecule MLN4924. MLN4924 acts as a broad inhibitor of Cullin-RING ligases (CRLs) by blocking Cullin neddylation (*18*), thus allowing us to narrow the search to either CRL or non-CRL ligase families. All our example Ub-GPS constructs bearing N-terminal glycine were stabilized upon treatment with MLN4924, implicating CRLs in the recognition of N-terminal glycine (Fig. 4C and fig. S7A).

Next, we sought to identify the specific CRL adaptor(s) responsible for recognition of the N-terminal glycine degron. Using dominant-negative constructs to inhibit each of the major Cullins, we determined that either Cul2 or Cul5 was responsible for the degradation of example Ub-GPS reporters harboring N-terminal glycine degrons (Fig. 4D and fig. S7B). Using these reporter substrates, we performed a series of CRISPR/Cas9–mediated genetic screens using a library of single-guide RNAs (sgRNAs) targeting known CRL2/5 substrate adaptor proteins (fig. S8A). Together, these screens identified ZYG11B as the CRL2 substrate adaptor responsible for recognition of the N-terminal glycine degron motif (Fig. 4E, fig. S8B, and data file S5). Intriguingly, ZER1, which is closely related to ZYG11B (29% amino acid identity) (fig. S8C), was enriched at or approaching the level of statistical significance in several screens, suggesting that these two related adaptors may

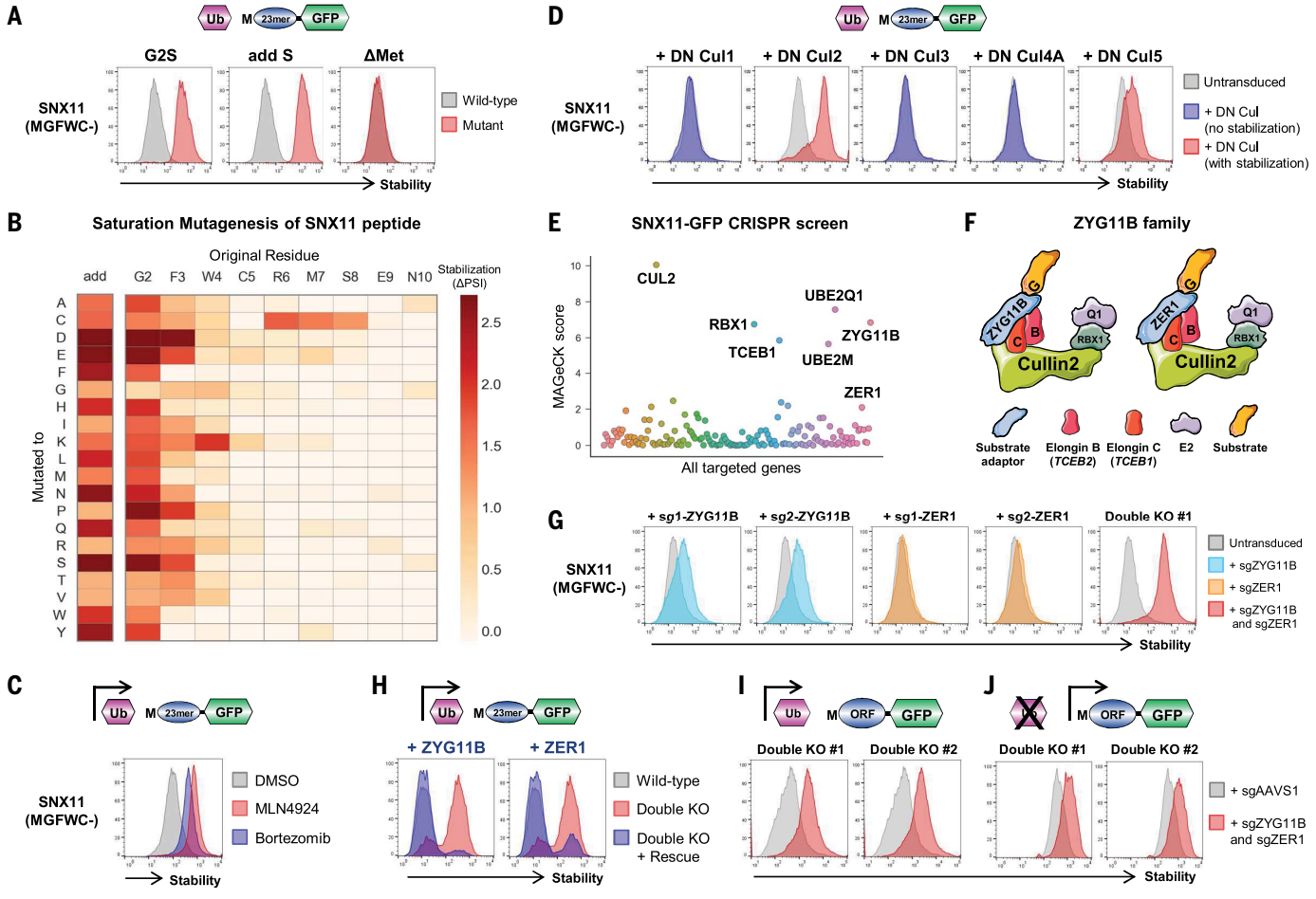

Fig. 4. Cul2^{ZYG11B} and Cul2^{ZER1} target N-terminal glycine. (**A**) Glycine at the N terminus can act as a potent degron. The N-terminal peptide derived from SNX11 and a mutant version that lacked the initiator methionine (ΔMet) were highly unstable, whereas mutant versions in which the terminal glycine was mutated to serine (G2S) or in which a serine residue was added between the initiator methionine and the glycine residue (add S) were not (fig. S6A). (**B**) Defining N-terminal glycine degrons through saturation mutagenesis. Each of the first 10 residues of the SNX11 peptide were mutated to all other possible residues, and their stabilities were measured by means of FACS and Illumina sequencing. The darker the color, the greater the degree of stabilization as compared with that of the wild-type sequence (fig. S6B). (**C** and **D**) Cul2 complexes target N-terminal glycine. Stabilization of the SNX11-GFP reporter (C) upon treatment with the CRL inhibitor MLN4924, and (D) after expression of dominant-negative (DN) versions of Cullins (fig. S7). (**E** and **F**) CRISPR screens identify the Cul2 substrate adaptors responsible for the recognition of N-terminal glycine. (E) Results of the SNX11-GFP reporter screen, which highlighted two CRL2 complexes (F) (fig. S8). (**G** to **J**) Cul2^{ZYG11B} and Cul2^{ZER1} cooperate to target N-terminal glycine. (G) CRISPR-mediated ablation of both ZYG11B and ZER1 was required for full stabilization of the SNX11-GFP reporter. (H) Exogenous expression of either ZYG11B or ZER1 rescued degradation of the SNX11-GFP reporter in cells lacking endogenous ZYG11B and ZER1. Knockout of ZYG11B and ZER1 stabilized full-length SNX11 fused to the N terminus of GFP, both (I) when expressed in the context of the Ub-GPS system or (J) without upstream ubiquitin fusion (fig. S9).

collaborate in the degradation of proteins that expose N-terminal glycine (Fig. 4F). The third member of the ZYG11 family, ZYG11A, did not score in any of the screens, which is consistent with RNA-sequencing data (*19*) showing that it is rarely expressed across human tissues (fig. S8, C and D).

To examine the possibility of cooperation between ZYG11B and ZER1, we performed individual CRISPR/Cas9–mediated gene disruption experiments, ablating the function of ZYG11B or ZER1 either alone or in combination. Loss of ZYG11B alone did indeed stabilize all of the peptide-GFP fusion proteins (Fig. 4G and fig. S9A), but whereas complete stabilization was observed for two of the reporters, only partial stabilization was observed for the others. By contrast, loss of ZER1 alone had little stabilizing effect on any of the reporters; however, simultaneous disruption of both ZER1 and ZYG11B resulted in complete stabilization (Fig. 4G and fig. S9A). Furthermore, ZYG11B and ZER1 both associated with putative substrates that bear N-terminal glycine degrons (fig. S9B), and exogenous expression of either ZYG11B or ZER1 alone in ZYG11B/ZER1 double-mutant cells fully restored the degradation of a peptide-GFP fusion whose stabilization required ablation of both endogenous ZYG11B and ZER1 (Fig. 4H). Last, we validated that $Cul2^{ZYG11B}$ and $Cul2^{ZER1}$ were able to mediate the degradation of full-length proteins that bear exposed glycine residues at their N termini (Fig. 4, I and J, and fig. S9, C to E).

To obtain a global view of the substrates targeted by these Cul2 complexes, we compared the stability of the Ub-GPS N-terminome library in wild-type cells with cells that lack either ZYG11B, ZER1, or both ZYG11B and ZER1 (fig. S10A and data file S3B). First, this revealed that ZYG11B and ZER1 share the majority of their substrates: There were 115 fusions stabilized in ZYG11B mutant cells and 36 stabilized in ZER1 mutant cells, whereas 488 were stabilized in the double-mutant cells. Sequence analysis of these shared substrates confirmed that N-terminal glycine was the most enriched feature while also highlighting preferred (F, G, H, K, and Y) and disfavored (D, E, I, P, S, and T) residues at the following position (fig. S10B). Of the substrates that were targeted solely by ZYG11B, over 90% encoded a glycine residue at the second position (fig. S10C). Intriguingly, there was no enrichment of N-terminal glycine among the substrates exclusively targeted by ZER1 (fig. S10D). This finding suggested that (i) any ZER1 substrates bearing an N-terminal glycine were also substrates for ZYG11B, and hence were still targeted for degradation in ZER1 mutant cells, and (ii) although N-terminal glycine was indispensable for recognition by ZYG11B, in some contexts ZER1 might recognize substrates that begin with residues other than glycine. We characterized one such substrate—the N-terminal peptide derived from KCNT2 (which begins MPYL)—in detail (fig. S11). In particular, saturation mutagenesis revealed that the hydrophobic residues encoded at the third and fourth position formed a critical part of the ZER1 degron,

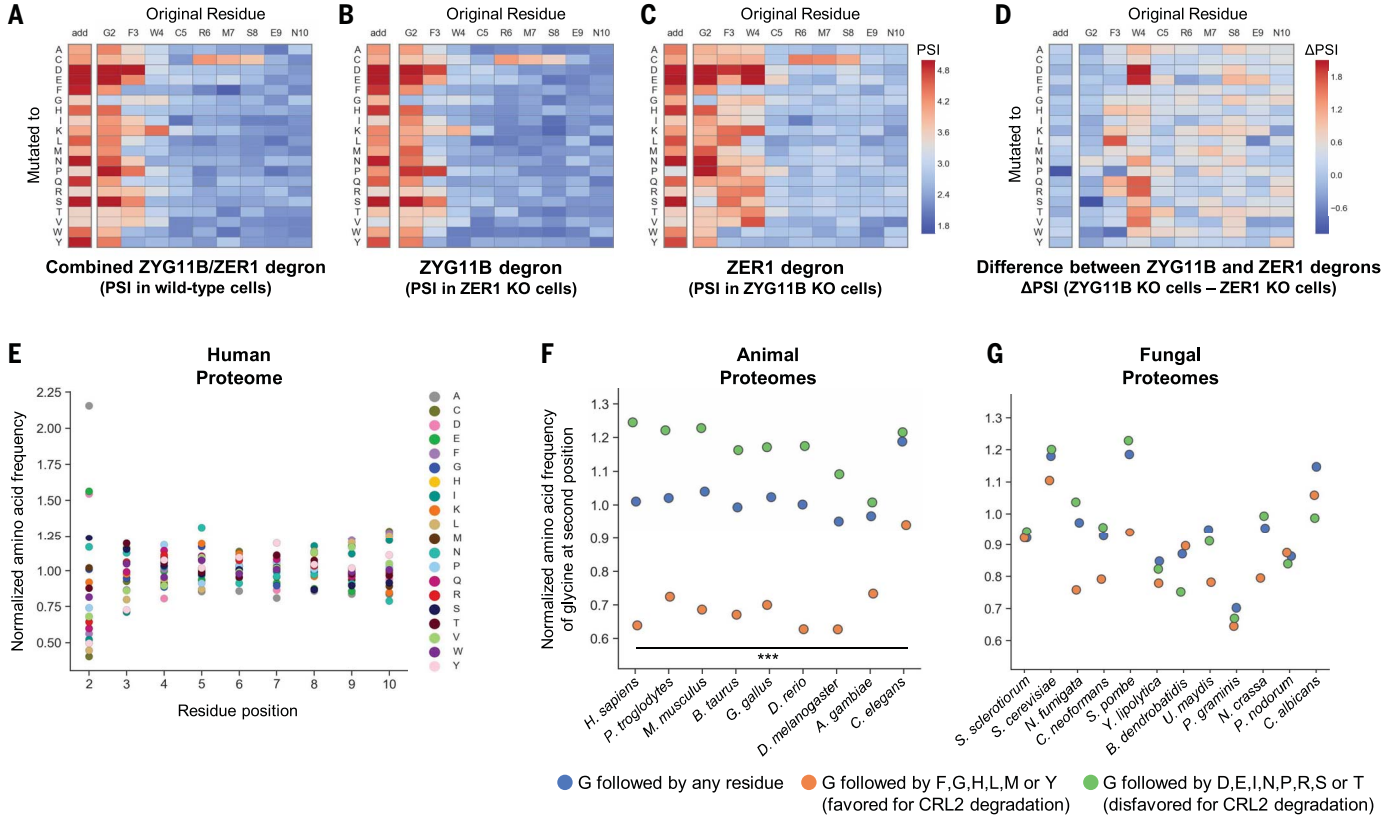

Fig. 5. N-terminal glycine degrons are depleted from metazoan proteomes. (**A** to **D**) Defining the degrons recognized by ZYG11B and ZER1 through saturation mutagenesis. Each of the first 10 residues of the SNX11 N-terminal peptide were mutated to all possible amino acids; the stability of each mutant in the resulting Ub-GPS library was measured in (A) wild-type, (B) ZER1 mutant, or (C) ZYG11B mutant cells. The color scale reflects the raw PSI measurement for each peptide-GFP fusion, so that the greater the intensity of the red color, the greater the stabilizing effect of the mutation. The heatmap in (D) illustrates the difference between the PSI in ZYG11B mutant cells versus ZER1 mutant cells; thus, a dark red color indicates mutations that prevent recognition by ZER1 but not by ZYG11B, whereas a dark blue color indicates mutations that permit recognition by ZER1 but not by ZYG11B (fig. S13). (**E**) Normalized amino acid frequencies across the first 10 residues (following the initiator methionine) of human proteins. (**F** and **G**) Depletion of N-terminal glycine degrons in metazoan proteomes. The normalized amino acid frequency of glycine encoded at the second position in the indicated proteomes is shown by the blue dots, and is further categorized depending on whether the glycine residue is followed by a residue favoring (orange dots) or disfavoring (green dots) CRL2-mediated degradation. The relationship observed across animal proteomes (F) is not apparent across fungal proteomes (G), which do not possess a ZYG11 ortholog. (***$P < 0.001$, Fisher's exact test)

whereas some more flexibility was tolerated at the second position (fig. S11G). However, the location of these residues relative to the front of the peptide remained critical because the addition of a single amino acid upstream of the proline residue prevented degradation (fig. S11G).

Defining the N-terminal glycine degrons recognized by ZYG11B and ZER1

To gain further insight into the specific degron motifs recognized by ZYG11B and ZER1, we examined a larger number of potential peptide-GFP substrates that begin with glycine (fig. S12). These could be divided into three categories: peptides fully stabilized upon mutation of ZYG11B alone (fig. S12A); peptides stabilized partially upon mutation of ZYG11B alone, but which required combined mutation of ZYG11B and ZER1 for complete stabilization (fig. S12B); and peptides for which full redundancy was observed between ZYG11B and ZER1 (fig. S12C). For the vast majority of the peptides in the latter two categories, an aromatic residue (H, F, or Y) was located downstream of the terminal glycine, supporting the idea that ZER1 might preferentially recognize bulky residues located further along the peptide chain (fig. S12D).

We tested this hypothesis more rigorously by repeating the saturation mutagenesis experiments in the genetic background of either ZYG11B ablation or ZER1 ablation (data file S4, B and C). The results for some representative peptides are shown in Fig. 5, A to D, and fig. S13. Mutations promoting stability in wild-type cells were identical to those promoting stability in ZER1 mutant cells (Fig. 5, A and B). Therefore, these residues comprise the minimal N-terminal glycine degron, which is recognized by ZYG11B. Conversely, the ZER1 degron (as revealed in ZYG11B mutant cells) is more extensive because mutations that were two or more residues downstream of the terminal glycine interfered with degradation (Fig. 5, C and D). Overall, these data support a model in which both ZYG11B and ZER1 target substrates with exposed glycine residues at their N-termini; however, the recognition motif for ZYG11B is relatively small, comprising just the terminal glycine and the following residue, whereas the recognition motif for ZER1 may extend three or more residues along the polypeptide chain and preferentially comprises amino acids with bulky aromatic side chains.

N-terminal glycine degrons are depleted from metazoan proteomes

GPS-peptidome technology has already identified a suite of degron motifs lying at the C terminus of human proteins (*13*). All of these degron motifs are depleted from the human proteome (*13*), suggesting evolutionary pressure to avoid degradation by E3 ligases that target terminal degrons. We thus examined the abundance of N-terminal glycine degrons in eukaryotic proteomes. As is the case for the residue at the extreme C terminus of eukaryotic proteins (*13*), the identity of the residue following the initiator methionine at the N terminus was far more variable than at all neighboring positions, suggesting that its properties are particularly important (Fig. 5E). Nonetheless, glycine was encoded at almost exactly the expected frequency at the second position across a range of metazoan model organisms (Fig. 5F, blue dots). However, classifying glycine residues as those favored (G followed by F, G, H, L, M, or Y) or disfavored (G followed by D, E, I, N, P, R, S, or T) for CRL2-mediated degradation revealed that, compared with sequences located internally, N-terminal glycine degron motifs are depleted from animal proteomes (Fig. 5F, orange dots), whereas N-terminal glycine motifs that are not efficiently recognized by ZYG11B and ZER1 are correspondingly enriched (Fig. 5F, green dots). As a control, we performed a similar analysis on a panel of reference fungal proteomes, which possess Cul2 but no ZYG11B-family ortholog (*20*). Consistent with the idea that there should be no selective pressure to avoid N-terminal glycine degrons in the absence of $Cul2^{ZYG11B}$ and $Cul2^{ZER1}$, no such relationship was observed as in animal proteomes (Fig. 5G). Thus, the avoidance of N-terminal glycine motifs appears to have shaped the composition of metazoan proteomes.

ZYG11B and ZER1 target protein fragments bearing N-terminal glycine after proteolytic cleavage

Endoproteolysis generates an additional source of terminal degrons (*21*–*23*). Caspase cleavage preferentially occurs immediately upstream of glycine residues (Fig. 6A). Of the ~1800 known human caspase cleavage sites, approximately one-third result in the exposure of glycine at the N terminus of the downstream fragment (*24*), suggesting a potential role for ZYG11B and ZER1 in the degradation of proteins cleaved during apoptosis. Moreover, in contrast to the situation at the native N-termini of human proteins (Fig. 5F), we found that N-terminal glycine degrons that favor CRL2-mediated degradation were enriched at caspase cleavage sites (Fig. 6B).

We used GPS to assess a potential role for ZYG11B and ZER1 in the removal of proteolytic fragments. We generated a Ub-GPS peptide library in which the 24 residues downstream of all caspase cleavage events annotated in Degrabase (*24*) and PROSPER (*25*) were fused to the N terminus of GFP, and we profiled the stability of these peptide-GFP fusions in wild-type cells versus combined ZYG11B/ZER1 mutant cells (Fig. 6C and data file S6). The results confirmed that $Cul2^{ZYG11B}$ and $Cul2^{ZER1}$ could target many caspase cleavage products: 225 substrates were stabilized >0.5 PSI units in both ZYG11B/ZER1 double-mutant lines, of which 219 (97%) harbored an N-terminal glycine residue (Fig. 6D; the GPS profiles of some example substrates are shown in Fig. 6E and fig. S14A).

We validated these findings in two ways. First, for a panel of example cleavage products exposing N-terminal glycine degrons, we verified that the full-length protein fragments downstream of the cleavage site were stabilized in ZYG11B/ZER1 double-mutant cells (Fig. 6F). Second, we demonstrated that these fragments would also be substrates for ZYG11B and ZER1 after endoproteolytic cleavage. Our initial attempts to perform these experiments by inducing the dimerization of caspase 9 (*26*) resulted in rapid cell death. Therefore, in order to decouple proteolytic cleavage from cell death, we engineered mutant versions of four example substrates in which the caspase cleavage site was replaced with the Tobacco Etch Virus (TEV) protease cleavage site (Fig. 6G). TEV protease recognizes the amino acid sequence ENLYFQ/G (where "/" represents the cleavage position), thus exposing an N-terminal glycine on the downstream fragment, and is active when expressed in mammalian cells (*27*, *28*). Upon expression of TEV protease, we observed destabilization of the downstream cleavage products that bear N-terminal glycine degrons in wild-type cells, but this effect was abrogated in ZYG11B/ZER1 double-mutant cells (Fig. 6G and fig. S14B). Thus, ZYG11B and ZER1 are likely to be involved in the clearance of proteolytic fragments after caspase cleavage during apoptosis.

ZYG11B and ZER1 function in the quality control of *N*-myristoylated proteins

Last, we considered whether the recognition of N-terminal glycine degrons might be conditionally regulated through posttranslational modifications. Intriguingly, *N*-myristoylation, the process through which the 14-carbon fatty acid myristate is attached to the N terminus of a subset of eukaryotic proteins (*29*), occurs exclusively on N-terminal glycine (Fig. 7A). Given that our mutagenesis experiments showed that addition of just a single amino acid to the N terminus prevented ZYG11B- and ZER1-mediated recognition, we reasoned that *N*-myristoylation would prevent CRL2-mediated degradation from N-terminal glycine. Thus, we hypothesized that ZYG11B and ZER1 might play an important role in "myristoylation quality control," degrading proteins that bear N-terminal glycine degrons conditionally exposed after a failure of *N*-myristoylation.

Given that the *N*-myristoyltransferase enzymes (NMT1 and NMT2 in human cells) require less than the first 20 residues for substrate recognition (*29*), we reasoned that the peptide-GFP fusion proteins expressed from our N-terminome Ub-GPS library should undergo native *N*-myristoylation. In order to examine the effect of *N*-myristoylation on protein stability, we profiled the N-terminome Ub-GPS library in the presence or absence of NMT1/2 (Fig. 7B and data file S3C). Although we were not able to generate clones in which both NMT1 and NMT2 were completely ablated after CRISPR/Cas9–mediated gene disruption—a finding consistent with the notion that *N*-myristoylation is an essential process (*30*)—we did isolate three clones that retained only residual levels of one NMT enzyme as assessed by means of immunoblot (Fig. 7C). When we analyzed the composition of all the peptide-GFP fusion proteins whose stability was substantially reduced in all three NMT1/2 mutant clones, N-terminal glycine was the most enriched

feature (Fig. 7D). Thus, a failure to undergo *N*-myristoylation can lead to instability of the unmodified protein.

To investigate a possible role for ZYG11B and ZER1 in this process, we examined the stability of a panel of example substrates (fig. S15A) in which N-terminal peptides derived from proteins known to undergo *N*-myristoylation (*31*) were expressed in the presence and absence of both NMT1/2 and ZYG11B/ZER1. These peptide-GFP fusion proteins were efficiently myristoylated, as evidenced by membrane localization in wild-type cells but not in NMT1/2 mutant cells (fig. S15B). Validating the screen results, in each case we observed destabilization of the peptide-GFP fusion protein upon loss of NMT1/2 (Fig. 7E, yellow histograms); moreover, ZYG11B and ZER1 were primarily responsible for this instability because complete or near-complete restabilization was observed upon ablation of both NMT1/2 and ZYG11B/ZER1 (Fig. 7E, purple histograms). The true magnitude of this effect is likely to be even greater because addition of the small-molecule NMT1/2 inhibitor IMP-1088 (*32*) to the NMT1/2 mutant clones, thus inhibiting the residual *N*-myristoyltransferase activity remaining in the cell, further enhanced the destabilization of the peptide-GFP substrates (fig. S15C). Moreover, the small degree of stabilization observed with some of the fusion proteins upon ablation of ZYG11B and ZER1 in wild-type (that is, NMT1/2-sufficient) cells (Fig. 7E, top row) suggested that some fraction of protein molecules do normally escape *N*-myristoylation, emphasizing the necessity for a degradative mechanism to remove these aberrant species.

Last, we wanted to validate that endogenous *N*-myristoylated proteins behaved in a similar manner. We observed a significant reduction in the steady-state levels of a panel of example substrates in NMT1/2 mutant cells, which was abrogated upon concurrent ablation of ZYG11B and ZER1 (Fig. 7F). However, unlike the complete or near-complete stabilization that we observed using the peptide-GFP fusion constructs

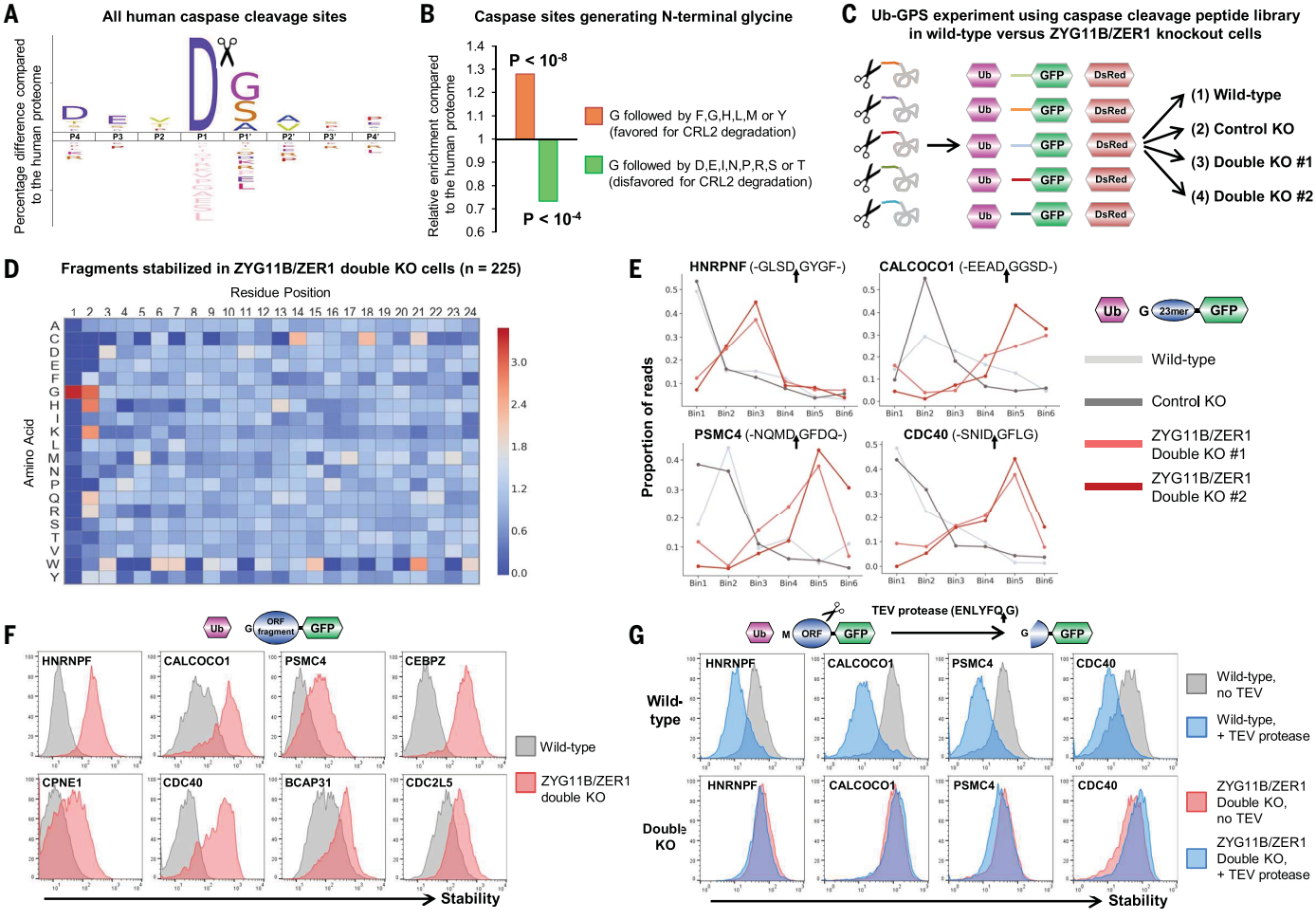

Fig. 6. ZYG11B and ZER1 target N-terminal glycine degrons generated through endoproteolytic cleavage. (**A** and **B**) Caspase cleavage preferentially generates fragments that bear N-terminal glycine. (A) Logoplot depicting the consensus sequence surrounding all caspase cleavage sites annotated in Degrabase (*24*). (B) Compared with their frequency across the human proteome, preferred glycine degrons (orange bar) are enriched at known caspase cleavage sites, whereas disfavored glycine degrons (green bar) are depleted. (**C** to **E**) Caspase cleavage events generate N-terminal glycine degrons targeted by ZYG11B and ZER1. (C) Schematic representation of the caspase cleavage product Ub-GPS screen. (D) Heatmap showing the relative enrichment (red) or depletion (blue) of each amino acid across all positions of the 24-amino acid peptide comparing peptides stabilized in both ZYG11B/ZER1 double mutant cells with the whole caspase cleavage site library. (E) Profiles of example substrates. Residues flanking the caspase cleavage site (indicated by arrows) are shown (fig. S14A). (**F** and **G**) CRL2-mediated degradation of proteolytic cleavage products bearing N-terminal glycine degrons. (F) The full-length downstream caspase cleavage products of the indicated proteins were expressed by using the Ub-GPS system, and their stability was assessed in wild-type (gray) and dual ZYG11B/ZER1 mutant cells (red) by means of flow cytometry. (G) The caspase site in the indicated full-length open reading frames (ORFs) was replaced with a TEV protease cleavage site. Upon TEV expression (blue histograms), destabilization of the downstream cleavage products bearing N-terminal glycine degrons was observed in wild-type cells (top row) but not in dual ZYG11B/ZER1 mutant cells (bottom row) (fig. S14B).

(Fig. 7E), here combined mutation of ZYG11B and ZER1 only resulted in partial restabilization. Thus, in the context of full-length proteins, multiple degrons in addition to N-terminal glycine may be exposed after a failure of *N*-myristoylation, rendering them substrates for additional E3 ligases. Altogether, these data demonstrate a physiological role for ZYG11B and ZER1 in the surveillance of myristoylated proteins: Successful *N*-myristoylation shields proteins from degradation, but a failure to undergo *N*-myristoylation results in the exposure of N-terminal glycine degrons and CRL2-mediated degradation (Fig. 7G).

Discussion

We exploited GPS technology to directly examine the contribution of N-terminal sequences to protein stability across the human proteome. Unexpectedly, in addition to targeting abnormal proteins that lack an initiator methionine, we discovered that UBR-family E3 ligases also targeted proteins with a native N terminus in which an arginine or lysine residue follows an intact initiator methionine. We also found that cysteine exposed at the N terminus of GFP conferred instability in a UBR-dependent manner. Nitric oxide–mediated oxidation of N-terminal cysteine renders it a substrate for arginylation by ATE1 and hence UBR-mediated degradation (*16*). However, here substrates that bear N-terminal cysteine were not stabilized to the same extent in ATE1 mutant cells as in cells that lack UBR proteins; thus, if UBR proteins do not directly bind N-terminal cysteine, an ATE1-independent pathway must exist that permits this class of degrons to be recognized by UBR E3 ligases.

Most notably, we uncovered an additional N-degron pathway centered on N-terminal glycine. There are intriguing mechanistic similarities between the ZYG11B- and ZER1-mediated recognition of N-terminal glycine degrons and the KLHDC2-, KLHDC3-, and KLHDC10-mediated recognition of C-terminal glycine degrons (*13*), with both processes involving multiple related members of CRL2 substrate adaptor families. Like the Kelch repeats found in the KLHDC family proteins, the leucine-rich repeats and the armadillo-like repeats present in the ZYG11 family adaptors also have the propensity to form solenoid structures (*33*), raising the possibility of a common structural mode through which

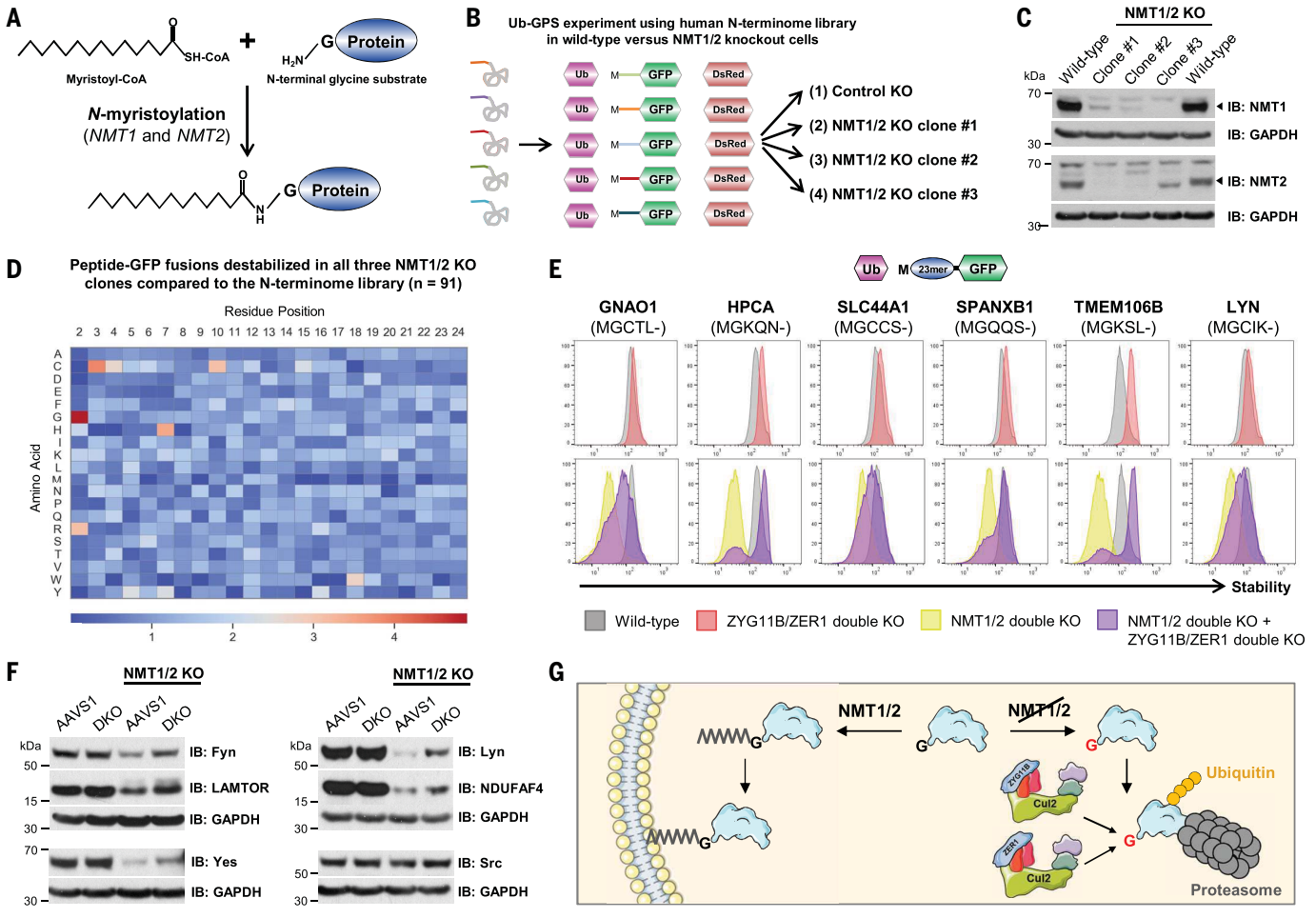

Fig. 7. Cul2^{ZYG11B} and Cul2^{ZER1} target proteins that fail to undergo *N*-myristoylation for proteasomal degradation. (**A**) *N*-myristoylation occurs on N-terminal glycine. (**B**) Schematic representation of the GPS screen designed to assess the effect of loss of *N*-myristoylation on protein stability. (**C**) Immunoblot validation of NMT1/2 knockout clones. Arrowheads indicate bands of the expected molecular weight. (**D**) Loss of *N*-myristoylation destabilizes peptide-GFP fusions that start with glycine. The heatmap shows the relative enrichment (red) or depletion (blue) of each amino acid across all positions of the 24-amino acid peptide, comparing the 91 peptides that exhibit substantial destabilization in all three NMT1/2 mutant clones relative to the whole N-terminome library. (**E** and **F**) ZYG11B and ZER1 target N-terminal glycine degrons exposed after a failure of *N*-myristoylation. (E) The first 24 amino acids from the indicated proteins were expressed as N-terminal fusions to GFP, and their stability in the indicated genetic backgrounds was measured by means of flow cytometry. The destabilization observed upon loss of NMT1/2 (gold histograms) is rescued in the absence of ZYG11B and ZER1 (purple histograms). (F) The abundance of the indicated myristoylated proteins was assessed by means of immunoblot in either control (AAVS1) or ZYG11B/ZER1 double-mutant cells (DKO), either with or without simultaneous ablation of NMT1/2. Src, which did not exhibit significant destabilization in NMT1/2 mutant cells in the GPS screen, is shown as a negative control. (**G**) Model depicting the role of Cul2^{ZYG11B} and Cul2^{ZER} in the quality control of *N*-myristoylated proteins.

terminal glycine residues are engaged (*34*). Furthermore, like their C-terminal counterparts, the ZYG11 family of substrate adaptors have also shaped the proteome, with N-terminal glycine degrons being broadly avoided across metazoa.

Our data suggests two contexts in which the targeting of N-terminal glycine degrons may play an important physiological role. *N*-myristoylation is a posttranslational modification that regulates the membrane localization and other properties of several hundred human proteins (*29*), a group that comprises notable members including Arf family GTPases, G protein α subunits, and Src family tyrosine kinases (*31*). We propose a model in which a failure of *N*-myristoylation conditionally exposes N-terminal glycine degrons to ZYG11B and ZER1, which are normally occluded upon successful modification. Further work will be required to ascertain whether other classes of terminal degrons function in analogous quality control pathways to ensure the efficient deposition of posttranslational modifications.

Furthermore, the strong enrichment for favored ZYG11B/ZER1 glycine degrons at the N-termini of known caspase cleavage products suggested a potential role for these CRL2 complexes during apoptosis, and we confirmed experimentally that many caspase cleavage events would generate substrates efficiently degraded by $Cul2^{ZYG11B}$ and $Cul2^{ZER1}$. Following glycine, the next most commonly generated N-terminal residue after caspase cleavage is serine, accounting for ~28% of annotated caspase sites. Intriguingly, in complete contrast to glycine, serine is the most stabilizing residue when exposed at the N terminus. Our caspase cleavage product GPS screen showed that fragments bearing N-terminal serine were generally extremely stable (fig. S14C). This may be useful where caspases need to activate a target, such as in the case of ataxia-telangiectasia mutated (ATM), whose C-terminal cleavage product acts in a dominant-negative manner to prevent DNA repair during apoptosis (*35*), or RAD21, whose C-terminal cleavage product acts as a pro-apoptotic factor (*36*).

The importance of this glycine-specific N-degron pathway to human biology is underscored by the frequency of heterozygous loss-of-function mutations in humans for both ZYG11B and ZER1 being far lower than would be predicted. ZYG11B and ZER1 both have a pLi value of 1 in the ExAC database (*37*), indicating that loss-of-function variants are strongly selected against in the heterozygous state, demonstrating potent haploinsufficiency and counter selection in humans. Misregulation of Src-family tyrosine kinases could be deleterious to development. In *Caenorhabditis elegans*, the ZYG11 ortholog is required for the metaphase-to-anaphase transition and M phase exit at meiosis II (*20*, *38*, *39*). In humans, ZYG11B and ZER1 are both expressed in the testes and ovaries, and hence a similar role in the regulation of meiosis could also explain the strong selection against loss-of-function mutations. Altogether, the comprehensive analysis of N-terminal degrons presented here has illuminated multiple aspects of N-degron proteolytic pathways and revealed that a family of E3 ligases specific for N-terminal glycine has shaped the human proteome.

Materials and methods

Cell Culture

HEK-293T (ATCC® CRL-3216) cells were grown in Dulbecco's Modified Eagle's Medium (DMEM) (Life Technologies) supplemented with 10% fetal bovine serum (HyClone) and penicillin/streptomycin (Thermo Fisher Scientific).

Transfection and lentivirus production

Lentivirus was generated through the transfection of HEK-293T cells using PolyJet In Vitro DNA Transfection Reagent (SignaGen Laboratories). Cells seeded at approximately 80% confluency were transfected as recommended by the manufacturer with the lentiviral transfer vector plus four plasmids encoding Gag-Pol, Rev, Tat and VSV-G. The media was changed 24 hours post-transfection and lentiviral supernatants collected a further 24 hours later. Cell debris was removed by centrifugation (800x *g*, 5 min) and virus was stored in single-use aliquots at -80°C. Transduction of target cells was achieved by adding the virus in the presence of 8 μg/ml hexadimethrine bromide (Polybrene, Sigma-Aldrich).

Inhibitors

The proteasome inhibitor Bortezomib was obtained from APExBio and the pan-CRL inhibitor MLN4924 was obtained from Active Biochem; both were used at a final concentration of 1 μM. The NMT1/2 inhibitor IMP-1088 was purchased from Cayman Chemical and was used at a final concentration of 1 μM for 24 hours.

Antibodies

Primary antibodies used in this study were: rabbit anti-UBR1 (Bethyl, A302-988A), rabbit anti-UBR2 (Bethyl, A305-416A), rabbit anti-UBR4 (Bethyl, A302-278A), rabbit anti-GFP (Abcam, ab290), rabbit anti-FOXJ3 (Bethyl, A303-107A), rabbit anti-ALKBH1 (Abcam, ab195376), rabbit anti-CHMP3 (Bethyl, A305-397A), mouse anti-vinculin (Sigma, V9131), rabbit anti-Fyn (Cell Signaling, 4023T), rabbit anti-LAMTOR (Cell Signaling, 8975T), rabbit anti-Yes (Cell Signaling, 3201S), rabbit anti-Lyn (Bethyl, A302-683A-T), rabbit anti-NDUFAF4 (ABclonal, A14345), rabbit anti-Src (Cell Signaling, 2123T) and rabbit anti-GAPDH (Cell Signaling, 5174). The HA and FLAG epitope tags were detected using rat anti-HA peroxidase (Sigma-Aldrich, 12013819001) and rabbit anti-FLAG peroxidase (Cell Signaling, #2044S), respectively. HRP-conjugated goat anti-mouse IgG and goat anti-rabbit IgG secondary antibodies were obtained from Jackson ImmunoResearch (#111-035-003).

Plasmids

Lentiviral vectors encoding dominant-negative Cullin constructs were a generous gift from W. Harper. For exogenous expression of CRL2 substrate adaptors, the pHRSIN-P_{SFFV}-GFP-WPRE-P_{PGK}-Hygro vector was used (a gift from P. Lehner), with the constructs cloned in place of GFP using the Gibson assembly method (NEBuilder HiFi Cloning Kit). Plasmids encoding ZYG11A and ZYG11B were obtained from Addgene [plasmids #110550 and #110551, deposited by E. Kipreos (*40*)], while an entry vector encoding ZER1 was obtained from the Ultimate ORF Clone collection (Thermo Fisher Scientific). A plasmid encoding TEV protease was also obtained from Addgene [plasmid #64276, deposited by X. Shu (*27*)].

For individual CRISPR/Cas9-mediated gene disruption experiments, the lentiCRISPR v2 vector was used (Addgene #52961, deposited by Feng Zhang). Oligonucleotides encoding the top and bottom strands of the sgRNAs were synthesized (IDT), annealed and phosphorylated (T4 PNK; NEB) and cloned into the lentiCRISPR v2 vector as described (*41*). Nucleotide sequences of the sgRNAs used were:

sg-AAVS1: GGGGCCACTAGGGACAGGAT
sg1-UBR1: GTGAGAGGATGGAAATCAGCG
sg2-UBR1: GATTCTAACTTGTGGACCGAA
sg1-UBR2: GAGGAGGAGAGAAGATGGCGT
sg2-UBR2: GTACCCAAAATCTACTGCAG
sg1-UBR4: GCCTCTCGAAGATGAACACCG
sg2-UBR4: GCTGACCCCTGGACAGACAG
sg-ATE1: GTATCAGGATCTCATAGACCG
sg1-ZYG11B: GCGCTCGTAAGGATCCTCGA
sg2-ZYG11B: GAAGCTCGAAGGCCAGAAAGC
sg1-ZER1: GTATGAGGAGGAGAACCCAGG
sg2-ZER1: GCCGCAGCAGGGACTCCACA
sg1-NMT1: GCAGGGTGTAGGGCTCCTGG
sg2-NMT1: GAAGCTCTACCGACTGCCAG
sg1-NMT2: GATAGACGGGGACAATGAGG
sg2-NMT2: GGACACGTGCGGGATAGACG

Flow cytometry

Analysis of HEK-293T cells by flow cytometry was performed on a BD LSRII instrument (Becton Dickinson) and the resulting data was analyzed using FlowJo. Cell sorting was performed on a MoFlo Astrios (Beckman Coulter).

Generation of Ub-GPS libraries

Human protein coding sequences were downloaded from the Gencode database (release 27). The first 72 nucleotides of entries that (i) started with a methionine residue, (ii) had a transcript_support_level equal to 1 or 2 and (iii) were common to both the Ensembl and Havana databases were included in the oligonucleotide design. After removal of identical 72-nucleotide sequences, the final N-terminome library consisted of a total of 24,638 sequences. The oligonucleotide pool was synthesized by Agilent Technologies and amplified by PCR (Q5 Hot Start High-Fidelity DNA Polymerase, NEB). The PCR product was then cloned into the Ub-GPS vector between a unique SalI site engineered into the 3′ end of the ubiquitin gene and a unique NdeI site at the 5′end of GFP using the Gibson assembly method (NEBuilder HiFi Cloning Kit), such that the resulting vector encoded the peptides immediately downstream of ubiquitin, followed by a

short linker (ATSALGT) and GFP (commencing SKGEEL-). At least 100-fold representation of the library was maintained at each step.

Ub-GPS libraries for saturation mutagenesis were generated in an identical manner. For each peptide selected for analysis, each amino acid encoded at position 2 through to position 10 was mutated to all other possible 19 amino acids. For each peptide 9 reference sequences were also synthesized, in which the same wild-type amino acid sequence was encoded by different nucleotide sequences.

Two databases were used to collate cleavage products for the caspase cleavage site Ub-GPS library: Degrabase (*24*) and PROSPER (*25*). All annotated cleavage sites in human proteins occurring after aspartic acid in each databases were included for oligonucleotide design, which, after removal of duplicates, resulted in a total of 2,234 sequences. Amino acid sequence were converted into nucleotide sequences using the following codons:

A: GCC, C: TGC, D: GAC, E: GAG, F: TTC, G: GGC, H: CAC, I: ATC, K: AAG, L: CTG, M: ATG, N: AAC, P: CCC, Q: CAG, R: AGA, S: TCC, T: ACC, V: GTG, W: TGG, and Y: TAC. The oligonucleotide pool was synthesized by Agilent Technologies and amplified and cloned into the Ub-GPS vector as above.

Ub-GPS screens

GPS plasmid libraries were packaged into lentiviral particles which were used to transduce HEK-293T cells at a multiplicity of infection of ~0.2 (achieving approximately 20% DsRed$^+$ cells) and at sufficient scale to achieve ~500-fold coverage of the library (a total of ~12 million transduced cells in the case of the human N-terminome library). Puromycin (1.5 μg/ml) was added two days post-transduction to eliminate untransduced cells. Surviving cells were pooled, expanded and then partitioned by FACS into six bins 7 days post-transduction based on the GFP/DsRed ratio. Genomic DNA was extracted from each of the pools separately (Gentra Puregene Cell Kit, Qiagen) and the fusion peptides amplified by PCR (Q5 Hot Start Polymerase, NEB) using a forward primer annealing to the end of the ubiquitin gene and a reverse primer annealing to the front of GFP; sufficient reactions were performed to amplify a total mass of DNA equivalent to the mass of genomic DNA from cells representing 500-fold coverage of the library. All PCR products were pooled, and one-tenth of the mix was purified using a spin column (Qiagen PCR purification kit). Finally, 200 ng of the purified PCR product was used as the template for a second PCR reaction using primers to add the Illumina P5 sequence and a 7 bp 'stagger' region to the 5′ end, and Illumina indexes and P7 sequence at the 3′ end. Samples to be multiplexed were then pooled, purified on an agarose gel (QIAEXII Gel Extraction Kit, Qiagen) and sequenced on an Illumina NextSeq instrument.

CRISPR screens

A custom sgRNA library was designed targeting 43 E2 enzymes, 11 core CRL components, and 109 CRL2/5 adaptors at a depth of 6 sgRNAs per gene. The sgRNA sequences together with flanking BbsI restriction enzyme recognition sites were synthesized by Twist Bioscience. The oligonucleotide pool was amplified by PCR (Q5 Hot Start Polymerase, NEB) and the product purified (Qiagen PCR purification kit) and digested with BbsI (NEB). The digested product was concentrated by ethanol precipitation and then visualized on a 10% TBE PAGE gel (Thermo Fisher Scientific) stained with SYBR Gold (Thermo Fisher Scientific). DNA was isolated from the 28 bp band using the "crush-and-soak" method, concentrated by ethanol precipitation, and then cloned into lentiCRISPR v2 (Addgene #52961) digested with BsmBI (NEB).

The sgRNA library DNA was packaged into lentiviral particles. HEK-293T cells stably expressing unstable peptide-GFP fusion proteins were transduced at a multiplicity of infection of ~0.3 at sufficient scale to maintain at least 1000-fold representation of the library. Untransduced cells were eliminated through puromycin selection commencing two days post-transduction. The top ~5% of the surviving cells based on the GFP/DsRed ratio were isolated by FACS, which was performed 7 days post-transduction. For each screen genomic DNA was extracted from both the sorted cells and the unselected library as a reference. The sgRNAs in both pools were amplified by PCR and sequenced on an Illumina NextSeq instrument.

Immunoprecipitation and immunoblotting

HEK-293T cells stably expressing epitope-tagged CRL2 substrate adaptors and peptide-GFP fusions were grown in 10 cm plates. Following treatment with Bortezomib (1 μM, 5 hours), cells were lysed in ice-cold lysis buffer (50 mM Tris, 100 mM NaCl, 0.5% NP-40, pH 7.5 supplemented with EDTA-free protease inhibitor tablet and Phos-Stop phosphatase inhibitor tablet (Roche)) for 30 min on ice. Nuclei were pelleted by centrifugation (14,000x *g*, 10 min, 4°C). Beads coated with anti-HA (Pierce anti-HA magnetic beads, Thermo Fisher Scientific) or anti-FLAG (anti-FLAG M2 magnetic beads, Sigma-Aldrich) antibodies were added to the supernatants and incubated with rotation overnight at 4°C. The beads were then washed three times with lysis buffer before bound proteins were eluted upon incubation with SDS-PAGE sample buffer (95°C, 10 min). Proteins were subsequently resolved by SDS-PAGE (NuPAGE Bis-Tris gels, Thermo Fisher Scientific) and transferred to a nitrocellulose membrane (Trans-Blot Turbo System, Bio-Rad) which was then blocked in 10% nonfat dry milk in PBS + 0.1% Tween-20 (PBS-T). The membrane was incubated with primary antibody overnight at 4°C, and then, following three washes with PBS-T, HRP-conjugated secondary antibody was added for 1 hour at room temperature. Following a further three washes in PBS-T, reactive bands were visualized using Western Lightning Plus ECL (Perkin Elmer) and HyBlot CL film (Denville Scientific).

Mass spectrometry

UBR KO clone 2 cells stably expressing peptide-GFP fusions growing in 15 cm plates were lysed as described above, and immunoprecipitation performed in a similar way using GFP-Trap_MA magnetic agarose beads (Chromotek). Elution of the peptide- GFP fusion proteins was achieved by treatment with 2 M glycine for 1 min, followed by neutralization with 1 M Tris base, pH 10.4. Eluted proteins were reduced using DTT (Thermo Fisher) and alkylated with iodoacetamide (Sigma). Following TCA precipitation (Sigma), proteins were digested with Glu-C (Thermo Fisher) then cleaned up on C-18 stage tips (3M).

Mass spectrometry data were collected using a Q Exactive mass spectrometer (Thermo Fisher) coupled with a Famos Autosampler (LC Packings) and an Accela600 liquid chromatography pump (Thermo Fisher). Peptides were separated on a 100 μm inner diameter microcapillary column packed with ~25 cm of Accucore C18 resin (2.6 μm, 150 Å, Thermo Fisher). Peptides were separated using a 120 gradient of 5 to 25% acetonitrile in 0.125% formic acid at a flow rate of ~300 nl/min. The scan sequence began with an Orbitrap MS1 spectrum with resolution 70,000, scan range 300–1500 Th, automatic gain control (AGC) target 1×10^5, maximum injection time 250 ms, and centroided data type. The top twenty precursors were selected for MS2 analysis which consisted of HCD (high-energy collision dissociation) with the following parameters: resolution 17,500, AGC 1×10^5, maximum injection time 100 ms, isolation window 1.6 Th, normalized collision energy (NCE) 27, and centroid spectrum data type. Unassigned charge states were excluded from MS^2 analysis, but singly charged species were included. Dynamic exclusion was set to automatic. Mass spectra were processed using a Sequest-based in-house software pipeline.

Bioinformatics

N-terminome Ub-GPS screen

Raw Illumina reads derived from each GPS bin were first trimmed of constant sequences derived from the Ub-GPS vector backbone using Cutadapt (*42*). Resulting 72 nt reads were mapped to the reference input library using Bowtie 2 (*43*), and count tables were generated from reads that aligned perfectly to the reference sequence. Following correction for sequencing depth, the protein stability index (PSI) metric was calculated for each peptide-GFP fusion. The PSI score is given by the sum of multiplying the proportion of reads in each bin by the bin number (1-6 in this case), thus yielding a stability score between 1 (maximally unstable) and 6 (maximally unstable): $\mathrm{PSI} = \sum_{i=1}^{6} R_i * i$ (where i represents the number of the bin and R_i represents the proportion of Illumina reads present for a peptide in that given bin i). Read counts and associated stability score for each peptide-GFP fusion are detailed in data file S1.

Prediction of destabilizing N-terminal motifs

The stability data derived from the Ub-GPS N-terminome screen was used to identify potential

destabilizing N-terminal degron motifs (Fig. 2, C and D). Varying exactly two residues at a time between position 2 and position 7, for all possible combinations of di-peptide motifs (allowing gaps) the mean PSI of all peptides containing that motif at the front of the peptide (that is, immediately following the initiator methionine) was compared to the mean PSI of all peptides containing the same motif at any internal location within the 24-nucleotide oligomer peptide. The full data for all possible N-terminal motifs is tabulated in data file S2.

N-terminome Ub-GPS screen in different genetic backgrounds

The Ub-GPS N-terminome screens with the UBR mutant clones and the ZYG11B and ZER1 mutant cells were performed in a similar manner as above, except that only the half of the N-terminome library comprising peptides bearing an initiator methionine was used. Read counts for all peptide-GFP fusions are detailed in data file S3A. Subsequently, comparisons between wild-type cells and combined ZYG11B/ZER1 mutant cells (data file S3B) and between wild-type, control (AAVS1) mutant and three NMT1/2 mutant clones (data file S3C) were performed in a similar way. In each case, a ΔPSI score was generated for each peptide-GFP fusion reflecting the difference in raw PSI scores between the wild-type or control mutant cells and the experimental mutant cells. For the plots shown in Fig. 3 and fig. S4, peptide-GFP fusions were defined as UBR substrates if they were stabilized >0.8 PSI units (Fig. 3E) or >0.6 PSI units (fig. S4, A to D) in the UBR KO clone compared to control cells, but also not stabilized >0.3 PSI units in either ZYG11B or ZER1 mutant cells. The logoplots shown in fig. S4, E to H were generated with iceLogo (*44*) and rendered using Seq2Logo (*45*): the "experimental set" comprised all peptides starting with the indicated motif that were identified as a UBR substrate in any of the three UBR KO clones, the "reference set" comprised all peptides in the N-terminome library starting with that same motif, and the "percentage difference" scoring system was used. Residues significantly enriched at $P < 0.05$ are displayed. For the heatmap shown in Fig. 7D, peptide-GFP fusions destabilized >0.5 PSI units in all three NMT1/2 mutant clones were included for analysis.

Saturation mutagenesis Ub-GPS screens

The heatmaps displayed in Figs. 3, G to I, and 4B and figs. S5, A to C, and S6 illustrate the difference between the PSI for each individual mutant peptide and the median PSI of all the unmutated peptides; the darker the red color, the greater the stabilizing effect of the mutation. For the heatmaps shown in Fig. 5, A to C, and fig. S13 the color scales indicate the raw PSI stability measurement, which lies between 1 (maximally unstable; dark blue) and 6 (maximally stable; dark red); the exception is the comparison between ZYG11B mutant and ZER1 mutant cells (right columns) where a ΔPSI score reflecting the difference between raw PSI score in ZYG11B mutant cells and ZER1 mutant cells for each peptide is depicted. The full data for all mutant peptides in all genetic backgrounds is detailed in data file S4, A to C.

CRISPR screens

Constant regions derived from the backbone of the lentiCRISPR v2 expression vector were removed from Illumina reads using Cutadapt, and count tables were generated from the remaining variable portion of the sgRNA sequences using Bowtie 2. The Model-based Analysis of Genome-wide CRISPR/Cas9 Knockout (MAGeCK) algorithm (*46*) was used to rank the performance of individual genes targeted by multiple sgRNAs enriched in the selected cells versus the unsorted populations. The full MAGeCK output for each screen is detailed in data file S5. For the scatterplots shown in Fig. 4E and fig. S8B, the MAGeCK score plotted on the y axis is calculated as the negative log10 of the "pos|score" value generated by MAGeCK.

Proteome composition analysis

Canonical protein sequences were downloaded from the Swiss-Prot database. For each position between position 2 and position 10 at the N terminus of the proteins the total abundance of each amino acid was quantified, expressed as a proportion of the total number of protein sequences, and then normalized to the mean proportion observed across the 9 N-terminal residues between position 2 and position 10. For the analysis of N-terminal glycine degrons shown in Fig. 5, F and G, we further categorized glycine residues as either "favored" for CRL2-mediated degradation through ZYG11B and ZER1 if they were followed by F, G, H, L, M or Y, or "disfavored" if followed by D, E, I, N, P, R, S or T. The mean abundance of $G_{favored}$ and $G_{disfavored}$ across the 8 N-terminal residues between position 3 and position 10 was then compared to their abundance at position 2. For the analysis of human caspase cleavage sites presented in Fig. 6A, all unique cleavage sites occurring downstream of aspartic acid (D) annotated in Degrabase 1.0 (*24*) were analyzed using iceLogo. In Fig. 6B, all unique cleavage sites occurring downstream of aspartic acid (D) and upstream of glycine (G) were analyzed; the frequency of $G_{favored}$ and $G_{disfavored}$ at the N terminus of these caspase cleavage products was compared to the frequency of $G_{favored}$ and $G_{disfavored}$ at all glycine residues in the human proteome.

Caspase cleavage site Ub-GPS screen

The Ub-GPS screen with peptides derived from human caspase cleavage sites was analyzed in the same way as above, generating a ΔPSI score for each peptide reflecting the difference in raw PSI scores between either control (AAVS1) mutant cells or combined ZYG11B/ZER1 double mutant cells versus wild-type cells (data file S6). For the heatmap shown in Fig. 6D, peptide-GFP fusions stabilized >0.5 PSI units in both ZYG11B/ZER1 double mutant cell lines but <0.25 PSI units in control knockout cells were included; the intensity of the colors represent the depletion (blue) or enrichment (red) of each amino acid comparing this pool of ZYG11B/ZER1 substrates to all peptides detected in the caspase cleavage site library.

REFERENCES AND NOTES

1. G. Kleiger, T. Mayor, Perilous journey: A tour of the ubiquitin-proteasome system. *Trends Cell Biol.* **24**, 352–359 (2014). doi: 10.1016/j.tcb.2013.12.003; pmid: 24457024
2. T. Ravid, M. Hochstrasser, Diversity of degradation signals in the ubiquitin-proteasome system. *Nat. Rev. Mol. Cell Biol.* **9**, 679–690 (2008). doi: 10.1038/nrm2468; pmid: 18698327
3. B. Mészáros, M. Kumar, T. J. Gibson, B. Uyar, Z. Dosztányi, Degrons in cancer. *Sci. Signal.* **10**, eaak9982 (2017). doi: 10.1126/scisignal.aak9982; pmid: 28292960
4. A. Bachmair, D. Finley, A. Varshavsky, In vivo half-life of a protein is a function of its amino-terminal residue. *Science* **234**, 179–186 (1986). doi: 10.1126/science.3018930; pmid: 3018930
5. A. Varshavsky, N-degron and C-degron pathways of protein degradation. *Proc. Natl. Acad. Sci. U.S.A.* **116**, 358–366 (2019). doi: 10.1073/pnas.1816596116; pmid: 30622213
6. B. Bartel, I. Wünning, A. Varshavsky, The recognition component of the N-end rule pathway. *EMBO J.* **9**, 3179–3189 (1990). doi: 10.1002/j.1460-2075.1990.tb07516.x; pmid: 2209542
7. A. Varshavsky, The N-end rule pathway and regulation by proteolysis. *Protein Sci.* **20**, 1298–1345 (2011). doi: 10.1002/pro.666; pmid: 21633985
8. C.-S. Hwang, A. Shemorry, A. Varshavsky, N-terminal acetylation of cellular proteins creates specific degradation signals. *Science* **327**, 973–977 (2010). doi: 10.1126/science.1183147; pmid: 20110468
9. A. Shemorry, C.-S. Hwang, A. Varshavsky, Control of protein quality and stoichiometries by N-terminal acetylation and the N-end rule pathway. *Mol. Cell* **50**, 540–551 (2013). doi: 10.1016/j.molcel.2013.03.018; pmid: 23603116
10. S.-J. Chen, X. Wu, B. Wadas, J.-H. Oh, A. Varshavsky, An N-end rule pathway that recognizes proline and destroys gluconeogenic enzymes. *Science* **355**, eaal3655 (2017). doi: 10.1126/science.aal3655; pmid: 28126757
11. I. Kats *et al*., Mapping degradation signals and pathways in a eukaryotic N-terminome. *Mol. Cell* **70**, 488–501.e5 (2018). doi: 10.1016/j.molcel.2018.03.033; pmid: 29727619
12. H.-C. S. Yen, Q. Xu, D. M. Chou, Z. Zhao, S. J. Elledge, Global protein stability profiling in mammalian cells. *Science* **322**, 918–923 (2008). doi: 10.1126/science.1160489; pmid: 18988847
13. I. Koren *et al*., The eukaryotic proteome is shaped by E3 ubiquitin ligases targeting C-terminal degrons. *Cell* **173**, 1622–1635.e14 (2018). doi: 10.1016/j.cell.2018.04.028; pmid: 29779948
14. F. Sherman, J. W. Stewart, S. Tsunasawa, Methionine or not methionine at the beginning of a protein. *BioEssays* **3**, 27–31 (1985). doi: 10.1002/bies.950030108; pmid: 3024631
15. T. Tasaki *et al*., A family of mammalian E3 ubiquitin ligases that contain the UBR box motif and recognize N-degrons. *Mol. Cell. Biol.* **25**, 7120–7136 (2005). doi: 10.1128/MCB.25.16.7120-7136.2005; pmid: 16055722
16. R.-G. Hu *et al*., The N-end rule pathway as a nitric oxide sensor controlling the levels of multiple regulators. *Nature* **437**, 981–986 (2005). doi: 10.1038/nature04027; pmid: 16222293
17. H.-K. Kim *et al*., The N-terminal methionine of cellular proteins as a degradation signal. *Cell* **156**, 158–169 (2014). doi: 10.1016/j.cell.2013.11.031; pmid: 24361105
18. T. A. Soucy *et al*., An inhibitor of NEDD8-activating enzyme as a new approach to treat cancer. *Nature* **458**, 732–736 (2009). doi: 10.1038/nature07884; pmid: 19360080
19. K. G. Ardlie *et al*., The Genotype-Tissue Expression (GTEx) pilot analysis: Multitissue gene regulation in humans. *Science* **348**, 648–660 (2015). doi: 10.1126/science.1262110; pmid: 25954001
20. S. Vasudevan, N. G. Starostina, E. T. Kipreos, The *Caenorhabditis elegans* cell-cycle regulator ZYG-11 defines a conserved family of CUL-2 complex components. *EMBO Rep.* **8**, 279–286 (2007). doi: 10.1038/sj.embor.7400895; pmid: 17304241
21. K. I. Piatkov, C. S. Brower, A. Varshavsky, The N-end rule pathway counteracts cell death by destroying proapoptotic protein fragments. *Proc. Natl. Acad. Sci. U.S.A.* **109**, E1839–E1847 (2012). doi: 10.1073/pnas.1207786109; pmid: 22670058

22. K. I. Piatkov, L. Colnaghi, M. Békés, A. Varshavsky, T. T. Huang, The auto-generated fragment of the Usp1 deubiquitylase is a physiological substrate of the N-end rule pathway. *Mol. Cell* **48**, 926–933 (2012). doi: 10.1016/j.molcel.2012.10.012; pmid: 23159736
23. K. I. Piatkov, J.-H. Oh, Y. Liu, A. Varshavsky, Calpain-generated natural protein fragments as short-lived substrates of the N-end rule pathway. *Proc. Natl. Acad. Sci. U.S.A.* **111**, E817–E826 (2014). doi: 10.1073/pnas.1401639111; pmid: 24550490
24. E. D. Crawford *et al*., The DegraBase: A database of proteolysis in healthy and apoptotic human cells. *Mol. Cell. Proteomics* **12**, 813–824 (2013). doi: 10.1074/mcp.O112.024372; pmid: 23264352
25. J. Song *et al*., PROSPER: An integrated feature-based tool for predicting protease substrate cleavage sites. *PLOS ONE* **7**, e50300 (2012). doi: 10.1371/journal.pone.0050300; pmid: 23209700
26. K. C. Straathof *et al*., An inducible caspase 9 safety switch for T-cell therapy. *Blood* **105**, 4247–4254 (2005). doi: 10.1182/blood-2004-11-4564; pmid: 15728125
27. T.-L. To *et al*., Rationally designed fluorogenic protease reporter visualizes spatiotemporal dynamics of apoptosis in vivo. *Proc. Natl. Acad. Sci. U.S.A.* **112**, 3338–3343 (2015). doi: 10.1073/pnas.1502857112; pmid: 25733847
28. T.-L. To *et al*., Rational design of a GFP-based fluorogenic caspase reporter for imaging apoptosis in vivo. *Cell Chem. Biol.* **23**, 875–882 (2016). doi: 10.1016/j.chembiol.2016.06.007; pmid: 27447051
29. M. H. Wright, W. P. Heal, D. J. Mann, E. W. Tate, Protein myristoylation in health and disease. *J. Chem. Biol.* **3**, 19–35 (2010). doi: 10.1007/s12154-009-0032-8; pmid: 19898886
30. S. H. Yang *et al*., *N*-myristoyltransferase 1 is essential in early mouse development. *J. Biol. Chem.* **280**, 18990–18995 (2005). doi: 10.1074/jbc.M412917200; pmid: 15753093
31. E. Thinon *et al*., Global profiling of co- and post-translationally N-myristoylated proteomes in human cells. *Nat. Commun.* **5**, 4919 (2014). doi: 10.1038/ncomms5919; pmid: 25255805
32. A. Mousnier *et al*., Fragment-derived inhibitors of human N-myristoyltransferase block capsid assembly and replication of the common cold virus. *Nat. Chem.* **10**, 599–606 (2018). doi: 10.1038/s41557-018-0039-2; pmid: 29760414
33. I. S. Gul, P. Hulpiau, Y. Saeys, F. van Roy, Metazoan evolution of the armadillo repeat superfamily. *Cell. Mol. Life Sci.* **74**, 525–541 (2017). doi: 10.1007/s00018-016-2319-6; pmid: 27497926
34. D.-V. Rusnac *et al*., Recognition of the Diglycine C-End Degron by $CRL2^{KLHDC2}$ Ubiquitin Ligase. *Mol. Cell* **72**, 813–822.e4 (2018). doi: 10.1016/j.molcel.2018.10.021; pmid: 30526872
35. G. C. Smith, F. d'Adda di Fagagna, N. D. Lakin, S. P. Jackson, Cleavage and inactivation of ATM during apoptosis. *Mol. Cell. Biol.* **19**, 6076–6084 (1999). doi: 10.1128/MCB.19.9.6076; pmid: 10454555
36. F. Chen *et al*., Caspase proteolysis of the cohesin component RAD21 promotes apoptosis. *J. Biol. Chem.* **277**, 16775–16781 (2002). doi: 10.1074/jbc.M201322200; pmid: 11875078
37. M. Lek *et al*., Analysis of protein-coding genetic variation in 60,706 humans. *Nature* **536**, 285–291 (2016). doi: 10.1038/nature19057; pmid: 27535533
38. R. Sonneville, P. Gönczy, Zyg-11 and cul-2 regulate progression through meiosis II and polarity establishment in *C. elegans*. *Development* **131**, 3527–3543 (2004). doi: 10.1242/dev.01244; pmid: 15215208
39. J. Liu, S. Vasudevan, E. T. Kipreos, CUL-2 and ZYG-11 promote meiotic anaphase II and the proper placement of the anterior-posterior axis in *C. elegans*. *Development* **131**, 3513–3525 (2004). doi: 10.1242/dev.01245; pmid: 15215209
40. R. S. Balachandran *et al*., The ubiquitin ligase $CRL2^{ZYG11}$ targets cyclin B1 for degradation in a conserved pathway that facilitates mitotic slippage. *J. Cell Biol.* **215**, 151–166 (2016). doi: 10.1083/jcb.201601083; pmid: 27810909
41. N. E. Sanjana, O. Shalem, F. Zhang, Improved vectors and genome-wide libraries for CRISPR screening. *Nat. Methods* **11**, 783–784 (2014). doi: 10.1038/nmeth.3047; pmid: 25075903
42. M. Martin, Cutadapt removes adapter sequences from high-throughput sequencing reads. *EMBnet J.* **17**, 10 (2011). doi: 10.14806/ej.17.1.200
43. B. Langmead, S. L. Salzberg, Fast gapped-read alignment with Bowtie 2. *Nat. Methods* **9**, 357–359 (2012). doi: 10.1038/nmeth.1923; pmid: 22388286
44. N. Colaert, K. Helsens, L. Martens, J. Vandekerckhove, K. Gevaert, Improved visualization of protein consensus sequences by iceLogo. *Nat. Methods* **6**, 786–787 (2009). doi: 10.1038/nmeth1109-786; pmid: 19876014
45. M. C. F. Thomsen, M. Nielsen, Seq2Logo: A method for construction and visualization of amino acid binding motifs and sequence profiles including sequence weighting, pseudo counts and two-sided representation of amino acid enrichment and depletion. *Nucleic Acids Res.* **40**, W281-7 (2012). doi: 10.1093/nar/gks469; pmid: 22638583
46. W. Li *et al*., MAGeCK enables robust identification of essential genes from genome-scale CRISPR/Cas9 knockout screens. *Genome Biol.* **15**, 554 (2014). doi: 10.1186/s13059-014-0554-4; pmid: 25476604

ACKNOWLEDGMENTS

We are grateful to C. Araneo and his team for FACS and J. Paulo for mass spectrometry. We thank A. Varshavsky, J. Wells, and E. Tate for advice. **Funding:** R.T.T. is a Sir Henry Wellcome Postdoctoral Fellow (201387/Z/16/Z). Z.Z. is a Croucher Foundation Honorary Ph.D. Scholar. This work was supported by an NIH grant (AG11085) to S.J.E. and J.W.H.; S.J.E. is an investigator with the Howard Hughes Medical Institute. **Author contributions:** Conceptualization, R.T.T., I.K., and S.J.E.; investigation, R.T.T., I.K., D.Y.R., Z.Z.; writing, R.T.T., I.K., and S.J.E; supervision, J.W.H. and S.J.E. **Competing interests:** The authors declare no competing interests. **Data and materials availability:** All data are available in the main text or the supplementary materials.

SUPPLEMENTARY MATERIALS

science.sciencemag.org/content/365/6448/eaaw4912/suppl/DC1
Figs. S1 to S15
Data Files S1 to S6
Reference (*47*)

26 December 2018; resubmitted 29 March 2019
Accepted 15 May 2019
10.1126/science.aaw4912

RESEARCH ARTICLE SUMMARY

NEURODEVELOPMENT

Structured spike series specify gene expression patterns for olfactory circuit formation

Ai Nakashima*, Naoki Ihara*, Mayo Shigeta, Hiroshi Kiyonari, Yuji Ikegaya, Haruki Takeuchi†

INTRODUCTION: The development of precise neural circuits is initially directed by genetic programming and subsequently refined by neural activity. In the mouse olfactory system, axons from various olfactory sensory neurons expressing the same olfactory receptor converge onto a few spatially invariant glomeruli, generating the olfactory glomerular map in the olfactory bulbs. During development, olfactory receptors instruct axon sorting to form discrete glomeruli. Olfactory receptors generate a combinatorial code of axon-sorting molecules whose expression is regulated by neural activity. However, it remains unclear how neural activity induces olfactory receptor–specific expression patterns of axon-sorting molecules.

RATIONALE: The prevailing model for the activity-dependent development of neural circuits postulates an interaction between pre- and postsynaptic neurons. In Hebbian plasticity, the correlated activity of pre- and postsynaptic neurons strengthens synaptic connections, whereas uncorrelated activity or lack of activity weakens them. However, this theory does not explain activity-dependent mechanisms in olfactory map formation. Axons of olfactory sensory neurons can converge to form glomerular-like structures even in mutant mice lacking synaptic partners, suggesting another activity-dependent mechanism for glomerular segregation. The involvement of neural activity in olfactory map formation has been demonstrated by experimental suppression of neural activity. Here, we asked how neural activity is involved in the expression of axon-sorting molecules regulating glomerular segregation.

ON OUR WEBSITE

Read the full article at http://dx.doi.org/10.1126/science.aaw5030

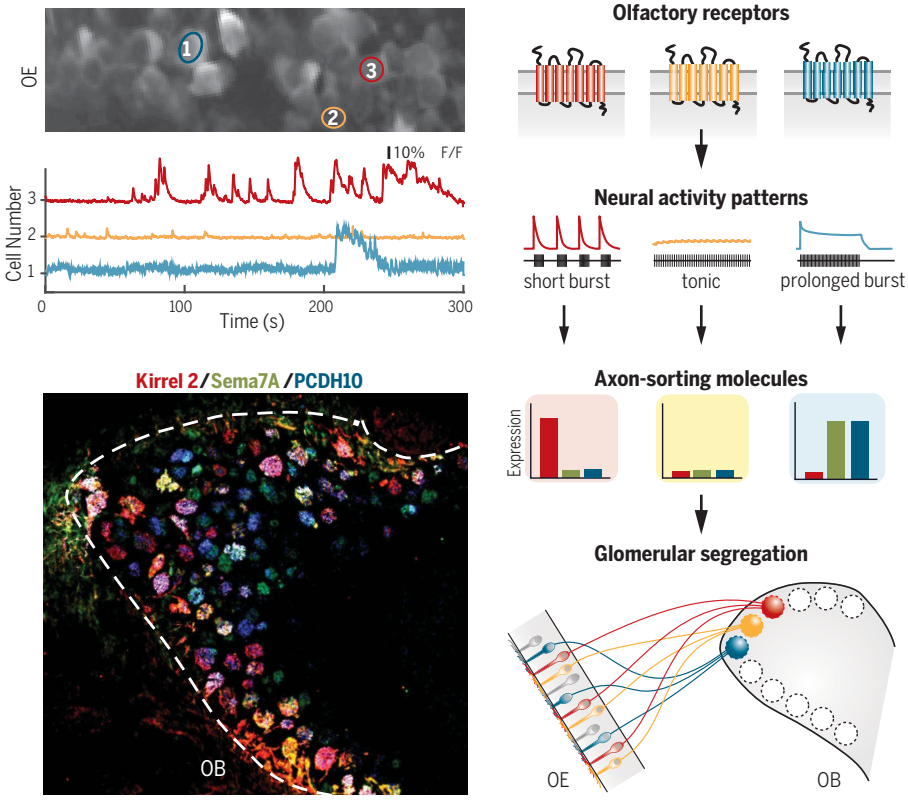

Firing pattern–dependent olfactory map formation. Top left: Diverse patterns of spontaneous neural activity in olfactory sensory neurons. Bottom left: A combinatorial expression pattern of axon-sorting molecules at axon termini of olfactory sensory neurons. Right: A model for activity-dependent olfactory map formation. OE, olfactory epithelium; OB, olfactory bulb. Axon-sorting molecules for glomerular segregation: red, Kirrel2 (kin of IRRE-like protein 2); green, Sema7A (semaphorin 7A); blue, PCDH10 (protocadherin 10).

RESULTS: We performed calcium imaging experiments and optogenetic stimulation to address how neural activity generates olfactory receptor–specific expression patterns of axon-sorting molecules. Calcium imaging of olfactory sensory neurons revealed that the temporal patterns of spontaneous neuronal spikes were not spatially organized, but rather were correlated with the olfactory receptor types. Receptor substitution experiments demonstrated that olfactory receptors determine spontaneous activity patterns. Moreover, optogenetically differentiated patterns of neuronal activity induced expression of corresponding axon-sorting molecules and regulated glomerular segregation.

CONCLUSION: We have demonstrated an instructive role of neural activity in olfactory map formation. We propose an activity-dependent mechanism, different from Hebbian plasticity theory, in which specific patterns of spontaneous activity determined by the expressed olfactory receptor type contribute to generating the combinatorial code of axon-sorting molecules for olfactory receptor–specific axon sorting.

Neural activity is involved in various aspects of brain development and function. Our findings show that in the olfactory system, gene expression that regulates neural circuit formation is dependent on neural firing patterns. With this strategy, neurons can generate variation through diversifying gene expression. The pattern-dependent gene regulation may also expand beyond development to plastic changes in neural circuits throughout the lifetime. ■

The list of author affiliations is available in the full article online.
*These authors contributed equally to this work.
†Corresponding author. Email: haruki-t@mol.f.u-tokyo.ac.jp
Cite this article as A. Nakashima *et al.*, *Science* **365**, eaaw5030 (2019). DOI: 10.1126/science.aaw5030

RESEARCH ARTICLE

NEURODEVELOPMENT

Structured spike series specify gene expression patterns for olfactory circuit formation

Ai Nakashima[1]*, Naoki Ihara[1]*, Mayo Shigeta[2], Hiroshi Kiyonari[2,3], Yuji Ikegaya[1,4], Haruki Takeuchi[1,5]†

Neural circuits emerge through the interplay of genetic programming and activity-dependent processes. During the development of the mouse olfactory map, axons segregate into distinct glomeruli in an olfactory receptor (OR)–dependent manner. ORs generate a combinatorial code of axon-sorting molecules whose expression is regulated by neural activity. However, it remains unclear how neural activity induces OR-specific expression patterns of axon-sorting molecules. We found that the temporal patterns of spontaneous neuronal spikes were not spatially organized but were correlated with the OR types. Receptor substitution experiments demonstrated that ORs determine spontaneous activity patterns. Moreover, optogenetically differentiated patterns of neuronal activity induced specific expression of the corresponding axon-sorting molecules and regulated axonal segregation. Thus, OR-dependent temporal patterns of spontaneous activity play instructive roles in generating the combinatorial code of axon-sorting molecules during olfactory map formation.

In the mammalian brain, the development of precise neural circuits is initially directed by intrinsic genetic programming and subsequently refined by neural activity (*1*–*3*). In the mouse olfactory system, individual olfactory sensory neurons (OSNs) express a single gene of a functional olfactory receptor (OR) out of >1000 OR genes (*4*–*6*). Axons from various OSNs expressing the same OR converge onto a few spatially invariant glomeruli, generating the olfactory glomerular map in the olfactory bulbs (OBs) (*7*–*9*). The olfactory glomerular map forms through two processes: global targeting and glomerular segregation (*10*, *11*). OSN axons are first guided to approximate target regions according to gradients of axon guidance molecules (*12*, *13*) and are subsequently sorted into specific glomerular structures in an activity-dependent manner (*11*, *14*–*16*). In glomerular segregation, OSN axons discriminate expressed OR types. Substitution of an OR-coding DNA sequence with another sequence results in allopatric generation of glomeruli that are distinct from the original ones (*17*, *18*). Further, suppression of spontaneous neural activity disrupts the glomerular segregation (*15*). However, it remains a mystery how neural activity mediates the OR-specific glomerular segregation.

The most prevailing model for the activity-dependent development of neural circuits postulates the interaction between pre- and postsynaptic neurons. In Hebbian plasticity (*19*), the correlated activity of pre- and postsynaptic neurons strengthens synaptic connections, whereas uncorrelated activity or lack of activity weakens them. However, this theory does not explain activity-dependent mechanisms for axon sorting before the formation of synapses. OSN axons are capable of converging to form glomerular-like structures even in mutant mice lacking synaptic partners (*20*, *21*). These findings suggest another activity-dependent mechanism for glomerular segregation.

OR molecules control the expression of various axon-sorting molecules, which serve to regulate glomerular segregation through their adhesive or repulsive interactions (*22*–*26*). These molecules exhibit both mosaic and glomerular-specific expression patterns (*27*). However, their spatial patterns are not identical in the OB. As a result, OR identity is represented as a unique combinatorial code of axon-sorting molecules at the axon termini, which provides the self-identification tags for OR-specific glomerular segregation. Because the expression of axon-sorting molecules is activity-dependent (*22*, *25*), neural activity is expected to bridge between the OR types and the combinatorial expression of the axon-sorting molecules. Previous studies reported that spontaneous firing rates are different among OSN classes in several species (*28*–*32*). However, it remains unclear whether neural activity functions in an instructive way or a permissive way; it is not clear whether specific features of neural activity patterns are important or whether the presence of neural activity is sufficient to trigger a predetermined gene expression. Here, we applied genetic approaches to address how neural activity generates OR-specific expression patterns of axon-sorting molecules.

Activity-dependent expression of axon-sorting molecules

On the basis of our previous study (*27*), we focused on Kirrel2, Sema7A, and PCDH10 as the axon-sorting molecules for glomerular segregation. Genetic knockout (KO) experiments demonstrated that these molecules are involved in neural circuit formation in the mouse olfactory system (*22*, *25*, *33*) (fig. S1). The expression levels of these molecules are uniquely correlated with OR types (*22*, *24*, *27*). However, the expression patterns differed among glomeruli in the OB (Fig. 1A). For example, Kirrel2 expression was high in the I7 glomeruli but low in the MOR28 and M71 glomeruli. In contrast, PCDH10 expression was high in the M71 glomeruli, middle in the I7 glomeruli, and low in the MOR28 glomeruli (Fig. 1, B and C). Our previous study showed that the expression levels of these molecules dropped substantially to undetectable levels in KOs of the cyclic nucleotide–gated (CNG) channel (*27*), a key component of the olfactory signal transduction pathway (*34*). High-KCl treatment of olfactory tissues in ex vivo culture conditions increased the expression of these genes, and this effect was blocked by the depletion of extracellular calcium ions or inhibition of the voltage-gated L-type calcium channel (fig. S2). These results indicate that calcium influx associated with neural activity is required for generating the combinatorial code of the axon-sorting molecules.

Visualizing OSN spontaneous activity

To examine the nature of OSN spontaneous activity, we used a Cre/*loxP* approach [*pGoofy-Cre*: *pCAG-LSL-GCaMP6f* (*Ai95D*) mice] to express the genetically encoded calcium indicator GCaMP6f (*35*) specifically in OSNs (Fig. 2A). In the OSN-specific GCaMP6f mice, action potentials were reliably detected as transient increases in the fluorescence intensities of GCaMP6f (fig. S3). Correlation analyses revealed that spontaneous calcium events were not spatially or temporally correlated between OSNs in ex vivo acute olfactory epithelium (OE) slices from neonatal mice (Fig. 2, A and B; see also movie S1), which suggested that spontaneous calcium transients are sporadic events and occur independent of neighboring OSNs. These results are in contrast to the spontaneous activity patterns observed in the developing retina, which generates temporally correlated activity among neighboring retinal

[1]Laboratory of Chemical Pharmacology, Graduate School of Pharmaceutical Sciences, University of Tokyo, Tokyo 113-0033, Japan. [2]Laboratory for Animal Resource Development, RIKEN Center for Biosystems Dynamics Research, 2-2-3 Minatojima Minami-machi, Chuo-ku, Kobe 650-0047, Japan. [3]Laboratory for Genetic Engineering, RIKEN Center for Biosystems Dynamics Research, 2-2-3 Minatojima Minami-machi, Chuo-ku, Kobe 650-0047, Japan. [4]Center for Information and Neural Networks, National Institute of Information and Communications Technology, Suita City, Osaka 565-0871, Japan. [5]Social Cooperation Program of Evolutional Chemical Safety Assessment System, LECSAS, Graduate School of Pharmaceutical Sciences, University of Tokyo, Tokyo 113-0033, Japan.
*These authors contributed equally to this work.
†Corresponding author. Email: haruki-t@mol.f.u-tokyo.ac.jp

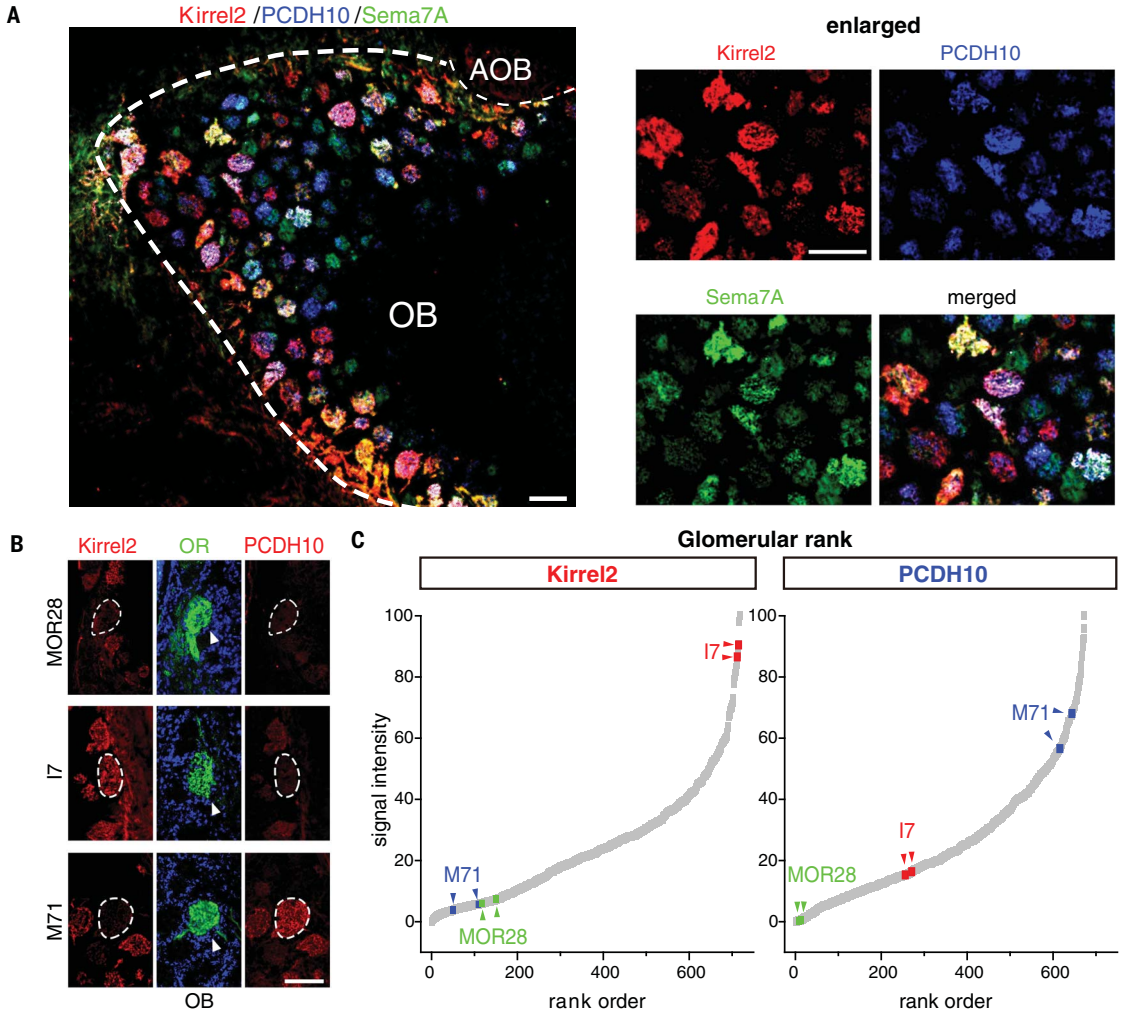

Fig. 1. OR-specific expression patterns of axon-sorting molecules. (**A**) Glomerulus-specific expression of axon-sorting molecules. A parasagittal OB section from a 2-week-old mouse was immunostained using antibodies to Kirrel2 (red), PCDH10 (blue), and Sema7A (green). Enlarged images are shown at the right. AOB, accessory olfactory bulb. Scale bars, 100 μm. (**B**) Expression levels of axon-sorting molecules in OSNs expressing specific ORs. The glomerular locations of MOR28-, I7-, and M71-expressing OSNs were identified by immunostaining with the indicated antibodies (indicated by arrowheads). Adjacent sections were immunostained using antibodies to Kirrel2 and PCDH10. Scale bars, 100 μm. (**C**) Rank order of expression levels of Kirrel2 and PCDH10. The signal intensities of Kirrel2 and PCDH10 were quantified for each glomerulus and plotted in order (N = 718 glomeruli for Kirrel2, N = 673 glomeruli for PCDH10).

ganglion cells and regulates precise circuit formation (*10*, *36*–*39*). In the CNG-KO mice, spontaneous activity was still present (*34*) (fig. S3E, see also movie S2) but in altered patterns; the event frequencies of calcium spikes and the inter-event intervals (IEIs) (frequency = 0.90 ± 1.02 times/min, IEI = 59.09 ± 61.52 s; mean ± SD, N = 230 cells) were lower and longer, respectively, relative to those in wild-type mice (frequency = 2.05 ± 2.48 times/min, IEI = 48.14 ± 53.09 s; mean ± SD, N = 252 cells). Because CNG channel–mediated activity is essential for the expression of *Kirrel2*, *Sema7A*, and *PCDH10* (*27*), these observations indicate that specific features of neural activity (e.g., frequency, IEI), rather than the presence of neural activity, are important for the expression of axon-sorting molecules, leading to the hypothesis that neural activity is instructive for glomerular segregation.

ORs determine spontaneous activity patterns

We next compared the temporal features of spontaneous calcium transients between OSNs expressing different OR types. We selected two types of OR-defined neurons based on the expression profiles of the axon-sorting molecules: (i) I7-expressing OSNs, in which expression levels of *Kirrel2* are high, and (ii) MOR28-expressing OSNs, in which expression levels of *Kirrel2* are low (Fig. 1, B and C, and fig. S4). We generated the transgenic mice *H-I7-Cre-mcherry* and *H-MOR28-Cre-mcherry* (hereafter abbreviated as *H-OR-Cre* lines), in which Cre recombinase was coexpressed with *I7* or *MOR28* (Fig. 2C and fig. S4). Because the forced expression of OR from a transgene suppresses endogenous OR expression (*6*, *40*, *41*), the monogenic OR expression is maintained in OSNs expressing the transgenes. The *H-OR-Cre* lines were then crossed with *Ai95D* mice to visualize spontaneous calcium transients of OSNs expressing specific ORs. We compared the features of calcium spikes, including baseline fluorescence, total event number, IEI, peak amplitude, coefficient of variation (CV), and rise and fall times of calcium spikes between I7- and MOR28-expressing neurons (N = 59 cells for I7, N = 61 cells for MOR28). We found that calcium transient patterns were significantly different between I7- and MOR28-expressing OSNs (Fig. 2C), even though both ORs were expressed under the control of the same *MOR23* promoter (*42*) (Fig. 2C and fig. S4A). I7-expressing OSNs exhibited calcium transients of higher amplitudes and higher frequencies than those of MOR28-expressing OSNs (Fig. 2, C and D). We conducted multidimensional scaling (MDS) to plot the datasets of I7- and MOR28-expressing OSNs according to relative distance (Fig. 2E). In the MDS space, OSNs expressing different ORs were significantly separated by a single line determined by the linear support vector machine (SVM) classifier (gray dashed line in Fig. 2E, F1 = 0.775, P < 0.0001), indicating that different ORs are sufficient to induce differing patterns of spontaneous calcium transients.

To overview a variety of calcium transient patterns in OSNs, we next collected the features of calcium transients from a large number of OSNs [N = 3214 cells; N = 59 for I7 (red), N = 61 for MOR28 (green), N = 45 for M71 (blue), and N = 3049 for randomly selected OSNs (gray)]. The dataset was dimension-reduced by principal components analysis (PCA). In two-dimensional PC space, OSNs were clustered depending on the expressed OR types (Fig. 2F and fig. S5). Taken together, this result indicates that OSNs expressing the same OR type exhibited similar temporal profiles of calcium transients.

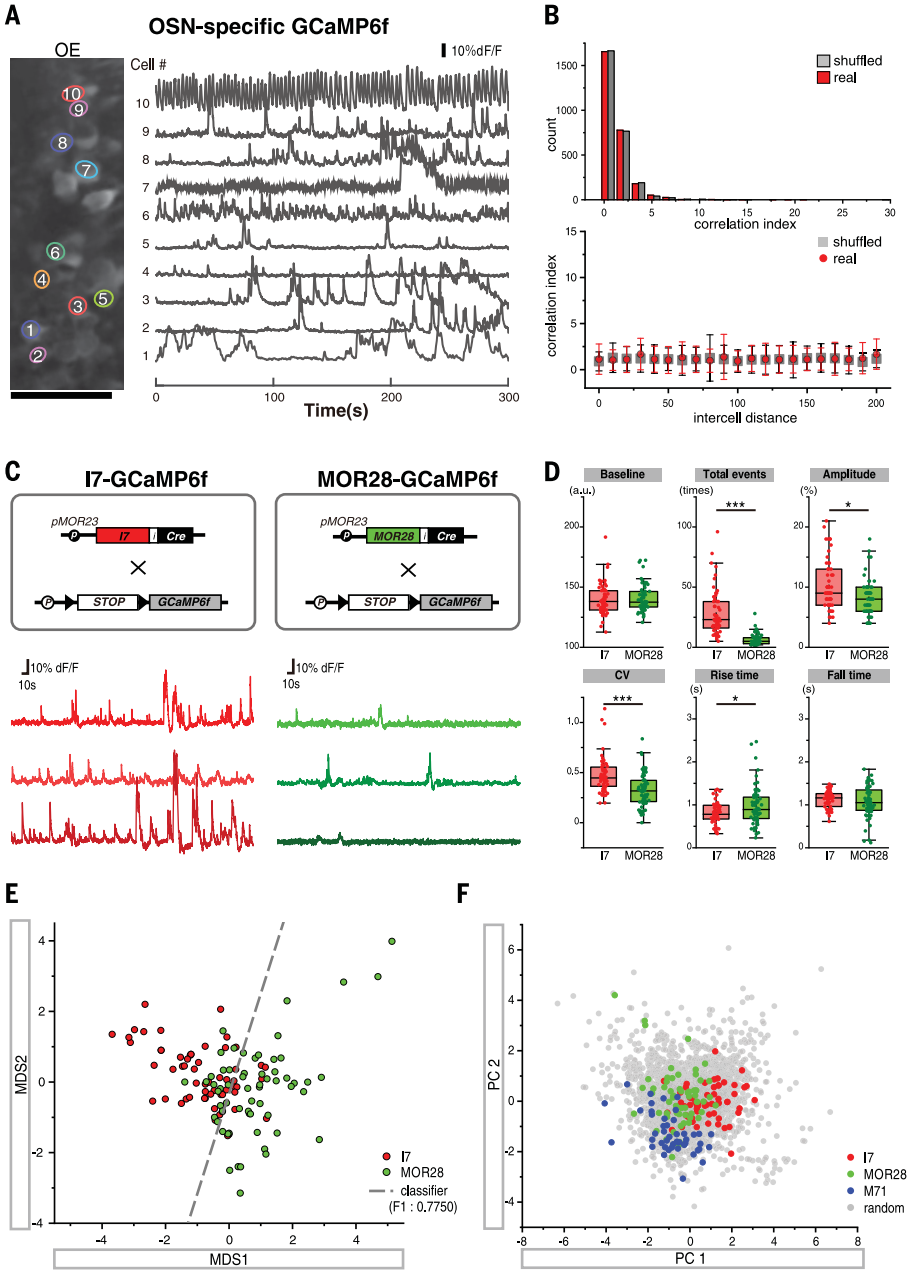

Fig. 2. Spontaneous activity patterns correlate with OR types. (**A**) An image of an OE acute slice. OSN calcium transients are shown at the right. Scale bar, 50 μm. (**B**) Pairwise cross-correlation analyses were performed for all possible pairs (N = 2701 pairs). Top: The distribution of the correlation indices for the real data was not significantly different from that for shuffled data (Mann-Whitney U test). Bottom: Correlation indices were plotted as a function of the intercell distance between cell pairs. Data are means ± SEM. (**C**) Top: *H-OR-Cre* lines were crossed with *Ai95D* mice. Bottom: Representative calcium transients. (**D**) Features of spontaneous calcium transients were analyzed for I7- or MOR28-expressing OSNs. Results are shown as box-and-whisker plots displaying the median and interquartile ranges. Outliers are 1.5 times the interquartile range (IQR) either above the third quartile or below the first quartile. CV, coefficient of variation. ***P < 0.001, *P < 0.05 (Mann-Whitney U test). (**E**) Multidimensional scaling (MDS) of the calcium imaging dataset of OR-defined OSNs. The support vector machine (SVM) classifier is shown as a gray dashed line. (**F**) PCA biplot of the calcium imaging dataset from 3214 OSNs.

Spike bursts increase *Kirrel2* expression

To assess the causal links between the neural activity patterns and the expression of axon-sorting molecules, we used an optogenetic approach to manipulate the neural activity of OSNs. OSN-specific channelrhodopsin-2 (ChR2) mice were generated by crossing *pGoofy-Cre* mice with *pCAG-LSL-ChR2* (*Ai32*) mice (*43*) (Fig. 3A, top). Blue light pulses (3 ms at ≤40 Hz) could precisely control the neural activity of OSNs at a single spike level, irrespective of the light power (fig. S6). The OSN-specific ChR2 mice were stimulated by blue light pulses with two different protocols, namely phasic burst stimulation (intraburst frequency, 10 Hz; action potentials in burst, 15; interburst interval, 15 s) and tonic stimulation (Fig. 3B). In both protocols, light-induced action potentials were maintained at the overall firing rate of 1 Hz because the median firing rate of the spontaneous activity of OSNs was 1.1 Hz (fig. S7). We illuminated the unilateral dorsolateral side of the OE with blue light pulses for 12 hours according to the protocols and compared the changes in the expression of axon-sorting molecules between the light-illuminated and shaded sides of the OE (Fig. 3A, bottom). We found that in the phasic burst protocol, *Kirrel2* was up-regulated in the light-stimulated side relative to the shaded side (Fig. 3B). However, no significant change was observed in the tonic protocol. *Kirrel2* expression was up-regulated in the phasic burst protocols when the interspike intervals (ISIs) of the induced spikes within bursts were less than 200 ms (Fig. 3C). Single-cell quantification further revealed that the intraburst frequency of the induced spikes had different impacts on *Kirrel2* up-regulation (ISI = 50 ms, d = 0.74; ISI = 100 ms, d = 1.54; ISI = 200 ms, d = 1.09) (Fig. 3D, left). *Kirrel2* expression increased even in MOR28-expressing OSNs, where the endogenous *Kirrel2* expression levels are low (Fig. 3D, right), indicating that the change in the expression levels of *Kirrel2* was not attributable to a difference in the OSN population. In addition, the induced spike numbers within bursts affected *Kirrel2* expression (Fig. 3E).

To find the relationship between endogenous spontaneous activity and optogenetically induced firing, we conducted SVM classification in terms of *Kirrel2* expression levels. The nonlinear SVM classifier based on endogenous activity patterns of *Kirrel2*-high (I7) and *Kirrel2*-low (MOR28 and M71) OSNs could predict the light stimulation–induced *Kirrel2* up-regulation (Fig. 3F, left). The optogenetic stimulation protocols that increased *Kirrel2* expression (Fig. 3F, a to d) were plotted onto the *Kirrel2*-high side of the graph, whereas those that did not change *Kirrel2* expression (Fig. 3F, e to g) were plotted onto the *Kirrel2*-low side. Further, OSNs in the I7 cluster frequently exhibited calcium transients with high amplitude that resembled phasic burst stimulation (Fig. 3F, right, calcium event frequency = 0.047 ± 0.031 Hz, calcium event amplitude = 10.25 ± 4.06%, mean ± SD). In contrast, such high-amplitude calcium transients were not frequently observed in the MOR28 and M71 clusters (MOR28, frequency = 0.011 ± 0.008 Hz, amplitude = 8.28 ± 2.98%, mean ± SD; M71, frequency = 0.036 ± 0.033 Hz, amplitude = 4.11 ± 1.17%, mean ± SD). Thus, we deduced that the phasic burst stimulations mimicked the physiological patterns of neural activity for *Kirrel2* expression.

In contrast to *Kirrel2*, the expression of *Sema7A* and *PCDH10* did not change during the series of experiments (Fig. 3C). A similar phenotype was also observed in the CNG-KO background, where

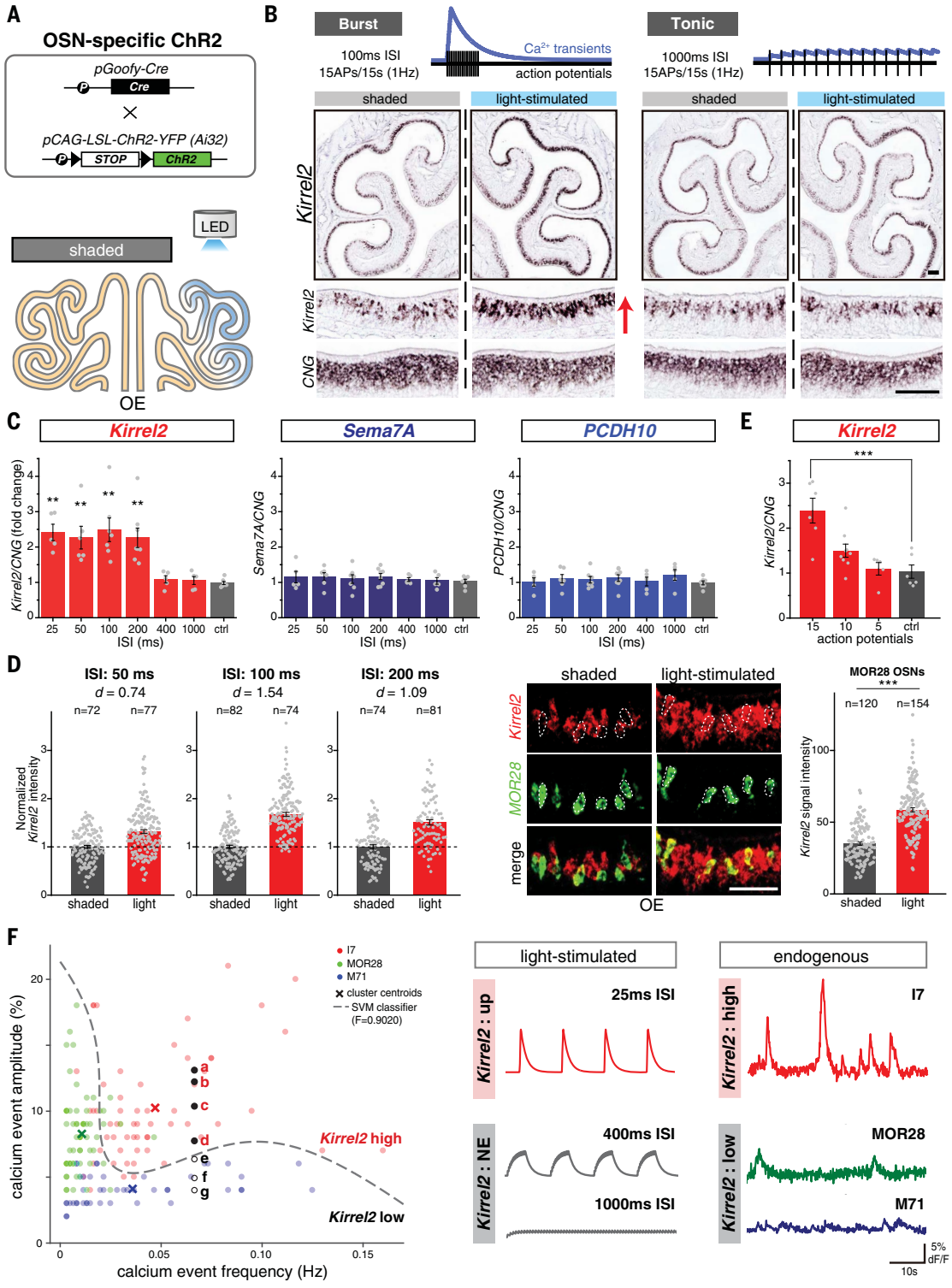

Fig. 3. Phasic burst stimulation increases *Kirrel2* expression. (**A**) Top: Transgenic constructs for the OSN-specific ChR2 mice. Bottom: Experimental schematic for the in vivo optogenetic stimulation. (**B**) In situ hybridization of the OE sections using probes for *Kirrel2* and *CNG* channel (mature OSN marker). (**C**) Relative expression levels of axon-sorting molecules were compared by quantitative RT-PCR; $N = 5$ to 8 mice per group. (**D**) Left: Single-cell analyses of gene expression changes. Right: Relative *Kirrel2* signal intensities in MOR28-expressing OSNs. $^{***}P < 0.001$ (Student *t* test). (**E**) Differential impacts of *Kirrel2* by protocols comprising different spike numbers. Relative *Kirrel2* levels were compared by quantitative RT-PCR; $N = 5$ to 9 mice per group. $^{**}P < 0.01$, $^{***}P < 0.001$ [one-way analysis of variance (ANOVA) with post hoc Tukey test in (C) and (E)]. Error bars in (C) to (E) denote SEM. (**F**) Left: Scatterplot of the calcium imaging data. The SVM classifier divides OSNs according to *Kirrel2* levels (gray dashed line). The expected calcium transients through light stimulation are also plotted: **a**, 25 ms ISI, 15 APs, 15 s; **b**, 50 ms ISI, 15 APs, 15 s; **c**, 100 ms ISI, 15 APs, 15 s; **d**, 200 ms ISI, 15 APs, 15 s; **e**, 400 ms ISI, 15 APs, 15 s; **f**, 200 ms ISI, 10 APs, 15 s; **g**, 200 ms ISI, 5 APs, 15 s. Right: Calcium transients nearest to the centroids of each OR cluster are compared with the expected calcium transients induced by light stimulation. NE, no effect. See also fig. S11. Scale bars, 50 μm.

endogenous calcium transients were more static (fig. S8). These results demonstrate that the spike bursts specifically up-regulate *Kirrel2* expression.

Prolonged burst stimulation increases *Sema7A* and *PCDH10*

We next sought to determine which pattern of neural activity was necessary for the expression of *Sema7A* and *PCDH10*. Because they showed similar protein distribution patterns at the OSN axon termini (27), there must be a common regulatory mechanism underlying their expression. We stimulated OSNs with various burst duration protocols ranging from 1.5 to 720 s (Fig. 4A). We kept the overall firing rate at 1 Hz and the spike frequency within bursts at 10 Hz. Optogenetic stimulation with various burst duration protocols revealed that *Sema7A* and *PCDH10* were up-regulated by burst durations for more than 10 s and 20 s, respectively (Fig. 4B). It is notable that the 360-s and 720-s burst duration protocols increased the expression of *Sema7A* and *PCDH10*, but not that of *Kirrel2* (Fig. 4, B and C).

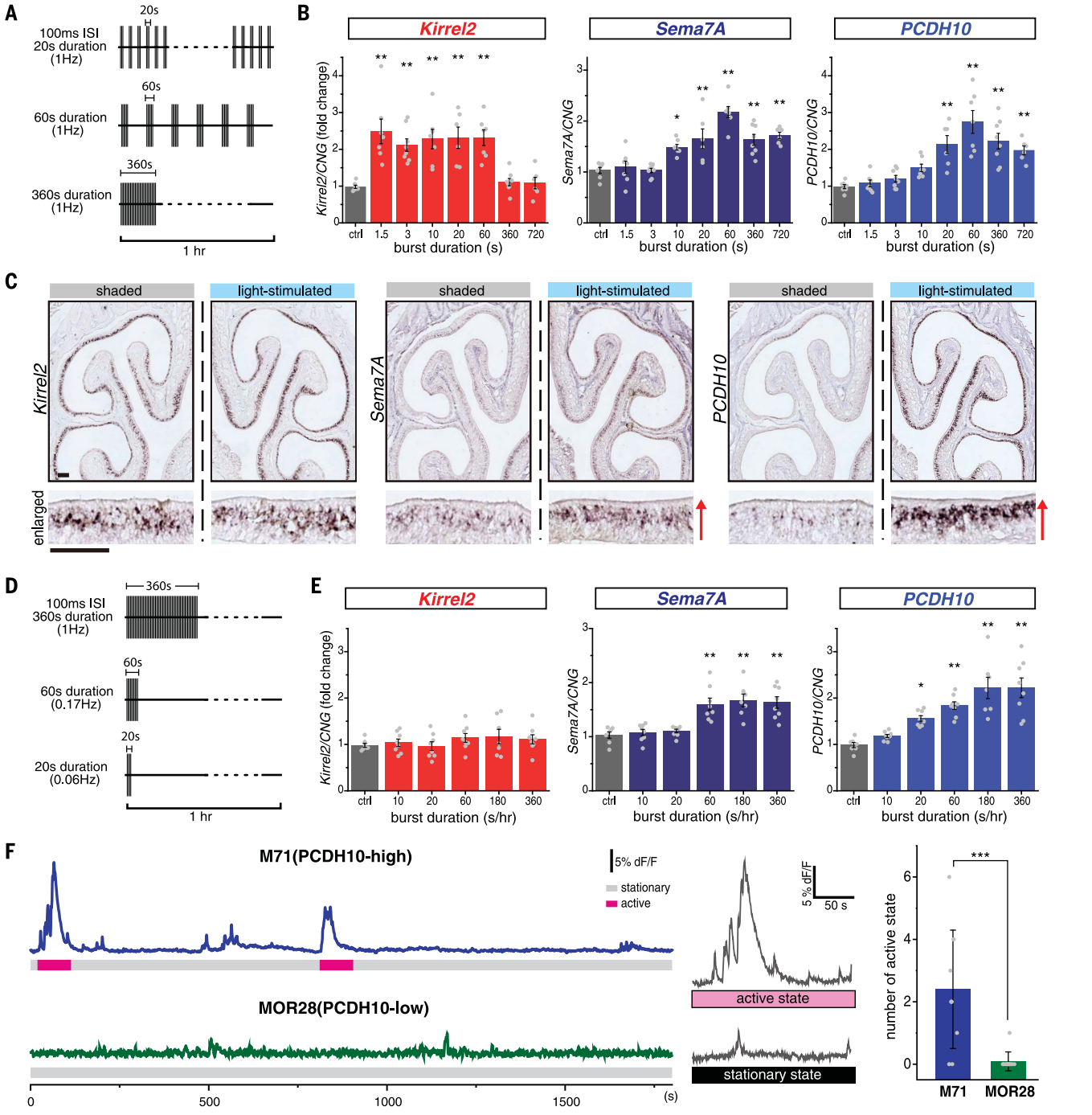

Fig. 4. Prolonged burst stimulation increases *Sema7A* and *PCDH10*. (**A**) Schematic showing various stimulation protocols. (**B**) Expression changes of axon-sorting molecules upon different light stimulation protocols. Quantitative analyses were performed as in Fig. 3C. Error bars denote SEM (N = 6 to 8 mice per group). (**C**) In situ hybridization of the OE sections from OSN-specific ChR2 mice illuminated by blue light with the long-duration protocol (ISI, 100 ms; burst duration per hour, 360 s). Enlarged photos are shown at the bottom. Scale bars, 50 μm. (**D**) Schematic showing various optogenetic stimulation protocols. (**E**) Expression changes of axon-sorting molecules upon various burst units. Quantitative analyses were performed as in Fig. 3C. Error bars denote SEM (N = 7 or 8 mice per group). $^{*}P < 0.05$, $^{**}P < 0.01$ [one-way ANOVA with post hoc Tukey test in (B) and (E)]. (**F**) Left: Long-term calcium imaging of *PCDH10*-high (M71) and *PCDH10*-low (MOR28) OSNs. Right: Number of active states per hour in M71- and MOR28-expressing OSNs. Data are means ± SD. N = 10 cells (M71), 11 cells (MOR28). $^{***}P < 0.001$ (Student t test).

To investigate the minimum duration of bursts required for the expression of *Sema7A* and *PCDH10*, we further tested the effects of various burst units by changing the burst duration irrespective of the firing rate of the induced spikes (Fig. 4D). To this end, OSNs were stimulated hourly with various types of single burst units (intraburst frequency, 10 Hz; burst duration, 10 to 360 s) for 12 hours. We found that both genes were up-regulated by prolonged bursts. The sensitivities to the burst duration differed between *Sema7A* and *PCDH10*; a 20-s burst duration induced the expression of *PCDH10*, but not that of *Sema7A* (Fig. 4E). The differential sensitivities of *Sema7A* and *PCDH10* to the burst durations may

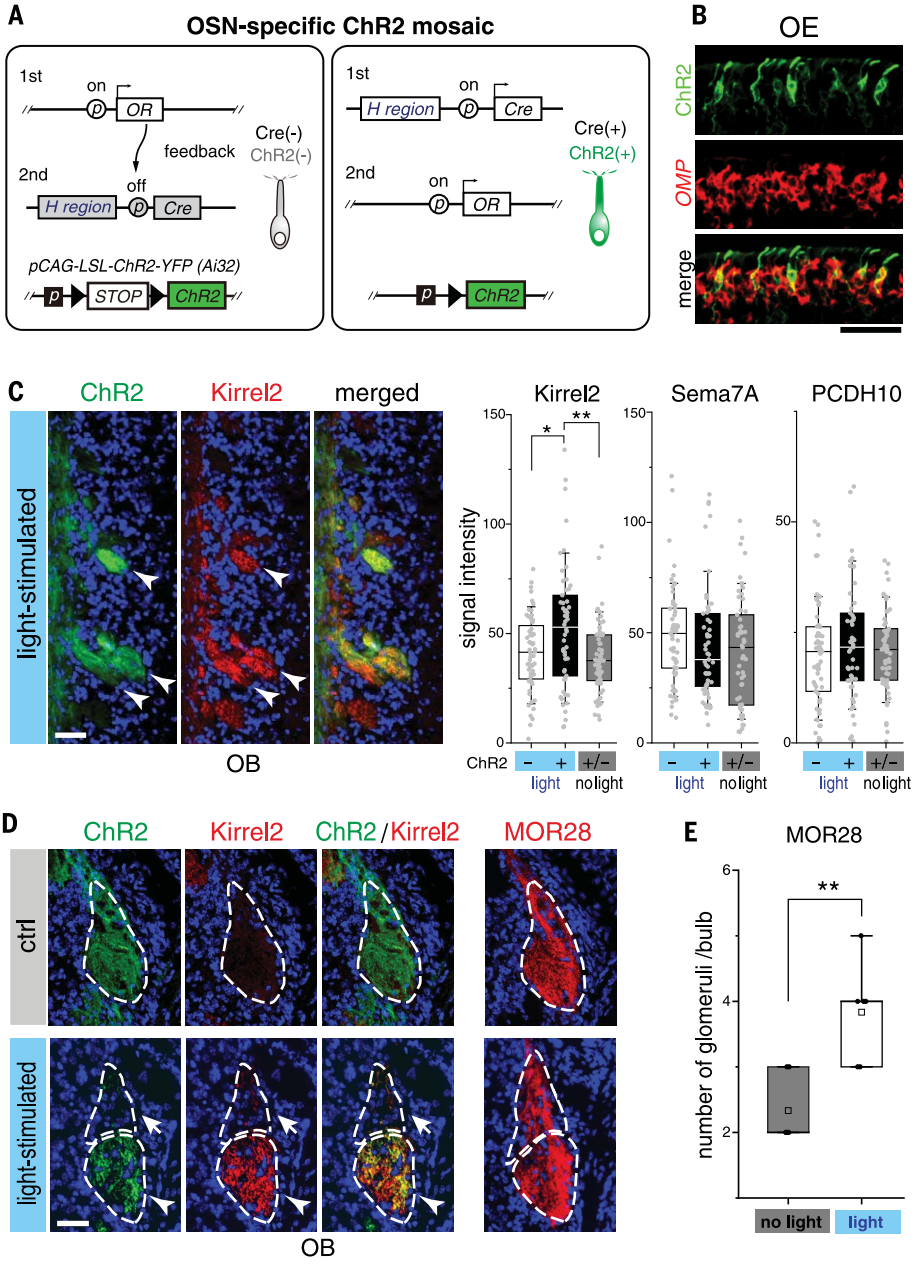

Fig. 5. Optogenetic stimulation affects axonal segregation. (**A**) Schematic for generating OSN-specific ChR2 mosaic mice. (**B**) Double staining of an OE section from the ChR2 mosaic mouse. An OE section was subjected to in situ hybridization using an *OMP* probe (red) and immunostaining with antibodies to green fluorescent protein (GFP) (green). (**C**) Immunostaining of an OB section with antibodies to GFP and Kirrel2 after chronic light stimulation (intraburst frequency, 10 Hz; APs within burst, 15; interburst interval, 15 s). Left: Kirrel2 up-regulation upon light stimulation is indicated by arrowheads. Right: Quantification of protein levels of axon-sorting molecules. $*P < 0.05$, $**P < 0.01$ (one-way ANOVA with post hoc Tukey test). See also data S5. (**D**) Immunostaining of OB sections using antibodies to Kirrel2, GFP, and MOR28. Kirrel2-positive and -negative MOR28^{+} axons are indicated by arrowheads and arrows, respectively. (**E**) Numbers of MOR28 glomeruli per OB in ChR2 mosaic mice with and without light stimulation. A glomerular structure was semiautomatically defined by immunofluorescence signals of vesicular glutamate transporter2 (VGlut2). Box and whiskers in all graphs represent 25th to 75th and 10th to 90th percentiles, respectively. Scale bars, 50 μm. $N = 6$ glomeruli, $**P < 0.01$ (Student t test).

explain their partially overlapping but different expression patterns in the OSN axon termini in the OBs (*27*). In a series of burst duration experiments (Fig. 4D), *Kirrel2* expression was not changed (Fig. 4E). These results indicate that *Sema7A* and *PCDH10* expression is up-regulated by protocols of low-frequency and long-duration bursts, whereas *Kirrel2* expression is up-regulated by protocols of high-frequency and short-duration bursts.

We also performed long-term calcium imaging for OSNs expressing *M71* and *MOR28* in which *PCDH10* expression levels are high and low, respectively (Fig. 1, B and C). As shown in Fig. 4F, both types of OSNs exhibited stationary states during the majority of the recorded time. However, we observed events of prolonged calcium elevation several times per hour in M71-expressing OSNs (Fig. 4F). We defined the active state according to the duration when OSNs showed a higher amplitude of calcium transients above average for >20 s. The active state in M71-expressing OSNs lasted for 34.14 ± 13.47 s with an IEI of 445.85 ± 376.03 s (mean ± SD), which is enough to induce *PCDH10* expression. In contrast, the active state was hardly observed in MOR28-expressing OSNs [0.09 ± 0.30 times/hour (N = 11 cells) versus 2.4 ± 1.90 times/hour for *M71*-expressing OSNs (N = 10 cells), means ± SD]. These results suggest that prolonged burst stimulations and their impact on gene expression mimicked physiological conditions.

Chronic optogenetic stimulation induces axonal segregation

To examine whether in vivo optogenetic stimulation indeed affects segregation of OSN axons, we conducted optogenetic stimulation for a prolonged period of time. For this purpose, we used *H-Cre* transgenic mice (*13*). In this mouse, Cre recombinase is expressed in a subset of OSNs as a result of the OR-mediated negative feedback signal (*6*). Therefore, ChR2-positive and ChR2-negative OSNs expressing the same OR can be generated in the same individuals by crossing the *H-Cre* transgenic mice with the *Ai32* mice (Fig. 5, A and B).

Neonatal OSN-specific ChR2 mosaic mice were stimulated for 5 to 6 hours per day with the phasic burst protocol used in Fig. 3B. After 1 week of light stimulation, we observed an increase in Kirrel2 proteins, but not in PCDH10 or Sema7A proteins, in ChR2-positive OSN axons (Fig. 5, C and D). The Kirrel2 up-regulation was also observed in the CNG-KO background where endogenous Kirrel2 expression is decreased (fig. S9). We found segregation of MOR28-expressing OSN axons according to ChR2 expression in the OB of the ChR2 mosaic mice (Fig. 5, D and E). A similar axonal phenotype was also found in I7-expressing OSN axons (fig. S10, A and B). The ChR2-dependent axonal segregation did not occur without light stimulation (Fig. 5, D and E, and fig. S10). These results indicate that the optogenetically induced phasic burst stimulation induced axonal segregation, presumably through Kirrel2 up-regulation.

Discussion

Hebbian plasticity explains the activity-dependent development of many neural circuits (*19*). Synchronous firing of presynaptic neurons, such as retinal waves in the visual system (*2*, *36*, *37*, *39*, *44*, *45*), is a prerequisite for the Hebbian plastic changes. In the present study, we did not observe spatial or temporal correlations for the spontaneous activities among OSNs (Fig. 2, A and B). Rather,

spontaneous activity patterns of OSNs were uniquely correlated with OR types. We also showed that differing neural activity patterns induced the expression of different axon-sorting molecules regulating axonal segregation. On the basis of these results, we propose an activity-dependent mechanism, different from the Hebbian plasticity theory, in which specific patterns of spontaneous activity determined by the expressed ORs contribute to generate the combinatorial code of axon-sorting molecules for OR-specific glomerular segregation.

Our calcium imaging analyses in OR substitution experiments demonstrated that ORs determine spontaneous activity patterns. How are spontaneous activity patterns regulated by ORs? It has been reported that G protein–coupled receptors (GPCRs), including ORs, produce unique levels of basal cAMP (cyclic adenosine monophosphate) in a ligand-independent manner (*12*, *46*, *47*). A plausible explanation is that the OR-derived basal activity contributes to the pattern of spontaneous activity. However, mutations of a GPCR that result in altered basal cAMP levels do not affect the expression of axon-sorting molecules in OSNs (*12*). Therefore, the OR-derived basal activity is unlikely to be a determinant of spontaneous activity patterns. In this study, we found that individual OSNs show different firing patterns in response to continuous optogenetic stimulation (fig. S6D). Moreover, several voltage-dependent calcium channels and transient receptor potential channels are expressed in a subset of OSNs (*48*–*51*). It is possible that the intrinsic membrane properties vary among OSNs expressing different OR types for OR-correlated patterns of spontaneous activity. However, the mechanisms linking the membrane properties to expressed ORs remain unknown.

In this study, we demonstrated the firing pattern–dependent expression of axon-sorting molecules by optogenetic stimulation. The SVM classification indicated that optogenetic stimulation experiments mimicked physiological conditions (Fig. 3F and fig. S11). We found that phasic, repetitive short bursts of neural activity induced *Kirrel2* expression, whereas prolonged durations of bursting activity induced the expression of *Sema7A* and *PCDH10*. Increased levels of *Kirrel2* were dependent on spike numbers and ISIs within bursts in the phasic burst stimulation (Fig. 3, D and E). The sensitivities to the burst duration might differ between *PCDH10* and *Sema7A*. We observed statistically significant up-regulation of *PCDH10* and *Sema7A* by burst durations of >20 s and >60 s, respectively (Fig. 4E). This firing pattern–dependent expression allows OSNs to separately regulate the types and levels of axon-sorting molecules to generate the combinatorial code for glomerular segregation (fig. S12).

How do OSNs decode the temporal patterns of their own neural activity into diverse expression of axon-sorting molecules? Previous studies have identified transcription factors that are activated by different patterns of calcium transients (*52*–*54*). For example, CaMKII (calcium/calmodulin-dependent protein kinase II) is activated by high-frequency calcium oscillations, whereas NFATs (nuclear factors of activated T cells) are activated by low-frequency oscillations (*55*). The differential properties (e.g., sensitivity, affinity, and kinetics) of calcium-responsive factors may provide a molecular basis for the differential readouts of neural activity patterns.

In the nervous system, neural activity is involved in various aspects of the neural development and plasticity—including cell type specification, dendritic branching, synaptic maturation, and learning and memory—through a complex program of gene regulation (*56*–*59*). Although several hundreds of genes have been identified as activity-dependent genes (*60*), their regulatory mechanisms and functions are not fully understood. In this study, we demonstrated firing pattern–dependent gene expression regulating neural circuit formation. With this strategy, neurons can generate variation through diversifying gene expression with only a single second messenger. The pattern-dependent regulation may also expand beyond development to the plasticity of neural circuits, which is the basis for learning and adapting to environmental changes throughout the lifetime.

Materials and methods

Mutant mice

All experimental procedures were performed with the approval of the animal experiment ethics committee of the University of Tokyo and Institutional Animal Care and Use Committee (IACUC) of RIKEN Kobe Branch, and in accordance with the guidelines for the care and use of laboratory animals of the University of Tokyo and RIKEN Kobe Branch. *H-Cre* mice were as described (*13*). *Ai95D*, *Ai32*, *M71-ires-Cre*, and CNG-KO mice were purchased from the Jackson Laboratory. *pGoofy-Cre* and *Kirrel2* conditional KO (RBRC06340) mice were generous gifts provided by Y. Yoshihara and H. Sakano, respectively. To generate the *H-I7* (accession no. CDB0537T: www2.clst.riken.jp/arg/TG%20mutant%20mice%20list.html) and *H-MOR28* (accession no. CDB0536T: www2.clst.riken.jp/arg/TG%20mutant%20mice%20list.html) minigene constructs, a 10.1-kb *Sac*I fragment containing the *MOR23* gene from a BAC clone of a C57BL/6 mouse (RP23-306I18) was subcloned into pBluescript II SK(+). The 2.1-kb *H enhancer* fragment (*22*) was attached to the 5′ end of the MOR23 minigene and an *ires-Cre-ires-mcherry* fragment was inserted into the 3′-UTR of the minigene. The 930-bp coding sequence of *MOR23* was replaced with that of *I7* or *MOR28*. The transgene sequences were excised by *Asc*I digestion, separated from the vector DNA by sucrose gradient centrifugation, and then microinjected into the pronuclei of CD-1 embryos.

Immunostaining and in situ hybridization

Immunostaining was performed largely as described (*22*). Mice were anesthetized with sodium pentobarbital (2.5 mg/animal) and perfused intracardially with 4% paraformaldehyde in phosphate-buffered saline (PBS). The olfactory bulb (OB) was embedded briefly in an optimal cutting temperature (OCT) compound (Tissue-Tek; Sakura Finetek) in liquid nitrogen. The olfactory epithelium (OE) was dissected and fixed overnight with 4% paraformaldehyde in PBS and decalcified in 0.5 M ethylenediaminetetraacetic acid for 8 to 10 hours at 4°C. Tissues were then incubated in 30% sucrose overnight at 4°C and embedded in an OCT compound in liquid nitrogen. Serial sections (10 μm for the OE, 12 μm for the OB) were prepared with CM3050 cryostat (Leica) and collected onto Matsunami adhesive silane-coated glass slides (Matsunami Glass). Slides were rinsed with PBS three times and incubated in a blocking buffer [5% skim milk in PBS with 0.2% Triton X-100 (PBST)] for 1 hour at room temperature (RT). After the blocking, the slides were incubated with primary antibodies overnight at RT. After being washed with PBST three times, the sections were treated with secondary antibodies (Molecular Probes) at a dilution of 1:400. The primary antibodies used in this study are listed in data S7. The VectaStain ABC Kit (Vector Laboratories Inc.) was used to obtain higher intensity in the immunostaining of ORs. In situ hybridization was performed as described (*13*). The sequences of the RNA probes that were used are listed in data S7. The full-length coding sequence for *mcherry* was subcloned into the pGEM-T vector (Promega) and used as a template.

Signal intensity measurement and statistical analysis

Optical and fluorescent images of sections were obtained using a BZ-X700 microscope (Keyence). A glomerular structure was defined by immunofluorescence signals of vesicular glutamate transporter2 (VGlut2), and staining intensities of Kirrel2, Sema7A, and PCDH10 within glomerulus were measured using ImageJ (NIH). After subtracting the background signals, staining intensities were divided by the highest staining intensity and were normalized to 100% (Fig. 1C). In Fig. 3D, signal intensities were rescaled such that the rescaled mean in the shaded side is 1. The data are presented as means ± SEM.

Optogenetic stimulation

Mice were placed on ice to anesthetize them by hypothermia and a skin incision was made over the dorsal surface of the head. Xylocaine jelly (2%, AstraZeneca) was applied to the bone overlying the OE as a local anesthetic, and a cover slip was placed over the bone to prevent the olfactory tissue from drying out. The olfactory sensory neurons (OSNs) were stimulated using 470-nm LEDs (Lex2; Brain Vision LLC). To stimulate the OE unilaterally, LEDs were placed directly outside the right side of the OE, whereas the other side was covered with thin aluminum to avoid light stimulation. After 12 hours of stimulation, the glass cover was removed from the skull and olfactory tissues were collected for reverse transcription polymerase chain reaction (RT-PCR) or in situ hybridization. For chronic stimulation, pups were wrapped tightly in gauze bandage

before stimulation and placed in an acrylic chamber. Blue LEDs were placed directly outside the dorsal side of the OE. After stimulation, pups were placed on a temperature-controlled heating pad before they were returned to their mothers. In all protocols, the light pulse duration was 3 ms with a power of 3 mW mm^{-2}. The timing, duration, and cycle of LED light stimulation were controlled with a pulse stimulator (Nihon Kohden).

RT-PCR

Quantitative PCR was performed as described (*13*). The expression levels of *Kirrel2*, *Sema7A*, and *PCDH10* were normalized to that of *CNG*. Primer sets and TaqMan probes used in this study were designed by Universal Probe Library (Roche) and Nihon Gene Research Laboratories Inc. (Miyagi). The primers and probe sequences used for RT-PCR are listed in data S7.

Slice preparation

Acute slices were prepared from neonatal mice (PD3-6). Mice were anesthetized and decapitated, and the olfactory tissue was embedded in 5% low-melting agar in Ringer's solution (125 mM NaCl, 2.5 mM KCl, 2 mM $CaCl_2$, 2 mM $MgCl_2$, 25 mM $NaHCO_3$, 10 mM HEPES, and 10 mM glucose) and cut into 200- to 300-μm-thick slices using a vibratome (Leica VT1200S) in ice-cold oxygenated artificial cerebrospinal fluid (aCSF; 125 mM NaCl, 2.5 mM KCl, 1 mM $MgCl_2$, 2 mM $CaCl_2$, 1.25 mM NaH_2PO_4, 25 mM $NaHCO_3$, and 10 mM glucose). Slices were briefly transferred to an interface chamber containing oxygenated artificial cerebrospinal fluid (aCSF) at RT.

Ex vivo culture

For ex vivo culture experiments, mice were anesthetized by hypothermia and were quickly decapitated. The nose was dissected en bloc to prepare intact septal nasal cartilage with epithelia. Samples were briefly transferred to an interface chamber containing oxygenated aCSF and were incubated at 35°C for 6 hours. After the incubation, OE samples were postfixed overnight with 4% paraformaldehyde in PBS.

Electrophysiological recording

Loose-patch recording was performed largely as described (*60*). Briefly, after anesthesia was achieved by hypothermia, mice were quickly decapitated, and the nose was dissected en bloc to prepare intact OE. The septal nasal cartilage with epithelia was placed in a submerged recording chamber with the mucus layer facing up and was continuously perfused with oxygenated aCSF at 35°C. For extracellular recording, pipettes with resistance of 4 to 8 MΩ were fabricated using the P-1000 micropipette puller (Sutter Instrument) and filled with aCSF. All recordings were performed using the Olympus BX51W0-I microscope. A 40× objective lens (0.8 numerical aperture, LUMplan FN; Olympus) was used to guide a patch pipette to individual OSNs. Recordings were performed in a loose patch configuration. A loose seal (resistance, 40 to 200 MΩ) was formed by applying gentle suction when an electrode tip contacted an OSN. Signals were band-filtered between 200 Hz and 5 kHz.

Calcium imaging and data analysis

Calcium imaging was conducted using acute slices of OE from mice expressing GCaMP6f. OE slices were placed in a recording chamber perfused with aCSF at 3 to 4 ml/s. Fluorophores were excited at 488 nm and visualized using a 507-nm long-pass emission filter. Videos were recorded at 10 frames/s for 10 min or 5 frames/s for 1 hour using a 40× water immersion objective lens (0.8 numerical aperture, CFI Apo 40XW NIR; Nikon), a Nipkow-disk confocal microscope (CSU-X1; Yokogawa Electric), and a cooled electron multiplying charge-coupled device camera (iXon DU897; Andor Technologies). Image acquisition was controlled by Andor Solis (Andor Technologies). The fluorescence change was measured as $(F_t - F_0)/F_0$, where F_t is the fluorescence intensity at a given time point and F_0 is the baseline. Automated quantification of the features of calcium transients was performed using FluoroSNNAP software (*61*). Principal components analyses were performed with Origin Pro (OriginLab). Multidimensional scaling (MDS) and support vector machine (SVM) classification were performed with MATLAB software. F1 score was calculated as a measure of the accuracy in the SVM classification (*62*).

Correlation analysis

To quantify the correlation between pairs of recorded cells, the correlation index (CI) was calculated as described (*33*, *40*). The formula was as follows:

$$\mathrm{CI} = \frac{N_{AB(-\Delta t,+\Delta t)}T}{N_{A(0,T)}N_{B(0,T)}2\Delta t}$$

where $N_{AB(-\Delta t,+\Delta t)}$ is the number of spikes from cell B that fall within $\pm\Delta t$ of any spike from A, T is the duration of the recording in seconds, and $N_{A(0,T)}$ and $N_{B(0,T)}$ are the total numbers of spikes detected from cells A and B during the recording. To evaluate the significance of deviations from the "random" baseline of the CI, surrogate data were generated through the random shuffling of real data. The spike coincidence time window in Fig. 2 was $\pm\Delta t$ = 200 ms.

REFERENCES AND NOTES

1. L. C. Katz, C. J. Shatz, Synaptic activity and the construction of cortical circuits. *Science* **274**, 1133–1138 (1996). doi: 10.1126/science.274.5290.1133; pmid: 8895456
2. L. A. Kirkby, G. S. Sack, A. Firl, M. B. Feller, A role for correlated spontaneous activity in the assembly of neural circuits. *Neuron* **80**, 1129–1144 (2013). doi: 10.1016/j.neuron.2013.10.030; pmid: 24314725
3. L. I. Zhang, M. M. Poo, Electrical activity and development of neural circuits. *Nat. Neurosci.* **4**, 1207–1214 (2001). doi: 10.1038/nn753; pmid: 11687831
4. L. Buck, R. Axel, A novel multigene family may encode odorant receptors: A molecular basis for odor recognition. *Cell* **65**, 175–187 (1991). doi: 10.1016/0092-8674(91)90418-X; pmid: 1840504
5. A. Chess, I. Simon, H. Cedar, R. Axel, Allelic inactivation regulates olfactory receptor gene expression. *Cell* **78**, 823–834 (1994). doi: 10.1016/S0092-8674(94)90562-2; pmid: 8087849
6. S. Serizawa *et al*., Negative feedback regulation ensures the one receptor–one olfactory neuron rule in mouse. *Science* **302**, 2088–2094 (2003). doi: 10.1126/science.1089122; pmid: 14593185
7. K. J. Ressler, S. L. Sullivan, L. B. Buck, Information coding in the olfactory system: Evidence for a stereotyped and highly organized epitope map in the olfactory bulb. *Cell* **79**, 1245–1255 (1994). doi: 10.1016/0092-8674(94)90015-9; pmid: 7528109
8. P. Mombaerts *et al*., Visualizing an olfactory sensory map. *Cell* **87**, 675–686 (1996). doi: 10.1016/S0092-8674(00)81387-2; pmid: 8929536
9. R. Vassar *et al*., Topographic organization of sensory projections to the olfactory bulb. *Cell* **79**, 981–991 (1994). doi: 10.1016/0092-8674(94)90029-9; pmid: 8001145
10. L. Luo, J. G. Flanagan, Development of continuous and discrete neural maps. *Neuron* **56**, 284–300 (2007). doi: 10.1016/j.neuron.2007.10.014; pmid: 17964246
11. H. Sakano, Neural map formation in the mouse olfactory system. *Neuron* **67**, 530–542 (2010). doi: 10.1016/j.neuron.2010.07.003; pmid: 20797531
12. A. Nakashima *et al*., Agonist-independent GPCR activity regulates anterior-posterior targeting of olfactory sensory neurons. *Cell* **154**, 1314–1325 (2013). doi: 10.1016/j.cell.2013.08.033; pmid: 24034253
13. H. Takeuchi *et al*., Sequential arrival and graded secretion of Sema3F by olfactory neuron axons specify map topography at the bulb. *Cell* **141**, 1056–1067 (2010). doi: 10.1016/j.cell.2010.04.041; pmid: 20550939
14. H. Takeuchi, H. Sakano, Neural map formation in the mouse olfactory system. *Cell. Mol. Life Sci.* **71**, 3049–3057 (2014). doi: 10.1007/s00018-014-1597-0; pmid: 24638094
15. C. R. Yu *et al*., Spontaneous neural activity is required for the establishment and maintenance of the olfactory sensory map. *Neuron* **42**, 553–566 (2004). doi: 10.1016/S0896-6273(04)00224-7; pmid: 15157418
16. A. S. Mobley *et al*., Hyperpolarization-activated cyclic nucleotide-gated channels in olfactory sensory neurons regulate axon extension and glomerular formation. *J. Neurosci.* **30**, 16498–16508 (2010). doi: 10.1523/JNEUROSCI.4225-10.2010; pmid: 21147989
17. T. Ishii *et al*., Monoallelic expression of the odourant receptor gene and axonal projection of olfactory sensory neurones. *Genes Cells* **6**, 71–78 (2001). doi: 10.1046/j.1365-2443.2001.00398.x; pmid: 11277098
18. P. Feinstein, P. Mombaerts, A contextual model for axonal sorting into glomeruli in the mouse olfactory system. *Cell* **117**, 817–831 (2004). doi: 10.1016/j.cell.2004.05.011; pmid: 15186781
19. D. O. Hebb, *The Organization of Behavior: A Neuropsychological Theory* (Wiley, 1949).
20. A. Bulfone *et al*., An olfactory sensory map develops in the absence of normal projection neurons or GABAergic interneurons. *Neuron* **21**, 1273–1282 (1998). doi: 10.1016/S0896-6273(00)80647-9; pmid: 9883721
21. J. A. St. John, H. J. Clarris, S. McKeown, S. Royal, B. Key, Sorting and convergence of primary olfactory axons are independent of the olfactory bulb. *J. Comp. Neurol.* **464**, 131–140 (2003). doi: 10.1002/cne.10777; pmid: 12898607
22. S. Serizawa *et al*., A neuronal identity code for the odorant receptor-specific and activity-dependent axon sorting. *Cell* **127**, 1057–1069 (2006). doi: 10.1016/j.cell.2006.10.031; pmid: 17129788
23. T. Cutforth *et al*., Axonal ephrin-As and odorant receptors: Coordinate determination of the olfactory sensory map. *Cell* **114**, 311–322 (2003). doi: 10.1016/S0092-8674(03)00568-3; pmid: 12914696
24. T. Kaneko-Goto, S. Yoshihara, H. Miyazaki, Y. Yoshihara, BIG-2 mediates olfactory axon convergence to target glomeruli. *Neuron* **57**, 834–846 (2008). doi: 10.1016/j.neuron.2008.01.023; pmid: 18367085
25. E. O. Williams *et al*., Delta Protocadherin 10 is Regulated by Activity in the Mouse Main Olfactory System. *Front. Neural Circuits* **5**, 9 (2011). doi: 10.3389/fncir.2011.00009; pmid: 21897809
26. G. Mountoufaris *et al*., Multicluster Pcdh diversity is required for mouse olfactory neural circuit assembly. *Science* **356**, 411–414 (2017). doi: 10.1126/science.aai8801; pmid: 28450637
27. N. Ihara, A. Nakashima, N. Hoshina, Y. Ikegaya, H. Takeuchi, Differential expression of axon-sorting molecules in mouse olfactory sensory neurons. *Eur. J. Neurosci.* **44**, 1998–2003 (2016). pmid: 27207328
28. J. Reisert, Origin of basal activity in mammalian olfactory receptor neurons. *J. Gen. Physiol.* **136**, 529–540 (2010). doi: 10.1085/jgp.201010528; pmid: 20974772
29. T. Connelly, A. Savigner, M. Ma, Spontaneous and sensory-evoked activity in mouse olfactory sensory neurons with defined odorant receptors. *J. Neurophysiol.* **110**, 55–62 (2013). doi: 10.1152/jn.00910.2012; pmid: 23596334

30. E. A. Hallem, M. G. Ho, J. R. Carlson, The molecular basis of odor coding in the Drosophila antenna. *Cell* **117**, 965–979 (2004). doi: 10.1016/j.cell.2004.05.012; pmid: 15210116
31. A. Dahanukar, E. A. Hallem, J. R. Carlson, Insect chemoreception. *Curr. Opin. Neurobiol.* **15**, 423–430 (2005). doi: 10.1016/j.conb.2005.06.001; pmid: 16006118
32. C. Y. Su, K. Menuz, J. R. Carlson, Olfactory perception: Receptors, cells, and circuits. *Cell* **139**, 45–59 (2009). doi: 10.1016/j.cell.2009.09.015; pmid: 19804753
33. R. J. Pasterkamp, J. J. Peschon, M. K. Spriggs, A. L. Kolodkin, Semaphorin 7A promotes axon outgrowth through integrins and MAPKs. *Nature* **424**, 398–405 (2003). doi: 10.1038/nature01790; pmid: 12879062
34. L. J. Brunet, G. H. Gold, J. Ngai, General anosmia caused by a targeted disruption of the mouse olfactory cyclic nucleotide-gated cation channel. *Neuron* **17**, 681–693 (1996). doi: 10.1016/S0896-6273(00)80200-7; pmid: 8893025
35. T. W. Chen *et al*., Ultrasensitive fluorescent proteins for imaging neuronal activity. *Nature* **499**, 295–300 (2013). doi: 10.1038/nature12354; pmid: 23868258
36. C. L. Torborg, M. B. Feller, Spontaneous patterned retinal activity and the refinement of retinal projections. *Prog. Neurobiol.* **76**, 213–235 (2005). doi: 10.1016/j.pneurobio.2005.09.002; pmid: 16280194
37. M. Meister, R. O. Wong, D. A. Baylor, C. J. Shatz, Synchronous bursts of action potentials in ganglion cells of the developing mammalian retina. *Science* **252**, 939–943 (1991). doi: 10.1126/science.2035024; pmid: 2035024
38. T. McLaughlin, C. L. Torborg, M. B. Feller, D. D. O'Leary, Retinotopic map refinement requires spontaneous retinal waves during a brief critical period of development. *Neuron* **40**, 1147–1160 (2003). doi: 10.1016/S0896-6273(03)00790-6; pmid: 14687549
39. T. A. Seabrook, T. J. Burbridge, M. C. Crair, A. D. Huberman, Architecture, Function, and Assembly of the Mouse Visual System. *Annu. Rev. Neurosci.* **40**, 499–538 (2017). doi: 10.1146/annurev-neuro-071714-033842; pmid: 28772103
40. A. Fleischmann *et al*., Mice with a "monoclonal nose": Perturbations in an olfactory map impair odor discrimination. *Neuron* **60**, 1068–1081 (2008). doi: 10.1016/j.neuron.2008.10.046; pmid: 19109912
41. M. Q. Nguyen, Z. Zhou, C. A. Marks, N. J. Ryba, L. Belluscio, Prominent roles for odorant receptor coding sequences in allelic exclusion. *Cell* **131**, 1009–1017 (2007). doi: 10.1016/j.cell.2007.10.050; pmid: 18045541
42. A. Vassalli, A. Rothman, P. Feinstein, M. Zapotocky, P. Mombaerts, Minigenes impart odorant receptor-specific axon guidance in the olfactory bulb. *Neuron* **35**, 681–696 (2002). doi: 10.1016/S0896-6273(02)00793-6; pmid: 12194868
43. L. Madisen *et al*., A toolbox of Cre-dependent optogenetic transgenic mice for light-induced activation and silencing. *Nat. Neurosci.* **15**, 793–802 (2012). doi: 10.1038/nn.3078; pmid: 22446880
44. R. O. Wong, M. Meister, C. J. Shatz, Transient period of correlated bursting activity during development of the mammalian retina. *Neuron* **11**, 923–938 (1993). doi: 10.1016/0896-6273(93)90122-8; pmid: 8240814
45. M. B. Feller, D. P. Wellis, D. Stellwagen, F. S. Werblin, C. J. Shatz, Requirement for cholinergic synaptic transmission in the propagation of spontaneous retinal waves. *Science* **272**, 1182–1187 (1996). doi: 10.1126/science.272.5265.1182; pmid: 8638165
46. B. K. Kobilka, X. Deupi, Conformational complexity of G-protein-coupled receptors. *Trends Pharmacol. Sci.* **28**, 397–406 (2007). doi: 10.1016/j.tips.2007.06.003; pmid: 17629961
47. R. A. Bond, A. P. Ijzerman, Recent developments in constitutive receptor activity and inverse agonism, and their potential for GPCR drug discovery. *Trends Pharmacol. Sci.* **27**, 92–96 (2006). doi: 10.1016/j.tips.2005.12.007; pmid: 16406086
48. M. Pyrski *et al*., Trpm5 expression in the olfactory epithelium. *Mol. Cell. Neurosci.* **80**, 75–88 (2017). doi: 10.1016/j.mcn.2017.02.002; pmid: 28188885
49. M. Pyrski *et al*., P/Q Type Calcium Channel Cav2.1 Defines a Unique Subset of Glomeruli in the Mouse Olfactory Bulb. *Front. Cell. Neurosci.* **12**, 295 (2018). doi: 10.3389/fncel.2018.00295; pmid: 30233329
50. N. Kanageswaran *et al*., Deep sequencing of the murine olfactory receptor neuron transcriptome. *PLOS ONE* **10**, e0113170 (2015). doi: 10.1371/journal.pone.0113170; pmid: 25590618
51. M. Omura, P. Mombaerts, Trpc2-expressing sensory neurons in the main olfactory epithelium of the mouse. *Cell Rep.* **8**, 583–595 (2014). doi: 10.1016/j.celrep.2014.06.010; pmid: 25001287
52. M. Behar, A. Hoffmann, Understanding the temporal codes of intra-cellular signals. *Curr. Opin. Genet. Dev.* **20**, 684–693 (2010). doi: 10.1016/j.gde.2010.09.007; pmid: 20956081
53. K. M. Tyssowski *et al*., Different Neuronal Activity Patterns Induce Different Gene Expression Programs. *Neuron* **98**, 530–546.e11 (2018). doi: 10.1016/j.neuron.2018.04.001; pmid: 29681534
54. E. Smedler, P. Uhlén, Frequency decoding of calcium oscillations. *Biochim. Biophys. Acta* **1840**, 964–969 (2014). doi: 10.1016/j.bbagen.2013.11.015; pmid: 24269537
55. H. Fujii *et al*., Nonlinear decoding and asymmetric representation of neuronal input information by CaMKIIα and calcineurin. *Cell Rep.* **3**, 978–987 (2013). doi: 10.1016/j.celrep.2013.03.033; pmid: 23602566
56. N. C. Spitzer, Electrical activity in early neuronal development. *Nature* **444**, 707–712 (2006). doi: 10.1038/nature05300; pmid: 17151658
57. P. L. Greer, M. E. Greenberg, From synapse to nucleus: Calcium-dependent gene transcription in the control of synapse development and function. *Neuron* **59**, 846–860 (2008). doi: 10.1016/j.neuron.2008.09.002; pmid: 18817726
58. Y. Chen, A. Ghosh, Regulation of dendritic development by neuronal activity. *J. Neurobiol.* **64**, 4–10 (2005). doi: 10.1002/neu.20150; pmid: 15884010
59. A. E. West, M. E. Greenberg, Neuronal activity-regulated gene transcription in synapse development and cognitive function. *Cold Spring Harb. Perspect. Biol.* **3**, a005744 (2011). doi: 10.1101/cshperspect.a005744; pmid: 21555405
60. S. W. Flavell, M. E. Greenberg, Signaling mechanisms linking neuronal activity to gene expression and plasticity of the nervous system. *Annu. Rev. Neurosci.* **31**, 563–590 (2008). doi: 10.1146/annurev.neuro.31.060407.125631; pmid: 18558867
61. T. P. Patel, K. Man, B. L. Firestein, D. F. Meaney, Automated quantification of neuronal networks and single-cell calcium dynamics using calcium imaging. *J. Neurosci. Methods* **243**, 26–38 (2015). doi: 10.1016/j.jneumeth.2015.01.020; pmid: 25629800
62. C. J. van Rijsbergen, *Information Retrieval* (Butterworths, ed. 2, 1979).

ACKNOWLEDGMENTS

We thank Y. Yoshihara for providing the *pGoofy-Cre* mice, H. Sakano for providing the *Kirrel2* conditional KO mice, and C. Greer, S. L. Zipursky, and K. Katori for their valuable comments. **Funding:** Supported by the Mitsubishi Foundation, the Takeda Science Foundation, the Japan Foundation for Applied Enzymology, the Kato Memorial Bioscience Foundation, the Japan Science and Technology Agency, PRESTO, JST ERATO grant JPMJER1801, the Human Frontier Science Program (RGP0019/2016), JSPS Grants-in-Aid for Scientific Research grant 18H05525, and JSPS KAKENHI grants 24370087, 15K21029, and 18K14712. This work was conducted partially as a program at the International Research Center for Neurointelligence (WPI-IRCN) of the University of Tokyo Institutes for Advanced Study. **Author contributions:** A.N., N.I., Y.I., and H.T. conceived the experiments; A.N., N.I., M.S., H.K., and H.T. performed the experiments and analyzed the data; all authors contributed to the writing the manuscript and provided helpful comments; and all authors read and approved the final manuscript. **Competing interests:** Authors declare no competing interests. **Data and materials availability:** All data are available in the manuscript or supplementary materials. All materials can be requested from H.T.

SUPPLEMENTARY MATERIALS

science.sciencemag.org/content/365/6448/eaaw5030/suppl/DC1
Figs. S1 to S12
Movies S1 and S2
Data S1 to S7

3 January 2019; accepted 23 May 2019
Published online 6 June 2019
10.1126/science.aaw5030

RESEARCH ARTICLES SUMMARY

CELL BIOLOGY

The heme-regulated inhibitor is a cytosolic sensor of protein misfolding that controls innate immune signaling

Mena Abdel-Nour, Leticia A. M. Carneiro, Jeffrey Downey, Jessica Tsalikis, Ahmed Outlioua, Dave Prescott, Leandro Silva Da Costa, Elise S. Hovingh, Armin Farahvash, Ryan G. Gaudet, Raphael Molinaro, Rob van Dalen, Charles C. Y. Lau, Farshad C. Azimi, Nichole K. Escalante, Aaron Trotman-Grant, Jeffrey E. Lee, Scott D. Gray-Owen, Maziar Divangahi, Jane-Jane Chen, Dana J. Philpott, Damien Arnoult*, Stephen E. Girardin*

INTRODUCTION: Innate immunity relies on several families of pattern recognition molecules (PRMs) that broadly recognize microbial motifs and danger signals. Upon activation, multiple PRMs assemble into very large protein complexes or "signalosomes," and some PRM adaptors, such as RIP2, MAVS, TRIF, and ASC, have even been shown to form amyloid-like filaments. The assembly of very large molecular structures needs to be tightly regulated to avoid accumulation of potential toxic protein aggregates, such as those causing neurodegeneration. However, the means by which PRM signalosome assembly is controlled remains poorly understood.

RATIONALE: The integrated stress response (ISR) is a highly conserved pathway that triggers eIF2α phosphorylation, a key checkpoint in the control of cellular responses to various stresses. While studying the impact of the ISR on innate immunity, we discovered that heme-regulated inhibitor (HRI), one of the four known eIF2α kinases, was essential for pro-inflammatory cytokine responses to intracellular bacterial pathogens. We sought to determine the underlying mechanism.

RESULTS: We found that HRI was critical for signaling downstream of NOD1 and NOD2, two intracellular PRMs of the nucleotide-binding domain leucine-rich repeat (NLR) protein superfamily that detect bacterial peptidoglycan and induce pro-inflammatory NF-κB signaling. Because HRI function had been previously associated with proteotoxicity, we speculated that it might control the assembly of NOD signalosomes. We indeed observed that HRI, together with the heat shock protein HSPB8, was necessary for the folding and release from endomembranes of NOD signalosomes after peptidoglycan stimulation. Presynthesized HSPB8 was released from HRI and was rapidly recruited to the PRM complex. Concomitantly, HRI was activated, triggering a pathway dependent on eIF2α, ATF4, and ATF3, which resulted in transcriptional up-regulation of HSPB8. The HRI/eIF2α/ATF4/HSPB8 signaling axis is thus critical for controlling the scaffolding of NOD signalosome and the sustained activation of NF-κB signaling. We further demonstrated that the HRI/eIF2α signaling axis was also essential for signaling downstream of MAVS and TRIF but dispensable for pathways dependent on MyD88 or STING; whether HSPB8 (or another HSP not yet identified) is involved in the HRI-dependent control of these multiple PRM pathways remains to be characterized. We further noticed that the PRM pathways regulated by HRI share the property that their adaptor proteins can form amyloid-like filaments in vitro. Indeed, overexpression of these proteins activated HRI, which suggests that potentially toxic molecular superstructures, such as self-assembling amyloid-like filaments, may be direct activators of the HRI signaling axis. In agreement with these findings, expression of α-synuclein, a protein that forms toxic amyloid filaments that are a pathological hallmark of Parkinson's disease, induced *ATF3* and *HSPB8* expression through HRI.

ON OUR WEBSITE

Read the full article at http://dx.doi.org/10.1126/science.aaw4144

CONCLUSION: The HRI/eIF2α/HSPB8 signaling axis identified here shares a remarkable homology with the unfolded protein response (UPR), which regulates protein folding in the endoplasmic reticulum. We propose that HRI, eIF2α, and HSPB8 define a novel cytosolic UPR (cUPR) essential for optimal innate immune signaling by large molecular platforms. Future studies should be aimed at delineating the role of the cUPR in the control and clearance of pro-aggregative proteins, such as those implicated in neurodegeneration. ■

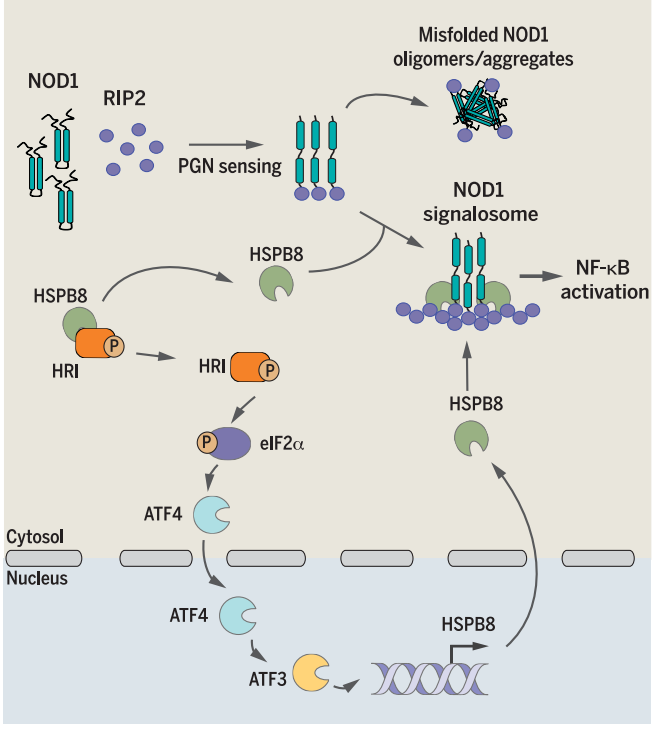

The cytoplasmic unfolded protein response controls NOD1 signaling. Upon detection of peptidoglycan (PGN), NOD1 and RIP2 undergo conformational changes, leading to the displacement of HSPB8 from HRI toward NOD1 signalosomes and subsequent NF-κB activation. Simultaneously, the dissociation of HSPB8 from HRI leads to the phosphorylation of eIF2α and the synthesis of ATF4 and ATF3, which induces de novo HSPB8 expression to sustain signaling.

The list of author affiliations is available in the full article online.
*Corresponding author. Email: stephen.girardin@utoronto.ca (S.E.G.); damien.arnoult@inserm.fr (D.A.)
Cite this article as M. Abdel-Nour *et al.*, *Science* **365**, eaaw4144 (2019). DOI: 10.1126/science.aaw4144

RESEARCH ARTICLE

CELL BIOLOGY

The heme-regulated inhibitor is a cytosolic sensor of protein misfolding that controls innate immune signaling

Mena Abdel-Nour[1], Leticia A. M. Carneiro[1]*, Jeffrey Downey[2], Jessica Tsalikis[1], Ahmed Outlioua[3,4], Dave Prescott[1,5], Leandro Silva Da Costa[3], Elise S. Hovingh[1], Armin Farahvash[1], Ryan G. Gaudet[6], Raphael Molinaro[1], Rob van Dalen[1]†, Charles C. Y. Lau[1,5], Farshad C. Azimi[1], Nichole K. Escalante[5]‡, Aaron Trotman-Grant[5], Jeffrey E. Lee[1], Scott D. Gray-Owen[6], Maziar Divangahi[2], Jane-Jane Chen[7], Dana J. Philpott[5], Damien Arnoult[3]§, Stephen E. Girardin[1]§

Multiple cytosolic innate sensors form large signalosomes after activation, but this assembly needs to be tightly regulated to avoid accumulation of misfolded aggregates. We found that the eIF2α kinase heme-regulated inhibitor (HRI) controls NOD1 signalosome folding and activation through a process requiring eukaryotic initiation factor 2α (eIF2α), the transcription factor ATF4, and the heat shock protein HSPB8. The HRI/eIF2α signaling axis was also essential for signaling downstream of the innate immune mediators NOD2, MAVS, and TRIF but dispensable for pathways dependent on MyD88 or STING. Moreover, filament-forming α-synuclein activated HRI-dependent responses, which suggests that the HRI pathway may restrict toxic oligomer formation. We propose that HRI, eIF2α, and HSPB8 define a novel cytosolic unfolded protein response (cUPR) essential for optimal innate immune signaling by large molecular platforms, functionally homologous to the PERK/eIF2α/HSPA5 axis of the endoplasmic reticulum UPR.

The integrated stress response (ISR) is an evolutionarily conserved signaling cascade through which cells can cope with their environment and adjust their metabolic status. Detection of various cellular stresses by the ISR is performed by four kinases: PKR (protein kinase R), GCN2 (general control nonderepressible 2), PERK (protein kinase RNA-like ER kinase), and HRI (heme-regulated inhibitor). PKR detects viral double-stranded RNA (dsRNA); GCN2 senses uncharged tRNAs that accumulate in cells lacking free amino acids (AA) (*1*, *2*); PERK detects accumulation of misfolded proteins in the endoplasmic reticulum (ER), also known as ER stress (*3*); and HRI responds to a broad range of stresses, including heme deprivation, oxidative stress, and heat shock (*4*–*7*), although cytosolic proteotoxicity may represent an overarching trigger for HRI (*8*). These four kinases phosphorylate eIF2α (eukaryotic initiation factor 2α) on Ser^{51}, which results in a temporary block in translation and transcriptional reprograming to cope with the encountered stress.

[1]Department of Laboratory Medicine and Pathobiology, University of Toronto, Toronto, ON, Canada. [2]Department of Microbiology and Immunology, McGill University, Montreal, QC, Canada. [3]INSERM U1197, Hôpital Paul Brousse, Bâtiment Lavoisier, 94807 Villejuif Cedex, France. [4]Molecular Genetics and Immunophysiopathology Research Team, Health and Environment Laboratory, Aïn Chock Faculty of Sciences, Hassan II University of Casablanca, Casablanca, Morocco. [5]Department of Immunology, University of Toronto, Toronto, ON, Canada. [6]Department of Molecular Genetics, University of Toronto, Toronto, ON, Canada. [7]Institute of Medical Engineering and Science, Massachusetts Institute of Technology, Cambridge, MA, USA.
*Present address: Instituto de Microbiologia, Federal University of Rio de Janeiro, Brazil. †Present address: Interfaculty Institute of Microbiology and Infection Medicine, Infection Biology, University of Tübingen, Tübingen, Germany. ‡Present address: Department of Pathology, Stanford University, Palo Alto, CA, USA.
§Corresponding author. Email: stephen.girardin@utoronto.ca (S.E.G.); damien.arnoult@inserm.fr (D.A.)

The HRI/eIF2α axis is required for inflammatory responses during infection

To characterize the role of the ISR in host responses to bacterial pathogens, we infected mouse embryonic fibroblasts (MEFs), expressing either the wild-type form of eIF2α or a knock-in (KI) mutation encoding the $Ser^{51} \rightarrow$ Ala (S51A) substitution, with *Salmonella*, *Shigella*, and *Listeria*, which induce eIF2α phosphorylation (*9*–*11*). In line with the established role of eIF2α phosphorylation in stress granule formation, infection with the three pathogens induced stress granule accumulation in wild-type but not KI MEFs (fig. S1, A to C). However, we surprisingly noticed that the secretion of pro-inflammatory cytokines (Fig. 1A and fig. S1, D to H) was blunted in KI MEFs relative to wild-type cells in response to the three pathogens in a manner independent of bacterial replication (fig. S1, I to K). The reduced secretion of Cxcl1 in the KI MEFs correlated with reduced expression of *Cxcl1* (Fig. 1B), showing that the ISR is required for transcriptional cytokine responses to infection. *Shigella* infection induced the expression of ATF3 and ATF4 (fig. S2), and as expected, up-regulation of the ISR-associated gene *Atf3* was dependent on eIF2α phosphorylation and ATF4, an essential transcription factor that, upon eIF2α phosphorylation, mediates transcriptional reprogramming during the ISR (*12*) (fig. S3).

In agreement with results obtained in KI cells, *Cxcl1* expression after *Shigella* infection was blunted in $Atf4^{-/-}$ MEFs (Fig. 1C). Down-regulation of *Shigella*-induced cytokine expression in ISR-deficient cells was not a consequence of exacerbated translation, as reduced translation was observed in $Atf4^{-/-}$ MEFs (fig. S4). Finally, the impact of acute inhibition of the ISR was analyzed by using ISRIB, a specific inhibitor of eIF2α phosphorylation. ISRIB treatment potently inhibited *IL8*, *ATF3*, and *GADD34* expression in *Shigella*-infected cells at doses that did not alter translation (fig. S5). Thus, phosphorylation of eIF2α is essential for pro-inflammatory and stress responses during bacterial infection.

We next aimed to identify the eIF2α kinases that mediate the ISR during bacterial infection. Our previous work has shown that invasive bacterial pathogens trigger GCN2 activation (*9*, *10*), but the contribution of the other eIF2α kinases remains undetermined. Upon infection of HeLa cells with *Shigella*, we observed the accumulation of a slower-migrating form of HRI, indicative of phosphorylation and activation, and this effect increased at later times of infection (Fig. 1D). As a control, treatment with arsenite, a known HRI inducer, resulted in full conversion of HRI to its slower-migrating form (Fig. 1D). HRI activation is also associated with its dissociation from Hsc70 (*13*); both *Shigella* infection and arsenite treatment induced HRI/Hsc70 dissociation (fig. S6). We next assessed the relative contributions of HRI and GCN2 in triggering the ISR during infection by knocking down their expression (fig. S7, A and B). Although the formation of stress granules after arsenite treatment or AA starvation depended on HRI and GCN2, respectively (figs. S7C and S8), we observed a partial contribution of each kinase to *Shigella*-induced stress granule formation and eIF2α phosphorylation (fig. S7, D and E). Transient knockdown of both HRI and GCN2 [double knockdown (DKD)] resulted in near-complete abolishment of stress granule formation and eIF2α phosphorylation after *Shigella* infection, relative to scrambled cells (Fig. 1E and fig. S7D), thus showing that HRI and GCN2 cooperate to trigger the ISR during *Shigella* infection.

We next analyzed the relative contributions of HRI and GCN2 to the transcriptional responses induced by *Shigella*. Whereas *ATF3* expression after arsenite treatment or AA starvation was dependent on HRI and GCN2, respectively (fig. S7F), *ATF3* induction during *Shigella* infection was dependent on both HRI and GCN2 (Fig. 1F). Moreover, the oxidative stress response gene *HMOX1* was induced in an HRI-dependent manner, whereas the AA metabolism gene *ASNS* was

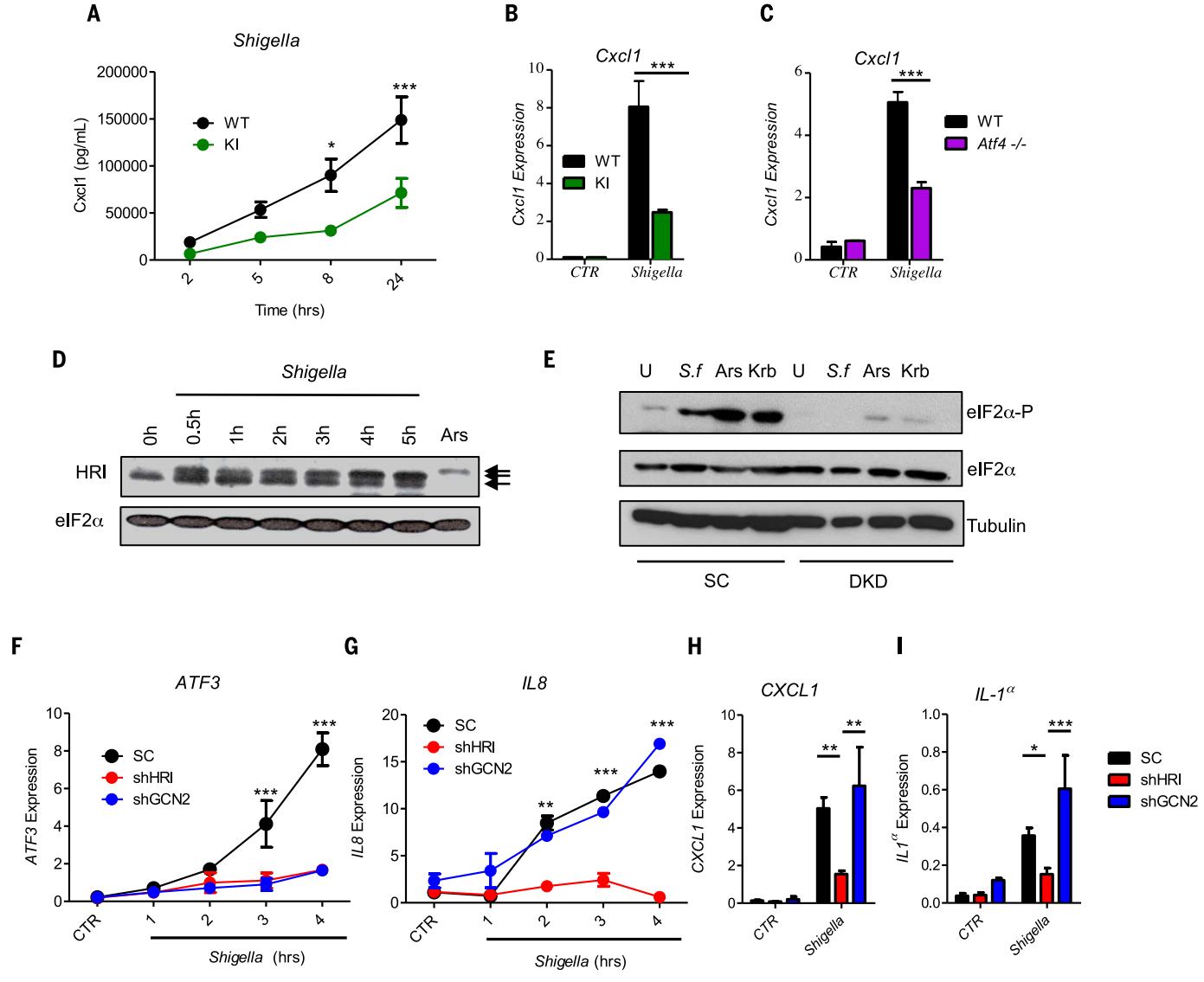

Fig. 1. The HRI/eIF2α axis is required for inflammatory responses during infection. (**A**) Cxcl1 secretion from the supernatants of wild-type (WT) and eIF2α S51A knock-in (KI) MEFs after infection with *Shigella* for the indicated times, as measured by ELISA. (**B** and **C**) Expression of *Cxcl1* in WT and KI MEFs (B) and WT and Atf4 knockout ($Atf4^{-/-}$) MEFs (C) left unstimulated (CTR) or after infection with *Shigella*. (**D**) HeLa cells infected with *Shigella* or treated for 1 hour with 300 μM sodium arsenite (Ars) and analyzed by immunoblotting. (**E**) HeLa cells transduced with lentiviral particles targeting a scrambled sequence (SC), both HRI and GCN2 [double knockdown (DKD)] left untreated (U), infected 1 hour with *Shigella* (*S.f*), treated 1 hour with 300 μM Ars or treated with Krebs-Ringer buffer (KRB) for 45 min and analyzed by immunoblotting. (**F** and **G**) Expression of *ATF3* (F) and *IL8* (G) in HeLa cells transduced with lentiviral particles targeting a scrambled sequence (SC), HRI (shHRI), or GCN2 (shGCN2) and infected with *Shigella*. (**H** and **I**) Expression of *CXCL1* (H) and *IL1α* (I) in scrambled, HRI KD, and GCN2 KD HeLa cells infected with *Shigella*. Data are means ± SD from three independent experiments. *$P < 0.05$, **$P < 0.01$, ***$P < 0.001$.

induced in a GCN2-dependent manner in *Shigella*-infected cells (fig. S7, G to J). During infection with *Shigella*, expression of *IL-8*, *CXCL1*, and *IL-1α* (Fig. 1, G to I) was strongly repressed in HRI knockdown (KD) cells, whereas knockdown of GCN2 had no effect. Down-regulation of *Shigella*-induced cytokine expression in HRI KD cells was not a consequence of exacerbated translation, as reduced translation was observed relative to scramble control and GCN2 KD cells (fig. S9). Thus, although both HRI and GCN2 are needed for the full ISR during *Shigella* infection, HRI is the sole eIF2α kinase controlling ISR-dependent pro-inflammatory responses to this pathogen (fig. S10).

HRI is essential for NOD1- and NOD2-driven inflammatory responses

In nonmyeloid cells, the NOD1/2–NF-κB axis is critical for inflammatory signaling in response to *Shigella* (*14*–*16*). After *Shigella* infection, NF-κB activation was blunted in HRI KD cells (Fig. 2A and fig. S11A). The decreased NF-κB response was not due to a lack of bacterial invasion or replication (fig. S11B) and was independent from translation regulation, because p65 nuclear translocation after *Shigella* infection occurred prior to translation arrest (fig. S12). In agreement with this finding, the expression of *Cxcl1* and *Il6* (Fig. 2, B and C) was markedly reduced in *Shigella*-infected $Hri^{-/-}$ MEFs relative to $Hri^{+/+}$ cells. Knockdown of HRI in HCT116 cells significantly blunted *IL-8* expression in response to the NOD1 and NOD2 ligands (Fig. 2D), which suggests that HRI directly controls NOD1/2-dependent signaling. As a control, we noted that the expression of

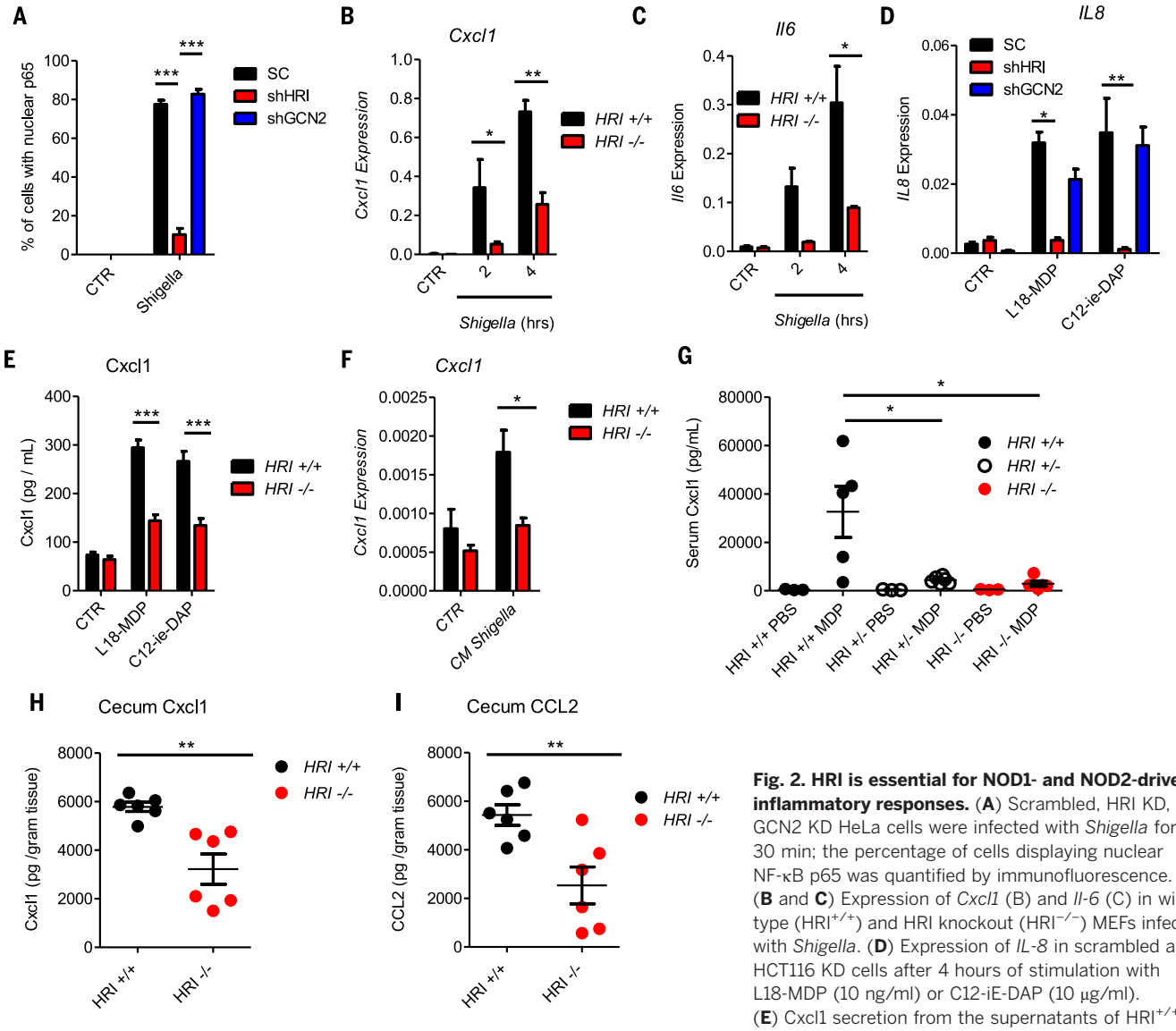

Fig. 2. HRI is essential for NOD1- and NOD2-driven inflammatory responses. (**A**) Scrambled, HRI KD, and GCN2 KD HeLa cells were infected with *Shigella* for 30 min; the percentage of cells displaying nuclear NF-κB p65 was quantified by immunofluorescence. (**B** and **C**) Expression of *Cxcl1* (B) and *Il-6* (C) in wild-type ($HRI^{+/+}$) and HRI knockout ($HRI^{-/-}$) MEFs infected with *Shigella*. (**D**) Expression of *IL-8* in scrambled and HCT116 KD cells after 4 hours of stimulation with L18-MDP (10 ng/ml) or C12-iE-DAP (10 μg/ml). (**E**) Cxcl1 secretion from the supernatants of $HRI^{+/+}$ and $HRI^{-/-}$ bone marrow–derived macrophages (BMDMs) stimulated for 6 hours with L18-MDP (10 ng/ml) or C12-iE-DAP (10 μg/ml), as measured by ELISA. (**F**) Expression of *Cxcl1* in intestinal organoids derived from $HRI^{+/+}$ and $HRI^{-/-}$ mice treated for 4 hours with *Shigella* conditioned medium (CM *Shigella*). (**G**) Serum Cxcl1 in $HRI^{+/+}$, HRI heterozygous ($HRI^{+/-}$), and $HRI^{-/-}$ mice after intraperitoneal injection with MDP, as measured by ELISA. (**H** and **I**) Cxcl1 (H) and CCL2 (I) in the cecum homogenate of $HRI^{+/+}$ and $HRI^{-/-}$ mice 4 days after infection with *Citrobacter rodentium*, as measured by ELISA. Graphs represent means ± SD from three to five independent experiments. *$P < 0.05$, **$P < 0.01$, ***$P < 0.001$ (two-way ANOVA followed by Tukey multiple-comparisons test).

NOD1 and *NOD2* was unaffected by HRI or GCN2 knockdown (fig. S13, A and B). Cxcl1 secretion was also reduced in $Hri^{-/-}$ bone marrow–derived macrophages (BMDMs) stimulated with NOD ligands either directly (Fig. 2E) or in synergy with lipopolysaccharide (LPS) stimulation (fig. S13C). Similarly, *Cxcl1* expression was reduced in $Hri^{-/-}$ organoids stimulated with *Shigella* culture supernatant (Fig. 2F). Intraperitoneal injection of the NOD2 ligand muramyl dipeptide (MDP) triggered a blunted secretion of Cxcl1 in the serum of $Hri^{-/-}$ mice relative to $Hri^{+/+}$ littermates (Fig. 2G), a reduced infiltration of neutrophils into the peritoneum (fig. S13, D and E), and a smaller release of interleukin (IL)–1β into the peritoneal cavity (fig. S13F). Similar effects were noted when $Hri^{-/-}$, $Hri^{+/-}$, or $Hri^{+/+}$ mice were injected with the NOD1 agonist FK-156 (fig. S13, G and H). To characterize the role played by HRI in an in vivo model of infection driven partly by NOD1 and NOD2 (*17*, *18*), we infected $Hri^{-/-}$ and $Hri^{+/+}$ mice with *Citrobacter rodentium*. Significantly less cecal Cxcl1, Ccl2, and serum Cxcl1 (Fig. 2, H and I, and fig. S13I), as well as a trend for reduced serum Ccl2 and cecal Il6 (fig. S13, J and K), were observed in *C. rodentium*–infected $Hri^{-/-}$ mice relative to $Hri^{+/+}$ littermates, in line with studies demonstrating reduced serum IL-6 in $Hri^{-/-}$ mice during *Listeria* infection (*19*). This blunted pro-inflammatory response was not due to differences in colonization, because both groups of mice displayed a similar bacterial burden (fig. S13L). Together, these results demonstrate a key role for HRI in controlling NOD1/2-driven pro-inflammatory responses in cell lines, in primary cells, and in vivo.

The HRI signaling axis controls the folding and solubility of NOD1 oligomers

We speculated that HRI might control NOD1/2 signaling at the level of complex formation. Scramble control or shHRI (short hairpin HRI) cells transfected with NOD1-HA (NOD1 fused to hemagglutinin) and either unstimulated or stimulated with C12-iE-DAP were lysed in non-ionic (NP-40) or ionic [radioimmunoprecipitation assay (RIPA)] buffers. Stimulation with C12-iE-DAP resulted in the release of NOD1 into the soluble fraction of NP-40–lysed cells, and analysis by blue

native polyacrylamide gel electrophoresis (PAGE) revealed that the released NOD1 was in the form of large oligomers (Fig. 3A, left panels). Interestingly, although NOD1 was expressed normally in shHRI cells, stimulation with C12-iE-DAP failed to release the protein into the soluble fraction, as it remained mainly insoluble (Fig. 3A, left panels). To determine whether NOD1 proteins did not form oligomers at all upon stimulation or whether those oligomers did form but could not be solubilized by NP-40, we performed a similar analysis in cells lysed with RIPA, which strips most non-transmembrane proteins from membranes. Using this buffer, NOD1 complexes could now be solubilized in shHRI cells, and blue native PAGE analysis revealed that they were constitutively found as large complexes (Fig. 3A, right panels). Thus, NOD1 forms large signaling platforms, or signalosomes, that are soluble in both ionic and non-ionic buffers in control cells, but these complexes can only be extracted by an ionic buffer in shHRI cells.

To gain better understanding of NOD1 complex formation in HRI-silenced cells, we transfected scramble control and shHRI cells with NOD1-HA and stimulated them with C12-iE-DAP, as above, or left them unstimulated (Fig. 3A). These cells were then lysed in RIPA buffer, and NOD1 complexes were immunoprecipitated and incubated with the dye SYPRO Orange, whose fluorescence increases when the dye binds hydrophobic patches or misfolded proteins. To control for the robustness of the assay, we denatured the NOD1 immunocomplexes and an unrelated purified protein by boiling, resulting in increased fluorescence (Fig. 3B and fig. S14, A and B). Whereas NOD1 oligomers displayed similar fluorescence in scramble versus shHRI cells in control conditions, stimulation with C12-iE-DAP resulted in a significant increase in fluorescence only in shHRI cells (Fig. 3C and fig. S14C), which suggests improper folding of the NOD1 complexes assembled after ligand stimulation in shHRI cells. In agreement with this finding, acute inhibition of eIF2α-dependent signaling with ISRIB also increased the hydrophobicity of NOD1 complexes in cells stimulated with C12-iE-DAP (Fig. 3D). Thus, the HRI/eIF2α signaling axis controls the assembly of the NOD1 signalosomes after ligand stimulation.

The HRI-eIF2α-HSPB8 loop is essential for NOD1 and NOD2 signaling

We next aimed to determine how HRI controls NOD signalosome assembly. Heat shock protein (HSP) chaperones regulate the assembly and stability of protein complexes, so we speculated that HRI might regulate NOD signalosome assembly through the expression and action of HSPs. In our earlier microarray analysis of *Shigella*-induced genes (*9*), *HSPB8* was among the most up-regulated genes and was the only HSP regulated by *Shigella* (fig. S15, A and B), an observation that we confirmed in wild-type MEFs (Fig. 4A). *Hspb8* was also up-regulated by the unfolded protein response (UPR)/ER stress inducer thapsigargin (Fig. 4A), whereas the UPR/ER stress chaperone *Hspa5* (also called BiP or GRP78) was induced by thapsigargin but not *Shigella* infection (fig. S16A). Thapsigargin also induced *HSPB8* and *HSPA5* expression in HCT116 cells (fig. S16, B and C) and primary murine intestinal organoids (fig. S16, D and E). Thus, both HSPB8 and HSPA5 are induced by UPR/ER stress, but HSPB8 is additionally up-regulated by infection. We also analyzed the kinetics of *HSPB8* induction by *Shigella* and observed that whereas the pro-inflammatory genes *IL8* and *CXCL1*, as well as the stress-induced genes *ATF3* and *GADD34*, were induced in a first wave (as early as 1 hour after infection), *HSPB8* was induced in a second wave, at 2 to 4 hours after infection (fig. S16, F to J).

To further characterize the pathway that controls *HSPB8* expression, we infected *Atf4*$^{-/-}$ MEFs and CRISPR-engineered *ATF3*$^{-/-}$ HCT116 cells (fig. S17A) with *Shigella* or stimulated them with thapsigargin. *Shigella*-induced up-regulation of *HSPB8* was ATF4-dependent (Fig. 4B) as well as ATF3-dependent (fig. S17B), in agreement with kinetics data showing that ATF3 is induced before HSPB8 (fig. S16, F to J), whereas induction by thapsigargin required neither ATF4 nor ATF3 (Fig. 4B and fig. S17B). In contrast, HSPA5 up-regulation by thapsigargin stimulation was partially dependent on ATF4 and did not require ATF3 (fig. S17, C and D), in agreement with the known reliance of HSPA5 expression on the IRE1α and ATF6 branches of the UPR (*20*, *21*). Moreover, *Hspb8* up-regulation by *Shigella* infection was abrogated in eIF2α KI MEFs (fig. S17E), although baseline levels of *Hspb8* mRNA and protein (fig. S17F) were higher in KI as compared to wild-type MEFs in uninfected cells, possibly as a result of higher baseline levels of *Atf3* (see fig. S3A). Finally, HRI but not GCN2 controlled *HSPB8* up-regulation after *Shigella* infection (Fig. 4C); this effect was specific, as HSP90 expression was unaffected by HRI knockdown (fig. S17G).

At baseline, protein levels of HSPB8 were lower in *Shigella*-infected shHRI cells than in scramble control or shGCN2 cells (fig. S17H). Moreover, by 30 min after *Shigella* infection, a decline of the protein HSPB8, but not HSP90 or Hsc70, was observed (fig. S17H), which suggests that HSPB8 chaperoning activity was engaged rapidly during infection and may result in its degradation. It is thus possible that the HRI-dependent transcriptional up-regulation of HSPB8 during infection represents a regulatory feedback loop to restore HSPB8 levels. Together, these results identify HSPB8 as a key HSP induced by *Shigella* infection through the HRI/eIF2α/ATF4/ATF3 signaling axis.

We then asked whether HSPB8 mediated the effects of HRI on NOD-dependent signaling. Short hairpin RNA (shRNA)–mediated silencing of HSPB8 (fig. S17I) strongly inhibited *Shigella*-induced *IL-8* up-regulation (Fig. 4D), whereas overexpression of HSPB8 in HRI KD cells or in HRI CRISPR knockout cells rescued *Shigella*-induced NF-κB signaling and inflammatory responses (Fig. 4E and figs. S18 and S19). Thus, the

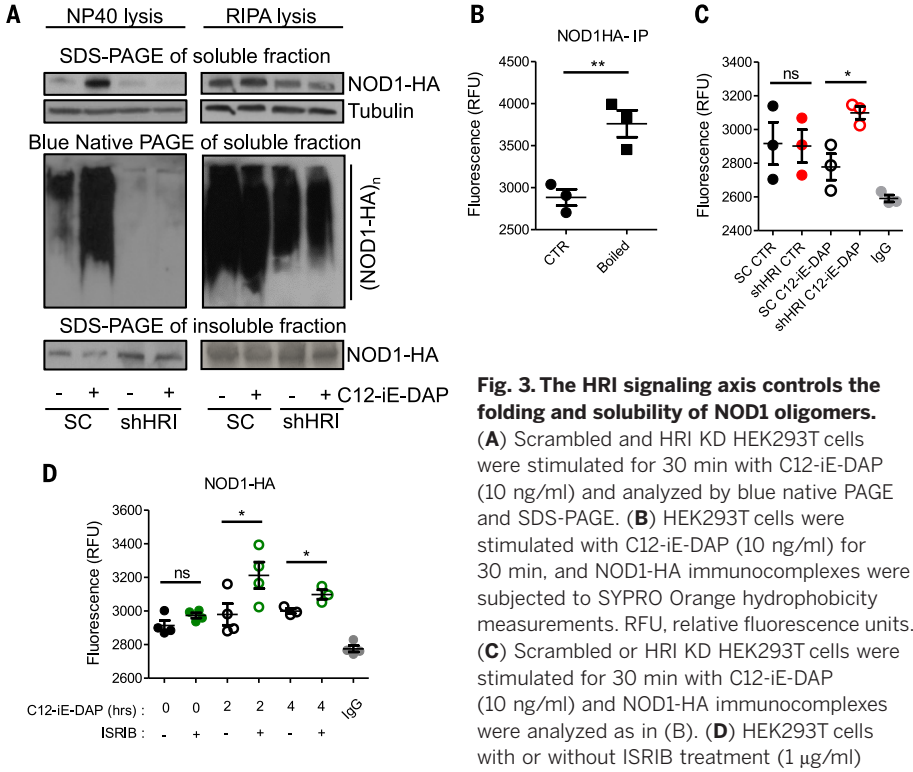

Fig. 3. The HRI signaling axis controls the folding and solubility of NOD1 oligomers. (**A**) Scrambled and HRI KD HEK293T cells were stimulated for 30 min with C12-iE-DAP (10 ng/ml) and analyzed by blue native PAGE and SDS-PAGE. (**B**) HEK293T cells were stimulated with C12-iE-DAP (10 ng/ml) for 30 min, and NOD1-HA immunocomplexes were subjected to SYPRO Orange hydrophobicity measurements. RFU, relative fluorescence units. (**C**) Scrambled or HRI KD HEK293T cells were stimulated for 30 min with C12-iE-DAP (10 ng/ml) and NOD1-HA immunocomplexes were analyzed as in (B). (**D**) HEK293T cells with or without ISRIB treatment (1 μg/ml) were stimulated with C12-iE-DAP (10 ng/ml) and NOD1-HA immunocomplexes were analyzed as in (B). Graphs represent means ± SD from three or four independent experiments. *P < 0.05, **P < 0.01; ns, not significant.

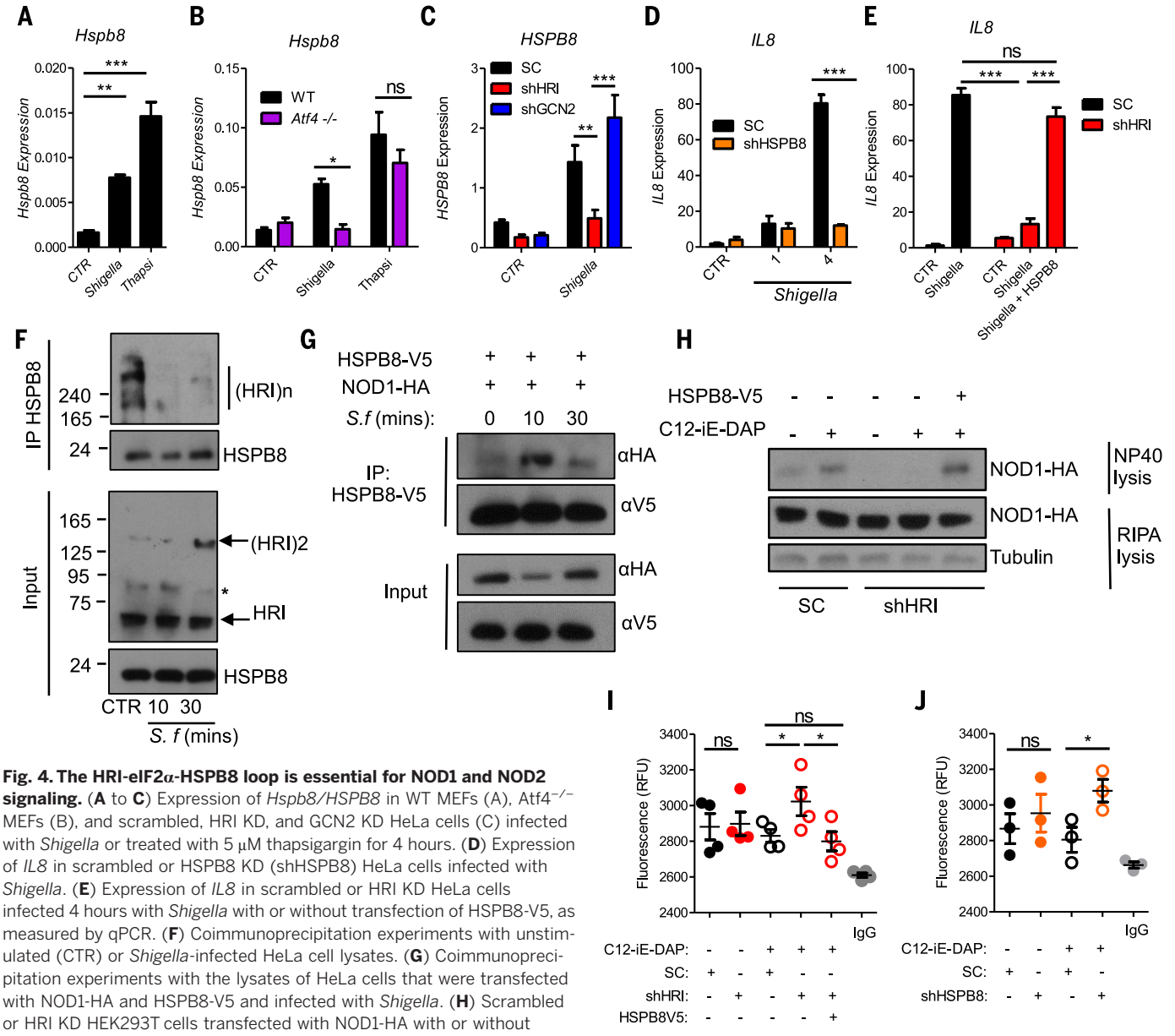

Fig. 4. The HRI-eIF2α-HSPB8 loop is essential for NOD1 and NOD2 signaling. (**A** to **C**) Expression of *Hspb8/HSPB8* in WT MEFs (A), Atf4$^{-/-}$ MEFs (B), and scrambled, HRI KD, and GCN2 KD HeLa cells (C) infected with *Shigella* or treated with 5 μM thapsigargin for 4 hours. (**D**) Expression of *IL8* in scrambled or HSPB8 KD (shHSPB8) HeLa cells infected with *Shigella*. (**E**) Expression of *IL8* in scrambled or HRI KD HeLa cells infected 4 hours with *Shigella* with or without transfection of HSPB8-V5, as measured by qPCR. (**F**) Coimmunoprecipitation experiments with unstimulated (CTR) or *Shigella*-infected HeLa cell lysates. (**G**) Coimmunoprecipitation experiments with the lysates of HeLa cells that were transfected with NOD1-HA and HSPB8-V5 and infected with *Shigella*. (**H**) Scrambled or HRI KD HEK293T cells transfected with NOD1-HA with or without HSPB8-V5 and analyzed as in Fig. 3A. (**I** and **J**) Scrambled or HRI KD HEK293T cells transfected with or without HSPB8-V5 (I) and scrambled or HSPB8 KD HEK293T cells (J) were stimulated for 30 min with C12-iE-DAP (10 ng/ml) and NOD1-HA complexes were subjected to SYPRO Orange hydrophobicity assays. Graphs display means ± SD from three to five independent experiments. *P < 0.05, **P < 0.01, ***P < 0.001. Asterisk in (F) denotes a nonspecific band.

HRI signaling axis regulates *Shigella*-induced pro-inflammatory NF-κB signaling through an HSPB8-dependent process.

We next aimed to uncover the mechanism through which the HRI-HSPB8 pathway regulates *Shigella*-induced pro-inflammatory NF-κB signaling. Drawing parallels with the UPR pathway in which activation occurs after displacement of chaperones to the proteins requiring refolding (*22*), we speculated that HRI might interact with HSPB8. Coimmunoprecipitation assays confirmed that HSPB8 interacted with HRI oligomers at the endogenous level, and the proteins rapidly dissociated after infection with *Shigella* (Fig. 4F). Concomitantly, an interaction between NOD1 immunocomplexes and HSPB8-V5 (HSPB8 fused to a V5 tag) was observed, which peaked at 10 min after infection (Fig. 4G). Thus, displacement of HSPB8 from HRI to forming NOD1 signalosomes may act as a signal for HRI activation. Notably, HSPB8 also interacted with NOD2 complexes and NOD2-HSPB8 interactions increased after MDP stimulation (fig. S20). Furthermore, ectopic expression of HSPB8 was sufficient to rescue the release of NP-40–soluble NOD1 complexes (Fig. 4H) and to reduce the hydrophobicity of NOD1 immunocomplexes in C12-iE-DAP–stimulated HRI KD cells (Fig. 4I). In agreement with these findings, silencing of HSPB8 increased the hydrophobicity of NOD1 immunocomplexes after stimulation with C12-iE-DAP (Fig. 4J). Thus, the HRI-HSPB8 axis regulates NOD1 signaling through the control of signalosome assembly and folding, and HSPB8 displacement from HRI to the NOD1 signalosome likely serves as a signal to trigger an HRI-dependent eIF2α-ATF4-ATF3 pathway inducing transcriptional up-regulation of HSPB8 for homeostatic regulation.

HRI differentially regulates PRM signaling

We next aimed to explore whether the HRI/eIF2α/HSPB8 axis regulates other pattern recognition molecule (PRM) pathways. We first investigated whether Toll-like receptor (TLR) signaling was

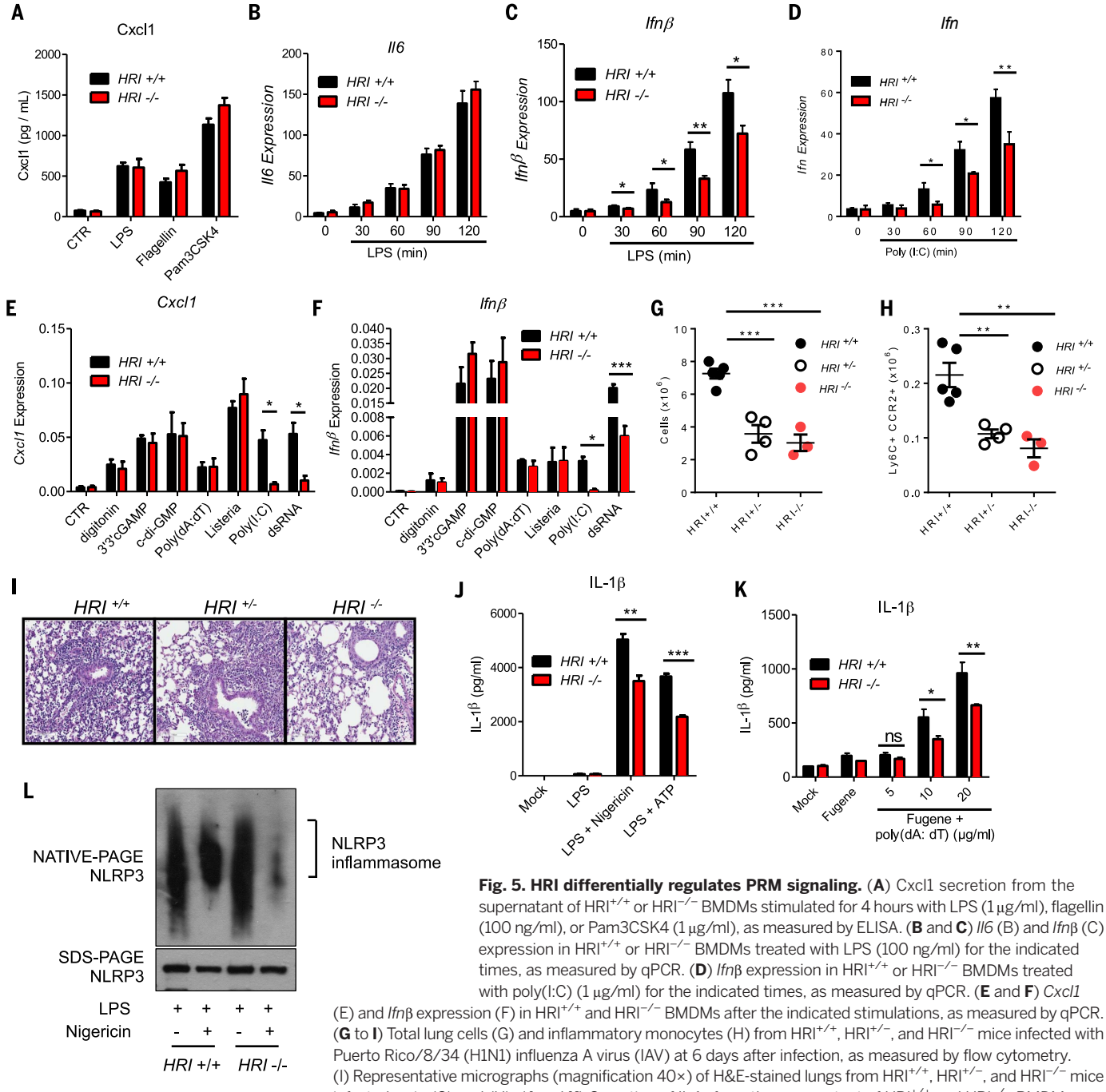

Fig. 5. HRI differentially regulates PRM signaling. (**A**) Cxcl1 secretion from the supernatant of HRI$^{+/+}$ or HRI$^{-/-}$ BMDMs stimulated for 4 hours with LPS (1 μg/ml), flagellin (100 ng/ml), or Pam3CSK4 (1 μg/ml), as measured by ELISA. (**B** and **C**) *Il6* (B) and *Ifn*β (C) expression in HRI$^{+/+}$ or HRI$^{-/-}$ BMDMs treated with LPS (100 ng/ml) for the indicated times, as measured by qPCR. (**D**) *Ifn*β expression in HRI$^{+/+}$ or HRI$^{-/-}$ BMDMs treated with poly(I:C) (1 μg/ml) for the indicated times, as measured by qPCR. (**E** and **F**) *Cxcl1* (E) and *Ifn*β expression (F) in HRI$^{+/+}$ and HRI$^{-/-}$ BMDMs after the indicated stimulations, as measured by qPCR. (**G** to **I**) Total lung cells (G) and inflammatory monocytes (H) from HRI$^{+/+}$, HRI$^{+/-}$, and HRI$^{-/-}$ mice infected with Puerto Rico/8/34 (H1N1) influenza A virus (IAV) at 6 days after infection, as measured by flow cytometry. (I) Representative micrographs (magnification 40×) of H&E-stained lungs from HRI$^{+/+}$, HRI$^{+/-}$, and HRI$^{-/-}$ mice infected as in (G) and (H). (**J** and **K**) Secretion of IL-1β from the supernatant of HRI$^{+/+}$ and HRI$^{-/-}$ BMDMs stimulated with LPS (100 ng/ml) for 3 hours alone or subsequently stimulated with 10 μM nigericin or 5 mM ATP for 45 min (J) and BMDMs primed for 4 hours with LPS (100 ng/ml) in Opti-MEM and stimulated with Fugene alone or transfected with poly(dA:dT) for 16 hours (K), as measured by ELISA. (**L**) HRI$^{+/+}$ and HRI$^{-/-}$ BMDMs were stimulated for 3 hours with LPS (100 ng/ml) and stimulated with 10 μM nigericin for 45 min, then analyzed by blue native PAGE. Bar graphs represent means ± SD from three to five independent experiments. *P < 0.05, **P < 0.01, ***P < 0.001 (one-way ANOVA followed by Tukey multiple-comparisons test).

influenced by HRI. Stimulation of scramble control cells or shHRI HCT116 with the TLR5 ligand flagellin triggered similar expression of *IL-8* (fig. S21A). Stimulation of *Hri*$^{+/+}$ and *Hri*$^{-/-}$ BMDMs with the TLR4, TLR5, and TLR2 ligands LPS, flagellin, and Pam3CSK4, respectively, induced similar secretion of Cxcl1 (Fig. 5A). In agreement with this finding, MyD88 signaling was similar in LPS-stimulated *Hri*$^{+/+}$ and *Hri*$^{-/-}$ BMDMs (Fig. 5B and fig. S21, B and C). In contrast, TRIF activation was blunted in LPS-treated *Hri*$^{-/-}$ BMDMs (Fig. 5C and fig. S21, B and D), which suggests that HRI regulates the TLR4/TRIF but not the TLR4/MyD88 signaling axis. Consistently, intraperitoneal injection of *Hri*$^{+/+}$, *Hri*$^{+/-}$, or *Hri*$^{-/-}$ mice with LPS triggered similar levels of serum Cxcl1 (fig. S21E). TLR3-TRIF signaling was also partially impaired in *Hri*$^{-/-}$ BMDMs (Fig. 5D and fig. S22). Furthermore, *Hri*$^{+/+}$ and *Hri*$^{-/-}$ BMDMs had similar expression of *Cxcl1* and *Ifnb* (Fig. 5, E and F) and secreted comparable amounts of interferon (IFN) α/β (fig. S23) after stimulation with inducers of the cGAS-STING pathway. In contrast, *Hri*$^{-/-}$ BMDMs expressed significantly less *Cxcl1* and *Ifnb* and secreted less type I IFNs in response to RIG-I-MAVS triggers (Fig. 5, E and F, and fig. S23). In agreement, no differences in STING-driven

inflammation were observable in $Hri^{+/+}$ and $Hri^{-/-}$ MEFs or BMDMs after infection with herpes simplex virus (HSV) (fig. S24). In contrast, a strong decrease of these markers, together with a reduced formation of MAVS oligomers, was noted in $Hri^{-/-}$ MEFs and BMDMs infected with the RIG-I-MAVS activator Sendai virus (SeV) (fig. S25). In agreement with a role for HRI in TRIF-dependent and MAVS-dependent responses, but not MyD88-dependent responses, we further noticed that acute inhibition of eIF2α phosphorylation using ISRIB significantly inhibited *Il6* and *Ifnb* induced by polyinosinic-polycytidylic acid [poly(I:C)] addition (TLR3-TRIF trigger) or transfection (MAVS trigger), and that it inhibited *Ifnb* induced by LPS (TLR4-TRIF trigger) without affecting *Il6* (TLR4-MyD88 trigger) (fig. S26). In support of the role of HRI in host defense against RNA viruses, we observed a significant blunting of immune cell recruitment and reduced damage in the lungs of $Hri^{-/-}$ mice at day 6 after infection with influenza A virus (Fig. 5, G to I, and fig. S27). Finally, heptose-1,7-bisphosphate (HBP) sensing by TIFA [tumor necrosis factor receptor–associated factor (TRAF)–interacting protein with forkhead-associated domain] also required HRI, as scramble control cells exhibited a robust induction of *IL-8* after stimulation with HBP-containing conditioned media from *gmhB*$^{-}$ *Neisseria meningitidis* (*14*), which was severely reduced in shHRI cells (fig. S28).

We then tested whether the NLRP3 inflammasome required HRI for signaling; NLRP3 differs from other PRMs tested so far, in that NLRP3 inflammasome assembly triggers rapid cell death and does not induce downstream transcriptional reprogramming. LPS-dependent priming of $Hri^{+/+}$ and $Hri^{-/-}$ BMDMs, which relies on the TLR4/MyD88 axis, resulted in comparable up-regulation of NLRP3 and pro–IL-1β in the lysates of $Hri^{+/+}$ and $Hri^{-/-}$ BMDMs (fig. S29A), in agreement with the results above. After LPS priming, stimulation with adenosine triphosphate (ATP) or nigericin yielded reduced release of mature IL-1β and cleaved caspase-1 into the supernatant of $Hri^{-/-}$ BMDMs (fig. S29A). In agreement with this result, we observed decreased secretion of IL-1β (Fig. 5J) and IL-18 (fig. S29B) in $Hri^{-/-}$ BMDMs. AIM2 inflammasome activity was also reduced in $Hri^{-/-}$ BMDMs (Fig. 5K and fig. S30). However, cell death induced by LPS transfection, which depends on the caspase-11 inflammasome (*23*), was unaffected in $Hri^{-/-}$ BMDMs, whereas caspase-1 activation and IL-1β release, which require NLRP3 (*24*), were similarly blunted (fig. S31). NLRP3 activation results in the assembly of a well-structured oligomeric inflammasome complex that can be resolved using native gel electrophoresis. Interestingly, stimulation of BMDMs with nigericin resulted in blunted assembly of endogenous NLRP3 inflammasomes in $Hri^{-/-}$ cells (Fig. 5L). Activation of the NLRP3 inflammasome further licenses assembly of ASC (apoptosis-associated speck-like protein containing CARD) prion-like polymers (*25*), which form specks. The endogenous ASC fibers and specks were reduced in $Hri^{-/-}$ BMDMs stimulated with nigericin (fig. S32). SYPRO Orange hydrophobicity measurements of NLRP3 inflammasome complexes after nigericin stimulation revealed greater hydrophobicity of NLRP3 inflammasomes in $Hri^{-/-}$ BMDMs (fig. S33), suggesting improper folding. However, ISRIB treatment had no impact on NLRP3 activation (fig. S34), which implies that HRI deficiency might induce a cellular state that affects NLRP3 inflammasome assembly but that the eIF2α/HSPB8 arm of the HRI signaling axis is likely not involved in the assembly or stability of the NLRP3 inflammasome. This is not unexpected, given that the NLRP3-ASC complex rapidly leads to pyroptotic cell death and does not induce signaling that modulates transcription. Together, these results reveal that HRI regulates NLRP3/ASC inflammasome assembly and function, although the underlying mechanism of how this regulation occurs remains to be elucidated.

HRI controls the cellular response to prefibrillar PRM adaptors and α-synuclein

We noticed that the PRM pathways regulated by HRI share the property that their adaptor proteins (RIP2 for NOD1/2, MAVS for RIG-I/MDA-5, TRIF for TLR3/TLR4, ASC for NLRP3/AIM2) can form amyloid-like fibrils in vitro. To begin elucidating the molecular requirements that trigger activation of the HRI/eIF2α/HSPB8 signaling axis and to test directly whether enforced assembly of these adaptors was sufficient to induce HRI-dependent signaling, we transfected scramble CTR versus HRI KD human embryonic kidney (HEK) 293T cells with various PRM adaptors. Overexpression of RIP2, MAVS, and TRIF resulted in an HRI-dependent induction of *IL8* and *HSPB8* (Fig. 6, A and B), which suggests that the assembly of PRM signalosome adaptors might be an essential step for HRI activation. In contrast, overexpression of MyD88, which assembles "myddosomes" with well-defined stoichiometry that, contrary to "TRIFosomes," do not form amyloid-like fibrils (*26*), induced *IL8* in an HRI-independent manner and did not up-regulate *HSPB8* (Fig. 6, A and B). Overexpression of ASC induced neither *IL8* nor *HSPB8* (Fig. 6, A and B), in agreement with our observation (see above) that NLRP3 inflammasome assembly is not controlled by the

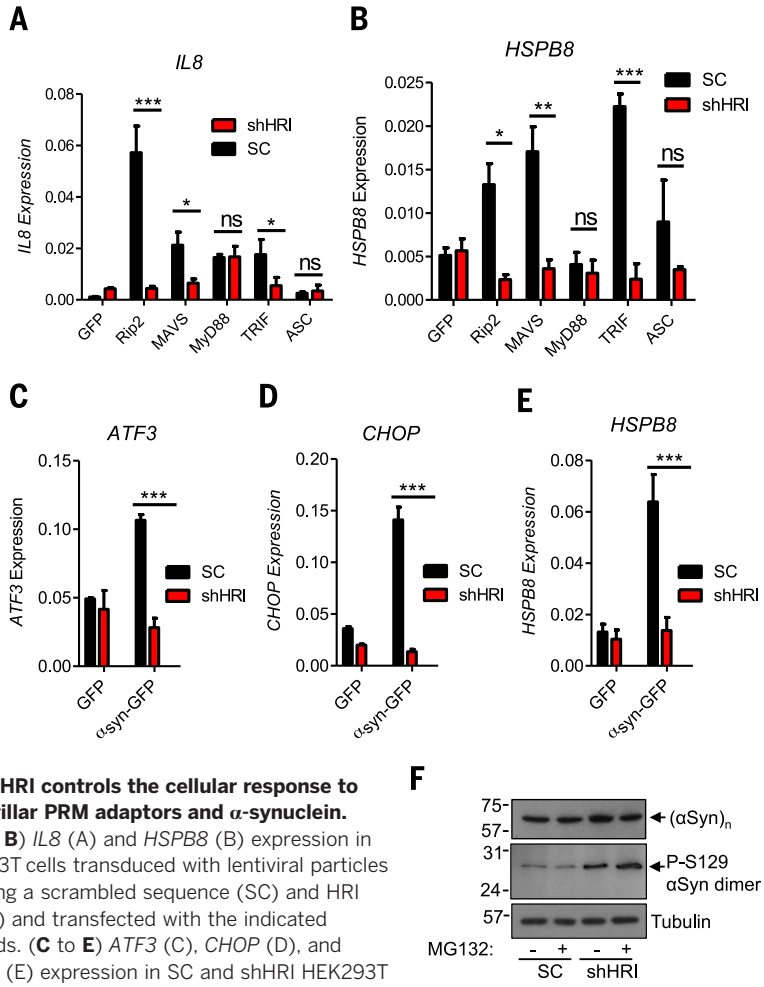

Fig. 6. HRI controls the cellular response to prefibrillar PRM adaptors and α-synuclein. (**A** and **B**) *IL8* (A) and *HSPB8* (B) expression in HEK293T cells transduced with lentiviral particles targeting a scrambled sequence (SC) and HRI (shHRI) and transfected with the indicated plasmids. (**C** to **E**) *ATF3* (C), *CHOP* (D), and *HSPB8* (E) expression in SC and shHRI HEK293T cells transfected with the indicated plasmids. (**F**) SC and shHRI SH-SY5Y cells treated with 5 μM MG132 for 4 hours and analyzed by Western blotting. Graphs represent means ± SD from three to five independent experiments. *P < 0.05, **P < 0.01, ***P < 0.001.

eIF2α/HSPB8 arm of HRI signaling. Moreover, we observed that necroptosis signaling, which involves amyloid-like fibrillar assembly of RIPK1/3 heterodimers (*27*), was also regulated by HRI (fig. S35). In agreement with this finding, overexpression of α-synuclein, a protein that forms toxic amyloid fibrils that are a pathological hallmark of Parkinson's disease (*28*), induced *ATF3*, *CHOP*, and *HSPB8* (Fig. 6, C to E) expression in an HRI-dependent manner. In the neuroblastoma cell line SH-SY5Y, HRI silencing induced accumulation of dimers of endogenous α-synuclein phosphorylated at Ser^{129} (Fig. 6F), which is indicative of misfolding (*29*). Together, these data suggest that HRI-dependent signaling may be essential for controlling the assembly and/or stability of amyloid-like fibrils in the cytosol.

Concluding remarks

Our data reveal that HRI controls the formation and folding of large PRM signalosomes in the cytosol, thereby affecting downstream innate immune signaling. Because HRI differentially regulates PRM signaling, the protein may be sensitive to specific molecular superstructures. This idea is supported by the finding that HRI-regulated PRMs rely on adaptor proteins that, at least in vitro, assemble filamentous structures. Considering that HRI is a stress-sensitive kinase of the ISR pathway, it is tempting to speculate that potentially toxic molecular superstructures, such as self-assembling amyloid-like fibrils or filaments, are direct activators of the HRI signaling axis. If this were the case, HRI could be involved in detecting and restricting the accumulation of cytosolic protein aggregates that are associated with neurodegenerative diseases, as hinted by our preliminary results with α-synuclein. Future biochemical studies should delineate the detailed nature of the (supra-)molecular structures that activate HRI.

The HRI/eIF2α/HSPB8 signaling axis shares a remarkable homology with the PERK-dependent branch of the UPR, which regulates protein folding in the ER. Indeed, the eIF2α kinase PERK senses the accumulation of misfolded proteins in the ER and is activated after dissociation with HSPA5, and earlier studies suggest the presence of a similar mechanism of regulation between the chaperone p58 and PKR (*30*). This pathway stimulates the up-regulation of stress-associated genes, such as the ER chaperone *HSPA5* that encodes BiP/GRP78. We thus propose that HRI and HSPB8 represent functional homologs of PERK and BiP, respectively, and that the HRI/eIF2α/HSPB8 signaling axis detects certain forms of cytosolic UPR (cUPR).

Materials and methods

Reagents and stimulations

To induce amino acid starvation, cells were rinsed three times with PBS and incubated in Krebs Ringer bicarbonate (KRB) buffer (118.5 mM NaCl, 4.74 mM KCl, 1.18 mM KH_2PO_4, 23.4 mM $NaHCO_3$, 5 mM glucose, 2.5 mM $CaCl_2$, and 1.18 mM $MgSO_4$, adjusted to pH 7.6 by titration with 1 N NaOH). Unless stated, chemicals and ligands were all obtained from Sigma or Invivogen, respectively. 3′cGAMP or c-di-GMP was delivered into cells by diluting ligands in digitonin permeabilization buffer [5 μg/ml for poly(dA:dT) and poly(I:C), 2 μg/ml for dsRNA] as described (*31*). For activation of AIM2, poly (dA:dT) was delivered using/FuGene. Supernatant was collected 16 hours after stimulation unless specified.

Cell lines

HeLa, HEK293T, HCT116, MEFs, L929, and SH-SY5Y cells were all cultured in DMEM with 10% FBS and 1% penicillin and streptomycin. Primary MEFs were prepared as described (*32*). Lentiviral knockdown was performed using the targeting sequences in table S1 as described (*33*). Bone marrow–derived macrophages (BMDMs) were prepared from the femurs and tibia of mice by obtaining bone marrow and incubating cells in RPMI with 20% conditioned media from L929 cells, 10% FBS, 1% penicillin and streptomycin, and 2 mM L-glutamine for 7 days. EIF2α knockin (KI) MEFs were obtained from R. J. Kaufman. ATF4 knockout MEFs were provided by R. Wek and were grown in DMEM with 10% FBS, 1% penicillin and streptomycin, and supplemented with 55 μM β-mercaptoethanol, nonessential amino acids (NEAA), and essential amino acids. CRISPR/CAS9 knockout cells were generated using the CRISPR-Cas9 system as described (*34*). THP-1 cells were grown in RPMI with 10% FBS supplemented with penicillin/streptomycin, NEAA, and 2-mercaptoethanol.

Mice

$Hri^{+/-}$ breeder mice were obtained from a previous study (*6*). Mice were bred and housed under SPF conditions at the Division of Comparative Medicine, University of Toronto. All experiments were performed with 7- to 11-week-old littermate mice from $HRI^{+/-}$ crosses. All mice experiments were approved by the local Animal Ethics Review Committee. Genotyping was performed with the primers shown in table S2.

Bacterial strains and in vitro bacterial infections

Infections with *Shigella flexneri*, *Salmonella* Typhimurium, and *Listeria monocytogenes* were performed as described (*9*, *10*). For *Shigella* infections where the time is not indicated, infections were performed for 4 hours. For *Listeria* infections of BMDMs, plates were centrifuged at 500*g* for 10 min after addition of bacteria, incubated at 37°C/5% CO_2 for 30 min, incubated with fresh gentamycin-containing medium (30 μg/ml), then left for an additional 2 hours. To measure bacterial replication, cells were infected as described above and lysed with PBS containing 0.1% Triton; lysate was serial-diluted and plated. *Shigella* conditioned medium was produced by using stationary phase cultures, pelleting bacteria by centrifugation (10,000*g* for 5 min) and filtering with a 0.22-μm syringe filter. *Neisseria gonorrhoeae* conditioned medium was purified as described (*35*).

Viral infections

Sendai virus and HSV were provided by D. Garcin and D. Boutolleau, respectively. Cells were incubated with Sendai virus (SeV at 40 HA/ml) or HSV (MOI of 5) diluted in serum-free DMEM and 2 hours later replaced with DMEM with 20% calf serum and antibiotics, incubated at 37°C. For influenza experiments, mice were intranasally (in 25 μl PBS) infected with a sublethal dose (50 plaque-forming units) with influenza A/Puerto Rico/8/34 virus provided by J. A. McCullers. All experiments were performed according to the animal research ethics board of McGill University.

Reverse transcription quantitative polymerase chain reaction (RT-qPCR)

Measurements of gene expression (unless otherwise specified) were performed by RT-qPCR. RT-PCR analysis was performed with SYBR green reagents as described (*9*). Murine and human qPCR primers used are listed in tables S3 and S4, respectively. For influenza infections, RNA was isolated using Qiazol reagent (Qiagen) and All-In-One RT MasterMix (abm) was used for cDNA synthesis. Table S5 indicates viral primers.

Western blots

Unless otherwise indicated, cells were lysed using RIPA. Lysates were centrifuged at 13,000*g* to separate out membrane fractions versus insoluble fractions and cytoplasmic proteins versus soluble fractions. The membrane fractions were resuspended in RIPA buffer with Laemmli blue loading buffer and boiled to obtain the insoluble fractions. Samples were run on acrylamide gels and transferred onto PVDF. Membranes were blocked with 5% milk in TBST and incubated with the indicated antibodies: mouse anti-tubulin (#T5168, Sigma, 1/10,000 dilution), rabbit anti-eIF2α (#9722S, NEB, 1/1000), rabbit anti-phospho-eIF2α (#9721, NEB, 1/1000), rabbit anti-HRI (#07-226, Upstate, 1/5000), anti-HRI polyclonal (*6*) (1/3000) rabbit anti-GCN2 (#ab137543, Abcam, 1/1000), monoclonal anti-HA tag (#G036, Abcam, 1/1000), monoclonal anti-Flag-Tag (#F3165, Sigma, 1/1000), rabbit anti-V5-Tag (#13202, NEB, 1/1000), rabbit anti-HSPB8 (#3059, cell signaling, 1/500), rabbit anti-HSP90 (#ab13492, Abcam, 1/3000), rabbit anti-Hsc70 (#ab51052, Abcam, 1/1000), rabbit anti-ERK (#9102, NEB, 1/4000), mouse anti-phospho-ERK (#9106, NEB, 1/4000), mouse anti-IκBα (#4814, NEB, 1/4000), rabbit anti-IκBα (# 9242, NEB, 1/2000), mouse anti-phospho-IκBα (#9246, NEB, 1/2000), rabbit anti-GAPDH (#G9545, Sigma, 1/20,000), mouse anti-caspase-1(p20) (#AG-20B-0042, Adipogen, 1/4000), mouse anti-NLRP3 (#AG-20B-0014, Adipogen, 1/4000), goat anti-mouse IL-1β (#AF-401-NA, R&D Systems, 1/1000), rabbit anti-IRF3 (#4302, NEB, 1/2000), rabbit anti-phospho-IRF3 (Ser396) (#4947, NEB), rabbit anti-NAK/TBK1 (EP611Y) (#ab40676, Abcam, 1/4000), rabbit anti-phospho-TBK1 (Ser172) (EPR2867(2)) (#ab109272, Abcam, 1/2000) or rabbit anti-phospho-TBK1/NAK (Ser172) (#5483, NEB, 1/2000), rabbit anti-MAVS (#4983, NEB, 1/2000) and rabbit anti-MAVS (M-300) (#sc-68881, Santa Cruz, 1/1000), rabbit

anti-STING/TMEM173 (#19851-1-AP, Proteintech, 1/2000), rabbit anti-ASC mouse specific (D2W8U) (#67824, NEB, 1/2000), rabbit polyclonal anti-ATF3 (H-90) (#sc22978, Santa Cruz, 1/1000), rabbit anti-ATF4 (D4B8) (#11815, NEB, 1/1000), mouse monoclonal anti-puromycin (4G11) (#MABE342, Millipore, 1/5000), rabbit anti-α-synuclein phospho-S129 (#ab51253, Abcam, 1/3000), mouse anti-α-synuclein (#ab1903, Abcam, 1/3000).

Immunofluorescence

Preparation of samples for immunofluorescence assays was performed as described (*11*). Antibodies were used as follows: anti-Tia-1, 1:100 (Santa Cruz); anti-p65, 1:100 (Abcam); anti-ASC, 1:400 (NEB).

Surface sensing of translation (SUnSEt) assay

SUnSEt assays were conducted as described (*11*).

Coimmunoprecipitation and SYPRO Orange experiments

For coimmunoprecipitation experiments, cells were lysed using RIPA buffer on ice and subsequently centrifuged at 13,000*g* for 3 min. Protein G beads (Pierce) were washed twice with RIPA buffer and centrifuged at 2000*g* for 10 min before adding lysate and the indicated antibodies. The immunoprecipitation reaction was incubated overnight at 4°C. Next, samples were centrifuged at 10,000*g* for 5 min, washed with RIPA buffer, resuspended in RIPA buffer with Laemmli blue loading buffer and boiled for 10 min. For hydrophobicity measurements, the immunoprecipitated samples were washed three times with PBS and resuspended in PBS. Samples were then incubated with a final concentration of 5× SYPRO Orange and fluorescence was measured using a RT-qPCR machine (300 nm excitation/470 nm emission) between 20° and 100°C. Hydrophobicity measurements of NOD1 were performed by transfecting HEK293T cells with NOD1-HA plasmid. Each dot on the scatterplots represents a data point from a unique experiment; $n = 3$ to 5 experiments were performed for each SYPRO Orange assay.

Intraperitoneal injections

Mice were injected intraperitoneally with 50 μg of MDP, 50 μg of FK-156, or 1 μg of LPS. Two hours after injection, mice were killed and whole blood was collected by cardiac puncture. To obtain the peritoneal lavage, 2 ml of PBS was injected into the peritoneal cavity, mixed briefly by massaging and collected. Peritoneal lavage was centrifuged for 10 min at 500*g*, the supernatant was used for ELISAs and the pelleted cells were used for flow cytometry.

In vivo Citrobacter *infections*

Citrobacter rodentium strain DBS 100 was cultured in LB medium overnight at 37°C. Bacterial colony-forming units (CFUs) were calculated after inoculation by plating on MacConkey agar. Mice were fasted overnight before being inoculated with 1×10^8 CFU bacteria in 200 μl volume by oral gavage. *C. rodentium* was obtained from P. Sherman (HSC, Toronto). Mice were killed 4 days after infection and the cecum and blood of mice collected for ELISA experiments.

Flow cytometry

Isolated peritoneal cells were sequentially incubated with the LIVE/DEAD Fixable Aqua Dead Cell Stain Kit (ThermoFisher Scientific), rat anti-mouse CD16/32 monoclonal antibody (clone 43, ThermoFisher), Alexa Fluor 700-conjugated rat anti-mouse Ly-6G (clone RB6-8C5, ThermoFisher), and APC-eFluor 780-conjugated rat anti-mouse CD11b (clone M1/70). For influenza infections, lungs were perfused with 10 ml of PBS, minced and digested in collagenase (150 U/ml) for 1 hour at 37°C and 5% CO_2. Single-cell suspensions were obtained by crushing cells through a 70-μm filter and stained with Fixable Viability Dye eFluor506 (eBioscience) for 20 min in PBS at 4°C, washed, then stained with anti-mouse CD16/32 (clone 93, eBioscience) in 0.5% BSA/PBS to block nonspecific binding for 5 min at 4°C. Finally, cells were stained with BUV395-conjugated rat anti-mouse CD45.2 (clone 104, BD Biosciences), PE-Cy7-conjugated rat anti-mouse CD11b (clone M170, BD Biosciences), Alexa Fluor 700-conjugated rat anti-mouse Ly6G (clone 1A8, BD Biosciences), and PE-conjugated rat anti-mouse CCR2 (clone 475301, R&D) and FITC-conjugated rat anti-mouse Ly6C (clone AC-21, BD Biosciences) in 0.5% BSA/PBS for 20 min at 4°C. Flow cytometry analysis was performed on an LSRFortessa X-20 Cell Analyzer or LSRFortessa Cell Analyzer (influenza) (BD Biosciences) via FACSDiva acquisition software (BD Biosciences), and analysis performed with FlowJo v10.3 (FlowJo, LLC).

Microarray analysis

Data from a previous report (*9*) were repurposed.

IFN protein quantification

Quantification of total IFN in the supernatants of BMDMs was performed using B16-Blue IFN α/β reporter cell lines as per the manufacturer's instructions (Invivogen).

Enzyme-linked immunosorbent assays (ELISAs)

ELISAs were performed according to the manufacturer's instructions. Cxcl1, IL-1β, IL-6, and murine CCL2 ELISA kits were obtained from R&D Systems. Measurements of IL-1β in response to NLRP3 stimulation and IL-6 measurements in macrophages were performed with kits from Thermofisher Scientific. Murine IFNβ ELISA and IL-18 ELISA kits were obtained from PBL Assay Science and MBL, respectively.

Transfections

For transient expression, transfections were performed with PEI MW25,000. HSPB8-V5 (*36*) and α-synuclein–GFP plasmids were obtained from Addgene. TIFA-flag was generated by S. D. Gray-Owen. NOD1-HA and NOD2-HA expression vectors were used in a previous study (*37*).

Luciferase

Luciferase assays were performed as described and adapted to HeLa cells (*37*).

Organoids

Murine organoid cultures were obtained and grown as described (*38*).

Histopathology

Lungs were excised and fixed in 10% formalin for 48 hours. Hematoxylin and eosin (H&E) staining was performed by the Histopathology Core of the RI-MUHC of McGill University and scanned up to 40× on the Aperio AT Turbo (Leica).

Blue native PAGE

Cells were lysed using either NP-40 lysis buffer to obtain cytoplasmic proteins and loosely membrane-associated proteins or RIPA to obtain all proteins. After lysis, experiments were performed as described (*35*).

Semi-denaturing detergent agarose gel electrophoresis (SDD-AGE)

For size estimation of MAVS aggregates, SDD-AGE was performed as described (*25*).

Cell death assays

Primed BMDMs [Pam_3CSK_4 (1 μg/ml) for 4 hours] were transfected with LPS using FuGene. LDH release was measured using LDH Cytotoxicity Detection Kit (Clontech). Percentages were obtained by comparing to Triton-lysed cells (100% cell death) and subtracting untreated controls.

Cell death was also quantified by monitoring propidium iodide (PI) incorporation (5 μg/ml) via fluorescence measurements over 24 hours on a microplate fluorimeter (Fluostar Omega, BMG Labtech).

ASC oligomerization

After stimulation, cells were lysed with cold PBS containing 0.5% Triton X-100 and centrifuged at 6000*g* for 15 min at 4°C. The pellets were washed twice in PBS and freshly prepared disuccinimidyl suberate (2 mM) was added to the resuspended pellets incubated with mixing for 30 min. The pellets were collected by centrifugation and redissolved in SDS-PAGE sample buffer.

Statistics

For analysis of data in fig. S16, B to E, a Student *t* test was used. For multiple comparisons, data was analyzed using analysis of variance (ANOVA) with Bonferroni post-test for cellular assays and Tukey post-test for in vivo experiments.

REFERENCES AND NOTES

1. T. E. Dever *et al.*, Phosphorylation of initiation factor 2α by protein kinase GCN2 mediates gene-specific translational control of GCN4 in yeast. *Cell* **68**, 585–596 (1992). doi: 10.1016/0092-8674(92)90193-G; pmid: 1739968
2. P. Zhang *et al.*, The GCN2 eIF2α kinase is required for adaptation to amino acid deprivation in mice. *Mol. Cell. Biol.* **22**, 6681–6688 (2002). doi: 10.1128/MCB.22.19.6681-6688.2002; pmid: 12215525
3. H. P. Harding, Y. Zhang, D. Ron, Protein translation and folding are coupled by an endoplasmic-reticulum-resident kinase.

Nature **397**, 271–274 (1999). doi: 10.1038/16729; pmid: 9930704
4. R. S. Ranu, Regulation of protein synthesis in rabbit reticulocyte lysates: The hemeregulated protein kinase (HRI) and double stranded RNA induced protein kinase (dRI) phosphorylate the same site(s) on initiation factor eIF-2. *Biochem. Biophys. Res. Commun.* **91**, 1437–1444 (1979). doi: 10.1016/0006-291X(79)91227-0; pmid: 526314
5. A. Yerlikaya, S. R. Kimball, B. A. Stanley, Phosphorylation of eIF2α in response to 26S proteasome inhibition is mediated by the haem-regulated inhibitor (HRI) kinase. *Biochem. J.* **412**, 579–588 (2008). doi: 10.1042/BJ20080324; pmid: 18290760
6. A. P. Han *et al*., Heme-regulated eIF2α kinase (HRI) is required for translational regulation and survival of erythroid precursors in iron deficiency. *EMBO J.* **20**, 6909–6918 (2001). doi: 10.1093/emboj/20.23.6909; pmid: 11726526
7. E. McEwen *et al*., Heme-regulated inhibitor kinase-mediated phosphorylation of eukaryotic translation initiation factor 2 inhibits translation, induces stress granule formation, and mediates survival upon arsenite exposure. *J. Biol. Chem.* **280**, 16925–16933 (2005). doi: 10.1074/jbc.M412882200; pmid: 15684421
8. D. Ron, Translational control in the endoplasmic reticulum stress response. *J. Clin. Invest.* **110**, 1383–1388 (2002). doi: 10.1172/JCI0216784; pmid: 12438433
9. I. Tattoli *et al*., Amino acid starvation induced by invasive bacterial pathogens triggers an innate host defense program. *Cell Host Microbe* **11**, 563–575 (2012). doi: 10.1016/j.chom.2012.04.012; pmid: 22704617
10. I. Tattoli *et al*., Listeria phospholipases subvert host autophagic defenses by stalling pre-autophagosomal structures. *EMBO J.* **32**, 3066–3078 (2013). doi: 10.1038/emboj.2013.234; pmid: 24162724
11. J. Tsalikis *et al*., Intracellular Bacterial Pathogens Trigger the Formation of U Small Nuclear RNA Bodies (U Bodies) through Metabolic Stress Induction. *J. Biol. Chem.* **290**, 20904–20918 (2015). doi: 10.1074/jbc.M115.659466; pmid: 26134566
12. H. P. Harding *et al*., An integrated stress response regulates amino acid metabolism and resistance to oxidative stress. *Mol. Cell* **11**, 619–633 (2003). doi: 10.1016/S1097-2765(03)00105-9; pmid: 12667446
13. V. Thulasiraman *et al*., Evidence that Hsc70 negatively modulates the activation of the heme-regulated eIF-2α kinase in rabbit reticulocyte lysate. *Eur. J. Biochem.* **255**, 552–562 (1998). doi: 10.1046/j.1432-1327.1998.2550552.x; pmid: 9738893
14. R. G. Gaudet *et al*., Innate Recognition of Intracellular Bacterial Growth Is Driven by the TIFA-Dependent Cytosolic Surveillance Pathway. *Cell Rep.* **19**, 1418–1430 (2017). doi: 10.1016/j.celrep.2017.04.063; pmid: 28514661
15. S. E. Girardin *et al*., Nod1 detects a unique muropeptide from gram-negative bacterial peptidoglycan. *Science* **300**, 1584–1587 (2003). doi: 10.1126/science.1084677; pmid: 12791997
16. S. E. Girardin *et al*., CARD4/Nod1 mediates NF-κB and JNK activation by invasive Shigella flexneri. *EMBO Rep.* **2**, 736–742 (2001). doi: 10.1093/embo-reports/kve155 pmid: 11463746
17. K. Geddes *et al*., Identification of an innate T helper type 17 response to intestinal bacterial pathogens. *Nat. Med.* **17**, 837–844 (2011). doi: 10.1038/nm.2391; pmid: 21666695
18. Y. G. Kim *et al*., The Nod2 sensor promotes intestinal pathogen eradication via the chemokine CCL2-dependent recruitment of inflammatory monocytes. *Immunity* **34**, 769–780 (2011). doi: 10.1016/j.immuni.2011.04.013; pmid: 21565531
19. W. Bahnan *et al*., The eIF2α Kinase Heme-Regulated Inhibitor Protects the Host from Infection by Regulating Intracellular Pathogen Trafficking. *Infect. Immun.* **86**, e00707-17 (2018). doi: 10.1128/IAI.00707-17; pmid: 29311243
20. B. M. Gardner, D. Pincus, K. Gotthardt, C. M. Gallagher, P. Walter, Endoplasmic reticulum stress sensing in the unfolded protein response. *Cold Spring Harb. Perspect. Biol.* **5**, a013169 (2013). doi: 10.1101/cshperspect.a013169; pmid: 23388626
21. J. Celli, R. M. Tsolis, Bacteria, the endoplasmic reticulum and the unfolded protein response: Friends or foes? *Nat. Rev. Microbiol.* **13**, 71–82 (2015). doi: 10.1038/nrmicro3393; pmid: 25534809
22. P. Walter, D. Ron, The unfolded protein response: From stress pathway to homeostatic regulation. *Science* **334**, 1081–1086 (2011). doi: 10.1126/science.1209038; pmid: 22116877
23. S. M. Crowley, B. A. Vallance, L. A. Knodler, Noncanonical inflammasomes: Antimicrobial defense that does not play by the rules. *Cell. Microbiol.* **19**, e12730 (2017). doi: 10.1111/cmi.12730; pmid: 28117938
24. N. Kayagaki *et al*., Non-canonical inflammasome activation targets caspase-11. *Nature* **479**, 117–121 (2011). doi: 10.1038/nature10558; pmid: 22002608
25. X. Cai *et al*., Prion-like polymerization underlies signal transduction in antiviral immune defense and inflammasome activation. *Cell* **156**, 1207–1222 (2014). doi: 10.1016/j.cell.2014.01.063; pmid: 24630723
26. C. E. Bryant, M. Symmons, N. J. Gay, Toll-like receptor signalling through macromolecular protein complexes. *Mol. Immunol.* **63**, 162–165 (2015). doi: 10.1016/j.molimm.2014.06.033; pmid: 25081091
27. J. Li *et al*., The RIP1/RIP3 necrosome forms a functional amyloid signaling complex required for programmed necrosis. *Cell* **150**, 339–350 (2012). doi: 10.1016/j.cell.2012.06.019; pmid: 22817896
28. I. Dikiy, D. Eliezer, Folding and misfolding of α-synuclein on membranes. *Biochim. Biophys. Acta* **1818**, 1013–1018 (2012). doi: 10.1016/j.bbamem.2011.09.008; pmid: 21945884
29. A. Oueslati, Implication of α-Synuclein Phosphorylation at S129 in Synucleinopathies: What Have We Learned in the Last Decade? *J. Parkinsons Dis.* **6**, 39–51 (2016). doi: 10.3233/JPD-160779; pmid: 27003784
30. S. J. Polyak, N. Tang, M. Wambach, G. N. Barber, M. G. Katze, The P58 cellular inhibitor complexes with the interferon-induced, double-stranded RNA-dependent protein kinase, PKR, to regulate its autophosphorylation and activity. *J. Biol. Chem.* **271**, 1702–1707 (1996). doi: 10.1074/jbc.271.3.1702; pmid: 8576172
31. J. J. Woodward, A. T. Iavarone, D. A. Portnoy, c-di-AMP secreted by intracellular *Listeria monocytogenes* activates a host type I interferon response. *Science* **328**, 1703–1705 (2010). doi: 10.1126/science.1189801; pmid: 20508090
32. L. H. Travassos *et al*., Nod1 and Nod2 direct autophagy by recruiting ATG16L1 to the plasma membrane at the site of bacterial entry. *Nat. Immunol.* **11**, 55–62 (2010). doi: 10.1038/ni.1823; pmid: 19898471
33. M. T. Sorbara *et al*., The protein ATG16L1 suppresses inflammatory cytokines induced by the intracellular sensors Nod1 and Nod2 in an autophagy-independent manner. *Immunity* **39**, 858–873 (2013). doi: 10.1016/j.immuni.2013.10.013; pmid: 24238340
34. M. T. Sorbara *et al*., Complement C3 Drives Autophagy-Dependent Restriction of Cyto-invasive Bacteria. *Cell Host Microbe* **23**, 644–652.e5 (2018). doi: 10.1016/j.chom.2018.04.008; pmid: 29746835
35. R. G. Gaudet *et al*., Cytosolic detection of the bacterial metabolite HBP activates TIFA-dependent innate immunity. *Science* **348**, 1251–1255 (2015). doi: 10.1126/science.aaa4921; pmid: 26068852
36. S. Carra, J. F. Brunsting, H. Lambert, J. Landry, H. H. Kampinga, HspB8 participates in protein quality control by a non-chaperone-like mechanism that requires eIF2α phosphorylation. *J. Biol. Chem.* **284**, 5523–5532 (2009). doi: 10.1074/jbc.M807440200; pmid: 19114712
37. J. Lee *et al*., pH-dependent internalization of muramyl peptides from early endosomes enables Nod1 and Nod2 signaling. *J. Biol. Chem.* **284**, 23818–23829 (2009). doi: 10.1074/jbc.M109.033670; pmid: 19570976
38. I. Tattoli *et al*., NLRX1 Acts as an Epithelial-Intrinsic Tumor Suppressor through the Modulation of TNF-Mediated Proliferation. *Cell Rep.* **14**, 2576–2586 (2016). doi: 10.1016/j.celrep.2016.02.065; pmid: 26971996

ACKNOWLEDGMENTS

Funding: Supported by Canadian Institutes of Health Research (CIHR) grants PJT-15319 and MOP-12353 (S.E.G.), Agence Nationale de Recherche sur le SIDA (ANRS) and foundation ARC (D.A.), CIHR team grant on chronic inflammation THC-13523 (D.J.P. and S.E.G.), and an Ontario Graduate Scholarship (M.A.N. and J.T.). **Author contributions:** M.A.N., L.A.M.C., J.D., J.T., A.O., D.P., L.S.D.C., E.S.H., A.F., R.M., R.V.D., C.C.Y.L., N.K.E., A.T.G., and D.A. performed experiments; R.G.G., S.D.G., F.C.A., J.E.L., and J.J.C. provided reagents; M.D. oversaw influenza infection experiments; S.E.G., D.J.P., and D.A. oversaw the project; and M.A.N. and S.E.G. wrote the original draft of the manuscript. **Competing interests:** R.G.G. and S.D.G. have filed patents concerning the therapeutic potential of heptose 1-phosphate and heptose 1,7-biphosphate. **Data and materials availability:** HRI knockout mice are available from J.J.C. under a material agreement with the Institute of Medical Engineering and Science, Massachusetts Institute of Technology. All data are available in the main text or supplementary materials.

SUPPLEMENTARY MATERIALS

science.sciencemag.org/content/365/6448/eaaw4144/suppl/DC1
Figs. S1 to S35
Tables S1 to S5

18 December 2018; resubmitted 16 April 2019
Accepted 7 June 2019
10.1126/science.aaw4144

RESEARCH ARTICLE

CRISPR BIOLOGY

RNA-guided DNA insertion with CRISPR-associated transposases

Jonathan Strecker[1,2,3,4], Alim Ladha[1,2,3,4], Zachary Gardner[1,2,3,4], Jonathan L. Schmid-Burgk[1,2,3,4], Kira S. Makarova[5], Eugene V. Koonin[5], Feng Zhang[1,2,3,4]*

CRISPR-Cas nucleases are powerful tools for manipulating nucleic acids; however, targeted insertion of DNA remains a challenge, as it requires host cell repair machinery. Here we characterize a CRISPR-associated transposase from cyanobacteria *Scytonema hofmanni* (ShCAST) that consists of Tn7-like transposase subunits and the type V-K CRISPR effector (Cas12k). ShCAST catalyzes RNA-guided DNA transposition by unidirectionally inserting segments of DNA 60 to 66 base pairs downstream of the protospacer. ShCAST integrates DNA into targeted sites in the *Escherichia coli* genome with frequencies of up to 80% without positive selection. This work expands our understanding of the functional diversity of CRISPR-Cas systems and establishes a paradigm for precision DNA insertion.

Prokaryotic clustered regularly interspaced short palindromic repeats (CRISPR) and CRISPR-associated proteins (Cas) systems provide adaptive immunity against foreign genetic elements via guide RNA–dependent DNA or RNA nuclease activity (*1*–*3*). CRISPR effectors, such as Cas9 and Cas12, have been harnessed for genome editing (*4*–*9*) and create targeted DNA double-strand breaks in the genome, which are then repaired by endogenous DNA damage repair pathways. Although it is possible to achieve precise integration of new DNA after Cas9 cleavage either through homologous recombination (*10*) or nonhomologous end-joining (*11*, *12*), these processes are inefficient and vary greatly depending on cell type. Homologous recombination repair is also tied to active cell division, making it unsuitable for postmitotic cells. Recently, an alternative approach for making point mutations on DNA has been developed that relies on using dead Cas9 (*13*) to recruit cytidine or adenine deaminases to achieve base editing of genomic DNA (*14*–*16*). However, base editing is restricted to nucleotide substitutions, and thus efficient and targeted integration of DNA into the genome remains a major challenge.

To overcome these limitations, we sought to leverage self-sufficient DNA insertion mechanisms, such as transposons. We explored bioengineering approaches of CRISPR-Cas effectors to facilitate DNA transposition (fig. S1). Cas9 binding to DNA generates an R-loop structure, exposing a substrate for enzymes that act on single-stranded DNA (ssDNA). By tethering nickase Cas9(D10A) to the ssDNA transposase TnpA from *Helicobacter pylori* IS608 (*17*, *18*), we observe targeted DNA insertions in vitro and in *Escherichia coli* that are dependent on TnpA transposase activity, Cas9 single guide RNA (sgRNA), and the presence of an insertion site within the ssDNA. However, the requirement of an ssDNA donor will necessitate continued development for efficient synthesis and delivery to cells.

A number of CRISPR-Cas systems lacking active nuclease domains have been identified previously, including minimal type I loci lacking the Cas3 helicase-nuclease (*19*) and type V loci containing a Cas12 effector with a naturally inactivated RuvC-like nuclease domain (*20*). The absence of nuclease domains raises questions about the biological function of these CRISPR-Cas systems that can bind but not cleave DNA. Recently, an association between Tn7-like transposons and subtype I-F, subtype I-B, or subtype V-K (formerly, V-U5) CRISPR-Cas systems was reported (*21*, *22*). The CRISPR-Cas–associated Tn7-like transposons contain *tnsA*, *tnsB*, *tnsC*, and *tniQ* genes (*21*), similar to the canonical Tn7 heterotrimeric TnsABC complex (*23*, *24*). Tn7 is targeted to DNA via two alternative pathways that are mediated, respectively, by TnsD, a sequence-specific DNA binding protein that recognizes the Tn7 attachment site (*25*, *26*), and TnsE, which facilitates transposition into conjugal plasmids and replicating DNA (*27*).

The association between Tn7-like transposons and CRISPR-Cas systems suggests that the transposons might have hijacked CRISPR effectors to generate R-loops in target sites and facilitate the spread of transposons via plasmids and phages (*21*). In the case of subtype V-K, the position of the CRISPR-Cas locus is frequently conserved in predicted transposons, suggesting that CRISPR-Cas is linked with transposition (*22*). However, because canonical Tn7 transposons often carry cargo genes with defense functions that are beneficial to the host cell (*24*), it is also possible that CRISPR-Cas may be cargo genes. To date, no functional data on transposon-encoded CRISPR-Cas systems have been reported. Here we show that Tn7-like transposons can be directed to target sites via CRISPR RNA (crRNA)–guided targeting and we elucidate the mechanism of crRNA-guided Tn7 transposition. We further demonstrate that Tn7 transposition can be reprogrammed to insert DNA into the genome of *E. coli*, highlighting the potential of using RNA-guided Tn7-like transposons for genome editing.

Characterization of a transposon associated with a type V CRISPR system

Among the transposon-encoded CRISPR-Cas variants, the subtype V-K are the simplest because they contain a single-protein CRISPR-Cas effector (*20*, *21*, *28*), Cas12k (formerly, C2c5). Subtype V-K systems are thus far limited to cyanobacteria, and the latest nonredundant set includes 63 loci that, in the phylogenetic tree of Cas12k, split into four major branches, covering a broad taxonomic range of Cyanobacteria (*22*). All V-K systems are embedded within predicted Tn7-like transposable elements with no additional *cas* genes, suggesting that, if they are active CRISPR-Cas systems, they might rely on adaptation modules supplied in trans. Of the 560 analyzed V-K spacers, only six protospacer matches were identified: three from cyanobacterial plasmids and three from single-stranded transposons of IS200 or IS650 families (*22*). These findings suggest that V-K systems might provide a biological advantage for the host transposons by directing integration into other mobile genetic elements, to enhance transposon mobility while minimizing damage to the host.

For experimental characterization, we selected two Tn7-like transposons encoding subtype V-K CRISPR-Cas systems [hereafter, CAST (CRISPR-associated transposase)]. The selected CAST loci were 20 to 25 kb in length and contained Tn7-like transposase genes at one end of the transposon with a CRISPR array and Cas12k on the other end, flanking internal cargo genes (Fig. 1A and fig. S2, A and B). We first cultured the cyanobacteria *Scytonema hofmanni* (UTEX B 2349) (Fig. 1B) and *Anabaena cylindrica* (PCC 7122) and performed small RNA sequencing to determine whether the CRISPR-Cas systems are expressed and active. For both loci, we identified a long putative trans-activating crRNA (tracrRNA) that mapped to the region between Cas12k and the CRISPR array, and in the case of *S. hofmanni* (ShCAST) we detected crRNAs 28 to 34 nucleotides (nt) long, consisting of 11 to 14 nt of direct repeat (DR) sequence with 17 to 20 nt of spacer (Fig. 1C and fig. S2C).

[1]Broad Institute of MIT and Harvard, Cambridge, MA 02142, USA. [2]McGovern Institute for Brain Research, Massachusetts Institute of Technology, Cambridge, MA 02139, USA. [3]Department of Brain and Cognitive Sciences, Massachusetts Institute of Technology, Cambridge, MA 02139, USA. [4]Department of Biological Engineering, Massachusetts Institute of Technology, Cambridge, MA 02139, USA. [5]National Center for Biotechnology Information, National Library of Medicine, National Institutes of Health, Bethesda, MD 20894, USA.
***Corresponding author. Email: zhang@broadinstitute.org**

To investigate whether ShCAST and AcCAST function as RNA-guided transposases, we cloned the four CAST genes (*tnsB*, *tnsC*, *tniQ*, and *Cas12k*) into a helper plasmid (pHelper) along with the endogenous tracrRNA region and a crRNA targeting a synthetic protospacer (PSP1). We predicted the ends of the transposons by searching for TGTACA-like terminal repeats surrounded by a duplicated insertion site (*21*) and constructed donor plasmids (pDonor) containing the kanamycin resistance gene flanked by the transposon left end (LE) and right end (RE). Given that CRISPR-Cas effectors require a protospacer adjacent motif (PAM) to recognize target DNA (*29*), we generated a target plasmid (pTarget) library containing the PSP1 sequence flanked by a 6N motif upstream of the protospacer. We coelectroporated pHelper, pDonor, and

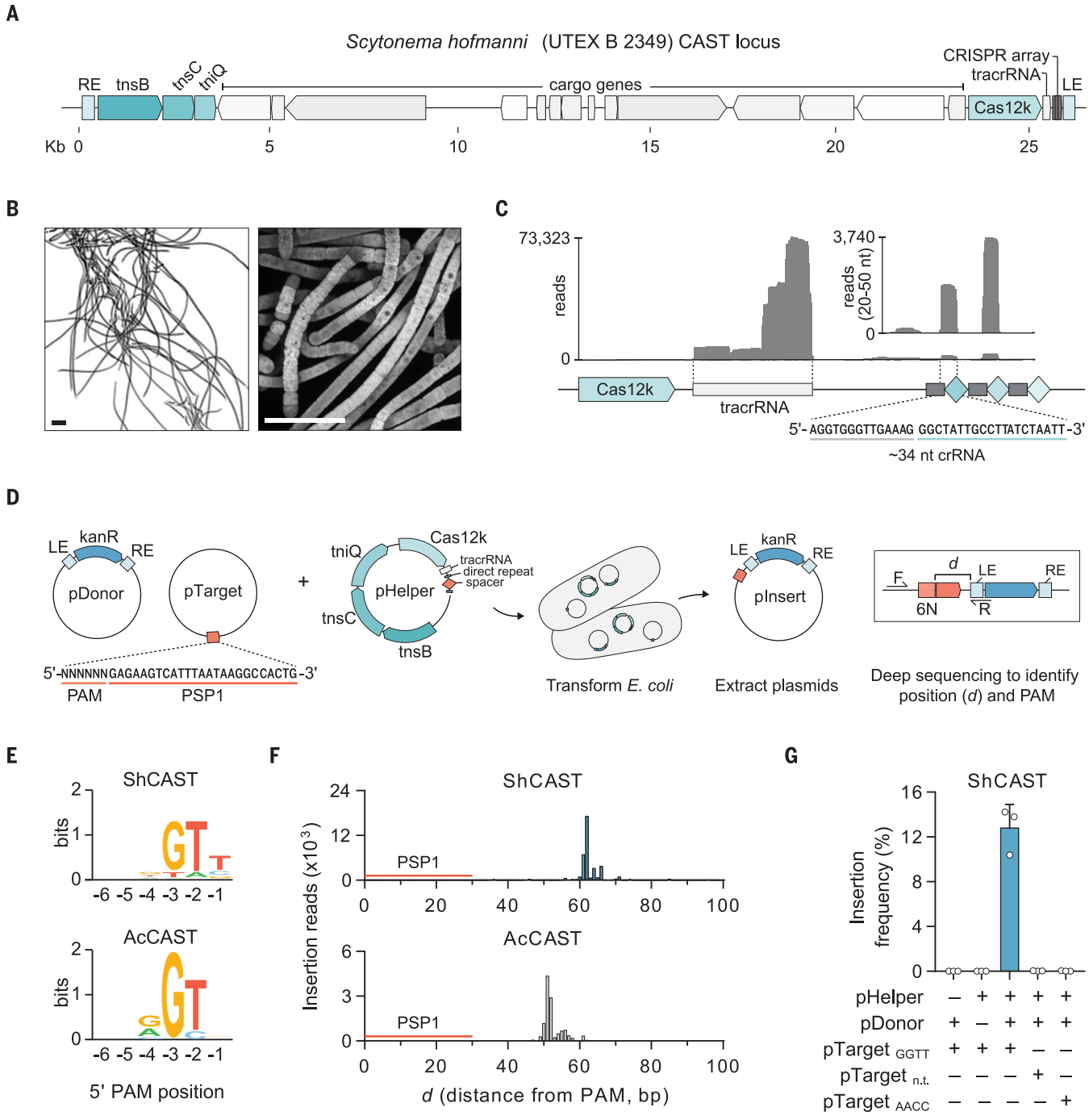

Fig. 1. Targeting requirements for CRISPR-associated transposase (CAST) systems. (**A**) Schematic of the *S. hofmanni* CAST locus containing Tn7-like proteins, the CRISPR-Cas effector Cas12k, and a CRISPR array. (**B**) Fluorescent micrograph of the cyanobacteria *S. hofmanni*. Scale bars, 40 μm. (**C**) Alignment of small RNA sequencing reads from *S. hofmanni*. The location of the putative tracrRNA is marked. (**D**) Schematic of experiment to test CAST system activity in *E. coli*. kanR, kanamycin resistance gene; F, forward primer; R, reverse primer. (**E**) PAM motifs for insertions mediated by ShCAST and AcCAST. (**F**) ShCAST and AcCAST insertion positions identified by deep sequencing. (**G**) Insertion frequency of ShCAST system in *E. coli* with pTarget substrates as determined by ddPCR. Error bars represent SD from $n = 3$ replicates. n.t., nontargeting.

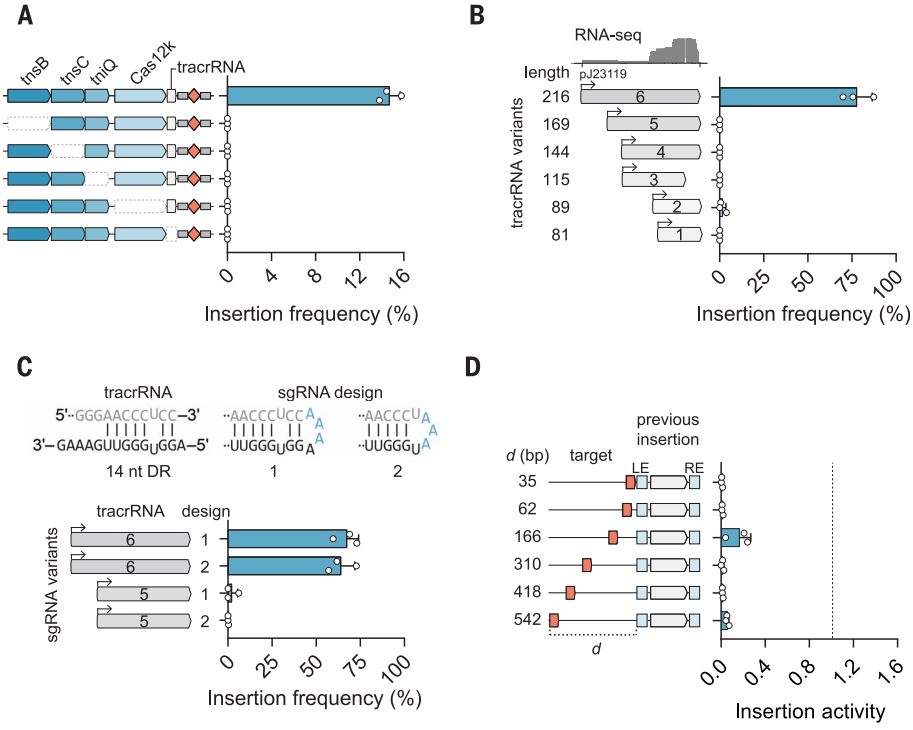

Fig. 2. Genetic requirements for RNA-guided insertions. (**A**) Genetic requirement of tnsB, tnsC, tniQ, Cas12k, and tracrRNA on insertion activity. Deleted components are indicated by a dashed outline. (**B**) Insertion activity of six tracrRNA variants expressed with the pJ23119 promoter. (**C**) Schematic of tracrRNA and crRNA base pairing and two sgRNA designs highlighting the linker sequence (blue). (**D**) Insertion activity into pTarget containing ShCAST transposon ends relative to activity into pTarget without previous insertion. Error bars represent SD from $n = 3$ replicates.

pTarget into *E. coli* and extracted plasmid DNA after 16 hours (Fig. 1D). We detected insertions into the target plasmid (pInsert) by polymerase chain reaction (PCR) for both ShCAST and AcCAST, and deep sequencing confirmed the insertion of the LE into pTarget. Analysis of PAM sequences in pInsert plasmids revealed a preference for GTN PAMs for both ShCAST and AcCAST systems, suggesting that these insertions result from Cas12k targeting (Fig. 1E and fig. S3, A and B). We next examined the position of the donor in pInsert products relative to the protospacer. Insertions were detected within a small window 60 to 66 base pairs (bp) downstream from the PAM for ShCAST and 49 to 56 bp downstream from the PAM for AcCAST (Fig. 1F). No insertions were detected in the opposite orientation for either system, indicating that CAST functions unidirectionally. Although DNA insertions could potentially arise from genetic recombination in *E. coli*, the discovery of an associated PAM sequence and the constrained position of insertions argues against this possibility.

To validate these findings, we transformed *E. coli* with ShCAST pHelper and pDonor plasmids along with target plasmids containing a GGTT PAM, an AACC PAM, and a scrambled nontarget sequence. We assessed insertion events by quantitative droplet digital PCR (ddPCR), which revealed insertions of the donor only in the presence of pHelper and a pTarget containing a GGTT PAM and crRNA-matching protospacer sequence (Fig. 1G). Additional experiments with 16 PAM sequences confirmed a preference for NGTN motifs (fig. S3C). As further validation, we recovered pInsert products and performed Sanger sequencing of both LE and RE junctions. All sequenced insertions were located 60 to 66 bp from the PAM and contained a 5-bp duplicated insertion motif flanking the inserted DNA (fig. S4), consistent with the staggered DNA breaks generated by Tn7 (*30*). Because Tn7 inserts into a CCCGC motif downstream of its attachment site, we hypothesized that the sequence within the insertion window might also be important for CAST function. We generated a second target library with an 8N motif located 55 bp from the PAM and again cotransformed the library into *E. coli* with ShCAST pHelper and pDonor followed by deep sequencing (fig. S5A). We observed only a minor sequence preference upstream of the LE in pInsert, with a slight T or A preference three bases upstream of the insertion site (fig. S5, B to D). ShCAST can therefore target a wide range of DNA sequences with minimal targeting rules. Together, these results indicate that AcCAST and ShCAST catalyze DNA insertion in a heterologous host and that these insertions are dependent on a targeting protospacer and a distinct PAM sequence.

Genetic requirements for RNA-guided insertions

We next sought to determine the genetic requirements for ShCAST insertions in *E. coli* and constructed a series of pHelper plasmids with deletions of each element. Insertions into pTarget required all four CAST proteins and the tracrRNA region (Fig. 2A). To better characterize the tracrRNA sequence, we complemented pHelper$_{\Delta tracrRNA}$ with various tracrRNA driven by the pJ23119 promoter. Expression of the 216-nt tracrRNA variant 6 alone was sufficient to restore DNA transposition (Fig. 2B). The 3′ end of the tracrRNA is predicted to hybridize with a crRNA containing 14 nt of the DR sequence, and we designed sgRNA testing two linkers between the tracrRNA and crRNA sequences. Both designs supported insertion activity in the context of the tracrRNA variant 6 (Fig. 2C). We observed that expression of tracrRNA or sgRNA with the pJ23119 promoter resulted in a fivefold increase in the insertion activity compared with the natural locus, suggesting that RNA was rate limiting during heterologous expression.

As ShCAST does not destroy the protospacer upon DNA insertion, we asked whether multiple insertions could occur in pTarget, or if these are inhibited, as with canonical Tn7 (*31*, *32*). We generated target plasmids containing LE + RE, or LE alone, and measured ShCAST transposition activity at six nearby protospacers. We observed a strong inhibitory effect on transposition at a protospacer 62 bp from the LE (<1% of relative activity to pTarget), and only 5.7% relative activity 542 bp from the LE (Fig. 2D), indicating that CAST transposon ends act in cis to prevent multiple insertions. The presence of LE alone resulted in a weaker inhibitory effect, and we observed 61.1% of activity at 542 bp away from the transposon end (fig. S6, A and B).

Our original pDonor contained 2.2 kb of cargo DNA, and we next tested the effect of donor length on ShCAST activity ranging from 500 bp to 10 kb. We observed a twofold higher insertion rate with a 500-bp donor and a similar rate of insertions with 10 kb of payload compared with the original pDonor (fig. S6C). We were unable to detect rejoined pDonor backbone during transposition in *E. coli* (fig. S6, D and E), suggesting that a linear donor backbone is formed, not a rejoined product, consistent with the known reaction products of canonical Tn7 (*30*, *33*). Finally, we investigated the requirement of the LE and RE transposon end sequences contained in pDonor for transposition. Removal of all flanking genomic sequences or the 5bp duplicated target sites had little effect on insertion frequency, and ShCAST tolerated truncations of LE and RE to 113 and 155 bp, respectively (fig. S7A). Removal of additional donor sequence completely abolished transposase activity, which is consistent with the loss of predicted Tn7 TnsB-like binding motifs (fig. S7, B and C).

In vitro reconstitution of ShCAST

Although our data strongly suggested that ShCAST mediates RNA-guided DNA insertion, to exclude

the requirement of additional host factors, we next sought to reconstitute the reaction in vitro. We purified all four ShCAST proteins (fig. S8A) and performed in vitro reactions using pDonor, pTarget, and purified RNA (Fig. 3A). Addition of all four protein components, crRNA, and tracrRNA resulted in DNA insertions detected by both LE and RE junction PCRs, as did reactions containing the four protein components and sgRNA (Fig. 3B). The truncated tracrRNA variant 5 was also able to support DNA insertion in vitro, in contrast with the activity observed in *E. coli*. ShCAST-catalyzed transposition in vitro occurred between 37° and 50°C and depended on adenosine triphosphate and Mg^{2+} (fig. S8, B and C). To confirm that in vitro insertions are in fact targeted, we performed reactions with target plasmids containing a GGTT PAM, an AACC PAM, and a scrambled nontarget sequence, and we could only detect DNA insertions into the GGTT PAM substrate with the target sequence (Fig. 3C). In vitro DNA transposition depended on all four CAST proteins, although we identified weak but detectable insertions in the absence of tniQ (Fig. 3D).

We were unable to detect DNA cleavage in the presence of Cas12k and sgRNA across a range of buffer conditions (fig. S8D), which is consistent with the predicted lack of nuclease activity of Cas12k. To determine whether other CRISPR-Cas effectors could also stimulate DNA transposition, we performed reactions with tnsB, tnsC, and tniQ, along with dCas9 and a sgRNA targeting the same GGTT PAM substrate. We were unable to detect any insertions after dCas9 incubation (Fig. 3E), which indicates that the function of Cas12k is not merely DNA binding, and that DNA transposition by CAST does not simply occur at R-loop structures. As final validation, we transformed in vitro reaction products into *E. coli* and performed Sanger sequencing to determine the LE and RE junctions. All sequenced donors were located in pTarget 60 to 66 bp from the PAM and contained duplicated 5-bp insertion sites, demonstrating complete reconstitution of ShCAST with purified components.

ShCAST mediates efficient and precise genome insertions in *E. coli*

To test whether ShCAST could be reprogrammed as a DNA insertion tool, we selected 48 targets in the *E. coli* genome and cotransformed pDonor and pHelper plasmids expressing targeting sgRNAs (Fig. 4A). We detected insertions by PCR at 29 of the 48 sites (60.4%) and selected 10 sites for additional validation (fig. S9A). We performed ddPCR to quantitate insertion frequency after 16 hours and measured rates up to 80% at PSP42 and PSP49 (Fig. 4B). This high efficiency of insertion was surprising given that insertion events were not selected for by antibiotic resistance, so we performed PCR of target sites to confirm. We detected the 2.5-kb insertion product in the transformed population (Fig. 4C). Restreaking transformed *E. coli* yielded pure single colonies, the majority of which contained the targeted insertion (fig. S9B), and the high efficiency of integration was maintained with a variety of donor DNA lengths (fig. S9C). We analyzed the position of genome insertions by targeted deep sequencing of the LE and RE junctions and observed insertions within the 60- to 66-bp window at all 10 sites (Fig. 4D and fig. S10A).

We next assayed the specificity of RNA-guided DNA transposition. We performed unbiased sequencing of donor insertion sites after Tn5 tagmentation of genomic DNA. We observed one prominent insertion site in each sample, which mapped to the target site and contained >50% of the total insertion reads (Fig. 4E). The remaining off-target reads were scattered across the genome, and analysis of the top off-target sites revealed strong overlap between samples, demonstrating that these events are independent of the guide sequence (fig. S10B and table S5). Top off-target sites were located near highly expressed loci such as ribosomal genes, serine-tRNA ligase, and enolase, although insertion frequency in these regions were all <1% of the on-target site (table S5). We identified one potential RNA-guided off-target after targeting of PSP42, which contains four mismatches to the guide sequence (fig. S10C). Together, these results indicate that ShCAST robustly and precisely inserts DNA into the target site.

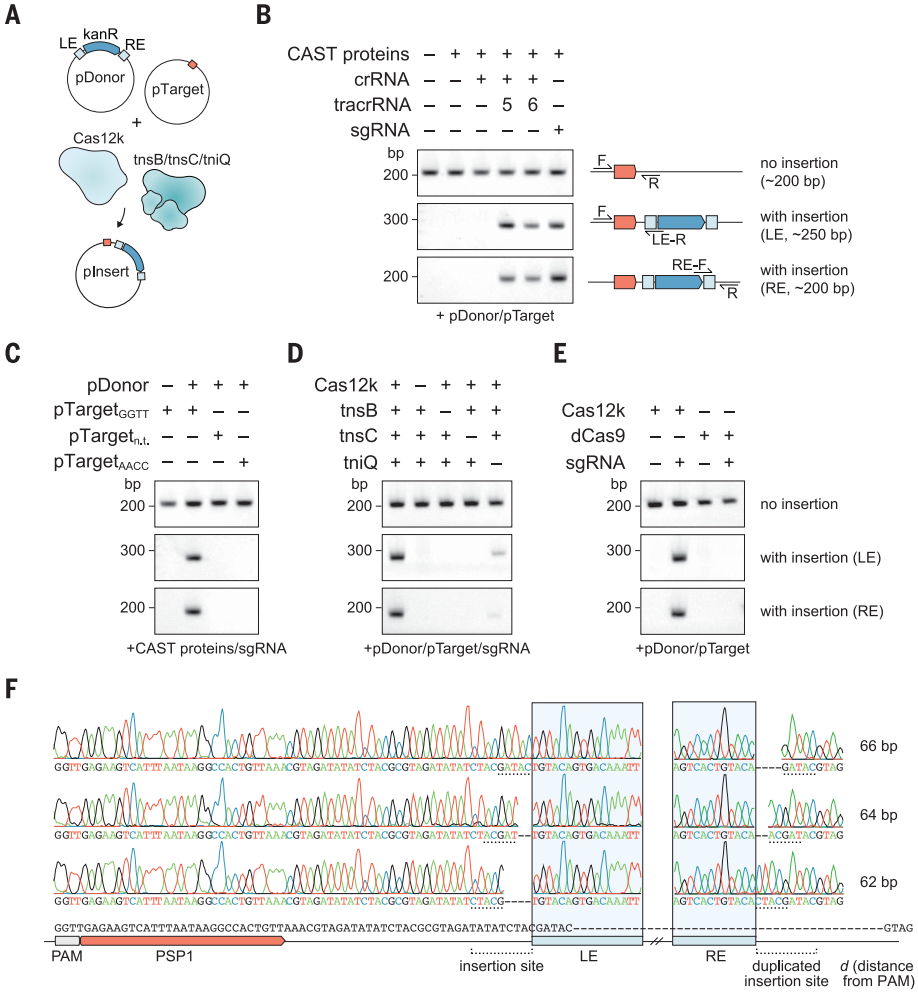

Fig. 3. In vitro reconstitution of an RNA-guided transposase. (**A**) Schematic of in vitro transposition reactions with purified ShCAST proteins and plasmid donor and targets. (**B**) RNA requirements for in vitro transposition. pInsert was detected by PCR for LE and RE junctions. All reactions contained pDonor and pTarget. Schematics indicate the location of primers and the expected product sizes for all reactions. (**C**) Targeting specificity of ShCAST in vitro. All reactions contained ShCAST proteins and sgRNA. (**D**) Protein requirements for in vitro transposition. All reactions contained pDonor, pTarget, and sgRNA. (**E**) CRISPR-Cas effector requirements for in vitro transposition. All reactions contained ShCAST proteins, pDonor, and pTarget. (**F**) Chromatograms of pInsert reaction products after transformation and extraction from *E. coli*. LE and RE elements are highlighted and the duplicated insertion sites denoted. For all panels, ShCAST proteins were used at a final concentration of 50 nM, and *n* = 3 replicates for all reactions were performed with a representative image shown.

Discussion

Here we demonstrate that CRISPR-Cas systems associated with Tn7-like transposon mediate RNA-guided DNA transposition and elucidate its mechanism. ShCAST mediates unidirectional insertions in a narrow window downstream of the target and inhibits repeated insertions into a single target site (Fig. 5). Although ShCAST and AcCAST exhibit similar PAM preferences, one notable difference is that their respective positions of insertion, relative to the PAM, differ by 10 to 11 bp, which roughly corresponds to one turn of DNA. Deeper exploration of microbial genomes is expected to uncover CAST systems with a range of diverse properties, including targeting preference and activity across different conditions.

Targeted DNA insertion by ShCAST results in the incorporation of LE and RE elements and

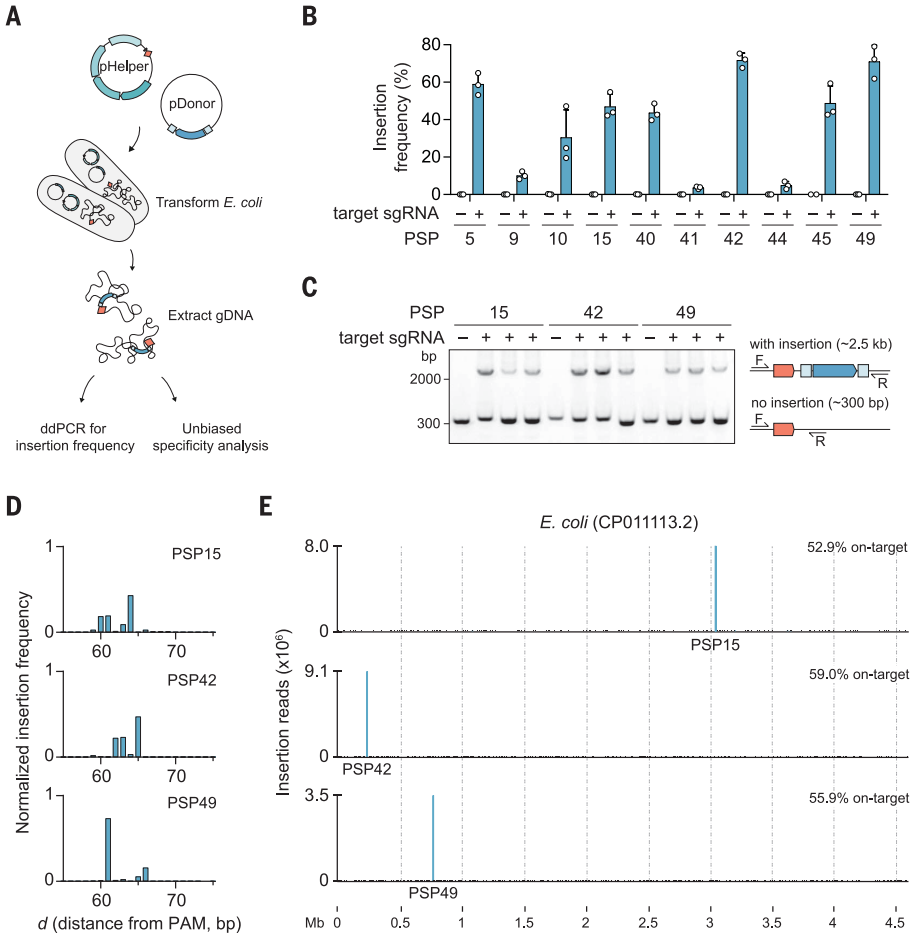

Fig. 4. ShCAST mediates genome insertions in *E. coli*. (**A**) Schematic of experiment to test for genome insertions in *E. coli*. (**B**) Insertion frequency at 10 tested protospacers after ShCAST transformation. Insertion frequency was determined by ddPCR on extracted genomic DNA. Error bars represent SD from $n = 3$ replicates. (**C**) Flanking PCR of three tested protospacers in a population of *E. coli* after ShCAST transformation. Schematics indicate the location of primers and the expected product sizes. (**D**) Insertion site position as determined by deep sequencing after ShCAST transformation. (**E**) Insertion positions determined by unbiased donor detection. The location of each protospacer is annotated along with the percent of total donor reads that map to the target.

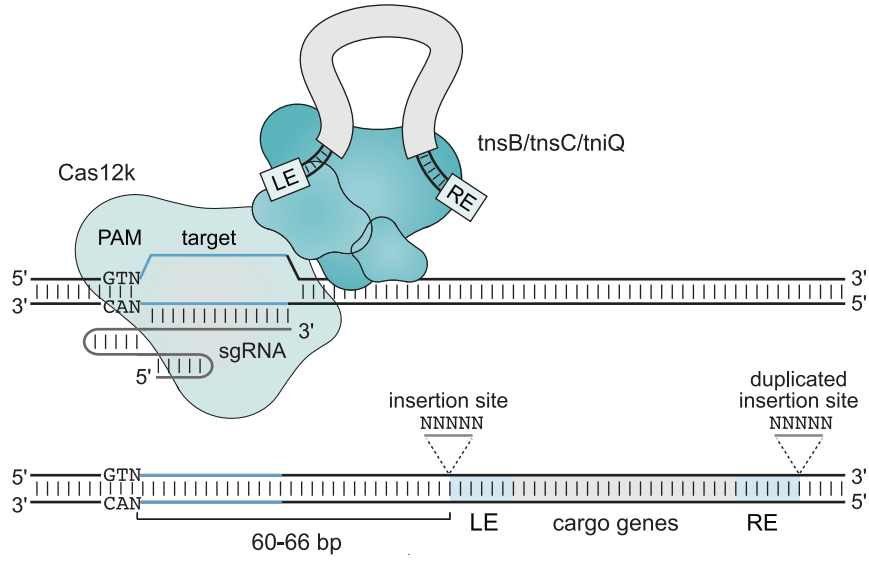

Fig. 5. Model for RNA-guided DNA transposition. The ShCAST complex that consists of Cas12k, TnsB, TnsC, and TniQ mediates insertion of DNA 60 to 66 bp downstream of the PAM. Transposon LE and RE sequences, along with any additional cargo genes, are inserted into DNA resulting in the duplication of 5-bp insertion sites.

is therefore not a scarless integration method. One potential generalizable strategy for the use of CAST in the therapeutic context would be to insert corrected exons into the intron before the mutated exon (fig. S11). CAST could also be used to insert transgenes into "safe harbor" loci (*34*) or downstream of endogenous promoters so that the expression of transgenes of interest can benefit from endogenous gene regulation.

Further studies should improve our understanding of the function of each transposase subunit in the CAST complex, notably, TniQ, which contains a predicted DNA binding domain. We originally hypothesized that TniQ is analogous to the site-specific DNA binding protein TnsD of Tn7 and, therefore, might be dispensable for RNA-guided insertions; however, we observed that TniQ is required for RNA-guided insertions in *E. coli*. The observation that in vitro transposition can occur to a limited extent in the absence of TniQ is compatible with a model in which TniQ facilitates the formation of the CAST complex and is not essential for catalytic function. Therefore, it might be possible to engineer simplified versions of CAST systems without TniQ or with fragments of TniQ.

Our analysis indicated that ShCAST is specific but, under overexpression conditions, can integrate at nontargeted sites in the *E. coli* genome via Cas12k-independent mechanisms, and this guide-independent integration seems to favor highly expressed genes. We also observed nontargeted insertions into pHelper in *E. coli* that were independent of Cas12k (fig. S12) and reminiscent of TnsE-mediated Tn7 insertions into conjugal plasmids and replicating DNA (*27*). Future protein engineering of the transposase components could improve the targeting specificity of CAST systems.

This work identifies a function for CRISPR-Cas systems beyond adaptive immunity that does not require Cas nuclease activity and provides a strategy for targeted insertion of DNA without engaging homologous recombination pathways, with a particularly exciting potential for genome editing in eukaryotic cells.

REFERENCES AND NOTES

1. R. Barrangou, P. Horvath, *Nat. Microbiol.* **2**, 17092 (2017).
2. P. Mohanraju *et al.*, *Science* **353**, aad5147 (2016).
3. L. A. Marraffini, *Nature* **526**, 55–61 (2015).
4. L. Cong *et al.*, *Science* **339**, 819–823 (2013).
5. P. Mali *et al.*, *Science* **339**, 823–826 (2013).
6. B. Zetsche *et al.*, *Cell* **163**, 759–771 (2015).
7. J. Strecker *et al.*, *Nat. Commun.* **10**, 212 (2019).
8. F. Teng *et al.*, *Cell Discov.* **4**, 63 (2018).
9. J.-J. Liu *et al.*, *Nature* **566**, 218–223 (2019).
10. M. Jasin, R. Rothstein, *Cold Spring Harb. Perspect. Biol.* **5**, a012740 (2013).
11. J. L. Schmid-Burgk, K. Höning, T. S. Ebert, V. Hornung, *Nat. Commun.* **7**, 12338 (2016).
12. K. Suzuki *et al.*, *Nature* **540**, 144–149 (2016).
13. L. S. Qi *et al.*, *Cell* **152**, 1173–1183 (2013).
14. A. C. Komor, Y. B. Kim, M. S. Packer, J. A. Zuris, D. R. Liu, *Nature* **533**, 420–424 (2016).
15. N. M. Gaudelli *et al.*, *Nature* **551**, 464–471 (2017).
16. K. Nishida *et al.*, *Science* **353**, aaf8729 (2016).
17. C. Guynet *et al.*, *Mol. Cell* **29**, 302–312 (2008).
18. O. Barabas *et al.*, *Cell* **132**, 208–220 (2008).
19. K. S. Makarova *et al.*, *Nat. Rev. Microbiol.* **13**, 722–736 (2015).
20. S. Shmakov *et al.*, *Nat. Rev. Microbiol.* **15**, 169–182 (2017).
21. J. E. Peters, K. S. Makarova, S. Shmakov, E. V. Koonin, *Proc. Natl. Acad. Sci. U.S.A.* **114**, E7358–E7366 (2017).
22. G. Faure *et al.*, *Nat. Rev. Microbiol.* 10.1038/s41579-019-0204-7 (2019).
23. R. J. Sarnovsky, E. W. May, N. L. Craig, *EMBO J.* **15**, 6348–6361 (1996).
24. J. E. Peters, N. L. Craig, *Nat. Rev. Mol. Cell Biol.* **2**, 806–814 (2001).
25. C. S. Waddell, N. L. Craig, *Proc. Natl. Acad. Sci. U.S.A.* **86**, 3958–3962 (1989).
26. C. S. Waddell, N. L. Craig, *Genes Dev.* **2**, 137–149 (1988).
27. J. E. Peters, N. L. Craig, *Genes Dev.* **15**, 737–747 (2001).
28. S. Hou *et al.*, *RNA Biol.* **16**, 518–529 (2019).
29. F. J. Mojica, C. Díez-Villaseñor, J. García-Martínez, C. Almendros, *Microbiology* **155**, 733–740 (2009).
30. R. Bainton, P. Gamas, N. L. Craig, *Cell* **65**, 805–816 (1991).
31. Z. Skelding, J. Queen-Baker, N. L. Craig, *EMBO J.* **22**, 5904–5917 (2003).
32. A. E. Stellwagen, N. L. Craig, *EMBO J.* **16**, 6823–6834 (1997).
33. M. C. Biery, F. J. Stewart, A. E. Stellwagen, E. A. Raleigh, N. L. Craig, *Nucleic Acids Res.* **28**, 1067–1077 (2000).
34. M. Sadelain, E. P. Papapetrou, F. D. Bushman, *Nat. Rev. Cancer* **12**, 51–58 (2011).

ACKNOWLEDGMENTS

We thank R. Macrae for critical reading of the manuscript and the entire Zhang laboratory for support and advice. We thank F. Chen for imaging *S. hofmanni*. **Funding:** J.S. is supported by the Human Frontier Science Program. F.Z. is a New York Stem Cell Foundation–Robertson Investigator. F.Z. is supported by NIH grants (1R01-HG009761, 1R01-MH110049, and 1DP1-HL141201); the Howard Hughes Medical Institute; the New York Stem Cell and Mathers Foundations; the Poitras Center for Affective Disorders Research at MIT; the Hock E. Tan and K. Lisa Yang Center for Autism Research at MIT; and by J. and P. Poitras. **Author contributions:** J.S. and F.Z. conceived of the project. J.S., A.L., and Z.G. performed bacterial experiments. J.S. purified CAST proteins and performed in vitro reactions. A.L. performed genome targeting experiments. A.L. performed insertion specificity analysis with help from J.L.S.-B. K.S.M. and E.V.K. identified CAST loci and performed bioinformatics analysis. F.Z. supervised the research and experimental design. J.S. and F.Z. wrote and revised the manuscript with input from all authors. **Competing interests:** J.S. and F.Z. are coinventors on U.S. provisional patent application no. 62/780,658 filed by the Broad Institute, relating to CRISPR-associated transposases. F.Z. is a cofounder of Editas Medicine, Beam Therapeutics, Pairwise Plants, Arbor Biotechnologies, and Sherlock Biosciences. **Data and materials availability:** Expression plasmids are available from Addgene under a uniform biological material transfer agreement; support forums and computational tools are available via the Zhang lab website (https://zhanglab.bio).

SUPPLEMENTARY MATERIALS

science.sciencemag.org/content/365/6448/48/suppl/DC1
Materials and Methods
Figs. S1 to S12
Tables S1 to S6
References (*35*–*38*)

4 May 2019; accepted 29 May 2019
Published online 6 June 2019
10.1126/science.aax9181

RESEARCH ARTICLE SUMMARY

CELL BIOLOGY

A COPII subunit acts with an autophagy receptor to target endoplasmic reticulum for degradation

Yixian Cui, Smriti Parashar, Muhammad Zahoor*, Patrick G. Needham*, Muriel Mari, Ming Zhu, Shuliang Chen, Hsuan-Chung Ho, Fulvio Reggiori, Hesso Farhan†, Jeffrey L. Brodsky†, Susan Ferro-Novick‡

INTRODUCTION: The unfolded protein response (UPR) maintains homeostasis of the endoplasmic reticulum (ER) through a variety of mechanisms, including ER-associated degradation (ERAD). ERAD recognizes terminally misfolded or unassembled proteins and retrotranslocates them across the ER membrane into the cytosol, where they are degraded by the proteasome. Certain disease-associated, aggregation-prone proteins, however, cannot be cleared by ERAD and are disposed of by other pathways. Aggregation-prone proteins have been linked to a variety of neurodegenerative diseases, including a diverse group of disorders characterized as hereditary spastic paraplegias. Thus, understanding how these alternate disposal pathways function has important medical implications.

RATIONALE: Autophagy of the ER (ER-phagy) is a disposal pathway that targets ER domains and sequesters them into autophagosomes for delivery to the vacuole or lysosome for degradation. When ER-phagy is induced, ER-phagy receptors recruit their binding partner, Atg8 in yeast or LC3 in mammals, to discrete sites on the ER to facilitate autophagosome formation. These sites are formed on a highly dynamic tubular ER network that is stabilized by Lnp1, a conserved protein that resides at the tubular ER junctions. Although ER-phagy occurs at discrete sites on the contiguous ER network, the receptors that load ER into autophagosomes are dispersed throughout the network. How specific sites on the ER are targeted for ER-phagy is unknown. We reasoned that cytosolic components might function with ER-phagy receptors to define these sites. COPII coat subunits were candidates for such factors because they are known to segregate membrane domains from the bulk ER. Correctly folded proteins destined to exit the ER are packaged by the COPII coat cargo adaptor complex Sec24-Sec23 into transport vesicles that bud from the ER and traffic to the Golgi.

RESULTS: In budding yeast, we discovered that the Sec24 paralog Lst1, which forms a COPII cargo adaptor complex with Sec23, is essential for ER-phagy. ER-phagy is typically induced in yeast with the drug rapamycin, a TOR (target of rapamycin) kinase inhibitor that mimics nutrient deprivation. Rapamycin treatment up-regulated the Atg40 ER-phagy receptor and increased the number of Atg40 puncta that colocalized with Lst1-Sec23. Atg40 also bound to Lst1. Other COPII coat subunits did not colocalize with or interact with Atg40. Highlighting the importance of ER dynamics in ER-phagy, the Lst1-Sec23 complex failed to colocalize with Atg40 puncta and Atg8 in Lnp1-depleted cells, which are defective in ER-phagy. Consistent with a role for Lst1 in packaging ER domains, Atg40 degradation during ER-phagy required Lst1. Furthermore, both Lst1 and Atg40 were needed to sequester ER domains into autophagosomes. We also found that ER stress induced by an overexpressed, aggregation-prone secretory protein up-regulated Atg40 expression to reduce protein aggregation in the ER. TOR-dependent autophagy transcriptional regulators, and not the UPR, modulated Atg40 expression. The role of Lst1 in ER-phagy appears to be conserved, because its mammalian homolog, SEC24C, was similarly required for ER-phagy. Specifically, we found that SEC24C was needed for the degradation of two mammalian ER-phagy receptors, FAM134B and RTN3. SEC24C function is especially critical in the central nervous system, because its depletion in postmitotic neurons leads to their death.

ON OUR WEBSITE

Read the full article at http://dx.doi.org/10.1126/science.aau9263

CONCLUSION: We discovered an unconventional function for a COPII cargo adaptor complex, Lst1/SEC24C-Sec23, in targeting domains of the ER for autophagy. Lst1/SEC24C-mediated ER-phagy was induced by nutrient deprivation or the expression of aggregation-prone proteins. In the latter case, ER-phagy prevented protein aggregation in the ER. Formation of Lst1/SEC24C-Sec23–containing ER-phagy sites (ERPHS) required Lnp1-stabilized ER junctions. ERPHS were found to be distinct from the Sec24-Sec23–containing ER exit sites (ERES) that bud canonical COPII-coated transport vesicles. Thus, our findings indicate that COPII cargo adaptors package distinct cargoes (ER domains or exported proteins) into membranes that are then directed onto alternate pathways, ER-phagy or the secretory pathway. The Lst1/SEC24C-Sec23 and Sec24-Sec23 cargo adaptor complexes could sort their distinct cargoes through an interaction with the cytoplasmic domain of an ER transmembrane protein: the ER-phagy receptor or an exported protein, respectively. These distinct ER-trafficking routes are regulated by separate stress-response pathways. ER-phagy depends on TOR-dependent autophagy transcriptional regulators, whereas protein homeostasis on the secretory pathway is modulated by the UPR. ■

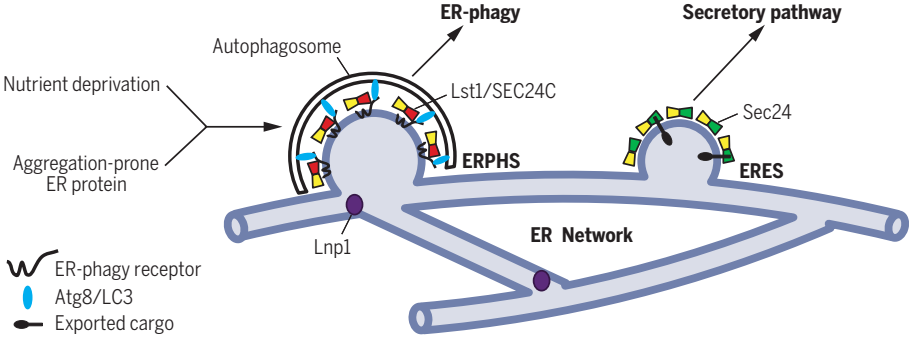

COPII cargo adaptors package cargoes onto two distinct pathways. ER-phagy, which can be induced by nutrient deprivation or expression of aggregation-prone proteins, occurs at ERPHS that contain Lst1/SEC24C-Sec23. The absence of Sec24 from the ERPHS distinguishes them from the Sec24-containing ERES, which bud conventional COPII vesicles that traffic to the Golgi. ER junctions stabilized by Lnp1 are important for the formation of the ERPHS.

The list of author affiliations is available in the full article online.
*These authors contributed equally to this work.
†These authors contributed equally to this work.
‡Corresponding author. Email: sfnovick@ucsd.edu

CELL BIOLOGY

A COPII subunit acts with an autophagy receptor to target endoplasmic reticulum for degradation

Yixian Cui[1], Smriti Parashar[1], Muhammad Zahoor[2]*, Patrick G. Needham[3]*, Muriel Mari[4], Ming Zhu[1], Shuliang Chen[1], Hsuan-Chung Ho[1], Fulvio Reggiori[4], Hesso Farhan[2]†, Jeffrey L. Brodsky[3]†, Susan Ferro-Novick[1]‡

The COPII-cargo adaptor complex Lst1-Sec23 selectively sorts proteins into vesicles that bud from the endoplasmic reticulum (ER) and traffic to the Golgi. Improperly folded proteins are prevented from exiting the ER and are degraded. ER-phagy is an autophagic degradation pathway that uses ER-resident receptors. Working in yeast, we found an unexpected role for Lst1-Sec23 in ER-phagy that was independent from its function in secretion. Up-regulation of the stress-inducible ER-phagy receptor Atg40 induced the association of Lst1-Sec23 with Atg40 at distinct ER domains to package ER into autophagosomes. Lst1-mediated ER-phagy played a vital role in maintaining cellular homeostasis by preventing the accumulation of an aggregation-prone protein in the ER. Lst1 function appears to be conserved because its mammalian homolog, SEC24C, was also required for ER-phagy.

Vesicle transport cargo adaptors sort and concentrate cargo into transport vesicles at specific stages of membrane traffic (*1*, *2*). At the endoplasmic reticulum (ER), the Sec24 subunit of the major COPII-cargo adaptor complex, Sec24-Sec23, binds to the cytosolic domain of ER transmembrane proteins and packages them into vesicles that traffic to the Golgi (*1*). Yeast also have two Sec24 paralogs, Iss1/Sfb2 (56% identity) and Lst1/Sfb3 (23% identity), which form secretory cargo adaptor complexes with Sec23. Mammals have four SEC24 isoforms. The mammalian SEC24 homologs (SEC24A and SEC24B) are 50% identical but only share 20% identity with the Lst1 homologs (SEC24C and SEC24D), which are also 50% identical to each other (*3*).

ER homeostasis is maintained by the unfolded protein response (UPR), which is up-regulated by ER stressors, such as the accumulation of unfolded or misfolded proteins in the ER. The UPR restores homeostasis by a variety of mechanisms, including the activation of signaling pathways that increase the production of the chaperones and enzymes that promote and regulate protein folding (*4*). To prevent improperly folded proteins from entering the secretory pathway, ER-associated degradation (ERAD) recognizes terminally misfolded proteins and retrotranslocates them into the cytosol for degradation by the proteasome (*5*). ERAD, however, is unable to clear all aberrant proteins from the ER (*6*). Macroautophagy (herein called autophagy) of the ER, or ER-phagy, could be part of a global ER stress response that restores cellular homeostasis when ERAD and/or the UPR fail to respond. There are two major types of autophagy pathways, bulk and selective (*7*). During starvation, bulk autophagy uses autophagosomes to scavenge cytoplasmic components for nutrients. To rapidly increase autophagosome number, COPII vesicles are rerouted to serve as a membrane source for bulk autophagy (*7*, *8*). Selective pathways instead use autophagy receptors to package cargo into autophagosomes. These cargoes include damaged or superfluous organelles, protein aggregates, and pathogens (*9*).

Although ER-phagy was initially described in 2005 (*10*), it was not until the first ER-phagy receptors were identified that the process was thought to be selective (*11*, *12*). ER-phagy occurs at discrete foci on the ER (*13*); however, the autophagy receptors that load ER into autophagosomes are dispersed throughout the contiguous network of the ER. How sites on the ER are targeted for ER-phagy is unclear. We reasoned that the cytosolic machinery that recognizes and binds to ER-phagy receptors may play a role in marking specific sites on the ER where autophagy will occur. Because COPII coat subunits are known to participate in membrane-budding events at the ER (*1*), we investigated whether coat subunits play a role in sequestering ER domains into autophagosomes during ER-phagy.

Lst1 is required for ER-phagy but not bulk autophagy

ER-phagy is typically induced in yeast by treating cells for 12 to 24 hours with rapamycin, a TOR (target of rapamycin) kinase inhibitor that mimics nutrient starvation (*10*, *11*). Rapamycin also up-regulates the expression of the ER-phagy receptor Atg40, which increases ER-phagy activity (*11*). Atg40, a reticulon-like ER membrane protein, is required for cortical and cytoplasmic ER degradation and also contributes to nuclear ER degradation. Nuclear ER turnover is predominantly facilitated by Atg39, a nucleophagy receptor (*11*).

We initiated our studies by investigating whether COPII coat subunits play a role in ER-phagy. The long incubation period with rapamycin to induce ER-phagy precluded us from analyzing temperature-sensitive mutants harboring COPII mutations because they die quickly at their restrictive temperature. The *lst1*Δ, *iss1*Δ, and *sec24-3A* mutants, however, do not appreciably impair growth or secretion (*14*, *15*). In *sec24-3A* cells, bulk autophagy is defective as a consequence of a failure to phosphorylate Sec24 at T324, T325, and T328 (*15*). Sec24 phosphorylation at these sites, which are conserved in Iss1, enables COPII-coated vesicles to bind the core autophagy machinery (*15*). We found a defect in the degradation of the ER protein Sec61 in *lst1*Δ, but not in the *sec24-3A iss1*Δ and *iss1*Δ mutants (Fig. 1, A to D, and fig. S1, A to C). One of the kinases that phosphorylates Sec24 during bulk autophagy, Hrr25 (*15*), was also dispensable for ER-phagy (fig. S1, D and E). Furthermore, Sec24 phosphorylation was not needed for pexophagy (fig. S2, A and B) and mitophagy (fig. S2, D and E). The degradation of Rtn1, which marks ER tubules, the edges of sheets, and the nuclear ER in a small fraction of cells (*16*), was also defective in the *lst1*Δ mutant (Fig. 1, E and F, and fig. S3, A and B). Similarly, a third ER protein, Per33, was degraded less efficiently in *lst1*Δ cells (fig. S3, C to F). Like Sec61, Per33 resides on the nuclear, cortical, and cytoplasmic ER (*17*). In addition to being induced by rapamycin, Lst1-mediated ER degradation was also induced by growth to the stationary phase (fig. S4, A to C).

To determine whether Lst1 functions in bulk autophagy, we measured the activation of vacuolar alkaline phosphatase (Pho8Δ60) 4 hours after starvation (fig. S4D), as well as the cleavage of green fluorescent protein (GFP)–autophagy-related protein 8 (Atg8) in the vacuole (fig. S4, E and F) 24 hours after rapamycin treatment (*18*). When bulk autophagy is induced, GFP-Atg8 and Pho8Δ60 are delivered to the vacuole, where Pho8Δ60 is activated by proteolytic cleavage. No defect in bulk autophagy was detected in *lst1*Δ cells by either assay.

Additionally, Lst1 was not needed for pexophagy (fig. S2, B and C), mitophagy (fig. S2, E and F), or the biosynthetic cytosol-to-vacuole targeting pathway (fig. S2G), which also uses autophagy machinery (*18*). Thus, Lst1 and its paralog, Sec24, appeared to function in different autophagy pathways. Although phosphorylation of the Sec24 membrane distal surface is required for bulk autophagy (*15*), it was dispensable for

[1]Department of Cellular and Molecular Medicine, University of California at San Diego, La Jolla, CA 92093, USA. [2]Institute of Basic Medical Sciences, Department of Molecular Medicine, University of Oslo, Sognsvannsveien 9, 0372 Oslo, Norway. [3]Department of Biological Sciences, University of Pittsburgh, Pittsburgh, PA 15260, USA. [4]Department of Biomedical Sciences of Cells and Systems, University of Groningen Medical Center, Groningen, Netherlands.
*These authors contributed equally to this work.
†These authors contributed equally to this work.
‡Corresponding author. Email: sfnovick@ucsd.edu

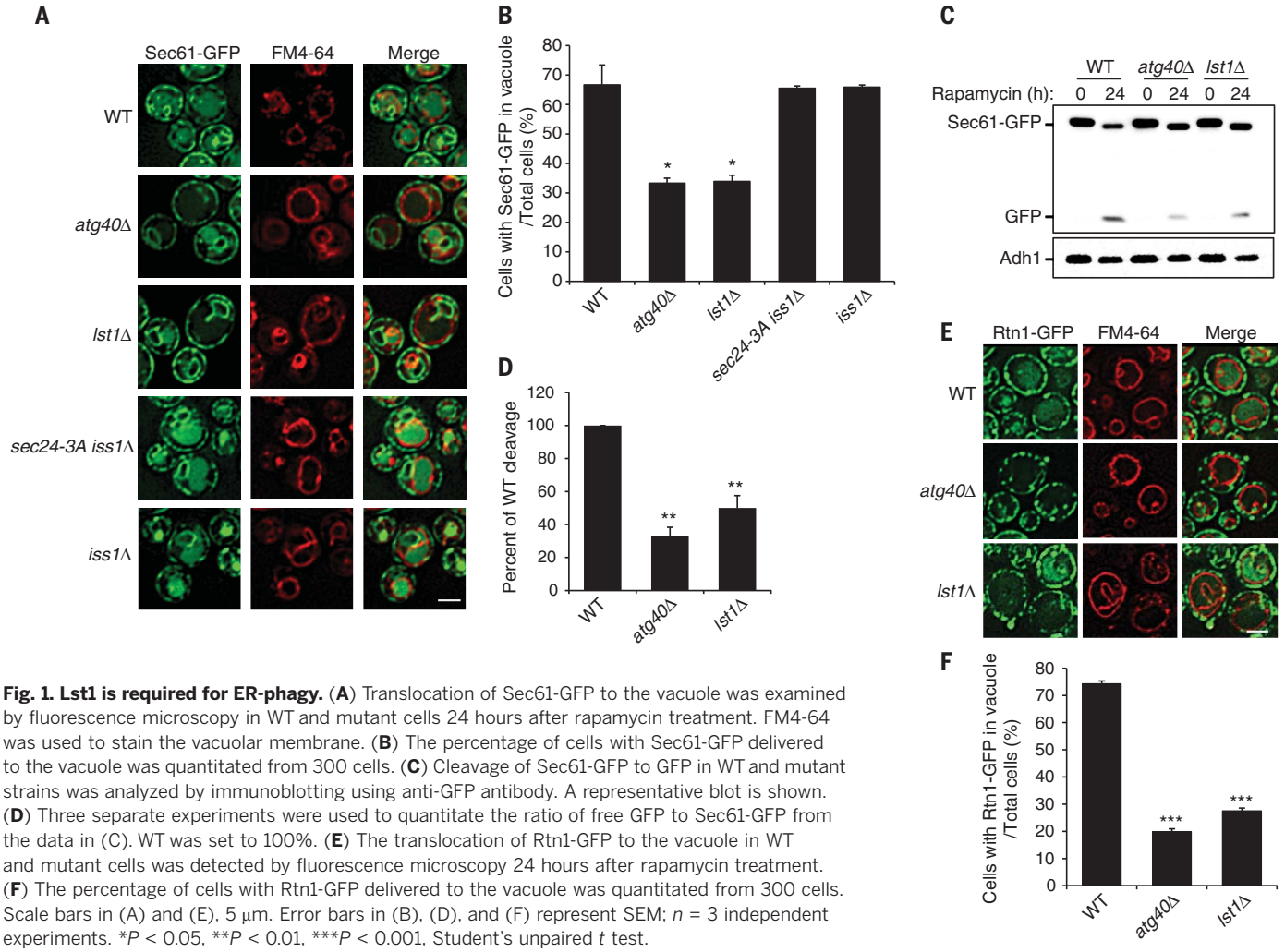

Fig. 1. Lst1 is required for ER-phagy. (**A**) Translocation of Sec61-GFP to the vacuole was examined by fluorescence microscopy in WT and mutant cells 24 hours after rapamycin treatment. FM4-64 was used to stain the vacuolar membrane. (**B**) The percentage of cells with Sec61-GFP delivered to the vacuole was quantitated from 300 cells. (**C**) Cleavage of Sec61-GFP to GFP in WT and mutant strains was analyzed by immunoblotting using anti-GFP antibody. A representative blot is shown. (**D**) Three separate experiments were used to quantitate the ratio of free GFP to Sec61-GFP from the data in (C). WT was set to 100%. (**E**) The translocation of Rtn1-GFP to the vacuole in WT and mutant cells was detected by fluorescence microscopy 24 hours after rapamycin treatment. (**F**) The percentage of cells with Rtn1-GFP delivered to the vacuole was quantitated from 300 cells. Scale bars in (A) and (E), 5 μm. Error bars in (B), (D), and (F) represent SEM; $n = 3$ independent experiments. $^{*}P < 0.05$, $^{**}P < 0.01$, $^{***}P < 0.001$, Student's unpaired t test.

ER-phagy. By contrast, Lst1 acted exclusively in ER-phagy.

Lst1 is primarily known for the formation of larger COPII-coated vesicles and the trafficking of glycosylphosphatidylinositol (GPI)–anchored proteins (*1*). Unlike Sec24, Lst1 cannot package the ER-Golgi fusion machinery (SNAREs) into COPII vesicles. Consequently, vesicles containing Lst1, but not Sec24, are unable to fuse with the Golgi (*19*). When we measured ER-phagy in two *lst1* mutants (*LST1*-B1 and *LST1*-B2) that disrupt the packaging of GPI-anchored proteins into COPII vesicles (*20*), no ER-phagy defect was observed (fig. S5, A to D). Thus, the role of Lst1 on the secretory pathway can be uncoupled from its contribution to ER-phagy. These results establish an unanticipated role for this conserved coat protein in autophagy.

Lst1 acts in concert with Atg40

Sec61-GFP–positive ER cisternae and foci accumulated in rapamycin-treated *atg40*Δ and *lst1*Δ mutants (fig. S6, A and B). Furthermore, the ER degradation defect in the *lst1*Δ*atg40*Δ double mutant was not significantly different from either single knockout (fig. S6, C to F). These findings implied that Lst1 and Atg40 function in the same pathway. Because increased levels of autophagy receptors increase ER-phagy and the number of ER-containing autophagosomes (*11*, *12*), ER-phagy receptors are thought to play a role in packaging ER into autophagosomes (*12*). To address if Lst1 works with Atg40 to perform this function, we induced Atg40 expression with rapamycin (*11*) and asked if this promotes an association with Lst1. To assess the colocalization of Lst1-3xGFP with Atg40-2xmCherry, we focused on noncortical Atg40 puncta because previous studies indicated that these more central puncta have greater accessibility to the autophagy machinery (*17*). Sec24-GFP and Sec13-GFP, a component of the COPII coat scaffold complex (Sec13-Sec31) (*1*), were examined as controls. Although all COPII coat subunits mark ER exit sites (ERES) in nutrient-rich growth conditions (*21*), only Lst1-3xGFP and its partner, Sec23-GFP, showed increased colocalization with Atg40-2xmCherry puncta (Fig. 2, A to C, and fig. S7, A to C). Unlike Atg40, Lst1 and Sec23 expression did not increase with rapamycin treatment (fig. S7D). The number of Lst1-3xGFP and Sec23-GFP puncta was also unchanged (fig. S7E). Although previous studies showed that *CUP1*-driven Atg40 overexpression only increased ER-phagy in the presence of rapamycin (*11*), overexpression was sufficient to drive Atg40 colocalization with Lst1 (fig. S8, A and B). Rapamycin also induced the expression of the nucleophagy receptor Atg39 (*11*) but did not induce the colocalization of Lst1 with Atg39 (fig. S8, C and D). Furthermore, Lst1 did not contribute to the degradation of the nuclear ER marker Hmg1 (fig. S8, E to H).

Selective autophagy receptors bind to the ubiquitin-like protein Atg8 at sites of autophagosome formation (*9*). Consistent with the proposal that Lst1 functions with Atg40 to target ER domains for degradation, rapamycin induced Atg8-Lst1 colocalization in wild-type (WT) but not *atg40*Δ cells (Fig. 2D and fig. S9A). By contrast, Atg8 showed increased colocalization with two COPII coat subunits required for bulk autophagy, Sec24 and Sec13 (*22*), in both WT and *atg40*Δ cells (Fig. 2D and fig. S9A). Because Sec23 is a binding partner for both

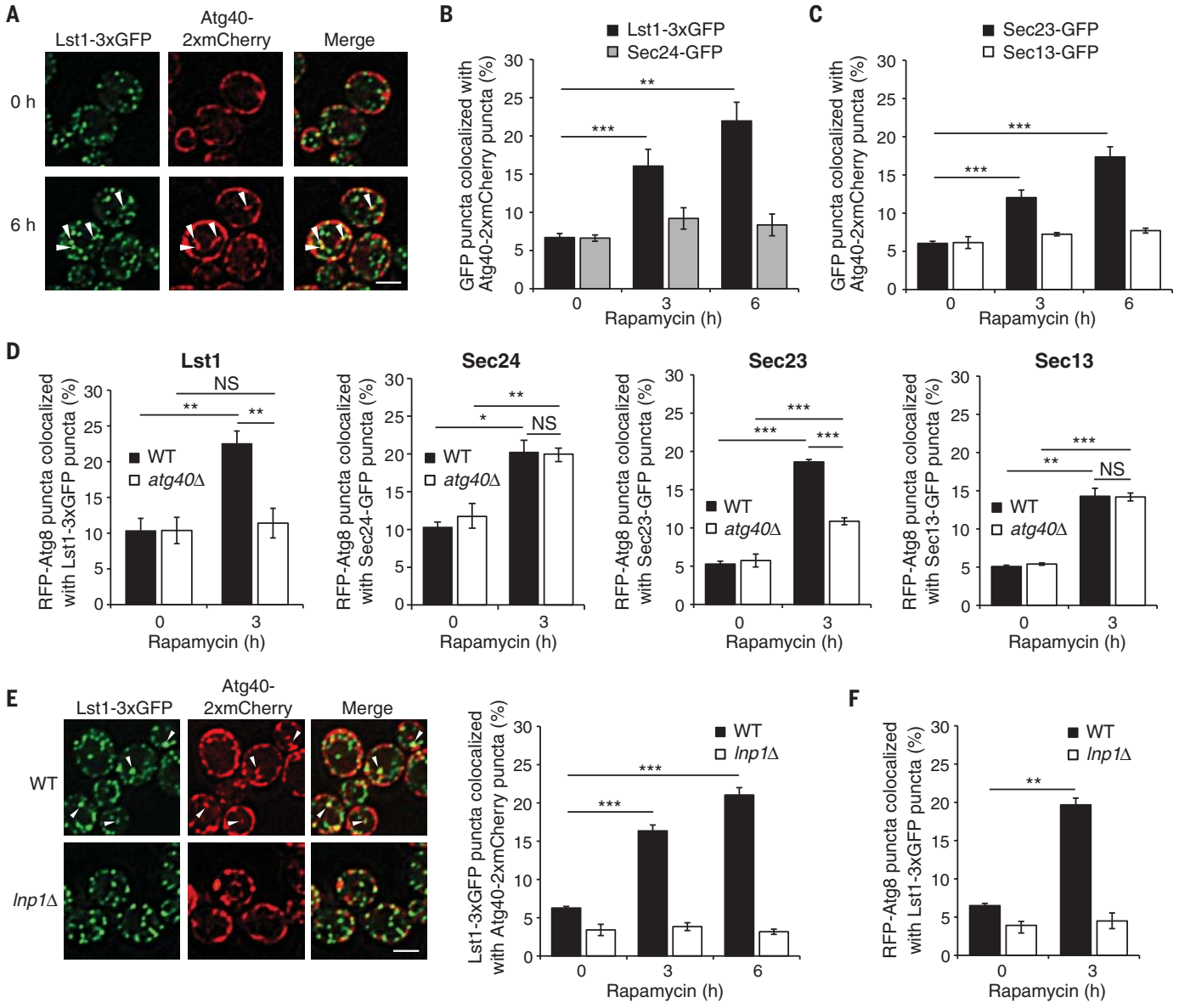

Fig. 2. Lst1 and Sec23 colocalize with Atg40 and Atg8 in rapamycin-treated cells. (**A**) Representative images of cells treated for 0 or 6 hours with rapamycin. Arrowheads indicate Lst1-3xGFP that colocalized with Atg40-2xmCherry puncta. (**B**) Bar graph showing the percentage of Lst1-3xGFP or Sec24-GFP colocalizing with Atg40-2xmCherry puncta. (**C**) Bar graph showing the percentage of Sec23-GFP or Sec13-GFP colocalizing with Atg40-2xmCherry puncta. (**D**) Cells were treated for 0 or 3 hours with rapamycin, and the RFP-Atg8 that colocalized with GFP-tagged COPII subunits was quantitated. (**E**) Left, arrowheads indicating Lst1-3xGFP that colocalized with Atg40-2xmCherry puncta 6 hours after rapamycin treatment. Quantitation is on the right. (**F**) Quantitation of RFP-Atg8 that colocalized with Lst1-3xGFP in WT and *lnp1*Δ cells. Scale bars in (A) and (E), 5 μm. Error bars in (B) to (F) represent SEM; $n = 3$ to 6 independent experiments. NS, not significant ($P \geq 0.05$); *$P < 0.05$, **$P < 0.01$, ***$P < 0.001$, Student's unpaired t test.

Lst1 and Sec24, the colocalization of Atg8 with Sec23 was only partially dependent on Atg40 (Fig. 2D and fig. S9A).

Next, we investigated whether ER organization is important for the colocalization of Lst1 with Atg40. Lnp1 is an ER protein that resides at and stabilizes the three-way junctions that form when two tubules fuse to each other (*23*). In its absence, ER network rearrangements are disrupted and Atg40 puncta fail to access the autophagy machinery (*17*). As a consequence, ER is not packaged into autophagosomes in *lnp1*Δ cells (*17*). We found that Lst1-3xGFP failed to colocalize with Atg40-2xmCherry (Fig. 2E and fig. S9B; also see Pearson's coefficient in fig. S9C) in *lnp1*Δ cells. Furthermore, even though Lst1-3xGFP and RFP-Atg8 puncta appeared unaltered in the *lnp1*Δ mutant, Atg8 also failed to colocalize with Lst1 (Fig. 2F and fig. S9D). We propose that Atg8-Lst1–colocalizing puncta (usually one per cell) represent active ER-phagy sites stabilized by Lnp1. Although Atg40 puncta tend to accumulate at the cell periphery in Lnp1-depleted cells (*17*), the distribution of Atg40 puncta was unperturbed in *lst1*Δ cells (fig. S9E).

The localization studies described above suggested that Lst1 and Atg40 interact with each other during ER-phagy. Lst1 could interact with Atg40 via its cytosolic domain (*11*); however, this possibility could not be tested because the cytoplasmic domain was unstable. We were also unable to express full-length Atg40 in bacteria. Instead, to address whether Lst1 interacts with

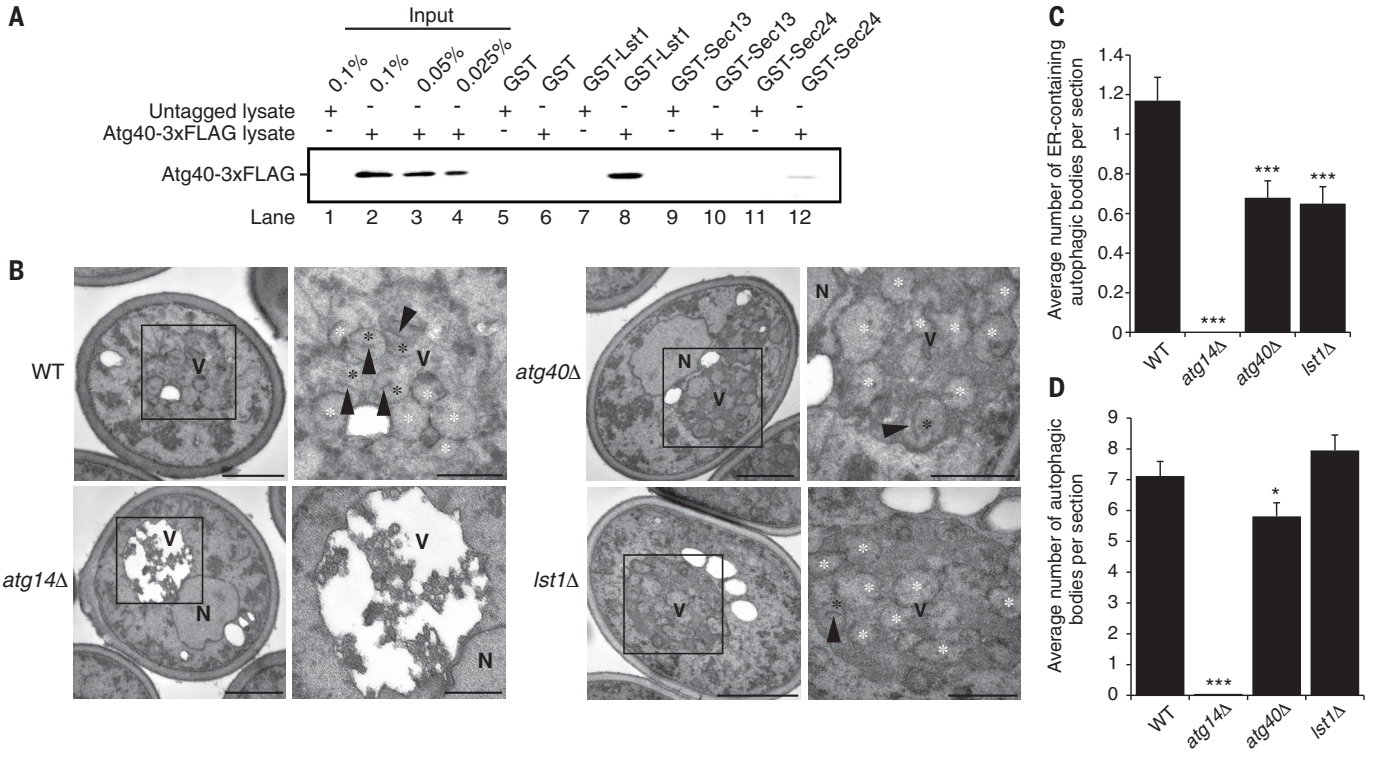

Fig. 3. Lst1 binds to Atg40 and facilitates the packaging of ER into autophagosomes. (**A**) Equimolar amounts (0.1 μM) of purified recombinant GST and GST fusion proteins were incubated with 2 mg of yeast lysate prepared from Atg40-3xFLAG-untagged or -tagged cells treated with rapamycin. (**B**) Representative electron micrographs of WT and *pep4*Δ strains treated for 12 hours with rapamycin. The boxed areas in the left panels are magnified on the right. Black asterisk, an autophagic body containing an ER fragment; white asterisk, an autophagic body lacking an ER fragment; arrowhead, an ER fragment inside an autophagic body. Scale bars in the left and right panels represent 1 μm and 500 nm, respectively. (**C**) Bar graph showing the average number of ER-containing autophagosomes. (**D**) Bar graph showing the average number of total autophagosomes. Error bars in (C) and (D) represent SEM; $n = 100$ cells. $^{*}P < 0.05$, $^{***}P < 0.001$, Student's unpaired t test. N, nucleus; V, vacuole.

Atg40, we performed binding studies with lysates prepared from untreated and rapamycin-treated cells expressing Atg40-3xFLAG. Atg40-3xFLAG from both lysates bound to purified, bacterially produced glutathione *S*-transferase (GST)–Lst1, but not to GST-Sec13, GST-Sec24 (Fig. 3A and fig. S10, A and C), or GST-Sec23 (fig. S10B). GST-Lst1 also failed to bind to two other ER proteins, Ufe1 and Yip1 (fig. S10D). These findings indicate that Lst1, but not Sec24 or other COPII coat subunits, binds to Atg40. Sec13-Sec31 could have failed to associate with Atg40 because the binding of Lst1-Sec23 to Atg40 sterically hindered its interaction. Supporting the proposal that the interaction of Atg40 with Lst1 is needed for ER-phagy, the rapamycin-induced degradation of Lst1-GFP required Atg40 and Atg40-GFP degradation required Lst1 (fig. S11, A to H).

To determine the number of ER-containing autophagosomes in the *lst1*Δ mutant, we examined cells depleted of the vacuolar protease Pep4 by conventional electron microscopy (Fig. 3, B to D). Although autophagic bodies were absent in the *atg14*Δ mutant, which blocks autophagosome formation (Fig. 3, B to D), the number of autophagosomes formed in the *lst1*Δ mutant was the same as that in WT (Fig. 3D). By contrast, a significant reduction in autophagic bodies that contained ER was observed in the *lst1*Δ mutant (Fig. 3, B and C). Consistent with the proposal that Lst1 works with Atg40 to package cortical and cytoplasmic ER into autophagosomes, the *lst1*Δ defect was comparable to that seen in *atg40*Δ cells (Fig. 3, B and C).

ER stress up-regulates Atg40

In mammalian cells, the putative ER-phagy receptor FAM134B targets ERAD-insensitive substrates to autophagy (*6*). How the ER communicates with the autophagy machinery when ERAD does not respond or is overwhelmed is unknown.

The Z variant of human alpha-1 antitrypsin (ATZ) is an aggregation-prone ERAD substrate that is also targeted to the lysosome via non–autophagosome-mediated (*24*) and autophagosome-mediated pathways (*25*, *26*). When ATZ is highly overexpressed in yeast under the inducible galactose promoter (*GAL1*), excess ATZ not degraded by ERAD is directed to the vacuole through two pathways, vacuolar protein sorting and autophagy (*27*). Blocking the latter pathway leads to the accumulation of ATZ aggregates in the ER (*27*). Currently, it is unknown whether this autophagosome-mediated pathway is ER-phagy. To determine whether ATZ aggregates in the absence of Atg40 or Lst1, microsomal membrane fractions prepared from WT, *atg14*Δ, *atg40*Δ, and *lst1*Δ cells were analyzed on sucrose gradients. Soluble ATZ was primarily found at the top of the WT gradient, whereas ATZ from mutant lysates was largely in the pellet (Fig. 4, A to C, and fig. S12, A and B). Aggregation appeared to result from a block in ER-phagy, because substantially less ATZ was observed in the pellet when lysates from the *lst1*-B1 mutant were examined (fig. S12C). The *lst1*-B1 mutant disrupts membrane traffic (*20*) but not ER-phagy (fig. S5). Aggregation was also specific to misfolded ATZ, because appreciably less WT M-variant alpha-1 antitrypsin (ATM) was observed in the pellet when lysates from *lst1*Δ or *atg40*Δ cells were examined (Fig. 4D). Consistent with this observation, a portion of the ATM, but not ATZ, was secreted (fig. S12D). Thus, only mutant alpha-1 antitrypsin aggregated in the ER in the absence of ER-phagy. It is notable that in the pancreas, the loss of the ER-phagy receptor CCPG1 leads to the accumulation of aggregated proteins in the ER (*13*).

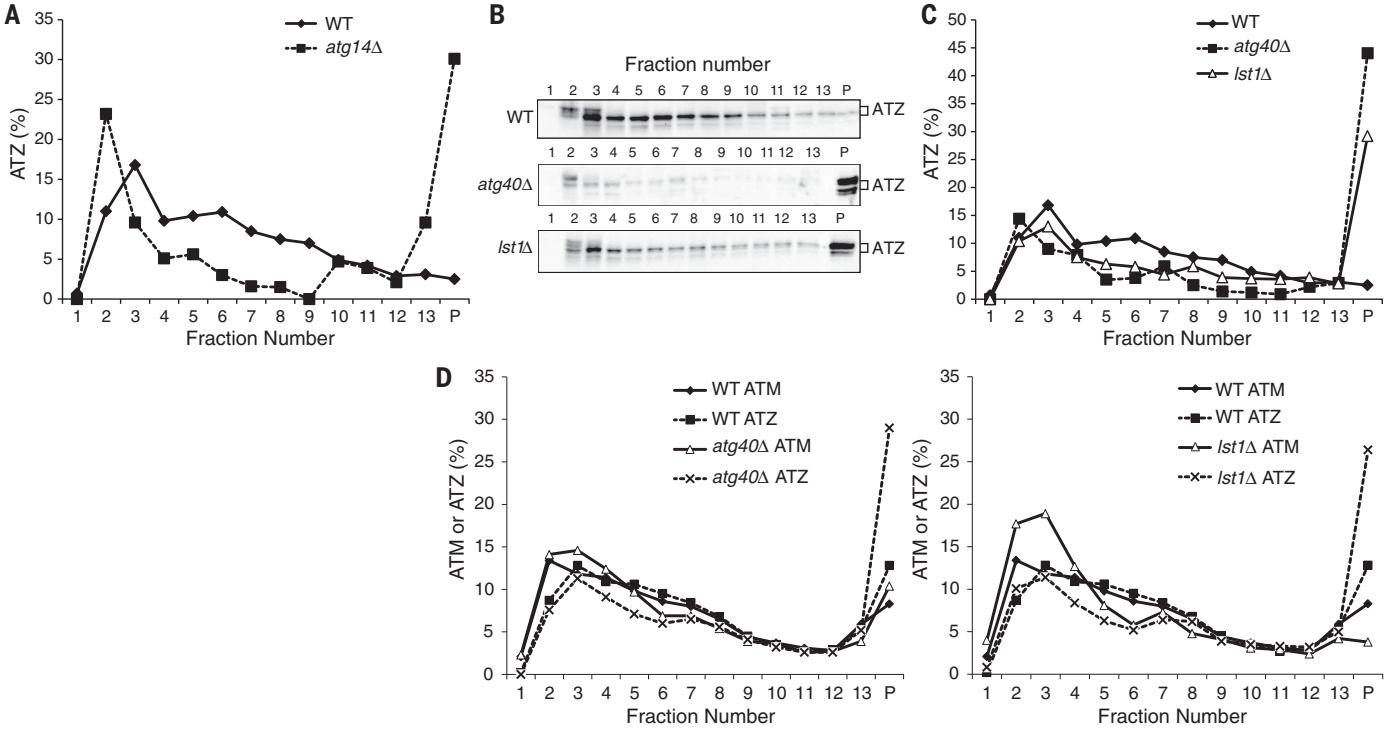

Fig. 4. ATZ aggregates accumulate in *atg40*Δ and *lst1*Δ mutants. Microsomal membrane fractions prepared from WT and mutant cells harboring plasmids expressing either ATZ (**A** to **D**) or ATM (D) were lysed in the presence of detergent and fractionated on a sucrose gradient. Gradient fractions were blotted with antibody directed against alpha-1 antitrypsin. Soluble alpha-1 antitrypsin was at the top of the gradient and aggregates remained in the pellet (P).

Previous studies showed that multiple COPII coat subunits, including Sec24 and Lst1, are targets of the UPR (*28*). To determine whether Atg40 is also a UPR target, we overexpressed ATZ in the presence or the absence of Ire1, an ER transmembrane kinase that triggers the UPR (*29*). ATZ induction enhanced Atg40 expression in WT cells (compare Fig. 5, A and B, with fig. S12E). Furthermore, Atg40 expression and ATZ accumulation were further enhanced in *ire1*Δ mutant cells, which block the UPR and augment ER stress (*4*, *29*) (Fig. 5, A and B). By contrast, overexpressed ATM did not increase Atg40 expression in the *ire1*Δ mutant (fig. S12F). To determine whether the loss of Atg40 induces the UPR, we examined pathway induction by flow cytometry in cells carrying an integrated UPR-regulated GFP reporter. Whereas the *atg39*Δ (Fig. 5C) and *sec24-3A iss1*Δ mutants behaved like WT (fig. S12G), the level of UPR induction in the *atg40*Δ and *lst1*Δ mutants was the same as that in an ERAD-deficient *hrd1*Δ strain (Fig. 5C) (*5*). Thus, although Atg40 was not found to be a UPR target, the UPR responded to the loss of ER-phagy.

Because Atg40 expression is not under the control of the UPR, we next sought to identify the pathway that regulates it. ER stress is known to modulate the expression of core autophagy machinery (*30*). Therefore, we considered the possibility that autophagy transcriptional regulators control Atg40 expression. Pho23, which associates with the histone deacetylase large complex (Rpd3L), is a transcriptional repressor of autophagy that modulates autophagosome abundance via Atg9 (*31*). We found that Atg40, but not the UPR targets Kar2 and Lst1, were up-regulated in the *rpd3*Δ and *pho23*Δ strains (Fig. 5, D and E). Atg40 and Atg9 mRNA levels also increased in these mutants (Fig. 5F), indicating that the Atg40 ER-phagy receptor is a target of the same transcriptional regulators that modulate Atg9 and other core autophagy machinery.

Mammalian SEC24C is required for ER-phagy

It was recently reported that SEC24A and SEC24B, but not SEC24C and SEC24D, contribute to bulk autophagy (*32*). To determine whether any of the SEC24 isoforms are required for ER-phagy in mammalian cells, we knocked down each of the four isoforms by small interfering RNA (siRNA) in U2OS cells (fig. S13A). We then monitored the delivery of two ER-phagy receptors, FAM134B and RTN3, to lysosomes in the Torin2 (TOR inhibitor2)–treated SEC24-depleted cells. We chose to examine these two mammalian ER-phagy receptors because Atg40 has a domain structure that is similar to FAM134B yet localizes to the tubular ER–like RTN3 (*12*, *33*). 3xFLAG-FAM134B was resistant to degradation in SEC24C-depleted cells, but sensitive in cells depleted of SEC24A, SEC24B, or SEC24D (Fig. 6A and fig. S13B). Moreover, the delivery of 3xFLAG-FAM134B to lysosomes (LAMP1) required SEC24C and ULK1, a component of the autophagosome biogenesis machinery (Fig. 6, B and C, and fig. S13C). The delivery of RTN3 to lysosomes was also SEC24C and ULK1 dependent (Fig. 6, D and E, and fig. S14). Thus, in mammals, as in yeast, TOR inhibition stimulated the delivery of ER to lysosomes via Lst1/SEC24C-mediated ER-phagy.

Discussion

Here, we report a noncanonical role for the COPII-cargo adaptor complex Lst1-Sec23 and show that it functions with the ER-phagy receptor Atg40 to specify ER domains for ER-phagy. By analogy to its role as a cargo adaptor in vesicle traffic (*20*), Lst1-Sec23 may sort ER domains into autophagosomes through an interaction with the cytoplasmic domain of Atg40 (fig. S15). Several lines of evidence highlight the key events mediated by Lst1 on this pathway. First, when Atg40 expression was up-regulated by the TOR inhibitor rapamycin, the Lst1-Sec23 complex associated with Atg40 puncta. Second, in accord with the proposal that the colocalization of Lst1 with Atg40 is needed for ER-phagy, Lst1 failed to colocalize with Atg40 and Atg8 in the *lnp1*Δ mutant. Lnp1 is needed for ER organization and the incorporation of ER into autophagosomes (*17*). Third, consistent with a role in ER packaging, Lst1 was required for the

degradation of Atg40, and the number of ER-containing autophagosomes was reduced in the *lst1*Δ mutant.

To date, six ER-phagy receptors have been identified in mammalian cells (*12*, *13*, *33*–*37*). Although some receptors respond to starvation, others only respond to ER stress, and some respond to both. Here, we have shown that Atg40 responds to starvation and ER stress. Atg40 was up-regulated by both rapamycin (*11*) and the overexpression of an aggregation-prone misfolded secretory protein (ATZ). In the latter case, the induction of Lst1-mediated ER-phagy reduced the level of aggregated ATZ in the ER (fig. S15). Consistent with the observation that a TOR inhibitor up-regulates Atg40 (*11*), we found that Atg40 expression is modulated by autophagy transcriptional regulators. Recent studies have shown that ER stress inhibits TOR (*38*). Thus, TOR-dependent autophagy transcriptional regulators may also modulate the up-regulation of ER-phagy receptors to reduce ER protein aggregation.

Our findings imply that a specific subcomplex of the COPII coat that contains Lst1-Sec23 binds to Atg40 to package ER domains into autophagosomes during ER-phagy (fig. S15). ER-phagy occurs at distinct sites on the ER that we have named ERPHS (ER-phagy sites). The absence of Sec24 from these sites distinguishes them from the Sec24-containing ERES that bud conventional COPII vesicles (fig. S15). Because previous studies in yeast did not reveal a substantial accumulation of cytosolic ER fragments during ER-phagy, it was suggested that ER domains are engulfed into autophagosomes on or in close proximity to the ER network (*10*) (fig. S15). We found that Lst1-GFP was degraded in the vacuole in an Atg40-dependent fashion (fig. S15), indicating that ER fragments were packaged into autophagosomes before they completely uncoated. Because the Lst1-Sec23 complex cannot package SNAREs, fragments that bud from the ER cannot fuse with the Golgi before their incorporation into autophagosomes.

The formation of ERPHS in yeast was dependent on the ER protein Lnp1, which is needed for stable three-way ER junctions (fig. S15) (*23*). Consistent with this observation, the mammalian ER-phagy receptor TEX264 concentrates and colocalizes with LC3 (the Atg8 homolog in mammals) at ER junctions (*36*, *37*). The localization of LNP1 to ER junctions depends on ATLASTIN, which is also required for ER-phagy (*16*, *39*, *40*). Furthermore, ATLASTIN 3 (ATL3) has recently been reported to be an ER-phagy receptor (*35*). Mutations in ATLASTIN and LNP1 are associated with hereditary spastic paraplegia (HSP) and HSP-like neuropathies (*41*, *42*). The ER-phagy receptor FAM134B, which is needed for both ER-phagy and autophagosome-independent ER-to-lysosome degradation (*12*, *24*), is linked to sensory neuron function (*12*).

The mammalian Lst1 homolog SEC24C was also required for the delivery of ER sheets (FAM134B) and tubules (RTN3) to lysosomes for degradation. This observation is in accord with recent data showing that the interactome for the ER-phagy receptor RTN3 includes SEC24C but not the other SEC24 isoforms (*33*). Although professional secretory cells are insensitive to SEC24C depletion, the loss of SEC24C in post-mitotic neurons leads to microcephaly and perinatal death (*43*). Whereas SEC24C and SEC24D are ~50% identical, their functions only partially overlap in the brain (*43*), and we did not detect a substantial role for SEC24D in ER-phagy. Because our experiments and the RTN3 interactome

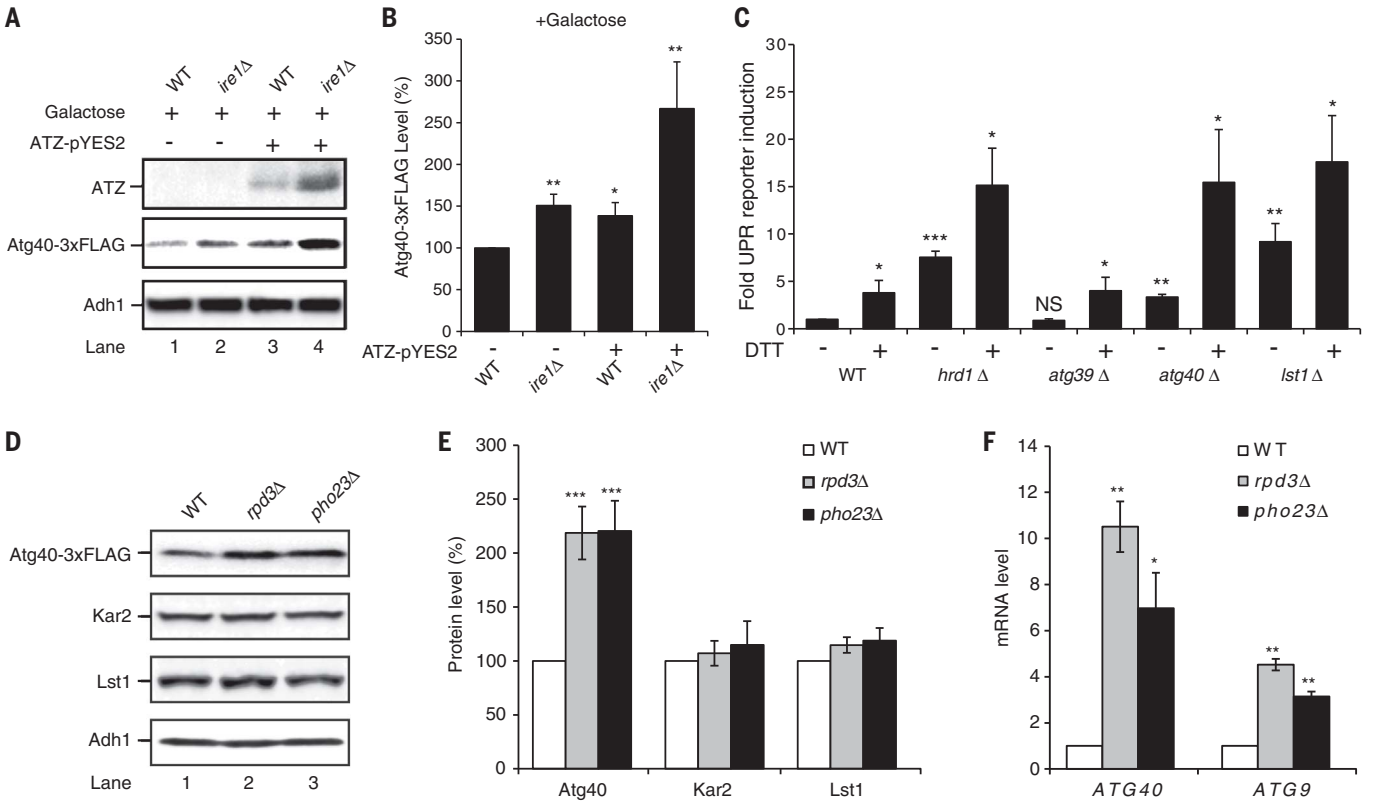

Fig. 5. Atg40 expression is regulated by the Rpd3-Pho23 complex. (**A**) Atg40 expression was examined 24 hours after growth in 2% galactose. Western blot analysis was performed on lysates to detect ATZ (top), Atg40-3xFLAG (middle), and Adh1 (bottom). (**B**) The data in (A) were normalized to Adh1 and WT (−ATZ) was set to 100%. (**C**) UPR induction was assayed by flow cytometry in the absence or presence of 8 mM dithiothreitol (DTT). WT (−DTT) was set to 1.0. (**D**) Atg40-3xFLAG, Kar2, and Lst1 levels were measured by Western blot analysis in the indicated strains. (**E**) The data in (D) were normalized to Adh1 and WT was set to 100%. (**F**) Quantitative reverse transcription–polymerase chain reaction was used to assess mRNA levels. The data were normalized to actin mRNA levels and WT was set to 1.0. Error bars in (B), (C), and (F) represent SEM; $n = 3$ independent experiments. Error bars in (E) represent SEM; $n = 4$ to 8 independent experiments. NS, not significant ($P \geq 0.05$); $^{*}P < 0.05$, $^{**}P < 0.01$, $^{***}P < 0.001$, Student's unpaired t test.

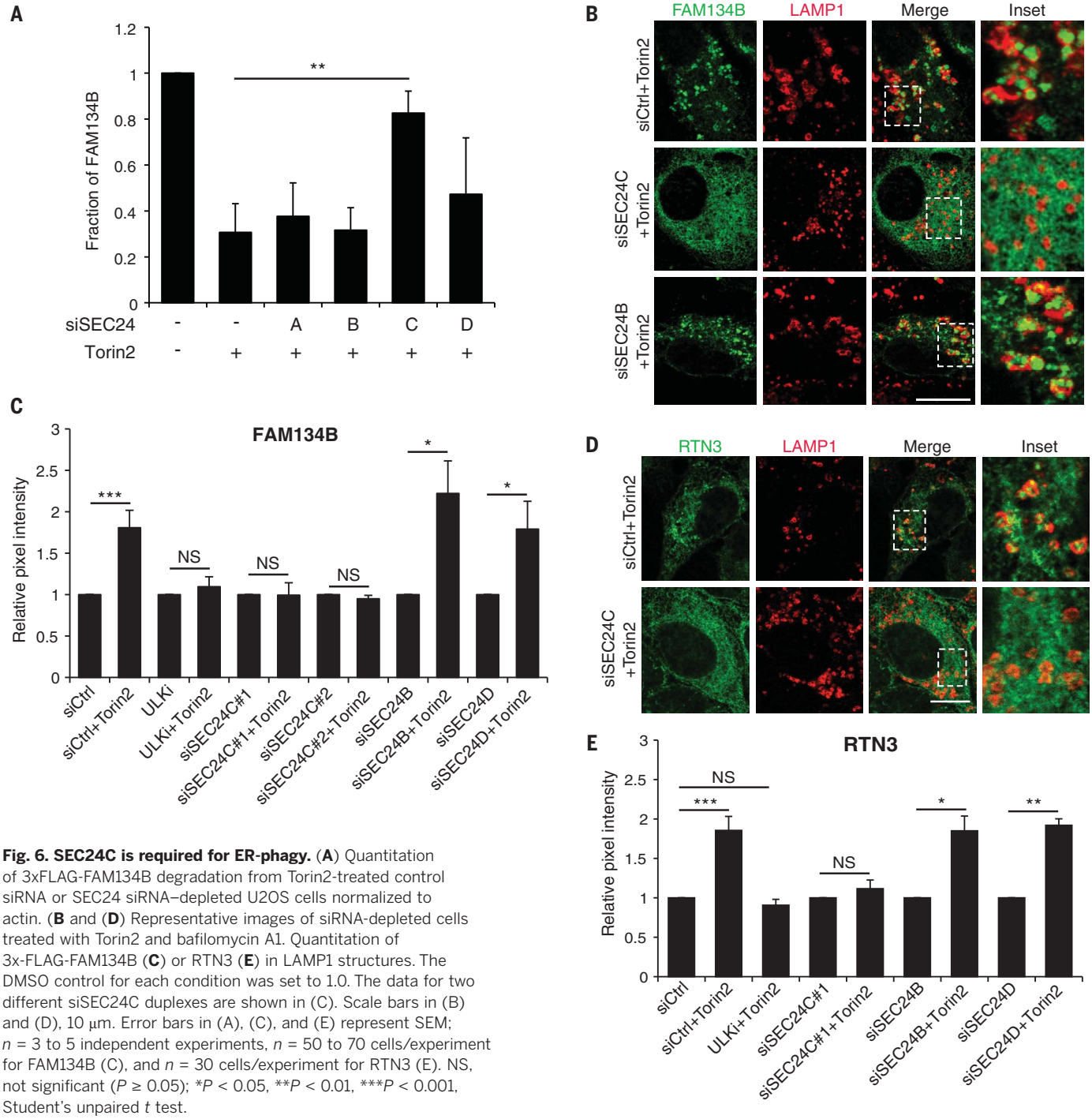

Fig. 6. SEC24C is required for ER-phagy. (**A**) Quantitation of 3xFLAG-FAM134B degradation from Torin2-treated control siRNA or SEC24 siRNA–depleted U2OS cells normalized to actin. (**B** and (**D**) Representative images of siRNA-depleted cells treated with Torin2 and bafilomycin A1. Quantitation of 3x-FLAG-FAM134B (**C**) or RTN3 (**E**) in LAMP1 structures. The DMSO control for each condition was set to 1.0. The data for two different siSEC24C duplexes are shown in (C). Scale bars in (B) and (D), 10 μm. Error bars in (A), (C), and (E) represent SEM; n = 3 to 5 independent experiments, n = 50 to 70 cells/experiment for FAM134B (C), and n = 30 cells/experiment for RTN3 (E). NS, not significant ($P \geq 0.05$); *$P < 0.05$, **$P < 0.01$, ***$P < 0.001$, Student's unpaired t test.

analysis both used U2OS cells, it remains formally possible that other cell types may require SEC24D for ER-phagy. These findings suggest that ER-phagy plays a crucial role in maintaining neuronal homeostasis.

In summary, we propose that in yeast and mammals, COPII cargo adaptors package different cargoes (secretory proteins or ER domains) into membranes and target them to distinct pathways. Our findings imply that ERES, which bud canonical COPII vesicles that traffic on the secretory pathway, are distinct from the ERPHS used in autophagy. The secretory and ER-phagy pathways also appear to be regulated by different stress-response pathways; secretory protein homeostasis is regulated by the UPR, whereas ER-phagy depends on TOR-dependent autophagy transcriptional regulators.

REFERENCES AND NOTES

1. N. Gomez-Navarro, E. Miller, *J. Cell Biol.* **215**, 769–778 (2016).
2. T. Kirchhausen, J. S. Bonifacino, H. Riezman, *Curr. Opin. Cell Biol.* **9**, 488–495 (1997).
3. B. L. Tang, J. Kausalya, D. Y. Low, M. L. Lock, W. Hong, *Biochem. Biophys. Res. Commun.* **258**, 679–684 (1999).
4. P. Walter, D. Ron, *Science* **334**, 1081–1086 (2011).
5. J. L. Brodsky, *Cell* **151**, 1163–1167 (2012).
6. A. Forrester *et al.*, *EMBO J.* **38**, e99847 (2019).
7. S. Davis, J. Wang, S. Ferro-Novick, *Dev. Cell* **41**, 23–32 (2017).
8. T. Shima, H. Kirisako, H. Nakatogawa, *J. Cell Biol.* **218**, 1503–1510 (2019).
9. A. L. Anding, E. H. Baehrecke, *Dev. Cell* **41**, 10–22 (2017).
10. M. Hamasaki, T. Noda, M. Baba, Y. Ohsumi, *Traffic* **6**, 56–65 (2005).
11. K. Mochida *et al.*, *Nature* **522**, 359–362 (2015).
12. A. Khaminets *et al.*, *Nature* **522**, 354–358 (2015).

13. M. D. Smith *et al*., *Dev. Cell* **44**, 217–232.e11 (2018).
14. K. J. Roberg, M. Crotwell, P. Espenshade, R. Gimeno, C. A. Kaiser, *J. Cell Biol.* **145**, 659–672 (1999).
15. S. Davis *et al*., *eLife* **5**, e21167 (2016).
16. S. Chen, P. Novick, S. Ferro-Novick, *Nat. Cell Biol.* **14**, 707–716 (2012).
17. S. Chen, Y. Cui, S. Parashar, P. J. Novick, S. Ferro-Novick, *Proc. Natl. Acad. Sci. U.S.A.* **115**, E6237–E6244 (2018).
18. D. J. Klionsky, A. M. Cuervo, P. O. Seglen, *Autophagy* **3**, 181–206 (2007).
19. E. Miller, B. Antonny, S. Hamamoto, R. Schekman, *EMBO J.* **21**, 6105–6113 (2002).
20. E. A. Miller *et al*., *Cell* **114**, 497–509 (2003).
21. H. Iwasaki, T. Yorimitsu, K. Sato, *FEBS Lett.* **589**, 1234–1239 (2015).
22. M. Hamasaki, T. Noda, Y. Ohsumi, *Cell Struct. Funct.* **28**, 49–54 (2003).
23. S. Chen *et al*., *Proc. Natl. Acad. Sci. U.S.A.* **112**, 418–423 (2015).
24. I. Fregno *et al*., *EMBO J.* **37**, e99259 (2018).
25. T. Kamimoto *et al*., *J. Biol. Chem.* **281**, 4467–4476 (2006).
26. T. Hidvegi *et al*., *Science* **329**, 229–232 (2010).
27. K. B. Kruse, J. L. Brodsky, A. A. McCracken, *Mol. Biol. Cell* **17**, 203–212 (2006).
28. K. J. Travers *et al*., *Cell* **101**, 249–258 (2000).
29. J. S. Cox, C. E. Shamu, P. Walter, *Cell* **73**, 1197–1206 (1993).
30. T. Yorimitsu, U. Nair, Z. Yang, D. J. Klionsky, *J. Biol. Chem.* **281**, 30299–30304 (2006).
31. M. Jin *et al*., *Curr. Biol.* **24**, 1314–1322 (2014).
32. Y. T. Jeong *et al*., *eLife* **7**, e42253 (2018).
33. P. Grumati *et al*., *eLife* **6**, e25555 (2017).
34. F. Fumagalli *et al*., *Nat. Cell Biol.* **18**, 1173–1184 (2016).
35. Q. Chen *et al*., *Curr. Biol.* **29**, 846–855.e6 (2019).
36. H. Chino, T. Hatta, T. Natsume, N. Mizushima, *Mol. Cell* **74**, 909–921.e6 (2019).
37. H. An *et al*., *Mol. Cell* **74**, 891–908.e10 (2019).
38. L. Luo *et al*., *J. Mol. Endocrinol.* **60**, 285–297 (2018).
39. J. R. Liang, E. Lingeman, S. Ahmed, J. E. Corn, *J. Cell Biol.* **217**, 3354–3367 (2018).
40. S. Wang, H. Tukachinsky, F. B. Romano, T. A. Rapoport, *eLife* **5**, e18605 (2016).
41. J. K. Fink, *Acta Neuropathol.* **126**, 307–328 (2013).
42. M. W. Breuss *et al*., *Am. J. Hum. Genet.* **103**, 296–304 (2018).
43. B. Wang *et al*., *J. Clin. Invest.* **128**, 3319–3332 (2018).

ACKNOWLEDGMENTS

We thank S. Ma for technical assistance during the early phase of these studies, R. Hampton for the 4xUPRE-GFP plasmid and the use of his flow cytometer, E. Miller for plasmids, and A. Lougheed for assistance in the preparation of figures. We also thank the UCSD School of Medicine microscopy core for use of their Volocity software. **Funding:** Salary support for S.F-N., Y.C., S.P., M.Z., S.C., and H.-C.H. was provided by the Alpha-1 Foundation and NIGMS under award nos. R01GM114111, R01GM115422, and R35GM131681. Salary support for P.G.N. and J.L.B was provided by NIH grants P30DK79307, 1R01GM75061, and R35GM131732. H.F. is supported by the Norwegian Research Council, the Norwegian Cancer Society, and the Ander Jahre Foundation. F.R. is supported by Marie Skłodowska-Curie Cofund (713660), Marie Skłodowska-Curie ITN (765912), ALW Open Program (ALWOP.310), ZonMW VICI (016.130.606), and ZonMW TOP (91217002) grants. M.M. is supported by an ALW Open Program grant (ALWOP.355). **Author contributions:** Y.C., S.P., M.Z., P.G.N., M.M., M.Z., S.C., H.-C.H., F.R., H.F., J.L.B., and S.F.-N. designed research and analyzed data; Y.C., S.P., M.Z., P.G.N., M.M., M.Z., S.C., and H.-C.H. performed research; and S.F.-N., J.L.B., F.R., Y.C., S.P., M.M., and H.F. wrote the paper. **Competing interests:** The authors declare no competing interests. **Data and materials availability:** All data are available in the main text or the supplementary materials.

SUPPLEMENTARY MATERIALS

science.sciencemag.org/content/365/6448/53/suppl/DC1
Figs. S1 to S15
Tables S1 and S2
References (*44*–*52*)

31 July 2018; resubmitted 13 April 2019
Accepted 12 June 2019
10.1126/science.aau9263

PROTEIN DYNAMICS

Proton uptake mechanism in bacteriorhodopsin captured by serial synchrotron crystallography

Tobias Weinert[1]*, Petr Skopintsev[1]†, Daniel James[1]†, Florian Dworkowski[2], Ezequiel Panepucci[2], Demet Kekilli[1], Antonia Furrer[1], Steffen Brünle[1], Sandra Mous[3], Dmitry Ozerov[4], Przemyslaw Nogly[3], Meitian Wang[2], Jörg Standfuss[1]

Conformational dynamics are essential for proteins to function. We adapted time-resolved serial crystallography developed at x-ray lasers to visualize protein motions using synchrotrons. We recorded the structural changes in the light-driven proton-pump bacteriorhodopsin over 200 milliseconds in time. The snapshot from the first 5 milliseconds after photoactivation shows structural changes associated with proton release at a quality comparable to that of previous x-ray laser experiments. From 10 to 15 milliseconds onwards, we observe large additional structural rearrangements up to 9 angstroms on the cytoplasmic side. Rotation of leucine-93 and phenylalanine-219 opens a hydrophobic barrier, leading to the formation of a water chain connecting the intracellular aspartic acid–96 with the retinal Schiff base. The formation of this proton wire recharges the membrane pump with a proton for the next cycle.

Proteins are intrinsically dynamic molecules that follow defined conformational rearrangements to drive the fundamental biochemistry of life. Structural studies of these dynamic processes are challenging, because structural intermediates are often short-lived. Pump-probe crystallography offers the opportunity to capture successive temporal snapshots of light-activated processes to study protein dynamics within the crystallographic lattice at the level of individual atoms, at physiological temperatures and on wild-type proteins (*1*).

X-ray free electron lasers (XFELs) and the emerging method of time-resolved serial femtosecond crystallography (TR-SFX) have brought exciting opportunities for structural biologists (*2*, *3*). Recent studies on photoactive yellow protein (*4*, *5*) show that TR-SFX is a powerful new tool for studying the structural dynamics of proteins within a crystalline environment. The ultrafast but bright x-ray pulses from these powerful linear accelerators outrun most radiation damage effects (*6*) and allow the use of small crystals, resulting in high protein activation levels (*4*). The serial injection of crystals further favors the study of nonreversible reactions and the collection of redundant datasets of high quality. The great potential of the TR-SFX method for studying membrane transport can be realized when comparing results (*7*) from freeze trapping studies of the light-driven proton pump bacteriorhodopsin (bR) to a whole series of structural states ranging from the femtosecond (*8*) to the early millisecond regime (*9*).

Primary energy conversion processes in biology are variations around one central theme: proton transfer across membranes. Time-resolved crystallographic studies provided much insight into how proton pumping is achieved in bR. In particular, they focused on the early events in the pumping cycle, including the ultrafast process of energy capture through photoisomerization of retinal (*8*) and the proton release step from the retinal Schiff base (SB) toward the extracellular side of the membrane (*9*). The fundamental piece missing in our dynamic view of proton transport is how the protein rearranges to reprotonate the SB from the cytoplasmic side to reload substrate for the next pumping cycle.

We answer this question by adapting injector-based serial crystallography for time-resolved measurements in the millisecond range at widely available synchrotron sources. Requirements for time-resolved crystallography using the Laue method were never met for bR (*7*). Therefore, pioneering works to determine the structures of spectroscopic intermediates were carried out using freeze-trapping and mutagenesis (*10*). Although mutagenesis and freeze trapping provide valuable insights and allow trapping of individual structural intermediates, major controversies remained because mutations modify critical activation switches and structures of mutants may not adequately reflect rearrangements in the native protein. Such structures may further suffer from radiation damage, are obtained at nonphysiological temperatures, and lack the temporal dimension critical to understanding protein dynamics. Serial millisecond crystallography (SMX) approaches work well with high-viscosity injectors (*11*), as the injectors extrude crystals slowly and allow sufficient x-ray exposure to collect high-resolution data with the photon flux available at synchrotrons (*12*). Our recent work has shown that modern high–frame-rate and low-noise detectors make SMX a viable method for routine room-temperature structure determination (*13*). By extending the setup with a simple class 3R laser diode, we enable time-resolved studies with millisecond time resolution (TR-SMX) and bring dynamic serial crystallography from the few operational XFELs to the large community of synchrotron users worldwide. We demonstrate the technology by recording the temporal evolution of two structurally distinct intermediate states of bR and their decay back to the dark state. The closed state obtained by TR-SMX at 0 to 5 ms shows the structural rearrangements necessary for proton release that are associated with the spectroscopic M-state of bR with comparable quality and in agreement with previous XFEL experiments. The open state that we obtained from data collected 10 to 15 ms after activation is characterized by large conformational rearrangements up to 9 Å on the cytoplasmic side, which have been associated with the spectroscopic N-state of bR and have not yet been resolved by dynamic crystallography. These open the protein for the formation of a Grotthuss proton wire, a transient water chain that allows the reprotonation of the SB from Asp^{96}, the primary proton donor at the cytoplasmic side of the membrane. The observations align with the classical alternate access model of membrane transport and further complete the dynamic view of vectorial proton transport in bR by resolving the critical proton uptake step at the end of the pumping cycle.

Time-resolved serial millisecond crystallography

The most straightforward experiment possible with our TR-SMX setup (Fig. 1) leaves the laser diode on while data from continuously light-activated protein molecules within the crystal are being collected. By comparing these data to serial data collected without illumination (fig. S1), it is possible to reveal dominant conformational changes in a photocycle analogous to steady-state spectroscopic techniques. From bR microcrystals with a size of about 35 μm by 35 μm by 3 μm, we collected 114,052 light and 119,374 dark diffraction patterns in the steady-state mode with data extending to a resolution of 1.8 Å (table S1). The quality of difference electron density maps [F_o(light) – F_o(dark)] improved with the number of included images with characteristic difference density peaks starting to plateau at about 10,000 images, indicating data convergence (fig. S2). The estimated activation level was 38% (see materials and methods) and resulted in well-resolved difference density map features, with the strongest positive and negative peaks at 7.3 and 8.5σ, respectively. Structure factor extrapolation allows selective refinement of the activated species in a crystal by removing the contribution of nonactivated states from structure factor amplitudes (*14*) (fig. S3 and materials and methods). Refinement against extrapolated steady-state data revealed two activated species

[1]Division of Biology and Chemistry–Laboratory for Biomolecular Research, Paul Scherrer Institut, 5232 Villigen, Switzerland. [2]Macromolecular Crystallography, Swiss Light Source, Paul Scherrer Institut, 5232 Villigen PSI, Switzerland. [3]Department of Biology, Institute of Molecular Biology and Biophysics, ETH Zurich, 8093 Zürich, Switzerland. [4]Science IT, Paul Scherrer Institut, 5232 Villigen, Switzerland.
***Corresponding author. Email: tobias.weinert@psi.ch**
†These authors contributed equally to this work.

of bR (table S2). Although one subspecies had been observed in previous TR-SFX structures obtained at 1.7 and 8.3 ms after photoactivation, which we termed the "closed" state, the second subspecies featured large rearrangements on the cytoplasmatic side, indicating that the dynamic view of proton pumping in bR had not yet been completed in the previous studies; hence, we termed this intermediate the "open" state (table S2).

To follow the rise and decay of these intermediates and to obtain separate structures, we developed a data collection scheme, which triggers the laser diode using a transistor–transistor logic signal issued from a delay generator to achieve laser exposure synchronized with data collection at the detector (Fig. 1). In this setup, bR crystals were exposed for 5 ms with laser light at the x-ray interaction region, while the photoreaction was tracked by collecting 5-ms-long timepoints over 40 consecutive frames. This data collection sequence was continuously repeated while new crystals were resupplied by the high-viscosity injector (*11*). After about 5 hours of data collection, each of the timepoints contained ~13,000 indexable diffraction patterns with the resolution extending to 2.3 Å (table S1).

Analysis of the data provides a "continuous" molecular movie of structural changes over 200 ms in time during which bR molecules complete their photocycle within the crystal. Within this time frame, we observe a long-term decay of difference map signal and complete restoration of the dark state within about 100 ms (movie S1). The rate of this long-term decay (fig. S4) and the evolution of structural states as determined by occupancy refinements (Fig. 1) occur within the temporal range established by time-resolved spectroscopy on bR crystals (*9*, *15*, *16*). Successive structural intermediates typically overlap, which presents a general problem for time-resolved experiments. Following the rise and decay of intermediates in small steps, as demonstrated here, allows one to choose time delays at which occurring intermediates can best be separated. These results demonstrate that time-resolved serial crystallography is not limited to XFEL sources but can also be done efficiently at synchrotrons. Results are of a quality comparable to that of our previous time-resolved studies at XFELs on the same crystals (fig. S5), even though the resolution

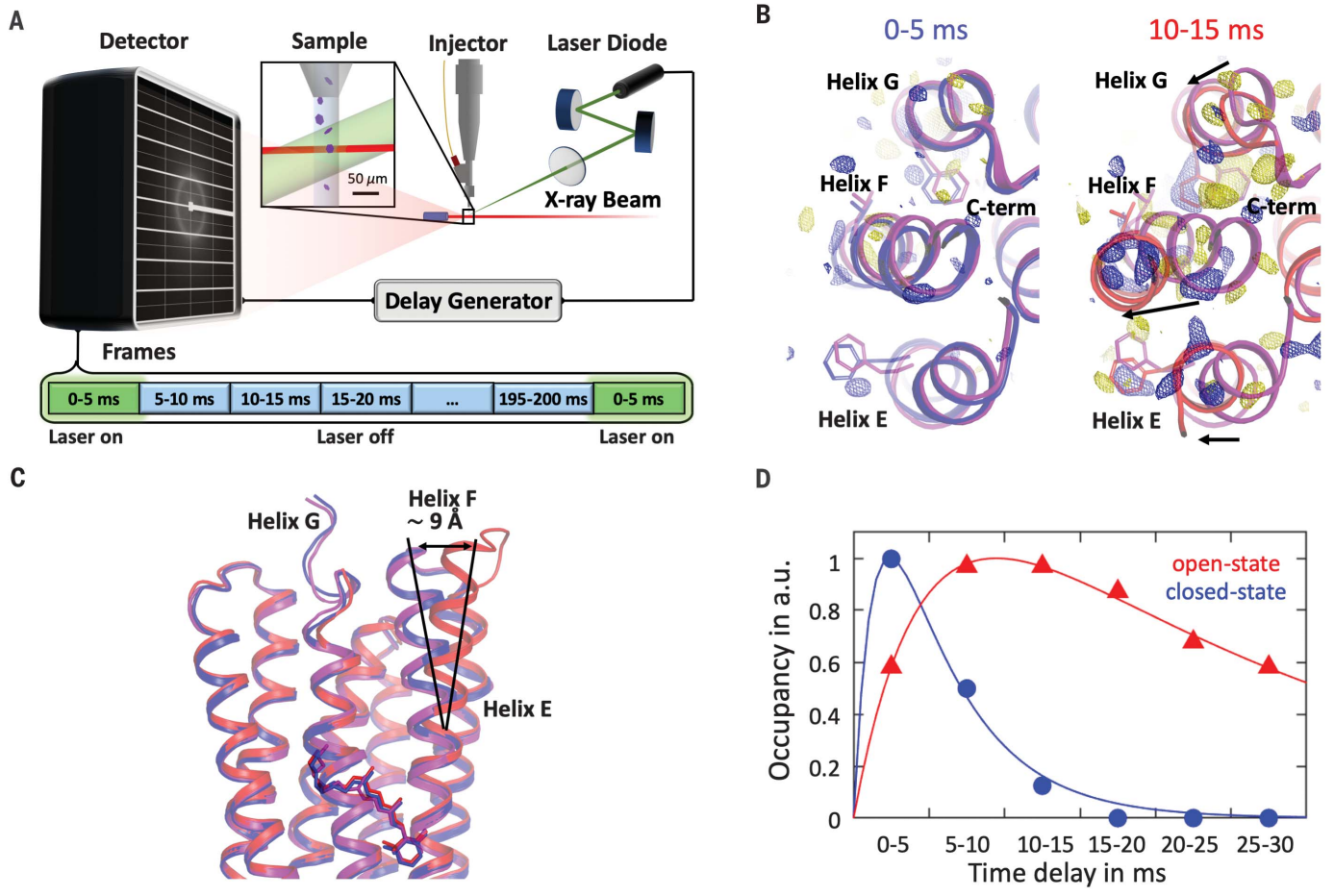

Fig. 1. Experimental setup and evolution of structural intermediates over time. (**A**) Experimental pump-probe setup and TR-SMX data collection. The laser (green) originates from a class 3R laser diode and is controlled by way of two steering mirrors before being focused to intersect with the extrusion path of the high-viscosity injector (gray) and the x-rays (red). The laser and detector are triggered by a delay generator. Running the detector at 200 Hz, the data collection cycle consists of 40 frames each 5-ms long. The laser is activated for 5 ms during collection of the first data frame and is then turned off for the remaining frames, during which the illuminated bR completes its photocycle. (**B**) Large-scale conformational changes on the cytoplasmic ends of helices E, F, and G at different timepoints [dark state in purple, closed state (0 to 5 ms) in blue, and open state (10 to 15 ms) in red] are evident in difference electron density maps [left: F_o(0 to 5 ms) − F_o(dark); right: F_o(10 to 15 ms) − F_o(dark) at 3σ with positive difference density in blue and negative difference density in yellow]. (**C**) Displacement occurs on the cytoplasmic side at the end of helix F. (**D**) Combining the dark-, closed- and open-state models included as alternative conformations into a single model and refining their occupancies against collected time-resolved data provide a measure of the structural evolution of the two intermediates over time. Biexponential fits against the normalized data are shown with solid lines. The fit resulted in decay times of 23.8 ± 2.7 ms for the open conformation and 4.7 ± 0.3 ms for the closed conformation.

was limited by the available photon flux. However, the resolution is compensated by high levels of activation from the millisecond-long light exposure, more accurate data from the use of a photon counting detector, and a more stable monochromatic beam, as previously observed during de novo phasing (*13*). Owing to the slow extrusion rate, less than 20 µl of prepared microcrystals were necessary to obtain these data, instead of milliliters needed for the XFEL experiments. The reduced sample consumption substantially lowers the entry barrier for time-resolved crystallographic studies. Although the simple TR-SMX setup implemented at the Swiss Light Source delivers excellent results, there is great potential to improve the method further. Pink beams (*17*) and diffraction-limited sources (*18*) optimize beam characteristics for faster data acquisition. The Hadamard transform method (*19*) and continued software development (*20*) are means to improve data analysis. Together with stronger nanosecond lasers, as well as new fast and accurate detectors (*21*), these improvements will allow the time resolution to be pushed from milliseconds into the lower microsecond regime to cover the majority of biologically relevant protein dynamics.

Completing the bR pumping cycle

The molecular movies of structural changes in bR are an impressive example of how XFEL sources can be used to understand biology (*7*). Our TR-SMX measurements extend the dynamic view of bR into the second half of the photocycle (Fig. 2), where the proton substrate is reloaded.

Refining the closed-state structure obtained by steady-state SMX against extrapolated data from the 0- to 5-ms timepoint (table S2), we obtained a good fit to M-state structures obtained by cryotrapping (*22*) or TR-SFX (*8*, *9*) [root mean square deviation (RMSD) of 0.46 Å for the cryo-trapped structure 1IW9, 0.40 Å for the 1.7-ms structure 5B6Z, and 0.27 Å for the 8.3-ms structure 6G7L]. Difference maps obtained from 10 to 15 ms onward, however, showed clear additional features at the cytoplasmic side of the protein (Fig. 1). When refining the open-state structure obtained by steady-state SMX against extrapolated 10- to 15-ms data, we obtained a better fit in the dark-state structures of the constitutively open Asp^{96}→Gly/Phe^{171}→Cys/Phe^{219}→Leu triple mutant [RMSD of 0.59 Å for the x-ray structure 4FPD (*23*) and 0.85 Å for the electron diffraction structure 1FBK (*24*)], which are considered analogous to the wild-type N-state obtained by photoactivation (fig. S6). The structural rearrangements in the open state (10 to 15 ms) with respect to the dark and closed states (0 to 5 ms) occur in the cytoplasmic ends of helices E, F, and G. The largest change in helix F corresponds to a movement of 9 Å measured at the Cα position of Glu^{166} (Fig. 1 and movie S2), which resembles the movement of helix 6 upon activation of structurally related G protein–coupled receptors (fig. S7). The magnitude of the motion is consistent with transient movements of helices F and G in the millisecond range observed by time-resolved spin labeling studies in purple membranes (*25*), suggesting that bR can complete the motion inside the crystal lattice (fig. S8). The final O-state does not accumulate well in bR crystals (*16*), possibly because crystal contacts, which change upon formation of the open state (fig. S8), affect the kinetics of the N-state to O-state transition inside the crystal. However, the O-state is in a fast equilibrium with the N-state (*26*), suggesting that no large structural rearrangements occur in the transition. The small changes upon relaxation of retinal from the cis-isomer back to the trans-isomer are spread out in time, with associated difference map features disappearing around the 35- to 40-ms timepoint (movie S1). Our TR-SMX experiment thus completes the crystallographic view of the bR photocycle, by revealing the structural rearrangements over the timeframe in which the M-state to N-state transition occurs inside crystals until the dark state is recovered.

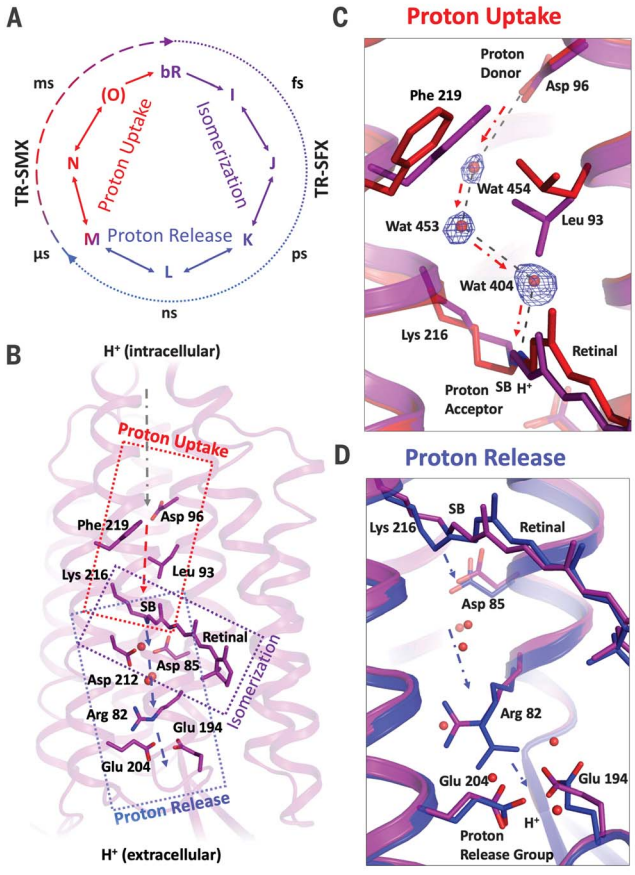

Fig. 2. Proton pumping in bacteriorhodopsin proceeds through three principal steps. (**A**) The proton pumping cycle in bR with spectroscopic intermediates (I, J, K, L, M, N, O) and the relevant time domains for the individual steps. (**B**) Overview of the three principal steps in the proton pumping cycle of bR. (**C**) At 10 to 15 ms, we observe the opening of the hydrophobic barrier between the primary proton donor Asp^{96} to the SB [dark state in purple, open state (10 to 15 ms) model in red]. The changes are accompanied by the ordering of three water molecules [positive F_o(10 to 15 ms) – F_o(dark) density in blue at 3σ]. (**D**) The 0- to 5-ms timepoint shows the rearrangements necessary for proton release, in agreement with previous XFEL studies (*8*, *9*) [dark state in purple, closed state (0 to 5 ms) model in blue]. Arrows indicate the direction of proton transfer reactions.

Structural changes in helices E and F involve large side-chain motions. The isomerizing retinal pushes against Trp^{182} in helix F starting at earlier timepoints (*9*). This motion continues in the transition from the closed state to the open state, driving the displacement of helix F and allowing the aromatic ring of Phe^{156} to move 9 Å and replace the ring of Phe^{171}. This alters the hydrophobic interaction network holding helix F in its original position. Moving helix F occurs concurrently with the disordering of the C terminus starting from Arg^{227} at the end of helix G (Fig. 3). By contrast, the structural changes in helix C are dominated by smaller side-chain rearrangements. The largest conformational change in helix C is a rotamer change of Leu^{93} matching a displacement of the nearby Phe^{219} side chain in helix G (movie S2). These changes create space for a chain of water molecules (Wat404, Wat453, Wat454) observed as strong positive difference map peaks [F_o(10 to 15 ms) – F_o(dark) above 3σ] connecting Asp^{96} on the cytoplasmic side with

the retinal SB (Fig. 2). Additional experimental evidence for such waters originates from a combination of Fourier transform infrared spectroscopy, site-directed mutagenesis, and molecular dynamic simulations (*27*, *28*). Our experimental results are consistent with molecular dynamic simulations showing that three waters are sufficient to close the gap and enable the proton transfer step to the SB (*28*). The positions of the three water molecules differ from those of the four waters observed in a freeze-trapping structure of the Val49Ala mutant (*29*), and the state trapped by mutagenesis lacks the large conformational changes on the cytoplasmic side. The constitutively open triple mutant Asp^{96}→Gly/Phe^{171}→Cys/Phe^{219}→Leu, by contrast, allowed trapping of N-like features without light activation (*23*). However, altering the side chains of these residues prevents formation of the water chain in the x-ray structure of the triple mutant (*23*) (fig. S5). Such controversies have long hindered the emergence of a consensus concerning large conformational changes in the late bR photocycle (*10*). The useful mutations by their very nature had to target functionally critical regions, which complicated interpretation. Our study resolves these discrepancies by showing the relevant arrangements in light-activated native bR measured at physiological temperatures and with real-time resolution.

Molecular mechanism of proton uptake

The structural transition fits well with the molecular mechanism of vectorial proton pumping (movie S2) (*30*). Mechanistically, bR can be divided into an extracellular half and a cytoplasmic half with retinal positioned at the center (Fig. 2). Light-induced isomerization of the retinal chromophore is the first principal step in the reaction and provides the energy for proton pumping. The energy is used in the second principal step to drive protein conformational changes on the extracellular side to transfer a proton from the retinal SB toward the extracellular release group via a hydrophilic interaction network of residues and water molecules. Transferring the proton to the release group removes the substrate from the center of the membrane.

In the third principal step, the protein has to adopt a different conformation to allow the SB to accept a proton from the intracellular side of the membrane. Preventing proton back leakage to the cytoplasmic side is critical for vectorial transport against a concentration gradient. In bR, this is achieved through a hydrophobic barrier between the primary acceptor of protons in the center (the SB) and the proton donor on the cytoplasmic side of the membrane (Asp^{96}). This 12-Å barrier has to be opened at the right time during each cycle to allow the SB to accept a new proton and recharge the system. Such a reprotonation switch has been suspected to involve larger conformational changes of the protein chain (*31*) in the late photocycle (i.e., M to N transition). Electron crystallography on bR mutants suggested opening on the cytoplasmic side and formation of a water channel to the retinal

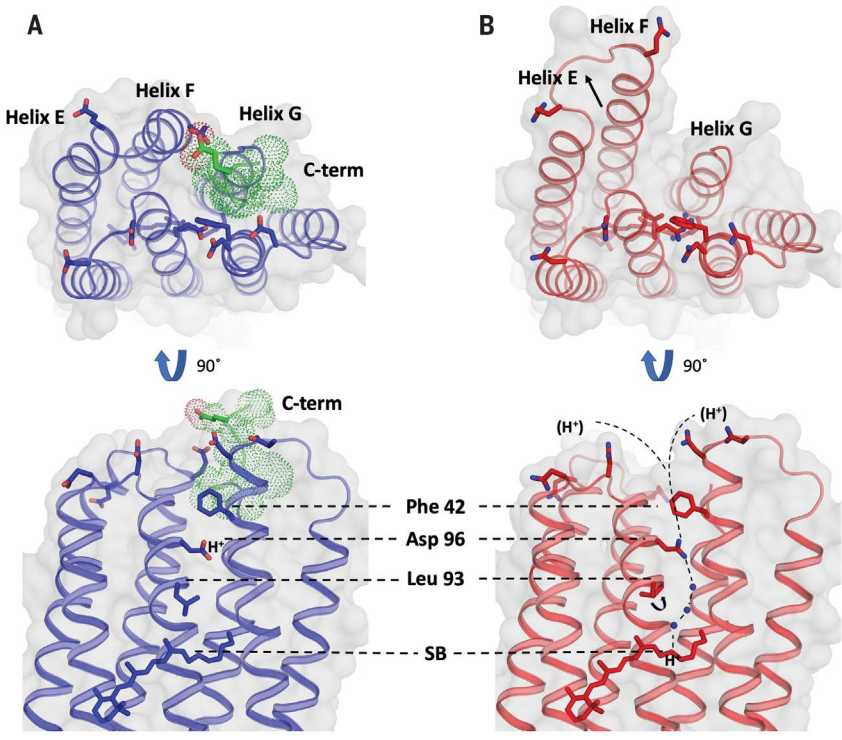

Fig. 3. Opening of the cytoplasmic side facilitates reprotonation. Rearrangements of helices E, F, and G between the closed state (0 to 5 ms) (**A**) and the open state (10 to 15 ms) (**B**) lead to disordering of the C terminus (green dotted spheres). Charged residues on the cytoplasmic surface are shown as sticks. The presumed proton position is indicated on either Asp^{96} or the SB, and the chain of ordered water molecules forming at 10 to 15 ms is shown in spheres.

(*24*, *32*). The formation of a water chain, oriented by the protein environment, could in principal act as a Grotthuss proton wire (*33*), bridging the hydrophobic barrier to deliver a new proton to the SB. Yet, despite numerous molecular dynamics simulations and structural studies (*10*), it remained unclear whether proton transfer occurs via rapidly exchanging waters in a channel (*23*) or via distinct water molecules rearranged by the protein environment (*28*). In addition to differences in methodology, discrepancies originate from the use of different starting models (fig. S5). The transition from the closed to the open bR conformation dominating the 10- to 15-ms timepoint provides direct evidence for the transient formation of such a chain of water molecules (Fig. 3). The rotation of Leu^{93}, together with Phe^{219}, creates space for three water molecules that connect the SB with the intracellular proton donor Asp^{96}, opening the hydrophobic barrier by altering the hydrophobic interaction network. Transferring the proton to the SB replenishes the substrate at the center of the membrane.

The structural rearrangements that we observe leave Asp^{96} covered by a single hydrophobic lid formed by Phe^{42}, making it accessible for reprotonation. Furthermore, structural changes to a cluster of residues acting as a proton funnel at the cytoplasmic side of the protein aid reprotonation of Asp^{96} (Fig. 3) (*34*), which may transiently proceed via an intracellular uptake cluster (*35*).

Time-resolved serial crystallography has revealed the structural reorganizations during proton uptake and release in bR with astounding detail and over many orders of magnitude in time. The alternating rearrangements on the extracellular and intracellular sides during the pumping cycle of bR agree with an alternate access model and may provide a template for understanding the principal transport steps in other membrane transport proteins. The large-scale motion of helix F further resembles the outward movement of transmembrane helix 6 in G protein–coupled receptors. Bringing time-resolved serial crystallography developed at XFELs to the broader scientific community using synchrotrons should provide tools to answer many other pressing questions in structural biology.

REFERENCES AND NOTES

1. R. Neutze, K. Moffat, *Curr. Opin. Struct. Biol.* **22**, 651–659 (2012).
2. I. Schlichting, *IUCrJ* **2**, 246–255 (2015).
3. H. N. Chapman, *Annu. Rev. Biochem.* **88**, 1–24 (2019).
4. J. Tenboer *et al.*, *Science* **346**, 1242–1246 (2014).
5. K. Pande *et al.*, *Science* **352**, 725–729 (2016).
6. K. Nass, *Acta Crystallogr. D Struct. Biol.* **75**, 211–218 (2019).
7. C. Wickstrand *et al.*, *Annu. Rev. Biochem.* **88**, annurev-biochem-013118-111327 (2019).
8. P. Nogly *et al.*, *Science* **361**, eaat0094 (2018).
9. E. Nango *et al.*, *Science* **354**, 1552–1557 (2016).

10. C. Wickstrand, R. Dods, A. Royant, R. Neutze, *Biochim. Biophys. Acta* **1850**, 536–553 (2015).
11. U. Weierstall *et al.*, *Nat. Commun.* **5**, 3309 (2014).
12. M. L. Grünbein, G. Nass Kovacs, *Acta Crystallogr. D Struct. Biol.* **75**, 178–191 (2019).
13. T. Weinert *et al.*, *Nat. Commun.* **8**, 542 (2017).
14. U. K. Genick *et al.*, *Science* **275**, 1471–1475 (1997).
15. P. Nogly *et al.*, *Nat. Commun.* **7**, 12314 (2016).
16. R. Efremov, V. I. Gordeliy, J. Heberle, G. Büldt, *Biophys. J.* **91**, 1441–1451 (2006).
17. A. Meents *et al.*, *Nat. Commun.* **8**, 1281 (2017).
18. M. Eriksson, J. F. van der Veen, C. Quitmann, *J. Synchrotron Radiat.* **21**, 837–842 (2014).
19. B. A. Yorke, G. S. Beddard, R. L. Owen, A. R. Pearson, *Nat. Methods* **11**, 1131–1134 (2014).
20. T. A. White *et al.*, *J. Appl. Crystallogr.* **49**, 680–689 (2016).
21. F. Leonarski *et al.*, *Nat. Methods* **15**, 799–804 (2018).
22. K. Takeda *et al.*, *J. Mol. Biol.* **341**, 1023–1037 (2004).
23. T. Wang *et al.*, *Structure* **21**, 290–297 (2013).
24. S. Subramaniam, R. Henderson, *Nature* **406**, 653–657 (2000).
25. N. Radzwill, K. Gerwert, H. J. Steinhoff, *Biophys. J.* **80**, 2856–2866 (2001).
26. G. Souvignier, K. Gerwert, *Biophys. J.* **63**, 1393–1405 (1992).
27. K. Gerwert, B. Hess, J. Soppa, D. Oesterhelt, *Proc. Natl. Acad. Sci. U.S.A.* **86**, 4943–4947 (1989).
28. E. Freier, S. Wolf, K. Gerwert, *Proc. Natl. Acad. Sci. U.S.A.* **108**, 11435–11439 (2011).
29. B. Schobert, L. S. Brown, J. K. Lanyi, *J. Mol. Biol.* **330**, 553–570 (2003).
30. K. Gerwert, E. Freier, S. Wolf, *Biochim. Biophys. Acta* **1837**, 606–613 (2014).
31. S. P. A. Fodor *et al.*, *Biochemistry* **27**, 7097–7101 (1988).
32. J. Vonck, *EMBO J.* **19**, 2152–2160 (2000).
33. N. Agmon, *Chem. Phys. Lett.* **244**, 456–462 (1995).
34. J. Riesle, D. Oesterhelt, N. A. Dencher, J. Heberle, *Biochemistry* **35**, 6635–6643 (1996).
35. V. A. Lorenz-Fonfria, M. Saita, T. Lazarova, R. Schlesinger, J. Heberle, *Proc. Natl. Acad. Sci. U.S.A.* **114**, E10909–E10918 (2017).

ACKNOWLEDGMENTS

We thank D.Oesterhelt and G.Schertler for providing purple membranes. **Funding:** For financial support, we acknowledge the Paul Scherrer Institute and the Swiss National Science Foundation for grants 31003A_141235, 31003A_159558 (to J.S.), and PZ00P3_174169 (to P.N.). This project received funding from the European Union's Horizon 2020 research and innovation program under the Marie-Sklodowska-Curie grant agreement no. 701646. **Author contributions:** T.W., P.S., M.W., and J.S. conceived the research with suggestions on laser setups from D.J. and F.D. Protein and microcrystals were prepared by A.F. and P.N. Slow crystal extrusion for the use at synchrotrons was optimized by P.S. and D.J. Synchronized diode and detector triggering was implemented by E.P. The pump-probe setup was built by D.J. and F.D. with suggestions from M.W. Data collection was done by T.W., P.S., D.J., A.F., D.K., S.B., F.D., D.O., P.N., M.W., and J.S. Data processing and structural refinements were done by T.W. The manuscript was written by T.W. and J.S. with contributions from all authors. **Competing interests:** The authors declare no competing interests. **Data and materials availability:** Coordinates, light amplitudes, dark amplitudes, and extrapolated structure factors for light activated data have been deposited in the Protein Data Bank (PDB) database under accession codes 6RNJ (TR-SMX closed state), 6RPH (TR-SMX open state), 6RQO (steady-state SMX activated state). Coordinates and dark state structure factors (steady-state SMX dark) have been deposited in the PDB database under accession code 6RQP.

SUPPLEMENTARY MATERIALS

science.sciencemag.org/content/365/6448/61/suppl/DC1
Materials and Methods
Supplementary Text
Figs. S1 to S8
Tables S1 and S2
References (*36*–*49*)
Movies S1 and S2

5 February 2019; accepted 11 June 2019
10.1126/science.aaw8634

REPORT

BIOCHEMISTRY

Conserved N-terminal cysteine dioxygenases transduce responses to hypoxia in animals and plants

Norma Masson[1]*, Thomas P. Keeley[1]*, Beatrice Giuntoli[2,3]*, Mark D. White[4]*†, Mikel Lavilla Puerta[3], Pierdomenico Perata[3], Richard J. Hopkinson[4]‡, Emily Flashman[4]§, Francesco Licausi[2,3]§, Peter J. Ratcliffe[1,5]§||

Organisms must respond to hypoxia to preserve oxygen homeostasis. We identify a thiol oxidase, previously assigned as cysteamine (2-aminoethanethiol) dioxygenase (ADO), as a low oxygen affinity (high-K_mO_2) amino-terminal cysteine dioxygenase that transduces the oxygen-regulated stability of proteins by the N-degron pathway in human cells. ADO catalyzes the conversion of amino-terminal cysteine to cysteine sulfinic acid and is related to the plant cysteine oxidases that mediate responses to hypoxia by an identical posttranslational modification. We show in human cells that ADO regulates RGS4/5 (regulator of G protein signaling) N-degron substrates, modulates G protein–coupled calcium ion signals and mitogen-activated protein kinase activity, and that its activity extends to other N-cysteine proteins including the angiogenic cytokine interleukin-32. Identification of a conserved enzymatic oxygen sensor in multicellular eukaryotes opens routes to better understanding and therapeutic targeting of adaptive responses to hypoxia.

Oxygen homeostasis is critical for most forms of life and is impaired in most human diseases. Previous work identified the hypoxia-inducible factor (HIF) prolyl hydroxylases as human oxygen sensors (*1*). These enzymes are low oxygen affinity (high-K_mO_2), 2-oxoglutarate (2-OG)–dependent dioxygenases that catalyze *trans*-4-prolyl hydroxylation of the transcription factor HIF (*2*, *3*) to target it for proteolysis. By this process, these hydroxylases regulate a broad range of transcriptional responses to hypoxia [reviewed in (*4*)]. Although the prolyl hydroxylation of HIF was unprecedented as a signaling mechanism, subsequent work has revealed different systems of enzymatic protein oxidation, which signal hypoxia in representatives of all four eukaryotic kingdoms (*5*–*7*). In each system, the protein oxidation event is linked to protein degradation.

Of particular interest is the Cys branch of the N-degron pathway (*8*). After the action of methionine aminopeptidases, oxidation of N-terminal cysteines creates a substrate for arginyltransferases, which catalyze the addition of this N-terminal destabilizing residue, promoting degradation. No cysteine-modifying enzyme was defined, but N-terminal cysteine oxidation was shown to be affected by nitric oxide (*9*) and, on the basis of in vitro studies, has been considered likely to be nonenzymatic. Subsequently, it was shown in plants that the Cys branch of the N-degron pathway controls the stability of ethylene response transcription factors (ERF-VII) (*10*, *11*). Further studies in *Arabidopsis thaliana* revealed that cysteine oxidation is catalyzed by a series of plant cysteine oxidases (PCOs), which act as oxygen sensors directing hypoxic adaptation (*7*, *12*). These findings led us to further investigate the mechanism of N-terminal cysteine oxidation in animals.

First, we created human osteosarcoma U-2OS and colon cancer RKO cells that stably express a fusion protein comprising N-terminal sequences that are sufficient for oxygen-dependent degradation of the ERF-VII transcription factor RAP2.12 (Related to APETALA2) in plants, linked to a green fluorescent protein (GFP):V5 reporter, and exposed these cells to hypoxia. To distinguish responses from those transduced by HIF, we also tested known inhibitors of the HIF prolyl hydroxylases that differ in their specificity both for other iron-dependent dioxygenases and nonenzymatic, metal-catalyzed oxidation. Exposure of the transfected cells to hypoxia and to the nonspecific iron chelator dipyridyl resulted in accumulation of the $RAP_{1\text{-}50}$:GFP:V5 reporter protein, but not that of a C2A mutant, without affecting reporter transcript levels (fig. S1). By contrast, neither reporter was activated by nonspecific 2-OG dioxygenase inhibitors [desferrioxamine (DFO) and dimethyloxalylglycine (DMOG)] or a HIF prolyl hydroxylase inhibitor, all of which robustly induced HIF (Fig. 1A). In cells exposed to hypoxia for 16 hours and then treated with cycloheximide before being reoxygenated or maintained in hypoxia, we found that hypoxia prolonged the reporter protein half-life from ~5 to 35 min (Fig. 1B and fig. S2). These findings demonstrated an iron- and oxygen-dependent activity in human cells that is distinct from that of the HIF prolyl hydroxylases and that operates on amino-acid sequences from plant RAP2.12, in a manner dependent on cysteine at position 2.

We next compared this response with that of members of the R4 group of RGS proteins, which are targets of the Cys branch of the N-degron pathway in humans and mice (*13*, *14*). Experiments on RKO cells stably expressing hemagglutinin (HA)-tagged RGS4 (RGS4:HA) and an RGS4:GFP fusion ($RGS4_{1\text{-}20}$:GFP), each encoding wild-type or C2A mutant sequences, revealed accumulation of wild-type, but not mutant, proteins in cells exposed to hypoxia and dipyridyl, but not DMOG or DFO (Fig. 1C and fig. S3). Endogenous RGS4 and RGS5 proteins in human neuroblastoma SH-SY5Y cells responded identically to the same set of compounds (Fig. 1D). Responses of these RGS proteins to graded hypoxia were further examined in a series of human (SH-5Y5Y, RKO, human endothelial EA.hy926) and mouse embryonic sarcoma (C3H/10T1/2) cells, revealing progressive accumulation of RGS4 or RGS5 proteins in response to physiological hypoxia (Fig. 1E and fig. S4). These changes were observed at the level of proteins and not mRNAs, with the exception of RGS4 in SH-SY5Y. Thus, plant and human reporter proteins and endogenous RGS proteins appeared to be regulated similarly, suggesting that human cells might regulate their stability using an enzyme(s) similar to the PCOs.

The human genome contains two thiol dioxygenases with a predicted structure similar to that of the PCOs, cysteine dioxygenase (CDO1) and an enzyme previously assigned as cysteamine (2-aminoethanethiol) dioxygenase (ADO) (*15*, *16*). Genes encoding these enzymes and PCO1 were cotransfected with a gene encoding RGS4:HA into human embryonic kidney 293T cells. Overexpressed ADO, but not CDO1, suppressed hypoxic induction of RGS4:HA in a manner dependent on cysteine at position 2 (Fig. 2A). At these levels of overexpression, RGS4:HA was not suppressed by PCO1. The ability of ADO to suppress RGS4:HA was inhibited by combined exposure to hypoxia and dipyridyl and ablated by H112A+H114A mutations (fig. S5) that prevent assembly of the catalytic iron center (*15*). These experiments indicated that the catalytic activity of overexpressed ADO was sufficient to suppress RGS4:HA.

We next inactivated ADO and CDO1 in SH-SY5Y and RKO cells using CRISPR/Cas9-mediated gene editing. Inactivation of ADO but not CDO1 led

[1]Ludwig Institute for Cancer Research, Nuffield Department of Medicine, University of Oxford, Oxford OX3 7FZ, UK. [2]Department of Biology, University of Pisa, Via Luca Ghini 13, 56126 Pisa, Italy. [3]Plantlab, Institute of Life Sciences, Scuola Superiore Sant'Anna, Via Guidiccioni 8/10, 56124 Pisa, Italy. [4]Chemistry Research Laboratory, University of Oxford, Mansfield Road, Oxford OX1 3TA, UK. [5]The Francis Crick Institute, 1 Midland Road, London NW1 1AT, UK.
*These authors contributed equally to this work.
†Present address: The University of Sydney, Sydney, NSW 2006, Australia.
‡Present address: University of Leicester, Leicester LE1 7RH, UK.
§These authors contributed equally to this work.
||Corresponding author. Email: peter.ratcliffe@ndm.ox.ac.uk

to constitutive up-regulation of endogenous and transfected RGS4 and RGS5 proteins irrespective of oxygen levels (Fig. 2B and figs. S6 and S7). In view of reported actions of nitric oxide on RGS proteins (*9*, *17*), we also tested responses to the nitric oxide donor DETA-NO in wild-type and ADO-deficient cells. Suppression of hypoxic RGS4 levels by DETA-NO in wild-type SH-SY5Y and RKO cells was also abrogated in ADO-deficient cells (fig. S8). Stable reexpression of ADO, but not overexpression of CDO1, suppressed levels of RGS proteins (figs. S7 and S9). Under these conditions, expression of PCO1 also suppressed RGS proteins and restored regulation by oxygen, demonstrating oxygen-dependent activity of the plant enzyme on endogenous human proteins. In SH-SY5Y cells, we then inactivated the arginyl-transferase ATE-1 that operates downstream

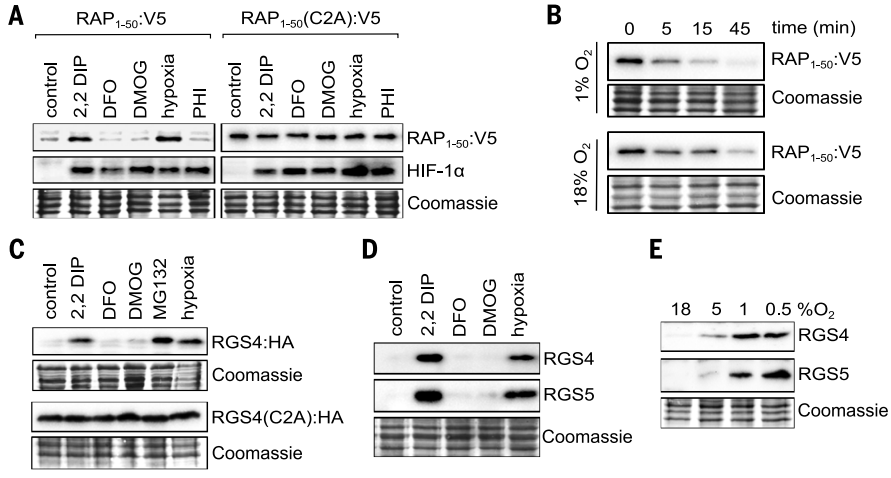

Fig. 1. Regulation of plant and animal N-degron substrates by oxygen in human cells. (**A**) Levels of fusion proteins linking the N-terminal 1-50 residues of plant RAP2.12 or a C2A mutant to a GFP:V5 cassette [$RAP_{1\text{-}50}$:V5; $RAP_{1\text{-}50}$(C2A):V5] in stably transfected U-2OS cells exposed to hypoxia or the indicated inhibitors. (**B**) $RAP_{1\text{-}50}$:V5 reporter protein half-life in cells incubated in hypoxia (16 hours, 1% O_2), treated with cycloheximide (100 μM, 10 min), and then maintained in hypoxia or reoxygenated for the indicated times. (**C**) C-terminal HA–tagged human RGS4 (RGS4:HA) or a C2A mutant in stably transfected RKO cells exposed to hypoxia or inhibitors. (**D** and **E**) Endogenous RGS4 and RGS5 proteins in SH-SY5Y cells exposed to inhibitors (D) or graded hypoxia (E). Similar patterns of response were observed for the plant fusion-protein reporter, transfected RGS4:HA, and endogenous RGS4/5 proteins; responses of exogenous proteins were abolished by C2A mutation. 2,2 DIP, 2,2-dipyridyl (100 μM); DFO, desferrioxamine (100 μM); DMOG, dimethyloxalylglycine (1 mM); PHI, prolyl hydroxylase inhibitor (125 μM); MG132, proteasomal inhibitor (25 μM). All exposures of cells to hypoxia or inhibitors were for 4 hours unless otherwise indicated. HIF-1α immunoblots are provided in (A) for comparison.

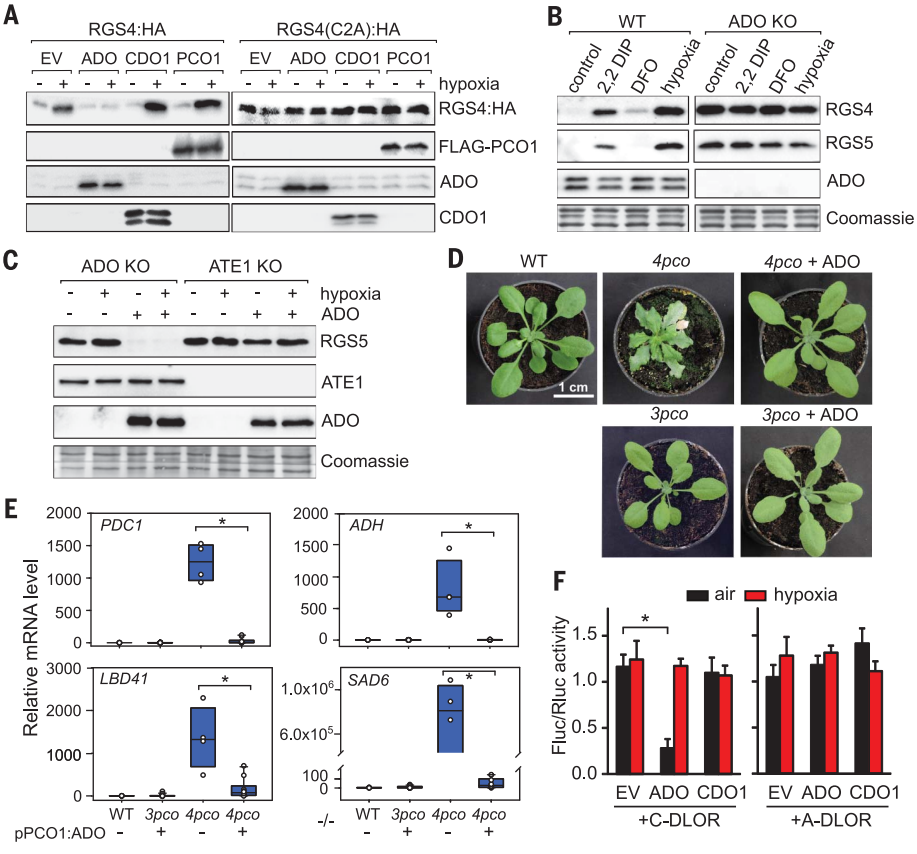

Fig. 2. ADO controls the oxygen-dependent Cys branch of the N-degron pathway. (**A**) RGS4:HA and RGS4(C2A):HA protein levels in 293T cells after coexpression with control (EV), ADO, CDO1, or PCO1. Cells were exposed to hypoxia (0.5% O_2, 16 hours) or maintained in air. Comparable enzyme levels were confirmed by separate FLAG immunoblotting. (**B**) Endogenous RGS4 and RGS5 proteins in ADO-deficient SH-SY5Y cells (ADO KO); RGS4 and RGS5 are constitutive and insensitive to iron chelators or hypoxia. (**C**) Overexpression of ADO does not repress constitutive stabilization of RGS5 in ATE1-deficient (ATE1 KO) cells. (**D**) Expression of human ADO restores the wild-type phenotype in *4pco A. thaliana* mutants; *3pco* mutants that did not manifest this phenotype were unaffected by ADO. (**E**) Box plots showing the relative mRNA level of hypoxia-inducible genes in wild-type and *pco* mutant plants that express ADO. ADO significantly reduced expression of the hypoxia-inducible genes *PDC1*, *ADH*, *LBD41*, and *SAD6* in *4pco* mutants. Data are shown as mean ± standard deviation (SD). *$P < 0.05$; Mann-Whitney rank-sum test with levels of non-hypoxia-inducible genes unchanged (fig. S10). (**F**) Relative luciferase activity (Fluc/Rluc) in *Saccharomyces cerevisiae* cells expressing C-DLOR (Cys) or A-DLOR (Cys to Ala mutant) reporter under aerobic and hypoxic conditions in the presence or absence of human ADO or CDO1. Data are shown as mean ± SD. *$P < 0.05$; two-way analysis of variance (ANOVA) followed by Holm-Sidak post hoc test.

of the proposed cysteine oxidation in the N-degron pathway. Up-regulation of RGS5 in ATE1- and ADO-deficient cells was similar, and was not suppressed by overexpression of ADO in ATE1-deficient cells (Fig. 2C). Thus, ADO is required for oxygen-dependent degradation of RGS proteins. This activity was dependent on the integrity of ATE1, consistent with ADO acting upstream of ATE1 in the N-degron pathway.

To determine whether ADO can complement deficient PCO in plants, we generated a PCO-depleted *A. thaliana* mutant by crossing plants in which four of the five known PCO (1, 2, 4, and 5) genes were inactivated by transferred DNA insertional mutagenesis. Homozygous quadruple *pco1/2/4/5* (*4pco*), but not triple *pco1/2/4* (*3pco*), mutant plants manifested severe developmental defects (Fig. 2D) and up-regulation of hypoxia-responsive genes under aerobic conditions (Fig. 2E). When human ADO, but not CDO1, was introduced into *4pco* plants under control of the PCO1 promoter, the constitutive upregulation of anaerobic genes in air was corrected and the plants developed normally (Fig. 2, D and E, and fig. S10). Consistent with complementation of defective PCO function, coexpression of ADO in *A. thaliana* protoplasts caused dose-dependent suppression of RAP2.12 luciferase fusion protein activity (fig. S10).

In budding yeast, cysteine is not a destabilizing N-terminal residue (*18*). To determine whether deficiency of an ADO-like enzyme might be responsible for the stability associated with N-cysteine in yeast, we introduced ADO or CDO1 into yeast cells together with a ratiometric reporter in which the activity of a RAP2.12-firefly luciferase fusion protein or a C2A mutant is normalized to *Renilla* luciferase (fig. S11). Expression of human ADO, but not CDO1, reduced the activity of, and conferred hypoxic regulation on, the $RAP_{2\text{-}28}$-FLuc protein, but not a C2A mutant (Fig. 2F and fig. S11). Consistent with this, phylogenetic analyses revealed potential ADO and CDO orthologs across most plants, animals, and at least some protist species but not fungi (fig. S12). Together, these findings explain the lack of activity of cysteine as a destabilizing residue in yeast but suggest that the pathway might otherwise operate widely in eukaryotic species.

Cross-complementation suggested that ADO catalyzes a form of N-terminal cysteine dioxygenation similar to that catalyzed by the PCOs. To test this, we produced recombinant human ADO and CDO1 in *E. coli*, reacted these enzymes with synthetic peptides corresponding to residues 2 to 15 of human RGS4 and RGS5, and examined the products by mass spectrometry (MS). We found that the peptides were modified by +32 Da mass addition by ADO, but not CDO1 (Fig. 3A and fig. S13), and that this modification was suppressed in anaerobic conditions (Fig. 3B). To confirm dioxygenation, we conducted the reactions in an atmosphere of $^{18}O_2$ or in the presence of ^{18}O-labeled water ($H_2{}^{18}O$). These experiments revealed a single +36 Da mass addition in $^{18}O_2$ and a single +32 Da mass addition in the presence of ^{18}O-labeled water, demonstrating that two oxygen atoms were incorporated directly into the peptide from molecular oxygen and confirming dioxygenation (Fig. 3B). MS2 assigned the modification to the N-terminal cysteine (fig. S14). Thus, human ADO catalyzes the dioxygenation of N-cysteine residues in RGS4 and RGS5 to cysteine sulfinic acid. Kinetic measurements on human ADO (Fig. 3C and fig. S15) revealed high turnover (k_{cat}) values of 20.1 and 16.9 s^{-1} on RGS4 and RGS5 peptides under atmospheric conditions, respectively, but marked sensitivity to oxygen (apparent $K_mO_2 > 500\ \mu M$). Thus, ADO resembles the HIF prolyl hydroxylase enzymes in manifesting a K_mO_2 that is significantly above the physiological range, a property that may underpin a role in oxygen homeostasis. Given the original assignment of ADO as a cysteamine dioxygenase, we also examined competition of N-cysteine peptide dioxygenation by free cysteamine and cysteine, but found inhibition only at high concentrations of these metabolites (IC_{50}, 37 and 13 mM, respectively, fig. S16).

RGS4 and RGS5 regulate heterotrimeric G protein signaling by enhancing Gα-coupled guanosine 5′-triphosphate hydrolysis and hence attenuating G protein signals. Because the catalytic activity of ADO lowers the levels of RGS4 and RGS5, ADO-deficient cells in which levels of these proteins are increased should manifest attenuation of G protein signaling on relevant pathways. Gα proteins can regulate the activity of mitogen-activated protein kinase (MAPK) pathways (*14*, *19*). Consistent with this, mouse cells and embryos with a defective N-degron pathway due to loss of the arginyltransferase ATE1 have been shown to exhibit reduced activation of MAPK kinase (*14*). We therefore assayed phosphorylation of MAPK (p44/p42) in ADO-deficient SH-SY5Y cells (Fig. 4A). These experiments revealed reduced levels of phosphorylated MAPK in ADO-deficient SH-SY5Y cells that were similar to levels of phosphorylated p44/p42 in ATE1-deficient SH-SY5Y cells. Reduction in phosphorylated p44/p42 was reversed by expression of ADO in ADO-knockout (KO), but not ATE1-KO, cells (Fig. 4B). To test the effects

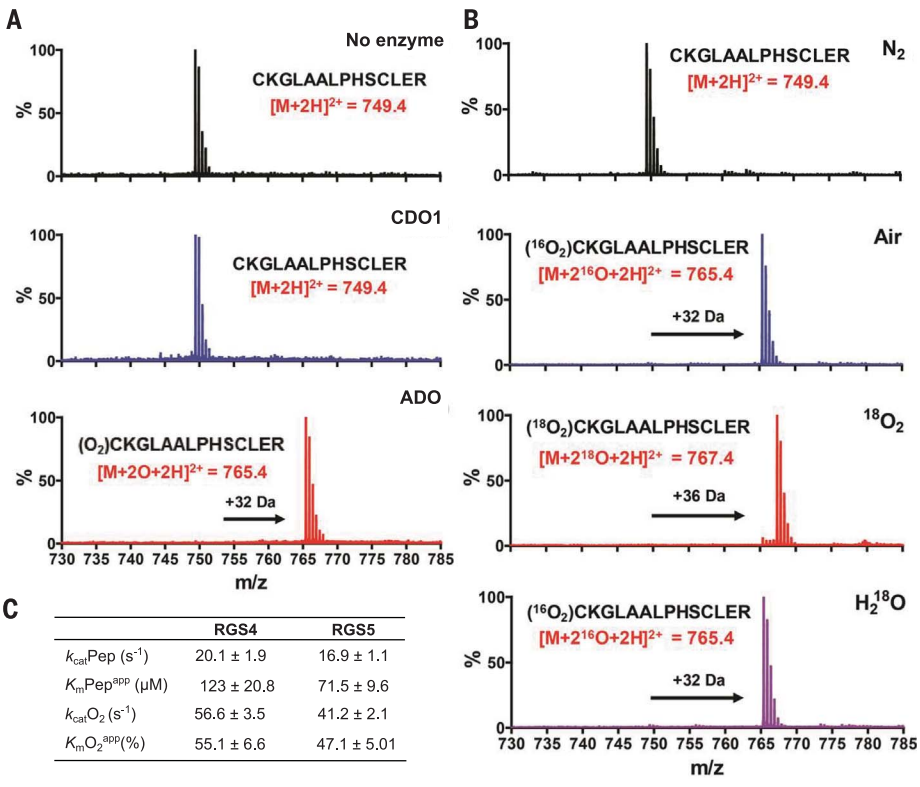

C

	RGS4	RGS5
k_{cat}Pep (s^{-1})	20.1 ± 1.9	16.9 ± 1.1
K_mPep^{app} (μM)	123 ± 20.8	71.5 ± 9.6
$k_{cat}O_2$ (s^{-1})	56.6 ± 3.5	41.2 ± 2.1
$K_mO_2{}^{app}$(%)	55.1 ± 6.6	47.1 ± 5.01

Fig. 3. ADO catalyzes the dioxygenation of the N-terminal Cys of RGS4/5 peptides. (**A**) MS results showing a mass shift of +32 Da when RGS5 N-terminal peptide was incubated with recombinant human ADO, but not with recombinant human CDO1. Similar results were obtained when an RGS4 N-terminal peptide was used (fig. S13). (**B**) The ADO-catalyzed +32 Da mass addition is absent when reactions were conducted under anaerobic (100% N_2) conditions; ^{18}O labeling demonstrates incorporation of two oxygen atoms derived directly from molecular O_2 and not H_2O. (**C**) Summary table of reaction kinetics for ADO-catalyzed dioxygenation of N-terminal RGS4/5 peptides. The influence of varying peptide concentration under atmospheric conditions (k_{cat}Pep and K_mPep^{app}) and O_2 levels using a fixed, nonlimiting concentration of peptide ($k_{cat}O_2$ and $K_mO_2{}^{app}$) were examined to determine sensitivities to both substrates. *m/z*, mass-to-charge ratio. Source data are provided in fig. S15.

of ADO on responses to a specific G protein–coupled agonist, we examined carbachol, a cholinergic agonist whose muscarinic receptor is coupled via Gαq to the regulation of intracellular Ca^{2+}. Attenuation of Ca^{2+} mobilization in response to carbachol (Fig. 4C), but not to the receptor-independent ionophore ionomycin (Fig. 4D), was observed in ADO-deficient cells and was reversed by reexpression of ADO. Given the complexity of interactions among RGS proteins and G protein–signaling pathways, we cannot be certain that these effects are entirely caused by effects of ADO on RGS4 and RGS5 proteins. Nevertheless, this study establishes a role for ADO in the regulation of G protein signaling, consistent with its role as a cysteine-modifying enzyme in the N-degron pathway regulating RGS proteins.

N-terminal sequence analyses of proteins encoded by plant and animal genomes have suggested the existence of many other potential substrates for the Cys branch of the N-degron pathway (*7*, *9*), and ADO is more widely expressed in human cells and tissues than is RGS4/5 (*20*). We therefore sought to determine whether ADO-mediated, oxygen-dependent regulation of human proteins extended beyond the identified RGS proteins. To pursue this, we first reacted recombinant ADO with a diverse series of peptides derived from proteins predicted to be processed to generate N-cysteine polypeptides and then measured dioxygenation (+32 Da mass shift) by MS. These experiments revealed substrate-dependent catalytic activity of ADO ranging from near zero to levels that were similar to those in experiments using RGS5 peptide (figs. S17 and S18). We then examined endogenous protein levels corresponding to peptide substrates that supported high [interleukin-32 (IL-32), Fig. 5A] or very low [asparagine synthetase (ASNS) and JunB] ADO-catalyzed dioxygenation using available antibodies. These experiments were conducted in the previously engineered ADO-deficient RKO cells because IL-32 was not detected in SH-SY5Y cells. Immunoblotting revealed that the abundance of IL-32, but not ASNS or JunB, was

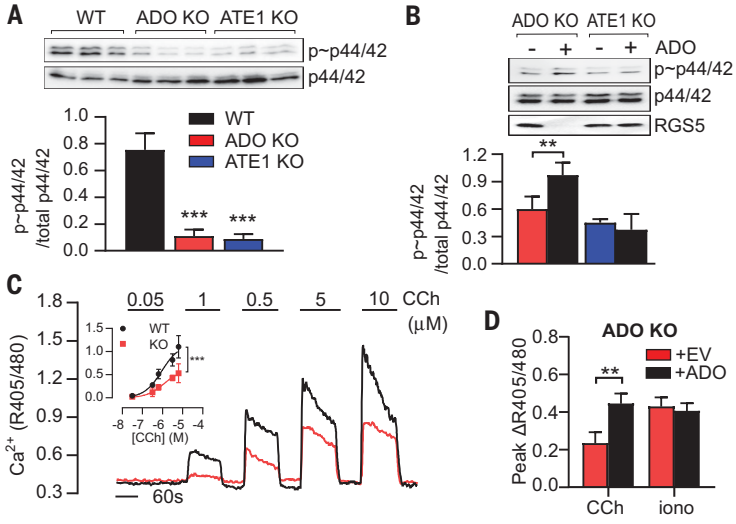

Fig. 4. ADO regulates G protein signaling. ADO regulates G protein signaling in SH-SY5Y cells. (**A**) MAPK (p44/42) phosphorylation in wild-type, ADO KO, and ATE1 KO cells. Immunoblot lanes represent separate biological replicates, with densitometric analysis provided below. Data are shown as mean ± SD. $n = 3$ independent clones. ***$P < 0.001$, one-way ANOVA with Holm-Sidak post hoc test. (**B**) Reexpression of ADO increases phosphorylated p44/42 in ADO KO, but not ATE1 KO cells. Data are shown as mean ± SD. $n = 3$ independent experiments. **$P < 0.01$, two-way ANOVA with Holm-Sidak post hoc test. (**C**) Carbachol (CCh)–stimulated rises in $[Ca^{2+}]_i$ are attenuated in ADO-deficient (KO) compared with wild-type (WT) cells. A representative trace is provided and mean peak change in R405/495 intensity at each CCh concentration is shown (inset). $n = 8$ to 12 individual cells. ***$P < 0.001$, three-parameter nonlinear regression analysis. (**D**) Ionomycin (0.1 μM) is equipotent at stimulating Ca^{2+} release in ADO KO cells infected with either control (EV) or ADO-containing lentivirus, whereas responses to CCh are recovered by ADO reexpression. Data are shown as mean ± SD. $n = 6$ to 7 individual cells. *$P < 0.05$, two-way ANOVA with Holm-Sidak post hoc test.

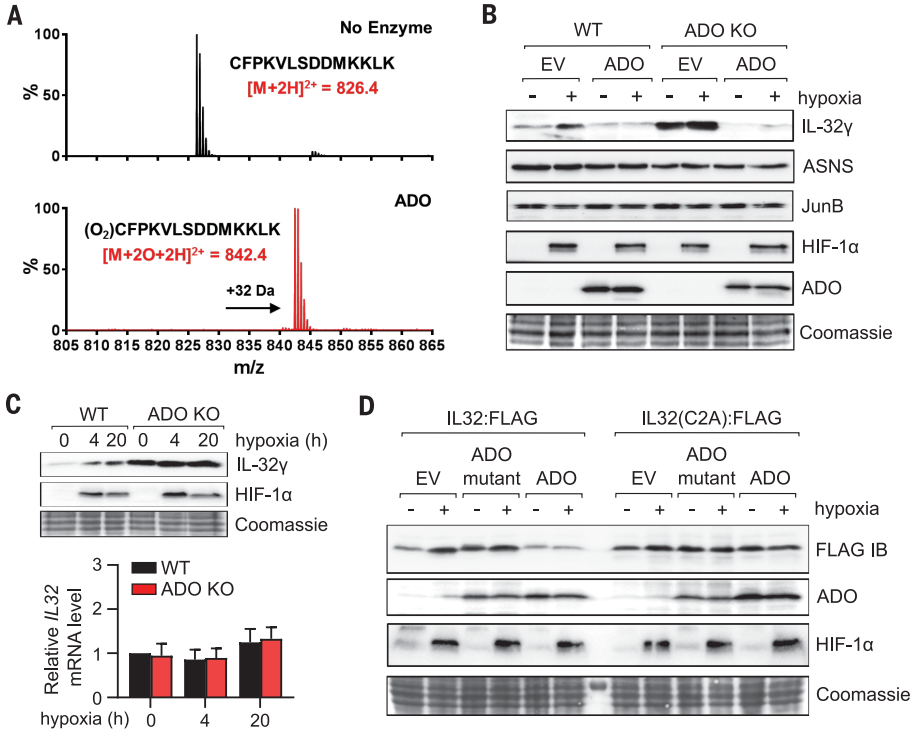

Fig. 5. IL-32 is a target of ADO-catalyzed N-terminal cysteine dioxygenation. (**A**) MS analyses of the indicated IL-32 N-terminal peptide incubated aerobically with or without recombinant ADO (1 hour at 37°C), showing a +32 Da shift when incubated with ADO, indicative of the addition of O_2. The small peak at ~845 *m/z* in the absence of ADO (top panel) was confirmed to correspond to a potassium adduct of the unoxidized peptide. (**B**) IL-32, but not asparagine synthetase (ASNS) or JunB, is regulated by hypoxia (1% O_2, 4 hours) and ADO in RKO cells. (**C**) ADO-dependent regulation of IL-32 by hypoxia is observed at the protein but not the mRNA level. (**D**) 293T cells cotransfected with plasmids encoding C-terminally FLAG-tagged IL-32 or an IL-32(C2A) mutant and either empty pRRL vector (EV), ADO, or a catalytically inactive ADO mutant (H112A+H114A), and exposed to hypoxia (1% O_2) for 16 hours. IL-32 levels were assessed using an anti-FLAG antibody. Hypoxic accumulation of IL-32 was evident in EV and mutant ADO, but not ADO, cotransfected cells, whereas C2A mutation abolished sensitivity to both hypoxia and ADO overexpression. Note that cotransfection with mutant ADO appears to increase basal levels of IL-32, consistent with possible competition with endogenous ADO for substrate binding.

increased in hypoxic cells, accumulated constitutively in ADO-deficient cells, and was reduced by reexpression of transfected ADO (Fig. 5B). Experiments in wild-type and ADO-deficient RKO cells confirmed IL-32 regulation at the protein but not the mRNA level (Fig. 5C). Further experiments confirmed dioxygenation of the N-terminal cysteine after reaction of the IL-32 peptide with recombinant ADO (fig. S18) and showed that this residue was necessary for ADO-mediated suppression of cotransfected IL-32 in cells (Fig. 5D). These findings demonstrate that ADO target proteins do extend beyond RGS proteins and identify human IL-32 as one such protein. The tested peptides represent only a small fraction of N-cysteine polypeptides that might be generated in cells and it is therefore likely that other ADO-regulated human targets exist. The transcriptional regulator LITTLE ZIPPER 2 and a component of Polycomb Repressor 2 Complex, VERNALIZATION 2, have recently been identified as new oxygen-regulated targets of the Cys branch of the N-degron pathway in plants (*21*, *22*). Given the emerging complexity of N-degron regulation (*8*), in which other processes may compete with ADO-catalyzed dioxygenation, it cannot be assumed that high levels of ADO catalysis on isolated peptides will necessarily predict physiological regulation by ADO, or indeed that all protein regulation by ADO operates through the same downstream pathways. Identification of human ADO as an enzymatic human oxygen sensor should open the way to understanding responses to hypoxia that are transduced by these pathways.

Conservation of ADO and the PCOs as human and plant oxygen sensors contrasts with the absence of conservation of their known substrates and with different challenges to oxygen homeostasis that are encountered by animals and plants. In plants, the ERF-VII pathway directs transcriptional responses to hypoxia that require time for the transcriptional output to engage adaptive responses. In animal cells, the principal process regulating transcriptional responses to hypoxia is the prolyl hydroxylation of HIF. By contrast, direct operation of ADO on the protein stability of signaling molecules has the potential to transduce more rapid responses to hypoxia than those mediated by the transcriptional output of HIF. RGS4 and RGS5 have been implicated in oxygen homeostasis in mammals through effects on the cardiovascular system and angiogenesis (*13*, *19*, *23*). IL-32 is an atypical cytokine that regulates proinflammatory cytokine networks and angiogenic growth factors (*24*, *25*). Although our findings identify ADO as an essential regulator of the responses of these proteins to hypoxia, it is of interest that RGS4, RGS5, and IL-32 have all been reported to be transcriptional targets of HIF (*26*–*28*). Consistent with the reported cell-type–specific regulation of RGS4 by HIF (*26*), we did observe induction of RGS4 mRNA by hypoxia in SH-SY5Y cells, but not in other cells. These findings predict that in specific cellular settings in which both systems are operative, the ADO and HIF prolyl hydroxylase systems will interact to generate physiological responses to hypoxia. In conclusion, our work defines an enzymatic human oxygen sensor, most likely operating physiologically on a shorter time scale than the transcriptional responses transduced by the HIF prolyl hydroxylases, and opens a new route to the investigation of adaptive responses to hypoxia, potentially including their therapeutic augmentation by catalytic inhibitors of ADO.

REFERENCES AND NOTES

1. A. C. R. Epstein *et al*., *Cell* **107**, 43–54 (2001).
2. M. Ivan *et al*., *Science* **292**, 464–468 (2001).
3. P. Jaakkola *et al*., *Science* **292**, 468–472 (2001).
4. W. G. J. Kaelin Jr., P. J. Ratcliffe, *Mol. Cell* **30**, 393–402 (2008).
5. C. M. West, H. van der Wel, Z. A. Wang, *Development* **134**, 3349–3358 (2007).
6. B. T. Hughes, P. J. Espenshade, *EMBO J.* **27**, 1491–1501 (2008).
7. D. A. Weits *et al*., *Nat. Commun.* **5**, 3425 (2014).
8. A. Varshavsky, *Proc. Natl. Acad. Sci. U.S.A.* **116**, 358–366 (2019).
9. R. G. Hu *et al*., *Nature* **437**, 981–986 (2005).
10. F. Licausi *et al*., *Nature* **479**, 419–422 (2011).
11. D. J. Gibbs *et al*., *Nature* **479**, 415–418 (2011).
12. M. D. White *et al*., *Nat. Commun.* **8**, 14690 (2017).
13. Y. T. Kwon *et al*., *Science* **297**, 96–99 (2002).
14. M. J. Lee *et al*., *Proc. Natl. Acad. Sci. U.S.A.* **102**, 15030–15035 (2005).
15. J. E. Dominy Jr. *et al*., *J. Biol. Chem.* **282**, 25189–25198 (2007).
16. M. H. Stipanuk, C. R. Simmons, P. Andrew Karplus, J. E. Dominy Jr., *Amino Acids* **41**, 91–102 (2011).
17. I. M. Jaba *et al*., *J. Clin. Invest.* **123**, 1718–1731 (2013).
18. A. Varshavsky, *Cell* **69**, 725–735 (1992).
19. C. Arnold *et al*., *FASEB J.* **32**, 2021–2035 (2018).
20. M. Uhlén *et al*., *Science* **347**, 1260419 (2015).
21. D. A. Weits *et al*., *Nature* **569**, 714–717 (2019).
22. D. J. Gibbs *et al*., *Nat. Commun.* **9**, 5438 (2018).
23. J. Hamzah *et al*., *Nature* **453**, 410–414 (2008).
24. C. A. Nold-Petry *et al*., *J. Immunol.* **192**, 589–602 (2014).
25. Y. J. E. Sloot, J. W. Smit, L. A. B. Joosten, R. T. Netea-Maier, *Semin. Immunol.* **38**, 24–32 (2018).
26. S. W. Olechnowicz, A. O. Fedele, D. J. Peet, *PLOS ONE* **7**, e44564 (2012).
27. Y. Jin *et al*., *J. Biol. Chem.* **284**, 23436–23443 (2009).
28. M. Zahoor *et al*., *Blood Adv.* **1**, 2656–2666 (2017).

ACKNOWLEDGMENTS

We thank J. Riepsaame for help with the creation of CRISPR-Cas9-edited cell lines, K. Buckler for guidance in Ca^{2+} measurements, E. Pires for mass spectrometry advice, G. Novi for crossing *A. thaliana* PCO mutants, and V. Shukla for help with yeast transformation. **Funding**: This work was supported by the Ludwig Institute for Cancer Research, the Wellcome Trust (grant no. 106241/Z/14/Z), Scuola Superiore Sant'Anna, and by Biotechnology and Biological Research Council (UK) New Investigator Grant BB/M024458/1. This work was also supported by the Francis Crick Institute, which receives its core funding from Cancer Research UK (FC001501), the UK Medical Research Council (FC001501), and the Wellcome Trust (FC001501). B. Giuntoli was supported by EMBO short-term fellowship 7233. **Author contributions**: P.J.R., F.L., and E.F. conceived the experiments; N.M., T.P.K., B.G., M.D.W., M.L.P., P.P., and R.J.H. designed and performed the experiments. P.J.R.., F.L., E.F., N.M., T.P.K., B.G., and M.D.W. wrote the manuscript. **Competing interests**: P.J.R. is a scientific cofounder of and holds equity in Reox Ltd., has served on the Research Advisory Board of GSK Ltd., and is coinventor on patents disclosing methods and means of assaying for HIF hydroxylase inhibitors and their use in the treatment of hypoxic diseases (US8535899, EP1379630), which have been licensed to Reox Ltd. P.J.R., F.L., E.F., N.M., T.P.K., B.G., and M.D.W. are inventors on a patent application related to this work (UK patent application no. 1908332.8). The other authors declare no competing interests. **Data and materials availability:** All data are available in the manuscript or the supplementary materials.

SUPPLEMENTARY MATERIALS

science.sciencemag.org/content/365/6448/65/suppl/DC1
Materials and Methods
Figs. S1 to S18
Reference (*29*)

9 November 2018; accepted 12 June 2019
10.1126/science.aaw0112

BEHAVIORAL ECONOMICS

Civic honesty around the globe

Alain Cohn[1]*, Michel André Maréchal[2]*, David Tannenbaum[3], Christian Lukas Zünd[2]

Civic honesty is essential to social capital and economic development but is often in conflict with material self-interest. We examine the trade-off between honesty and self-interest using field experiments in 355 cities spanning 40 countries around the globe. In these experiments, we turned in more than 17,000 lost wallets containing varying amounts of money at public and private institutions and measured whether recipients contacted the owners to return the wallets. In virtually all countries, citizens were more likely to return wallets that contained more money. Neither nonexperts nor professional economists were able to predict this result. Additional data suggest that our main findings can be explained by a combination of altruistic concerns and an aversion to viewing oneself as a thief, both of which increase with the material benefits of dishonesty.

Honest behavior is a central feature of economic and social life (*1*, *2*). Without honesty, promises are broken, contracts go unenforced, taxes remain unpaid, and governments become corrupt. Such breaches of honesty are costly to individuals, organizations, and entire societies. For example, losses due to tax evasion in the United States are estimated in the hundreds of billions of dollars each year (*3*), and the cost of corruption and other illicit financial flows in developing countries has been estimated at up to US$1.3 trillion annually—an amount roughly equal in size to the gross domestic product of Australia (*4*, *5*).

In this Report, we examine how acts of civic honesty, where people voluntarily refrain from opportunistic behavior, are affected by monetary incentives to act otherwise. Although there is robust experimental literature on the conditions that give rise to honest behavior (*6*–*11*), little is known about how material incentives affect civic honesty, particularly in field settings. Understanding the relationship between civic honesty and material incentives is not only practically relevant but also theoretically important.

Theories of honesty make different predictions about the role of material incentives. Classic economic models based on rational self-interest suggest that, all else being equal, honest behavior will become less common as the material incentives for dishonesty increase (*12*). Models of human behavior that incorporate altruistic or other-regarding preferences also predict that dishonesty will rise with increasing incentives, as self-interest virtually always dominates over concerns for the welfare of others—we care about others but not as much as we care about ourselves (*13*–*15*). As a result, self-interest will play an increasingly prominent role in behavior as the material incentives for dishonesty grow. Psychological models based on self-image maintenance predict that people will cheat for profit so long as their behavior does not require them to negatively update their self-concept (*7*, *16*). However, it is unclear ex ante whether self-image concerns will become more or less important as the incentives for dishonesty increase and also what form that relationship will take. A further complication is that most of the experimental literature on honest behavior involves modest financial stakes, has been conducted in laboratory settings (where people understand their behavior is being observed), and tends to rely on populations from Western, educated, industrialized, rich, and democratic societies (*17*).

We conducted a series of large-scale field experiments across the globe to examine how financial incentives influence rates of civic honesty. We turned in "lost" wallets and experimentally varied the amount of money left in them, which allowed us to determine how monetary stakes affect return rates across a broad sample of societies and institutions. Our experiments take inspiration from classic "lost letter" studies, which examine behavior in naturalistic settings, but provide tighter experimental control than past studies (*18*, *19*).

We visited 355 cities in 40 countries and turned in a total of 17,303 wallets. We typically targeted five to eight of the largest cities in a country, with roughly 400 observations per country. Wallets were turned in to one of five types of societal institutions: (i) banks; (ii) theaters, museums, or other cultural establishments; (iii) post offices; (iv) hotels; and (v) police stations, courts of law, or other public offices. These institutions serve as useful benchmarks because they are common across countries and typically have a public reception area where we could perform the drop-offs.

Our wallets were transparent business card cases, which we used to ensure that recipients could visually inspect without having to physically open the wallet (fig. S1). Our key independent variable was whether the wallet contained

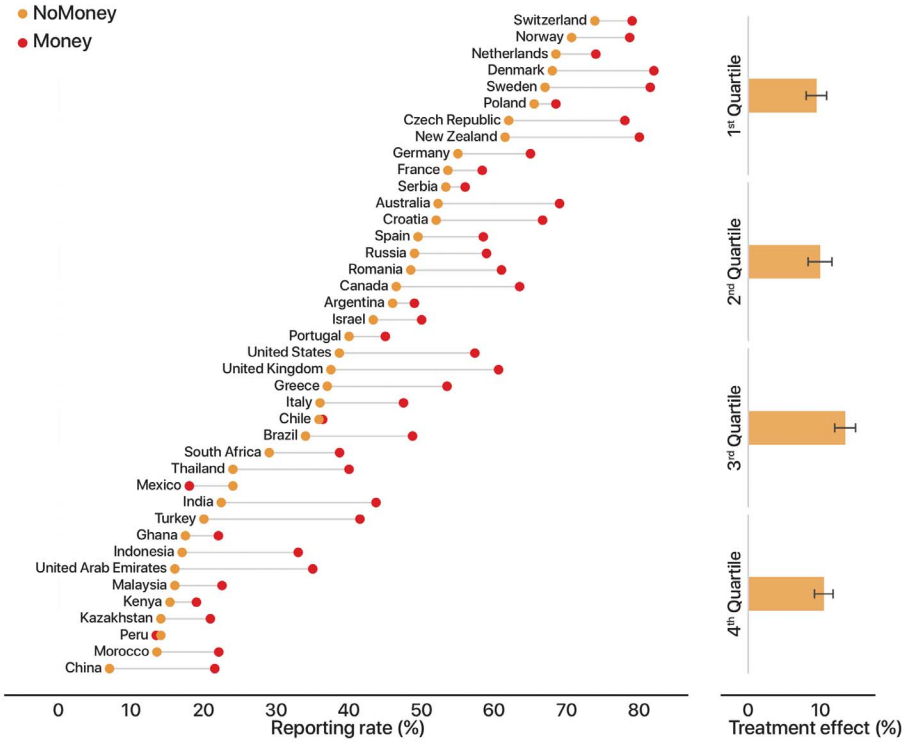

Fig. 1. Share of wallets reported in the NoMoney and Money conditions, by country. (**Left**) Share of wallets reported in NoMoney (US$0) and Money (US$13.45) conditions, by country. The amount of money in the wallet is adjusted according to each country's purchasing power. (**Right**) Average difference between Money and NoMoney conditions across quartiles based on absolute reporting rates in the NoMoney condition. Error bars represent standard errors of the mean.

[1]School of Information, University of Michigan, Ann Arbor, MI, USA. [2]Department of Economics, University of Zurich, Zurich, Switzerland. [3]Department of Management, University of Utah, Salt Lake City, UT, USA.
*Corresponding author: Email: adcohn@umich.edu (A.C.); michel.marechal@econ.uzh.ch (M.A.M.)

money, which we randomly varied to hold either no money or US$13.45 ("NoMoney" and "Money" conditions, respectively). We used local currencies and, to ensure comparability across countries, adjusted the amount according to each country's purchasing power. Each wallet also contained three identical business cards, a grocery list, and a key. The business cards displayed the owner's name and email address and we used fictitious but commonplace male names for each country. Both the grocery list and business cards were written in the country's local language to signal that the owner was a resident.

After walking into the building, one of our research assistants (from a pool of 11 male and 2 female assistants) approached an employee at the counter and said, "Hi, I found this [pointing to the wallet] on the street around the corner." The research assistant then placed the wallet on the counter and pushed it over to the employee, saying, "Somebody must have lost it. I'm in a hurry and have to go. Can you please take care of it?" The assistant then exited the building without leaving contact details or requesting written proof of having turned in the wallet. Our key outcome measure was whether recipients contacted the owner to return the wallet. We created a unique email address for each wallet and recorded emails that were sent within 100 days of the initial drop-off. Complete methods and results, including additional robustness checks such as testing for experimenter effects, can be found in the supplementary materials.

As shown in the left panel of Fig. 1, our cross-country experiments return a remarkably consistent result: citizens were overwhelmingly more likely to report lost wallets containing money than those without. We observed this pattern for 38 of our 40 countries, and in no country did we find a statistically significant decrease in reporting rates when the wallet contained money. On average, adding money to the wallet increased the likelihood of being reported from 40% in the NoMoney condition to 51% in the Money condition ($P < 0.0001$). This result holds when controlling for a number of recipient and situational characteristics (table S8). Furthermore, although rates of civic honesty vary substantially from country to country, the absolute increase in honesty across conditions was stable. As shown in the right panel of Fig. 1, the average treatment effect is roughly equal in size across quartiles based on absolute reporting rates.

Citizens displayed greater civic honesty when the wallets contained money, but perhaps this is because the amount was not large enough to be financially meaningful. To examine this possibility, we also ran a "BigMoney" condition in three countries (the United States, the United Kingdom, and Poland) that increased the money inside the wallet to US$94.15, or seven times the amount in our original Money condition. As shown in Fig. 2, reporting rates in all three countries increase even further when the wallets contained a sizable amount of money. Pooled across the three countries, reporting rates increased from 46% in the NoMoney condition to 61% in the Money condition and topped out at 72% in the BigMoney condition ($P < 0.0001$ for all pairwise comparisons) (table S9).

We next turn to the question of why people are especially likely to return a lost wallet when it contains more, rather than less, money. Our study design allows us to rule out several possible explanations. We first explored the possibility that recipients were worried about legal penalties for failing to return a wallet, especially when the wallet contained larger amounts of money. To address this issue, we examined whether relative reporting rates were affected by (i) the presence of other individuals when receiving the lost wallet, (ii) the presence of security cameras in the building, and (iii) state-level variation in lost property laws in the United States. Civic honesty should increase as a function of these variables if recipients are concerned about possible punishment or the probability of detection, yet we find that none of these factors explain meaningful variation in reporting rates across treatment conditions (tables S14 to S16). A second explanation is that because we only measured whether recipients reported a lost wallet, recipients in the money conditions may have been more likely to return the wallets while pocketing the cash. We conducted an audit on a subset of wallets reported to us and did not find support for this explanation: more than 98% of the money in the wallets we collected was returned. A third possible explanation is that recipients expected a bigger finder's fee upon returning wallets with larger amounts of money. In national representative surveys conducted in the United States, the United Kingdom, and Poland, we asked respondents what size of reward they would expect upon returning a wallet with the amounts of money we used in our studies. We fail to find evidence that people expect a larger reward for returning a wallet with more money in it (table S17).

Having ruled out these three possible explanations, we next formulate and test a simple behavioral model that captures the pattern of results observed in the data (full model details can be found in the supplementary materials). In our framework, civic honesty is determined by the interplay between four components: (i) the economic payoff of keeping the wallet, (ii) the fixed effort cost of contacting the wallet's owner, (iii) an altruistic concern for the owner's welfare, and (iv) the costs associated with negatively updating one's self-image as a thief (what we call theft aversion).

A key feature of our framework is that altruistic concerns are affected by the contents of the wallet thought to be valuable to the owner, whereas concerns of theft aversion are only affected by the contents of the wallet that are also valuable to the recipient (e.g., money). To distinguish between these two motivations, we conducted a "Money-NoKey" condition in our U.S., U.K., and Poland locations with wallets identical to our Money condition but which did not contain a key. Unlike money, the key is valuable to the owner but not to the recipient, and so any difference between the Money and Money-NoKey conditions can be ascribed to altruistic

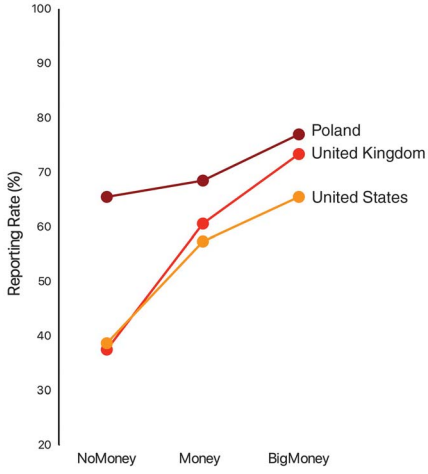

Fig. 2. Reporting rates as a function of monetary stakes. Share of wallets reported in the NoMoney (US$0), Money (US$13.45), and BigMoney (US$94.15) conditions.

concerns. As shown in table S10, recipients were, on average, 9.2 percentage points more likely to report a wallet with a key than one without ($P = 0.0001$ when results are pooled across countries). This suggests that recipients reported a lost wallet partly because they were concerned about the harm they would impose on the owner by not reporting it.

The second part of our framework—which is crucial to explaining the increase in reporting rates for wallets with larger amounts of money—involves the aversion to viewing oneself as a thief. Using nationally representative surveys conducted in the United States, the United Kingdom, and Poland, we asked respondents to imagine receiving a wallet from one of our four conditions (NoMoney, Money, BigMoney, and Money-NoKey) and to rate the extent to which failing to return that wallet would feel like stealing on a scale from 0 (not at all) to 10 (very much). Respondents reported that failing to return a wallet would feel more like stealing when the wallet contained a modest amount of money than when it contained no money and that such behavior would feel even more like stealing when the wallet contained a substantial amount of money ($P \leq 0.007$ for all pairwise comparisons) (table S11). This tells us that the self-image cost of failing to return the wallet likely increases with the amount of money in the wallet, which is consistent with our behavioral data on wallet reporting rates. By contrast, we fail to observe a reliable difference in "feels like stealing" scores when comparing wallets that contained the same amount of money but differed in whether they also contained a key (Money versus Money-NoKey; $P = 0.259$). This tells us that concerns of theft aversion are likely tied to contents that are valuable to the recipient, such as the amount of money inside the wallet, but not to other contents that are only valuable to the owner. Although survey responses do not always generalize to real behavior and should be interpreted carefully,

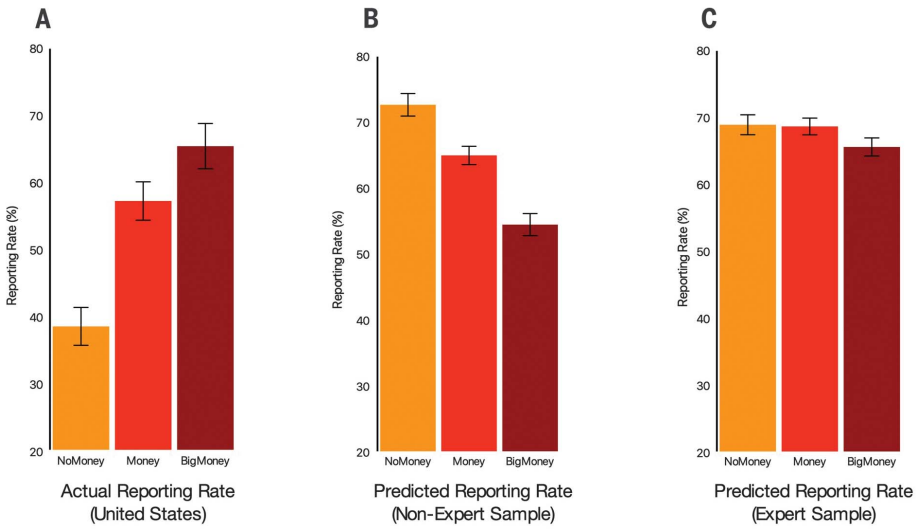

Fig. 3. Actual versus predicted reporting rates. (**A**) Actual reporting rates in the United States for each condition (n = 800 observations). Error bars represent robust standard errors. (**B**) Average predicted reporting rates for the United States by our nonexpert sample (n = 299 individuals). Error bars represent robust standard errors clustered by participants. (**C**) Average predicted reporting rates for the United States by our expert sample of academic economists (n = 279 individuals). Error bars represent robust standard errors clustered by participants.

these findings are consistent with the hypothesis that larger monetary payoffs for dishonesty are also associated with increased psychological costs and that the increase in psychological costs can outweigh the marginal economic benefits of dishonesty.

In a final set of studies, we investigated whether people anticipate this form of civic honesty. We asked a sample of 299 participants to predict reporting rates in the United States for wallets containing US$0, US$13.45, and US$94.15 (corresponding to our NoMoney, Money, and BigMoney conditions). To encourage accuracy, we notified respondents that the most accurate among them would be awarded a cash bonus. As shown in Fig. 3B, we find that respondents' beliefs were at odds with the behavioral data (Fig. 3A). Respondents predicted that rates of civic honesty would be highest when the wallet contained no money (mean predicted reporting rate M = 73%, SD = 29), lower when the wallet contained a modest amount of money (M = 65%, SD = 24), and lower still when the wallet contained a substantial amount of money (M = 55%, SD = 29). The average predicted change in reporting rates from condition to condition was significantly different from the actual change in reporting rates (P < 0.001 for all pairwise comparisons). As the amount of money increased, 64% of respondents incorrectly predicted that reporting rates would decrease and 18% correctly predicted that reporting rates would increase (P < 0.001 by a sign test). Additional questioning suggests that respondents' predictions reflected a mental model of human behavior that exaggerates the role of narrow self-interest (*20*, *21*). When wallets contained more money, respondents expected self-interest to grow and altruistic concerns for the owner to fade, and they gave little weight to the influence of theft aversion on reporting rates (see table S13).

The general public incorrectly predicts how citizens will respond as the monetary value of the wallet increases, but perhaps professional economists will be more accurate. We asked a sample of 279 top-performing academic economists to make the same set of predictions. Like our nonexperts, this sample also did not expect reporting rates to increase for wallets with larger amounts of money. As shown in Fig. 3C, respondents on average predicted that rates of civic honesty would be higher in the NoMoney and Money conditions (M = 69%, SD = 25 and M = 69%, SD = 21, respectively) than in the BigMoney condition (M = 66%, SD = 23). These predictions were again significantly different from the actual changes we observe across conditions (P < 0.001 for all pairwise comparisons). However, the degree of miscalibration among economists was less severe than in our nonexpert sample. As the amount of money increased, 49% of economists incorrectly predicted that reporting rates would decrease and 29% correctly predicted that reporting rates would increase (P < 0.001 by a sign test).

We conducted field experiments in 40 countries to examine whether people act more dishonestly when they have a greater economic incentive to do so, and we found the opposite to be true. Citizens were more likely to return wallets that contained relatively larger amounts of money. This finding is robust across countries and institutions and holds even when economic incentives for dishonesty are substantial. Our results are consistent with theoretical models that incorporate altruism and self-image concerns, but they also suggest modification in that nonpecuniary motivations directly interact with the material benefits gained from dishonest behavior. When people stand to heavily profit from engaging in dishonest behavior, the desire to cheat increases but so do the psychological costs of viewing oneself as a thief—and sometimes the latter will dominate the former.

Our findings also represent a distinctive dataset for examining cross-country differences in civic honesty. Honesty is a key component of social capital (*22*), and here we provide an objective measure to supplement the large body of work that has traditionally examined social capital using subjective survey measures (*2*, *23*–*25*). Using average reporting rates across countries, we find substantial variation in rates of civic honesty, ranging from 14 to 76%. This variation largely persists even when controlling for a country's gross domestic product, suggesting that other factors besides a country's wealth are also at play. In the supplementary materials, we provide an analysis suggesting that economically favorable geographic conditions, inclusive political institutions, national education, and cultural values that emphasize moral norms extending beyond one's in-group are also positively associated with rates of civic honesty. Future research is needed to identify how these and other factors may contribute to societal differences in honest behavior.

REFERENCES AND NOTES

1. K. J. Arrow, *Philos. Public Aff.* **1**, 343–362 (1972).
2. Y. Algan, P. Cahuc, *Annu. Rev. Econ.* **5**, 521–549 (2013).
3. IRS, *Tax Gap Estimates for Tax Years 2008–2010* (Internal Revenue Service, 2016).
4. D. Kar, S. Freitas, *Illicit Financial Flows from Developing Countries over the Decade Ending 2009* (Global Financial Integrity, 2011).
5. World Development Indicators 2017 (World Bank, 2017).
6. T. Ellingsen, M. Johannesson, *Econ. J.* **114**, 397–420 (2004).
7. N. Mazar, O. Amir, D. Ariely, *J. Mark. Res.* **45**, 633–644 (2008).
8. S. Shalvi, F. Gino, R. Barkan, S. Ayal, *Curr. Dir. Psychol. Sci.* **24**, 125–130 (2015).
9. S. Gächter, J. F. Schulz, *Nature* **531**, 496–499 (2016).
10. J. Abeler, D. Nosenzo, C. Raymond, "Preferences for truth-telling," IZA Discussion Paper No. 10188, Institute for the Study of Labor (IZA), 2016.
11. U. Gneezy, A. Kajackaite, J. Sobel, *Am. Econ. Rev.* **108**, 419–453 (2018).
12. G. S. Becker, *J. Polit. Econ.* **76**, 169–217 (1968).
13. E. Fehr, K. M. Schmidt, *Q. J. Econ.* **114**, 817–868 (1999).
14. G. Charness, M. Rabin, *Q. J. Econ.* **117**, 817–869 (2002).
15. R. Fisman, S. Kariv, D. Markovits, *Am. Econ. Rev.* **97**, 1858–1876 (2007).
16. S. Duval, R. A. Wicklund, *A Theory of Objective Self Awareness* (Academic Press, 1972).
17. J. Henrich, S. J. Heine, A. Norenzayan, *Nature* **466**, 29 (2010).
18. C. B. Merritt, R. G. Fowler, *J. Abnorm. Psychol.* **43**, 90–93 (1948).
19. S. Milgram, L. Mann, S. Harter, *Public Opin. Q.* **29**, 437–438 (1965).
20. J. Kruger, T. Gilovich, *J. Pers. Soc. Psychol.* **76**, 743–753 (1999).
21. D. T. Miller, R. K. Ratner, *J. Pers. Soc. Psychol.* **74**, 53–62 (1998).
22. L. Guiso, P. Sapienza, L. Zingales, "Civic capital as the missing link," in *Handbook of Social Economics*, J. Benhabib, A. Bisin, M. O. Jackson, Eds. (North-Holland, 2011), vol. 1, pp. 417–480.
23. E. L. Glaeser, D. I. Laibson, J. A. Scheinkman, C. L. Soutter, *Q. J. Econ.* **115**, 811–846 (2000).
24. P. Nannestad, *Annu. Rev. Polit. Sci.* **11**, 413–436 (2008).

25. A. Alesina, P. Giuliano, *J. Econ. Lit.* **53**, 898–944 (2015).

ACKNOWLEDGMENTS

For helpful discussions, we thank J. Abeler, M. Bauer, A. Bütikofer, S. DellaVigna, E. Fehr, R. Fisman, S. M. Garcia, J. Henrich, M. Johannesson, E. Kamenica, J. G. Lambsdorff, V.-L. Mui, N. Netzer, A. Oswald, D. Pope, G. Rao, A. Shleifer, P. Smeets, R. Thaler, F. Zilibotti, and audiences at various conferences and seminars. We thank J. Aeberhard, M. Baumann, K. Ben Hassine, D. Bigliel, T. Braschler, P. Bühri g, F. Caderas, C. Gabaglio, C. Kaut, V. Korbel, F. Noldin, N. Ruvidic, N. Sampl, B. Scherrer, M. Schwarz for outstanding research assistance and A. Saurer for excellent technical assistance. **Funding:** Financial support was provided by the Gottlieb Duttweiler Institute. **Author contributions:** A.C. and M.A.M. developed the research idea and designed the study. A.C., M.A.M., and C.L.Z. conducted the lost wallets experiments and nationally representative surveys. A.C., M.A.M., C.L.Z., and D.T. conducted the prediction studies. All authors analyzed the data and wrote the manuscript. **Competing interests:** None of the authors have any competing interests. **Data and materials availability:** Replication data files are available online at https://dataverse.harvard.edu/dataverse/honesty.

SUPPLEMENTARY MATERIALS

science.sciencemag.org/content/365/6448/70/suppl/DC1
Materials and Methods
Supplementary Text
Figs. S1 to S15
Tables S1 to S20
References (*26*–*111*)

23 July 2018; accepted 30 May 2019
Published online 20 June 2019
10.1126/science.aau8712

LIGHT METALS

Large plasticity in magnesium mediated by pyramidal dislocations

Bo-Yu Liu[1]*, Fei Liu[1]*, Nan Yang[1], Xiao-Bo Zhai[2], Lei Zhang[3], Yang Yang[4], Bin Li[4]†, Ju Li[5], Evan Ma[6], Jian-Feng Nie[7,8]†, Zhi-Wei Shan[1]†

Lightweight magnesium alloys are attractive as structural materials for improving energy efficiency in applications such as weight reduction of transportation vehicles. One major obstacle for widespread applications is the limited ductility of magnesium, which has been attributed to $\langle c+a \rangle$ dislocations failing to accommodate plastic strain. We demonstrate, using in situ transmission electron microscope mechanical testing, that $\langle c+a \rangle$ dislocations of various characters can accommodate considerable plasticity through gliding on pyramidal planes. We found that submicrometer-size magnesium samples exhibit high plasticity that is far greater than for their bulk counterparts. Small crystal size usually brings high stress, which in turn activates more $\langle c+a \rangle$ dislocations in magnesium to accommodate plasticity, leading to both high strength and good plasticity.

Magnesium is the lightest structural metal, with a density about 35% and 77% less than that of aluminum and steel, respectively (*1*). Magnesium alloys are actively being developed because of their potential usefulness for improving energy efficiency across the automobile, aircraft, and aerospace industries, in which the weight savings translate to lower energy consumption. However, the generally limited ductility of Mg at room temperature makes the processing and forming of profiles and components difficult and costly. Consequentially, low ductility has become one major obstacle that hampers the widespread applications of Mg products.

The ductility of Mg is intimately related to the fundamental behaviors of pyramidal $\langle c+a \rangle$ dislocations (fig. S1), which are the major contributor to *c*-axis strain (*2*, *3*). High ductility of Mg should therefore be achievable by generating more $\langle c+a \rangle$ dislocations (*4*–*7*). However, $\langle c+a \rangle$ dislocations are thought to be intrinsically unstable by readily transforming into sessile structures that cannot contribute to plastic strain (*8*–*10*). In light of this generally accepted understanding, proposed alloy design strategies primarily stabilize the $\langle c+a \rangle$ dislocation and prevent the glissile-to-sessile transformation (*11*). The glissile-to-sessile transformation is not observed in some recent simulation studies (*12*–*14*), in which $\langle c+a \rangle$ dislocations glide on pyramidal planes, even though the actual slip plane is under debate (*15*, *16*). Controversy surrounds the fundamental behavior of $\langle c+a \rangle$ dislocations, such as their ability to accommodate plastic strain and their slip pathways. This creates difficulties in rationalizing the mechanical behavior and for alloy design. We exploited in situ transmission electron microscope (TEM) mechanical testing (*17*, *18*), three-dimensional (3D) image reconstruction, and atomistic simulations to resolve the prevailing uncertainties. Our results document large plastic strains mediated by abundant $\langle c+a \rangle$ dislocations gliding on both pyramidal I $\{10\bar{1}1\}$ and pyramidal II $\{11\bar{2}2\}$ planes.

We performed in situ TEM mechanical testing at room temperature on submicrometer-size pillars of Mg single crystals (table S1). The pillars were fabricated by focused ion beam milling and tested inside TEM (fig. S2). We compressed the pillars along their *c* axis (Fig. 1 and movie S1), with the misalignment angle at less than 5°. In this condition, the $\langle c \rangle$ or $\langle a \rangle$ dislocation slip and $\{10\bar{1}2\}$ deformation twinning are all difficult to generate. We also conducted controlled experiments with the electron beam switched off and confirmed that the electron beam we used had no obvious effect on the mechanical behavior of the tested samples (fig. S3). We performed $\mathbf{g} \cdot \mathbf{b}$ analyses (where $\mathbf{g}$ is the diffraction vector and $\mathbf{b}$ is the Burgers vector) to determine the Burgers vector of dislocations (*19*).

All the pillars we tested underwent uniform deformation and exhibited fairly large dislocation-mediated plastic strains without failure (Fig. 1 and fig. S4). Dislocations were generated successively from the top region of the pillar, propagated gradually toward the bottom part of the pillar. With further deformation of the pillar, individual dislocations became difficult to image because their density was too high (Fig. 1C); therefore, we found it hard to analyze the Burgers vectors of these dislocations. To circumvent this difficulty, we used trapezoidal-shaped samples to generate

[1]Center for Advancing Materials Performance from the Nanoscale (CAMP-Nano) and Hysitron Applied Research Center in China (HARCC), State Key Laboratory for Mechanical Behavior of Materials, Xi'an Jiaotong University, Xi'an 710049, People's Republic of China. [2]College of Science, Xi'an University of Science and Technology, Xi'an 710054, People's Republic of China. [3]MOE Key Laboratory for Nonequilibrium Synthesis and Modulation of Condensed Matter, School of Science, Xi'an Jiaotong University, Xi'an 710049, People's Republic of China. [4]Department of Chemical and Materials Engineering, University of Nevada, Reno, NV 89557, USA. [5]Departments of Nuclear Science and Engineering and Materials Science and Engineering, Massachusetts Institute of Technology, Cambridge, MA 02139, USA. [6]Department of Materials Science and Engineering, Johns Hopkins University, Baltimore, MD 21218, USA. [7]Department of Materials Science and Engineering, Monash University, Melbourne, Victoria, 3800, Australia. [8]International Joint Laboratory for Light Alloys (Ministry of Education), College of Materials Science and Engineering, Chongqing University, Chongqing 400044, People's Republic of China.
*These authors contributed equally to this work.
†Corresponding author. Email: zwshan@xjtu.edu.cn (Z.-W.S.); jianfeng.nie@monash.edu (J.-F.N.); binl@unr.edu (B.L.)

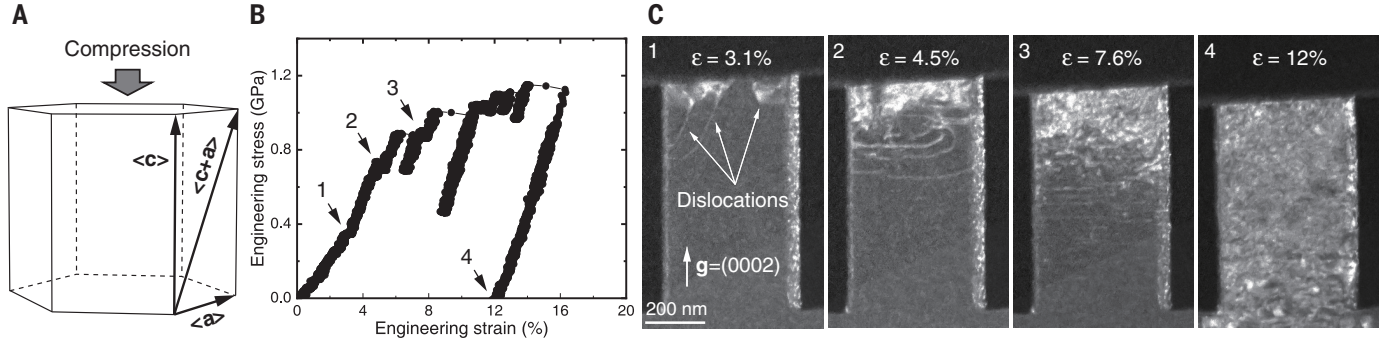

Fig. 1. In situ TEM compression test showing that dislocation slip is responsible for the plastic deformation of an Mg single-crystal pillar under *c*-axis compression. (**A**) Hexagonal unit cell showing the loading orientation. (**B**) Stress-strain curve. (**C**) Snapshots showing an increase in dislocation density during compression. The dark-field TEM observation is conducted under a two-beam condition. Electron beam direction ~$[\bar{2}110]$ (*a* axis). ε, engineering strain.

a stress gradient from the sample top to root (Fig. 2). During compression, we retracted the flat punch once dislocations appeared at the root (movie S2). Although the top was severely deformed, and its image contrast was complex, dislocations in regions near the sample root were all clearly visible. The Burgers vectors of these dislocations have both $\langle c \rangle$ and $\langle a \rangle$ components, and hence they are $\langle c + a \rangle$. Presumably, the generation and slip of the $\langle c + a \rangle$ dislocations effectively accommodates the plastic strain.

The $\langle c + a \rangle$ dislocations we observed in our study usually exhibited half-loop and zig-zag configurations (fig. S5A), similar to the $\langle c + a \rangle$ dislocations observed in bulk Mg (*4*, *20*–*22*). We believe the existence of such configurations suggests that $\langle c + a \rangle$ dislocations have both edge and screw characters and are thus of mixed type. The half loop shown in Fig. 3A formed at the top-right corner of the pillar and expanded continuously toward the lower-left corner during straining until it reached the pillar surface (fig. S6 and movie S3). This observation indicated to us that the $\langle c + a \rangle$ mixed dislocations are glissile, contributing to the plastic deformation, implying that $\langle c + a \rangle$ edge and screw dislocations are also glissile. For some $\langle c + a \rangle$ dislocations, some of their segments lie parallel to the intersection of pyramidal and basal planes and are also perpendicular to the Burgers vector. Hence, they are of edge type (see geometry analyses in fig. S5). Such edge segments are glissile (Fig. 3B and movie S4). Examination of other half loops and edge segments indicated that they are all glissile (fig. S7 and movie S5). Moreover, we observed reversible motion of $\langle c + a \rangle$ dislocations under cyclic loading (fig. S8 and movie S6). This indicates that the $\langle c + a \rangle$ dislocations retained their identity and mobility rather than becoming sessile. The mobility of the $\langle c + a \rangle$ dislocations was further supported by our atomistic simulation in which $\langle c + a \rangle$ dislocations nucleated during *c*-axis compression and glided on the pyramidal planes (figs. S9 and S10 and movie S7).

The straight segments lying parallel to the pyramidal-basal intersection were reported previously (*20*). The presence of such long segments has been attributed to low mobility of $\langle c + a \rangle$ edge dislocations (*20*), formation of sessile dislocation locks along the pyramidal-basal intersection (*23*), and dissociation of $\langle c + a \rangle$ dislocations into partials and basal stacking fault (*8*). Here, we propose that such rectilinear configuration can also result from the formation of dislocation dipole (Fig. 3C and movie S5). A straight dislocation dipole can form when a dislocation is pinned (marked by the yellow cross). The arrangement of the dipole and its two neighboring segments, 1 and 2, gave rise to an ε shape. Under the applied stress, segments 1 and 2 glided toward the left, accompanied by the elongation of the dipole. The geometry analysis indicated that this dipole was pure edge. During further straining, segments 1 and 2 formed a junction, leaving debris behind. The dislocation dipole and debris were both sessile, which can serve as obstacles to other

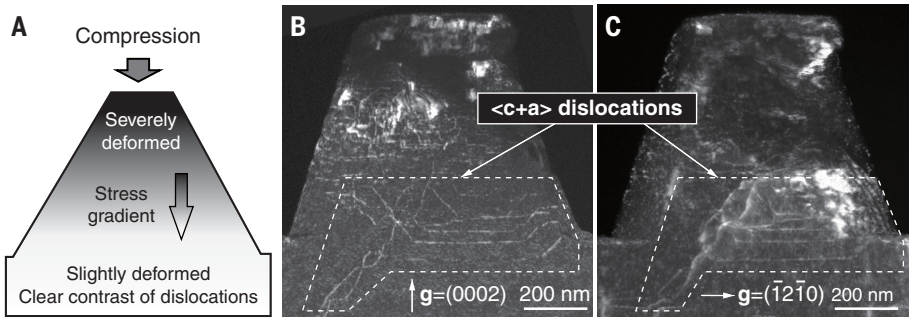

Fig. 2. Diffraction contrast analyses of $\langle c + a \rangle$ dislocations in a deformed trapezoidal sample. (**A**) Schematic illustration of the testing configuration. The pillar root is four times larger than the top. (**B** and **C**) Dark-field TEM images recorded from the same region. Electron beam direction ~[1̄010].

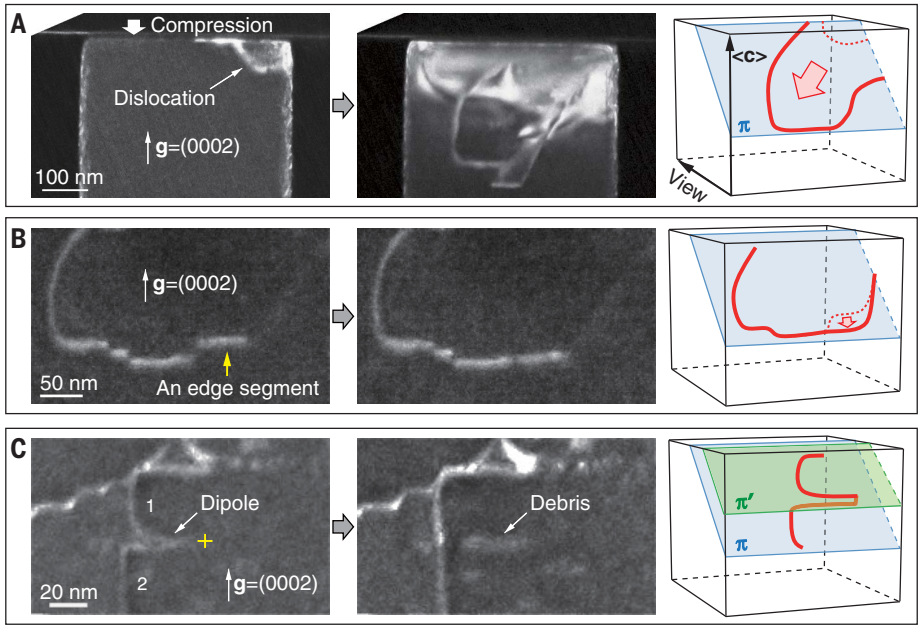

Fig. 3. In situ TEM showing the motion of $\langle c + a \rangle$ dislocations in different samples. (**A**) Expansion of a half loop. (**B**) Motion of an edge segment. (**C**) Formation of a dislocation dipole and debris. Electron beam direction ~[2̄110]. Schematic drawings of the moving dislocations are shown right to the TEM images. Symbol π refers to the pyramidal plane, and π′ is an adjacent pyramidal plane parallel to π. The red dashed line refers to the previous location of the moving dislocation.

dislocations. A likely mechanism for dipole formation by way of cross-slip is shown in fig. S11, similar to what has been proposed in other hexagonal structures such as zinc (*24*).

The formation of such a dislocation dipole requires cross-slip between two different pyramidal planes. Comparison of these two pyramidal planes is shown in fig. S12. Although the cross-slip of $\langle c + a \rangle$ dislocations between pyramidal I and II planes was studied in a computer simulation (*25*), cross-slip has not been unambiguously confirmed by experiments. Traditionally, the $\langle c + a \rangle$ slip plane is determined by slip-trace analyses, which is usually compounded by the lack of 3D information. We used a series of TEM images to construct 3D tomography to reveal the configuration and slip plane of $\langle c + a \rangle$ dislocation (fig. S13 and movies S8 and S9). Figure 4 shows 3D tomography of three $\langle c + a \rangle$ dislocations generated in *c*-axis compression. All three dislocations exhibit a curvilinear shape, indicating that they are mixed dislocations. When the pyramidal II plane is edge on, the projection of dislocation 1 becomes straight and lies on the trace of the pyramidal II plane, indicating that its gliding plane is pyramidal II (Fig. 4B). Similarly, the slip plane of dislocation 3 is pyramidal I (Fig. 4C). Dislocation 2 lies on two adjacent pyramidal II planes, indicating that cross-slip occurred. Further gliding of its segments on the two pyramidal planes would generate a dislocation dipole.

Our submicrometer-size Mg single crystals exhibit both higher strength and plasticity than

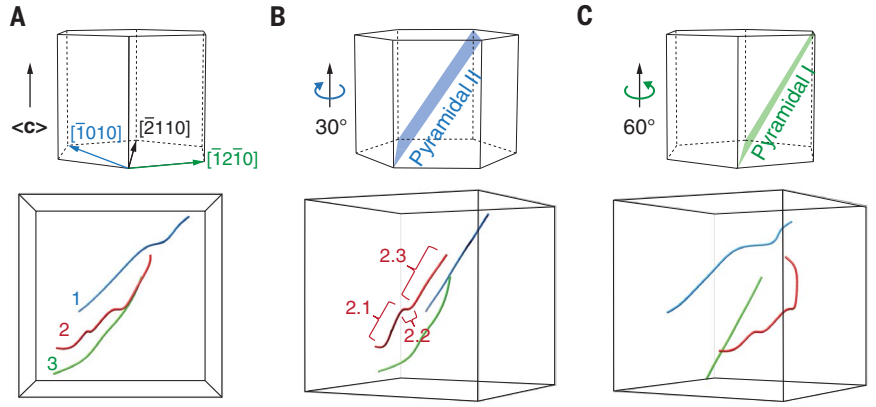

Fig. 4. 3D reconstruction revealing the pyramidal I and II gliding planes and cross-slip of $\langle c + a \rangle$ dislocations. The hexagonal unit cells indicate the viewing directions and the two pyramidal planes. (**A**) Viewing direction is [$\bar{2}$110]. Three curvilinear dislocations are selected for 3D analyses. (**B**) Viewing direction is [$\bar{1}$010]. In this orientation, the pyramidal II plane is edge on. Dislocation 1 is projected as a straight line, and hence, its slip plane is pyramidal II. For dislocation 2, segments 2.1 and 2.3 lie in different but nearby pyramidal II planes, indicating cross-slip of this dislocation. (**C**) Viewing direction is [$\bar{1}2\bar{1}0$]. The pyramidal I plane is edge on. Dislocation 3 is projected as a straight line, and therefore, its slip plane is pyramidal I.

their bulk counterpart (*26*), leading to a phenomenon of "smaller is stronger and more ductile." This phenomenon likely originates from the following factors. Small crystals usually have few preexisting dislocations, and therefore, a large amount of stress is required to nucleate dislocations. Once nucleated, dislocations can readily escape to the surfaces before dislocation multiplication, necessitating increasing stress levels to nucleate other dislocations or activate other dislocation sources to continue plasticity. Such size effects result in high stress in submicrometer-size Mg, which in turn activates abundant $\langle c + a \rangle$ dislocations to accommodate more plasticity. Another reason for the good plasticity is the rich surface sources for dislocations per unit volume, due to the large surface-to-volume ratio, which enables profuse dislocations to be generated successively from the crystal surface. Moreover, deformation twinning, which often occurs in bulk Mg under *c*-axis straining and introduces shear localization and stress concentration (*27*), is not seen in our pillars. Therefore, no potential twin-induced crack initiation sites exist in the pillars, which may also contribute to the improved plasticity. Furthermore, in a more general case, the stress concentration associated with a flaw in the tiny crystal is expected to be small, as the stress concentration factor is related to the flaw length over the flaw-tip radius. Our small crystal dimension limits this flaw aspect ratio. This prevents premature failure and allows the small crystal to maximize its potential ductility.

Our findings provide information on the mobility of pyramidal dislocations and its relationship with plasticity in pure Mg of small sizes, as well as insights into strategies for achieving long-sought plasticity in Mg that is traditionally difficult to form at room temperature. Simultaneously promoting dislocations and suppressing deformation twinning can be an effective strategy in this regard. Our experimental strategy can be extended to understanding the behavior of other hexagonal metals by identifying which microstructures promote or degrade properties such as strength and ductility.

REFERENCES AND NOTES

1. T. M. Pollock, *Science* **328**, 986–987 (2010).
2. M. H. Yoo, *Metall. Mater. Trans. A* **12**, 409–418 (1981).
3. S. Agnew, D. Brown, C. Tome, *Acta Mater.* **54**, 4841–4852 (2006).
4. S. Sandlöbes *et al.*, *Acta Mater.* **60**, 3011–3021 (2012).
5. S. Sandlöbes *et al.*, *Acta Mater.* **70**, 92–104 (2014).
6. S. R. Agnew, L. Capolungo, C. A. Calhoun, *Acta Mater.* **82**, 255–265 (2015).
7. S. Sandlöbes *et al.*, *Sci. Rep.* **7**, 10458 (2017).
8. Z. Wu, W. A. Curtin, *Nature* **526**, 62–67 (2015).
9. Z. Wu, W. A. Curtin, *Scr. Mater.* **116**, 104–107 (2016).
10. R. Ahmad, Z. Wu, S. Groh, W. A. Curtin, *Scr. Mater.* **155**, 114–118 (2018).
11. Z. Wu, R. Ahmad, B. Yin, S. Sandlöbes, W. A. Curtin, *Science* **359**, 447–452 (2018).
12. Y. Tang, J. A. El-Awady, *Acta Mater.* **71**, 319–332 (2014).
13. A. Kumar, B. M. Morrow, R. J. McCabe, I. J. Beyerlein, *Mater. Sci. Eng. A* **695**, 270–278 (2017).
14. Z. Ding *et al.*, *Acta Mater.* **146**, 265–272 (2018).
15. H. Fan, J. A. El-Awady, *Mater. Sci. Eng. A* **644**, 318–324 (2015).
16. K. Y. Xie, Z. Alam, A. Caffee, K. J. Hemker, *Scr. Mater.* **112**, 75–78 (2016).
17. B. Y. Liu *et al.*, *Nat. Commun.* **5**, 3297 (2014).
18. B.-Y. Liu *et al.*, *J. Mater. Sci. Technol.* **34**, 1061–1066 (2018).
19. Materials and methods are available as supplementary materials.
20. T. Obara, H. Yoshinga, S. Morozumi, *Acta Metall.* **21**, 845–853 (1973).
21. J. Geng, M. F. Chisholm, R. K. Mishra, K. S. Kumar, *Philos. Mag.* **95**, 3910–3932 (2015).
22. J. Jain, P. Cizek, K. Hariharan, *Scr. Mater.* **130**, 133–137 (2017).
23. B. Li, Q. W. Zhang, S. N. Mathaudhu, *Scr. Mater.* **134**, 37–41 (2017).
24. P. B. Price, *Philos. Mag.* **5**, 873–886 (1960).
25. M. Itakura, H. Kaburaki, M. Yamaguchi, T. Tsuru, *Phys. Rev. Lett.* **116**, 225501 (2016).
26. C. M. Byer, B. Li, B. Cao, K. T. Ramesh, *Scr. Mater.* **62**, 536–539 (2010).
27. M. R. Barnett, *Mater. Sci. Eng. A* **464**, 8–16 (2007).

ACKNOWLEDGMENTS

We acknowledge Z. Zhang (Hefei University of Technology) for providing the Mg single crystals; Q. J. Li (Johns Hopkins University) for fruitful discussions; and P. Zhang, C. W. Guo, and D. L. Zhang (Xi'an Jiaotong University) for assistance in focused ion beam and TEM experiments. We also appreciate the support from the International Joint Laboratory for Micro/Nano Manufacturing and Measurement Technologies and the Collaborative Innovation Center of High-End Manufacturing Equipment. **Funding:** The authors acknowledge the support from the National Key Research and Development Program of China (2017YFB0702001), National Natural Science Foundation of China (51601141, 51621063, 11504290, and 11834018), 111 Project 2.0 (BP2018008), China Postdoctoral Science Foundation (2016M600788), and the Science and Technology Department of Shaanxi Province (2016KTZDGY-04-03 and 2016KTZDGY-04-04). E.M. was supported by the U.S. Department of Energy (BES-DMSE no. DE-FG02-16ER46056). B.L. acknowledges the support from U.S. National Science Foundation (CMMI-1635088). J.-F.N. acknowledges the support from the Australian Research Council. J.L. was supported by NSF DMR-1410636. **Author contributions:** J.-F.N. and Z.-W.S. designed and supervised the project. B.-Y.L., F.L., and N.Y. performed the in situ TEM experiments and carried out the data analysis. X.-B.Z., B.-Y.L., and L.Z. carried out the 3D image reconstruction. Y.Y. and B.L. carried out the simulation and interpreted the results. J.L. and E.M. contributed to the interpretations of the observations. B.-Y.L., J.-F.N., B.L., E.M., and Z.-W.S. wrote the paper. All authors contributed to discussions of the results. **Competing interests:** The authors declare no competing interests. **Data and materials availability:** All data are available in the manuscript or the supplementary materials.

SUPPLEMENTARY MATERIALS

science.sciencemag.org/content/365/6448/73/suppl/DC1
Materials and Methods
Figs. S1 to S13
Table S1
Movies S1 to S9
References (*28*–*32*)

5 December 2018; accepted 8 May 2019
10.1126/science.aaw2843

RESTORATION ECOLOGY

The global tree restoration potential

Jean-Francois Bastin[1]*, Yelena Finegold[2], Claude Garcia[3,4], Danilo Mollicone[2], Marcelo Rezende[2], Devin Routh[1], Constantin M. Zohner[1], Thomas W. Crowther[1]

The restoration of trees remains among the most effective strategies for climate change mitigation. We mapped the global potential tree coverage to show that 4.4 billion hectares of canopy cover could exist under the current climate. Excluding existing trees and agricultural and urban areas, we found that there is room for an extra 0.9 billion hectares of canopy cover, which could store 205 gigatonnes of carbon in areas that would naturally support woodlands and forests. This highlights global tree restoration as our most effective climate change solution to date. However, climate change will alter this potential tree coverage. We estimate that if we cannot deviate from the current trajectory, the global potential canopy cover may shrink by ~223 million hectares by 2050, with the vast majority of losses occurring in the tropics. Our results highlight the opportunity of climate change mitigation through global tree restoration but also the urgent need for action.

Photosynthetic carbon capture by trees is likely to be among our most effective strategies to limit the rise of CO_2 concentrations across the globe (*1*–*3*). Consequently, a number of international initiatives [such as the Bonn Challenge, the related AFR100, and the New York Declaration on Forests (*4*, *5*)] have established ambitious targets to promote forest conservation, afforestation, and restoration at a global scale. The latest special report (*1*) by the Intergovernmental Panel on Climate Change (IPCC) suggests that an increase of 1 billion ha of forest will be necessary to limit global warming to 1.5°C by 2050. However, it remains unclear whether these restoration goals are achievable because we do not know how much tree cover might be possible under current or future climate conditions or where these trees could exist.

Previous efforts to estimate global tree cover potential have scaled existing vegetation estimates to the biome or ecoregion levels to provide coarse approximations of global forest degradation (*6*, *7*). However, quantitatively evaluating which environments could support trees requires that we build models using direct measurements of tree cover (independent of satellite-derived models) from protected areas, where vegetation cover has been relatively unaffected by human activity. With enough observations that span the entire range of environmental conditions, from the lowest to the highest possible tree cover, we can interpolate these "natural tree cover" estimates across the globe to generate a predictive understanding of the potential tree cover in the absence of human activity.

To explore the determinants of potential tree cover, we used 78,774 direct photo-interpretation measurements (data file S1) (*8*) of tree cover across all protected regions of the world (fig. S1) (*9*, *10*). Using global environmental layers (table S1) (*11*), we examined how climate, edaphic, and topographic variables drive the variation in natural tree cover across the globe. The focus on protected areas is intended to approximate natural tree cover. Of course, these regions are not entirely free of human activity (*11*), presenting slightly lower tree cover than expected in some regions or higher tree cover than expected in other regions because of low fire frequency, but these ecosystems represent areas with minimal human influence on the overall tree cover. We then used a random forest machine-learning approach (*12*) to examine the dominant environmental drivers of tree cover and generated a predictive model (Fig. 1) that enables us to interpolate potential tree cover across terrestrial ecosystems. The resulting map—Earth's tree carrying capacity—defines the tree cover per pixel that could potentially exist under any set of environmental conditions, with minimal human activity (Fig. 2A). This work is directly underpinned by our systematic dataset of direct tree cover measurements (entirely independent of climate and modeled remote sensing estimates) (*13*) across the globe (fig. S1) (*10*).

Across the world's protected areas (fig. S2), tree cover ranged between peaks of 0% in dry desert and 100% in dense equatorial forest, with fewer values falling between these two extremes (figs. S2 and S3). We paired these tree cover measurements with 10 global layers of soil and climate data (table S1) (*11*). Our resulting random forest model had high predictive power [coefficient of determination (R^2) = 0.86; intercept = −2.05% tree cover; slope = 1.06] (Fig. 1); rigorous *k*-fold cross-validation (fig. S4A) (*11*) revealed that our model could explain ~71% of the variation in tree cover without bias (R^2 = 0.71; intercept = 0.34% tree cover; slope = 0.99) (fig. S3, B and C). Our *k*-fold cross-validation approach also allows us to generate a spatially explicit understanding of model uncertainty (figs. S5 and S6) (*11*). Across all pixels, the mean standard deviation around the modeled estimate is ~9% in tree cover (28% of the mean tree cover) (figs. S5 and S6) (*11*). As such, these models accurately reflected the distribution of tree cover across the full range of protected areas. We then interpolated this random forest model across all terrestrial ecosystems using all 10 soil and climate variables to project potential tree cover across the globe under existing environmental conditions.

The resulting map reveals Earth's tree carrying capacity at a spatial resolution of 30 arc sec (Fig. 2A). The model accurately predicts the presence of forest in all existing forested land on the planet (fig. S7A) but also reveals the extent of tree cover that could naturally exist in regions beyond existing forested lands. The most recent Food and Agriculture Organization of the United Nations (FAO) definition of "forest" corresponds to a land of at least 0.5 ha covered by at least 10% tree

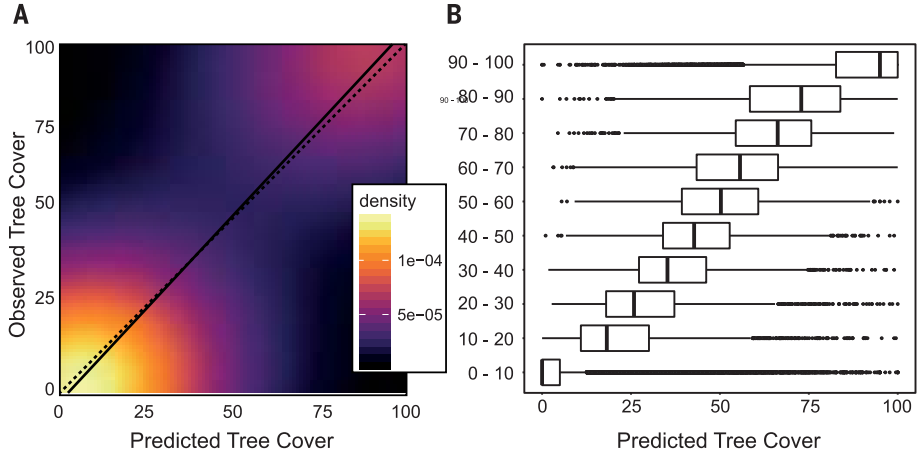

Fig. 1. Predicted vs. observed tree cover. (**A** and **B**) The predicted tree cover (*x* axes) compared with the observed tree cover (*y* axes). (A) Results as a density plot, with the 1:1 line in dotted black and the regression line in continuous black (intercept = −2% forest cover; slope = 1.06; R^2 = 0.86), which shows that the model is un-biased. (B) Results as boxplots, to illustrate the quality of the prediction in all tree cover classes.

[1]Crowther Lab, Department of Environmental Systems Science, Institute of Integrative Biology, ETH-Zürich, Zürich, Switzerland. [2]Food and Agriculture Organization of the United Nations, Rome, Italy. [3]Department of Environmental Systems Science, Institute of Integrative Biology, ETH-Zürich, Zürich, Switzerland. [4]Centre de Coopération Internationale en la Recherche Agronomique pour le Développement (CIRAD), UR Forest and Societies, Montpellier, France.
*Corresponding author. Email: bastin.jf@gmail.com

cover and without agricultural activity or human settlements (*14*). Using this definition, our map reveals that about two-thirds of terrestrial land, 8.7 billion ha, could support forest (table S2). That value is 3.2 billion ha more than the current forested area (fig. S7A) (*11*, *15*). We estimate that 1.4 billion ha of this potential forest land is located in croplands (>99%) and urban areas (<1%), as delineated by the European Space Agency's global land cover model (fig. S7B and table S2) (*16*), and 1.5 billion ha with croplands as delineated by Fritz *et al*. (fig. S7C and table S2) (*17*). Therefore, ~1.7 billion to 1.8 billion ha of potential forest land (defined as >10% tree cover) exists in areas that were previously degraded, dominated by sparse vegetation, grasslands, and degraded bare soils.

To avoid the pitfalls of categorical forest definitions, we also evaluated the tree canopy cover in a truly continuous scale (fig. S8). We refer to "canopy cover" as the area of the land that is covered by tree crown vertically projected to the ground (for example, 50% of tree cover over 1 ha corresponds to 0.5 ha of canopy cover) (fig. S8). By accounting for all levels of tree cover (from 0 to 100%), this approach balances the relative contribution of different forest types (such as woodlands, open forest, and dense forest) and of wooded lands outside forests (such as savannas) across the globe.

In total, 4.4 billion ha of canopy cover can be supported on land under existing climate conditions (pixel uncertainty = 28%; global uncertainty <1%) (table S2) (*11*). This value is 1.6 billion ha more than the 2.8 billion ha existing on land today (*10*, *15*). Of course, much of the land that could potentially support trees across the globe is currently used for human development and agriculture, which are necessary for supporting an ever-growing human population. On the basis of both the European Space Agency's global land cover model (*16*) and on Fritz and colleagues cropland layer (*17*), we estimate that 0.9 billion hectares are found outside cropland and urban regions (Fig. 2, B and C, and table S2) (*11*) and may represent regions for potential restoration. More than 50% of the tree restoration potential can be found in only six countries (in million hectares: Russia, +151; United States, +103; Canada, +78.4; Australia, +58; Brazil, +49.7; and China, +40.2) (data file S2), stressing the important responsibility of some of the world's leading economies. By comparing our country-level results to the commitments of 48 countries in the Bonn Challenge (*4*), we can provide a scientific evaluation of the country-level restoration targets. Approximately 10% of countries have committed to restoring an area of land that considerably exceeds the total area that is available for restoration (data file S2). By contrast, over 43% of the countries have committed to restore an area that is less than 50% of the area available for restoration. These results reinforce the need for better country-level forest accounting, which is critical for developing effective management and restoration strategies. Of course, it remains unclear what proportion of this land is public or privately owned, and so we cannot identify how much land is truly available for restoration. However, at a global scale, our model suggests that the global forest restoration target proposed by the IPCC (*1*) of 1 billion ha (defined as >10% tree cover) is undoubtedly achievable under the current climate. By scaling these forest area calculations by biome-level mean estimates of carbon storage (*18*, *19*), we estimate that vegetation in the potential restoration areas could store an

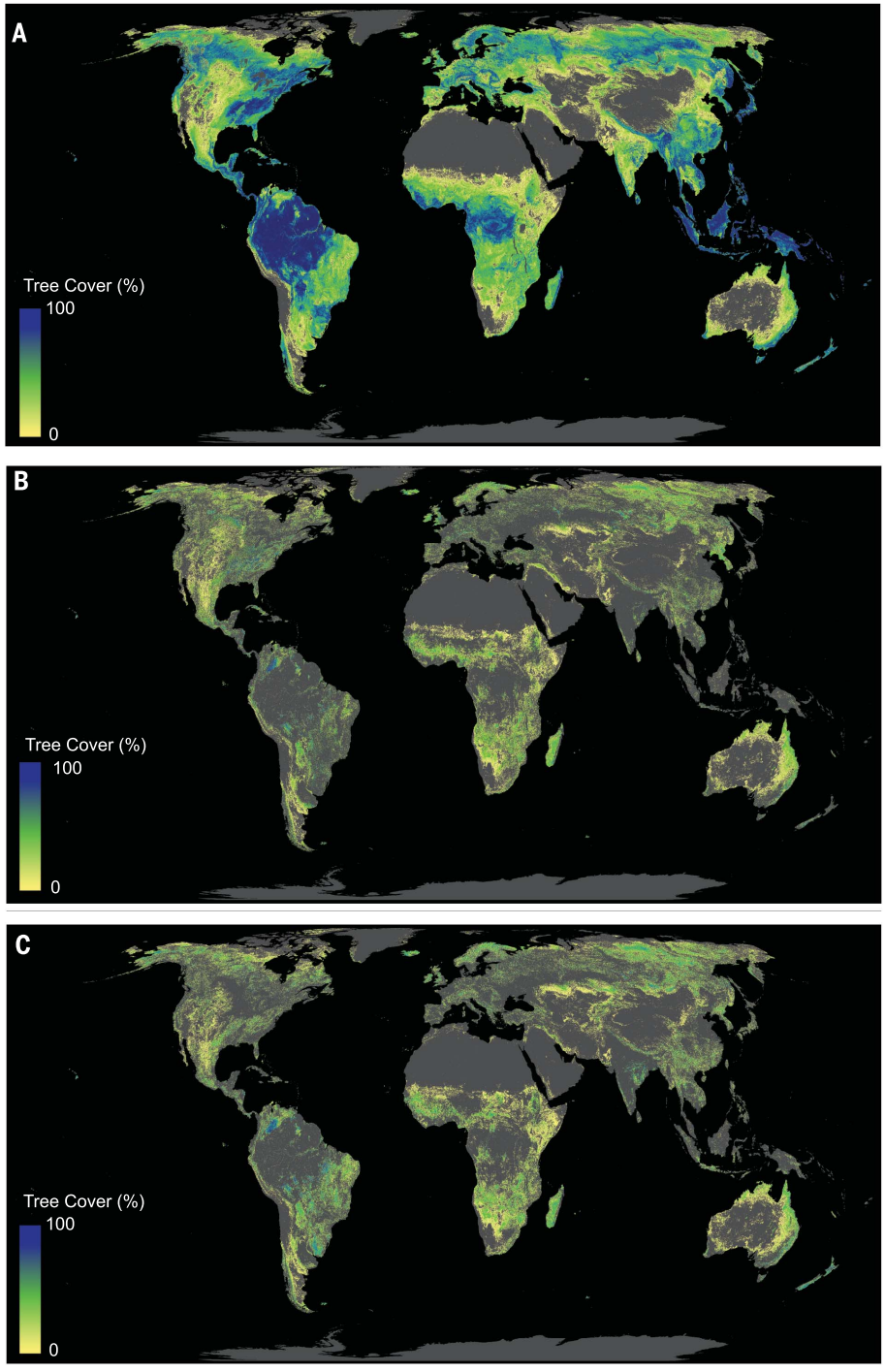

Fig. 2. The current global tree restoration potential. (**A**) The global potential tree cover representing an area of 4.4 billion ha of canopy cover distributed across the world. (**B** and **C**) The global potential tree cover available for restoration. Shown is the global potential tree cover (A), from which we subtracted existing tree cover (*15*) and removed agricultural and urban areas according to (B) Globcover (*16*) and (C) Fritz *et al*. (*17*). This global tree restoration potential [(B) and (C)] represents an area of 0.9 billion ha of canopy cover (table S2).

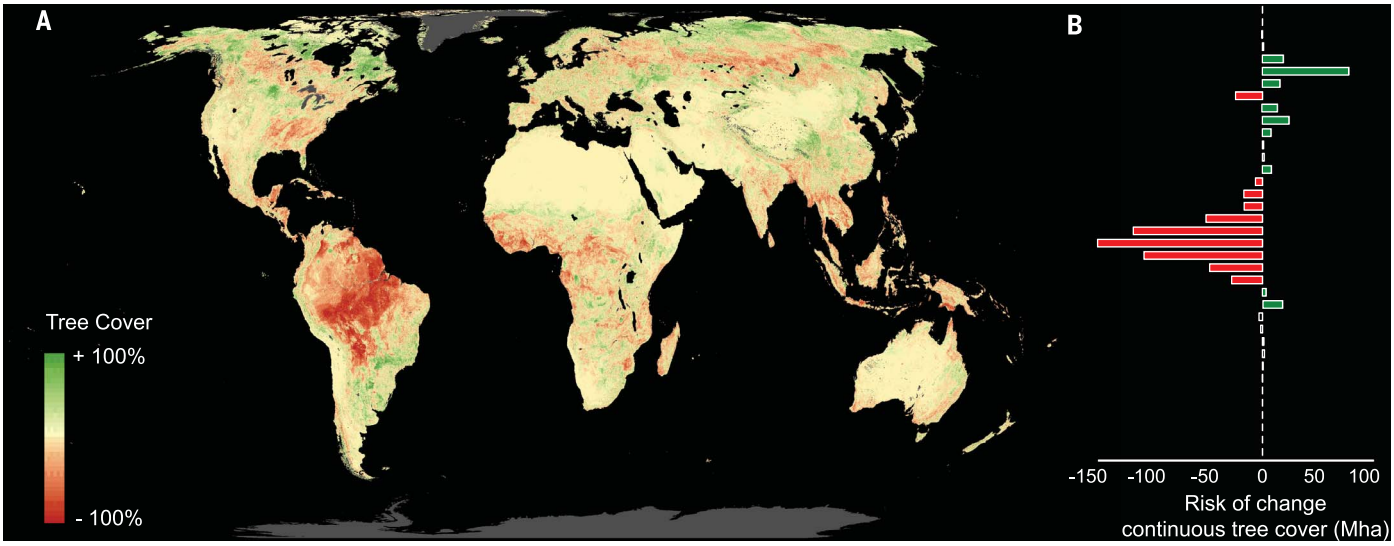

Fig. 3. Risk assessment of future changes in potential tree cover. (**A**) Illustration of expected losses in potential tree cover by 2050, under the "business as usual" climate change scenario (RCP 8.5), from the average of three Earth system models commonly used in ecology (cesm1cam5, cesm1bgc, and mohchadgem2es). (**B**) Quantitative numbers of potential gain and loss are illustrated by bins of 5° along a latitudinal gradient.

additional 205 gigatonnes of carbon (GtC) if they were restored to the status of existing forests (table S2).

Our model accurately depicts the regions where tree growth is possible under existing environmental conditions. However, changing climate conditions may alter the area of land that could support forest growth over the rest of the century, a point that needs to be considered when developing long-term restoration projects. We tested this possibility by rerunning our potential tree cover model under future climate conditions, projected under three Earth System Models (*10*) and two Representative Concentration Pathways (RCP) scenarios (RCP 4.5 and 8.5) (*1*). Under both scenarios, the global tree carrying capacity is lower than the present day potential because of reductions in the potential area of tropics. This is in stark contrast to most current model predictions, which expect global tree cover to increase under climate change (*20*). Although warming is likely to increase tree cover in cold regions with low tree cover (for example, in northern boreal regions such as Siberia) or with existing open forests (such as in tropical drylands) (Fig. 3), our model highlights the high probability of consistent declines of tropical rainforests with high tree cover. Because the average tree cover in the expanding boreal region (30 to 40%) is lower than that in declining tropical regions (90 to 100%), our global evaluation suggests that the potential global canopy cover will decrease under future climate scenarios, even if there is a larger total forest area with >10% tree cover. Therefore, despite potential increases in canopy cover in boreal (~130 Mha), desertic (~30 Mha), montane (~30 Mha), and temperate (~30 Mha) regions, the potential loss of forest habitat in tropical regions (~450 Mha) leads to a global loss of 223 Mha of potential canopy cover by 2050, corresponding to 46 GtC (Fig. 3B and table S3). Such risks of loss do not account for future changes in land use, such as pasture and cattle raising (*7*), which might also contribute to the urgency of the situation.

These models of future changes in tree cover potential reveal insights into how the structure of vegetation might change over time. Of course, these models are characterized by high uncertainty because, unlike the present-day interpolations, we rely on extrapolation of our machine-learning models outside of the existing range of global climate conditions. These extrapolations cannot be considered to be future projections of potential forest extent because they do not incorporate any of the ecological, hydrological, and biogeochemical feedbacks that would be associated with changes in forest cover. For example, it is possible that elevated CO_2 concentrations under future climate scenarios might enhance the growth of those existing trees, although recent evidence suggests that increased growth rate does not necessarily translate to increase of carbon storage (*21*). However, our approach has a strong predictive power to describe the potential tree cover in the absence of humans under any given set of future climate scenarios.

The global photointerpretation dataset offers the capacity to characterize the potential tree cover under any given set of environmental conditions. The resulting openly accessible map can serve as a benchmark map to assess restoration opportunities (such as tree planting and natural assisted regeneration) around the globe, with a tree cover of reference that respects the natural ecosystem type (for example, from wooded savannah to dense forest). However, restoration initiatives must not lead to the loss of existing natural ecosystems, such as native grasslands, that can support huge amounts of natural biodiversity and carbon. Using existing global land-cover layers (*15*–*17*), our maps reveal that there is likely to be space for at least an additional 0.9 billion ha of canopy cover. If these restored woodlands and forests were allowed to mature to a similar state of existing ecosystems in protected areas, they could store 205 GtC. Of course, the carbon capture associated with global restoration could not be instantaneous because it would take several decades for forests to reach maturity. Nevertheless, under the assumption that most of this additional carbon was sourced from the atmosphere, reaching this maximum restoration potential would reduce a considerable proportion of the global anthropogenic carbon burden (~300 GtC) to date (*1*). This places ecosystem restoration as the most effective solution at our disposal to mitigate climate change.

REFERENCES AND NOTES

1. Intergovernmental Panel on Climate Change (IPCC), *An IPCC Special Report on the Impacts of Global Warming of 1.5 °C Above Pre-Industrial Levels and Related Global Greenhouse Gas Emission Pathways* (IPCC, 2018).
2. B. W. Griscom *et al.*, *Proc. Natl. Acad. Sci. U.S.A.* **114**, 11645–11650 (2017).
3. S. L. Lewis, C. E. Wheeler, E. T. A. Mitchard, A. Koch, *Nature* **568**, 25–28 (2019).
4. United Nations Environment Programme (UNEP), The Bonn Challenge (2011).
5. UN Climate Summit, New York Declaration on Forests (2014).
6. P. Potapov, L. Laestadius, S. Minnemeyer, *Global Map of Potential Forest Cover* (World Resources Institute, 2011).
7. K.-H. Erb *et al.*, *Nature* **553**, 73–76 (2018).
8. A. Bey *et al.*, *Remote Sens.* **8**, 807 (2016).
9. United Nations Educational, Scientific and Cultural Organization (UNESCO), *The World Database on Protected Areas* (UNESCO, 2011).
10. Materials and methods are available as supplementary materials.
11. K. R. Jones *et al.*, *Science* **360**, 788–791 (2018).
12. L. Breiman, *Mach. Learn.* **45**, 5–32 (2001).
13. J.-F. Bastin *et al.*, *Science* **356**, 635–638 (2017).
14. Food and Agriculture Organization (FAO), *Global Forest Resources Assessment 2020: Terms and Definitions* (FAO, 2018).

15. M. C. Hansen *et al*., *Science* **342**, 850–853 (2013).
16. O. Arino *et al*., *Global Land Cover Map for 2009 (GlobCover 2009)* (European Space Agency, Université catholique de Louvain, PANGAEA, 2012).
17. S. Fritz *et al*., *Glob. Chang. Biol.* **21**, 1980–1992 (2015).
18. Y. Pan *et al*., *Science* **333**, 988–993 (2011).
19. J. Grace, J. Jose, P. Meir, H. S. Miranda, R. A. Montes, *J. Biogeogr.* **33**, 387–400 (2006).
20. X.-P. Song *et al*., *Nature* **560**, 639–643 (2018).
21. U. Büntgen *et al*., *Nat. Commun.* **10**, 2171 (2019).

ACKNOWLEDGMENTS

We warmly thank all the members of the Crowther lab team, not listed as coauthors of the study, for their incredible support. We also are very grateful to the Google Earth Outreach team for allowing us the storage expansion for our laboratory. **Funding:** This work was supported by grants to T.W.C. from DOB Ecology, Plant-for-the-Planet, and the German Federal Ministry for Economic Cooperation and Development. The data collection was partially supported by the International Climate Initiative of the Federal Ministry for the Environment, Nature Conservation, Building and Nuclear Safety of Germany. **Author contributions:** J.-F.B. conceived the study. J.-F.B. and D.R. performed the analyses. J.-F.B., Y.F., C.G., D.M., M.R., D.R., C.M.Z., and T.W.C. wrote the manuscript. **Competing interests:** The authors declare that there are no competing interests. **Data and materials availability:** All data are available in the manuscript or the supplementary materials. The global tree cover potential map, corresponding to Fig. 2A, is accessible online for visualization at https://bastinjf_climate.users.earthengine.app/view/potential-tree-cover, the Earth engine script to produce the map is accessible online at https://code.earthengine.google.com/ee5cf5186b5ad0f659cc7a43054f072c, and all related layers are accessible online at www.crowtherlab.com or upon request to the corresponding author.

SUPPLEMENTARY MATERIALS

science.sciencemag.org/content/365/6448/76/suppl/DC1
Materials and Methods
Figs. S1 to S12
Tables S1 to S3
References (*22*–*29*)
Data Files S1 and S2

21 February 2019; accepted 21 May 2019
10.1126/science.aax0848

CHEMICAL PHYSICS

Direct mapping of curve-crossing dynamics in IBr by attosecond transient absorption spectroscopy

Yuki Kobayashi[1]*, Kristina F. Chang[1], Tao Zeng[2], Daniel M. Neumark[1,3]*, Stephen R. Leone[1,3,4]*

The electronic character of photoexcited molecules can abruptly change at avoided crossings and conical intersections. Here, we report direct mapping of the coupled interplay between electrons and nuclei in a prototype molecule, iodine monobromide (IBr), by using attosecond transient absorption spectroscopy. A few-femtosecond visible pulse resonantly excites the ($B^3\Pi_{0^+}$), Y(0^+), and Z(0^+) states of IBr, and the photodissociation dynamics are tracked with an attosecond extreme-ultraviolet pulse that simultaneously probes the I-4*d* and Br-3*d* core-level absorption edges. Direct comparison with quantum mechanical simulations unambiguously identifies the absorption features associated with adiabatic and diabatic channels at the B/Y avoided crossing and concurrent two-photon dissociation processes that involve the Y/Z avoided crossing. The results show clear evidence for rapid switching of valence-electronic character at the avoided crossing.

The conventional picture of a photoexcited molecule smoothly evolving toward a product state on a single potential surface is invalid when degeneracies between neighboring states induce nonadiabatic interactions (*1*–*3*). Molecular dynamics that involve avoided crossings and conical intersections have been of fundamental interest in chemical physics since the seminal Landau-Zener model pioneered in the 1930s (*4*, *5*). It is now widely accepted that nonadiabatic interactions play key roles in broad classes of photochemical reactions, such as photoisomerization in the retinal chromophore (*6*) and photostability of DNA base pairs against ultraviolet radiation (*7*). Realization of laser-based control of nonadiabatic processes represents a pivotal milestone in recent progress of molecular spectroscopy (*8*, *9*).

Despite these successes, real-time observation of electronic dynamics in nonadiabatic regions remains elusive (*10*). Conceptually, electronic character can rapidly change in synchrony with nuclear motion. Experimentally, few-femtosecond time resolution is required for the probe, and the intrinsic degeneracy makes it challenging to obtain state-resolved information. Several experimental methods have been applied to this end (*11*–*15*), including high-harmonic spectroscopy (*16*) and ultrafast electron diffraction (*17*). Recent theoretical studies predicted that transient absorption spectroscopy in the x-ray/extreme-ultraviolet (XUV) range offers a distinct and powerful route to measure excited-state dynamics around nonadiabatic regions, with core-level absorption capturing the marked reorganization of valence electrons (*18*, *19*). Core-level absorption has superb state resolution (*20*); not only spin-orbit fine structure but even near-degenerate electronic states in nonadiabatic regions can be clearly resolved, as we demonstrate in this work. The probe step of core-to-valence transitions, being free of strong-field processes, can be directly simulated with quantum-chemistry calculations (*21*). Furthermore, when combined with high-harmonic generation–based attosecond light sources, this all-optical method has the potential to attain subfemtosecond probing time resolution (*22*).

Here, we report attosecond transient absorption mapping of valence-electron dynamics accompanying visible-light excitation of iodine monobromide (IBr), a prototype molecule for nonadiabatic photodissociation dynamics (*23*, *24*). Our primary focus is the switching of electronic character ensuing at an avoided crossing between excited $B(^3\Pi_{0^+})$ and Y(0^+) states. An outline of the experiment is depicted in Fig. 1A. Photodissociation is triggered by a few-femtosecond visible pump pulse [wavelength (λ) = 530 nm, $\Delta\lambda$ = 70 nm, 8 fs, 15 μJ] (Fig. 1B), which selectively excites the visible absorption band of IBr (Fig. 1B) (*25*) and minimizes the unfavorable ionization effects that arise in more conventional experiments in which intense near-infrared excitation is used (*26*). In the probe step after a delay time τ, an attosecond XUV pulse produced through high-harmonic generation is introduced (45 to 72 eV, ~200 as) (Fig. 1C), which encodes the time evolution of the photoexcited molecule in the characteristic core-to-valence absorption signals. The XUV probe pulse simultaneously detects the two core-level absorption edges of IBr: the $N_{4,5}$ edge (4*d* orbitals) of iodine and the $M_{4,5}$ edge (3*d* orbitals) of bromine. This feature enables full tracking of both photofragment electronic states, providing considerably more insight than experiments in which only one fragment is tracked (*15*).

The potential energy curves of IBr are shown in Fig. 1D. Multiple avoided crossings are present in diatomic interhalogens because of the strong spin-orbit couplings of the halogen atoms and the absence of *g*-*u* symmetry for heteronuclear diatomics (*23*, *24*). Two physical pictures are invoked to describe the dynamics at avoided crossings (*27*); in a diabatic picture, electronic states conserve their character as they move along the reaction coordinate, whereas in an adiabatic picture, electronic states are eigenstates of the electronic Hamiltonian and are subject to switching of electronic character. The visible pump pulse excites the molecule to an attractive $B(^3\Pi_{0^+})$ state, which undergoes an avoided crossing with a repulsive Y(0^+) state [distance of crossing (R_c) = 3.3 Å]. In the diabatic channel at the B/Y avoided crossing (Fig. 1D, inset), the photoexcited molecule remains on the attractive $B(^3\Pi_{0^+})$ potential, conserving its electronic character, and evolves toward the spin-orbit excited $I(^2P_{3/2})$ + $Br^*(^2P_{1/2})$ asymptote. In the adiabatic channel (Fig. 1D, inset), the photoexcited molecule transfers to the repulsive Y(0^+) potential, rapidly switching its electronic character, and proceeds to the ground $I(^2P_{3/2})$ + $Br(^2P_{3/2})$ asymptote. The nonadiabatic coupling is of intermediate strength for the B/Y avoided crossing of IBr, and the measured dissociation ratio between the diabatic and adiabatic channels is approximately 3:1 (*28*). In the experiments, resonance-enhanced two-photon processes are also observed for the visible pump pulse, which reaches a peak-field intensity of ~5×10^{13} W/cm^2. An electronic-structure analysis reveals a large transition dipole moment (~3 D) associated with the B → Y transition (*26*). The Y(0^+) state undergoes an avoided crossing with the higher Z(0^+) state (R_c = 2.8 Å), and the dissociation across the Y/Z avoided crossing leads to the $I^*(^2P_{1/2})$ + $Br(^2P_{3/2})$ asymptote. The B → Z transition is also possible but of less importance (~20% compared with B → Y) and is not considered further here.

We first analyzed the transient absorption spectrum of the dissociation products (Fig. 2A, recorded at delay times from 215 to 245 fs). The differential optical density (ΔOD) is defined as a logarithmic ratio of the transmitted XUV spectra with and without the visible pump pulse. Iodine and bromine atoms each exhibit three absorption lines in the I 4*d* → 5*p* and Br 3*d* → 4*p* series: 45.9, 46.7, and 47.6 eV for I and 64.5, 65.1, and 65.6 eV for Br, corresponding to the $^2P_{3/2} \rightarrow {}^2D_{5/2}$, $^2P_{1/2} \rightarrow {}^2D_{3/2}$, and $^2P_{3/2} \rightarrow {}^2D_{3/2}$ transitions, respectively (*29*, *30*). In Fig. 2A, the product ratio between the Br and Br* atoms calculated from the XUV absorption amplitudes is Br*/Br = 3.3, which is in reasonable agreement with a previous measurement at 525-nm excitation (Br*/Br = 3.0) (*28*). At the same time, a sizable signal from the I* atom is observed, yielding a product ratio of I*/I = 0.5. The appearance energy of the I* atom (~2.8 eV) is higher than the center photon energy of the visible pump pulse (~2.3 eV); thus, this signal is attributed to two-photon (or

[1]Department of Chemistry, University of California, Berkeley, CA 94720, USA. [2]Department of Chemistry, Carleton University, Ottawa, Ontario K1S5B6, Canada. [3]Chemical Sciences Division, Lawrence Berkeley National Laboratory, Berkeley, CA 94720, USA. [4]Department of Physics, University of California, Berkeley, CA 94720, USA.
*Corresponding author. Email: ykoba@berkeley.edu (Y.K.); dneumark@berkeley.edu (D.M.N.); srl@berkeley.edu (S.R.L.)

multiphoton) visible-excitation processes. A group of weak absorption signals at 55 to 58 eV corresponds to the I $4d \rightarrow np$ ($n > 5$) Rydberg series (*31*).

Transient absorption spectra as a function of delay time are shown in Fig. 2B. The measurements are carried out from −16 to 245 fs delay time at 1.5-fs intervals. To calculate ΔOD, the pump-on/pump-off XUV spectra were each averaged over 200 frames (40 laser pulses per frame). In Fig. 2B, the excited-state absorption (ΔOD > 0) is shown in bright colors, and the ground-state bleach (ΔOD < 0) is shown in gray shades. The observed ground-state bleach features, both in the I-4*d* and Br-3*d* windows, exhibit signatures of vibrational coherences in the ground $X(^1\Sigma_{0^+})$ state [isotopic averages: vibrational frequency (ω_e) = 268 m^{-1}, anharmonicity ($\omega_e x_e$) = 0.8 cm^{-1}, vibrational period (T) = 125 fs] (*32*). In previous studies, vibrational coherences in the neutral ground states launched by strong-field ionization were reported (*33*, *34*). In this work, the excitation mechanism is a resonant single-photon process, and distinct nodal structures are observed in the oscillating absorption signals. We performed quantum wave-packet simulations to compute the core-level absorption spectra, and the observed features are reproduced by taking coherences in the v = 0, 1, and 2 vibrational states (fig. S3). The mechanism for the overtone (v = 2) excitation is attributed to a stimulated Raman process enhanced by resonant visible-light coupling between the $X(^1\Sigma_{0^+})$ and $B(^3\Pi_{0^+})$ states.

The details of the excited-state absorption in the I-4*d* and Br-3*d* windows are shown in Fig. 3, A and B, respectively. The early time signals (0 to 50 fs) exhibit sweeping shifts to lower photon energy, which is indicative of molecular dissociation proceeding on the $B(^3\Pi_{0^+})$ potential. The evolution of the photoexcited molecule at the B/Y avoided crossing is encoded in the subsequent temporal window (50 to 80 fs) (Fig. 3, A and B, dashed boxes), and the corresponding absorption traces taken at 6-fs intervals are shown in Fig. 3, C and D (50, 56, 62, 68, 74, and 80 fs). The sharp absorption features associated with the I*(46.7 eV) and Br*(65.1 eV) atoms are nearly invariant with respect to delay time. These atomic fragments conceivably originate from two-photon processes that occur on a shorter time scale, an assignment that was corroborated with ab initio simulations. The other broad signals (indicated in Fig. 3 with arrows labeled "diabatic" and "adiabatic") exhibit dramatic variations both in the absorption amplitude and energy. As already mentioned, the diabatic channel at the B/Y avoided crossing leads to the I + Br* asymptote (Fig. 1D), and the associated wave packet conserves its electronic character. In the experimental results of the Br-3*d* window (Fig. 3D), the absorption signal that exhibits continuous shifts to lower photon energy converges to the Br* absorption line and hence is assigned to the diabatic channel. In the adiabatic channel, however, the photoexcited molecule changes the electronic character and proceeds to the ground I + Br

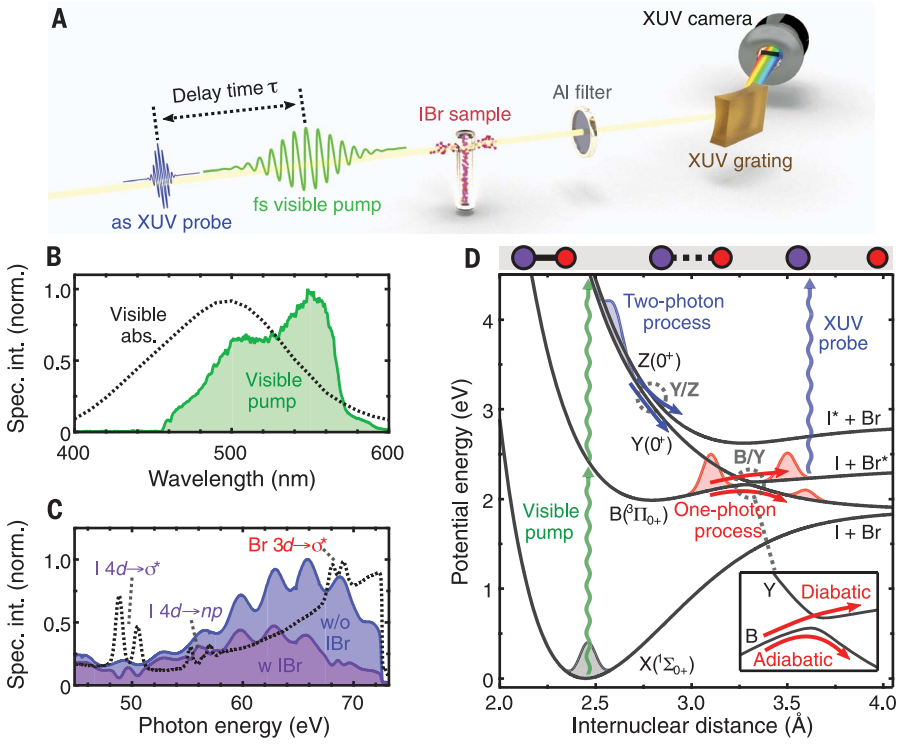

Fig. 1. Outline of experiment. (**A**) Illustration of the experimental setup. (**B**) Spectral intensity of the visible pump pulse (green area) and visible-absorption band (extinction coefficient) of IBr (black dashed curve) measured previously in (*25*). (**C**) Spectral intensity of the XUV probe pulse recorded with (purple area) and without (blue area) the IBr sample and the optical density (black dashed curve) calculated from the two spectra. The I-4*d* and Br-3*d* edges are covered by the broadband XUV spectrum. (**D**) Adiabatic potential energy curves of IBr, with the visible and XUV excitation pathways indicated with vertical arrows. The red and blue wave packets indicate the dissociation pathways from one-photon and two-photon processes, respectively. Avoided crossings are formed between the B and Y states (R_c = 3.3 Å) and Z and Y states (R_c = 2.8 Å). (Inset) The adiabatic and diabatic channels at the B/Y avoided crossing.

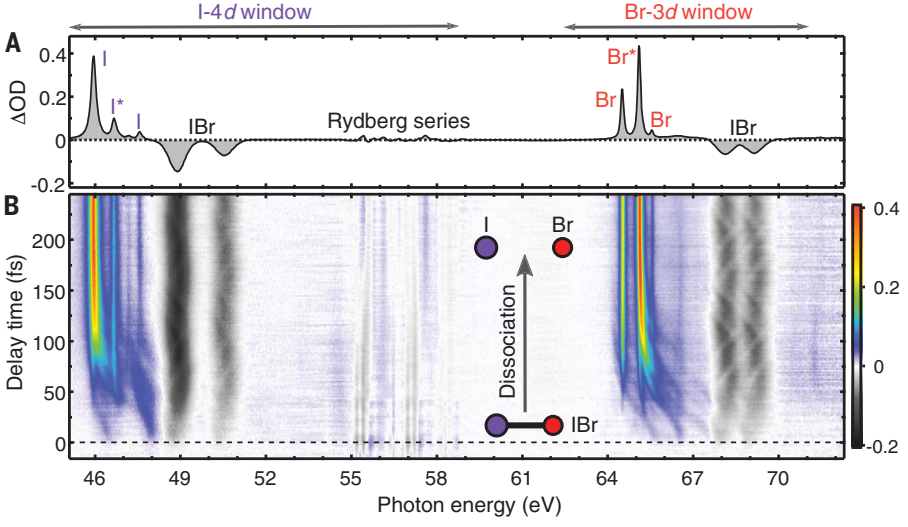

Fig. 2. Core-level transient absorption spectra of IBr. (**A**) Transient absorption spectrum of the dissociation products recorded at delay times from 215 to 245 fs. (**B**) Delay-time-resolved transient absorption spectra. At zero delay time, the visible pump pulse initiates the dissociation processes, and excited-state signal (bright colors) as well as ground-state bleach (gray shades) emerge. The dissociation proceeds toward the positive delays.

asymptote (Fig. 1D). In the experimental results (Fig. 3D), the Br absorption line suddenly emerges accompanied by no energy shift at a separate photon energy. The discontinuous evolution of the Br signal is a manifestation of the new electronic character acquired from the neighboring $Y(0^+)$ state. In the I-4*d* window (Fig. 3C), the XUV absorption signals associated with the diabatic and adiabatic channels are not as widely separated as in the Br-3*d* window because the same I atom is produced in both channels. Nonetheless, the continuous shifts to lower photon energy and the sudden emergence of the sharp I signal are distinctly resolved, leading to consistent assignments of the B/Y avoided-crossing signals.

To gain more detailed insight into the transitory molecular features, we performed ab initio simulations of the core-level absorption spectra (*26*). The valence and core-excited electronic structures were computed by means of spin-orbit generalized multiconfigurational quasi-degenerate perturbation theory (SO-GMC-QDPT) (*21*, *35*), and from these, the XUV absorption strengths were obtained. Nonadiabatic dissociation dynamics were simulated fully quantum mechanically by numerically solving the time-dependent Schrödinger equation. The initial wave packets were taken to be in the Franck-Condon region of the $B(^3\Pi_{0^+})$ state (one-photon process) or on the $Y(0^+)$ state (two-photon process) to model the relevant visible-light excitations.

Simulated results for the one-photon process are shown in Fig. 3, E and F. The sweeping energy shifts in the early time window are successfully reproduced by the simulation. The $B(^3\Pi_{0^+})$ state in the Franck-Condon region has a $[\sigma^2\pi^4\pi^{*3}\sigma^{*1}]$ configuration and is probed by the core-level transitions to the π^* and σ^* orbitals. The observed absorption lines reflect the multiplet structures of the core-excited states that originate from the spin-orbit couplings in the core (I-4*d*, Br-3*d*) and valence (π, π^*) orbitals (fig. S6). Some features are broadened and less pronounced in the experiments compared with the simulations, which we attribute to the finite spectral width of the visible pump pulse and the nuclear wave-packet motion on the repulsive core-excited potentials. The absorption traces in the temporal window for the B/Y avoided crossing (50 to 80 fs) are shown in Fig. 3, G and H, with assignments of the diabatic and adiabatic channels directly made from the wave-packet simulations. The continuous (diabatic) and discontinuous (adiabatic) evolution of the XUV absorption signals exhibits an excellent match with the experiments, providing clear confirmation of the experimental signal assignments at the B/Y avoided crossing.

The origin of the I* and part of the Br* signals is verified with the two-photon simulations (Fig. 3, I and J). The simulated I* signal (Fig. 3I) matches the experimental result (Fig. 3A) both in time and absorption energy. Passage through the Y/Z avoided crossing (Fig. 1D) is calculated to occur in ~25 fs. These early time dynamics are not as clearly resolved in the experiments because of the spectral broadening from the fast dissociative motion in the two-photon processes. Calculated absorption strengths of the $Y(0^+)$ and $Z(0^+)$ states are provided in fig. S7 for future reference. The Br* atom is produced by way of the wave packet adiabatically transferring from the repulsive $Y(0^+)$ potential to the attractive $B(^3\Pi_{0^+})$ potential at the B/Y avoided crossing. As such, in the simulation, the switching of electronic character causes abrupt emergence of the Br*

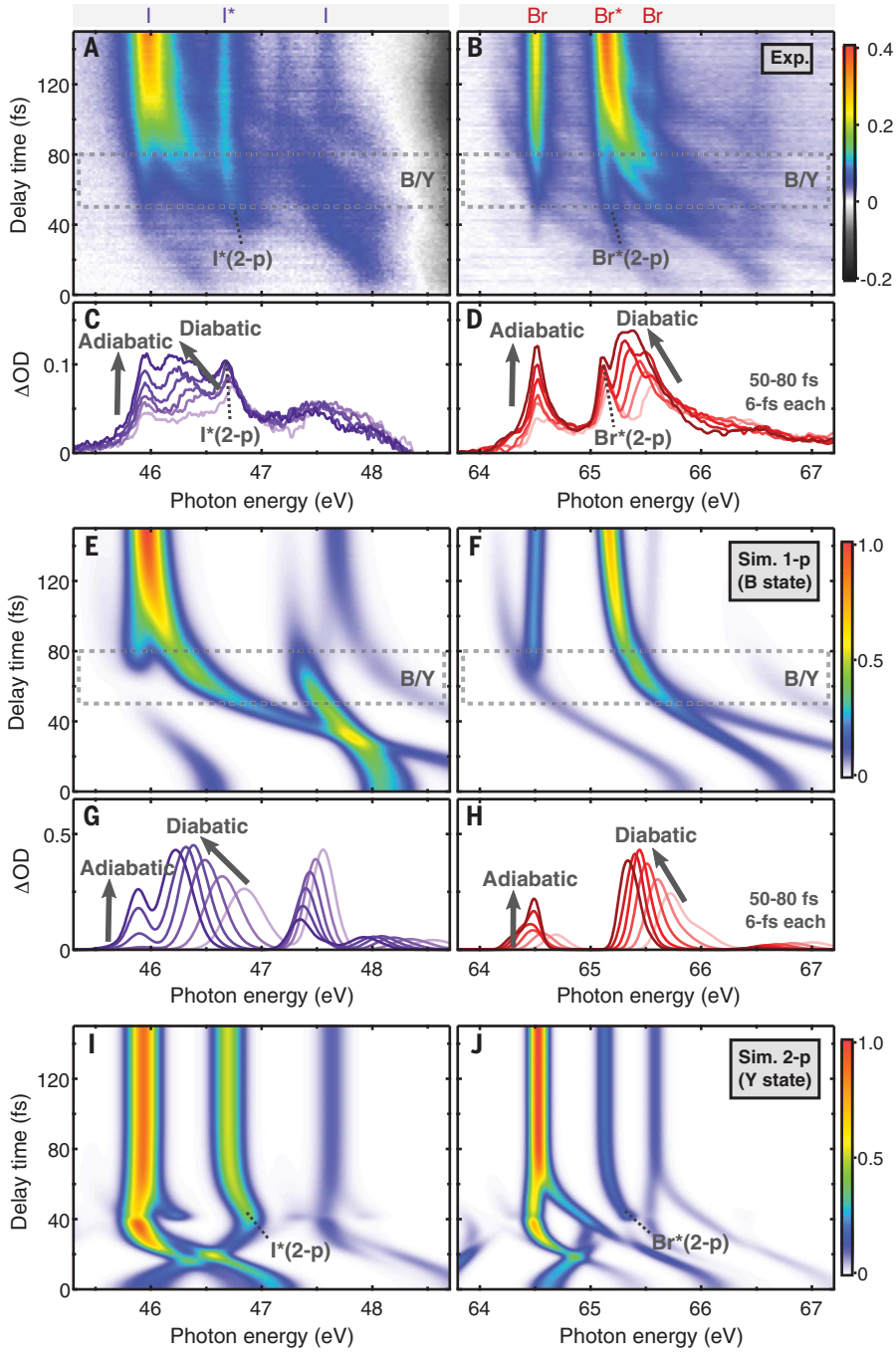

Fig. 3. Experimental and simulated spectra of nonadiabatic dissociation dynamics. (**A** and **B**) Experimental absorption spectra in the (A) I-4*d* and (B) Br-3*d* windows, respectively. The temporal window for the B/Y avoided crossing is highlighted with dashed boxes. (**C** and **D**) Absorption spectra taken from the experimental results at delay times of 50, 56, 62, 68, 74, and 80 fs. The assignments at the adiabatic and diabatic channels at the B/Y avoided crossing are denoted. (**E** to **H**) One-photon (1-p) simulation results shown for the comparison with the experimental results (A) to (D). (**I** and **J**) Two-photon (2-p) simulation results that reproduce the early time emergences of the I* and Br* signals. The absorption signals in the one-photon and two-photon simulations are normalized independently.

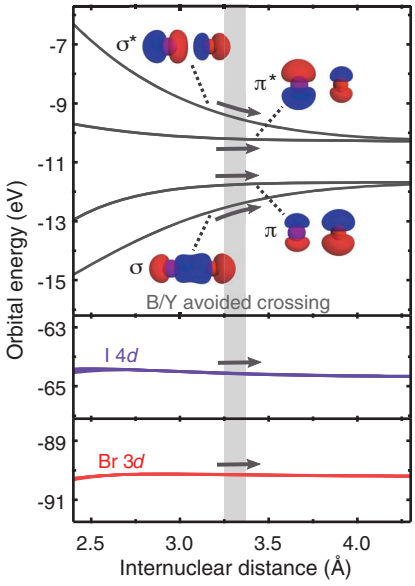

Fig. 4. Orbital energies as a function of internuclear distance. The energy difference between the core and valence orbitals are closely tied to the observed absorption energies. Around the B/Y avoided crossing (gray area), the energies of the core orbitals and valence π/π^* orbitals are nearly invariant, whereas those of the σ/σ^* orbitals show increase or decrease versus internuclear distance. The displayed molecular orbitals are computed at R_c = 3.3 Å.

signal (Fig. 3J), and the corresponding absorption feature is resolved at ~40-fs delay time in the experimental results (Fig. 3B).

To further investigate the electronic-structure information at the B/Y avoided crossing imprinted in the core-level absorption spectra, we examined the orbital energies and electron configurations. The energies of the active molecular orbitals are shown in Fig. 4 as a function of internuclear distance computed at the level of multiconfigurational self-consistent field (MCSCF). The energy differences between the core and valence orbitals are closely tied to the observed absorption energies. The exact description of the electronic states requires multiconfigurational treatments and inclusion of spin-orbit couplings, as is done in the SO-GMC-QDPT calculations (*26*). The energies of the I-4*d* and Br-3*d* orbitals are nearly invariant throughout the reaction coordinate. This insensitivity to internuclear distance indicates that the observed energy shifts in the diabatic channel (or no shift in the adiabatic channel) reflect the energy variations in the valence orbitals alone. As for the valence orbitals, the energy gradients quantified at the B/Y avoided crossing (gray area) are +1.5 eV/Å and −1.7 eV/Å for σ and σ*, respectively, but only +0.3 eV/Å and −0.2 eV/Å for π and π*, respectively. These trends indicate that the π and π* orbitals are effectively no longer contributing to the variation of the potential energies when the wave packet reaches the avoided crossing. A more direct clue to the electronic-character switching is obtained from the electronic configurations computed for each adiabatic state (*36*–*38*). Just before the avoided crossing, the $B(^3\Pi_{0^+})$ state is a mixed configuration of $[\sigma^2\pi^4\pi^{*3}\sigma^{*1}]$ and $[\sigma^2\pi^3\pi^{*4}\sigma^{*1}]$; a single vacancy lies in σ*, and the other vacancy is distributed between π and π*. After the photoexcited molecule adiabatically transfers to the repulsive $Y(0^+)$ potential, the main configuration changes to $[\sigma^2\pi^3\pi^{*3}\sigma^{*2}]$, where the σ* orbital is fully occupied, and the two vacancies lie in the π and π* orbitals. A physical picture emerges from these results: The vacancy in the valence orbitals switches from σ* to π/π* at the B/Y avoided crossing, giving rise to new core-level absorption signals with no further energy shifts, reflecting the energy invariance of the π and π* orbitals versus internuclear distance.

The visible-absorption band of IBr is a key benchmark system for curve-crossing dynamics. We applied attosecond transient absorption spectroscopy in combination with the SO-GMC-QDPT calculations of the electronic structures and revealed the switching of the valence-orbital vacancy from σ* to π/π* at the B/Y avoided crossing. This intuitive picture was obtained by the powerful ability of the attosecond XUV pulse to sensitively encode the energies and occupancies of valence orbitals in the core-to-valence absorption spectra of IBr. The valence-electronic structure not only determines the strength of chemical bonds, it also governs the reactivity of a molecule as represented by frontier-orbital theory; unraveling the dramatic evolution of valence-electronic structures around nonadiabatic regions will greatly extend knowledge of photochemical reactions. Application of ultrafast x-ray/XUV light sources in the explorations of chemical dynamics is an actively advancing field of research (*39*, *40*), and this work shows the great promise of attosecond transient absorption spectroscopy for mapping the evolution of valence electrons in larger molecular systems.

REFERENCES AND NOTES

1. G. A. Worth, L. S. Cederbaum, *Annu. Rev. Phys. Chem.* **55**, 127–158 (2004).
2. B. G. Levine, T. J. Martínez, *Annu. Rev. Phys. Chem.* **58**, 613–634 (2007).
3. M. P. Bircher *et al.*, *Struct. Dyn.* **4**, 061510 (2018).
4. L. D. Landau, *Phys. Z. Sowjetunion* **2**, 46 (1932).
5. C. Zener, R. H. Fowler, *R. Soc. London Ser. A* **137**, 696–702 (1932).
6. D. Polli *et al.*, *Nature* **467**, 440–443 (2010).
7. T. Schultz *et al.*, *Science* **306**, 1765–1768 (2004).
8. B. J. Sussman, D. Townsend, M. Y. Ivanov, A. Stolow, *Science* **314**, 278–281 (2006).
9. M. E. Corrales *et al.*, *Nat. Chem.* **6**, 785–790 (2014).
10. S. R. Leone *et al.*, *Nat. Photonics* **8**, 162–166 (2014).
11. S. Takeuchi *et al.*, *Science* **322**, 1073–1077 (2008).
12. M. C. E. Galbraith *et al.*, *Nat. Commun.* **8**, 1018 (2017).
13. A. von Conta *et al.*, *Nat. Commun.* **9**, 3162 (2018).
14. A. E. Boguslavskiy *et al.*, *J. Chem. Phys.* **148**, 164302 (2018).
15. H. Timmers *et al.*, *Nat. Commun.* 10.1038/s41467-019-10789-7 (2019).
16. H. J. Wörner *et al.*, *Science* **334**, 208–212 (2011).
17. J. Yang *et al.*, *Science* **361**, 64–67 (2018).
18. S. P. Neville *et al.*, *Faraday Discuss.* **194**, 117–145 (2016).
19. S. P. Neville, M. Chergui, A. Stolow, M. S. Schuurman, *Phys. Rev. Lett.* **120**, 243001 (2018).
20. R. Geneaux, H. J. B. Marroux, A. Guggenmos, D. M. Neumark, S. R. Leone, *Philos. Trans. A Phys. Eng. Sci.* **377**, 20170463 (2019).
21. Y. Kobayashi, T. Zeng, D. M. Neumark, S. R. Leone, *Struct. Dyn.* **6**, 014101 (2019).
22. F. Krausz, M. Ivanov, *Rev. Mod. Phys.* **81**, 163–234 (2009).
23. M. S. Child, R. B. Bernstein, *J. Chem. Phys.* **59**, 5916–5925 (1973).
24. M. S. Child, *Mol. Phys.* **32**, 1495–1510 (1976).
25. D. J. Seery, D. Britton, *J. Phys. Chem.* **68**, 2263–2266 (1964).
26. Materials and methods are available as supplementary materials.
27. T. Van Voorhis *et al.*, *Annu. Rev. Phys. Chem.* **61**, 149–170 (2010).
28. E. Wrede *et al.*, *J. Chem. Phys.* **114**, 2629–2646 (2001).
29. L. Nahon, P. Morin, F. C. Farnoux, *Phys. Scr.* **T41**, 104–112 (1992).
30. G. O'Sullivan, C. McGuinness, J. T. Costello, E. T. Kennedy, B. Weinmann, *Phys. Rev. A* **53**, 3211–3226 (1996).
31. L. Nahon, P. Morin, *Phys. Rev. A* **45**, 2887–2893 (1992).
32. R. E. Willis Jr., W. W. Clark III, *J. Chem. Phys.* **72**, 4946–4950 (1980).
33. E. R. Hosler, S. R. Leone, *Phys. Rev. A* **88**, 023420 (2013).
34. Z. Wei *et al.*, *Nat. Commun.* **8**, 735 (2017).
35. T. Zeng, *J. Chem. Phys.* **146**, 144103 (2017).
36. S. Patchkovskii, *Phys. Chem. Chem. Phys.* **8**, 926–940 (2006).
37. R. Li *et al.*, *J. Quant. Spectrosc. Radiat. Transf.* **133**, 271–280 (2014).
38. T. Matsuoka, S. Yabushita, *J. Phys. Chem. A* **119**, 9609–9620 (2015).
39. M. Chergui, A. H. Zewail, *ChemPhysChem* **10**, 28–43 (2009).
40. P. M. Kraus, M. Zürch, S. K. Cushing, D. M. Neumark, S. R. Leone, *Nat. Rev. Chem.* **2**, 82–94 (2018).
41. Y. Kobayashi, K. Chang, T. Zeng, D. Neumark, S. Leone, Direct mapping of curve crossing dynamics in IBr by attosecond transient absorption spectroscopy, UC Berkeley Dash, Dataset (2019); doi:10.6078/D10X1Z.

ACKNOWLEDGMENTS

Funding: This work, Y.K., and K.F.C. were supported by the National Science Foundation (NSF) (CHE-1660417). Y.K., K.F.C., D.M.N., and S.R.L. also acknowledge the funding from the U.S. Army Research Office (ARO) (W911NF-14-1-0383). T.Z. acknowledges the Natural Sciences and Engineering Research Council (NSERC) of Canada for research funding (RGPIN-2016-06276) and also Carleton University for the start-up grant (186853). Some of the computations by Y.K. were performed by using workstations at the Molecular Graphics and Computation Facility (MGCF) at the University of California, Berkeley, which is supported by the National Institutes of Health (NIH) (S10OD023532). Y.K. also acknowledges financial support from the Funai Overseas Scholarship.
Author contributions: Y.K., D.M.N., and S.R.L. conceived the experiments. Y.K. and K.F.C. performed the attosecond transient absorption measurements. T.Z. developed the SO-GMC-QDPT code. Y.K. performed the electronic-structure calculations and quantum-mechanical simulations. Y.K. analyzed the results and wrote the manuscript, with inputs from all authors.
Competing interests: The authors declare no competing interests. **Data and materials availability:** The experimental results of the attosecond transient absorption measurements are archived in the Dash repository (*41*).

SUPPLEMENTARY MATERIALS

science.sciencemag.org/content/365/6448/79/suppl/DC1
Materials and Methods
Supplementary Text
Figs. S1 to S8
Tables S1 and S2
References (*42*–*60*)

5 March 2019; accepted 11 June 2019
10.1126/science.aax0076

MARINE ECOLOGY

The great Atlantic *Sargassum* belt

Mengqiu Wang[1], Chuanmin Hu[1]*, Brian B. Barnes[1], Gary Mitchum[1], Brian Lapointe[2], Joseph P. Montoya[3]

Pelagic *Sargassum* is abundant in the Sargasso Sea, but a recurrent great Atlantic *Sargassum* belt (GASB) has been observed in satellite imagery since 2011, often extending from West Africa to the Gulf of Mexico. In June 2018, the 8850-kilometer GASB contained >20 million metric tons of *Sargassum* biomass. The spatial distribution of the GASB is mostly driven by ocean circulation. The bloom of 2011 might be a result of Amazon River discharge in previous years, but recent increases and interannual variability after 2011 appear to be driven by upwelling off West Africa during boreal winter and by Amazon River discharge during spring and summer, indicating a possible regime shift and raising the possibility that recurrent blooms in the tropical Atlantic and Caribbean Sea may become the new norm.

The Sargasso Sea is named after the floating mats of *Sargassum* seaweed, first reported by Christopher Columbus in the 15th century. These seaweed attract fish, shrimp, crabs, birds, and turtles (*1*–*3*), providing essential habitats and serving as hotspots for biodiversity and productivity. Two species of *Sargassum*, *S. fluitans* and *S. natans*, are the most abundant in the Sargasso Sea and the Gulf of Mexico (*1*, *4*), which are notably connected by ocean currents.

Large quantities of *Sargassum* have recently been reported in the central Atlantic Ocean and the Caribbean Sea (*5*–*14*), accompanied by frequent beaching events that have caused serious environmental, ecological, and economic problems (*15*, *16*). Numerous workshops have been held to develop strategies to respond to *Sargassum* inundations (*17*, *18*). A critical question is whether a regime shift in the atmospheric and/or oceanic climatic conditions has led to the recent changes. Several hypotheses have been proposed concerning the relative roles of warming temperatures, climate change, and nutrient enrichment (*19*–*23*), but the lack of large-scale *Sargassum* data has prevented investigators from reaching a solid conclusion.

We attempt to address this question using long-term satellite data, numerical models, and field measurements. The 19-year record of observations from the Moderate Resolution Imaging Spectroradiometer (MODIS) satellite instrument reveals a recent, recurrent *Sargassum* belt extending across the Intra-Americas Sea and the tropical Atlantic (Fig. 1). The environmental and field data, along with numerical models, help us to understand the formation of this great Atlantic *Sargassum* belt (GASB), the connectivity between different regions, as well as the mechanisms behind the tipping point in 2011 and interannual variations in subsequent years.

[1]College of Marine Science, University of South Florida, Tampa, FL, USA. [2]Harbor Branch Oceanographic Institute, Florida Atlantic University, Fort Pierce, FL, USA. [3]School of Biological Sciences, Georgia Institute of Technology, Atlanta, GA, USA.
*Corresponding author. Email: huc@usf.edu.

The entire monthly sequence of *Sargassum* abundance distributions (movie S1) shows that from 2000 to 2010, the central Atlantic showed very low abundance (*5*, *6*, *12*, *13*), with occasional small quantities near the Amazon River mouth from August to November. The first massive *Sargassum* bloom in the central Atlantic started in 2011 (*6*), and in later years the bloom developed to a GASB extending from West Africa to the Caribbean Sea and into the Gulf of Mexico (Fig. 1 and movie S1).

The GASB formed in the summer months (Northern Hemisphere in this paper) of 2011–2018 except in 2013 (Fig. 1C). In 2015 and 2018, the GASB showed the highest coverage, extending >8850 km and carrying a wet biomass of >9 million tons (>20 million tons in June 2018) (*24*). Once reaching the Gulf of Mexico, the belt followed the Loop Current and Gulf Stream to enter the North Atlantic Ocean. Some *Sargassum* were transported directly into the North Atlantic from the central west Atlantic following the Antilles Current (Fig. 1C).

Although multiple sources of *Sargassum* may exist, the shape of the GASB is consistent with advection by the ocean circulation patterns in the tropical Atlantic. Through particle-tracking numerical experiments that account for both physical transport and biological growth, the July GASB patterns were well reproduced by forward tracking of simulated *Sargassum* particles for 6 months (fig. S1). This holds true even when a uniform particle distribution is used to initialize the model, although a more realistic initialization using MODIS observations led to improved model performance in reproducing the GASB patterns in July (*25, 26*) (fig. S1, A and B). Furthermore, after accounting for biological factors under various scenarios, *Sargassum* density in the tropics could be captured even more accurately (fig. S1).

In both July and January, most of the simulated *Sargassum* particles in the central Atlantic are traced back to the same region, with a very weak connection to West Africa and almost no connection to the North Atlantic or Caribbean Sea (fig. S2) (*25*). This suggests that the major blooms in the central Atlantic likely developed locally rather than from seed populations in the Sargasso Sea. The weak connection between West Africa and the central Atlantic (fig. S2B) indicates that some *Sargassum* may enter the central Atlantic from West Africa and bloom there. These observations match well with previous modeling work emphasizing the role of North Equatorial Recirculation Region (NERR) as a potential source region (*19*–*21*, *27*) and other modeling efforts on the regional connections (*28*, *29*). Field measurements of species compositions (*30*) also suggest that the Sargasso Sea is unlikely to be the main source of the blooms in the central Atlantic.

It is natural to ask, then, what conditions in the central Atlantic triggered the first *Sargassum* bloom in 2011? Small amounts of *Sargassum* existed in the central Atlantic in previous years (movie S1), representing the seed populations. In 2009, higher-than-usual nutrients from the Amazon River discharge (*31*) (Fig. 2B and figs. S3A and S4C), as well as from upwelling in the eastern Atlantic (Fig. 2D, fig. S4D, and table S2), could stimulate *Sargassum* growth (*32*, *33*), allowing massive blooms to occur. A related question is, why did a massive bloom not occur in 2010? We suggest that this was due to higher-than-usual sea surface temperatures (hereafter, SSTs) in 2010 (Fig. 2D), which, according to laboratory experiments (*34*) (fig. S5) and our analyses of satellite-derived *Sargassum* change rates (*26*), would suppress *Sargassum* growth. In 2011, the SSTs were more suitable for *Sargassum* growth and the recycled nutrients from previous years and new nutrients from the current year would have created the correct conditions to initiate a massive bloom. Also, the low salinity induced by a large freshwater input from 2009 and 2010 would likely hinder *Sargassum* growth (*34*). A reasonable scenario of the 2011 bloom is therefore that nutrient accumulations from 2009 due to stronger upwelling in the eastern Atlantic and excessive Amazon River discharge in the western Atlantic provided the initial conditions, whereas high temperature and low salinity in 2010 delayed the bloom until 2011.

After 2011, the *Sargassum* abundance in the central Atlantic showed similar seasonality as in the Gulf of Mexico, with increased abundance from January to June and decreased abundance from July to December (Fig. 3B and fig. S6). Considering the weak seasonality in insolation in the tropics, this seasonality might be the result of an innate biological clock (circannual rhythm), as exists in other brown seaweeds (*35*), combined with the seasonal nutrient supply (*26*). Such a mechanism is discussed further in the supplementary materials.

In 2012, a *Sargassum* bloom first developed in spring and summer, but decreased rapidly from August to December. The earlier growth could have been a result of higher nutrient supply from upwelling processes and lower SSTs in the central east Atlantic from winter 2011 to spring 2012, whereas the rapid decrease after August could have been due to the overall lower nutrient supply from the Amazon River during 2010–2011 and the relatively higher SSTs after late summer. By January 2013, most *Sargassum* disappeared

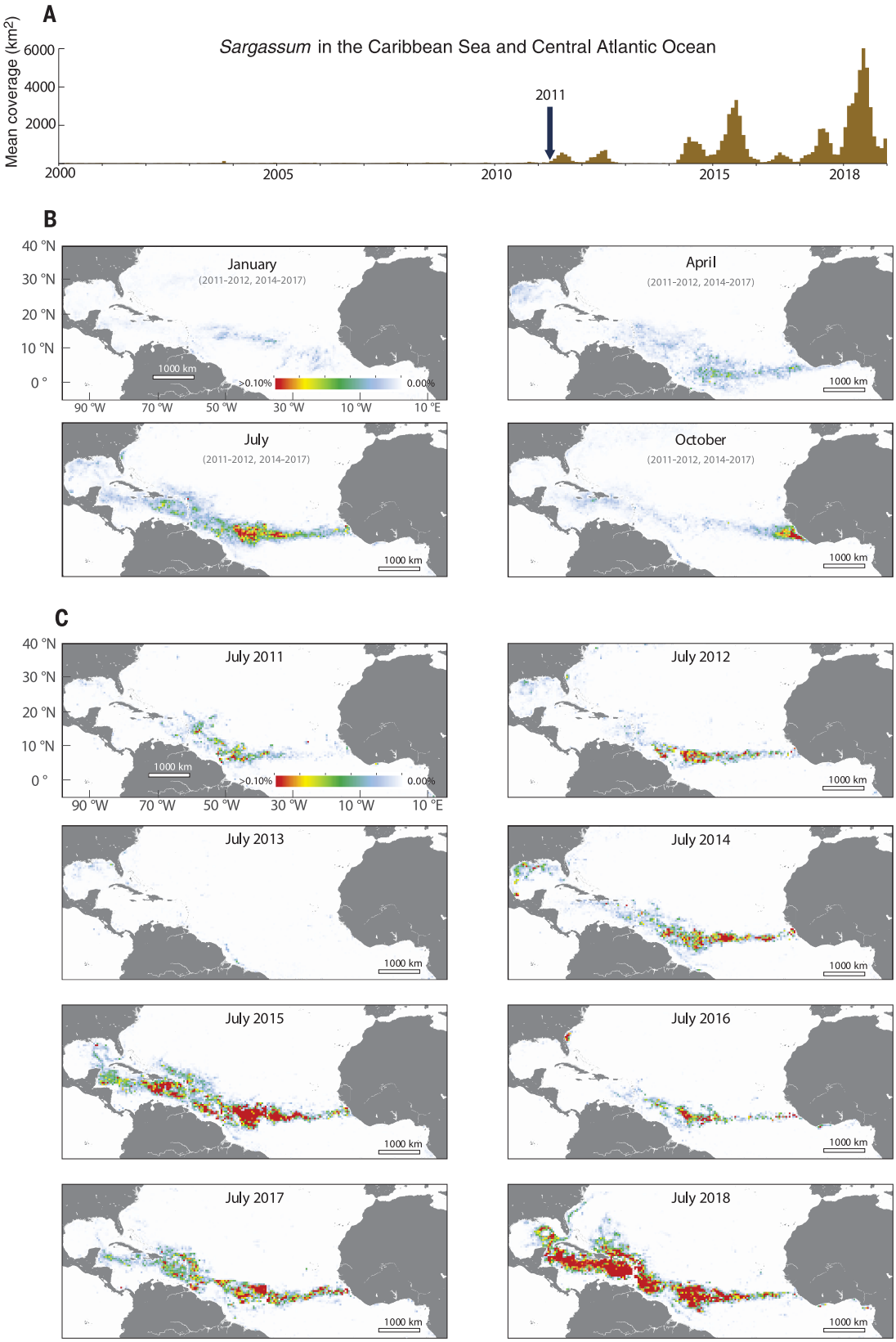

Fig. 1. *Sargassum* distributions in the Gulf of Mexico and the Atlantic Ocean. (**A**) Monthly mean *Sargassum* areal coverage in the Caribbean Sea and the central Atlantic Ocean, with a maximum of ~ 6000 km^2 or >20 million tons in June 2018. The year mark starts from January. (**B**) Monthly mean *Sargassum* density (% cover) in January, April, July, and October of 2011–2017 after excluding the nonbloom year of 2013. (**C**) Monthly mean *Sargassum* density for the month of July from 2011 to 2018. The GASB is observed in all years except 2013.

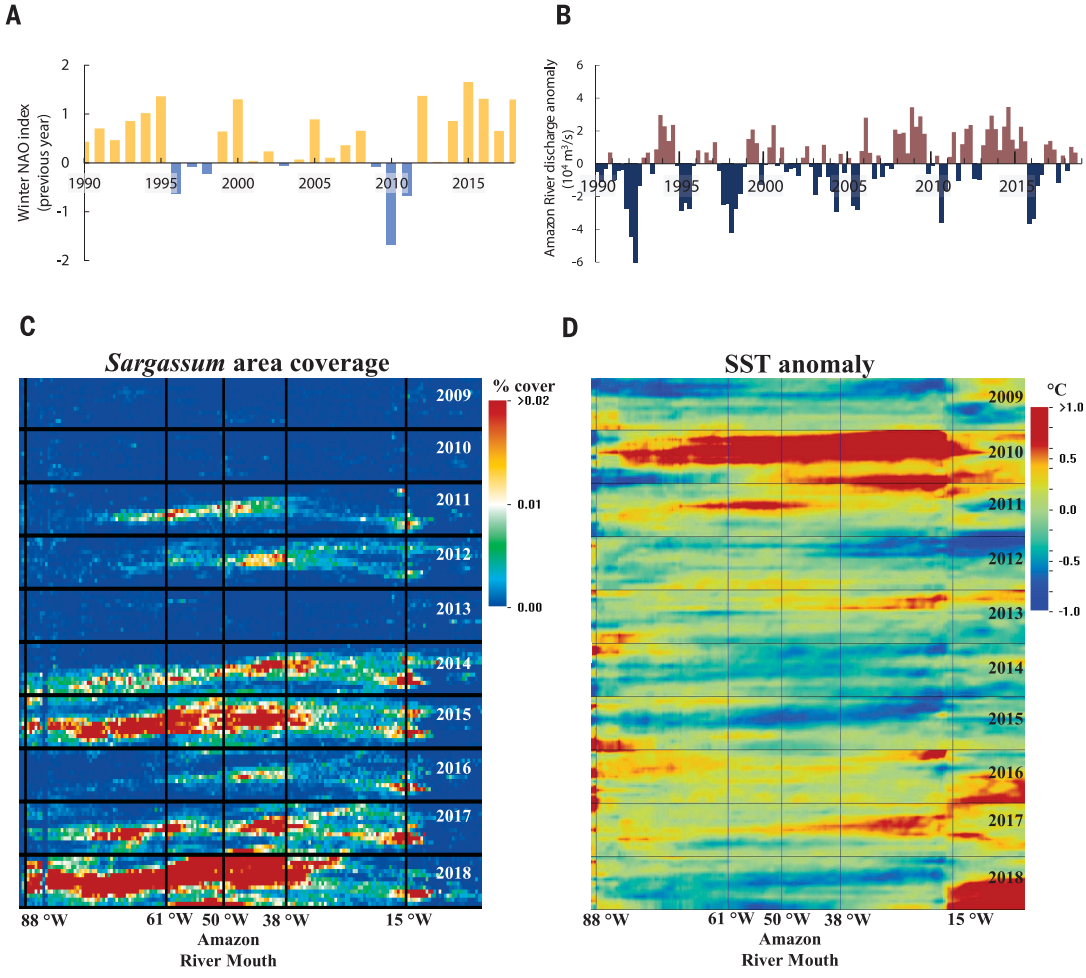

Fig. 2. Environmental conditions and climate indices used to explain interannual changes of GASB. (**A**) Mean NAO index averaged from December to February (winter NAO) for 1990–2018. (**B**) Seasonal mean discharge anomaly of the Amazon River from 1990 to 2018 measured at the Obidos station. (**C**) Latitude-averaged (from 5°S to 23°N) *Sargassum* monthly areal coverage density from 2009 to 2018. (**D**) Latitude-averaged monthly mean SST anomaly from 2009 to 2018. In (C) and (D), the vertical lines mark the locations of 88°W, 61°W, 50°W, 38°W, and 15°W, representing the Yucatan peninsula coast, Barbados coast, the Amazon River mouth, the middle of the central Atlantic, and the West Africa coast, respectively.

across the central Atlantic (movie S1). The reduced seed populations from 2012, higher SSTs in the growth phase, and limited nutrients together appeared to lead to a nonbloom year in 2013 (table S2 and movie S1).

In 2014, *Sargassum* grew rapidly during spring and summer. Unlike 2011, the first *Sargassum* aggregation was identified in early January in the central east Atlantic. This rapid growth can likely be attributed to the nutrient enrichment from the West Africa upwelling from winter 2013 to spring 2014 (table S2). The bloom continued to develop when reaching the central west Atlantic, where the *Sargassum* was nourished by high riverine nutrients accumulated in 2013–2014 (table S2 and Fig. 2B). The favorable growth conditions (higher nutrients and lower SSTs) in the central east Atlantic and central west Atlantic would also have sustained the winter bloom, providing higher-than-usual seed populations to initiate the massive bloom in 2015 (table S2).

In 2015, although the initial *Sargassum* growth rate was not as high as that in 2014, the seed population was much larger than it was in previous years. This, along with higher nutrients from the central east Atlantic in spring and early summer as well as from the Amazon River from 2014 to 2015, led to a massive *Sargassum* bloom in 2015 (table S2). The higher concentrations of *Sargassum* required more nutrients to sustain, which would also explain the lower change rate in spring 2015 (Fig. 3, A and B). From fall to winter, *Sargassum* decreased faster than in 2014 under comparatively warmer waters and reduced nutrients (table S2). This significant decrease continued until February 2016.

In 2016, only a small amount of *Sargassum* survived from 2015 and it was located in the central east Atlantic. The early growth was limited by the lower nutrient supply from West African upwelling from winter 2015 to spring 2016 (table S2). When the *Sargassum* was transported eastward to the central east Atlantic after December 2016, however, it grew faster because of local nutrient enrichments (table S2), providing seed populations for the 2017 bloom.

In 2017, the bloom generally developed faster than in 2016 possibly as a result of higher nutrient supplies from the Amazon River and the West Africa upwelling since winter 2016 (table S2). During winter 2017, the *Sargassum* change rate was much higher than it was in 2016, which would also have benefited from the lower SSTs and the higher availability of nutrients. The large amount of *Sargassum* that developed in the winter months helped to form the bloom in 2018.

Overall, the recent bloom events show connections to nutrient enrichment and climatic variations. Higher wintertime North Atlantic Oscillation (NAO) values in the bloom years correlated well with lower SSTs and stronger upwelling (Fig. 2) (*36*, *37*). Evidence for nutrient enrichment is also found in the *Sargassum* nutrient compositions. Specifically, the N:P ratios of the recent neritic samples show an increasingly P-limited growth compared with the historical baselines, which would be a result of long-term nutrient enrichment, especially N enrichment, in recent years (*24*). Other evidence to support recent nutrient

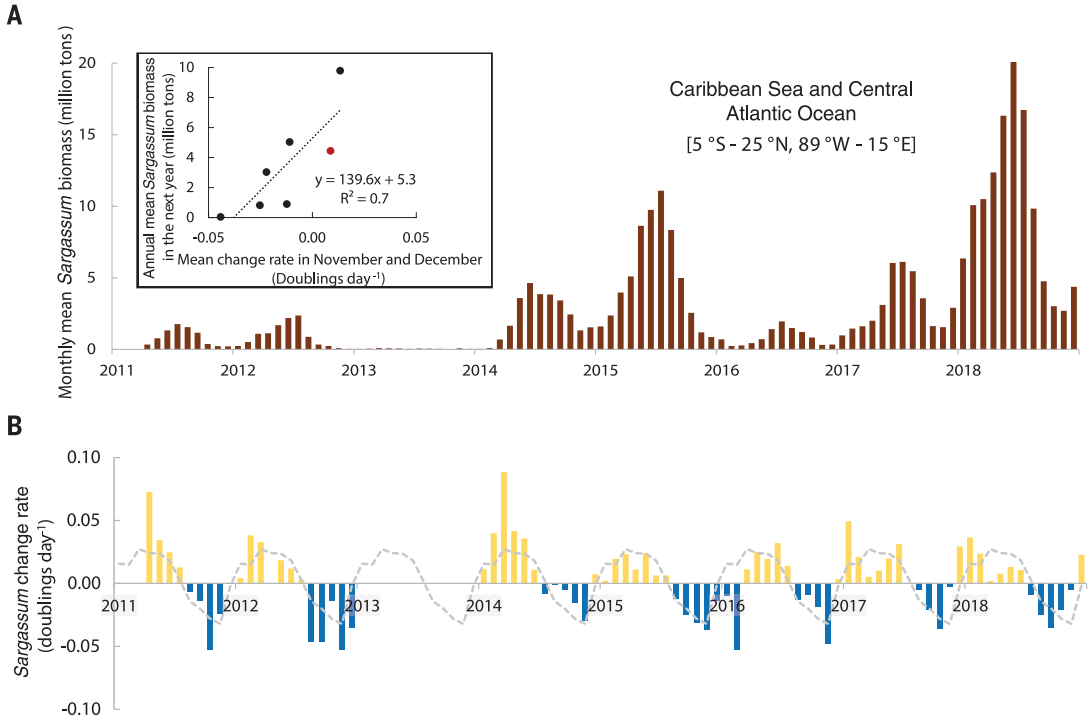

Fig. 3. *Sargassum* biomass and change rate from April 2011 to December 2018. (**A**) Monthly mean *Sargassum* biomass in the Caribbean Sea and central Atlantic. These estimates represent lower bounds because satellite measurements are insensitive to *Sargassum* accumulations in the vertical direction. The inset shows the correlation between the mean change rate in November and December (derived from the mean biomass change from October to December) with the annual mean *Sargassum* biomass in the next year. The red dot marks the data from 2019 (biomass averaged between January and April 2019) (**B**) *Sargassum* monthly change rate since 2011. The gray dashed line marks the climatological change rate between 2011 and 2018 except for 2013.

enrichment in the central west Atlantic comes from increased deforestation and fertilizer use in Brazil and increased water-column nitrogen from 2010 to 2018 (fig. S4).

The interannual changes in *Sargassum* blooms could be accounted for by changes in seed populations and oceanographic conditions, but a critical question remains: Can we predict future blooms based on these hindcast analyses? The following conditions appear to be associated with massive *Sargassum* blooms at magnitudes comparable to those in 2015 and 2018: (i) large seed populations during winter as a result of the previous year's bloom; (ii) higher nutrient supply from the West Africa upwelling in winter months, which can be inferred from higher chlorophyll levels and lower SSTs in satellite imagery; and (iii) higher nutrient supply from the Amazon River input but normal or lower SSTs during the current year. If these conditions are met, then a massive bloom is likely to occur in the central Atlantic, followed by severe beaching events in the Caribbean Sea in later months. Furthermore, during November to December, the *Sargassum* change rates showed negative correlations with SSTs (fig. S7, A and B), suggesting that the former might serve as an indicator for possible blooms in the following year (Fig. 3A, inset), with a lead time of at least 3 to 4 months.

Finally, we recognize that there are active discussions within the research community on the mechanisms driving the recent trends of *Sargassum* blooms. The explanation presented here is based on the physical connectivity across several regions, on the analysis of several environmental factors, on limited field studies, and on the satellite-based *Sargassum* observations. These modeling and observationally based analyses, although reasonable to the best of our knowledge, still require validation in the future and admittedly may not rule out other explanations. Conversely, the recurrent GASB clearly shows a regime shift after 2011 in bloom patterns and possibly in oceanographic conditions as well. A critical question is whether we have reached the point where recurrent GASB and beaching events may become the new norm. Under continued nutrient enrichment due to deforestation and fertilizer use in agriculture (fig. S4), along with the substantial mass of *Sargassum* seed populations lingering in the tropics (movie S1), the answer is likely positive, and more recent satellite observations between January and April 2019 also support this interpretation. However, the considerable *Sargassum* accumulations along the pathway of the GASB underline the need for multidisciplinary research to better understand their ecological and biogeochemical impacts (*24*, *38*), as well as their impacts on coastal environments, tourism, economies, and human health (*39*), especially if the role of *Sargassum* changes from that of an essential habitat to that of a severe and perpetual nuisance.

REFERENCES AND NOTES

1. J. N. Butler, B. F. Morris, J. Cadwallader, A. W. Stoner, Studies of *Sargassum* and the *Sargassum* community (Bermuda Biological Station, special publication no. 22, 1983).
2. T. L. Casazza, S. W. Ross, *Fish Bull.* **106**, 348–363 (2008).
3. B. Witherington, S. Hirama, R. Hardy, *Mar. Ecol. Prog. Ser.* **463**, 1–22 (2012).
4. J. N. Butler, A. W. Stoner, *Deep Sea Res. Part I Oceanogr. Res. Pap.* **31**, 1259–1264 (1984).
5. J. F. Gower, S. A. King, *Int. J. Remote Sens.* **32**, 1917–1929 (2011).
6. J. Gower, E. Young, S. King, *Remote Sens. Lett.* **4**, 764–773 (2013).
7. A. S. Maurer, E. De Neef, S. Stapleton, *Front. Ecol. Environ.* **13**, 394–395 (2015).
8. O. Oyesiku, A. Egunyomi, *Afr. J. Biotechnol.* **13**, 1118–1193 (2014).
9. M. T. M. de Széchy, P. M. Guedes, M. H. Baeta-Neves, E. N. Oliveira, *Check List* **8**, 638–641 (2012).
10. V. Smetacek, A. Zingone, *Nature* **504**, 84–88 (2013).
11. C. Hu, B. Murch, B. Barnes, M. Wang, J.-P. Maréchal, J. Franks, D. Johnson, B. Lapointe, D. Goodwin, J. Schell, A. Siuda, *Sargassum* watch warns of incoming seaweed (Eos, 2016).
12. M. Wang, C. Hu, *Remote Sens. Environ.* **183**, 350–367 (2016).
13. M. Wang, C. Hu, *Geophys. Res. Lett.* **44**, 3265–3273 (2017).
14. K. Langin, Mysterious masses of seaweed assault Caribbean islands (2018); https://www.sciencemag.org/news/2018/06/mysterious-masses-seaweed-assault-caribbean-islands.
15. J. Partlow, G. Martinez, Mexico deploys its navy to face its latest threat: Monster seaweed (2015); https://www.washingtonpost.com/world/the_americas/mexico-deploys-its-navy-to-face-its-latest-threat-monster-seaweed/2015/10/28/cea8ac28-710b-11e5-ba14-318f8e87a2fc_story.html?noredirect=on&utm_term=.212b01de8055

16. J. Rawlins-Bentham, *Sargassum*: A National Emergency & Energy Source (2018); http://gisbarbados.gov.bb/blog/sargassum-a-national-emergency-energy-source/
17. *Sargassum* and Oil Spills Monitoring Pilot Project for the Caribbean and Adjacent Regions Workshop; www.ioc-unesco.org/index.php?option=com_oe&task=viewEventRecord&eventID=2270
18. French-American workshop on *Sargassum*; www.tamug.edu/mars/tides/
19. J. S. Franks, D. R. Johnson, D. S. Ko, G. Sanchez-Rubio, J. R. Hendon, M. Lay, Unprecedented influx of pelagic *Sargassum* along Caribbean Island coastlines during summer 2011, in *Proceedings of the 64th Annual Gulf and Caribbean Fisheries Institute* (GCFI, 2011), pp. 6–8.
20. J. S. Franks, D. Johnson, D. S. Ko, Retention and growth of pelagic *Sargassum* in the north equatorial convergence region of the Atlantic Ocean: A hypothesis for examining recent mass strandings of pelagic *Sargassum* along Caribbean and West Africa shorelines, in *Proceedings of the 67th Annual Gulf and Caribbean Fisheries Institute* (GCFI, 2014), p. 136.
21. D. Johnson, D. Ko, J. Franks, P. Moreno, G. Sanchez-Rubio, *Proc. Gulf Caribb. Fish. Inst.* **65**, 102–103 (2013).
22. B. E. Lapointe, L. W. Herren, A. Feibel, C. Hu, Evidence of nitrogen-fueled blooms of pelagic *Sargassum* in the Gulf of Mexico, in *Proceedings of the 68th Annual Gulf and Caribbean Fisheries Institute* (GCFI, 2015), pp. 419–420.
23. S. Djakouré, M. Araujo, A. Hounsou-Gbo, C. Noriega, B. Bourlès, *Biogeosciences Discuss.* (2017).
24. M. Wang *et al*., *Geophys. Res. Lett.* **45**, 12359–12367 (2018).
25. M. Wang, thesis, University of South Florida (2018).
26. See the supplementary materials.
27. J. S. Franks, D. R. Johnson, D. S. Ko, *Gulf Caribb. Res.* **27**, SC6–SC11 (2016).
28. M. T. Brooks, V. J. Coles, R. R. Hood, J. F. Gower, *Mar. Ecol. Prog. Ser.* **599**, 1–18 (2018).
29. N. F. Putman *et al*., *Prog. Oceanogr.* **165**, 205–214 (2018).
30. J. M. Schell, D. S. Goodwin, A. N. Siuda, *Oceanography* **28**, 8–10 (2015).
31. E. M. Johns *et al*., *Fish. Oceanogr.* **23**, 472–494 (2014).
32. B. E. Lapointe, *Limnol. Oceanogr.* **40**, 625–633 (1995).
33. B. E. Lapointe, L. E. West, T. T. Sutton, C. Hu, *J. Exp. Mar. Biol. Ecol.* **458**, 46–56 (2014).
34. M. D. Hanisak, M. A. Samuel, *Hydrobiologia* **151**, 399–404 (1987).
35. K. Lüning, *Eur. J. Phycol.* **29**, 61–67 (1994).
36. P. C. Pardo, X. A. Padín, M. Gilcoto, L. Farina-Busto, F. F. Pérez, *Clim. Res.* **48**, 231–246 (2011).
37. T. E. Cropper, E. Hanna, G. R. Bigg, *Deep Sea Res. Part I Oceanogr. Res. Pap.* **86**, 94–111 (2014).
38. P. Baker *et al*., *Deep Sea Res. Part II Top. Stud. Oceanogr.* **148**, 21–34 (2017).
39. D. Resiere *et al*., *Lancet* **392**, 2691 (2019).

ACKNOWLEDGMENTS

We thank NASA for providing MODIS data for this analysis. We thank B. Murch for editorial comments, D. English, J. Cannizzaro, and R. Brewton for help in collecting and analyzing *Sargassum* samples, F. Hernandez for providing ship opportunity, and S. Weber and E. Strope for assistance with field sampling and nutrient analyses. M.W. and C.H. thank S. Murawski, D. Naar, and Y. Liu (University of South Florida) for useful discussions during the development of M.W.'s dissertation. We also thank D. Johnson and J. Franks for useful discussions on ocean circulations.

Funding: This work was funded by the U.S. NASA Ocean Biology and Biogeochemistry Program (NNX14AL98G, NNX16AR74G) and Ecological Forecast Program (NNX17AE57G), NOAA RESTORE Science Program (NA17NOS4510099), the JPSS/NOAA Cal/Val project (NA15OAR4320064), the National Science Foundation (NSF-OCE-0934025 and NSF-OCE-1737078), and by a William and Elsie Knight Endowed Fellowship. **Author contributions**: M.W.: methodology, data processing and analyses, visualization, and writing; C.H.: conceptualization, methodology, funding acquisition, project administration, coordination, supervision, advising, and writing; B.B.: data processing; G.M.: supervision and modeling; B.L.: project administration and supervision; J.P.M.: field measurement and analysis. **Competing interests:** The authors declare no competing interests. **Data and materials availability:** All data used in this study are available in the main text or the supplemental materials. All *Sargassum*-relevant imagery data products are available through the *Sargassum* Watch System (SaWS, https://optics.marine.usf.edu/projects/saws.html). Data have been deposited at the National Centers for Environmental Information with the accession number 0190272.

SUPPLEMENTARY MATERIALS

science.sciencemag.org/content/365/6448/83/suppl/DC1
Materials and Methods
Supplementary Text
Figs. S1 to S7
Tables S1 and S2
References (*40*–*50*)
Movie S1

25 January 2019; accepted 22 May 2019
10.1126/science.aaw7912

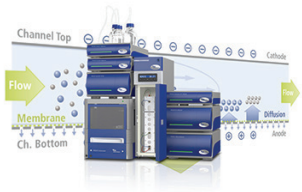

Field-Flow Fractionation System
The EAF2000 from Postnova Analytics combines the principles of electrical and asymmetrical field-flow fractionation (FFF) in a single platform. In this system, electrical and cross-flow fields are applied simultaneously across the FFF channel, enabling separation by size and simultaneous measurement of particle charge based on electrophoretic mobility. Combining these two powerful separation techniques in one platform opens the door to characterizing complex samples that have proven resistant using other techniques. EAF2000 can be used to separate and characterize complex proteins, antibodies, and viruses as well as charged nanoparticles, colloids, and polymers.
Postnova Analytics
For info: +49-(0)-8191-985-6880
www.postnova.com

Horizontal and Vertical Gel Electrophoresis Equipment
Syngene announces its range of robust horizontal and vertical gel electrophoresis equipment. Featuring sturdy injection-molded construction and corrosion-resistant platinum electrodes, all tanks offer a robust, leak-proof environment, guaranteeing user safety and long product life. With a choice of four sizes, the horizontal gel units (SynMini, SynMidi, SynChoice, and SynMaxi) allow scientists to run gels as small as 7 cm × 7 cm up to 20 cm × 20 cm. Each tank comes with two or three (for the SynChoice) sizes of cleverly designed, indentation-free, UV-transparent gel trays and a choice of combs in four different thicknesses. Syngene's SynPAGE and SynWave vertical electrophoresis tanks come in two sizes and can be used with 10 cm × 10 cm or 20 cm × 20 cm gels to run up to four handcast (additional plates required) or two commercial precast gels from any major supplier. For cost-effective versatility, scientists wanting to transfer their proteins to Western blots can also fit the new Syngene tanks with a modular blotting insert.
Syngene
For info: 800-686-4407
www.syngene.com/product-category/electrophoresis

DNA Sequencing Platform
Pacific Biosciences launches it latest DNA sequencing platform—the Sequel II System—delivering highly accurate long reads. The system includes the new SMRT Cell 8M as well as chemistry, instrument control software, and the SMRT Link software package. Using Sequel II, customers can comprehensively detect human variants ranging in size from single-nucleotide changes to large, complex structural variants. The system is also ideal for standard applications such as de novo assembly of large genomes and whole-transcriptome analysis using the Iso-Seq method. High-fidelity reads can enable comprehensive human variant detection with ≥95% precision and recall of structural variants, ≥99% precision and recall of single-nucleotide variants, and ≥96% precision and recall of insertions and deletions with as little as 15-fold coverage.
Pacific Biosciences
For info: 650-521-8000
www.pacb.com/sequel

Next-Generation Objectives
Olympus introduces its next-generation X Line objectives. Ultrathin lenses manufactured by a revolutionary polishing technique enable the objectives to simultaneously boost numerical aperture, flatness, and chromatic correction—providing exceptional image quality for researchers and clinicians alike. Olympus has harnessed this proprietary technology to deliver its high-performance X Line objectives for clinical and research applications as well as UPLAPO-HR objectives, the world's first plan-corrected apochromat objectives with a numerical aperture of 1.5 for total internal reflection fluorescence (TIRF) microscopy and superresolution applications. The new objectives will deliver significant improvements to a plethora of research and clinical applications without the need to change or upgrade imaging systems.
Olympus
For info: 704-877-8801
www.olympus-lifescience.com

Mass Spectrometry Systems
Waters offers two new high-resolution mass spectrometry systems. The SELECT SERIES Cyclic IMS seamlessly integrates cyclic ion mobility (cIM) technology into a high-performance research-grade time-of-flight mass spectrometer enabling limitless experimental potential. By providing high levels of flexibility through inlets and acquisition modes, the SYNAPT XS delivers greater freedom of analytical choice, supporting scientific creativity and technical success for any application.
Waters Corporation
For info: 800-252-4752
www.waters.com

Triple Quad LC/MS-MS System
The SCIEX Triple Quad 5500+ LC-MS/MS System – QTRAP Ready delivers superior quantitative results in a single injection workflow. When you activate the optional QTRAP functionality, your instrument acts as a linear ion trap. This allows you to acquire even more data from your sample without sacrificing the sensitivity or quality of your multiple reaction monitoring (MRM) analysis. The QTRAP technology incorporates additional scan types, such as MRM3 (MS/MS/MS), enhanced product ion scans, and many more. The additional scans can run at the same time you are acquiring your MRM, without any impact on performance or data quality. Whether you are focusing on pharmaceutical drug discovery workflows, clinical research, food and beverage testing, complex environmental analysis, or academic studies, or searching for answers from crucial forensic samples, the 5500+ system is equipped to handle the challenge.
SCIEX
For info: 877-740-2129
sciex.com

Electronically submit your new product description or product literature information! Go to www.sciencemag.org/about/new-products-section for more information.

Newly offered instrumentation, apparatus, and laboratory materials of interest to researchers in all disciplines in academic, industrial, and governmental organizations are featured in this space. Emphasis is given to purpose, chief characteristics, and availability of products and materials. Endorsement by *Science* or AAAS of any products or materials mentioned is not implied. Additional information may be obtained from the manufacturer or supplier.

University of Zurich[UZH]

Faculty of Science

The Faculty of Science at the University of Zurich invites applications for an

Assistant Professor Tenure Track in Digital Bioinorganic Chemistry

We are seeking candidates with an outstanding track record to build an internationally recognized research program in digital bioinorganic chemistry. While all areas of biological inorganic chemistry will be considered, upon equal qualifications, preference will be given to applicants with an interest in research directions complementing those of existing groups. This professorship lies within the UZH Digital Society Initiative and hence its research must have a strong link to aspects of digitalization, e.g. Big Data, bioinformatics, simulations, spectroscopy, high throughput, machine learning, or data mining. The selected candidate is expected to lead an independent research group linking experimental and computational methods and to participate in teaching at all levels of the BSc, MSc and PhD programs. The University of Zurich has an established program for career progression allowing promotion to associate and full professor upon successful evaluation.

The University of Zurich provides generous research support, including dedicated funds for personnel, running expenses and competitive start-up packages. Moreover, the successful applicant is expected to acquire external research funding. Zurich's scientific environment encompasses a rich spectrum of diverse activities spanning physical to biomedical research that provides extensive opportunities for collaboration with research groups at the University of Zurich and other leading Swiss research institutions.

The employment conditions for this position follow the legal regulations of the University of Zurich (please see www.prof.uzh.ch/de.html), including part-time options. The University of Zurich is an equal opportunities employer and in particular strives to increase the percentage of women in leading positions (please see https://www.mnf.uzh.ch/en/mnf-gleichstellung.html). Therefore, qualified female researchers are particularly encouraged to apply. The city of Zurich combines a stimulating cultural scene in a modern European city with easy access to beautiful natural surroundings.

Academics with the appropriate qualifications are kindly invited to submit their applications including:
– a curriculum vitae
– lists of publications and research funding,
– a detailed research plan and a teaching outline
– names and contact details of three referees

Please upload your application to http://www.mnf.uzh.ch/dbc by July 31, 2019.

For further information, please contact Prof. Dr. Roger Alberto (email: ariel@chem.uzh.ch).

Science Translational Medicine | AAAS
INTEGRATING SCIENCE, ENGINEERING, AND MEDICINE

ASSOCIATE or SENIOR EDITOR for SCIENCE TRANSLATIONAL MEDICINE

The American Association for the Advancement of Science (AAAS) and *Science Translational Medicine* are seeking a talented scientist, physician scientist or clinician interested in biomedical/translational research to join the *Science Translational Medicine* editorial team in Washington DC, USA or Cambridge, UK.

This editorial position is a fulltime position designed for a PhD scientist, MD/PhD physician scientist or MD clinician with research experience. We seek applicants who have a broad interest in translational research, the ability to rigorously and critically evaluate scientific and/or clinical research papers, as well as excellent communication and networking skills. Outstanding candidates in any biomedical field will be considered; expertise in one or more of the following fields would be an advantage: metabolism, diabetes/obesity, liver disease, gastroenterology, cell and gene therapy, respiratory disorders, clinical trials.

The tasks include but are not limited to:
- Manage the evaluation, review, and editing of submitted research manuscripts in a broad range of biomedical fields
- Judge the scientific value of research and select reviewers for submitted manuscripts
- Discuss and make recommendations regarding manuscripts and reviewer comments with the editorial team, members of the Board of Reviewing Editors, and the authors
- Write short summaries of research papers for publication
- Guide authors on manuscript revisions and edit the manuscripts for scientific content and style
- Follow manuscripts through the production process to ensure material is published in a timely manner
- Commission and edit Review, Perspective and Focus articles on a broad range of topics
- Commission and edit review and opinion content for special issues
- Foster relationships and communication with the scientific community through meetings, lab visits and professional contacts
- Represent *Science Translational Medicine* at scientific meetings nationally and internationally.

The minimum qualifications to be competitive and considered for the position are:
- Mastery of one or more biomedical fields typically acquired through completion of a doctoral or medical degree in at least one biomedical or clinical research field
- 2 to 5 years post PhD or MD experience, including postdoctoral research experience in one or more translational fields and multiple publications
- Ability to work constructively as a member of a tight-knit dynamic team
- Comprehensive knowledge of scientific research methods in order to discuss technical issues with authors
- Excellent outreach skills in order to effectively recruit top research papers to the journal
- Exceptional written, communication, and listening skills in order to communicate with authors and reviewers in evaluating, editing and modifying manuscripts
- Prior scientific editorial experience is not essential but is preferred

Application Process
Submit a resume and cover letter outlining qualifications and interest in the position by August 6, 2019. Applications are reviewed on a rolling basis. We will contact you with next steps if you are selected for an interview.

Application link: **http://bit.ly/2WvSsv6**

AAAS is the world's largest general scientific membership organization. Please visit the AAAS careers website **http://www.aaas.org/page/employment-aaas** to get more information, and to apply online.

AAAS is an Equal Opportunities Employer. All qualified applicants will receive consideration for employment without regard to race, color, religion, sexual orientation, gender, gender identity, national origin, age, disability, veteran status, or other protected category. AAAS uses E-Verify to confirm the employment eligibility of all newly hired employees.

UNIVERSITY OF CENTRAL FLORIDA

Professor and Dean, College of Optics and Photonics

The University of Central Florida (UCF) invites applications and nominations for the position of dean of the College of Optics and Photonics. The College of Optics and Photonics, which houses CREOL (Center for Research and Education in Optics and Lasers), is one of the world's foremost institutions for research and education in optics and photonics.

Located in Orlando, UCF is one of the nation's most dynamic metropolitan research universities. We are seeking a visionary leader for the college. The dean of the college is responsible for working with the faculty to foster excellence in research and education while continuing to reinforce the role of the college within the university and industry. As the academic and administrative leader of the college, the dean's responsibilities will include, but are not limited to: fiscal management, strategic planning, and academic programs.

The next dean of the College of Optics and Photonics shall possess:

- a strong commitment to advance research, teaching, and learning;
- an ability and willingness to advocate for student success and faculty excellence;
- evidence of advancing diversity and inclusivity;
- the ability to inspire the college's faculty, students and staff, university community, industry partners, donors, and alumni to dedicate their time and talent in pursuit of a shared vision for the college;
- a strong understanding of current trends and research directions in optics and photonics essential for promoting and accelerating research and discovery in the college;
- a working knowledge of the industry, its main challenges and strategic directions for the future.

The position reports to the provost and vice president for Academic Affairs.

The College of Optics and Photonics offers M.S. and Ph.D. degrees in Optics and Photonics and a B.S. degree in Photonic Science and Engineering. The faculty engage in a broad spectrum of research covering all areas of optics and photonics, ranging from fundamental physics to device and systems research.

The college has 35 core faculty members, and over 20 faculty members from other UCF colleges with joint appointments, about 50 research scientists and postdoctoral scholars, over 140 graduate students, and 150 undergraduate students. The college is home to the Center for Research and Education in Optics and Lasers (CREOL), the Florida Photonics Center of Excellence (FPCE), the Townes Laser Institute (TLI), the Townes Institute for Science and Technology Experimentation Facility (TISTEF), and the Institute for the Frontier of Attosecond Science and Technology (iFAST). Additional information is available at https://www.creol.ucf.edu.

UCF and its 13 colleges provide opportunities to more than 68,000 students, offering 189 bachelor's and master's degrees, and 32 doctoral programs. Students come from all 50 states and over 147 countries. A priority on diversity and inclusiveness led UCF to co-found the University Innovation Alliance, a consortium of large public research universities committed to better serving first-generation, low-income students. U.S. News & World Report ranked UCF the 10th "Most Innovative School" in its Best Colleges 2019 report. Additionally, UCF is one of 56 public universities with the Carnegie Foundation's highest designation in two categories: community engagement and very high research activity. As one of the largest universities in the country, UCF is committed to innovative community partnerships, world-class research with local and global impact and the integration of technology and learning. For additional information about the University of Central Florida, please visit www.ucf.edu.

Minimum Qualifications
Applicants must hold an earned doctorate from an accredited institution in a related field; have a strong research record and commitment to teaching; have a strong understanding of academic affairs; and have credentials to be appointed at the level of full professor with tenure at the college.

Preferred Qualifications
Preference will be given to applicants with demonstrated leadership experience in higher education, industry, or government lab, and a strong recognition in the field.

Additional Application Materials Required
UCF requires all applications and supporting documents to be submitted electronically through the Human Resources website, **https://jobs.ucf.edu/en-us/job/497427/professor-and-dean-college-of-optics-and-photonics**. In addition to completing the online application, candidates must upload a letter of interest, a complete CV, and contact information for three (3) professional references.

References will be contacted only for short-listed candidates after notification.

The position will remain open until filled. Screening of applications will begin August 15, 2019.

Please contact the search committee chair, Dr. Michael Georgiopoulos, at michaelg@ucf.edu with questions, nominations and expressions of interest about the position.

Equal Employment Opportunity Employer
As an Equal Opportunity/Affirmative Action Employer, UCF encourages all qualified applicants to apply, including women, veterans, individuals with disabilities, and members of traditionally underrepresented populations. UCF 's Equal Opportunity Statement can be viewed at: http://eeo.ucf.edu/documents/PresidentsStatement.pdf. As a Florida public university, UCF makes all application materials and selection procedures available to the public upon request.

Tenured Professor in Developmental Biology

Department of Molecular and Cellular Biology
Faculty of Arts & Sciences, Harvard University

MCB
Department of Molecular and Cellular Biology

The Department of Molecular and Cellular Biology at Harvard University seeks to appoint a tenured professor in developmental biology, with an emphasis on studying fundamental biological questions in either conventional or unconventional model systems. We are particularly excited about candidates who employ modern quantitative methods such as, but not limited to, imaging, genomics, and computation. The appointment is expected to begin on July 1, 2020 or as soon as feasible. The professor will teach and advise at the undergraduate and graduate levels. The Department offers an interactive research community with broad interests, state of the art animal facilities and core facilities for imaging, proteomics, genomics and bioinformatics, and close association with wider Harvard science initiatives such as the Quantitative Biology Initiative, the Harvard Stem Cell Institute, the Center for Brain Science, the Broad Institute, and the Center for Nanoscale Systems.

A doctorate degree is required. Applications should include: curriculum vitae, a research vision statement describing future plans, a teaching statement describing teaching approach and philosophy, and a statement describing efforts to encourage diversity, inclusion, and belonging, including past, current, and anticipated future contributions in these areas.

Candidates are encouraged to apply by September 1, 2019. Applications will be reviewed until the position is filled. We anticipate interviewing short-listed candidates beginning in the first weeks of October.

We are deeply committed to improving the diversity of Harvard's faculty and scientific community. We strongly encourage applications from women and other underrepresented groups.

Submit applications to:
http://academicpositions.harvard.edu/postings/9093

For information contact Polina Kehayova | kehayova@fas.harvard.edu | **www.mcb.harvard.edu**

HARVARD UNIVERSITY

We are an equal opportunity employer and all qualified applicants will receive consideration for employment without regard to race, color, religion, sex, national origin, disability status, protected veteran status, gender identity, sexual orientation, pregnancy and pregnancy-related conditions or any other characteristic protected by law.

CAREER OPPORTUNITY

Faculty Position, Cell and Molecular Biology

Memphis, TN

St. Jude Children's Research Hospital
Finding cures. Saving children.
ALSAC • DANNY THOMAS, FOUNDER

The Department of Cell and Molecular Biology seeks applicants for faculty positions at all levels (Assistant, Associate or Full). St. Jude Children's Research Hospital offers a remarkable opportunity to perform cutting-edge research with outstanding, long-term institutional support and exceptional core facilities in an environment of open collaboration.

Successful applicants will possess a Ph.D., M.D., or both; and present a vibrant research program with potential for interaction both within the department and across the institution.

Interested applicants should submit a CV and a 2-page letter of research accomplishments and future interests. Applicants for Assistant Member positions should have three letters of recommendation. Applicants for Associate/ Full Member positions should send contact information for three references.

J. Paul Taylor, M.D., Ph.D.
Chair, Department of Cell and Molecular
St. Jude Children's Research Hospital
262 Danny Thomas Place
Memphis, TN 38105
marquetta.nebo@stjude.org
Apply online: **bit.ly/facultycellbiology**

St. Jude Children's Research Hospital is an equal opportunity employer.

Tulane University
SCHOOL OF MEDICINE

Assistant Professor-Tenure Track

The Department of Pharmacology at Tulane University School of Medicine is currently recruiting faculty members with a Ph.D. or equivalent degree for tenure-track position at the level of Assistant or Associate Professor. Areas of preferred expertise include **Vascular Biology, Mitochondrial Biology, and Neuroscience**.

This position will be supported by significant laboratory space, competitive salaries and excellent start-up packages. The requirements for Assistant Professor include a minimum of two years of postdoctoral research experience and for Associate Professor a minimum of three years of experience at the level of Assistant Professor and a NIH R01 or other significant extramural funding.

The successful candidate is expected to develop and maintain a research program related to cardiovascular disease that is complimentary to the department's strengths, using pharmacology principles, theories, concepts, methods and techniques in order to design studies, manage projects and carry out investigations. Additionally, the candidate must maintain scholarly activity. Teaching duties will include delivery of lectures to graduate and medical students as well as participation in active learning sessions of graduate and medical students. The candidate will be required to provide service to the department and institution by serving on committees. Additionally, specific duties and distribution of effort in teaching, research, and service duties will be determined by the Department Chair and subject to change based on the needs of the department.

Tulane University is an Affirmative Action and Equal Opportunity Employer and is committed to providing equal employment opportunity to qualified persons without regard to race, sex, religion, national origin, age, disability, gender identity, veteran's status, or any other status or classification protected by federal, state or local law.

To submit an application, please apply online through the Tulane University employment portal. Use the following link: **http://apply.interfolio.com/62633**, or copy/paste into your browser; then click "Apply for this Job" to fill out an application and submit your documents. Please do not send documents via email.

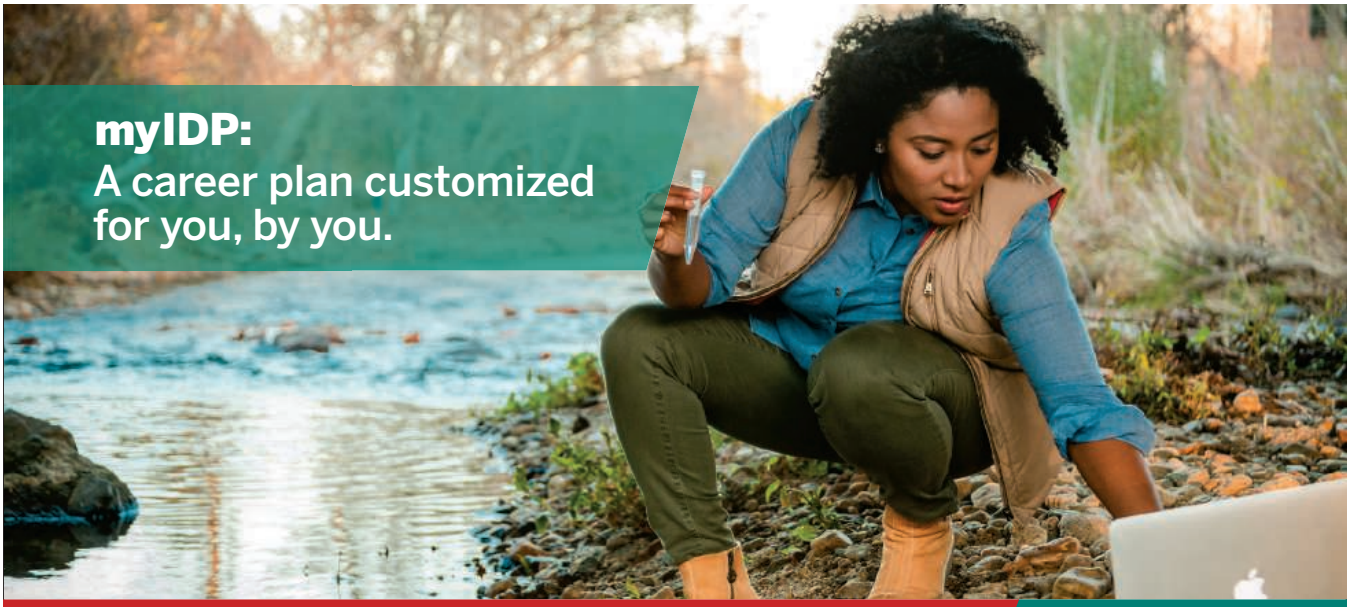

GOVERNMENT OF INDIA

Ministry of Human Resource Development (Department of Higher Education) Technical Section - I

Appointment of Director, IIT Kharagpur

Applications are invited for appointment to the post of Director of Indian Institute of Technology (IIT) at Kharagpur. The Director of an IIT is the academic and administrative head of the Institution. He/she is expected to have a minimum of 5 years' administrative experience and leadership qualities to head an Institute of National importance. The candidate/person should be a Ph.D. with first class or equivalent at the preceding degree, preferably in a branch of Engineering. In exceptional cases, candidates with Science, Mathematics or Management degrees may be considered. He/she should have an outstanding academic record throughout and a minimum of 10 years teaching experience as a Professor in a reputed Engineering or Technology Institute or University and should have guided Ph.D. students. The applicant should preferably be less than 60 years of age on the last date of receipt of the applications. The post carries a fixed pay of Rs. 2,25,000/- (Revised) per month, with allowances as per rules.

2. Interested individuals may apply giving their detailed resume in the prescribed format clearly bringing out research, teaching, industry-academia collaborations and administrative achievements, alongwith a two-page justification in support of their candidature, a two-page vision statement for the institution and contact details of at least two distinguished individuals well acquainted with their work. The application typed in the prescribed format along with enclosures may be sent by Registered/Speed Post to **The Under Secretary (TS.1), Department of Higher Education, Ministry of Human Resource Development, Room No. 428 "C" Wing, Shastri Bhawan, New Delhi -110 001 so as to reach the Ministry on or before 20th July, 2019.** The detailed advertisement and the format of application is available on the website (**www.mhrd.gov.in**).

By **Kate Bredbenner**

One Ph.D., hold the pastries

I never thought I would spend so much of my time and money setting up still-life–worthy displays of flaky croissants and shiny fruit for people who are judging my science, and that of my colleagues. Yet that's the expectation: At my university, and many others, students bring food to our thesis committee meetings and defenses, adding to the already sky-high pressure. My first taste of it came 5 years ago, for my first committee meeting. I prepared furiously. I meticulously proofread my written proposal and aligned all the figures. My slides all used the same font. I had even prepared some extra slides to address possible questions my judges might ask. Even so, I was sure the meeting was doomed—because I didn't know how to make coffee.

In my mind, one drop of burnt coffee would cause my judges to kick me aside like a stray dog. One bite of stale pastry would put them in a mood so foul I would be carted back to the humble Pennsylvania town where I grew up, then forced into my high school job as a Wendy's drive-thru operator. Of course, I knew logically that these things were unlikely to happen, but the pressure of a committee meeting often sends logic out the window.

So in the hours before the meeting, when I should have been looking over my slides, skimming key papers, or even relaxing a bit, I was standing numbly in front of the lab coffee maker—a Rubik's Cube I couldn't solve. Discouraged, I tackled a problem more within my reach: plating the fresh almond croissants I had trekked 20 blocks uptown to fetch earlier that morning. (I had made the mistake of wearing my meeting outfit—a button-down that made me feel like a capable adult—and the humidity had left me with pit stains like a character in a deodorant commercial; good thing I had a backup outfit.)

But once the croissants were settled on the wooden cutting board and the perfectly ripe grapes were in their cute owl-decorated bowl, I turned back to the dreaded coffee maker and felt my perfectly prepared world crumbling around me. Out of the corner of my eye, I saw Joan. One year ahead of me in grad school, Joan had already been through the gauntlet I was about to face. Even more important, she was a fervent coffee drinker.

"Hey Joan!" I yelped, trying to keep my cool. "How would you like to help me make coffee for my meeting?" She gave me a knowing look, the kind of look that says she's been there and come out the other side. Of course, she agreed to help.

"Committees shouldn't expect students to provide lavish spreads."

In the end, the meeting went fine. But my lack of coffee-making knowledge shook my confidence in my abilities as a scientist more than it should have.

Since then, the grad students in my lab have made a pact to help each other with snacks for these meetings. This year, we banded together to create a delectable offering for Joan's thesis defense. She had been through all our committee meetings with us, and if we could help her with some sandwiches and a fruit salad, we were going to do it. She didn't need the stress of remembering when to hit the button on the coffee maker while also remembering the molecular weights of all the proteins in the nuclear pore complex.

Our camaraderie doesn't make the expectation less of a burden, though. Graduate students want to do everything in our power to please our committee members as we describe our research plans and show we are capable scientists. But that should mean spending time preparing and thinking, not stressing ourselves out to buy and serve croissants. I'm lucky to have some of the best fellow grad students-slash-event planners anyone could ask for, but many students don't have this sort of network or tradition.

The solution is easy: Committees shouldn't expect students to provide lavish spreads, or anything at all. We shouldn't have to spend our money buying overpriced fruit salad or know how to make coffee to be considered successful graduate students. Our research should be enough. ■

Kate Bredbenner is a graduate fellow at Rockefeller University in New York City. Send your career story to SciCareerEditor@aaas.org.

ILLUSTRATION: ROBERT NEUBECKER